

FLOW AND HEAT TRANSFER FOR
MULTIPLE TURBULENT IMPINGING SLOT JETS

by

Nabil Raymond Saad

A thesis submitted to the Faculty of Graduate Studies and Research
in partial fulfilment of the requirements for the degree of
Doctor of Philosophy.

Department of Chemical Engineering
McGill University
Montreal

August, 1981

To

Suzanne and Alexandre

ABSTRACT

Flow field and heat transfer characteristics were defined for multiple confined turbulent slot jets with exhaust ports located symmetrically between the jets.

For a 3-slot jet system, average Nusselt number, \overline{Nu} , is up to 80% greater with symmetric outflow than with cumulative spentflow with one-sided outflow.

A key dimensionless geometric parameter, S/H , was found for both flow and heat transfer. For $S/H > 1.5$, multiple slot jets are effectively an assembly of single jets. At $(S/H)_{ce} = 1.5$, interaction begins under the exit port centerline. Below the critical value $(S/H)_{co} = 0.7$, interaction depresses stagnation point Nusselt number.

A general correlation of \overline{Nu} with flow and geometric parameters was established. \overline{Nu} was found to be a maximum at $H/w = 5$ and $S/H = .5$.

Application of throughflow at the impingement surface enhances \overline{Nu} by a maximum of 30% for Reynolds number = 10200 and 22800. A throughflow rate was found above which convective heat transfer decreases with throughflow.

RESUME

On a étudié expérimentalement l'écoulement et le transfert thermique sur la surface réceptrice de plusieurs jets confinés rectangulaires turbulents avec des portes de sortie situées symétriquement entre les jets.

On a trouvé que la valeur moyenne du nombre de Nusselt, \bar{Nu} , pour le système de trois jets rectangulaires avec portes de sortie symétriques est jusqu'à 80% plus élevé que celui obtenu pour un système équipé d'une porte de sortie à écoulement transversale.

On a trouvé un paramètre non-dimensionnel géométrique, S/H , d'importance vitale pour l'expression d'écoulement et de transfert thermique. Lorsque $S/H > 1.5$ le système de jets multiples rectangulaire ressemble à un montage de jets simples. Lorsque $(S/H)_{ce} = 1.5$, une interaction entre les jets se produit sous la porte de sortie. Pour une valeur au dessous du point critique $(S/H)_{co} = 0.7$ cette interaction abaisse la valeur du nombre de Nusselt au point de stagnation.

On a établi une corrélation générale entre \bar{Nu} et les paramètres géométriques ainsi que ceux d'écoulement. On a trouvé que \bar{Nu} atteint son maximum lorsque $H/w = 5$ et $S/H = 0.5$.

On a trouvé que l'aspiration au travers de la surface d'impact poreuse augmente \bar{Nu} d'un maximum de 30% pour un nombre de Reynolds de 10200 et de 22800. On a aussi trouvé un taux d'aspiration au-dessus duquel le transfert thermique diminue avec l'aspiration.

ACKNOWLEDGEMENTS

The author wishes to express his sincere gratitude and appreciation to all those who, in various ways, contributed to this work.

To Dr W.J.M. Douglas for his constructive advice and continuous encouragement.

To Dr A.S. Mujumdar for interesting and fruitful discussions on many aspects of this work.

To the Pulp and Paper Research Institute of Canada for the award of a post-graduate scholarship and the use of their various facilities.

To the Paper Industry Management Association for the award of the Canadian Division Annual Scholarship.

To the research group committee members: Drs R.H. Croton, T. Obot, Messrs A. van Heiningen, B. Huang, O. Polat, Mrs S. Polat and to fellow graduate student Mr A. Menon for many valuable comments.

To Messrs A. Krish and A. Gagnon of the Chemical Engineering Workshop of McGill University, and D.P.W. Pounds and W. Davidson of the PPRIC Machine Shop for their help in constructing the equipment.

To Mr W. Abdel Messeh of Pratt and Whitney of Canada for allowing two leaves of absence to complete this work.

To Mrs C. Marchesseau, Miss L. Vanasse, Messrs V. Jariwala and D. Tan for help while working as summer students.

To Miss P. Fong and Mrs D. Ross for their great care, patience and excellent typing of the manuscript.

To Mr B. Gavin for his excellent and efficient preparation of the figures at short notice.

To my family, my wife and my son for their continued moral support.

TABLE OF CONTENTS

	<u>Page</u>
ABSTRACT	i
RESUME	ii
ACKNOWLEDGEMENTS	iii
TABLE OF CONTENTS	iv
LIST OF FIGURES	viii
LIST OF TABLES	xvii
NOMENCLATURE	xix
 <u>CHAPTER 1. INTRODUCTION</u>	 1
1.1 Background Information	1
1.2 Objectives and Scope	3
 <u>CHAPTER 2. LITERATURE REVIEW</u>	 6
2.1 Introduction	6
2.2 Flow Field of Turbulent Impinging Jets	6
2.2.1 Free Jet Region	7
2.2.2 Impingement Region	9
2.2.3 Wall Jet Region	10
2.2.4 Arrangement for Outflow after Impingement	11
2.2.4.1 Unconfined Multiple Impinging Slot Jet Studies	12
2.2.4.2 Confined Multiple Impinging Slot Jet Studies	14
2.3 Heat Transfer at the Impingement Surface	16
2.3.1 Analytical Studies	16
2.3.2 Experimental Studies	18

2.3.2.1	Single Impinging Slot Jet Studies	19
2.3.2.2	Multiple Impinging Slot Jet Studies	20
2.4	Effect of Suction	27
2.4.1	Flow Studies	27
2.4.2	Heat Transfer Studies	31
2.5	Summary	31
<u>CHAPTER 3.</u>	<u>EXPERIMENTAL APPARATUS</u>	33
3.1	Introduction	33
3.2	General Description of the Apparatus	33
3.2.1	Impingement and Exhaust Air Systems	38
3.2.2	Suction Air System	42
3.2.3	Vertical and Horizontal Traversing of the Impingement Surface	47
3.2.4	Impingement Surface Temperature Control	49
3.3	Flow Measurements	52
3.3.1	Velocity and Turbulence Measurements	54
3.3.2	Static Pressure Measurements	55
3.4	Heat Transfer Measurements	56
3.4.1	Porous Plate	56
3.4.2	Temperature Measurements	59
3.4.3	Heat Flux Measurements	61
3.5	Test Procedure	67
<u>CHAPTER 4.</u>	<u>RESULTS AND DISCUSSION: FLOW</u>	
4.1	Introduction	69
4.2	Range of Geometric and Flow Parameters	71
4.3	Flow Characteristics at the Nozzle Exit	76
4.4	Flow Field Downstream from the Nozzle Exit	85
4.4.1	Single Jet Flow Downstream from the Nozzle Exit	88
4.4.2	Multiple Jet Flow Downstream from the Nozzle Exit	109

4.5	Flow Field at the Impingement Surface	116
4.5.1	Impingement Flow for a Single Confined Slot Jet	116
4.5.2	Impingement Flow for the Multiple Slot Jet System	120
4.6	Effect of Throughflow at the Impingement Surface	150
4.7	Summary and Conclusions	161
<u>CHAPTER 5.</u>	<u>RESULTS AND DISCUSSION: HEAT TRANSFER</u>	174
5.1	Introduction	174
5.1.1	Range of Geometrical and Flow Parameters	174
5.1.2	Basis of Local Nusselt Number	177
5.2	Confined Multiple Slot Jet Systems with Symmetrical and One-Sided Outflow	181
5.2.1	Laboratory Representation of Multiple Slot Jet Systems	182
5.2.2	Effect on Heat Transfer of One-Sided Cumulative Spentflow	188
5.3	Stagnation Point Heat Transfer	202
5.4	Lateral Profiles of Heat Transfer	226
5.4.1	Effect of Reynolds Number and Geometrical Parameters on Profiles of Nu_x	226
5.4.2	Differentiation of Multiple from Single Jets by the Criterion of Flow Cell Proportions, S/H	248
5.4.3	Effect of Flow Cell Proportion on Nu_x Profiles at Various Levels of Reynolds Number and Spacing	251
5.4.4	Analysis of Confined Multiple Jets as a Closed System	266
5.5	Average Heat Transfer	278
5.6	Effect on Heat Transfer of Throughflow at the Impingement Surface	310
5.7	Summary and Conclusions	329
<u>CHAPTER 6.</u>	<u>CONTRIBUTIONS TO KNOWLEDGE</u>	340
<u>CHAPTER 7.</u>	<u>RECOMMENDATIONS FOR FUTURE WORK</u>	344
REFERENCES		346

	<u>Page</u>
<u>APPENDIX 1.</u> VALUES OF TURBULENT VELOCITY FOR $Re_j = 11000$	A1
<u>APPENDIX 2.</u> VALUES OF AVERAGE HEAT TRANSFER COEFFICIENTS OVER THE ENTIRE RANGE OF GEOMETRICAL AND FLOW PARAMETERS	A4
<u>APPENDIX 3.</u> CALCULATION OF REYNOLDS NUMBER	A7
<u>APPENDIX 4.</u> DESIGN CRITERIA FOR THE HEAT FLUX SENSOR	A12
<u>APPENDIX 5.</u> HEAT TRANSFER ERROR ANALYSIS	A18
A5.1 Analysis of Uncertainties Based on Single-Sample Experiments	A18
A5.2 Statistical Analysis of Uncertainties Based on Repeated Experiments	A23
<u>APPENDIX 6.</u> UNCERTAINTIES IN STATIC PRESSURE AT THE IMPINGEMENT SURFACE	A32
<u>APPENDIX 7.</u> VALUES OF SURFACE HEAT FLUX WITH AND WITHOUT THROUGHFLOW	A33

LIST OF FIGURES

<u>Figure</u>	<u>Caption</u>	<u>Page</u>
1.1	Schematic Diagram of Test Section	5
2.1	Flow Field of Turbulent Impinging Jets	8
2.2	Alternate Outflow Configurations in Systems of Multiple Impinging Slot Jets	13
2.3	Effect of Hot-Film Probe on Local Heat Transfer Profile	23
2.4	Effect of Re_j on \overline{Nu} for $f = 2, 4$ and 8% and $H/w = 4$	28
2.5	Effect of Re_j on \overline{Nu} for $f = 4\%$ and $H/w = 8, 16$ and 24	29
3.1	Schematic Diagram of the Apparatus	35
3.2	Photograph of the Facility	37
3.3	Dimensions of Jet Nozzles	40
3.4	Photograph of Jet Nozzles	41
3.5	Schematic Diagram of Test Section	43
3.6	Photograph of Test Section	44
3.7	Suction Box	46
3.8	Impingement Surface with Heat Flux Sensor	48
3.9	Schematic Diagram of Temperature Controller	51
3.10	Heating Circuit for the Heat Flux Sensor	53
3.11	Multimanometer Panel	57
3.12	36 AWG Chromel Constantan Thermocouple	60
3.13	Section through Porous Bronze Heat Flux Sensor	62
3.14	Section through Porous Bronze Heat Flux Sensor	63
3.15	Heat Flux Sensor Flush Mounted on the Impingement Surface	66
4.1	Impinging Jet Systems Used for Measurements of the Flow Field	70
4.2	Geometrical Variables (w , S/w and f) of the Multiple Confined Impinging Slot Jet System	72

<u>Figure</u>	<u>Caption</u>	<u>Page</u>
4.3	Profiles of Mean Velocity and Turbulence Intensity at the Nozzle Exit for $\bar{w} = 2.5$ mm and 3.3 mm	79
4.4	Profiles of Mean Velocity and Turbulence Intensity at the Nozzle Exit for $w = 5.0$ mm	80
4.5	Profiles of Mean Velocity and Turbulence Intensity at the Nozzle Exit for $w = 10.0$ mm	81
4.6	Profiles of Mean Velocity and Turbulence Intensity at the Nozzle Exit for $w = 13.3$ mm	82
4.7	Lateral Profiles of Axial Fluctuating Velocity at $z/w = 16$	89
4.8	Lateral Profiles of Turbulence Intensity at $z/w = 16$	91
4.9	Lateral Profiles of Mean Velocity and Turbulence Intensity at $z/w = 0$ and 1	93
4.10	Profiles of Fluctuating Velocity at the Jet Centerline	95
4.11	Profiles of Turbulence Intensity at the Jet Centerline	97
4.12	Profiles of Mean Velocity at the Jet Centerline	102
4.13	Mean Velocity Decay at the Jet Centerline	104
4.14	Mean Velocity at the Jet Centerline	106
4.15	Lateral Profiles of Axial Mean Velocity at $z/w = 16$	108
4.16	Jet Half-Width	110
4.17	Lateral Profile of Static Pressure at the Impingement Surface for a Single Slot Jet	118
4.18	Lateral Profile of Static Pressure at the Impingement Surface for a Single Slot Jet	119
4.19	Schematic Diagrams of Flow Cell Proportions $S/H = 6, 3$ and 1.5	122
4.20	Schematic Diagrams of Flow Cell Proportions $S/H = 1.5, 0.75$ and 0.375	123
4.21	Lateral Profile of Static Pressure at the Impingement Surface for Multiple Slot Jets at $S/H = 3$	125
4.22	Lateral Profile of Static Pressure at the Impingement Surface for Multiple Slot Jets at $S/H = 0.75$	127

<u>Figure</u>	<u>Caption</u>	<u>Page</u>
4.23	Lateral Profile of Static Pressure at the Impingement Surface for Multiple Slot Jets at $S/H = 0.375$	128
4.24	Superimposed Lateral Profiles of Static Pressure at the Impingement Surface for Multiple Slot Jets at $S/H = 3$	129
4.25	Superimposed Lateral Profiles of Static Pressure at the Impingement Surface for Multiple Slot Jets at $S/H = 0.75$	130
4.26	Superimposed Lateral Profiles of Static Pressure at the Impingement Surface for Multiple Slot Jets at $S/H = 0.375$	131
4.27	Lateral Profiles of Static Pressure at the Impingement Surface for Single and Multiple Slot Jets at $H/w = 4$	133
4.28	Lateral Profiles of Static Pressure at the Impingement Surface for Single and Multiple Slot Jets at $H/w = 8$	134
4.29	Lateral Profiles of Static Pressure at the Impingement Surface for Single and Multiple Slot Jets at $H/w = 16$	135
4.30	Effect of Impingement Surface Spacing on Stagnation Pressure for Single and Multiple Slot Jets	137
4.31	Lateral Profiles of Static Pressure at the Impingement Surface for Multiple Slot Jets for $f = 2.06\%$	139
4.32	Lateral Profiles of Static Pressure at the Impingement Surface for Multiple Slot Jets for $f = 8.313\%$	140
4.33	Effect of Reynolds Number on Lateral Profiles of Static Pressure at the Impingement Surface for Multiple Slot Jets for $S/H = 6$	143
4.34	Effect of Reynolds Number on Lateral Profiles of Static Pressure at the Impingement Surface for Multiple Slot Jets for $S/H = 3$	144
4.35	Effect of Reynolds Number on Lateral Profiles of Static Pressure at the Impingement Surface for Multiple Slot Jets for $S/H = 1.5$	145
4.36	Effect of Reynolds Number on Lateral Profiles of Static Pressure at the Impingement Surface for Multiple Slot Jets for $S/H = 1.5$	146
4.37	Effect of Reynolds Number on Lateral Profiles of Static Pressure at the Impingement Surface for Multiple Slot Jets for $S/H = 0.75$	147

<u>Figure</u>	<u>Caption</u>	<u>Page</u>
4.38	Effect of Reynolds Number on Lateral Profiles of Static Pressure at the Impingement Surface for Multiple Slot Jets for $S/H = 0.375$	148
4.39	Effect of H/w Impingement Surface Spacing on Lateral Profiles of Static Pressure for Multiple Slot Jets for $S/H = 1.5$	151
4.40	Effect of Throughflow on Lateral Profiles of Axial Mean Velocity	156
4.41	Effect of Throughflow on Lateral Profiles of Turbulence Intensity	160
5.1	Impinging Jet Systems Used for Heat Transfer Measurements at the Impingement Surface	175
5.2	Effect of Impingement Surface Spacing on Lateral Profiles of Nu_x for Confined Multiple Slot Jet Systems with Symmetrical ($f = 1.56\%$) and One-Sided Outflow	183
5.3	Effect of Impingement Surface Spacing on Lateral Profiles of Nu_x for Confined Multiple Slot Jet Systems with Symmetrical ($f = 3.125\%$) and One-Sided Outflow	184
5.4	Effect of Jet Reynolds Number on Lateral Profiles on Nu_x for Confined Multiple Slot Jet Systems with Symmetrical ($f = 3.125\%$) and One-Sided Outflow	185
5.5	Effect of Percent Open Area on Lateral Profiles of Nu_x for Confined Multiple Slot Jet Systems with Symmetrical and One-Sided Outflow	186
5.6	Superimposed Profiles of Nu_x for Confined Multiple Slot Jet Systems with Symmetrical ($f = 1.56\%$) and One-Sided Outflow	189
5.7	Superimposed Profiles of Nu_x for Confined Multiple Slot Jet Systems with Symmetrical ($f = 3.125\%$) and One-Sided Outflow	190
5.8	Superimposed Profiles of Nu_x for Confined Multiple Slot Jet Systems with Symmetrical and One-Sided Outflow and $Re_j = 20740, 10740$ and 5700	191
5.9	Superimposed Profiles of Nu_x for Confined Multiple Slot Jet Systems with Symmetrical ($f = 1.56, 3.125$ and 8.313%) and One-Sided Outflow	192
5.10	Effect of Impingement Surface Spacing on \overline{Nu} , Nu_o , Nu_{max} - Nu_{min} and $\Delta x/w$ for Confined Multiple Slot Jet Systems with Symmetrical ($f = 1.56\%$) and One-Sided Outflow	196

<u>Figure</u>	<u>Caption</u>	<u>Page</u>
5.11	Effect of Impingement Surface Spacing on \overline{Nu} , Nu_o , $Nu_{max}-Nu_{min}$ and $\Delta x/w$ for Confined Multiple Slot Jet Systems with Symmetrical ($f = 3.125\%$) and One-Sided Outflow	197
5.12	Effect of Jet Reynolds Number on \overline{Nu} , Nu_o , $Nu_{max}-Nu_{min}$ and $\Delta x/w$ for Confined Multiple Slot Jet Systems with Symmetrical ($f = 3.125\%$) and One-Sided Outflow	198
5.13	Effect of Percent Open Area on \overline{Nu} , Nu_o , $Nu_{max}-Nu_{min}$ and $\Delta x/w$ for Confined Multiple Slot Jet Systems with Symmetrical and One-Sided Outflow	199
5.14	Schematic Presentation of the Finite Lateral Size of the Heat Flux Sensor ($s = 3.7$ mm) with Respect to the Nozzle Width for $w = 13.3$ mm and 3.3 mm	204
5.15	Effect of Impingement Surface Spacing on Nu_o for Confined Single Impinging Slot Jet	206
5.16	Effect of Impingement Surface Spacing on Nu_o for Multiple Jet System ($f = 1.56\%$)	212
5.17	Effect of Impingement Surface Spacing on Nu_o for Multiple Jet System ($f = 2.06\%$) and for Single Jet System ($w = 3.3$ mm and $Re_j = 10270$)	213
5.18	Effect of Impingement Surface Spacing on Nu_o for Multiple Jet System ($f = 3.125\%$)	214
5.19	Effect of Impingement Surface Spacing on Nu_o for Multiple Jet System ($f = 6.25\%$) and for Single Jet System ($w = 10.0$ mm and $Re_j = 10910$)	215
5.20	Effect of Impingement Surface Spacing on Nu_o for Multiple Jet System ($f = 8.313\%$) and for Single Jet System ($w = 13.3$ mm and $Re_j = 10770$)	216
5.21	Effect of Impingement Surface Spacing on Nu_o for Multiple Jet System ($f = 2.06, 6.25$ and 8.313%) for $Re_j = 5500$ 11000 and 22000 (nominal)	221,222 223
5.22	Effect of Jet Reynolds Number on Nu_o for Multiple Jet System ($H/w = 8$)	224
5.23	Effect of Jet Reynolds Number on Nu_o for Multiple Jet System ($H/w = 16$)	225
5.24	Stagnation Point Heat Transfer Correlation for Multiple Impinging Jet System Compared to that for Single Impinging Jet System of Gardon and Akfirat (1966)	227
5.25	Bandwidth of the Scatter of Experimental Data from the Correlation Line	228

<u>Figure</u>	<u>Caption</u>	<u>Page</u>
5.26	Effect of Jet Reynolds Number on Lateral Profiles of Nu_x for $f = 2.06\%$ and $H/w = 4$	229
5.27	Effect of Jet Reynolds Number on Lateral Profiles of Nu_x for $f = 6.25\%$ and $H/w = 4$	230
5.28	Effect of Jet Reynolds Number on Lateral Profiles of Nu_x for $f = 8.313\%$ and $H/w = 4$	231
5.29	Effect of Jet Reynolds Number on Lateral Profiles of Nu_x for $f = 1.56$ and 2.06% and $H/w = 8$	237
5.30	Effect of Jet Reynolds Number on Lateral Profiles of Nu_x for $f = 3.125$ and 6.25% and $H/w = 8$	238
5.31	Effect of Jet Reynolds Number on Lateral Profiles of Nu_x for $f = 8.313\%$ and $H/w = 8$	239
5.32	Effect of Jet Reynolds Number on Lateral Profiles of Nu_x for $f = 1.56$ and 2.06% and $H/w = 16$	242
5.33	Effect of Jet Reynolds Number on Lateral Profiles of Nu_x for $f = 3.125$ and 7.25% and $H/w = 16$	243
5.34	Effect of Jet Reynolds Number on Lateral Profiles of Nu_x for $f = 8.33\%$ and $H/w = 16$	244
5.35	Effect of Jet Reynolds Number on Lateral Profiles of Nu_x for $f = 1.56$ and 2.06% and $H/w = 24$	245
5.36	Effect of Jet Reynolds Number on Lateral Profiles of Nu_x for $f = 3.125$ and 6.25% and $H/w = 24$	246
5.37	Effect of Flow Cell Proportion on Centerline Nusselt Number for Multiple Jets Relative to a Single Jet	250
5.38	(a) Nu_x Profiles as a Function of x/H for $Re_j = 10800$ (nominal) and $S/H = 1$	253
5.38	(b) Normalized Nu_x/Nu_o Profiles as a Function of x/H for $Re_j = 10800$ (nominal) and $S/H = 1$	254
5.39	Effect of Flow Cell Proportion on Lateral Profiles of Nu_x for $H/w = 4$ and $Re_j = 11000$ (nominal)	255
5.40	Effect of Flow Cell Proportion on Lateral Profiles of Nu_x for $H/w = 8$ and $Re_j = 11000$ (nominal)	256
5.41	Effect of Flow Cell Proportion on Lateral Profiles of Nu_x for $H/w = 16$ and $Re_j = 11000$ (nominal)	257

<u>Figure</u>	<u>Caption</u>	<u>Page</u>
5.42	Effect of Flow Cell Proportion on Lateral Profiles of Nu_x for $H/w = 24$ and $Re_j = 11000$ (nominal)	258
5.43	Effect of Flow Cell Proportion on Lateral Profiles of Nu_x for $H/w = 4$ and $Re_j = 5400$	260
5.44	Effect of Flow Cell Proportion on Lateral Profiles of Nu_x for $H/w = 8$ and $Re_j = 5500$ (nominal)	261
5.45	Effect of Flow Cell Proportion on Lateral Profiles of Nu_x for $H/w = 16$ and $Re_j = 550000$ (nominal) and Nu_x Profiles of Gardon and Akfirat (1966)	262
5.46	Effect of Flow Cell Proportion on Lateral Profiles of Nu_x for $H/w = 24$ and $Re_j = 5500$ (nominal)	263
5.47	Effect of Flow Cell Proportion on Lateral Profiles of Nu_x for $H/w = 4$ and $Re_j = 22000$ (nominal)	264
5.48	Effect of Flow Cell Proportion on Lateral Profiles of Nu_x for $H/w = 8$ and $Re_j = 22000$ (nominal) and Nu_x Profile of Cadek and Zerkle (1970)	265
5.49	Lateral Profiles of T_x , Nu_x and Nu_{xb} for Single and Multiple Jet System at $Re_j = 10790$, $S/H = 0.5$ and $H/w = 16$	269
5.50	Lateral Profiles of T_x , Nu_x and Nu_{xb} for Single and Multiple Jet System at $Re_j = 11000$, $S/H = 0.33$ and $H/w = 24$	271
5.51	(a) Lateral Profiles of T_x , Nu_x and Nu_{xb} for Multiple Jet System at $Re_j = 10790$, $S/H = 2$ and $H/w = 16$	273
5.51	(b) Lateral Profiles of T_x , Nu_x and Nu_{xb} for Multiple Jet System at $Re_j = 3300$, $S/H = 2$ and $H/w = 16$	274
5.52	(a) Lateral Profiles of T_x , Nu_x and Nu_{xb} for Multiple Jet System at $Re_j = 10790$, $S/H = 4$ and $H/w = 8$	275
5.52	(b) Lateral Profiles of T_x , Nu_x and Nu_{xb} for Multiple Jet System at $Re_j = 3330$, $S/H = 4$ and $H/w = 8$	276
5.53	Effect of Re_j on \overline{Nu} for $H/w = 8$ and $0.75 \leq S/H \leq 4.0$	281

<u>Figure</u>	<u>Caption</u>	<u>Page</u>
5.54	Effect of Re_j on \overline{Nu} for $H/w = 16$ and $0.375 \leq S/H \leq 2.0$	282
5.55	Effect of Re_j on \overline{Nu} for $H/w = 24$ and $0.33 \leq S/H \leq 1.33$	283
5.56	Effect of Flow Cell Proportion on the Slope n for $Nu = C Re_j^n$	284
5.57	Effect of S/H on \overline{Nu} for $Re_j = 5500$ and $H/w = 8, 16$ and 24 and Nu of Schuh and Pettersson (1966)	286
5.58	Effect of S/H on Nu for $Re_j = 11000$ and $H/w = 8, 16$ and 24 for Multiple and Single Jet Systems	287
5.59	Effect of S/H on \overline{Nu} for $Re_j = 15000$ and $H/w = 8, 16$ and 24	288
5.60	Effect of H/w on \overline{Nu} for $Re_j = 5500$ and $0.375 \leq S/H \leq 2$	292
5.61	Effect of H/w on Nu for $Re_j = 11000$ and $0.375 \leq S/H \leq 6$	293
5.62	Effect of H/w on \overline{Nu} for $Re_j = 15000$ and $0.375 \leq S/H \leq 2$	294
5.63	Effect of Flow Cell Proportion on the Slope m for $Nu = C(H/w)^{-m}$	295
5.64	Effect of H/w on \overline{Nu} for $f = 6.25\%$ and $Re_j = 5400, 10910$ and 21720	297
5.65	Average Heat Transfer Correlations for Non-Interacting and for Interacting Jets	299
5.66	Average Heat Transfer for $Re_j = 11000, H/w = 8, 16$ and 24 and $0.33 \leq S/H \leq 4$: Correlation and Experiment	302
5.67	(a) Effect of R_j on \overline{h} for $H/w = 8$ and $0.75 \leq S/H \leq 4$	307
5.67	(b) Effect of R_j on \overline{h} for $H/w = 16$ and $0.375 \leq S/H \leq 2$	308
5.67	(c) Effect of R_j on \overline{h} for $H/w = 24$ and $0.33 \leq S/H \leq 1.33$	309
5.68	Effect of Throughflow at the Impingement Surface on Lateral Profiles of Nu_{xt} for $Re_j = 10200, H/w = 8$ and $S/H = 1.5$	311

<u>Figure</u>	<u>Caption</u>	<u>Page</u>
5.69	Effect of Throughflow at the Impingement Surface on Lateral Profiles of Nu_{xt} for $Re_j = 22800$, $H/w = 8$ and $S/H = 1.5$	312
5.70	Effect of Throughflow at the Impingement Surface on Lateral Profiles of Nu_{xt} for $Re_j = 29100$, $H/w = 8$ and $S/H = 1.5$	313
5.71	Effect of Throughflow at the Impingement Surface on St_{xt}/St_x for $Re_j = 10200$, $H/w = 8$ and $S/H = 1.5$: Theory and Experiment	314
5.72	Effect of Throughflow at the Impingement Surface on St_{xt}/St_x for $Re_j = 22800$, $H/w = 8$ and $S/H = 1.5$: Theory and Experiment	315
5.73	Effect of Throughflow at the Impingement Surface on St_{xt}/St_x for $Re_j = 29100$, $H/w = 8$ and $S/H = 1.5$: Theory and Experiment	316
5.74	Effect of Throughflow at the Impingement Surface on St_{gt}/St_o for $Re_j = 10200$, 22800 and 291000: Theory and Experiment	317
5.75	Effect of Throughflow at the Impingement Surface on St_t/St for $Re_j = 10200$, 22800 and 29100: Theory and Experiment	318
5.76	Effect of Throughflow Parameters B_t and b_t on $\overline{St_t}/\overline{St_o}$, St_{ot}/St_o for $Re_j = 10200$, 22800 and 29100	319
A3.1	Discharge Coefficient for ASME Elliptic Nozzle	A8
A4.1	Boundary Conditions for the Heat Flux Sensor Numerical Simulation	A15
A4.2	Temperature Profile Throughout the Thickness of the Heat Flux Sensor	A16

LIST OF TABLES

<u>Table</u>	<u>Title</u>	<u>Page</u>
2.1	Experimental Conditions and Heat Transfer Correlations for Multiple Impinging Slot Jet Studies	22
4.1	Geometrical Parameters of the Confined Multiple Impinging Slot Jet System	73
4.2	Flow Parameters of the Confined Multiple Impinging Slot Jet System	75
4.3	Geometrical and Flow Parameters of the Multiple Jet System for Analysis of Nozzle Exit Flow Conditions	78
4.4	Jet Centerline Velocity at the Nozzle Exit and at 16w from the Nozzle Exit for $Re_j = 11000$	86
4.5	Geometrical Parameters of the Multiple Jet System for Analysis of Free Jet Development	87
4.6	Jet Half-Width for Analysis of Free Jet Development	115
4.7	Geometrical and Flow Parameters of the Multiple Jet System for Analysis of Impingement Surface Flow Conditions	117
4.8	Flow Parameters of the Confined Single Jet System for Analysis of Effect of Throughflow at the Impingement Surface	153
4.9	Criteria for Transition between Non-Interacting and Interacting Multiple Confined Slot Jet Systems	169
5.1	Geometrical and Flow Parameters of the Multiple Jet System for Analysis of Impingement Heat Transfer	178
5.2	Geometrical and Flow Parameters of the Multiple Jet System for Analysis of Heat Transfer with Symmetrical and One-Sided Outflow	187
5.3	Geometric Configuration for Maximum \overline{Nu}	305
5.4	Flow Parameters of the Confined Single Jet System for Analysis of Effect of Throughflow at the Impingement Surface	312

<u>Table</u>	<u>Title</u>	<u>Page</u>
A1.1	Fluctuating Velocity at the Jet Centerline for $w = 2.5\text{mm}$	A1
A1.2	Fluctuating Velocity at the Jet Centerline for $w = 3.3\text{mm}$	A1
A1.3	Fluctuating Velocity at the Jet Centerline for $w = 5.0\text{mm}$	A2
A1.4	Fluctuating Velocity at the Jet Centerline for $w = 10.0\text{mm}$	A2
A1.5	Fluctuating Velocity at the Jet Centerline for $w = 13.3\text{mm}$	A3
A2.1	Average Heat Transfer Coefficient for $f = 1.56\%$	A4
A2.2	Average Heat Transfer Coefficient for $f = 2.06\%$	A4
A2.3	Average Heat Transfer Coefficient for $f = 3.125\%$	A5
A2.4	Average Heat Transfer Coefficient for $f = 6.25\%$	A5
A2.5	Average Heat Transfer Coefficient for $f = 8.313\%$	A6
A3.1	Uncertainties in Re_j for the Study of Flow at the Impingement Surface ^j	A10
A3.2	Uncertainties in Re_j for the Study of Heat Transfer at the Impingement Surface	A10
A5.1	Error Analysis for High Heat Transfer Testing Conditions	A24
A5.2	Error Analysis for Low Heat Transfer Testing Conditions	A25
A5.3	Repeated Experiments for $f = 1.56\%$, $H/w = 8$ and $Re_j = 10790$	A29
A5.4	Repeated Experiments for $f = 6.25\%$, $H/w = 24$ and $Re_j = 5400$	A30
A7.1	Local Heat Flux at the Impingement Surface for $H/w = 8$, $Re_j = 10200$ and $U_s = 0, 0.1$ and 0.15 m/s	A33
A7.2	Local Heat Flux at the Impingement Surface for $H/w = 8$, $Re_j = 22800$ and $U_s = 0, 0.15$ and 0.3 m/s	A34
A7.3	Local Heat Flux at the Impingement Surface for $H/w = 8$, $Re_j = 29100$ and $U_s = 0, 0.2$ and 0.3 m/s	A35

NOMENCLATURE

A_s	free surface area of the heat flux sensor (for convection), mm^2
C	conductance of insulation (marinite) W/K
C_d	discharge coefficient
C_p	specific heat, J/kg-K
c_1	normalized location of kinematic origin of free jet as in equation (2.1)
c_2	normalized location of geometric origin of free jet as in equation (2.2)
c_3	normalized location of kinematic origin of wall jet as in equation (2.3)
c_4	normalized location of geometric origin of wall jet as in equation (2.4)
E	linearized voltage, volts
$(\overline{e^2})^{0.5}$	root-mean-square voltage, volts
H	impingement surface spacing from nozzle exit, mm
H_G	geometric origin of the jet, mm
H_o	kinematic virtual origin of the jet, mm
\bar{h}	average heat transfer coefficient, $\text{W/m}^2\text{-K}$
h_o	stagnation point heat transfer coefficient, $\text{W/m}^2\text{-K}$
h_x	local heat transfer coefficient, $\text{W/m}^2\text{-K}$
K_1	constant in equations (2.1) and (4.1)
K_2	constant in equations (2.2) and (4.4)
K_3	constant in equation (2.3)
K_4	constant in equation (2.4)
k	air thermal conductivity at the nozzle exit, W/m-K
l	transverse length of the nozzle, mm
L	lateral length of the nozzle (Fig. 3.3), mm

P_l	heat loss, W
P_s	heat into the sensor, W
ΔP	pressure relative to ambient, N/m^2 (Pa)
ΔP_j	pressure difference across the nozzle jet, N/m^2 (Pa)
ΔP_o	stagnation pressure relative to ambient, N/m^2 (Pa)
ΔP_s	pressure difference across the permeable impingement surface, N/m^2 (Pa)
ΔP_x	impingement surface static pressure relative to ambient, N/m^2 (Pa)
$Q_{cond.}$	heat transfer by conduction, W
$Q_{conv.}$	heat transfer by convection, W
$Q_{rad.}$	heat transfer by radiation, W
Q_t	heat carried by throughflow, W
R_j	fan energy at the nozzle exit per unit heat transfer area, W/m^2
R_{lw}	resistance of the lead wire, ohms
R_p	resistance of the precision shunt, ohms
R_s	resistance of the heating wire, ohms
S	jet centerline-to-exit port centerline spacing, mm
S_o	hot wire sensitivity factor
s	lateral length of the heat flux sensor, mm
T_{b1}	temperature at the back surface of the insulation, $^{\circ}C$
T_{b2}	temperature at the back surface of the sensor, $^{\circ}C$
T_j	jet temperature at the nozzle exit, $^{\circ}C$
T_s	impingement surface temperature, $^{\circ}C$
Tu_a	arrival turbulence intensity
T_w	temperature of impingement surface at steady state, $^{\circ}C$

T_x	air temperature after impingement, °C
ΔT	$T_s - T_j$, °C
ΔT_x	$T_s - T_x$, °C
t	thickness of the nozzle block = nozzle length (Figure 3.3), mm
U	axial mean velocity, m/s
U_j	local mean velocity at the nozzle exit, m/s
U_j^*	U_j averaged across nozzle width, m/s
U_{jo}	nozzle exit centerline mean velocity, m/s
U_o	centerline mean velocity, m/s
U_s	throughflow velocity at the impingement surface, m/s
u	instantaneous fluctuating velocity, m/s
u'	axial fluctuating velocity, $(\overline{u^2})^{0.5}$, m/s
u'_j	fluctuating velocity at location of U_j , m/s
u'_{jo}	fluctuating velocity at location of U_{jo} , m/s
u'_o	fluctuating velocity at location of U_o , m/s
V	lateral mean velocity, m/s
V_m	maximum lateral mean velocity, m/s
V_h	voltage across the heating wire, volts
V_p	voltage across the precision resistance, volts
w	nozzle width, mm
x	lateral distance, mm
$x_{0.5}$	jet half width, mm
y	perpendicular distance from impingement surface, mm
z	axial distance from nozzle exit, mm
$z_{0.5}$	distance from impingement surface where $U = 0.5 U_m$ (Equation (2.4))

Greek Letters

μ	air dynamic viscosity, Pa·s
ν	air kinematic viscosity, m^2/s
ρ	air density, kg/m^3
α	thermal diffusivity, m^2/s
ϵ_H	eddy diffusivity, m^2/s

Dimensionless Variables

b_b	blowing parameter
b_t	transpiration parameter $\left(\frac{\rho U_s}{\rho U_j^*}\right) \frac{1}{f} \frac{St_t}{f}$
B_t	alternate transpiration parameter, $(U_s/U_j^*)/St$
f	nozzle area-to-impingement surface area, $w/2S$
H/w	impingement surface spacing from nozzle exit
\overline{Nu}	average Nusselt number, $\overline{h}w/k$
Nu_e	Nusselt number under the exhaust port centerline, $h_e w/k$
Nu_o	stagnation point Nusselt number, $h_o w/k$
Nu_x	local Nusselt number, $h_x w/k$
Nu_{xb}	local Nusselt number based on bulk temperature, $h_{xb} w/k$
Nu_{xt}	local Nusselt number with throughflow, $h_{xt} w/k$
Pr	Prandtl number, $\mu C_p/k$
Re_j	Reynolds number at the nozzle exit, $U_j^* w/\nu$
\overline{St}	average Stanton number, $\overline{h}/\rho C_p U_j^*$
St_o	stagnation point Stanton number, $h_o/\rho C_p U_j^*$
\overline{St}_t	average Stanton number with throughflow, $h_t/\rho C_p U_j^*$

St_x	local Stanton number, $h_w / \rho C_p U_j^*$
St_{xt}	local Stanton number with throughflow, $h_{xt} / \rho C_p U_j^*$
S/H	flow cell proportion
$(S/H)_c$	critical flow cell proportion
$(S/H)_{co}$	upper critical limit of the flow cell proportion
$(S/H)_{ce}$	lower critical limit of the flow cell proportion
S/w	jet centerline-to-exit port centerline spacing
u'/U	turbulence intensity
x/w	dimensionless lateral distance
z/w	dimensionless axial distance

CHAPTER 1

INTRODUCTION

1.1 Background Information

Convective transport under impinging jets attracts attention because of high transfer rates relative to those for parallel flows. Impinging jets of various configurations are therefore used to cool, heat or dry surfaces in a number of industrial applications. In addition to the basic advantage of high transfer rates, impinging jets have the potential for fine control of local rates by adjusting the geometry and/or the local flow rate. For some industrial applications this capability is of great importance. Depending to some extent upon the application either round or slot jets may be used, either individually, in a single row or in a multiple configuration.

Cold jets are currently used in such industrial applications as cooling of electronic components, paper mill calender rolls and turbine hardware. In the turbine vane cooling application two-dimensional arrays of jets are used to cool the midchord region of the vane which has a trailing edge discharge. The studies of Saad, Mujumdar and Douglas (1980) indicate that the local heat transfer rate between the inner surface of the airfoil envelope and the coolant is significantly affected by the cumulative crossflow resulting from the "spent" flow from upstream jets.

Heated jets are used in a number of important industrial applications such as tempering of glass, anti-icing of aircraft wings and windshield surfaces, and drying of photographic films, textiles and paper. For high speed drying of newsprint the "Papridryer" process employs a combination of impingement and through-drying (Burgess et al., 1972a, b). In the Papridryer

the hot gas from the multiple confined slot jets, after impingement, exits from exhaust ports located in the confinement hood between adjacent jet nozzles. This outflow configuration avoids the undesirable consequences of cumulative crossflow and allows recovery of spentflow.

As discussed subsequently in Chapter 2, transport processes under multiple impinging slot jets have received relatively little attention in spite of current and potential industrial significance. Also, there are distinct shortcomings among the few existing studies. Gardon and Akfirat (1966) and Schuh and Pettersson (1966) studied the heat transfer for unconfined multiple impinging jets. Such systems have little industrial relevance because lack of confinement of the jets into a closed system allows entrainment by the jets of fluid from the surroundings, which is undesirable, and moreover is inconsistent with the typical need to recover the spentflow. Furthermore, those studies provide no information as to the geometric and flow conditions for which heat transfer for a multiple slot jet system deviates from that of an assembly of equivalent single jets.

The only previous study of a confined multiple jet system is that of Martin (1977) who measured average mass transfer under multiple slot jets. Unfortunately, in that study the outflow did not occur through exhaust ports in the confinement surface but was constrained to exit only in the transverse direction through the open sides at the ends of the slot nozzles. As a consequence the transport rate at the impingement surface was highly nonuniform in the direction of the nozzle length, a characteristic which is quite unacceptable in industrial applications such as the drying of paper where uniformity of transport rate in the transverse direction is essential.

In a confined multiple slot jet system, if the spentflow is not removed through exhaust ports located between each inlet nozzle in the confinement

surface, the consequence is for a cumulative crossflow to occur along the impingement surface. Thus the effect of crossflow on transfer rates is another important aspect of the design of multiple jet systems.

As in the Papiridryer process, the application of moderate throughflow, i.e. from simultaneous application of suction across the wet web, is expected to have a favourable influence on transport rates. Thus the combination of impingement flow and throughflow should further enhance heat transfer rates. This has been noted by van Heiningen, Mujumdar and Douglas (1976) and Saad, Douglas and Mujumdar (1977) for single slot and single round jets, respectively.

The effect of throughflow at the impingement surface, on the flow characteristics of a two-dimensional air jet, was studied by Abdul-Wahab, Mujumdar and Douglas (1975). Baines and Keffer (1977) and Obot (1981) presented some results on the influence of throughflow on lateral mean velocity and turbulence intensity profiles for single slot and single round impinging jets, respectively. These data show a qualitatively similar trend as to the effect of throughflow on lateral wall jet flow, a trend which suggests an enhancement of impingement surface transport rates.

Since for the industrially important applications such as drying of paper and cooling of hot components in turbine engine, the knowledge of the effect of crossflow and the effect of throughflow at the surface on impingement heat/mass transfer rates is needed, and in view of the lack of this information in the literature the present study was undertaken.

1.2 Objectives and Scope

The objective of the present study is therefore to investigate the heat transfer characteristics of turbulent confined multiple impinging slot jets,

with and without throughflow at the impingement surface (Figure 1.1). In order to develop a basic understanding of the phenomena of convective heat transfer for such a system the scope of the study was extended to include characterizing the flow field.

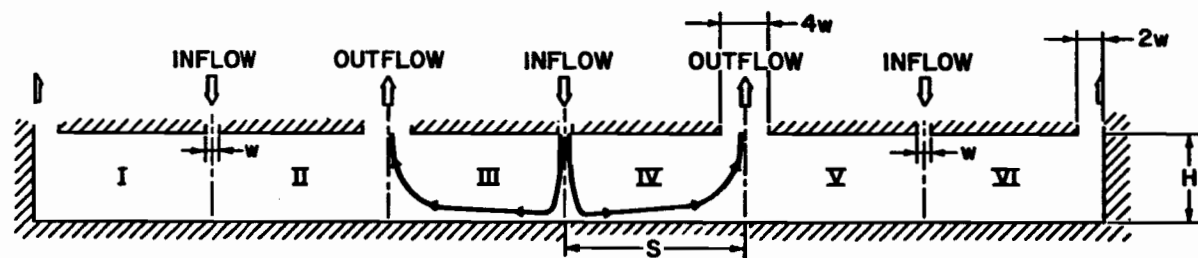
More specifically, for the flow study the objectives were:

- (1) To characterize mean velocity and turbulence aspects of the flow field for each set of nozzles used, in single and multiple configurations.
- (2) To characterize the flow field at the impingement surface by measuring the static pressure distribution.
- (3) To study the effect of throughflow at the impingement surface.

For the heat transfer investigation the objectives were:

- (1) To investigate local and average convective heat transfer for multiple confined turbulent slot jets with exhaust ports alternating with nozzles to give an impingement system without cross-flow.
- (2) To establish criteria for interaction between adjacent jets.
- (3) To study the effect of cumulative crossflow on heat transfer rates.
- (4) To study the effect on impingement heat transfer of throughflow at the impingement surface.

A totally new experimental heat transfer facility was designed to accomplish the above objectives.



MULTIPLE CONFINED IMPINGING SLOT JET SYSTEM WITH NOZZLES AND EXIT PORTS
LOCATED ALTERNATELY IN CONFINEMENT SURFACE

FIGURE 1.1 Schematic Diagram of Test Section

CHAPTER 2

LITERATURE REVIEW

2.1 Introduction

While extensive studies have been made of transport processes under single and multiple round impinging jets, less attention has been devoted to corresponding studies for single and multiple slot impinging jets. Earlier reviews by Arganbright and Resch (1971), Mujumdar and Douglas (1972), Livingood and Hrycak (1973) focussed on single impinging jet studies, while the more recent reviews by Martin (1977) and Obot et al. (1979) concentrated mainly on presentation of correlations for both single and multiple impinging jets to permit comparison and choice for design applications. These reviews have not clarified a number of aspects concerning transport processes under multiple impinging slot jets, a prime orientation of the present work.

The present review focusses particularly on the effects of various geometrical configurations for the relatively few studies of multiple slot jet systems which have been reported. Specifically, this analysis first deals briefly with the characteristics of single slot jets, as a standard of comparison for multiple jet studies, then with the flow and impingement surface transport phenomena characteristics of multiple slot jets on solid surfaces, and finally the effect of throughflow at the impingement surface on flow and transfer rates.

2.2 Flow Field of Turbulent Impinging Jets

The flow field of turbulent impinging jets comprises several distinct

regions, the free jet, impingement, wall jet and outflow regions, as identified in Figure 2.1.

2.2.1 Free Jet Region

The effect on mean velocity of interaction between the jet and the fluid into which it discharges penetrates the centerline of the jet flow at some distance from the nozzle exit. The potential core defines the shrinking region where this effect on mean velocity has not yet been felt. The corresponding outward movement of the interaction between the jet and the fluid into which it discharges is reflected in the steadily increasing width of the jet downstream from the nozzle exit.

In the free jet region the high lateral gradients in axial mean velocity which exist directly under the nozzle walls constitute a region of correspondingly high generation of turbulence. Thus the turbulence level in the free jet increases rapidly after discharge, including within the potential core region where mean velocity is unchanged from that at the nozzle exit.

Following the potential core region there is the developing region (transition region) which varies from about $5w$ to $7w$ from the nozzle exit. This variation depends mainly on nozzle geometry and the initial flow conditions upstream of the nozzle and at the nozzle wall as shown by Bradshaw (1966), Flora and Goldschmidt (1969) and Hill (1976).

Provided that the impingement surface spacing from the nozzle is sufficiently large there is a region of established flow which has the same characteristics as the corresponding established flow region for a free jet in the absence of an impingement surface. In this region axial mean velocity characteristics of the jet may be characterized by the rate of decay of centerline mean velocity and the rate of spreading. Centerline mean velocity, U_o , de-

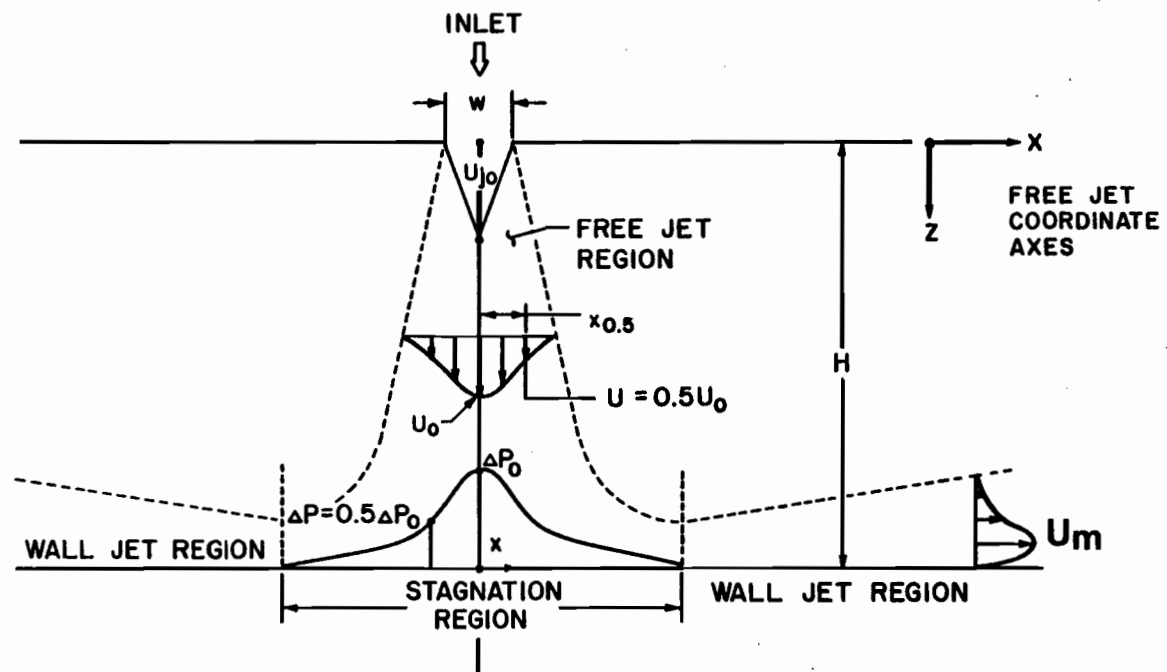


FIGURE 2.1. Flow Field of Turbulent Impinging Jets

creases inversely with distance from the nozzle exit, z , while jet half-width, $x_{0.5}$, defined as the lateral distance from the jet centerline at which axial mean velocity equals one-half of its maximum, is proportional to axial distance, z . Thus

$$U_o/U_{jo} = K_1(z/w - c_1)^n \quad (2.1)$$

and,

$$x_{0.5}/w = K_2(z/w - c_2)^m \quad (2.2)$$

where K_1 and K_2 are the slopes, with respect to axial distance, of the centerline mean velocity decay and the free jet half-width, respectively, and c_1 and c_2 are the normalized locations of kinematic and geometric origins of the jet, respectively. Note that, for a slot jet, $n = -0.5$ and $m = 1$. As free jet are described extensively in texts such as Hinze (1959), Abramovitch (1963), Schlichting (1968), Rajaratnam (1976) and Townsend (1976), no further comment is required here.

2.2.2 Impingement Region

As the jet approaches the impingement surface, pressure increases corresponding to decrease in axial mean velocity. The impingement region is considered to extend to a certain axial position away from the surface. This location is taken as the start of deviation of centerline axial velocity from the value for the equivalent free jet. The axial extent of the impingement region was measured by Schauer and Eustis (1963) and Beltaos and Rajaratnam (1973). In the first study measurements were made at only a single spacing, $H/w = 40$, while in the latter study measurements were made over the range

$21 \leq H/w \leq 65.7$. The agreement between these two sets of data is good; the extent of the stagnation region from the impingement surface was found to vary from 20 to 30% of the jet spacing. In a similar fashion Gutmark et al. (1978) in their study of the turbulence structure on the centerline of a two-dimensional impinging jet found that, for $H/w = 20$, the deviation from a free jet does not extend further than $0.2 H$ from the impingement surface.

The lateral extent of the impingement region is defined as the distance from the stagnation point where the static pressure gradient becomes negligible. For $21 \leq H/w \leq 65.7$ and $5270 \leq Re_j \leq 9400$, Beltaos and Rajaratnam (1974) found this distance to be around $0.35H$ from the stagnation line.

With respect to turbulence in the impingement region, Russell and Hatton (1972) reported measurements of turbulent shear stress, turbulent kinetic energy and eddy diffusivity in the impingement region of a plane slot jet confined between parallel walls. Their concern was with the prediction method proposed by Wolfshtein (1967). They found that despite the high degree of uncertainties in measurements due to the very high turbulence level in the stagnation region, the order of magnitude agreement with theory was still encouraging.

2.2.3 Wall Jet Region

Downstream of the impingement region is the wall jet region where, for fully developed flow the rate of decay of maximum lateral velocity, U_m , and the spreading rate expressed in terms of the wall jet half-width, $z_{0.5}$, may be represented by

$$U_m/U_{j0} = K_3(x/w - c_3)^n \quad (2.3)$$

and,

$$z_{0.5}/w = K_4(x/w - c_4)^m \quad (2.4)$$

where K_3 and K_4 are the slopes of the maximum lateral velocity decay and the wall jet half-width, respectively, and c_3 and c_4 are the normalized locations of kinematic and geometric origins of the wall jet, respectively. Wall jet half-width, $z_{0.5}$, is defined as the distance from the impingement surface where $U = 0.5 U_m$. Note that for an impinging slot jet $n = -0.5$ and $m = 1$ as was found by Beltaos and Rajaratnam (1973) and by Schauer and Eustis (1963).

In their theoretical prediction of wall jet flow for a single impinging slot jet, Cadek and Zerkle (1970) adopted Glauert's (1956) two-layer approach to model the wall jet region. The two-layer approach implies that the wall jet region can be divided into two parts, an inner layer where effect of the wall is the dominant feature and an outer layer which has characteristics of a free jet flow. Cadek and Zerkle (1970), employing the usual two-dimensional boundary layer assumptions along with the measured free jet data, predicted for $x/w = 7$ the profile normal to the impingement surface of lateral mean velocity. Their profiles agree well with the lateral mean velocity distributions measured in the wall jet by Beltaos and Rajaratnam (1973) for a single turbulent impinging slot jet.

2.2.4 Arrangement for Outflow after Impingement

Of all features of impinging jet studies, the aspect of how the jet outflow leaves after impingement has been least satisfactorily treated. As use of an unconfined jet is the simplest arrangement for laboratory experimental studies, this arrangement has been used for almost all studies of sin-

gle and multiple impinging jets. Unconfined jets easily entrain large amounts of fluid from the environment into the impingement flow. For the case of turbulent round impinging jets, Obot (1981) has reviewed the information available which indicates that entrainment by unconfined jets may increase the jet flow to 250% of that at the nozzle exit. Even for the simplest case of a jet discharging into an environment of the same fluid at the same temperature entrainment will affect the flow field and subsequently the impingement surface transport characteristics.

2.2.4.1 Unconfined Multiple Impinging Slot Jet Studies

Most studies of multiple impinging slot jets have been made with the impingement flow unconfined, thus forming a free outflow boundary condition as shown in Figure 2.2(a). This corresponds to the studies of Korger and Krizek (1965), Gardon and Akfirat (1966), Schuh and Pettersson (1966) and Scheuter and Dosdogru (1971). Unconfined impinging jet systems have little industrial relevance because entrainment by the jets of fluid from the surroundings is generally undesirable. Furthermore, lack of confinement is inconsistent with the typical need to recover the exhaust flow for purposes such as heat recovery.

Gardon and Akfirat (1966) measured the static pressure at the impingement surface for a system of three unconfined impinging slot jets spaced at $16w$ ($2S/w = 16$). At a relatively small nozzle-to-impingement surface spacing, $H/w = 4$, and jet Reynolds number $Re_j = 5500$ they found that the pressure distribution in the impingement region of the middle jet is substantially the same as that for a single unconfined impinging jet. However in the region where the deflected jets approach one another, i.e. outside the impingement region, while the static pressure at the impingement surface remains atmo-

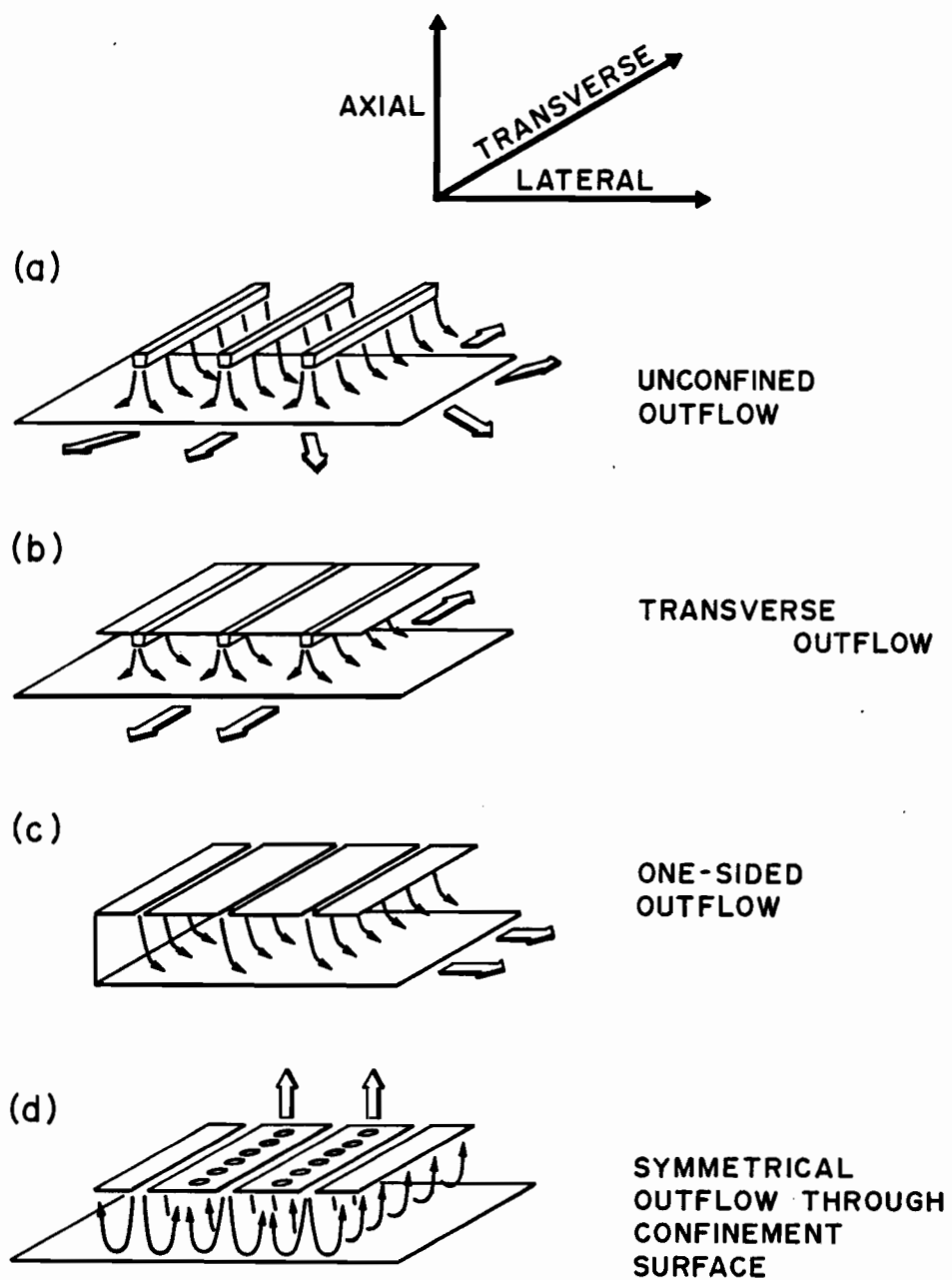


FIGURE 2.2. Alternate Outflow Configurations in Systems of Multiple Impinging Slot Jets

spheric for a single impinging jet, that for the multiple jets increases. This positive pressure gradient causes first a thickening of the boundary layer then flow separation from the impingement surface. This behaviour is manifested by marked secondary peaks in static pressure at points midway between adjacent nozzles. For a large nozzle-to-impingement surface spacing, $H/w = 16$, they found that the pressure distribution in the impingement region for a multiple unconfined slot jet system is much less peaked than that for the corresponding single jet, in that the stagnation pressure is decreased while there is an increase in the static pressure beyond $2w$ from the stagnation point. These observations indicate that for a nozzle to impingement surface spacing, $H/w = 16$, equal to the internozzle spacing, $2S/w = 16$, the inlet jet and outflows are highly interacting. Thus while in the corresponding single jet the flow spreads through substantially stationary air, the inlet jet in a multiple unconfined jet system flows countercurrent to the stream which constitutes the outflow after impingement. The overall effect found by Gardon and Akfirat is a considerable reduction in heat transfer rate at the impingement surface, as discussed subsequently.

2.2.4.2 Confined Multiple Impinging Slot Jet Studies

Martin and Schlünder (1973) in their study of multiple impinging slot jets used a confinement surface at the inlet slot nozzles, as portrayed in Figure 2.2(b). With the outflow exiting in the transverse direction only, they found that the discharge rate from the nozzles varied transversely, as was quite predictable. The pressure drop in the transverse direction for the transverse outflow naturally caused a transverse variation in pressure drop across the nozzle slots, and hence a variation in nozzle flow in the same direction. This increase in nozzle exit flow rate towards the edge of the array

further increased the transverse variation in outflow which would exist even if the nozzle exit flow were uniform. The transport characteristics at the impingement surface were of course found to follow the same transverse variation. This variation in the transverse direction is generally unacceptable in industrial applications such as drying of paper, where uniformity of transport rates in this direction is an important specification. The design used for their study thus has little practical relevance.

The third type of outflow, shown in Figure 2.2(c), is used in turbine vane cooling where the flow for a system of multiple confined impinging jets is constrained to exit from one lateral side while the three other sides are closed. As reported by Saad et al. (1980), and later by Florschuetz et al. (1981) for a confined array of jets with one-sided exhaust as shown in Figure 2.2(c), the cumulative crossflow, which increases in lateral (stream) direction, correspondingly reduces the driving force and hence reduces rates of transport phenomena at the impingement surface. Although these studies reported the effect of cumulative crossflow for an array of staggered round jets, this effect, expressed as attenuation in transport phenomena, would apply also for one-sided outflow from an array of slot jets. Further investigation of this important effect, not previously reported in the literature, forms part of the work of the present study.

The fourth type of outflow from a multiple confined slot jet system is shown in Figure 2.2(d) where outflow after impingement exhausts through circular ports located between neighbouring slot nozzles. This was the outflow for the proposed "Papridryer" process which constitutes a combination of impingement and through-drying of paper (Burgess et al., 1972a, b). With respect to the alternatives depicted on Figure 2.2 this outflow configuration avoids the undesirable consequences of interaction with the surroundings that

are associated with system (a), the flow nonuniformity in the transverse direction associated with system (b), and cumulative crossflow effects of system (c).

The report by Burgess et al. on the Papridryer does not include measurements to characterize the flow in this interesting system. In fact, no study of flow for a multiple confined impinging jet system with symmetrical, two-dimensional outflow has yet been published.

2.3 Heat Transfer at the Impingement Surface

In this section a review of analytical and experimental studies of impingement heat transfer from slot jets is presented.

2.3.1 Analytical Studies

Two main categories of theoretical approaches have been adopted for impinging jet calculations:

- (a) inviscid flow-boundary layer approach, and
- (b) iterative finite difference methods for solution of the full governing equations.

Undoubtedly the assumption of inviscid flow is a great simplification, but it presents difficulty in the location of the free stream boundary, which is one major drawback of this method. Shen (1962) suggested an iterative procedure to position the free stream boundary, then Schnurr et al. (1972) extended this approach with a new relaxation technique that computed the pressure distribution at the impingement surface from the calculated velocity potential. The large discrepancy of such predictions relative to experimental data is due to flow separation that cannot be predicted by the parabolic boundary layer calculation. Moreover, as the inviscid flow solution does not

include the turbulent nature of the flow field, it fails to define the turbulent boundary conditions to the boundary layer equations. For instance Gardon and Akfirat (1965), Cartwright and Russell (1967) and Cadek and Zerkle (1970) reported that both profiles at the nozzle exit of jet axial mean velocity and turbulence intensity affect the heat transfer when a single slot jet is spaced at $H/w > 3$. Using the potential flow method of Michell (1890) and Ehrick (1955), Miyazaki and Silberman (1972) found that the local heat transfer for impinging slot jet was independent of nozzle-to-impingement surface spacing higher than $3w$. This discrepancy is partially due to the potential flow assumption which predicts no change in the mainstream velocity for $H/w > 3$.

Solution of the full governing equations by finite difference methods was used by van Heiningen et al. (1976b), Saad et al. (1977) and Huang et al. (1978) to predict flow and heat transfer for single impinging laminar slot and round jets. Transport rates at the impingement surface were found to be relatively insensitive to nozzle-to-impingement surface spacing $1.5 < H/w < 12$, a prediction which compared well with experimental data of Sparrow and Lee (1975) and Schlotz and Trass (1970) for laminar slot and round impinging jets, respectively. On the other hand all predicted characteristics of laminar impinging jets were found to be a sensitive function of inlet jet velocity profile between the limits of parabolic and flat profile.

Concerning prediction of turbulent impinging jets, the approach of solving the full governing equations like the boundary layer approach encounters the problem of appropriate modeling of turbulence. Although some models such as those proposed by Gosman et al. (1969) and Gosman et al. (1976), produced acceptable predictions for some recirculating flows, these models are based empirical constants obtained from experimental data for certain flow

configurations. Application of such models to an unknown and highly complex flow such as impinging jets is subject to unavoidable uncertainties. Wolfshtein (1967), Gosman et al. (1976), Folley and Whitelaw (1977) and van Heiningen et al. (1977) found significant discrepancies between predicted and measured data, especially at the stagnation region. In their studies using this approach van Heiningen et al. (1977) attributed the deviation of predicted from experimental measurements in the stagnation region to inapplicability of the "log law" as a boundary condition in this region. Another remaining shortcoming of this approach is that with turbulence model used to date, investigators using this approach have not been able to predict the transition from laminar to turbulent flow that occurs at smaller values of H/w ($H/w < 7$). This transition is believed to have been established by the experimental studies of Gardon and Akfirat (1966) and Cadek and Zerkle (1970).

It may be concluded therefore that although it is evident that development of improved analytical solutions for turbulent transport processes deserves continuing attention and development, experimental measurements are still essential, especially for complex flows such as system of multiple impinging jets.

2.3.2 Experimental Studies

Most of the impingement heat transfer studies reported in this section are based on use of a steady state technique with the heat transfer surface maintained either at a uniform temperature or at uniform heat flux, the two standard boundary conditions. A few studies were derived from an unsteady state technique in which the initial condition was a uniform temperature heat transfer surface. Analysis of multiple impinging slot jet studies is preceded by a review of investigations with a single impinging slot jet.

2.3.2.1 Single Impinging Slot Jet Studies

Metzger (1962) used an unsteady state technique to obtain average Nusselt number, \overline{Nu} , for an isothermal heat transfer surface subjected to a single unconfined slot jet. Over the range $1490 \leq Re_j \leq 3700$ ($0.25 \leq w \leq 2.04$ mm), \overline{Nu} was found to be at a maximum at $H/w = 8$. This observation was confirmed later by Gardon and Akfirat (1966), who improved the resolution of heat transfer measurements remarkably. They used a 0.90 mm diameter heat flux sensor to measure the convective heat transfer rate from an isothermal heated impingement surface to a slot jet. For $450 \leq Re_j \leq 22000$ and $1.59 \leq w \leq 6.35$ mm Gardon and Akfirat obtained values of local Nusselt number, Nu_x , over a wide range of nozzle-to-impingement surface spacing ($2 < H/w < 80$). For $2 \leq H/w \leq 6$ they measured a secondary peak in Nu_x that begins immediately after the end of the acceleration (impingement) region where the disappearance of the stabilizing streamwise pressure gradient leads to a steep rise to turbulence intensity that triggers transition to a turbulent boundary layer. This secondary peak in Nu_x was also measured by Korger and Krizek (1966), Kumada and Mabuchi (1970), Schlünder et al. (1970) and Cadek and Zerkle (1970). While the first two groups used the naphthalene sublimation technique, Schlünder et al. computed local mass transfer rates by measuring the rate of water removal from uniformly moist, parallel strips of porous stoneware subjected to an impinging slot jet of unsaturated air. Although the results of these authors agree to within $\pm 10\%$ for value of average Nusselt number, \overline{Nu} , the scatter in local value, Nu_x , is as high as $\pm 20\%$, especially at the stagnation point. Such discrepancies are believed to be due in part to differences in turbulence levels at the nozzle exit. Unfortunately none of these investigators provided any detail informations of turbulence characteristics at the nozzle exit and downstream from the nozzle exit.

The industrially more important configuration involving use of a confinement surface at the same spacing from the impingement surface as the nozzle exit was studied by Folayan and Whitelaw (1977) for a single impinging slot jet cooling a heated surface. The experiments were carried out for one Reynolds number, $Re_j = 7100$, and for a range of spacing, H/w , between 2 and 12. For $H/w = 2$ their results indicated that the value of Nusselt at the stagnation point, Nu_o , was independent of whether or not a confinement surface was present. However, at $5 \leq H/w \leq 12$ Nu_o was consistently lowered by use of the confinement surface, and this trend continued away from the stagnation point. The finding that the effect of confinement for the case of impingement cooling of a hot surface is to cause a decrease in local and average heat transfer may be attributed to the effect of the confinement surface in reducing entrainment of air from the surroundings into the impingement flow. For the case of a single turbulent round jet, Obot (1981) has documented that at $Re_j = 80000$ the effect of confinement is to reduce entrainment by about 4.5%. Obot (1981) found that confinement did not affect turbulence significantly either along the jet centerline or along the impingement surface.

2.3.2.2 Multiple Impinging Slot Jet Studies

Of the limited data which have been reported for transport phenomena at the impingement surface for the industrially important case of multiple slot jets, the most significant data are for the jets unconfined as shown in Figure 2.2(a). Four studies of this kind, those of Korger and Krizek (1966), Gardon and Akfirat (1966), Schuh and Pettersson (1966) and Scheuter and Dosdogru (1971) have been reported. For the case of confined multiple impinging slot jets, the only study published, that of Martin and Schlünder (1973), is with the unique arrangement for the outflow after impingement that is shown in

Figure 2.2(b). The experimental conditions and proposed heat transfer correlations of these studies are listed in Table 2.1.

As the results of Scheuter and Dosdogru (1971) shown in Figure 2.3 contain a fundamental error, their data are not included in Table 2.1. These authors used a hot-film probe, which has been used widely as skin friction device, to measure local heat transfer. They used a DISA film probe mounted flush with the impingement surface of an unheated plate. Surface heat transfer distributions obtained this way exhibited a minimum at the stagnation point, thus conflicting with all other studies which invariably show a maximum at this location. The profile of Gardon and Akfirat (1966) is shown for contrast in Figure 2.3. The error of Scheuter and Dosdogru derives from the fact that for the impingement region the Reynolds analogy is not valid, as has been pointed out with reference to impingement heat transfer studies by van Heiningen, Mujumdar and Douglas (1976a). Schauer and Eustis (1963) measured the wall shear stress from velocity profiles and the heat transfer rates by a direct method. When the shear stress is correctly measured, as in their study, it must of course be zero at the stagnation point, in sharp contrast with the bell-shaped heat transfer profile. It should be noted that a completely different situation exists when the surface surrounding the hot-film probe is heated to the same temperature as the hot film, which then becomes a heat flux meter.

In Table 2.1 and in the discussion to follow frequent reference is made to a dimensionless geometric parameter, S/H . The concept of characterizing multiple impinging slot jet systems by the dimensionless S/H parameter was in fact not used by any previous investigator. Rather, this concept was introduced only in the present investigation. The analysis of multiple slot jet systems with symmetric outflow as systems comprising assemblies of repeated

TABLE 2.1. Experimental Conditions and Heat Transfer Correlations for Multiple Impinging Slot Jet Studies

Authors	Range of Parameters of Reported Experiments						Correlations and Range of Validity
	Re_j	w (mm)	S/w	f (%)	H/w	(S/H)*	
Korger and Krizek (1966) (L.M.T.), (M.U.)	6500 21500	5.0 10.0	5-33 7.5	1.5-10 6.67	8 6	0.63-4.13 1.25	No correlations could be obtained due to limited experiments.
Gardon and Akfirat (1966) (L.H.T.), (M.U.)	5500 11000 22000	3.2	8-16	3.13-6.25	4-40	0.2-4.0	$\overline{Nu} = 0.66 Re_j^{0.62} f^{0.38} (H/w)^{-0.31}$ $7000 < Re_j < 120000$; $8 < S/w < 32$; $H/w > 8$
Schuh and Pettersson (1966) (A.H.T.), (M.U.)	1260 6300 31600	1.0 1.0 5.0	2.5-50 2.5-50 2.5-10	1.0-20 1.0-20 5.0-20	2-16 2-16 2-16	0.25-25 0.25-25 0.25-5	$\overline{Nu} = 0.46 Re_j^{0.598} f^{0.372}$ $1200 < Re_j < 100000$; $2.5 < S/w < 50$; $H/w = 4$
Martin and Schlünder (1973) (A.M.T.), (M.C.)	750-20000	1.5-18	2.5-55	0.9-21.2	2-80	0.12-27.5	$\frac{\overline{Sh}}{Sc^{0.42}} = \frac{\overline{Nu}}{Pr^{0.42}} = 0.84 f_o^{0.75} \left[\frac{Re_j}{f/f_o + f_o/f} \right]^{0.667}$ $f_o = [60 + (H/w - 4)^2]^{-0.5}$ $750 < Re_j < 20000$; $2.5 < S/w < 55$; $2 < H/w < 80$

* S/H geometric parameter is not used in any of the investigations listed.

NOTE: (L.H.T.) = local heat transfer measurements
(A.H.T.) = average heat transfer measurements
(L.M.T.) = local mass transfer measurements
(A.M.T.) = average mass transfer measurements
(M.C.) = multiple confined jet system
(M.U.) = multiple unconfined jet system

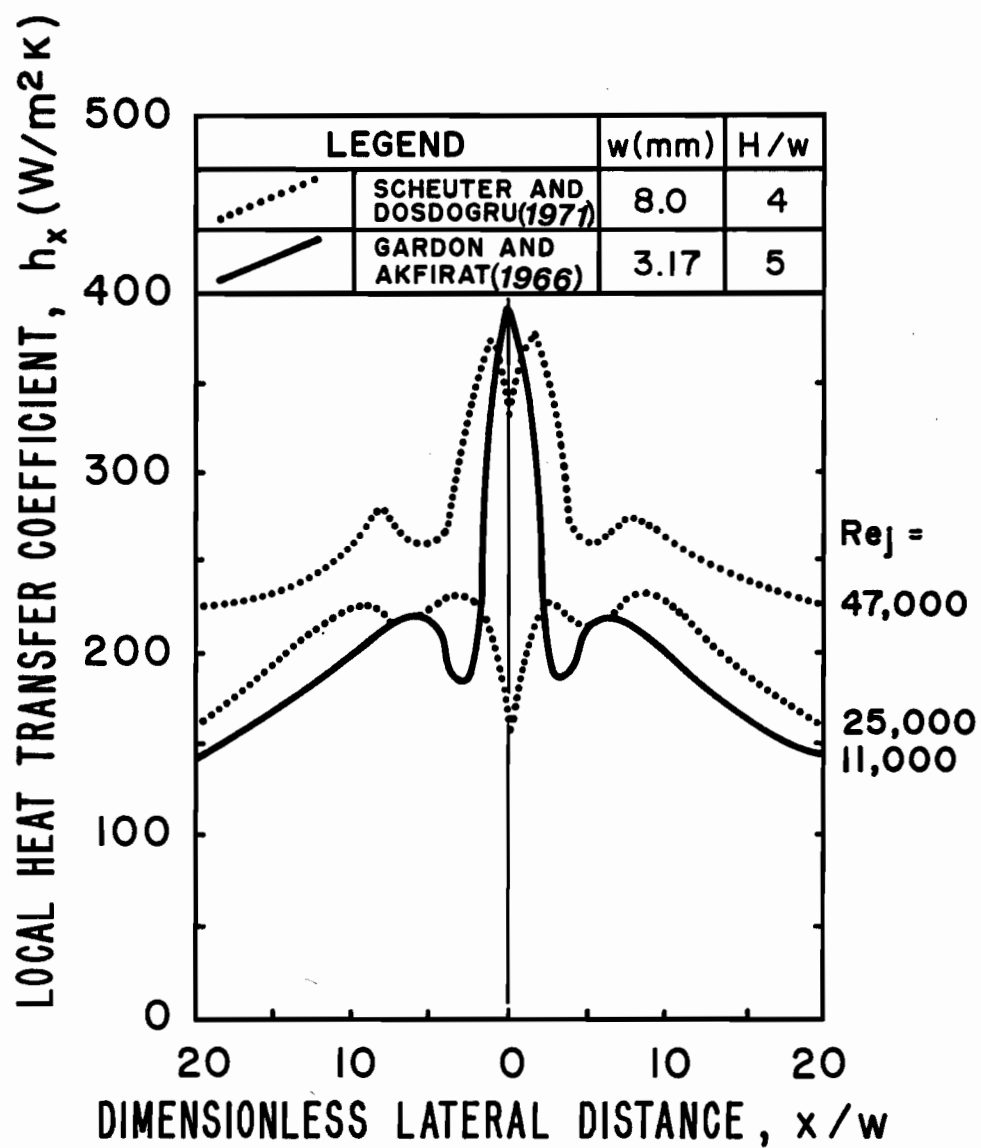


FIGURE 2.3. Effect of Hot-Film Probe on Local Heat Transfer Profile

"flow cells" of proportions S/H is proposed and validated in an extensive section of Chapter 4. Because of the success of this new perspective for the multiple slot jet system of the present investigation, the parameter of flow cell proportion, S/H , has been used in the re-interpretation of the results of previous investigators.

Korger and Krizek (1966), using the naphthalene sublimation technique, measured local mass transfer from the impingement surface over the limited range of parameters shown in Table 2.1. Their results show that with decreasing S/H from 4.13 to 0.63 the impingement surface mass transfer profile for the system of multiple jets departs from that for a single jet, in that the stagnation peak decreases and a secondary peak appears midway between adjacent stagnation peaks. Their mass transfer profiles also show that these secondary peaks increase over their operating conditions which correspond to flow cells of decreasing width, S/H . For instance, at $Re_j = 21500$, $H/w = 6$ and $S/w = 7.5$, (i.e. equivalent to $S/H = 1.25$) the secondary peak was found to be of similar magnitude to that at the stagnation line. Unfortunately these authors did not comment on these significant differences between single and multiple jets. Incredibly, they recommended use of single jet correlations for multiple jets regardless of the spacing S/w even though their own results showed major differences between the single and multiple jet cases.

Over a relatively wider range of parameters as shown in Table 2.1 Gardon and Akfirat (1966), using the steady state technique at uniform surface temperature, reported similar heat transfer profiles. For their conditions which correspond for a multiple jet system to a relatively wide flow cell, i.e. $S/H = 2$, (i.e. for their combination of $S/w = 8$ and $H/w = 4$) the pressure and heat transfer distribution in the impingement region of the middle jet is nearly the same as that for single jet. However in the region where the de-

flected jets converge (midway between neighbouring jet centerlines) the pressure was higher than for the equivalent single impinging jet. They believed that the associated adverse pressure gradient is high enough to cause flow separation which manifests itself in the marked secondary peak in heat transfer midway between adjacent jet centerlines. Their results for $S/w = 8$, $H/w = 16$ (equivalent to $S/H = 0.5$) indicated lower values for both impingement surface pressure and heat transfer, relative to the equivalent single jet. This reduction for the multiple slot jet case was most pronounced for their combination of $S/w = 8$ with $H/w = 40$ (equivalent to $S/H = 0.2$). Not only were the heat transfer profiles significantly lowered, but the maxima and minima in these profiles were reduced to only about 15% on either side of the average value. For the $S/w = 8$, $H/w = 40$ condition ($S/H = 0.2$), the amount of entrainment in this unconfined system and the interaction and mixing between adjacent jets would of course be very large. Gardon and Akfirat proposed a heat transfer correlation that covers a wide range of S/w ($8 < S/w < 32$), and jet Reynolds number $7000 < Re_j < 120000$.

Schuh and Pettersson (1966) reported average heat transfer data for a similar system of unconfined multiple slot jets using a steady state technique at a uniform surface temperature. Over the wide range of internozzle spacing $2.5 < S/w < 50$, for all values of H/w , i.e. $H/w = 2, 8$ and 16 , they found a maximum heat transfer to occur at $S/w = 7$ and $H/w = 8$, which would correspond to $S/H = 0.88$. They reported no explanation of this optimum because of lack of detail of their flow and local heat transfer investigation. For widely spaced jets, $S/w > 25$ at $H/w = 8$ (i.e. $S/H > 3$) their results show good agreement with those reported by Metzger (1962) for a single impinging slot jet. On the other hand for the same impingement surface spacing, $H/w = 8$, but at closer jet-to-jet spacing, S/w of 12 and 4 , combinations which would corre-

spond to S/H of 1.5 and 0.5, they reported heat transfer rates lower than those for single jet by Metzger (1962).

In summary for this unconfined system of multiple slot jets the range of values of flow cell proportions, S/H , at which heat transfer becomes less than that for a single jet was found to be $S/H < 1.5$ for Korger and Krizek (1966), at some value of S/H larger than 0.5 but less than 2 for Gardon and Akfirat (1966) and some value of S/H less than 1.5 for Schuh and Pettersson (1966). One limitation on the applicability of the results of these three investigations is the fact that the unconfined outflow arrangement is not what is needed for some important industrial applications. Moreover, the results do not indicate clearly what are the conditions at which heat transfer for a multiple slot jet system begins to be less than that for an assembly of equivalent single jets. However the results are sufficient to indicate that this reduction starts for flow cells somewhat narrower than $S/H = 2$.

To eliminate the changes in impingement surface heat or mass transfer caused by the mixing and entrainment from the surroundings associated with an unconfined system, Martin and Schlünder (1973) used a confined jet system as shown in Figure 2.2(b). As a consequence of the flow exiting in the transverse direction the impingement flow was 3-dimensional and the transport characteristics at the surface varied in the lateral and transverse directions. At a number of locations in the transverse direction they measured a laterally averaged rate of evaporation of water from strips of stoneware. Because of the serious flow nonuniformity in the transverse direction, as detailed in the previous section, they obtained laterally averaged mass transfer rates at the ends of the nozzle slot which were as much as 2.3 times the minimum rate at the midway location of the slot. Although an extensive amount of data was taken and correlated, their complex correlation is of limited value because of

the transverse variation of mass transfer rates which is generally unacceptable in industrial applications.

For $H/w = 4$, Figure 2.4 compares the correlation of Martin and Schlünder (1973) and Schuh and Pettersson (1966). The disagreement between the two sets of results at all values of f ($f = 2, 4$ and 8%) may be attributed to the lowering of impingement surface transfer rates of Martin and Schlünder due to the spent outflow in the transverse direction and also to the presence of confinement surface.

For $f = 4\%$, the effect of Re_j on average heat transfer, \overline{Nu} , is shown in Figure 2.5 for 3 values of H/w (8, 16 and 24). From this figure it can be seen that the correlation of Martin and Schlünder (1973) is close to that of Gardon and Akfirat (1966), since for the former at higher value of jet spacing (H/w) than 4 the effect of spent outflow on the transverse heat (mass) transfer profile is decreased.

2.4 Effect of Suction

Jets impinging on a permeable surface through which fluid may pass constitutes an industrially important configuration. Such an application is the proposed "Papridryer" process, a combination of impingement and through-drying of paper (Burgess et al., 1972a, b). In this process the range of the ratio of suction velocity to the average velocity at the nozzle exit is $0.045 < U_s/U_j^* < 0.45\%$.

2.4.1 Flow Studies

The effect of suction on impingement flow field appears in only three previous studies. Abdul-Wahab et al. (1975) and Baines and Keffer (1977) studied flow characteristics of a slot impinging jet on a permeable impingement surface. More recently a more comprehensive study on the effect of

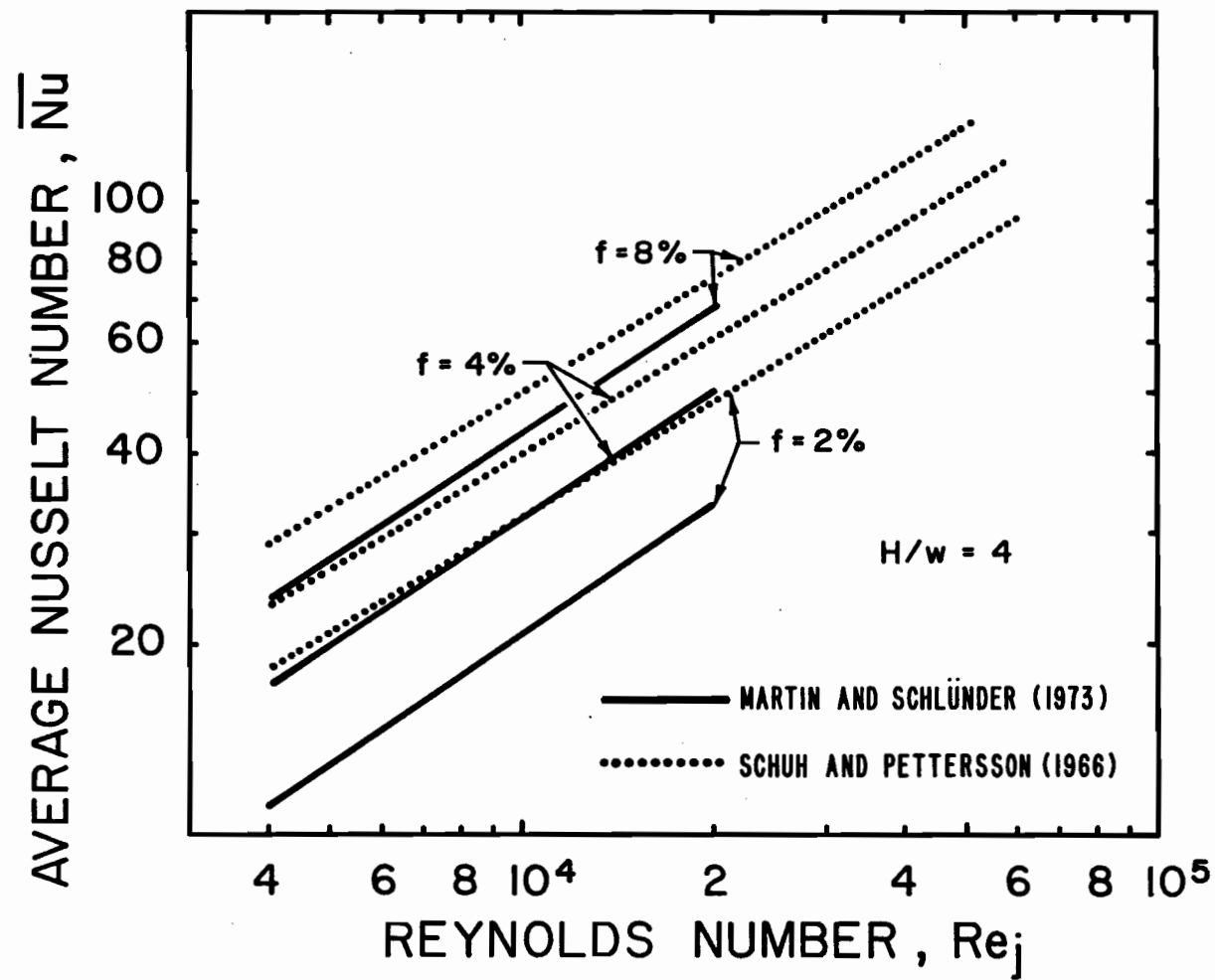


FIGURE 2.4. Effect of Re_j on \overline{Nu} for $f = 2, 4$ and 8% and $H/w = 4$

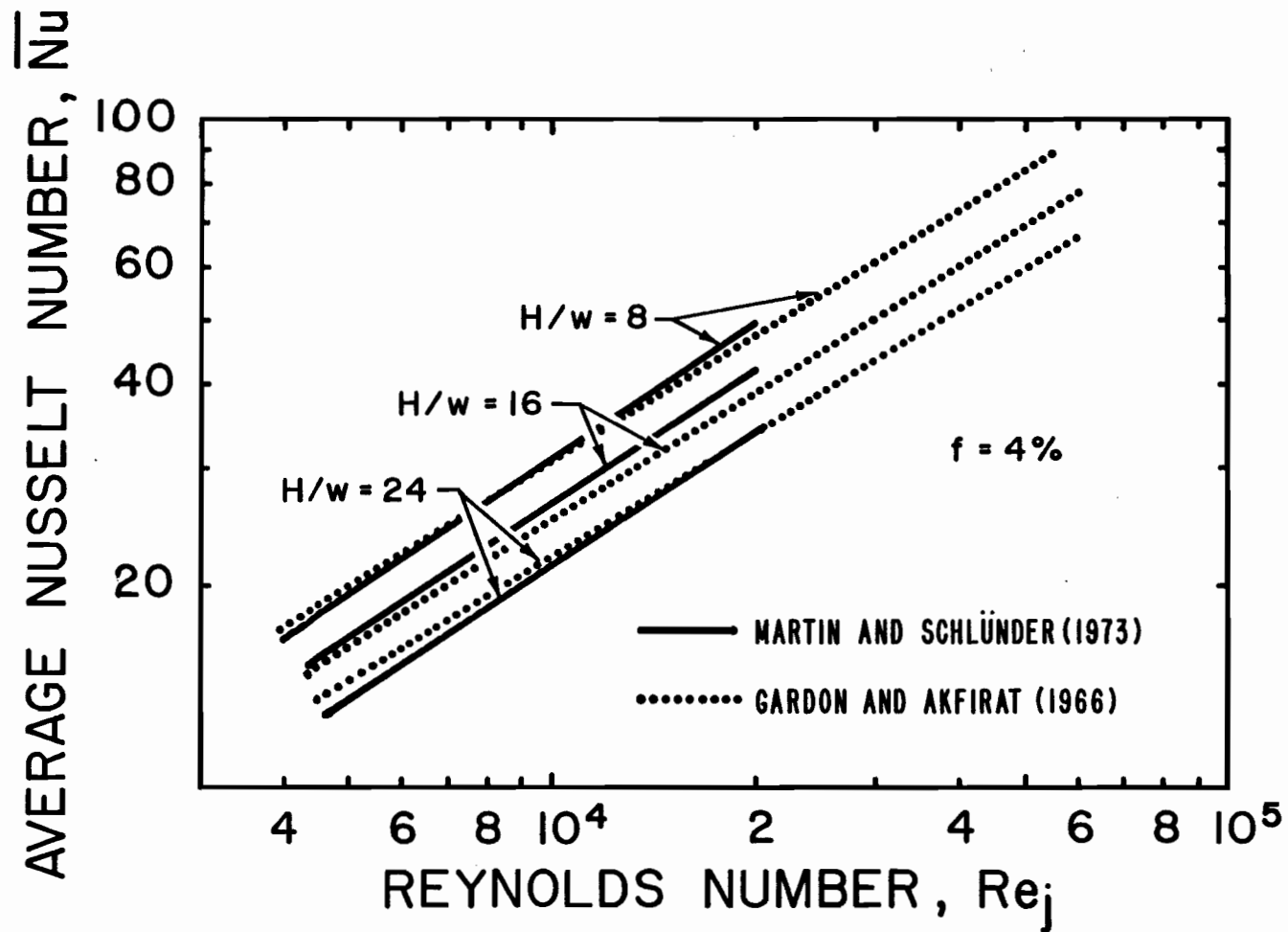


FIGURE 2.5. Effect of Re_j on \overline{Nu} for $f = 4\%$ and $H/w = 8, 16$ and 24

suction on axial and lateral flow was reported by Obot (1981) for a single round jet impinging on a permeable surface. In the exploratory study of Abdul-Wahab et al. the suction velocity was varied between $0.21 < U_s < 0.43$ m/s, for a jet exit velocity of $U_j^* = 13.5$ m/s, equivalent to $Re_j = 5680$, thus producing values of $U_s/U_j^* = 1.5$ and 3.2% . All measurements were made prior to impingement of the jet on the permeable surface. The results show a faster decay of the jet centerline mean velocity with suction than without and a reduction across the jet of the axial fluctuating velocity component. On the contrary, for $Re_j = 38000$, Obot (1981) found that a suction velocity of $U_s = 0.25$ m/s ($U_s/U_j^* = 0.8\%$) at a flat impingement surface subjected to a round jet caused a significant increase in axial mean velocity, no consistent effect on fluctuating velocity and thus some reduction in turbulence intensity in the developing jet region. For quite a high jet Reynolds number, $Re_j = 80000$, a suction velocity of $U_s = 0.25$ m/s ($U_s/U_j^* = 0.42\%$) produced no measurable effects on mean velocity and turbulence in the developing jet region. In the wall jet region application of suction $0.2 < U_s/U_j^* < 0.8\%$ caused both an increase in lateral velocity and a slight decrease in turbulence intensity adjacent to the impingement surface and a decrease in the boundary layer thickness. Both effects result in increasing the velocity gradient at the impingement surface.

With suction imposed on a rotating drum surface to produce values of throughflow velocity that varied up to $U_s/U_j^* = 0.29\%$ for $U_j^* = 52.7$ m/s ($Re_j = 6600$), Baines and Keffer found that the local surface shear stress increased throughout the entire profile by roughly a constant amount, sufficient that the average shear stress increased by 12% . In the wall jet region the maximum lateral velocity measured above the impingement surface was increased slightly by suction.

The data from Obot (1981) and Baines and Keffer (1977) show a qualitatively similar trend as to the effect of suction on lateral wall jet flow, a trend which suggests an enhancement of impingement heat transfer. However no quantitative information is available on this variable of considerable industrial importance.

2.4.2 Heat Transfer Studies

For a laminar impinging jet the effect of suction on momentum and heat transfer at the surface was predicted in computer simulation studies of van Heiningen et al. (1976b) for a slot jet, and by Saad (1976), Huang (1977) and Li (1977) for a round jet. At $H/w = 5$, $Re_j = 100$ and $U_s/U_j^* = 1\%$, the results of van Heiningen et al. indicated a small effect throughout the surface. At $H/w = 8$ and 12 and for $Re_j = 950$, the results of Saad, Douglas and Mujumdar showed that at $x/w = 0$ and $x/w = 1.3$ heat transfer increased by 10 and 30% respectively when compared to the case without suction. With suction, the heat transfer profiles presented by Huang and by Li show similar trends.

For the turbulent case, the effect of suction on impingement heat transfer under a single round jet was studied experimentally by Obot (1975). At $H/w = 6$, $Re_j = 20000$ and 28000 and $0.24 \leq U_s/U_j^* \leq 0.32\%$ the heat transfer rates increased by a constant amount from the stagnation point (10% increase) out to $x/w = 13$ (75% increase).

2.5 Summary

From the review of flow and heat transfer studies of slot impinging jets no information was found as to the effect of geometrical and flow parameters on confined multiple impinging jet systems without spentflow interaction and with uniform spanwise transport characteristics. Also it was found that even

for the case of single impinging slot jet, there has been little attention to the industrially important configuration of a closed system with a confinement surface.

In summary it is noted that in spite of their industrial significance, transport processes under multiple impinging jets have received relatively little attention in the prior literature and that there are distinct shortcomings among the few existing studies. Since mixing of inlet jet fluid with the ambient and interaction of jets with spentflow may cause significant changes in heat transfer rate, the lack of such a study in a confined impingement system is regrettable. Neither has there been any study of multiple slot jets impinging on a permeable surface.

CHAPTER 3

EXPERIMENTAL APPARATUS

3.1 Introduction

An experimental facility was designed to permit high resolution measurement of local heat transfer rates at a permeable heat transfer surface under a set of confined multiple impinging slot jets. The working fluid was air at nearly ambient temperature and the heat transfer was from the heated impingement surface to the impinging jet. The facility was constructed to permit study of the effect of four fundamental parameters; the spacing, nozzle-to-impingement surface; the ratio, nozzle area:impingement surface area; Reynolds number of the jet; and uniform suction at the permeable impingement surface. For characterization of the flow field the design also allowed flow measurements from nozzle exit to impingement surface and pressure profiles at the latter. The flow field in the absence of suction was characterized using an impermeable impingement surface.

3.2 General Description of the Apparatus

The apparatus shown schematically in Figure 3.1 and in a photograph in Figure 3.2 provided control of four general systems: flow of impingement and exhaust air; suction through impingement surface; horizontal and vertical traversing of the impingement surface; and impingement surface temperature control, including the heat flux sensor. Details of these systems are provided in the four sections which follow.

FIGURE 3.1. Schematic Diagram of the Apparatus

1. Honeycomb
2. 100 Mesh Screen
3. Nozzle Plate
4. Side Wall
5. Impingement Surface
6. Current Measurement
7. Voltage Measurement
8. DC Power Supply
9. Heat Flux Sensor
10. Suction Box
11. Impingement Surface Spacing Adjustment
12. Plenum Chamber
13. Screw for Horizontal Traversing
14. Level Table
15. Blower to Induce Throughflow
16. Electrical Heaters: Control Panel
17. Suction Hose
18. Chromel-Constantan Thermocouples
19. Thermocouple Temperature Read-Out
20. Butterfly Valve
21. Main Flow Silencer
22. Air Supply Fan Turbobl原因
23. Inlet Air Silencer
24. Header
25. Multimanometer Panel
26. Air Inlet Filter
27. Bleed Flow Silencer

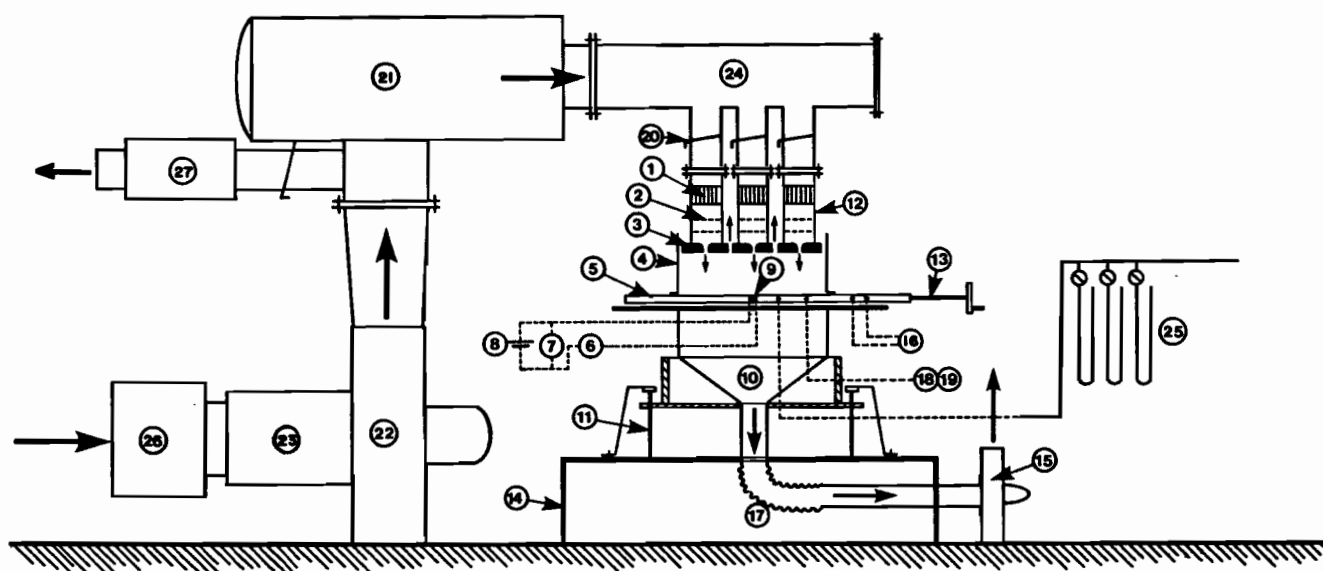


FIGURE 3.1. Schematic Diagram of the Apparatus

FIGURE 3.2. Photograph of the Facility

1. Air Inlet Filter
2. Bleed Flow Silencer
3. Main Flow Silencer
4. Header
5. Plenum Chamber
6. Manometer
7. Impingement Surface
8. Horizontal Traversing System
9. Suction Box
10. Thermocouple Selector Switch
11. Digital Voltmeter
12. Digital Printer
13. Vertical Traversing System
14. DC Power Supply
15. Temperature Controller
16. Two-Pen Recorder
17. Multimanometer Panel
18. Hot Wire System
19. Oscilloscope
20. Suction Pipe
21. Variable Resistor

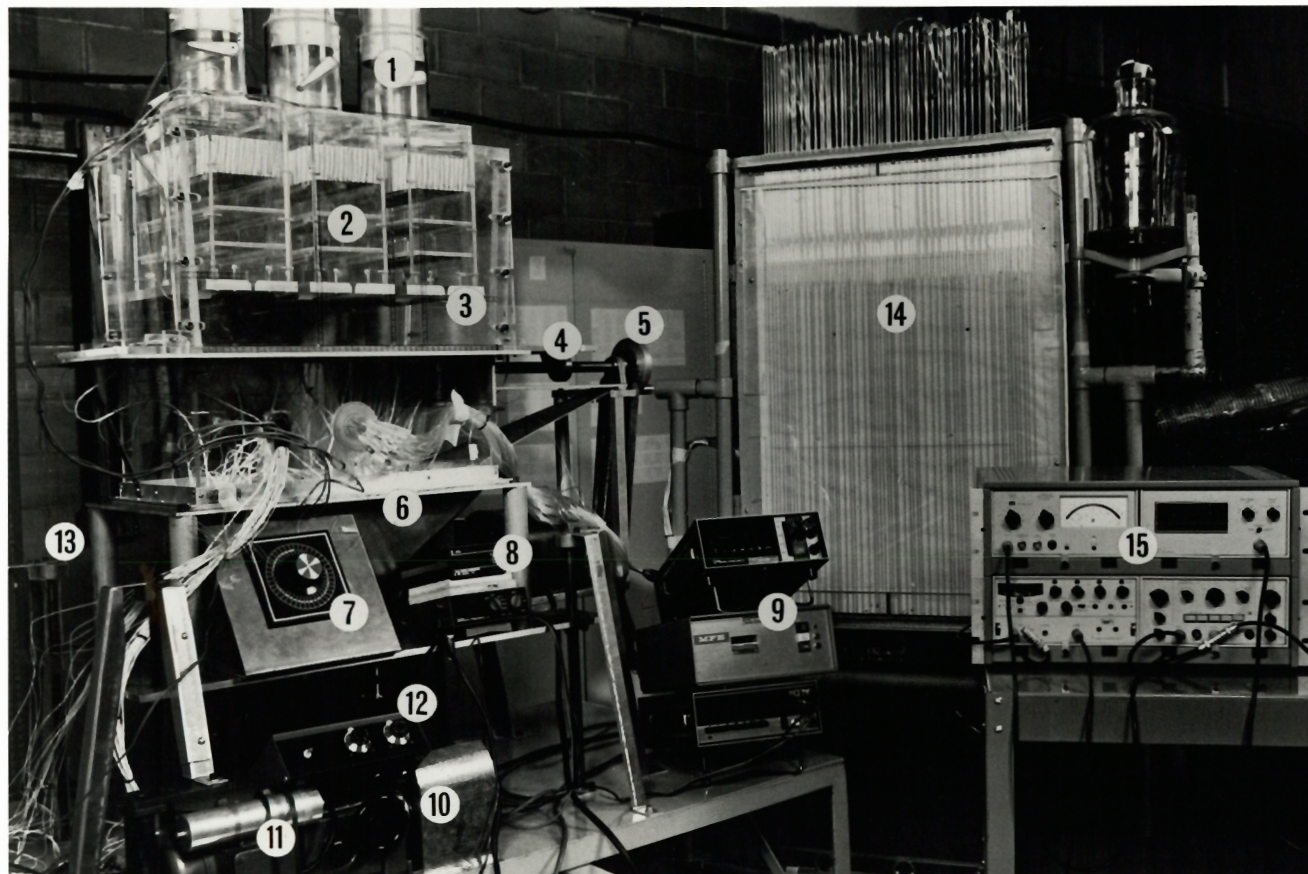


FIGURE 3.2. Photograph of the Facility

3.2.1 Impingement and Exhaust Air System

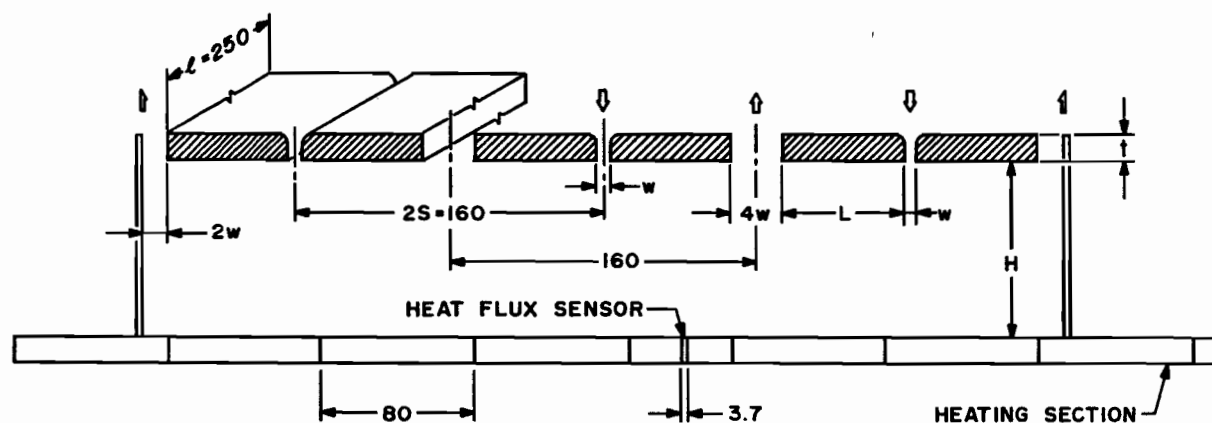
Ambient air passes sequentially through the inlet air filter, silencer, blower, bleed flow control valve with silencer, main flow silencer, cylindrical header plenum chamber, slot jet nozzle assembly (three in parallel), the test section and the exhaust ports, as illustrated on Figure 3.1.

Dust removal was required to prevent accumulation of dirt particles on the impingement surface during runs without suction and was essential to avoid clogging of the porous impingement plate under suction conditions. Therefore the ambient air was drawn into the turboblower through a filter-silencer (North American Mfg. Co., Cleveland, Ohio) with a one micron retention felt-type filter inside a metallic mesh filter element. The intake silencer reduced noise by absorption of objectionable sound frequencies. The capacity of the turboblower was $0.9 \text{ m}^3/\text{s}$ (2000 cfm) at 115% of motor rating, and its differential head 10342 N/m^2 (41 inches of water). The turboblower, with its 15 H.P., 550 Volt/3 phases/60 Hz motor, was mounted on a 900 lb seismic base to minimize vibration. A manually controlled valve provided adjustment of a bleed flow to prevent overheating of the motor for experiments at low flow rate, while a safety stop electric power controller (Cutler-Hamam, Montreal) was set to shut off the motor at an upper temperature limit of around 50°C . Two additional silencers were used, one on the bleed flow line, the other on the main flow line (Acoustex of Canada Ltd., Toronto). The three silencers reduced the overall sound pressure level by 6 decibels, and the maximum weighted sound level was found to be 70 decibels.

Air passed from the main blower discharge silencer through a flanged aluminum header, 200 mm diameter. The header supplied air to three 100 mm O.D., 160 mm long aluminum pipes, welded at 90° to the header at a spacing between centerlines of 160 mm. Each of these pipes contained a manually

operated butterfly valve for control of flow rate to each plenum chamber. These rectangular plexiglass plenum chambers (250 mm deep and 100 mm x 250 mm in cross-section, 250 mm being the length of the slot nozzles) adapted the flow from the 100 mm circular inlet to the 250 mm slot nozzle entrance. Air entering the well aligned plenum chambers passed through a layer of aluminum honeycomb to straighten the flow, then through two 100 mesh screens spaced 50 mm apart to dampen turbulence and generate uniform flow upstream of the nozzle exit. The slot nozzle plate was likewise spaced 50 mm below the second screen as shown in Figure 3.2. The plenum-to-nozzle contraction ratio was sufficiently large (in the range 7:1 to 40:1) so that, combined with the screens, conditions at the nozzle exit were a flow with well damped turbulence and a uniform velocity profile in the spanwise direction of the jet, as documented subsequently.

Aluminum nozzles in five configurations enabled study of effect of the ratio, nozzle area:impingement surface area, termed the percentage open area, from $f = 1.56\%$ to $f = 8.313\%$. While using one set of plenum chambers and hence a fixed spacing (160 mm) between adjacent slot jets, five values of percentage open area, f , were obtained with a single test section by using five sets of nozzle plates of varying nozzle width, w . The nozzles were machined according to the American Society of Mechanical Engineers Standard (1971) for short, elliptic entry, round nozzles, using nozzle hydraulic diameter D_H , in place of pipe diameter. The five sets of 250 mm long, geometrically similar nozzles, 2.5, 3.3, 5.0, 10.0 and 13.3 mm wide, are shown in Figures 3.3 and 3.4. The centerlines of the elliptic nozzles of square exit ports were equidistant, with the width of the latter in most cases set at four times the nozzle width ($4w$) in order to minimize pressure loss through the exit and the length of the straight portion of the nozzle was equal to



ℓ/w	$f, \%$	S/w		Set No	w	t	L
100	1.562	32		1	2.5	7.45	73.75
75	2.083	24		2	3.3	9.9	71.75
50	3.125	16		3	5.0	14.8	67.50
25	6.250	8		4	10.0	29.2	55.00
18.75	8.333	6		5	13.3	38.7	55.00

NOTE: DIMENSIONS ARE IN mm.

FIGURE 3.3. Dimensions of Jet Nozzles

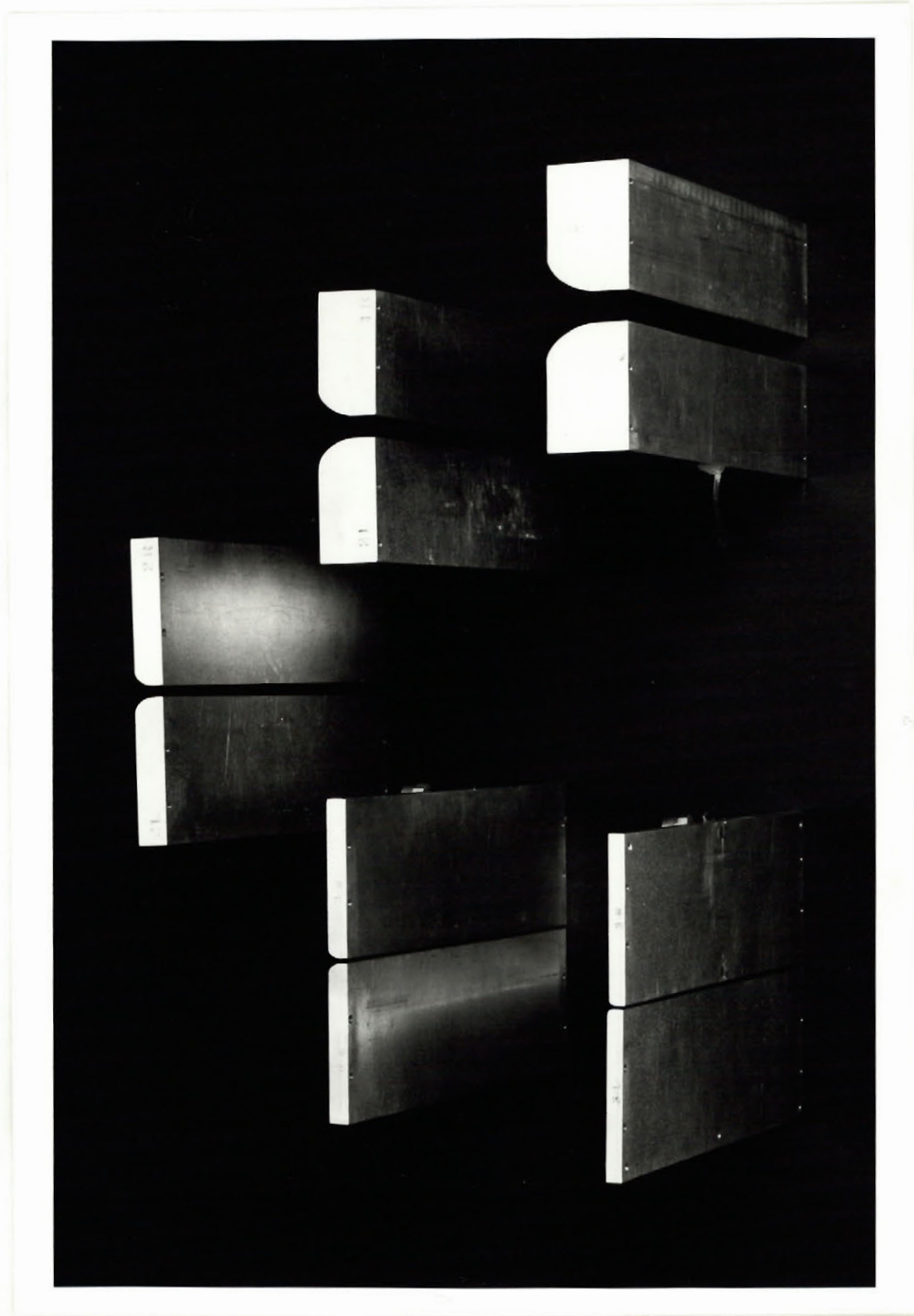


FIGURE 3.4. Photograph of Jet Nozzles

the nozzle width, i.e. $t/w = 1$. The nozzle aspect ratio l/w varied from 100:1 to 18.75:1. These high values of l/w assured two-dimensionality of flow at the nozzle exit over effectively all the span. The pressure difference across the nozzle plate was measured from static taps and the discharge coefficient for each nozzle is shown in Appendix 3. A chromel constantan thermocouple was mounted at the nozzle exit for measurement of jet temperature, T_j .

From the nozzle exit the jet discharged into the test section (480 mm x 250 mm) as shown in Figures 3.5 and 3.6. The test section was composed of four confinement walls and the impingement surface. A key feature of this experimental design was that impingement flow was exhausted through ports located midway between neighbouring jets. Thus symmetrical flow without cross-flow of air after impingement was achieved. The two plexiglass retaining walls prevented the jets from spreading in the transverse direction, thereby maintaining their two-dimensional character, a feature missing from some earlier work. The two end walls, i.e. the confinement walls parallel to the principal axis of the slot nozzles, were located at a position corresponding to the mid-point of an exit port, i.e. the exit ports at each end were half the width of the other exit ports as they accommodated only half the flow of the other ports. For each test case a fine adjustment on the position of each end wall was used to achieve this flow specification. Furthermore, static pressure measurements on the impingement plate were used to control the uniformity and similarity of the three inlet jets. The end walls were provided with a variable area slit that allowed hot wire traversing of the jet flow system. The impingement plate is described in detail subsequently.

3.2.2 Suction Air System

Suction at the impingement surface was obtained by mounting a permeable

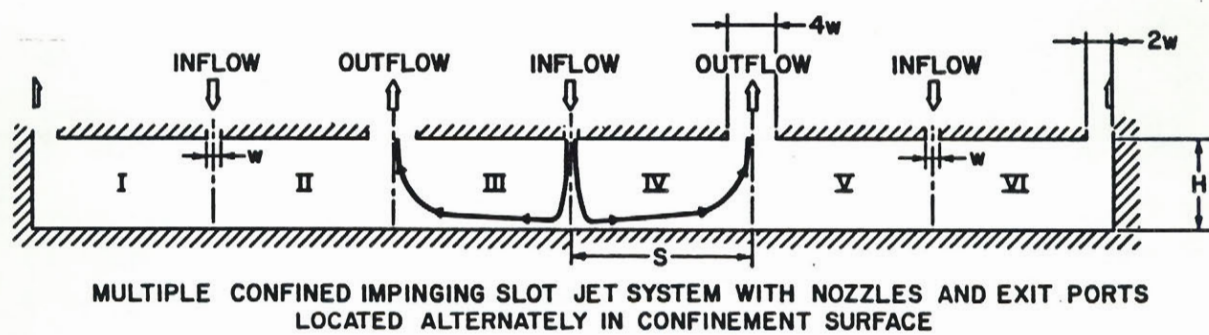


FIGURE 3.5. Schematic Diagram of Test Section

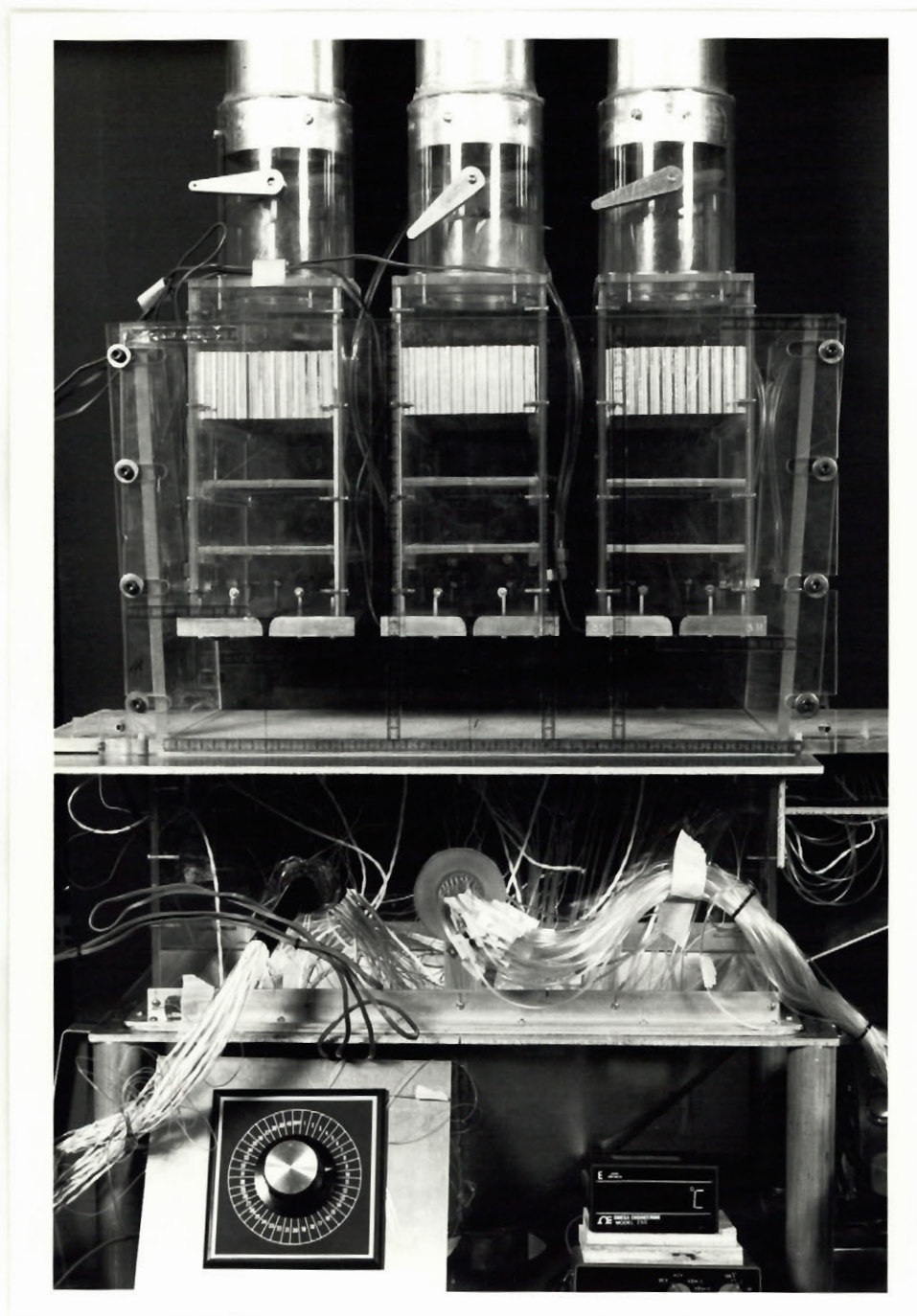


FIGURE 3.6. Photograph of Test Section

impingement plate on a suction box. The upper part of the suction box was made of plexiglass, 250 mm high and 480 mm x 250 mm cross-section, as shown in Figure 3.7. The lower part of the suction box, the diffuser section, was made of aluminum sheet metal. Both parts of the suction box may be seen in Figures 3.1 and 3.2. The upper edge of the suction box, which provided an air-tight mounting for the plate, was framed flush with 50 mm wide x 4 mm thick aluminum, thus providing additional support to the test section and retaining walls. Each lead wire from the instrumented lower surface of the test plate traversed the wall of the suction box through an air-tight pin connection. Similarly a number of slits were machined on each 480 mm side of the suction box to avoid damage to the lead wires during horizontal traversing of the impingement plate. Provision was made to enclose these slotted sides of the suction box to prevent ambient air from entering. This was achieved by enveloping the sides with thick nylon film. Thermocouples at various locations in the suction box indicated the temperatures of the through air, as will be described subsequently.

Air withdrawn from the suction box through the flexible hose, required to permit vertical positioning of the impingement surface-suction box unit, passed successively through an orifice flow meter, centrifugal blower, air intake tank and rotary blower with silencer. The high pressure head, rotary blower (Iesson Electric Corporation), powered by 10 H.P., 550 Volt/3 phase/60 Hz motor, provided the higher suction flow rates. It was connected in series through a 200 litres air intake tank with a centrifugal blower (North American Co., Cleveland) powered by 3 H.P., 550 Volt/3 phase/60 Hz motor. A gate valve controlled the intake mass flow ratio between ambient air and air from the centrifugal blower. Another gate valve, located upstream of the centrifugal blower, was used to control low suction flow rates when the



FIGURE 3.7. Suction Box

rotary blower was not operated. The suction flow rate was determined from a calibrated orifice meter installed in the suction line (76 mm diameter PVC pipe), 20 pipe diameters downstream from the suction box. Depending on the range of suction flow, the pressure drop across the orifice was determined by either a Meriam fluid, U-tube manometer or by a micromanometer (Wilh. Lambrecht KG Göttingen - Type 655).

3.2.3 Vertical and Horizontal Traversing of the Impingement Surface

Obtaining a complete heat transfer rate profile in the direction cross-wise to the fixed position nozzle slots was achieved by horizontal traversing of the impingement surface, with its single heat flux sensor as shown in Figure 3.8, over a lateral distance of 320 mm. Horizontal traversing was aided by mounting teflon ribbon on the 4 mm wide aluminum support strips which, as noted in the previous section, were attached to the two 480 mm edges of the suction box. One end of the impingement plate, the right-hand end as seen on Figures 3.1 and 3.2, was connected to a screw rod supported on an inclined beam fixed in turn to the suction box. The screw rod was mounted to a gear driven through a chain by 1/3 H.P. variable speed AC electric motor. The screw rod motion was controlled through the motor by means of a specially designed variable transformer with an on-off timer option. Traversing distance and stopping time at a particular position were thereby controlled. A stopping time of around 30 minutes was found to be sufficient to ensure steady state conditions of the heat flux sensor. A manual traversing option, used particularly during the qualification runs, was obtained by providing easy disengagement of the chain from the electric motor. The location of the sensor was read from scale attached to the side wall.

Variation in one of the fundamental parameters of this study, the im-

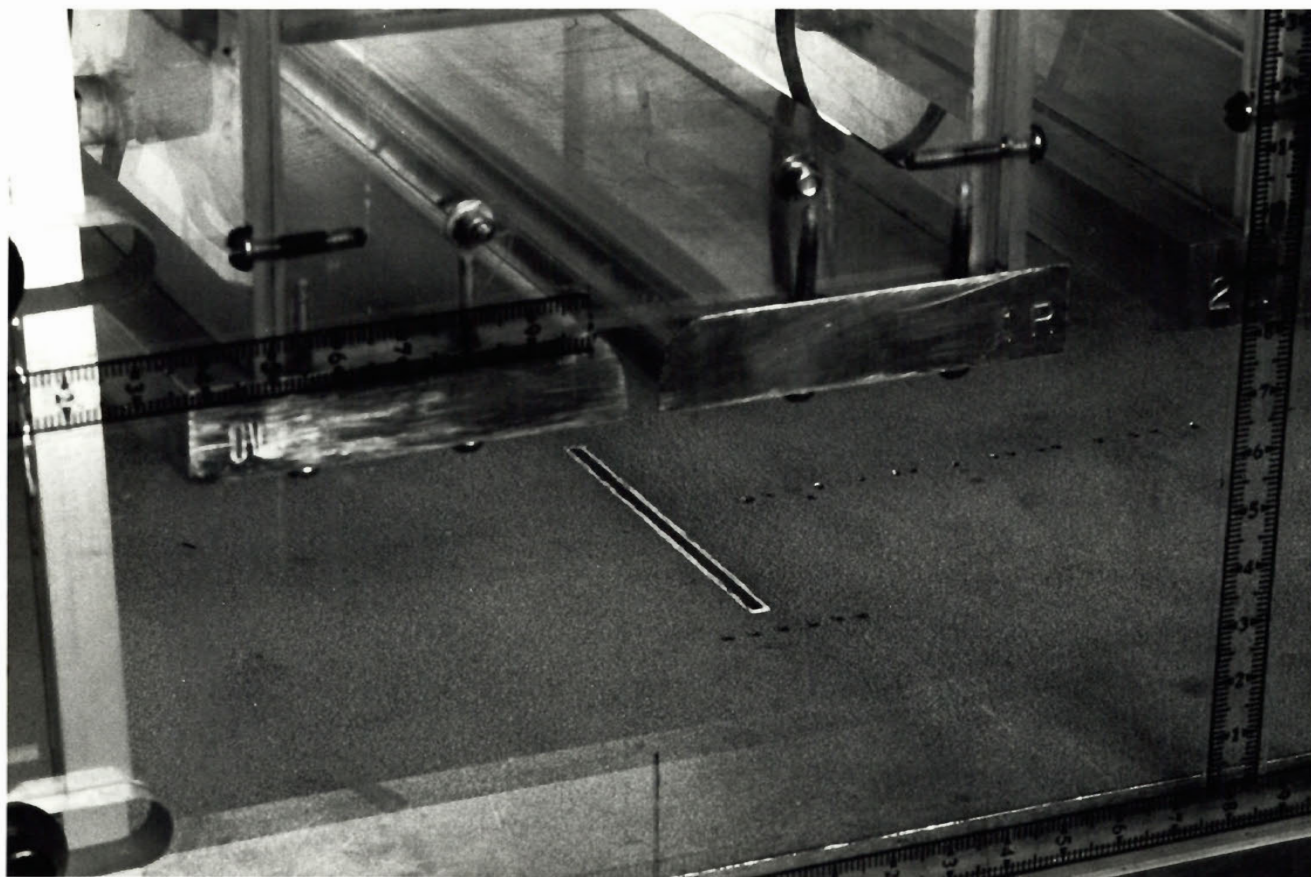


FIGURE 3.8. Impingement Surface with Heat Flux Sensor

pingement surface spacing from the jet nozzle, was achieved by providing a gear mechanism for adjusting the vertical position of the impingement surface-suction box unit under a multiple jet nozzle assembly maintained at a fixed position. This vertical positioning mechanism was designed to achieve the range of impingement surface spacing, $4 \leq H/w \leq 24$, for all widths ($w = 2.5$ to 13.3 mm) of nozzles used. The suction box supporting the impingement plate was mounted on a supporting plate, Figure 3.6, which in turn was mounted at its four corners on screw rod. Each screw rod was installed on a gear supported by two copper rings fixed on a level table. The four gears were controlled by a main gear through a chain. In turn the main gear was powered by a bidirectional variable speed, $1/3$ H.P., 12 lb-in torque (0-1800 RPM) electric motor. The motor was actuated by a double pole, double-throw switch. The main supporting table was accurately leveled until the impingement surface was parallel to the jet nozzle assembly. Each of the four table wheels were mounted on a screw rod for leveling. The impingement surface spacing was monitored by means of an accurate scale on the retaining walls.

3.2.4 Impingement Surface Temperature Control

As the overall experimental design involved determination of steady state impingement heat transfer profiles for the case of the isothermal boundary condition, a system was required for achieving a uniform isothermal impingement surface temperature under conditions of a highly non-uniform heat transfer at this surface. For impingement air at ambient temperature this objective was achieved by provision of an impingement plate electrical heating system sectioned into twelve independently controlled units. The AC power to each of these twelve plate heaters was controlled independently by a proportional controller (Model 872, RFL Industries Inc., Boonton, N.J.).

Each heater consisted of a single length of 24 AWG (0.5 mm diameter) Inconel wire, electrically insulated with a magnesium oxide layer, then shielded with a stainless steel sheath (O.D. 1.0 mm). This heater wire was laced back and forth in grooves machined in the back surface of impingement plate as shown in Figure 3.7. The end of each heater wire, after being stripped, was silver welded to 24 AWG single string copper leads, then placed inside a ceramic tubing for insertion into the groove. For each heater wire one lead was connected to a variable resistor, then to the ground bus bar, while the other lead was connected to another bus bar. A proportional controller connected to these bus bars closed the circuit. The controller, when rated for 115 AVC to a load higher than 100 watts, was specified to control the temperature within $\pm 0.1^{\circ}\text{C}$. The control circuit resistance was therefore increased by including an extra, variable (dummy) resistance to bring the controller power output to at least 100 watts at the lower impingement flow conditions. A thermistor located in a hole drilled to about 0.2 mm from the impingement surface closed the feedback loop of the controller. The thermistor semiconductor bead was located in a glass tubing, 0.8 mm diameter. Its two electrically insulated lead wires, 150 mm long, were connected to the controller unit. The negative temperature coefficient of resistance thermistor used operated between 30,000 and 300 ohms over 10°C to 130°C . In the proportional temperature controller used, the transmitter, controller and final control element comprise one integrated electronic circuit as shown in Figure 3.9. A temperature variation actuates the bridge system, causing a variable gain amplifier to supply a proportional signal to a Triac (bidirectional thyristor) firing circuit, thus ensuring proper Triac turn-on time. The Triac was mounted on a heat sink channel to assure good heat dissipation. Thus the number of integral cycles supplied to the heating wire was proportional to

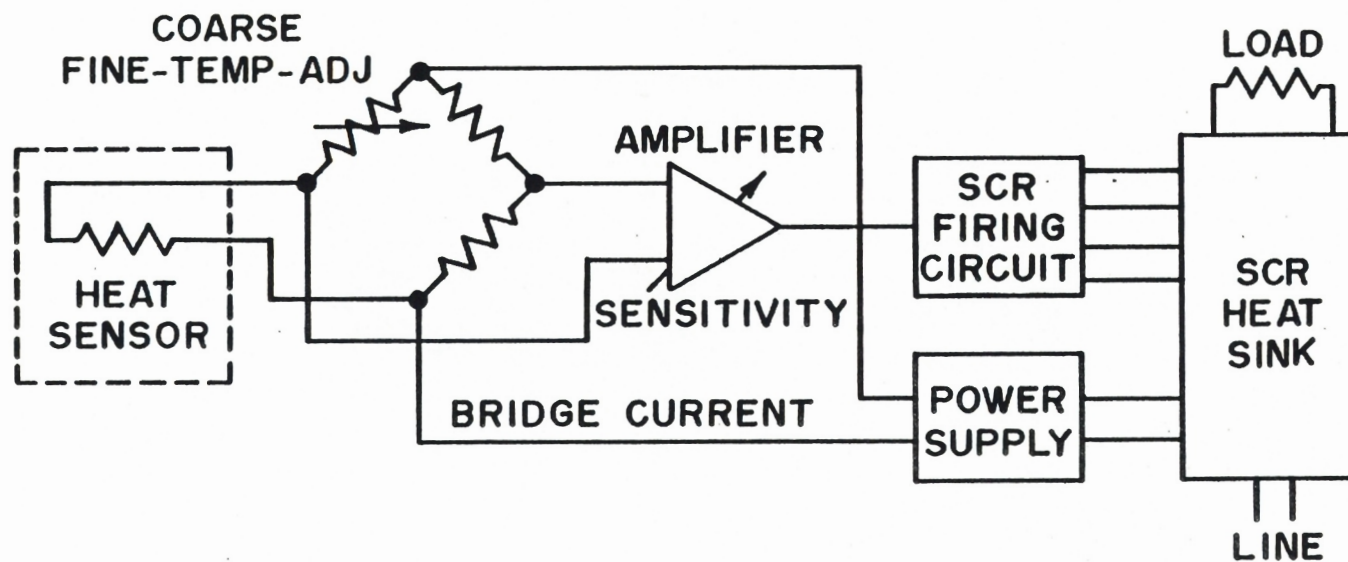


FIGURE 3.9. Schematic Diagram of Temperature Controller

the temperature deviation from the set point. The power switching Triac was pulsed into conduction as the line voltage passed through zero, thereby eliminating current surges which cause radio frequency interference (RFI). Radiated RFI could falsely trigger electronic instruments and computers located near the generating source.

While the 12-element electrical heating and control system described above served to maintain the required isothermal boundary condition for heat transfer at the impingement surface, a much more precisely controlled heat flux sensor was located centrally in the spanwise direction of the impingement plate, insulated from the plate. While details of the heat flux sensor design are presented in Section 3.4, the temperature control aspect is described here along with that for the entire impingement surface. The temperature of the sensor, 78.5 mm x 3.7 mm, was regulated manually by a variable voltage DC power supply (Model LP-410A-FM Lamda Electronics, Melville, L.I., N.Y.). The sensor heater, a 78.8 mm length of the same 1.0 mm O.D. insulated Inconel wire as used for the remainder of the plate, was located inside a single groove on the back surface of the sensor. One end of the heater was connected to a high precision, low resistance shunt (Leeds & Northrup Co.) through copper leads similar to those noted earlier, then to the ground bar. The other end was connected to the other bus bar, and the DC power supply connected to the bars. The sensor heater power was determined from the voltage drop across the heater and across the precision shunt in the heater circuit as shown in Figure 3.10.

3.3 Flow Measurements

The following two sections describe the instrumentation and procedures used for measuring mean velocity and axial turbulence for the jet and for

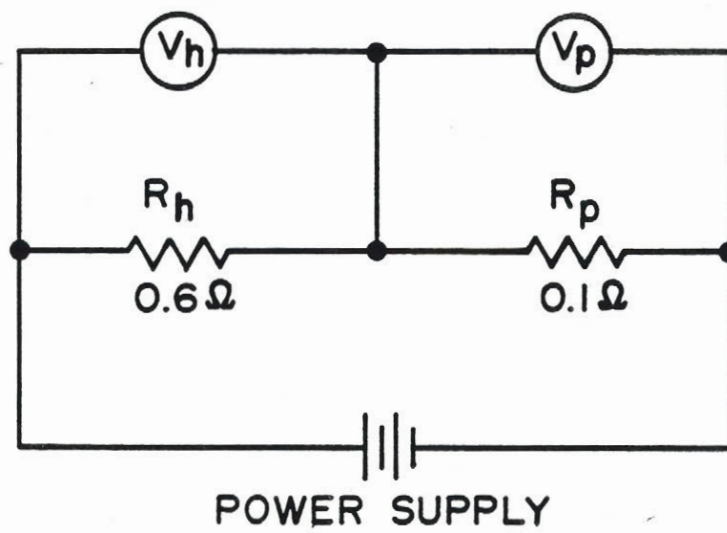


FIGURE 3.10. Heating Circuit for the Heat Flux Sensor

mean static pressure along the impingement surface.

3.3.1 Velocity and Turbulence Measurements

Turbulence measurements were made using the following DISA 55M System: a constant temperature anemometer (DISA 55M01), an electronic linearizer (DISA 55D10), a DC digital voltmeter (DISA 55D31), a root-mean square voltmeter (DISA 55D35) and a Tektronix 466 dual beam storage scope. The probe was mounted on a (DISA 55H21) probe holder which was in turn screwed concentrically to a 20 mm diameter tube (probe support) entering the test section from the 250 mm long end wall. The probe was mounted on a manual traversing mechanism (United Sensor and Control Corporation, Watertown, Mass.), with Vernier-type graduations, in increments of 0.5 mm. The traversing unit could rotate to any angular position. Both Vernier and protractor were friction loaded with adjustable springs and balls for easy accurate rotation to any angle. The unit was mounted on a heavy tripod which, as it was designed for use for high speed photography, was sufficiently robust to minimize probe vibration.

A standard (DISA 55P04 and 55P14) right angle, single wire probe was used to measure axial mean velocity (U) and fluctuating velocity (u') along the jet centerline and downstream of the nozzle exit. The gold-plated hot wire probes, 1.2 mm long and 5 μ m diameter, caused minimal disturbance to the flow around the sensitive part of the wire. Integration times for the mean voltages were 10 seconds, while the RMS voltmeter was set at a time constant of three seconds. Standard procedures were followed to obtain the linearized signal from the single wire probe. The calibration of each hot wire probe was verified after each test run. For the linearized system, mean velocity and axial fluctuating velocity component were calculated from

$$U = E/S_o \quad (3.1)$$

$$u' = (\overline{u^2})^{0.5} = (\overline{e^2})^{0.5}/S_o \quad (3.2)$$

where S_o is the sensitivity factor determined experimentally from calibration of the hot wire. The probe was calibrated in situ on the jet axis at 1 mm from the exit plane of the ASME nozzle, which generated a flat mean velocity profile and low turbulence level. This calibration was done on the basis of Pitot tube measurements at corresponding values of jet flow rate. The constant temperature anemometer was operated at an overheat ratio (the difference between operating and cold probe resistance values, divided by the latter value) equal to 0.8. The thermal stability of the electronic equipment was maintained by allowing the units to remain powered during the course of the experimental work even when the instruments were not in use. The calibration of the hot wire was done at steady state air jet temperature which was around 10°C higher than ambient air.

3.3.2 Static Pressure Measurements

Static pressures were measured with 1 mm O.D. stainless steel tube (0.76 mm I.D.) pressure taps which were spaced 5 mm apart in the streamwise direction along the midspan centerline of a plexiglass impingement plate built for the purpose of mapping impingement surface pressure profiles. At one streamwise location, close to the mid-point of this impingement plate, 10 static taps were located in the spanwise direction, i.e. along a line at 90° to the other 38 taps. The spanwise pressure profile was obtained at various streamwise locations by horizontal traversing of the plate. The pressure from the static taps through tygon tube was measured by two Statham

unbonded strain gauge differential pressure transducers (range 0-6.9 and 0-1.1 KN/m²). Both units were equipped with calibrated zeroing bridge. A Data Precision Inc. (Model 3400, Waterfield, Mass.) digital voltmeter was used to read this pressure transducer. A 48 port scanivalve (Scanivalve Corp., San Diego, Calif.) facilitated switching between the static pressure taps.

The heat transfer impingement plate was also equipped with 64 taps, 1 mm O.D. stainless steel tube (0.76 mm O.D.), spaced from 5-7 mm apart (depending on the location of heating wire) in the streamwise direction along the midspan centerline of the plate, and was built for the purpose of monitoring pressure profile before and during the heat transfer measurements. Each tap was connected to a manometer leg, while the other leg of each U-tube was connected through a manifold to the manometer fluid supply bottle. The 64-branch multimanometer panel, Figure 3.11, was mounted on a variable angle inclined manometer board to allow greater precision at low pressures. During heat transfer experiments the static pressure profile on the impingement surface was continuously displayed on this inclined multimanometer panel.

3.4 Heat Transfer Measurements

The following three sections provide descriptions of the porous plate, the instrumentation, and procedures used for measuring temperature and heat flux distribution along the impingement surface.

3.4.1 Porous Plate

The 10 mm x 760 mm x 250 mm plate (Arrow Sintered Products Company, Forest Park, Illinois) was produced by vibrating spherical particles of

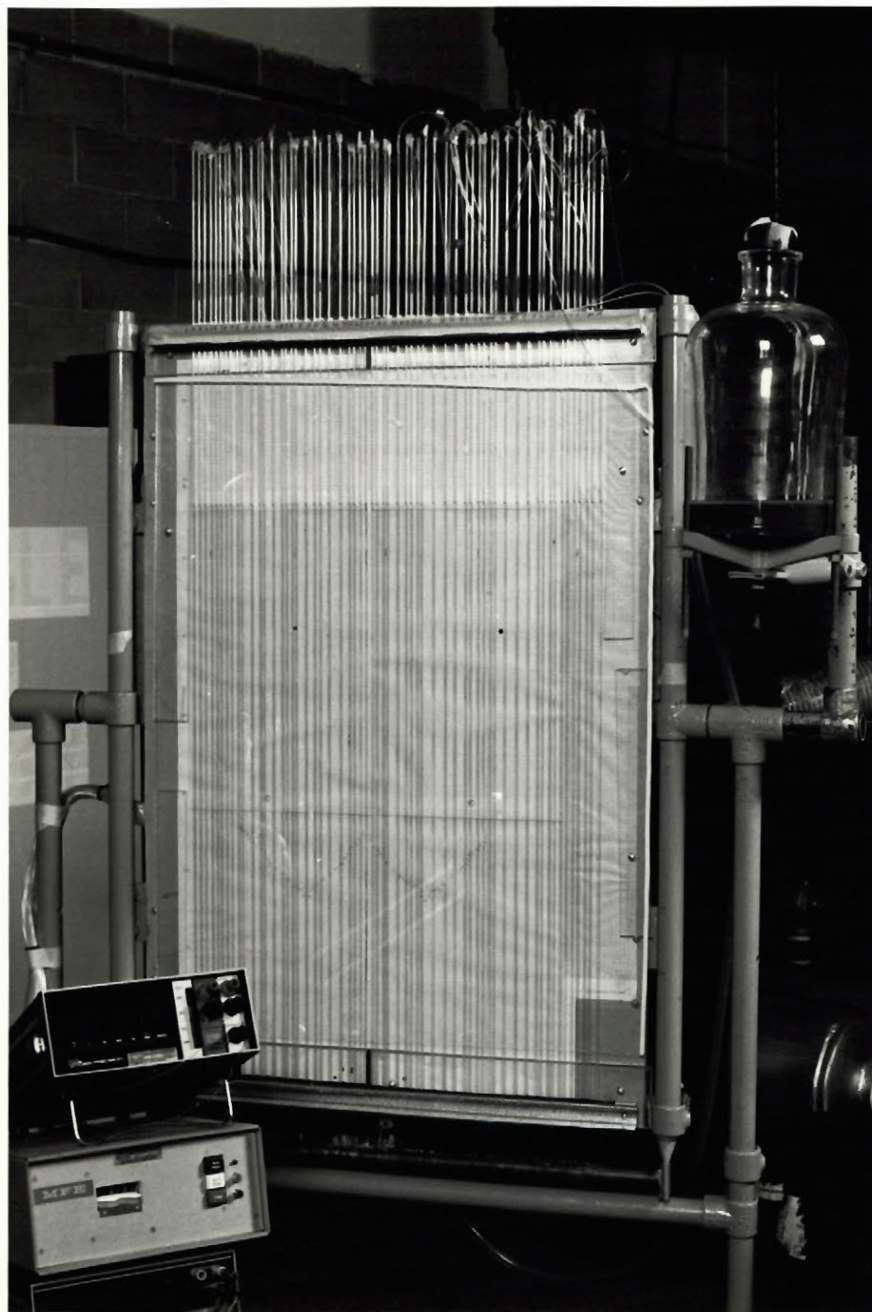


FIGURE 3.11. Multimanometer Panel

copper coated with tin (90 Cu - 10 Sn) into a mold, then sintering to bond all particles into a bronze plate of uniform porosity and excellent strength. The porosity of the plate was approximately 45%, its density, $520.4 \text{ kg}_m/\text{m}^3$. The controlled porosity structure matrix gave uniform thermal properties. The particle size distribution was controlled by selective screening to eliminate both the larger particles which would cause a rough surface, and the very fine particles which tend to agglomerate during the sintering process. The particle diameter before sintering ranged from 0.020 to 0.08 mm, with an average diameter of 0.05 mm. The plate surface roughness, measured by 0.127 mm radius stylus, was found to be 1.25 to 5 μm RMS which was found to be lower than the critical roughness. With a statistically small number of exceptions, the particles are aligned so that the crests of particles are in the same plane. To the touch the surface feels smooth.

In summary the porous plate may be described as follows:

Size: 10 mm x 760 mm x 250 mm

Composition: Special grade bronze filter made from 0.02 to 0.08 mm spherical sintered bronze particles.

Surface Finish: 1.25-5.00 μm (RMS) measured with a 0.0127 mm radius stylus.

Uniformity of permeability is an important requirement in the study of phenomena affected by normal throughflow. Permeability measurements on the plate were made before and after its instrumentation and installation. The suction air flow system was operated on 50 mm^2 square area of the plate by sealing the remaining areas on both faces with plexiglass board. The flow rate in the suction system through that 50 mm^2 spot and the pressure drop across the plate was measured. These measurements provided the value of the local resistance to flow through the test area. Permeability maps were therefore constructed by making measurements on different spots over the

surface of the plate. Similar permeability variation measurements made after the plate was instrumented with thermocouples and heater wires produced similar results. The permeability of the instrumented plate was found to be uniform within $\pm 10\%$.

3.4.2 Temperature Measurements

All temperature measurements on the impingement plate were made using 36 AWG Chromel-Constantan (OMEGA Type E) thermocouples (Figure 3.12). All thermocouples were brought to a manual selector switch (Omega Engineering, Stanford, Conn.) for read-out. The thermocouples were made sufficiently long so that the thermocouple wire itself could be used for the connection to the selector switch. To avoid introducing sharp temperature gradients in any of the thermocouples they were all thermally guarded with teflon tubing. The entire thermocouple circuit used a single electronic ice point compensator built in the digital temperature read-out, Omega Model 250. Impingement surface thermocouples were epoxied into 1.0 mm diameter holes precision drilled from the back surface of the plate to within 0.2 mm of the top impingement surface. These thermocouple temperatures were taken to be the plate surface temperature. These thermocouples were installed by partially filling the holes with a high thermal conductivity epoxy resin using a hypodermic needle, then inserting the thermocouple to the bottom of the hole. This procedure resulted in a small collar of epoxy squeezing up around the thermocouple at the plate back surface. Examination of every installation from the top impingement surface revealed no case of bleeding through the epoxy.

The 24 AWG Inconel heating wire, shielded with stainless steel and insulated with magnesium oxide, was imbedded in grooves spaced at 5 mm (except in the sensor region) on the lower surface of the plate. Both ends of each heater were stripped for silver soldering to the 26 AWG copper leads to the

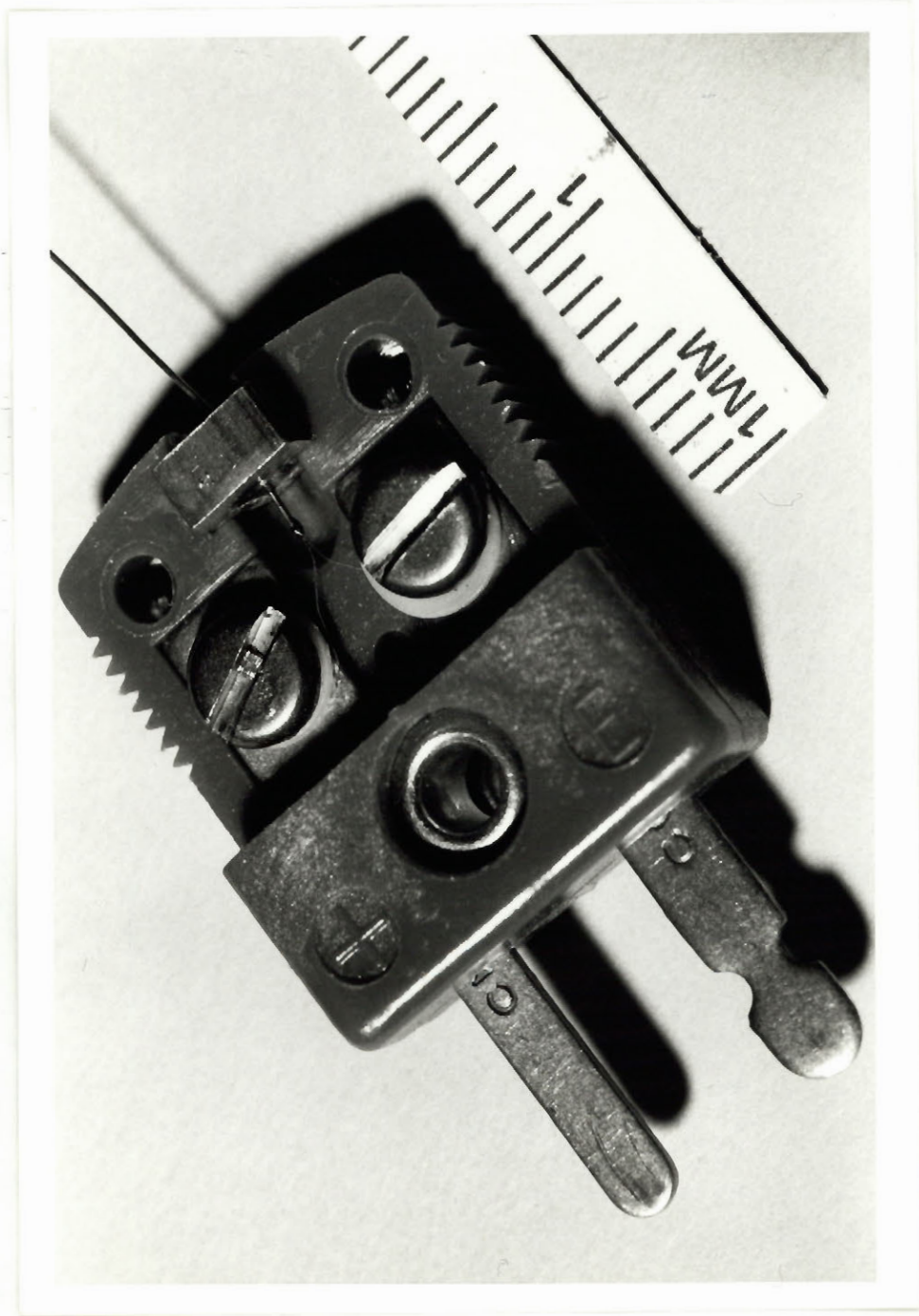


FIGURE 3.12. 36 AWG Chromel Constantan Thermocouple

temperature controller. A 0.3 mm thick layer of teflon ribbon was inserted in the groove on top of the wire, thereby reducing heat dissipation while also securing the wire in place.

3.4.3 Heat Flux Measurements

For determination under multiple slot jets of the heat transfer profile in the streamwise direction where this profile is highly non-uniform, one design would be installation of a large number of small heat flux sensors in an impingement surface which is fixed with respect to the jets. An alternate design would be to construct an impingement surface with a single, high precision heat flux sensor but with provision for traversing the impingement surface in the streamwise direction with respect to the jets, i.e. in the direction 90° to the length of the slots. The latter design, a simple and better alternative, was used in the present study. Traversing of the impingement surface in the streamwise direction was carried out in a stepwise manner, i.e. with the surface being held at each desired location for a period sufficiently long that steady state temperature conditions were obtained before measurements were made and the surface traversed to the next position.

The heat flux meter (Figures 3.13 and 3.14), the central feature of the design, comprised the 13th separately heated section of the porous bronze impingement surface, but differed from the other 12 heated sections in that it was thermally insulated from the surrounding plate, was instrumented so that the electric power dissipated by heat transfer from it could be measured precisely, and was much smaller, i.e. sufficiently small to achieve the objective of measuring a streamwise local value of the highly non-uniform heat flux. The transverse length of the heat flux sensor was set at 78.5 mm, i.e. to cover about the central one-third of the nozzle spanwise dimension (250 mm)

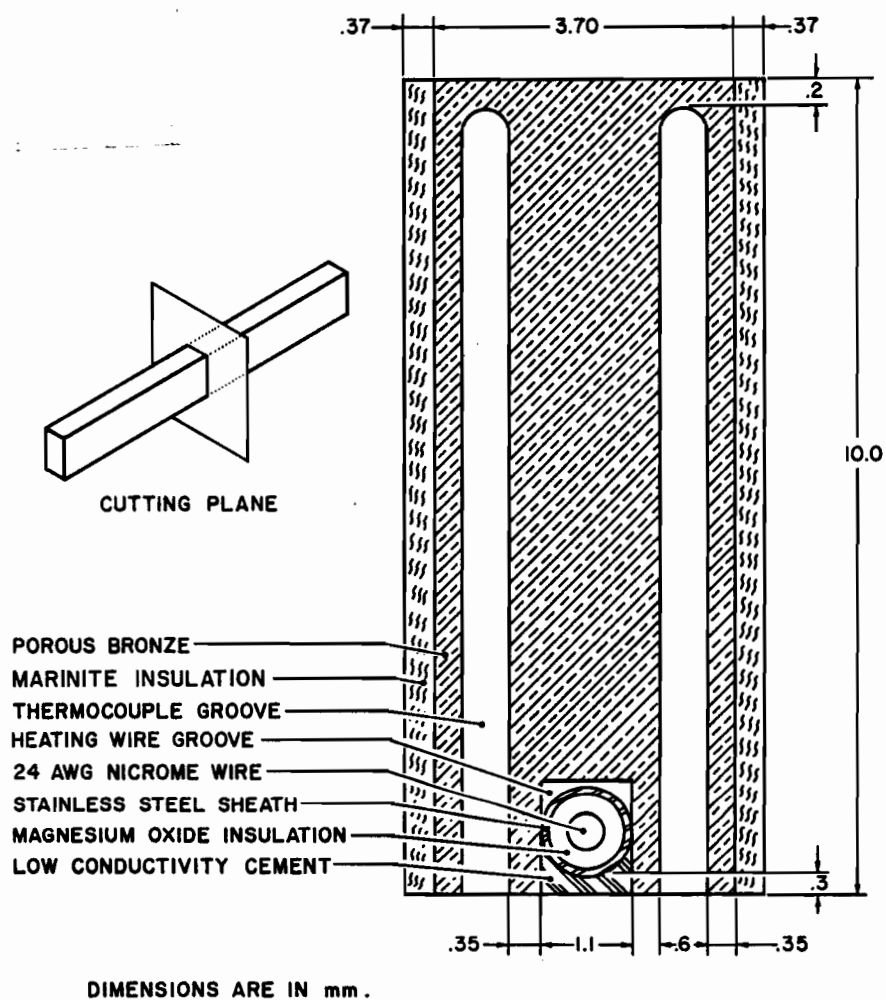


FIGURE 3.13. Section through Porous Bronze Heat Flux Sensor

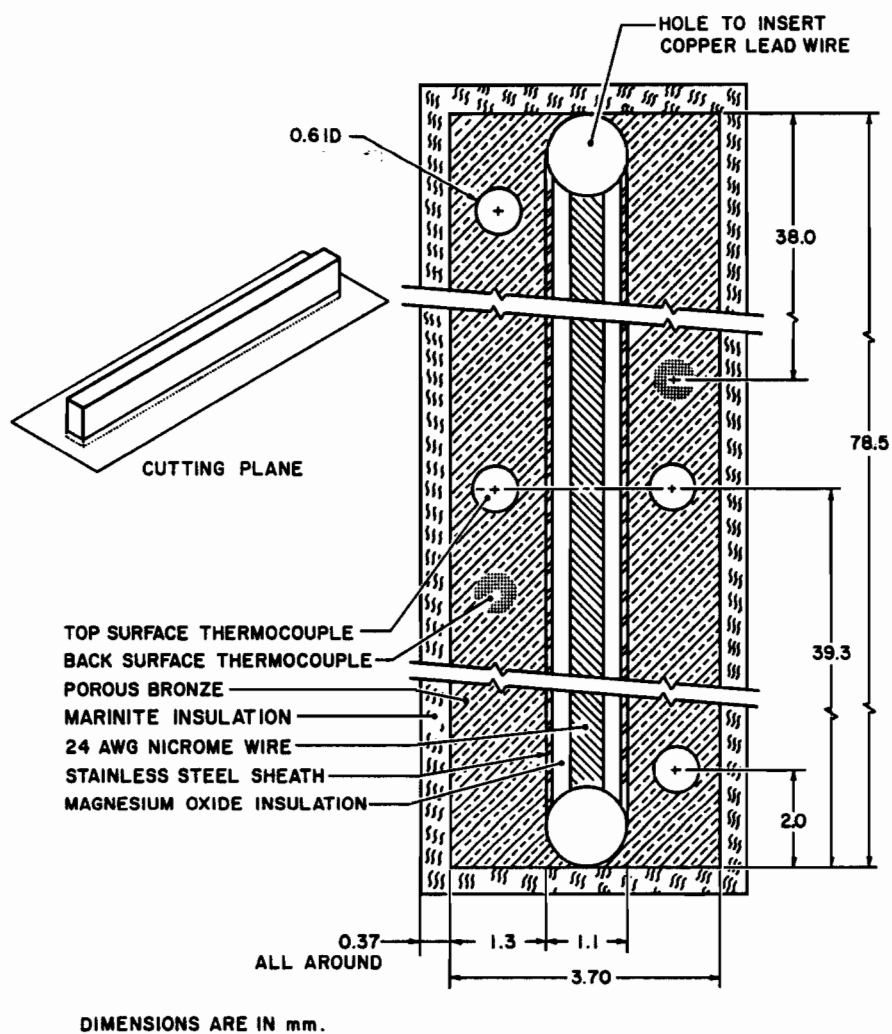


FIGURE 3.14. Section through Porous Bronze Heat Flux Sensor

of the impingement surface. Measurements of static pressure in the spanwise direction confirmed that this length of the sensor was such that it did not approach the wall effect region adjacent to the 480 mm length side walls.

Determining the width of the sensor was much more difficult, as this dimension involves choice of an optimum dimension between conflicting requirements. Thus the narrower the sensor, the closer the approach to a true local value in the streamwise direction of heat flux. However, the narrower the sensor, the greater the percentage cross-sectional area of the porous bronze sensor that is blocked by the electric heating wire, and the less typical the sensor is the porous bronze impingement surface of which it is meant to be a representative element. In order to make the best choice of width of the sensor the two-dimensional heat conduction partial differential equation was solved for various values of sensor width (see Appendix 4) with the appropriate boundary conditions.

The maximum temperature variation across the lateral width of heat transfer surface of the sensor (over the entire range of the experiments) by four thermocouples, located as shown in Figure 3.14, was found to be 0.1°C . The temperatures of the impingement surface varied by at the most 0.1°C from the sensor temperature, thus assuring a very close approach to the constant temperature boundary condition and minimizing driving force for lateral heat conduction between the sensor and the plate. Lateral heat transfer by conduction between the sensor and the plate was further reduced by thermally insulating the sensor with 0.37 mm of Marinite-36 asbestos cement (Johns Manville Ltd., Montreal) as shown in Figures 3.13 and 3.14.

For experiments without throughflow (which represents more than 90% of the experimental program) the heat loss from the grooved lower surface of the sensor was minimized by mounting a 250 mm x 100 mm x 10 mm sheet of

Marinite-36 asbestos cement (Johns Manville Ltd., Montreal) to cover the heat flux sensor and adjacent plate. The temperature of the grooved surface of the sensor was measured from two thermocouples (Figure 3.14) epoxied into a 0.5 mm deep groove and likewise, two thermocouples were inserted at the back surface of the marinite insulation. Thus the heat loss from this face for experiments without throughflow could be calculated using the known thermal conductivity of the marinite. For experiments with throughflow, the marinite board was removed and the heat loss convected by the through air from this face was estimated.

Assembly of the heat flux sensor into the corresponding slot machined in the test plate shown in Figure 3.15 was carried out with great care to assure smoothness of joints. Various methods of reworking and finishing small irregularities in the porous bronze surface established that the porosity of the plate was almost unaffected by mild compressive working provided there is no shearing of the surface. Thus minor irregularities around the sensor after assembly in the plate were "ironed out" using a polished steel roller without affecting the local permeability. In the final step the top irregularities of the teflon insulation gap were filled with plastic putty and shaved flush. The final joint lines could not be detected by touch.

The heating circuit shown in Figure 3.10 consisted of an Inconel heating wire ($R_h = 0.6 \Omega$) embedded in the heat flux sensor and a precision resistance ($R_p = 0.1 \Omega$). A variable DC power supply Lamda LP-410A-FM (Manville, L.I., N.Y.) was manually adjusted to achieve the desired sensor surface temperature. The precision resistance, R_p , was used for calculation of the current, the voltage, V_p , being measured by a 5.5 digits multimeter, Model 3500 (Data Precision, Wakefield, Mass.). The voltage drop, V_h , across the heating wire, R_h , was measured by a 3.5 digits multimeter, Model 175 (Data Precision).

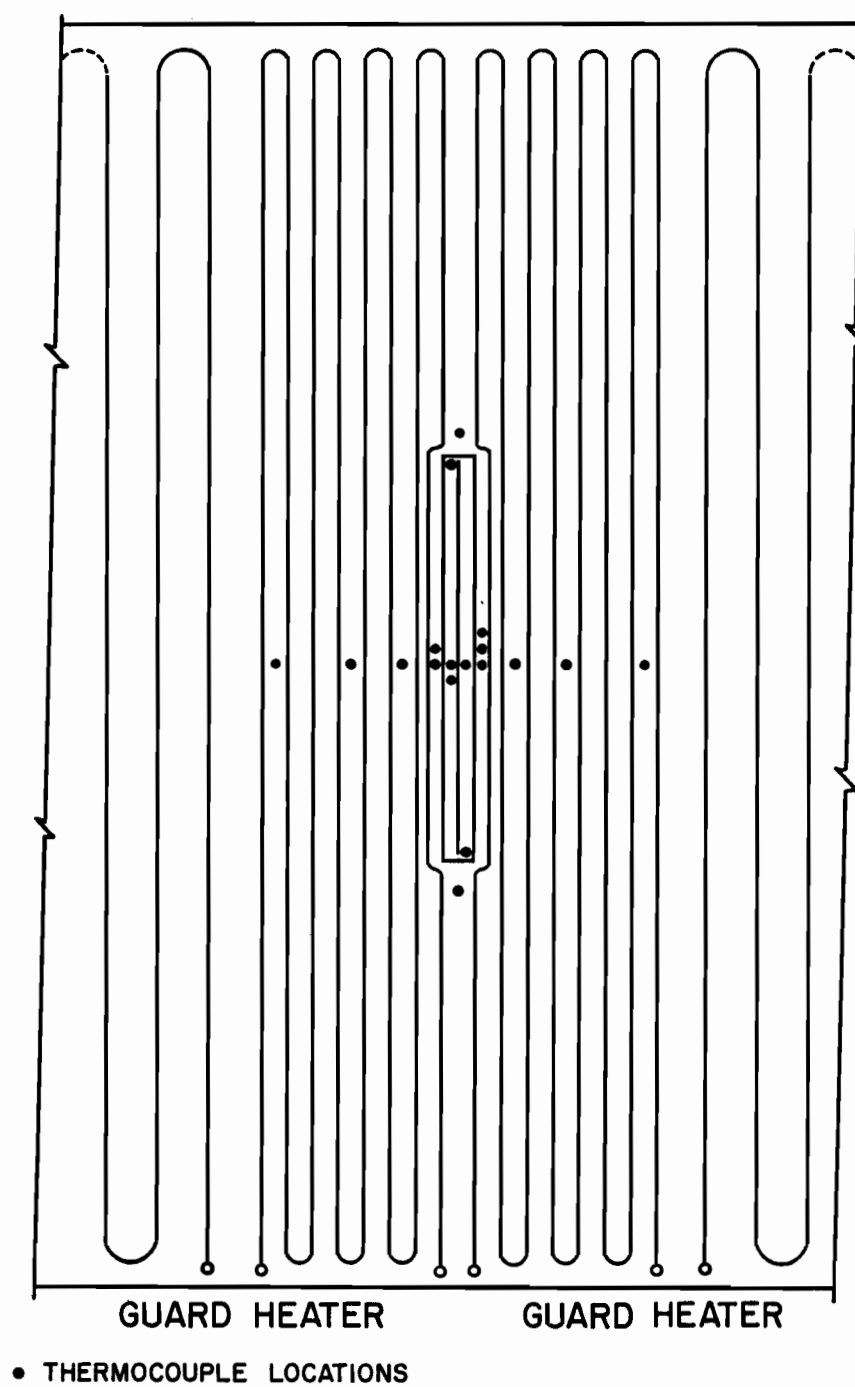


FIGURE 3.15. Heat Flux Sensor Flush Mounted on the Impingement Surface

At steady state the convective heat transfer with zero throughflow is

$$Q_{\text{conv.}} = P_s - Q_{\text{cond.}} - Q_{\text{rad.}} \quad (3.3)$$

where $Q_{\text{cond.}}$ and $Q_{\text{rad.}}$ (the heat loss by conduction and radiation, respectively) are evaluated as shown in Appendix 5 and P_s is calculated from

$$P_s = V_h (V_p / R_p) - (V_p / R_p)^2 R_{lw} \quad (3.4)$$

where R_{lw} is the resistance of the lead wire. The local heat transfer coefficient is therefore calculated as

$$h_x = \frac{Q_{\text{conv.}}}{A_s (T_s - T_j)} \quad (3.5)$$

where T_s and T_j are the steady state sensor free surface temperature and the jet temperature at the nozzle exit, respectively. The impingement surface heat transfer coefficient with the presence of throughflow is calculated as shown subsequently in Section 5.6.

3.5 Test Procedure

Each heat transfer experiment was begun by measuring the static pressure distribution at the impingement surface with no power to the plate, in order to assure flow symmetry. The position of the two end walls was fine-tuned to ensure that exactly one-half of one nozzle inflow left each of the end ports. Power to the impingement surface heaters was then switched on and monitoring was started for achieving steady state surface temperature, isothermal to within $\pm 0.1^\circ\text{C}$. Following recording of all variables at the steady state condition, the plate was traversed to the next station under the jet

array and a new steady state monitoring started. The analysis of experimental uncertainties is presented in Appendix 5.

CHAPTER 4

RESULTS AND DISCUSSION: FLOW

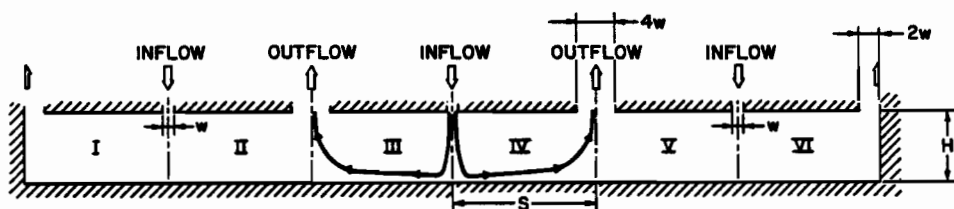
4.1 Introduction

As impingement heat transfer depends on the corresponding flow field, the present chapter is devoted to the documentation of the flow prior to the presentation in the succeeding chapter of the analysis of heat transfer for the impingement system under study.

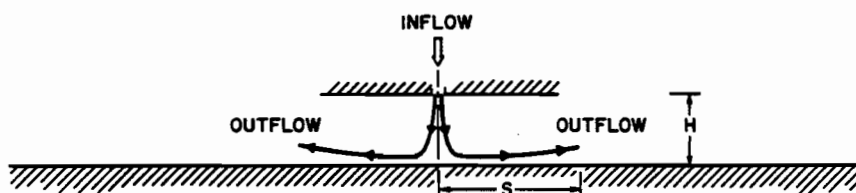
The multiple confined slot jet system with exhaust ports located symmetrically between jets which is of prime interest in this study is illustrated schematically at the top of Figure 4.1. In order to document differences between multiple and single confined slot jets, flow field measurements were also made for the corresponding single confined jet system, illustrated at the middle of Figure 4.1, where the impingement surface was the same as that for multiple jets. The single jet system was obtained by removing the nozzle blocks for the two outside jets, hence the confinement surface comprised the two central jet nozzle blocks. The third configuration shown on Figure 4.1, used for study of effect of throughflow, was obtained by blocking the exit ports and the two outer nozzles and by removing the end walls to permit lateral outflow.

Between the points of jet inflow and outflow for systems of confined jets shown in Figure 4.1 the flow field comprises the free jet, impingement and wall jet regions. Thus the flow field analysis is presented successively for the region at the nozzle exit (Section 4.3), in the free jet (Section 4.4), and along the impingement surface, including the impingement and wall jet regions (Section 4.5). In Sections 4.4 and 4.5 the cases of both single jet and multiple jet systems, as shown on Figure 4.1, are analyzed in order to document conditions for which the latter deviates significantly from the former.

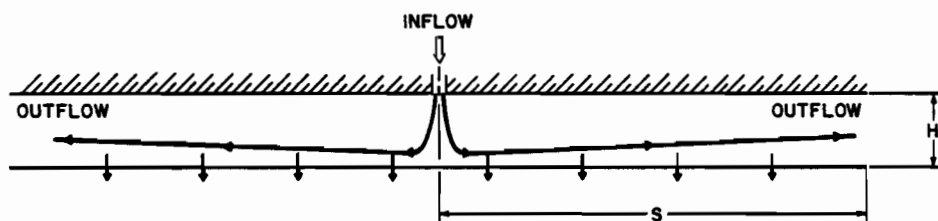
Finally, the effect of throughflow at the impingement surface is analyzed



MULTIPLE CONFINED IMPINGING SLOT JET SYSTEM WITH NOZZLES AND EXIT PORTS LOCATED ALTERNATELY IN CONFINEMENT SURFACE



SINGLE CONFINED IMPINGING SLOT JET WITH LATERAL OUTFLOW



SINGLE CONFINED IMPINGING SLOT JET WITH THROUGHFLOW AT THE IMPINGEMENT SURFACE

FIGURE 4.1. Impinging Jet Systems Used for Measurements of the Flow Field

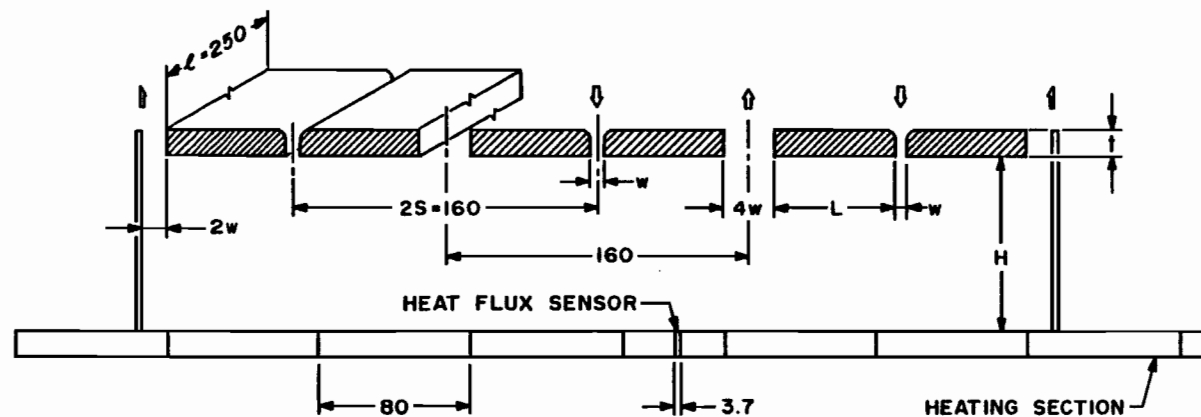
in Section 4.6 followed by the summary and conclusions, Section 4.7.

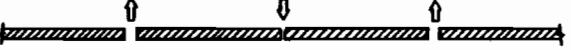
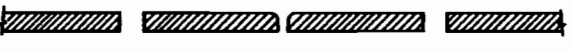



4.2 Range of Geometric and Flow Parameters

Impingement flow and heat transfer for the multiple confined jet system with exhaust ports located symmetrically between jets shown in Figure 4.1 were studied over a wide range of geometrical and flow parameters. Comprehension of the results discussed subsequently will be facilitated by presentation at the outset of the entire range of geometrical parameters, with the corresponding dimensionless variables, and likewise of the entire range of flow parameters.

The geometrical variables (Figures 4.1 and 4.2) are nozzle width w , spacing between the confinement surface and the impingement surface, H , and distance between centerlines of adjacent inlet nozzles and exit ports, S . The five values of nozzle width used in the present investigation, Figure 4.2, are 2.5, 3.3, 5, 10 and 13.3 mm. For reasons detailed in Chapter 3, the value of S was fixed at 80 mm, hence both dimensionless centerline spacing, S/w , and fractional open area, $f = w/2S$ are unique functions of nozzle width. Thus for each value of w the equivalent set of values, S/w and f , are tabulated in Figure 4.2 and at the top of Table 4.1.

Use of values of H over the range 4 to 400 mm provided a range in values of dimensionless confinement surface-to-impingement surface spacing, H/w , from 4 to 24 as noted on Table 4.1. The other geometric proportion listed, defined for the first time in the present study, S/H , characterizes the shape, i.e. the ratio of width to depth, of the basic flow cell which recurs in the multiple impinging jet system. Flow cell width is the centerline spacing, inlet nozzle-to-exit port, while flow cell depth is the spacing



l/w	$f, \%$	S/w		Set No	w	t	L
100	1.562	32		1	2.5	7.45	73.75
75	2.083	24		2	3.3	9.9	71.75
50	3.125	16		3	5.0	14.8	67.50
25	6.250	8		4	10.0	29.2	55.00
18.75	8.333	6		5	13.3	38.7	55.00

NOTE: DIMENSIONS ARE IN mm.

FIGURE 4.2. Geometrical Variables (w , S/w and f) of the Multiple Confined Impinging Slot Jet System

TABLE 4.1. Geometrical Parameters of the Confined Multiple Impinging Slot Jet System

w (mm)	2.5	3.3	5.0	10.0	13.3
S/w	32	24	16	8	6
f, %	1.56	2.06	3.125	6.25	8.313
H/w	S/H				
4	-	6	-	2	1.5
8	4	3	2	1	0.75
16	2	1.5	1	0.5	0.375
24	1.33	1.0	0.67	0.33	-

between impingement surface and confinement surface, the inlet nozzles and exit ports being continuous with the confinement surface. The present experimental apparatus comprised 6 flow cells, identified on Figure 4.1 as I to VI. The widest flow cell, $S/H = 6$, corresponds to combination of a wide internozzle spacing, $S/w = 24$ ($w = 3.3$ mm), with the smallest confinement-to-impingement surface spacing, $H/w = 4$. At the other extreme, the narrowest flow cell used, $S/H = 0.33$, results from the narrow internozzle spacing $S/w = 8$ ($w = 10$ mm) and the largest impingement surface spacing, $H/w = 24$. It may be noted that the multiple jet system illustrated on Figure 4.1 corresponds to an intermediate flow cell proportion of $S/H = 2$.

The flow parameters are similarly presented in Table 4.2. Experiments were run at a number of levels of nominal jet Reynolds number, Re_j , from 3500 to 45,000, for which the corresponding values of nozzle exit mean velocity, U_j^* , are tabulated as well in Table 4.2. Air viscosity and density for Re_j were evaluated at the nozzle exit temperature. So that the flow could be considered incompressible, the maximum value of U_j^* did not exceed Mach number of 0.3. While the nominal, i.e. target values of Re_j are listed in Table 4.2, subsequent references to experimental results always give the actual value of Re_j , generally close to the Table 4.2 nominal values.

The record of all values of geometrical and flow parameters used in the present study, Tables 4.1 and 4.2, constitutes a key reference to facilitate understanding of results throughout this thesis.

The values of geometrical and flow parameters listed in Tables 4.1 and 4.2 were chosen to encompass the wide range of parameters for two major industrial applications, impingement drying of paper and impingement cooling of turbine vanes. With respect to the first area of industrial application,

TABLE 4.2. Flow Parameters of the Confined Multiple Impinging Slot Jet System

w (mm)	S/w	f, %	Re _j (nominal)	U _j [*] (m/s)
2.5	32	1.56	3500	24.6
			5500	38.7
			11000	77.5
3.3	24	2.06	3500	18.7
			5500	29.3
			11000	58.7
			18500	98.7
			21000	112.0
5.0	16	3.125	5500	19.4
			7500	26.4
			11000	38.7
			18500	65.2
			21000	73.9
10.0	8	6.25	5500	9.7
			11000	19.4
			18500	32.6
			22000	38.7
13.3	6	8.313	11000	14.6
			18500	24.5
			22000	29.0
			30000	39.7
			45000	59.5

the proposed "Papridryer" process represents a projected combination of impingement and through-drying of paper (Burgess et al., 1972a, b). For their laboratory apparatus and mill-test "Papridryer" the range of fractional open area was $1.33 < f < 1.67\%$ and the range of spacing between confinement and impingement surfaces was $10 < H/w < 16$. In terms of the characterization of flow cell proportions introduced for multiple slot jet systems in the present study, the range of S/H for their test units was $2 < S/H < 3$, a range which corresponds to the wider flow cells tabulated in Table 4.1. Further, in these experimental Papridryers the jet velocity at the slot nozzle exit was between 60 to 100 m/s and jet temperature in the range $250\text{--}450^{\circ}\text{C}$. The corresponding jet exit Reynolds numbers were in the range $1000 < Re_j < 3000$, based on $w = 1.3\text{ mm}$ for the mill dryer.

The second industrial application consists of a two-dimensional array of jets to cool the midchord region of airfoils (Saad et al., 1980), for turbo-fan and turbo-prop engines. In this application the range of fractional open area is $3 < f < 10\%$ and the range of spacing between confinement and impingement surfaces is $3 < H/w < 15$. Thus this application produces flow cells in the range $0.34 < S/H < 5$, which covers the entire range recorded for the present study in Table 4.1. In this industrial application the jet velocity at the slot nozzle exit is between 30 and 200 m/s at the jet temperature in the range $250\text{--}500^{\circ}\text{C}$, i.e. corresponding to jet exit Reynolds number, $500 < Re_j < 6000$ based on $w = 1.3\text{ mm}$ for a typical engine design.

4.3 Flow Characteristics at the Nozzle Exit

A key variable in study of transport phenomena at the impingement surface under a system of confined multiple impinging jets is the ratio

jet nozzle area:impingement surface area, referred to here as percent open area, f . For a confined multiple jet system, the nozzles constitute openings in the confinement surface, hence the terminology "open area ratio". For the case of slot jets this is equivalent to the ratio, nozzle width: internozzle spacing, i.e. $w/2S$. For reasons documented in Section 3.2.1, the alternative of varying percent open area by varying internozzle spacing was rejected in favor of varying nozzle width for a fixed internozzle spacing. The nozzle geometry selection, i.e. short nozzles ($t/w = 1$) with ASME standard elliptic entry shape, was made with the objective of having for all cases a uniform boundary condition for the inlet jet, i.e. flat velocity profile and low uniform turbulence across the jet at the nozzle exit. Thus the objective was to achieve dynamic similarity for all nozzles. As nozzle width, w , was varied over the limits 2.5 to 13.3 mm in order to cover a wide range in open area, f , 1.56 to 8.313%, it was necessary at the outset of this study to document the effect of the large variation of nozzle width on degree of uniformity of the inlet jet boundary condition. Hence the effect of nozzle width on axial mean velocity and axial turbulence at the nozzle exit will now be examined.

Measurements of axial mean velocity, U_j , and axial fluctuating velocity, u' , mainly on the middle jet, were made for typical values of jet Reynolds number as shown in Table 4.3. The centerline mean velocity profile along the nozzle exit spanlength, l , was found to be uniform up to 5 mm from the end of the 250 mm span. Profiles of axial mean and fluctuating velocity, U_j and u' , across the nozzle width, normalized respectively with respect to U_{j0} and U_j , are recorded for all five values of w in Figures 4.3 through 4.6. It is well established that short nozzles of elliptic (contoured) entry produce profiles of mean and turbulent velocity which are

TABLE 4.3. Geometrical and Flow Parameters of the Multiple Jet System for Analysis of Nozzle Exit Flow Conditions

w (mm)	S/w	f, %	Re _j	U _j [*] (m/s)
2.5	32	1.56	10800	76
3.3	24	2.06	10300 18700	55 99.7
5.0	16	3.125	10800 18700	38 65.8
10.0	8	6.25	11000 18700	19.4 33
13.3	6	8.313	10800 18700	14.3 24

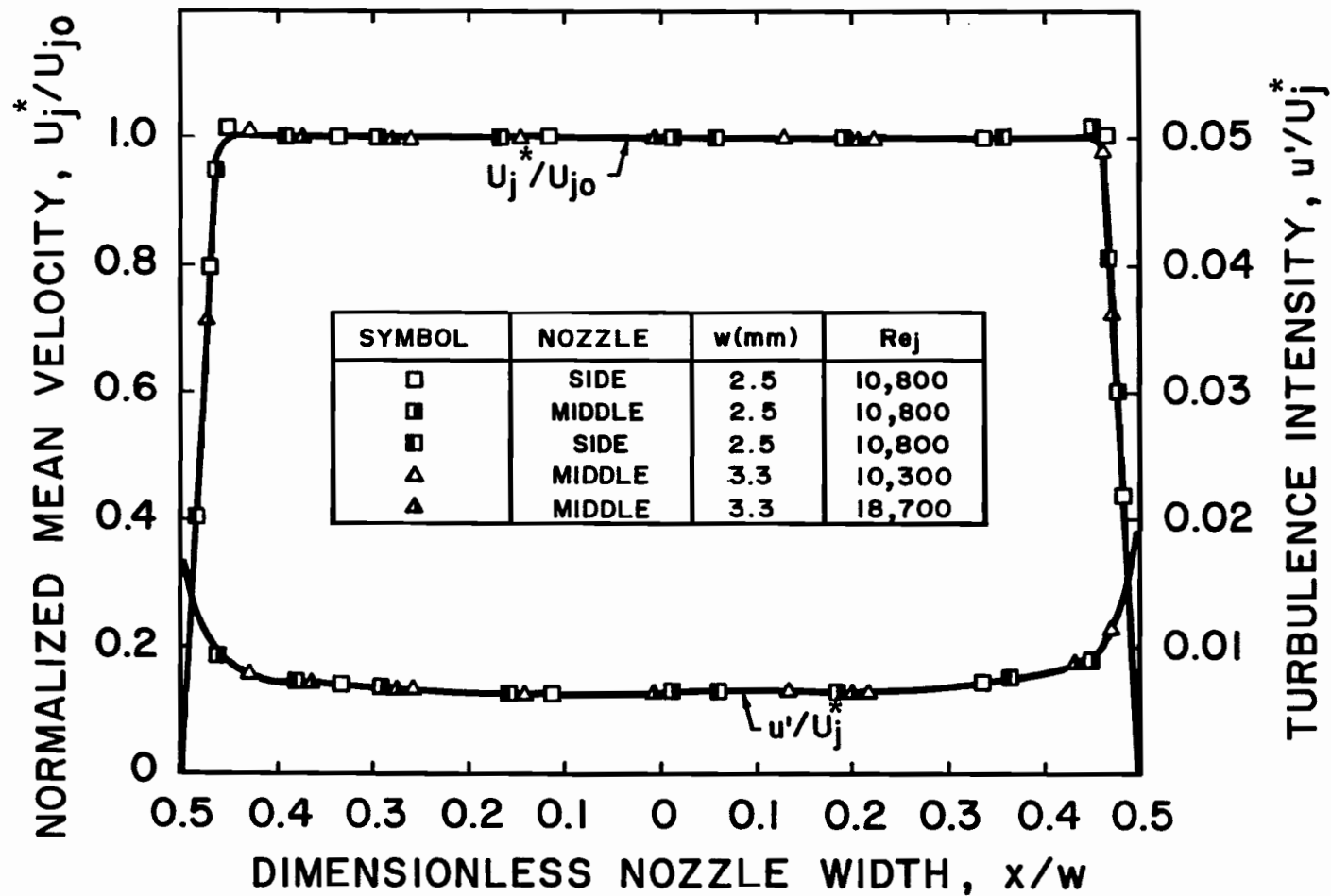


FIGURE 4.3. Profiles of Mean Velocity and Turbulence Intensity at the Nozzle Exit for $w = 2.5 \text{ mm}$ and 3.3 mm

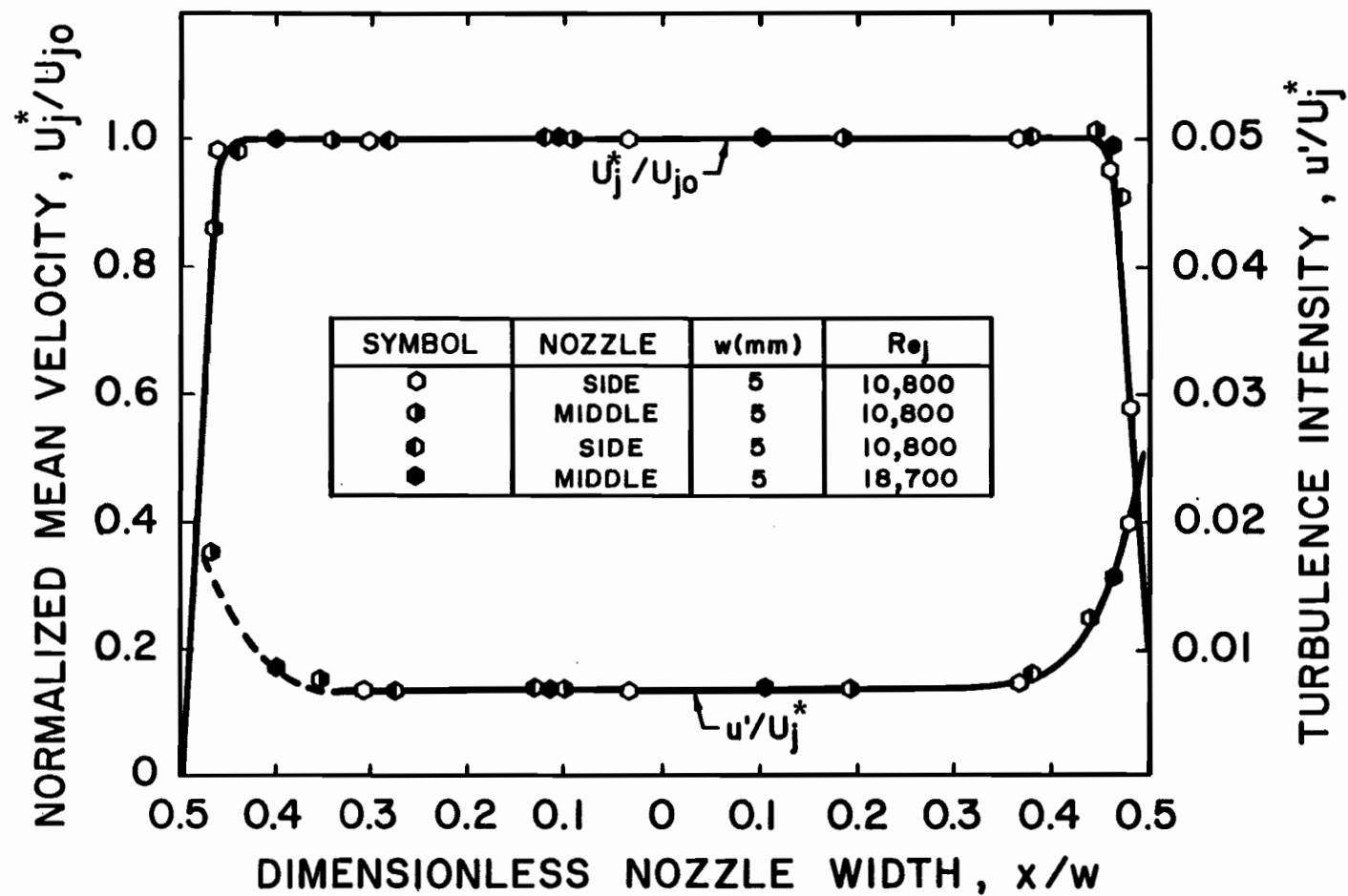


FIGURE 4.4. Profiles of Mean Velocity and Turbulence Intensity at the Nozzle Exit for $w = 5.0$ mm

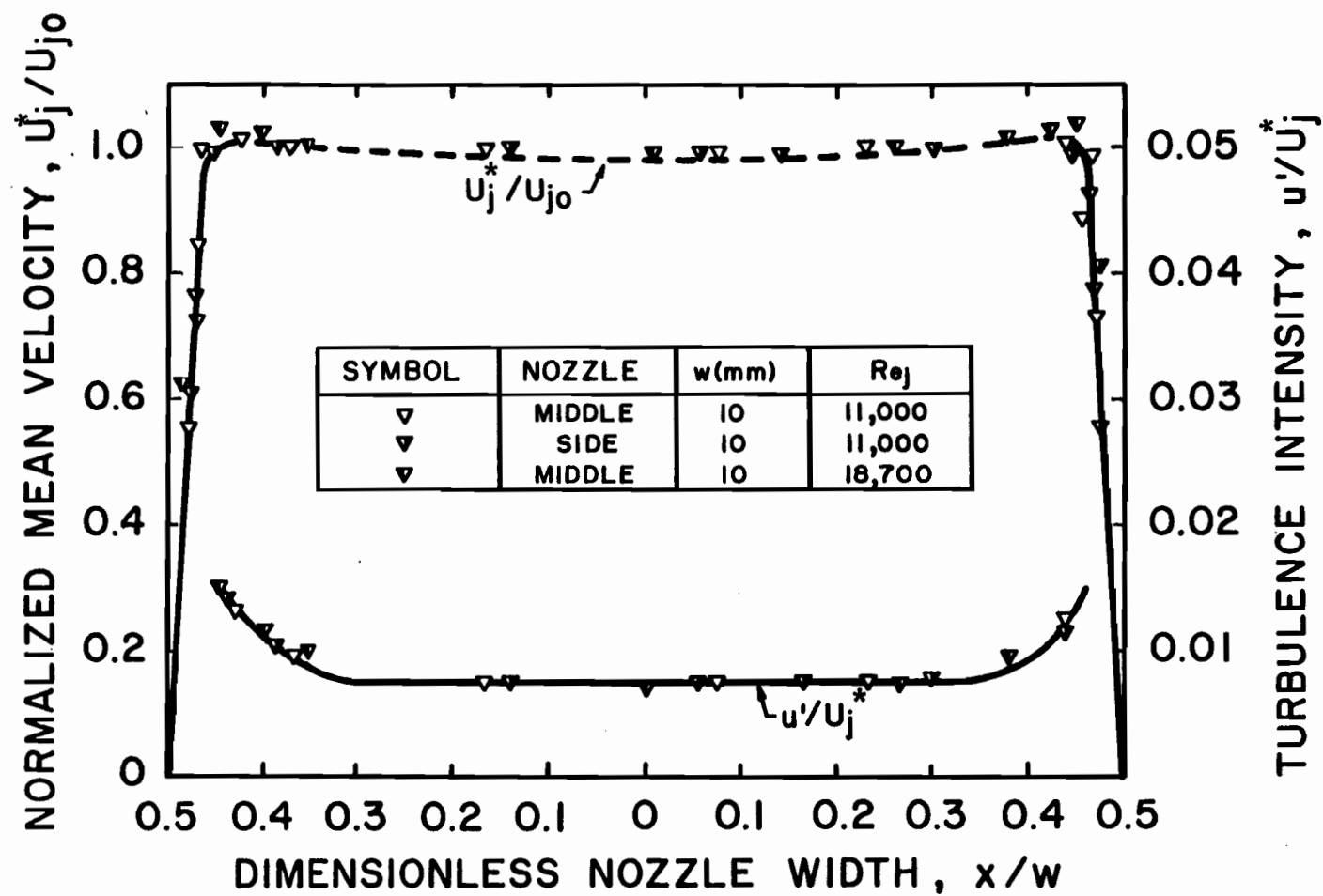


FIGURE 4.5. Profiles of Mean Velocity and Turbulence Intensity at the Nozzle Exit for $w = 10.0$ mm

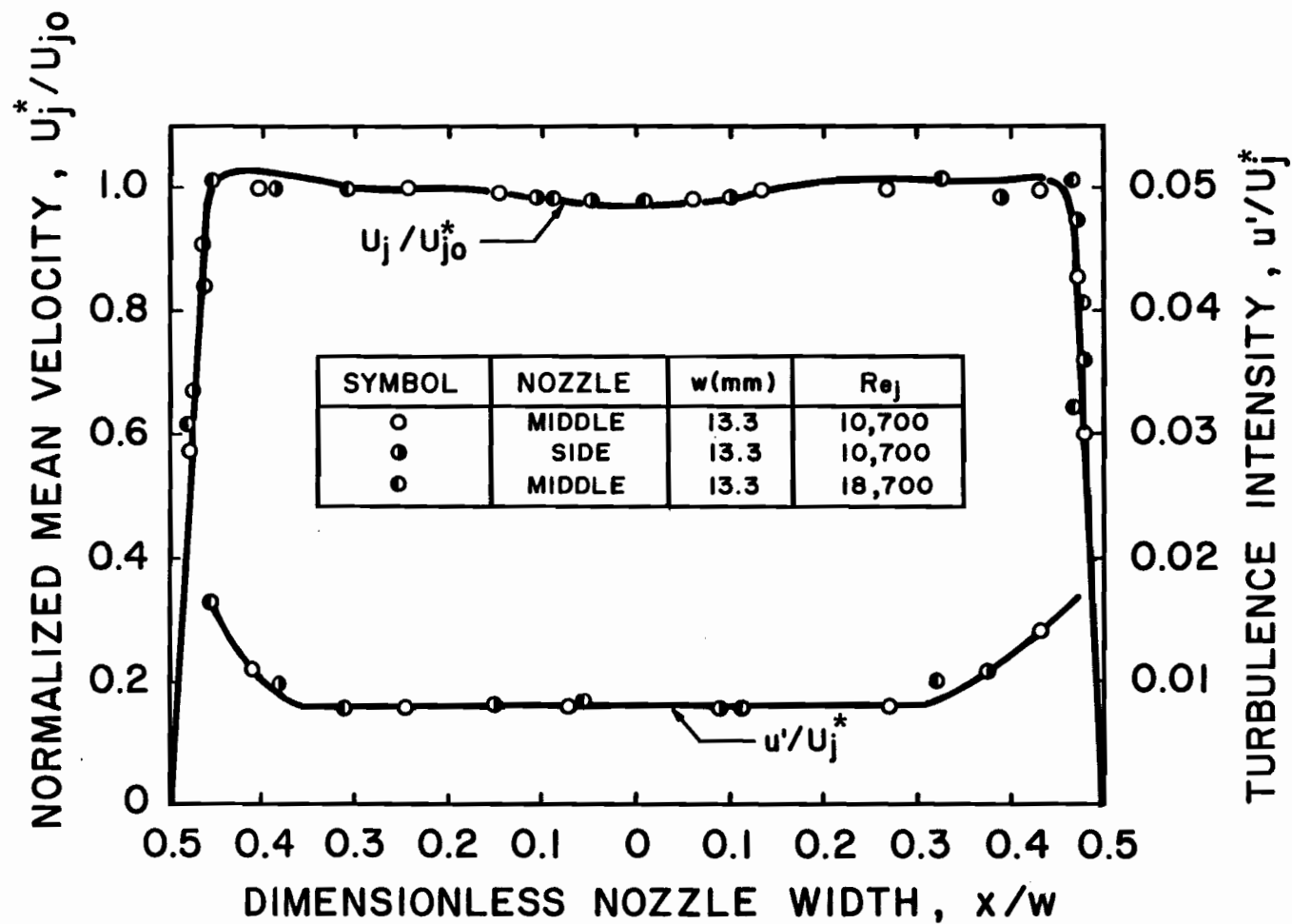


FIGURE 4.6. Profiles of Mean Velocity and Turbulence Intensity at the Nozzle Exit for $w = 13.3$ mm

very far from the limit for fully developed flow. Rather, such nozzles produce an exit profile of mean velocity which is uniform from the nozzle centerline over the central region of the nozzle almost to the nozzle wall, and an axial turbulence profile which over the central region of the nozzle is uniform and at a level much below that for the corresponding fully developed flow.

With respect to mean axial velocity, Figures 4.3 through 4.6 confirm that in the present study these profiles at the nozzle exit were flat over approximately the central 90% of the nozzle width, dropping very sharply to zero only over the last 5% of the width. For the two widest nozzles (10 and 13.3 mm) the mean velocity profiles display a very slight minimum around the centerline, which may be attributed to the correspondingly smaller ratio of area contraction to these wide nozzles from the 100 mm plenum chamber immediately upstream of the nozzle. Thus the plenum-to-nozzle contraction ratio, in the range 40:1 to 20:1 for the three narrowest nozzles, is only 10:1 and 7:1 for the two widest nozzles. This deviation from uniformity of mean velocity profile for the two nozzles of smallest contraction ratio, while discernable, is only about 2% from a completely flat profile, hence is not a significant effect for the present study.

With respect to axial turbulence at the nozzle exit, it is well-known that turbulence intensity is depressed in the strongly accelerating flow in a short elliptically contoured entry nozzle. This general effect is observed on Figures 4.3 through 4.6 where the profiles of turbulence intensity across the nozzle are seen to be flat at a value of less than 1% intensity in the central region, rising to about 2% at the closest location to the nozzle wall that was measured. These low turbulence levels contrast sharply to the corresponding values for fully developed channel flow of around 3% at the

centerline and about 30% near the source of turbulence generation at the wall. With respect to the effect of nozzle width on turbulence intensity in the central region, reference to the tabulated data shows that over the range $10800 < Re_j < 18700$ this level increases in a small but consistent way from 0.65% for the two narrowest nozzles, successively to 0.7%, 0.75% and 0.8% as w increases to 5, 10 and 13.3 mm. As the flow cross-section upstream of the nozzle (the 100 mm wide plenum chamber) is constant, it is evident from these results that the larger the ratio in area contraction between the upstream channel and the nozzle throat, the greater is the suppression of turbulence intensity at the latter position. As this contraction of area and corresponding acceleration of flow is one cause of the suppression of turbulence, the increasing suppression with the increasing contraction and acceleration noted above is the expected behavior.

In the larger perspective that turbulence intensity in the jet increases very rapidly downstream from the nozzle exit, for example to the order of 15% at 8 nozzle widths downstream along the nozzle centerline and higher than that level away from the centerline, it might appear trivial to observe at the nozzle exit small differences in axial turbulence intensity over the range 0.65-0.8%. However, it will be seen subsequently that, although small, these differences at the nozzle exit due to the nozzle width are not negligible because in fact these differences grow to become quite significant downstream from the nozzle exit and ultimately affect heat transfer at the impingement surface.

It remains only to be noted that over the range $10800 < Re_j < 18700$ and for any particular nozzle, no effect of Reynolds number on turbulence intensity at the nozzle exit can be observed.

It was noted at the outset of Section 4.2 that it had been hoped the

use of short ($t/w = 1$) elliptical entry nozzles would achieve the objective of having for all cases of the heat transfer study a uniform boundary condition of inlet jet, i.e. a single profile for mean velocity and turbulence intensity. Examination of the profiles of Figures 4.3-4.6 at the nozzle exit indicates that at this location that ideal was achieved to a considerable extent, but not entirely.

In the subsequent section this examination of the general flow boundary condition for heat transfer at the impingement surface is extended to inspection of the flow field downstream from the nozzle exit, first for a single jet, then for the multiple jet system.

4.4 Flow Field Downstream from the Nozzle Exit

Development of a single free jet and multiple impinging jets was studied at the middle jet position for a typical value of Reynolds number at the nozzle exit, $Re_j = 11000$. Thus w and U_j^* were varied inversely, keeping their product, and hence Re_j constant. For all values of w at $Re_j = 11000$, corresponding values of U_{j0} at the nozzle exit and U_o at $16w$ from the nozzle exit are presented in Table 4.4. For the study of single free jet development the impingement surface was located at 30 times nozzle width. As measurements were taken only as far as $18w$ from the nozzle exit, no influence from the impingement surface existed over the region studied.

Similarly, development of the free jet region in a multiple impinging jet system was studied over a range of geometrical configurations, shown in Table 4.5, sufficiently wide so as to include systems in which the jets are effectively non-interacting as well as systems of interacting multiple impinging jets. This range, duplicated subsequently in the study of the flow field at the impingement surface as well, was chosen to provide a comparison

TABLE 4.4. Jet Centerline Velocity at the Nozzle Exit and at
16w from the Nozzle Exit for $Re_j = 11000$

w (mm)	S/w	f, %	U_{jo} (m/s)	U_o (m/s) at $z/w = 16$
2.5	32	1.56	77.5	45.7
3.3	24	2.06	58.7	34.5
5.0	16	3.125	38.7	22.4
10.0	8	6.25	19.4	11.3
13.3	6	8.313	14.5	8.3

TABLE 4.5. Geometrical Parameters of the Multiple Jet System for Analysis of Free Jet Development

w (mm)	S/w	f, %	H/w	S/H
10.0	8	6.25	8	1.0
13.3	6	8.313	8	0.75
10.0	8	6.25	16	0.5
13.3	6	8.313	16	0.375

of development of the free jet for the multiple impinging jet system with that for a single jet.

For the single free jet the axial flow field is presented through profiles in both lateral and jet centerline directions, Figures 4.7 to 4.16. Due to the lack of reliability of results in the extremely high turbulence field away from the jet centerline obtained with the hot wire anemometry instrumentation used in this study, only results along the jet centerline, Figures 4.10 to 4.12, are presented for the multiple jet system.

4.4.1 Single Jet Flow Downstream from the Nozzle Exit

Development of the free jet flow field is discussed by examining first axial fluctuating velocity and turbulence intensity, then axial mean velocity. This sequence is chosen as development of axial mean velocity can only be understood through consideration of the development of axial turbulence. It will be recalled that the rate of turbulent transport of axial mean momentum between lateral regions of high and low axial momenta depends on level of turbulence, i.e. the higher the turbulence, the higher the rates of turbulent transport of momentum. Therefore, the sequence of analysis of turbulence downstream from the nozzle exit will be to inspect, first, lateral profiles of axial turbulence, then axial profiles of turbulence, and subsequently to examine the axial mean velocity via axial and lateral profiles.

For the five lateral profiles of axial fluctuating velocity at $16w$ downstream from the nozzle, shown in Figure 4.7 for $Re_j = 11000$, the values of u' for each profile are divided by a constant, i.e. by the value of U_0 for that nozzle width. This treatment of the u' profiles is purely a matter of plotting convenience, as values of u' cover an inconveniently large range. Only at the centerline of the jet ($x/w = 0$) are the values of u'/U_0

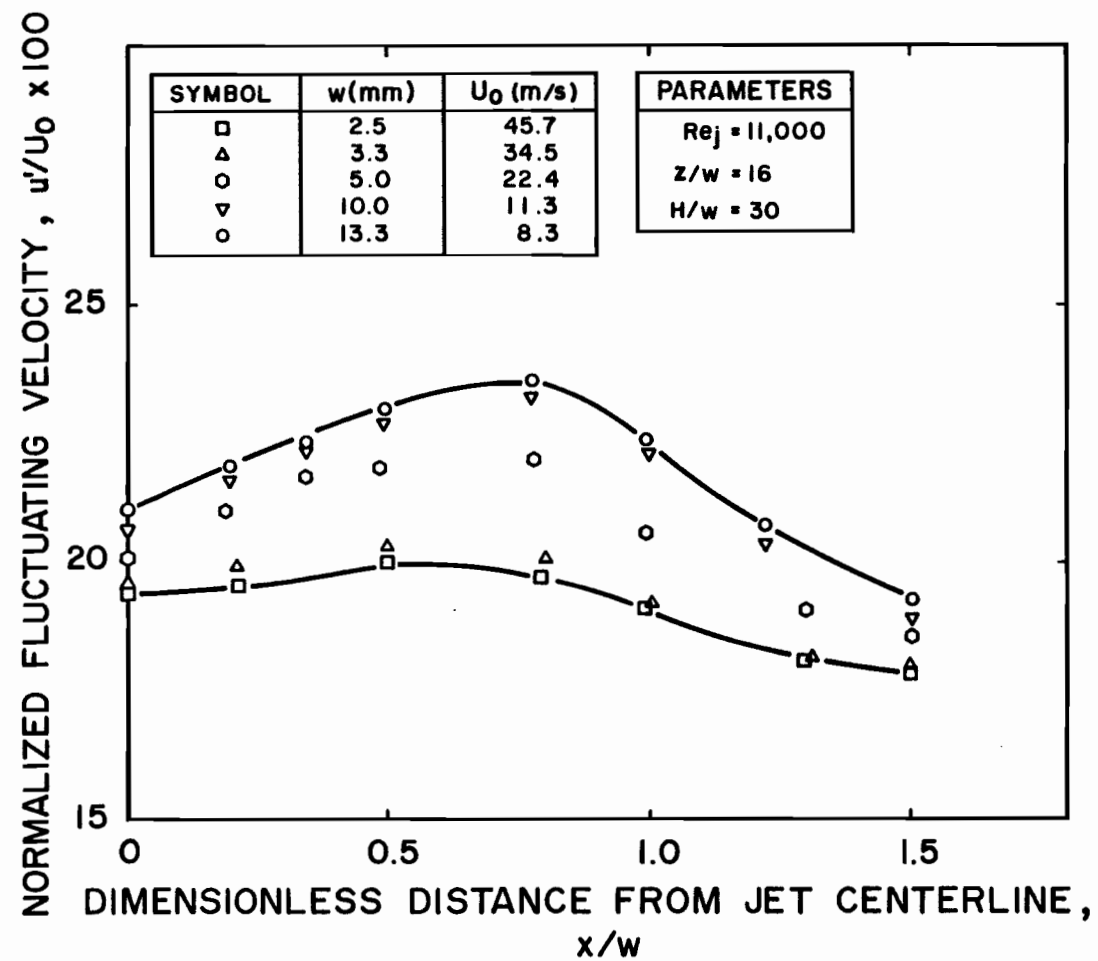


FIGURE 4.7. Lateral Profiles of Axial Fluctuating Velocity at $z/w = 16$

in Figure 4.7 values of turbulence intensity. For simplicity on Figure 4.7 and on similar subsequent figures, lines are shown only through the data for the two limiting values of w .

The values of u'/U_0 at the jet centerline, when viewed with reference to the u'/U_j^* values of Figures 4.3 to 4.6 at the nozzle exit, reveal that turbulence intensity increases very greatly, from a level of 0.65%-0.8% at the nozzle exit to 19%-21% at $16w$ downstream from the nozzle. Subsequent axial profiles of turbulence velocity will show that in fact, by $16w$ from the nozzle, u'/U_0 has already passed through a maximum and is decreasing. As is well-established for confined flow and shown in Figures 4.3 to 4.6, for flow at the nozzle exit the peak in turbulence velocity and turbulence intensity is very close to the nozzle wall ($x/w = 0.5$), the region of highest gradient in mean axial velocity. Downstream of the nozzle exit turbulence increases rapidly at all lateral positions as it is transported laterally in both directions from the region of generation around $x/w = 0.5$ where the gradient in mean axial velocity is highest. Thus the peak in lateral profiles of u' remains in the same general vicinity, relatively close to $x/w = 0.5$, although by $16w$ downstream the turbulence velocity peaks have drifted outwards somewhat to the region about $0.6-0.75 x/w$ from the nozzle centerline because of the general outwards mean velocity of the laterally expanding jet. Discussion of the other trend evident on Figure 4.7, i.e. the effect of the parameter, w , for data at one value of Re_j , will be considered following presentation of Figure 4.8.

With the axial turbulence for the cases shown in Figure 4.7 expressed alternately as intensity of turbulence, the resulting five lateral profiles at $16w$ downstream from the nozzle exit are shown in Figure 4.8. Whereas the u' lateral profiles downstream of the nozzle exit remain peaked at loca-

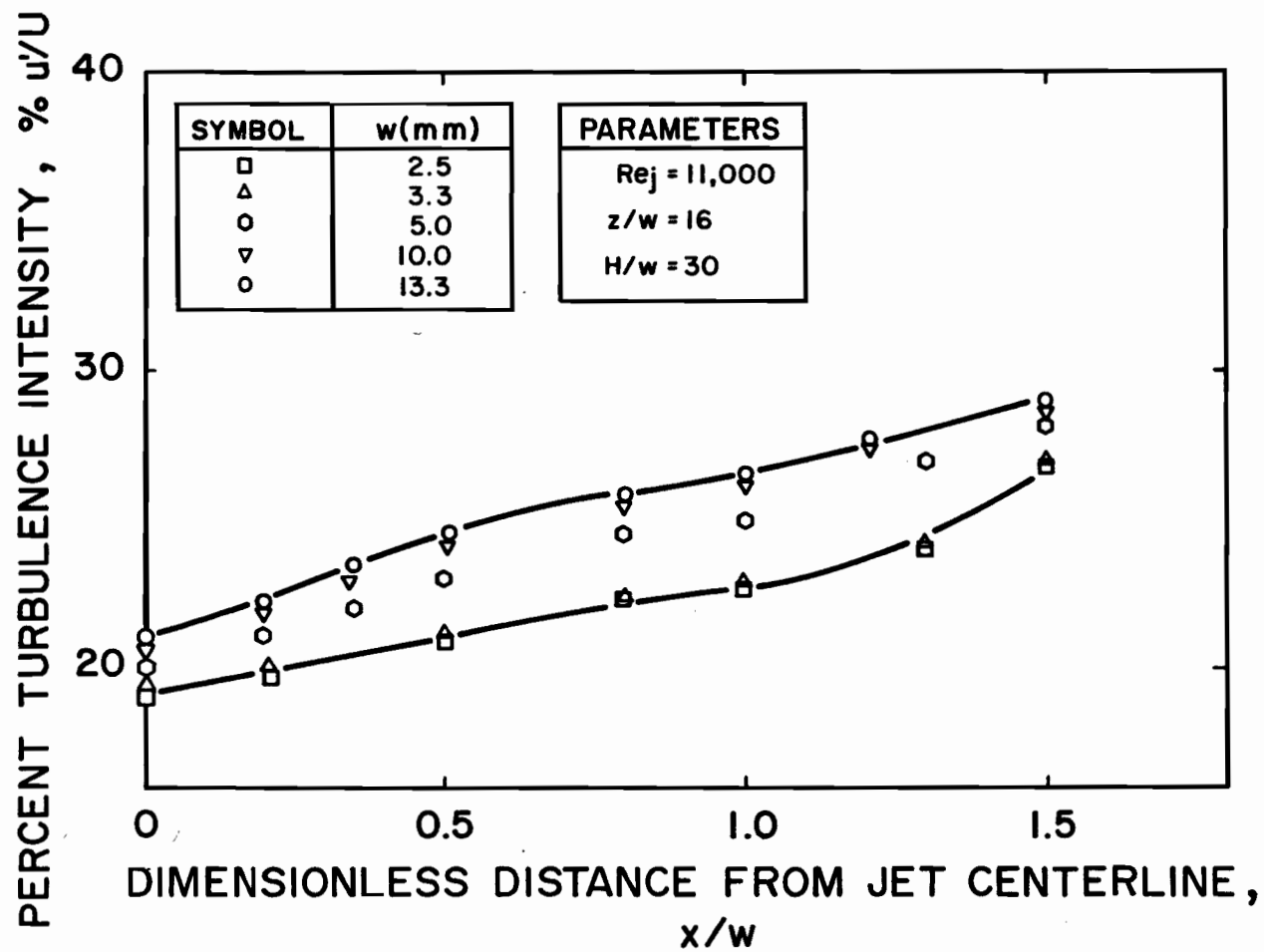


FIGURE 4.8. Lateral Profiles of Turbulence Intensity at $z/w = 16$

tions never far from that of the nozzle wall, the corresponding downstream lateral profiles in turbulence intensity, although in the order of 30 times higher than at the nozzle exit, display a relatively flat minimum at the centerline and increase continuously out as far as it was considered reasonable for turbulence measurements to be made. The fact that lateral profiles of turbulence intensity increase continuously outwards from the centerline whereas the corresponding turbulence velocity profiles exhibit maxima reveals at that/some distance from the jet centerline the local axial mean velocity decreases more rapidly with lateral distance than does local axial fluctuating velocity. As will be seen subsequently, the lateral profiles in axial mean velocity, which are almost square at the nozzle exit, do indeed become relatively Gaussian in shape downstream from the nozzle exit, with a decrease in mean velocity much more rapid than that for fluctuating velocity displayed by Figure 4.7.

It should further be noted from Figure 4.8 that even at a fixed Reynolds number ($Re_j = 11000$) the turbulence intensity downstream from the nozzle is not independent of nozzle width, i.e. turbulence intensity increases with increasing nozzle width. Thus the same trend as noted at constant Reynolds number at the nozzle exit in the previous section, does not damp out downstream of the nozzle, but is clearly present even at $16w$ from the nozzle. Therefore, incorporating nozzle width, w , in the dimensionless parameter, Re_j , unfortunately does not yield data which are totally independent of w . Further consideration of this flow characteristic will appear later.

Because the lateral profiles of Figures 4.7 and 4.8 are considerably downstream ($16w$) from the nozzle exit, it is of interest to examine through Figure 4.9 a lateral profile at only $1w$ downstream from the nozzle. With

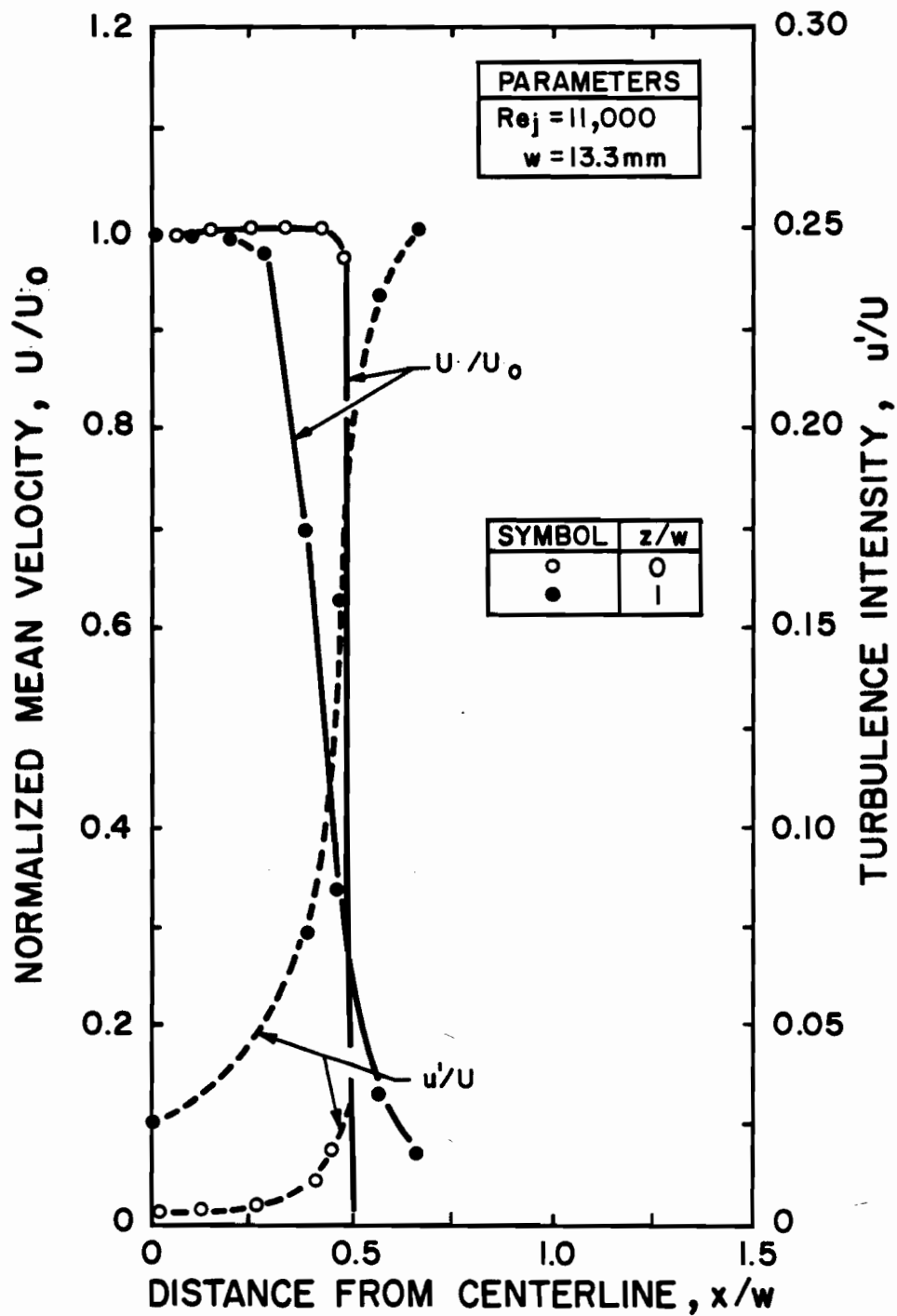


FIGURE 4.9. Lateral Profiles of Mean Velocity and Turbulence Intensity at $z/w = 0$ and 1

respect to axial mean velocity, Figure 4.9 shows the very rapid transition from the almost square velocity profile at the nozzle exit to a very considerably rounded profile at only $1w$ downstream from the nozzle. Figure 4.9 further demonstrates the extremely rapid rate of turbulence generation immediately downstream of the nozzle exit. Thus from a very narrow peak around 2% turbulence intensity at the nozzle exit the intensity of turbulence has by only $1w$ from the nozzle increased to a much broader, much higher peak of about 25%, with even the level at the jet centerline up to about 2.5% intensity. The axial profiles of turbulence shown subsequently will further illuminate the development of the velocity and turbulence field downstream from the nozzle.

Having presented lateral profiles downstream from the nozzle exit in Figures 4.3 to 4.9, this examination will now be extended via axial profiles through this flow field for the same value of Reynolds number at the nozzle exit, i.e. $Re_j = 11000$. Figures 4.10 and 4.11 present jet centerline profiles of axial turbulent velocity and turbulence intensity, thus complementing the lateral profiles of Figures 4.7 and 4.8. As noted at the outset, axial and lateral profiles of axial mean velocity will be presented subsequent to Figures 4.7 to 4.11 concerning axial turbulence.

Figure 4.10 portrays two sets of data; the band of data for five values of w for single jets which pass through maxima, and the four axial profiles for multiple slot jets, which do not display maxima. The single slot jet data are considered here, while the multiple jet data will be discussed in the next section. It should also be noted that, as in the case of Figure 4.7, the values of u' for each profile in Figure 4.10 are divided by a constant, i.e. by the value of U_{j0} , the value of centerline mean velocity at the nozzle exit as listed in Table 4.4. This treatment of u' pro-

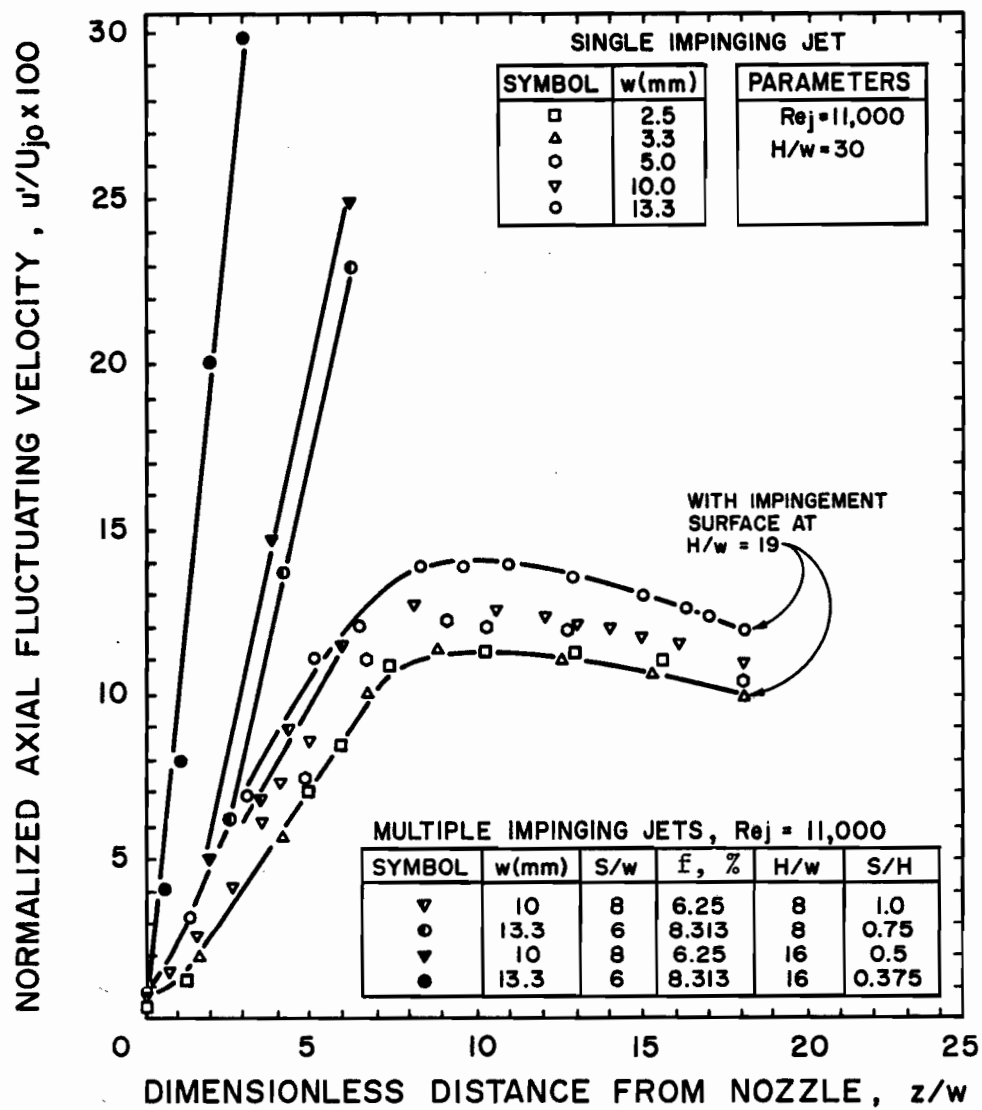


FIGURE 4.10. Profiles of Fluctuating Velocity at the Jet Centerline

files has the effect of reducing for graphical representation the inconveniently large range of values of u' and, because of the choice of constant, results in all axial profiles beginning at $z/w = 0$ on Figure 4.10 at the value of percent turbulence intensity at the nozzle exit. At all other values of z/w these values should not be misinterpreted as percent intensity, which they clearly are not, but rather as suitably compressed axial profiles of fluctuating velocity, u' . The values of u' are shown in Appendix 1.

The centerline fluctuating velocity in Figure 4.10 begins to rise rapidly immediately after the jet leaves the nozzle exit, i.e. turbulence increases even through the first $3w$ to $4w$ from the nozzle exit which constitutes the potential core region in which centerline mean velocity remains unaffected. Thus Figure 4.10 supplements the trend at $z/w = 1$ already evident from Figure 4.9. The centerline turbulent velocity continues its rapid increase within the development region, i.e. up to $7w$ from the nozzle, due to intense mixing, reaches a maximum around $z/w = 8$, then declines with increasing distance from the nozzle exit. Discussion of the effect of the parameter, w , on the profiles of u' can better be considered following presentation of Figure 4.11.

The fact that the sharp rise of u' begins immediately after the nozzle exit warrants comment. Flow at the exit of a short ($t/w = 1$), contoured entry nozzle is far from a self-preserving flow. From the source of turbulence adjacent to the nozzle wall there exist at the nozzle exit a rapid rate of lateral transport of turbulence directed towards the jet centerline where turbulence is a minimum. So at the nozzle exit the unstable flow from a short, contoured entry nozzle is in a condition of rapid lateral transport of axial turbulence from the wall to the jet centerline, as may be seen from Figures 4.3 through 4.6. Then immediately after the nozzle exit there is a

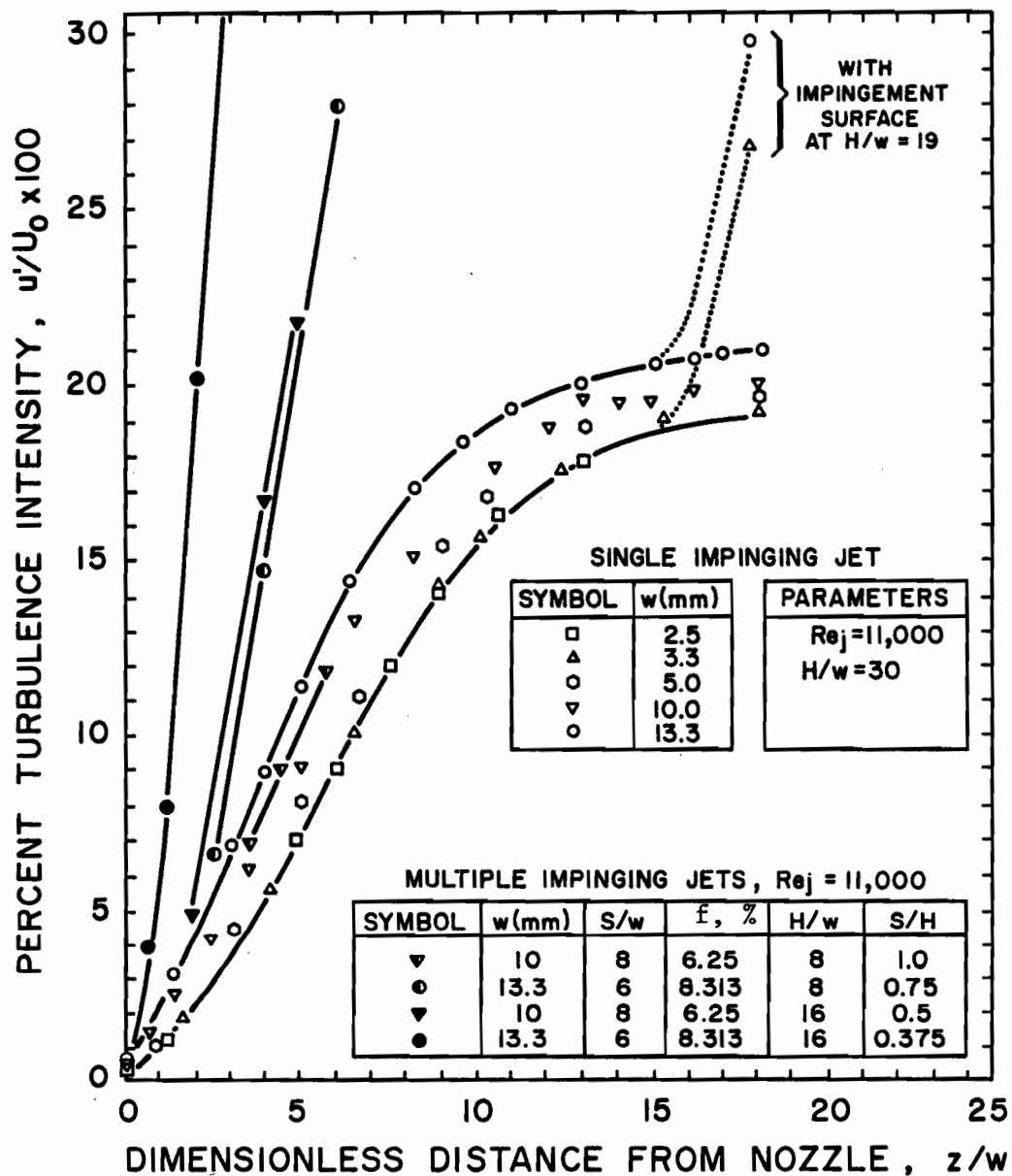


FIGURE 4.11. Profiles of Turbulence Intensity at the Jet Centerline

new source of turbulence, also at around $x/w = 0.5$, namely the interaction between the high velocity jet and the low velocity surrounding fluid, i.e. a region of very high gradient in axial mean velocity. Although it is well-known that it takes about $3w$ to $4w$ downstream of exit of short contoured entry nozzles before the dissipation of axial momentum reaches the jet centerline, i.e. the so-called length of potential core within which axial mean velocity remains constant. There is with respect to turbulence development downstream from such short nozzles no corresponding region where u' does not increase with axial distance. These contrasting effects concerning axial mean velocity and axial turbulence velocity indicate that downstream from short contoured nozzles the rate of lateral transport of turbulence is evidently much higher than the rate of lateral transport of axial momentum.

With respect to development of turbulence downstream of the nozzle exit it is also relevant to record that the hot wire signal displayed on an oscilloscope during lateral traversing $1w$ downstream from the nozzle exit reveals that the velocity therein undergoes increasingly violent low frequency oscillations which persist as the probe was moved downstream. At $z/w = 4$, i.e. near the end of the potential core, the lower frequency components are gradually masked by higher frequency components. Thus the rapid increase of axial turbulence within the potential core could be attributed to the random low frequency oscillations which reflect large scale disturbance that diffuse laterally very rapidly from the mixing region inwards to the centerline and, of course, outwards as well. The effects of lateral diffusion of large scale disturbances into the potential core region may be the cause of lateral distribution of u' at various axial location, Figures 4.7 and 4.9. For developed jets Sato and Hiroshi (1960), Minh and Hoopes (1972), Bradshaw (1966) and Obot (1981) found that the

highest value of u' is around the central location of the mixing region, i.e. half way between the shear layer and the centerline. Therefore, the lateral spreading of the shear layer at a given axial location has two effects; an inward spreading toward the jet centerline that consumes the core and initiates the decay in centerline velocity, and an outward spreading that increases the shear layer interface with the surroundings and enhances entrainment of ambient fluid by the jet. Both of these effects should tend to intensify the mixing process. As a final comment in this connection, it may be noted that the location of maxima in turbulence velocity ($z/w = 8$) in Figure 4.10 correspond to the location of maxima in the frequency of generation of eddies found by Yokobori et al. (1978).

In the same way that lateral profiles of turbulent velocity of Figure 4.7 were followed by lateral profiles of turbulent intensity of Figure 4.8, the axial profiles of turbulent velocity of Figure 4.10 are now presented in Figure 4.11 as axial profiles of turbulence intensity. As on Figure 4.10 for lateral profiles, the axial profiles of Figure 4.11 display two sets of data, i.e. the band of data for 5 values of nozzle width for single slot jets at a fixed $Re_j = 11000$, and another set of data for multiple slot jets. Again the single free jet data are considered first as a point of reference, then the multiple jet data are discussed in the next section.

Up to the end of the transition region (i.e. $z/w = 7$) all profiles of centerline turbulence intensity, u'/U_0 , of Figure 4.11 show trends similar to those noted on Figure 4.10 for the u' profiles. However, beyond $z/w = 7$, the turbulence intensity continues to rise, thus indicating that mean centerline velocity, U_0 , in the developed free jet region decays at higher rate than does axial fluctuating velocity u' . Although the u' profiles at $z/w = 18$ show no influence of the impingement surface located at $H/w = 19$,

i.e. one nozzle width from the impingement surface, the drop of U_0 to zero at the stagnation point starts at about $4w$ from the impingement surface, as will be seen in Figure 4.12. Thus this lack of effect of the impingement surface on u' over the region for which U_0 drops rapidly is what is responsible for the sudden increase of intensity of turbulence, u'/U_0 near the impingement surface, as can be seen from Figure 4.11. This remarkable rise in turbulence intensity when the flow enters the impingement region from a relatively stable level of about 18-20% at $4w$ from the impingement surface, i.e. to about 27-30% at $1w$ from impingement, is therefore entirely the result of a drop in mean velocity U_0 at a nearly constant centerline fluctuating velocity u' .

Because of the representation of u' profiles in Figure 4.10 in terms of u'/U_{j0} , consideration of the effect of the parameter, w , was not included in that discussion. However, from Figure 4.11 it can be seen that for all values of $0 \leq z/w \leq 18$ the turbulence intensity consistently increases with nozzle width. For instance, over the range $0 \leq z/w \leq 4$ and $Re_j = 11000$, the jet centerline turbulence intensity for the largest nozzle, $w = 13.3$ mm, is around 50% higher than that for the smallest nozzle, $w = 2.5$ mm. The absolute differences in turbulence intensity as a function of nozzle width remain about the same further downstream, but the relative differences of course become much smaller as turbulence intensity increases. For the same $Re_j = 11000$, the lateral turbulence profiles at $z/w = 0$, Figures 4.3 through 4.6, and that at $z/w = 16$, Figure 4.8, showed the same trend for the effect of nozzle width. So even though the dependence of turbulence level on w becomes relatively less significant as the jet becomes fully developed, i.e. with increasing distance from the nozzle exit, incorporating w in the dimensionless parameter Re_j unfortunately does not yield data completely indepen-

dent of w . As noted at the outset, development of jet mean velocity can better be understood through examination of turbulence. Thus subsequent to the presentation of lateral and axial turbulence profiles in Figures 4.7 through 4.11, axial mean velocity development downstream of the nozzle exit will now be inspected through profiles along the jet centerline, Figures 4.12 through 4.14 and lateral profiles, Figures 4.15 and 4.16.

As for the two preceding figures Figure 4.12 portrays two sets of data for $Re_j = 11000$; the band of data for values of nozzle width for a single jet, enclosed between the solid lines, and another band of data for multiple impinging jets. The lower limit of the multiple jet data, that for $S/H = 0.375$, the narrowest flow cell, is indicated by a dotted line. A dashed line identifies data for the next size flow cell, $S/H = 0.5$. As data for the widest flow cell, $S/H = 1$, occur in a congested region this limit is not indicated by a line. These data are values of jet centerline mean velocity, U_o , normalized with respect to that at the nozzle exit, U_{jo} , shown in Table 4.4 for all values of w . The single jet data are considered now, the multiple jet data in the following section.

As shown in Figure 4.12 the mean centerline velocity of a single jet remains constant from the nozzle exit, $z/w = 0$, down to around $z/w = 3-4$, then decreases at a constant rate. With the presence of an impingement surface at $z/w = 19$, U_o starts its drop to zero at the stagnation point at a distance of about $4w$ from that surface. This distance is similar to that reported by Gutmark et al. (1978).

The mean centerline velocity profiles of Figure 4.12 display the familiar regions documented by previous workers, i.e. the potential core, developing jet, developed jet, and impingement regions, and therefore do not require discussion here. The only aspect meriting comment is a trend at constant

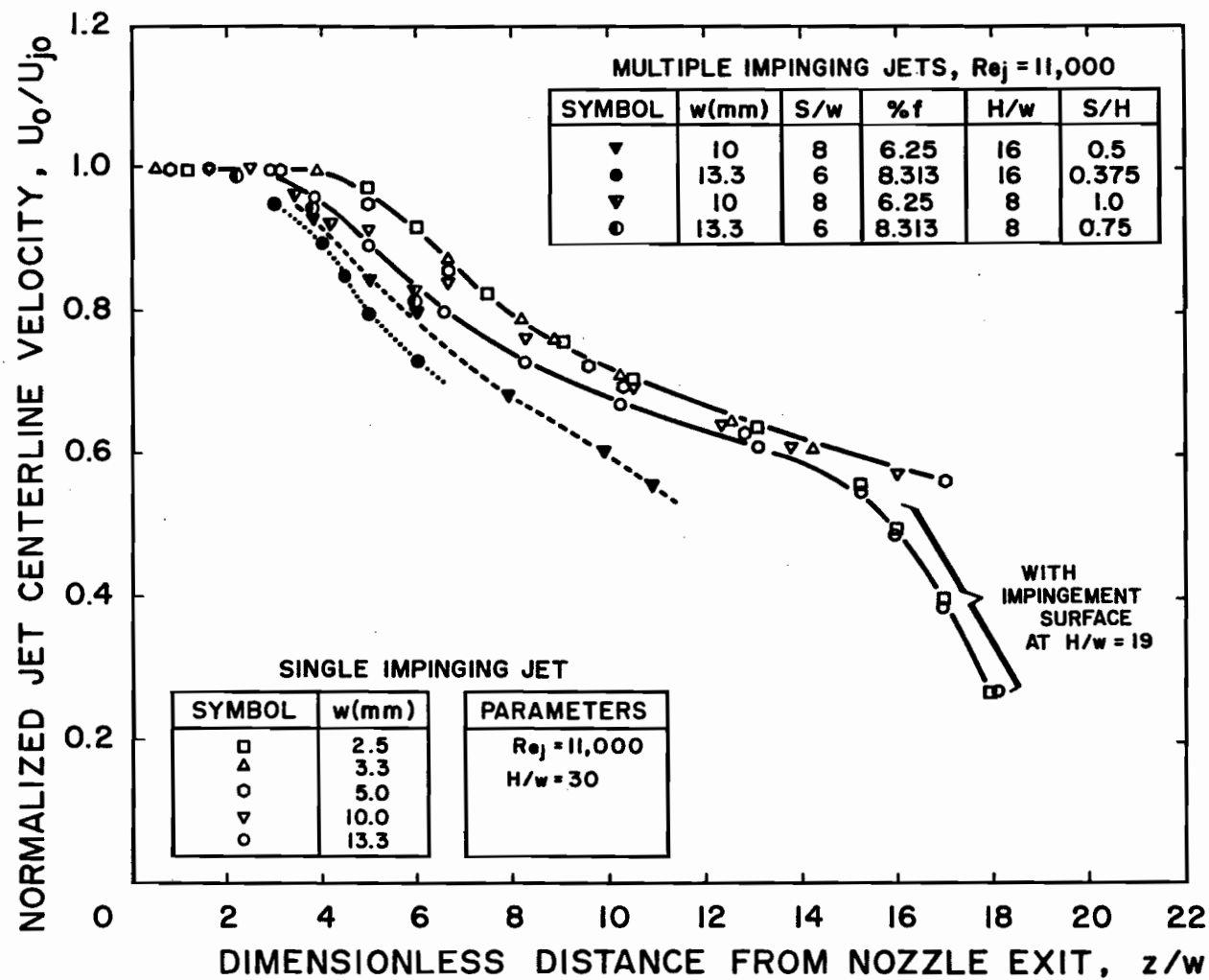


FIGURE 4.12. Profiles of Mean Velocity at the Jet Centerline

Reynolds number for some dependence of length of potential core on nozzle width. This effect may be seen more clearly from Figure 4.13 where the profile is expressed in terms of $(U_{jo}/U_o)^2$, as proposed by previous studies (Flora and Goldschmidt, 1969) who suggested the following form of empirical correlation,

$$(U_o/U_{jo})^{-2} = K_1(z/w - H_o/w) \quad (4.1)$$

The kinematic virtual origin, H_o/w , is the intercept of velocity decay lines with the abscissa. For only the limiting values of nozzle width, i.e. $w = 2.5$ and 13.3 mm, the velocity decay lines are illustrated in Figure 4.13. The kinematic origin moves away from the nozzle geometric origin consistently with increasing w , as tabulated on this figure. Thus the length of the potential core produced by the largest nozzle ($w = 13.3$ mm) is $1.15w$ shorter than that produced by the smallest nozzle ($w = 2.5$ mm). Flora and Goldschmidt (1969) found, for a similar short, $t/w = 1$, elliptic contoured nozzle ($w = 12.7$ mm and $Re_j = 17000$), the location of the kinematic origin to be at $1w$ upstream of the nozzle exit, $H_o/w = 1$; this agrees quite well with the present findings. The reduction of potential core length with increasing w corresponds to the increase of centerline turbulence with w as illustrated by Figure 4.11. As noted earlier, the rate of turbulent transport of axial momentum between lateral regions depends on the level of turbulence. Thus there is consistency between the experimental findings here that the larger the nozzle, the higher the turbulence, the earlier the decay of the centerline mean velocity, and the shorter the potential core.

Hills, Jenkins and Gilbert (1975) found a decreasing potential core length with decreasing jet velocity only when the initial nozzle boundary layer is laminar or in transition, and reported the effect to be dependent

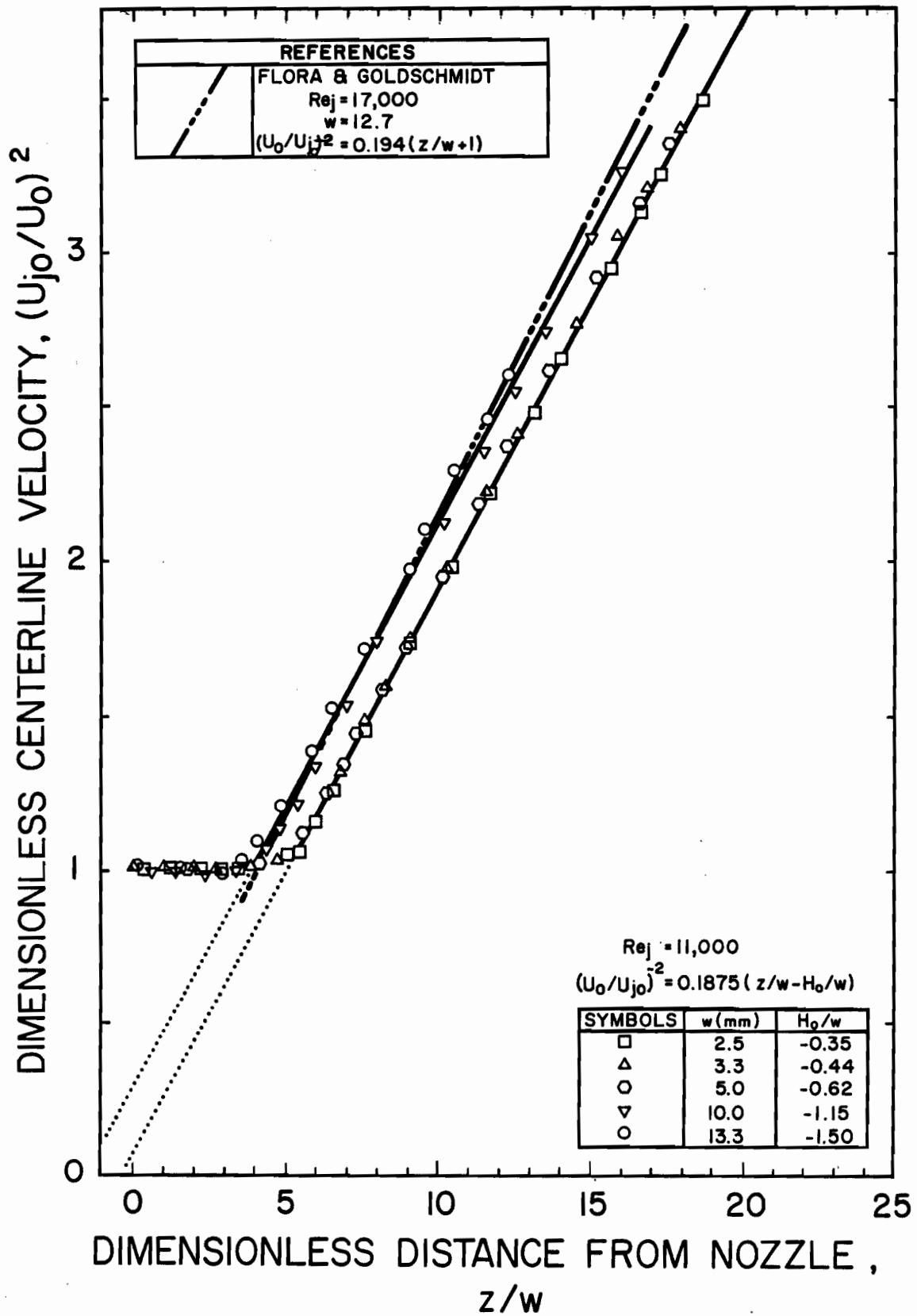


FIGURE 4.13. Mean Velocity Decay at the Jet Centerline

upon the turbulence characteristics upstream of the nozzle. In an attempt at explaining this phenomenon, Bradshaw (1966) attributed the decrease of potential core length with increasing w to the high level of Reynolds stresses in the boundary layer relative to the shear layer. The shear layer in turn produces a large scale structure of periodic disturbances that are more suppressed for a turbulent boundary layer.

Thus for the same jet Reynolds number, $Re_j = 11000$, a larger nozzle with lower exit mean velocity produces a flow field downstream of the nozzle exit that is more susceptible to disturbances from large scale structures, causing an earlier decay of centerline mean velocity hence a shorter potential core, while narrower nozzle suppresses these disturbances due to its higher acceleration.

Although the onset of decay of centerline mean velocity is to some extent a function of w , its decay rate, K_1 , remains constant as shown in Figure 4.14 where the profiles appear as a function of downstream distance corrected for the displacement with w . The complete results thereby converge to a single curve that decays with the inverse of the square root of the corrected distance as follows:

$$U_o/U_{jo} = 2.31[(z - H_o)/w]^{-0.5} \quad (4.2)$$

The intercept, 2.31, compares well with that found by Flora and Goldschmidt (1969).

After discussing the effect of w on jet centerline mean velocity, its effect away from that centerline is now considered. Similar to turbulence lateral profiles reported in Figures 4.7 and 4.8, lateral profiles of axial mean velocity, U , measured at $z/w = 16$ for $Re_j = 11000$ and for all values of w , are given on Figure 4.15. The lateral distance, x , was non-

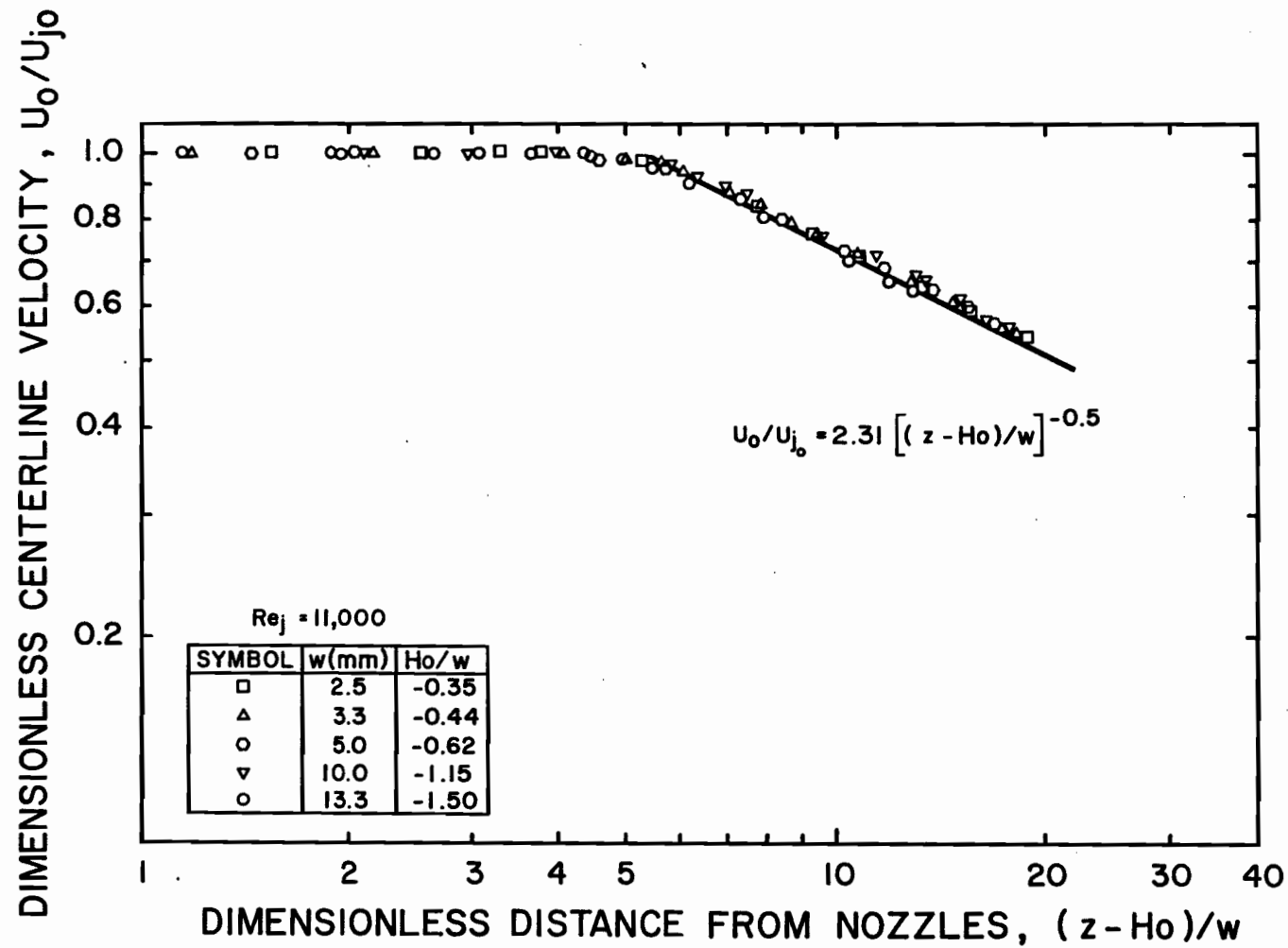


FIGURE 4.14. Mean Velocity at the Jet Centerline

dimensionalized with respect to the jet half width $x_{0.5}$, defined as the distance from jet centerline at which $U = 0.5 U_0$. At $z/w = 16$, $x_{0.5}/w$ can be obtained from Figure 4.16 as shown subsequently. Unlike the flat velocity profiles obtained at the nozzle exit, $z/w = 0$, as in Figures 4.3 through 4.6, the velocity profiles at $z/w = 16$ in Figure 4.15 present the limit for developed flow. These profiles are therefore well represented by Reichardt's solution:

$$U/U_0 = \exp - [0.693(x/x_{0.5})^2] \quad (4.3)$$

Since the dependence of this velocity profile upon w starts from the nozzle exit and continues all the way downstream, it is better discussed based on data in Figure 4.16 as shown subsequently.

Although no lateral profiles of axial mean velocity are given for other locations from the nozzle exit, i.e. $0 < z/w < 17$, additional information on the development of axial mean velocity in the lateral direction is presented in terms of jet half width $x_{0.5}$, which expresses the spreading characteristics of the free jet. Hence at $Re_j = 11000$ and for all values of w , $x_{0.5}/w$ was plotted versus the distance from the nozzle exit, z/w , as proposed by Flora and Goldschmidt who suggested the following form of empirical correlation,

$$x_{0.5}/w = K_2(z/w - H_G/w) \quad (4.4)$$

The geometric origin, H_G/w , the intercept of the half velocity lines with the abscissa, is also a measure of the displacement of these lines from the geometric origin of the jet, $z/w = 0$.

From immediately after the nozzle exit to around 3-4w downstream, i.e. within the potential core region, the jet half width remains effectively

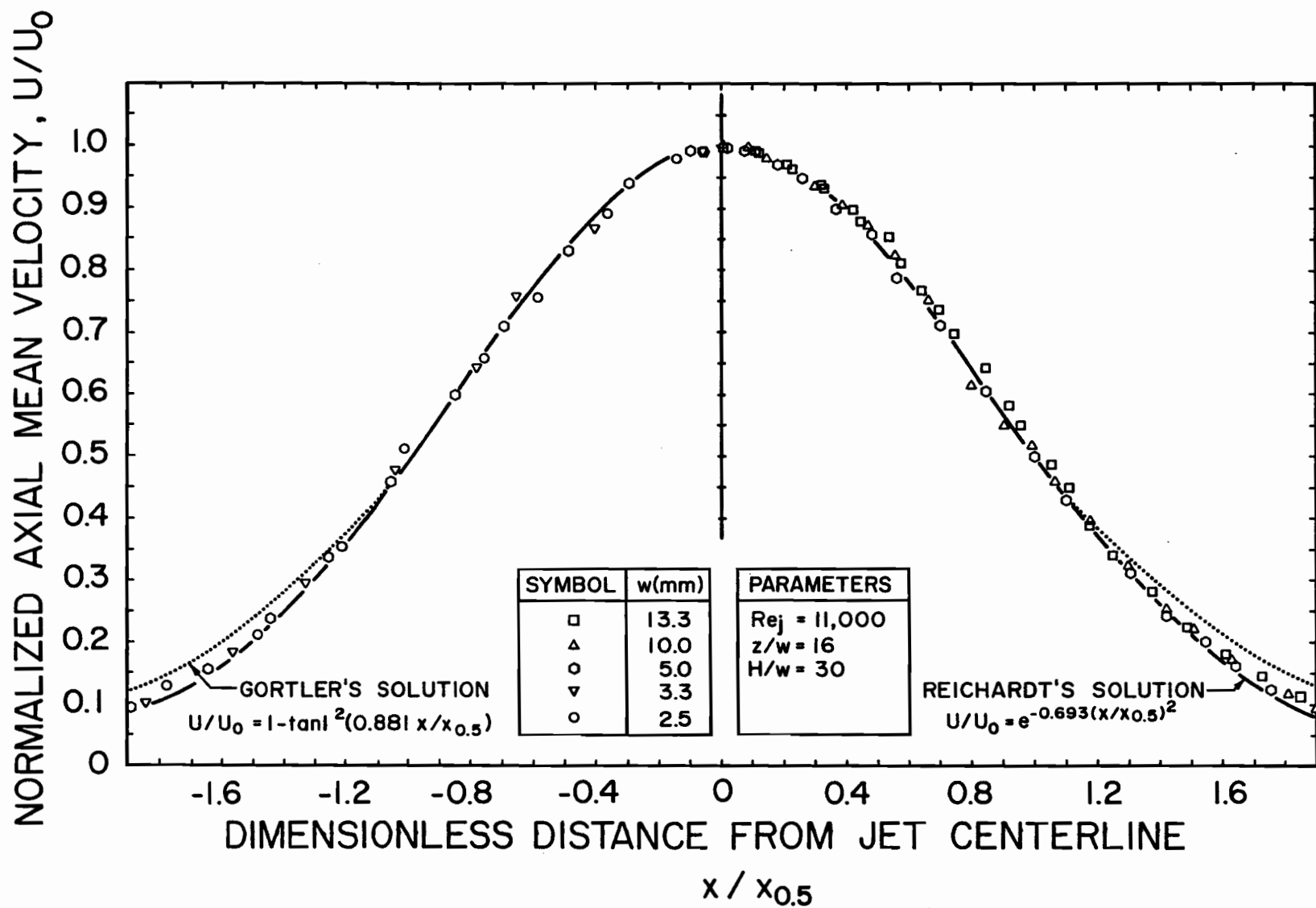


FIGURE 4.15. Lateral Profiles of Axial Mean Velocity at $z/w = 16$

equal to $0.5w$. Downstream of this region the spreading is observed to increase at a constant rate $K_2 = 0.119$, by a family of curves which are displaced consistently from the jet centerline with increasing w . Similarly to Figure 4.13, i.e. for only the limiting values of nozzle width, i.e. $w = 2.5$ mm and 13.3 mm, the intercepts of the half velocity lines (spreading lines) with the abscissa are illustrated in Figure 4.16. The kinematic origin, H_G/w , moves away from the nozzle geometric origin consistently with w , as tabulated in this figure. These results agree well with those of Flora and Goldschmidt (1969) as shown in Figure 4.16. The dependence of jet spreading upon w is consistent with that of centerline velocity decay shown earlier.

Numerous aspects of measurements of the flow field can now be integrated. At constant jet Reynolds number, $Re_j = 11000$, the wider nozzle shows a more turbulent flow field because with its smaller contraction ratio from the plenum chamber there is a less suppression of turbulence, hence a higher turbulence level at the nozzle exit, which in turn initiates a more turbulent jet at the nozzle exit, an effect which continues downstream from the nozzle exit. This high turbulence level in jets from larger nozzles at constant Re_j produces higher rates of lateral transport of momentum, hence a shorter potential core, earlier onset of axial mean velocity decay as well as earlier lateral spreading with axial distance downstream.

After analysis of the flow field for a single jet, attention may now be turned to the more challenging case of multiple impinging jets.

4.4.2 Multiple Jet Flow Downstream from the Nozzle Exit

For the confined multiple impinging jet system with slot exhaust ports alternating symmetrically between slot jet nozzles which is under study, a

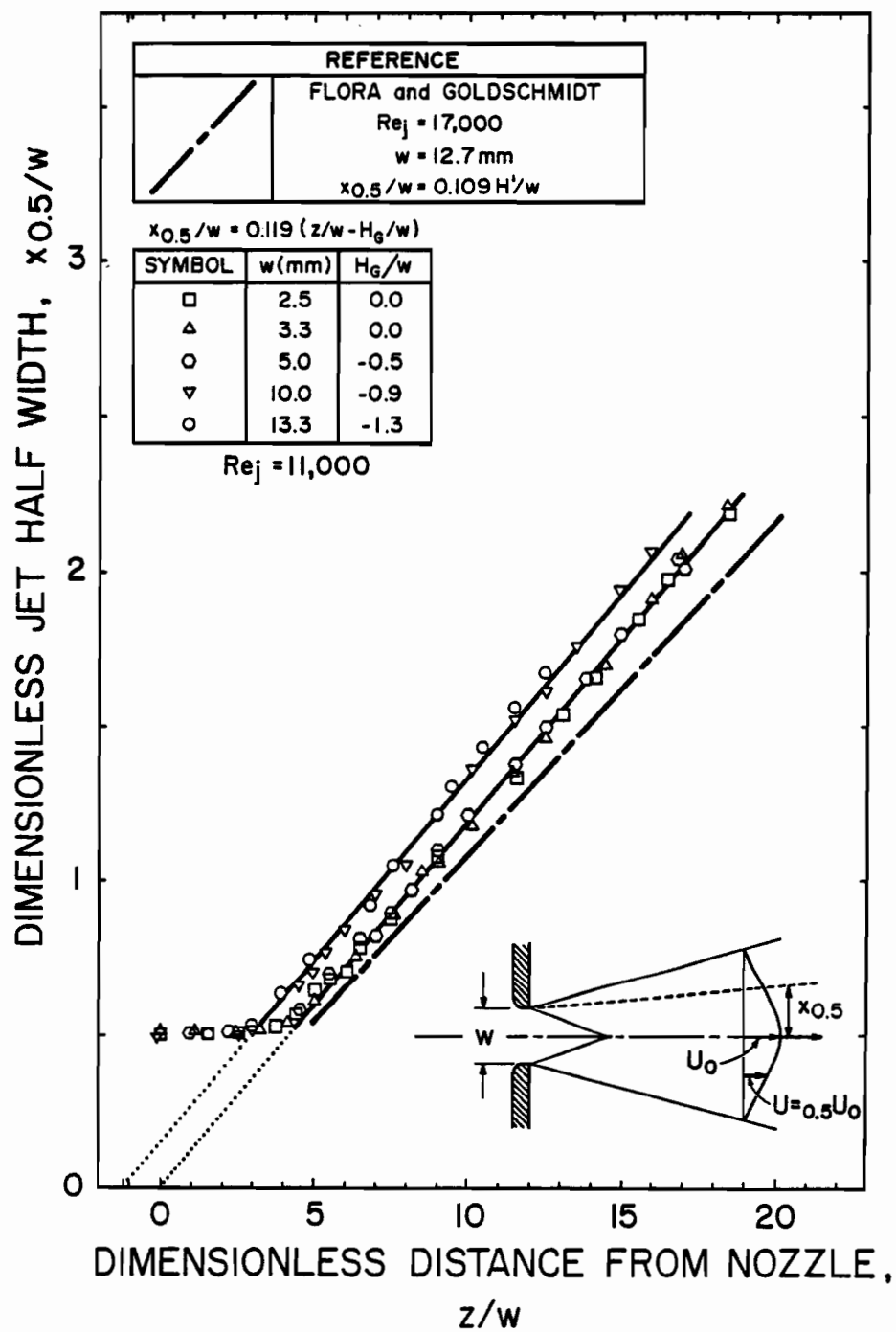


FIGURE 4.16. Jet Half-Width

central feature of analysis of results is the concept developed here of a "flow cell". This concept identifies the basic flow unit which is repeated, in pairs, for as many slot nozzles as such a multiple jet system may contain. As indicated in Figure 4.1, the test facility comprising 3 slot nozzles constructed for the present study contains 6 flow cells. It is evident from Figure 4.1 that even when the geometric and flow parameters for a single and a multiple jet system are identical, the flow field in a flow cell of the latter must be different from that for the corresponding single jet, at least over the region away from the jet centerline. However, it is also evident from consideration of Figure 4.1 that for a multiple jet system with jet nozzles and exhaust ports spaced sufficiently far apart, interaction from the outflow would not extend to the jet centerline. In impinging jets conditions along the jet centerline assume exceptional importance because they affect the high rates of transport of heat and/or mass in the near stagnation region of the impingement surface.

This perspective establishes the basis of the importance of knowing how to characterize conditions for which the jet centerline flow in a multiple jet system does not differ from that of a single jet at the same geometrical and flow parameters. Further, under conditions for which jet centerline flow characteristics do deviate from those for the equivalent single jet a logical basis of categorizing such conditions is needed. The dimensionless parameter, S/H , flow cell geometric proportions, introduced in the present study will be seen to be most useful in this regard. In subsequent discussion, the terms "non-interacting" or "interacting" will be used to describe the contrasting cases when the jet centerline flow conditions are the same as or different from those for the equivalent single jet.

From Table 4.1 it will be recalled that the experimental facility of the present study could be adjusted to provide flow cells for which the dimensionless parameter, S/H , varied between the limits of 0.33 and 6. For the specific purpose of studying the effect of multiple jets on jet centerline flow conditions, a sub-set of just four geometrical parameters from the right-hand side of Table 4.1 was selected, specifically two values of inter-jet spacing, $S/w = 8$ and 6 for two values of confinement surface-to-impingement surface spacing, $H/w = 8$ and 16. This sub-set covered a range in flow cell proportions, S/H , between 0.375 and 1, which was sufficient to cover the range from non-interacting to highly interacting multiple jets, the objective of this part of the investigation. These four sets of geometrical parameters, taken from the complete listing of Table 4.1, are reproduced in Table 4.5, this time in order of the value of the respective flow cell proportion, S/H , because of the central importance of the latter parameter.

The set of Figures 4.10, 4.11 and 4.12 document the dependence on geometrical parameters, particularly on S/H , the flow cell proportion, of axial fluctuating velocity, axial turbulence intensity, and axial mean velocity, respectively, along the jet centerline.

With respect to profiles of fluctuating velocity, it is apparent from Figure 4.10 that there is relatively little difference in centerline fluctuating velocity between a single and a multiple jet system for a flow cell of $S/H = 1$. More precisely, the data indicate that axial fluctuating velocity is only marginally higher perhaps by 15%, for a multiple jet system cell of $S/H = 1$, relative to an equivalent single jet. It can be seen that for the multiple jet system this profile was measured out to about $z/w = 6$, i.e. only about $2w$ from the impingement surface at $H/w = 8$. Although a slight effect on centerline fluctuating velocity may then be ascribed to interaction

in this multiple jet system, a satisfactory approximation would be to characterize the $S/H = 1$ flow cell as effectively a non-interacting jet at the jet centerline, at least as indicated by measurement of centerline turbulence velocity.

For the narrower flow cell, $S/H = 0.75$, Figure 4.10 indicates that at about $2.5w$ from the nozzle exit the single and multiple jet centerline profiles of fluctuating velocity are indistinguishable. However, beyond $z/w = 2.5$ the multiple jets are obviously strongly interacting all the way to the jet centerline. Thus by $z/w = 6$, i.e. $2w$ from the impingement surface, the centerline fluctuating velocity for the multiple jet system at $S/H = 0.75$ is effectively double that for the equivalent single jet, which constitutes strong interaction indeed. For the next narrower flow cell, $S/H = 0.5$, Figure 4.10 indicates that the interaction between the multiple jets reaches the centerline earlier yet, at about $z/w = 2.0$. For the narrowest flow cell, $S/H = 0.375$, the multiple jets are so strongly interacting there is no discernable distance from the nozzle exit before the centerline displays a penetrating interaction. By only $z/w = 0.5$ the centerline fluctuating velocity for the $S/H = 0.375$ flow cell is already about double that for the equivalent single jet and by $z/w = 3$ the centerline fluctuating velocity is about 4 times as high.

If axial turbulence intensity rather than turbulence velocity is taken as the criterion to characterize the onset of the extent of interaction at the jet centerline for multiple jet systems, Figure 4.11 indicates essentially the identical conclusions as did Figure 4.10 for fluctuating velocity.

If axial mean velocity rather than any turbulence variable were taken as the criterion for interaction along the jet centerline of multiple slot jet systems, Figure 4.12 would provide the indication. Here we see quali-

tatively the same effects as for the turbulence variables on Figures 4.10 and 4.11, although the magnitude of the effects on mean velocity are less, especially in the jet development region. It is clear that the narrowest flow cell, $S/H = 0.375$, results in a more rapid decay of centerline mean velocity than for the reference single jet case. The trend with S/H remains consistent, i.e. for $S/H = 0.5$ there is significantly less interaction at the centerline, at $S/H = 0.75$ some interaction is apparent, while for a flow cell of $S/H = 1$ the effect is marginal, approximately within the range of accuracy of the measurement.

From analysis of the interdependence between turbulence and mean velocity presented earlier in connection with single jet results, it is of course entirely predictable that as the multiple jet interaction effect is to enhance levels of turbulence, the interaction effect on axial mean velocity would be to cause more rapid decay of centerline velocity, which is of course the direction of these effects as documented on Figure 4.12.

As another view of when multiple slot jets become interacting it is instructive to examine the relationship between jet half-width and flow cell proportions, as may be done by reference to Table 4.6. In the center section of this table are listed the values of jet half-width for single jets for a number of combinations of values of w and H/w . In the right-hand section the jet half-widths, $x_{0.5}/w$, are re-expressed as $x_{0.5}/S$. By inspection of the correlation between S/H and $x_{0.5}/S$ one may conclude that multiple jets begin to be interacting along the jet centerline when the jet half-width reaches about 15% of the spacing between jet and exhaust centerlines.

The question of the extent of interaction between jets in multiple slot jet systems will recur in the following section concerned with the flow

TABLE 4.6. Jet Half-Width for Analysis of Free Jet Development

<div> <div>w (mm)</div> <div>H/w</div> </div>	S/H			$x_{0.5}/w$			$x_{0.5}/S$		
	5.0	10.0	13.3	5.0	10.0	13.3	5.0	10.0	13.3
8	2	1	0.75	1.01	1.06	1.11	0.06	0.13	0.18
16	1	0.5	0.375	1.96	2.01	2.06	0.13	0.25	0.34
24	0.67	0.33	-	2.96	2.96	-	0.18	0.37	-

$$x_{0.5}/w = 0.119(z/w - H_G/w)$$

field at the impingement surface, for which the concepts of flow cells and the flow cell geometric parameter, S/H , developed in the present section will find further utility.

4.5 Flow Field at the Impingement Surface

After characterizing the flow first at the nozzle exit for all values of w over the range $10800 \leq Re_j \leq 18700$, then downstream from the nozzle exit over a range of size of flow cells $0.375 \leq S/H \leq 1$ at $Re_j = 11000$, the effect at the impingement surface of these parameters, i.e. geometrical and flow parameters, for the multiple slot jet system illustrated in Figure 4.1 will now be presented. A wide spectrum of flow cell geometry, i.e. $0.375 \leq S/H \leq 6$, covering the range from interacting to non-interacting multiple impinging jets, was tested over the entire range of jet Reynolds number, $5000 < Re_j < 43800$.

Flow at the impingement surface is analyzed through examination of static pressure profiles as this sensitive variable can be measured accurately. Presentation continues the pattern of the previous section, i.e. results are considered first for the single impinging jet, then for multiple impinging jets, both systems as represented on Figure 4.1.

4.5.1 Impingement Flow for a Single Confined Slot Jet

Static pressure profiles were obtained for a single jet with $w = 3.3$ and 13.3 mm, and $H/w = 4, 8$ and 16, at $Re_j = 20700$, over a length $S = 80$ mm. These geometrical parameters correspond to some of those listed in Table 4.7 for the multiple jet system.

Lateral profiles of static pressure normalized with respect to pressure at the stagnation point, $\Delta P/\Delta P_o$, are presented in Figures 4.17 and 4.18.

TABLE 4.7. Geometrical and Flow Parameters of the Multiple Jet System for Analysis of Impingement Surface Flow Conditions

Table 4.7(a)

w (mm)	S/w	$f, \%$	H/w	S/H	Re_j	ΔP_o (N/m^2)	$\Delta P_o / \Delta P_j$
3.3	24	2.06	4	6	5000	427	0.8
					9500	1560	0.86
					20700	7260	0.9
			8	3	5000	340	0.64
					9500	1248	0.69
					20700	5808	0.72
			16	1.5	5000	200	0.38
					9500	750	0.41
					20700	2880	0.36
13.3	6	8.313	4	1.5	20700	432	0.84
					30000	917	0.89
					43800	2095	0.91
			8	0.75	20700	334	0.65
					30000	709	0.69
					43800	1620	0.70
			16	0.375	20700	102	0.2
					30000	205	0.2
					43800	459	0.19

Table 4.7(b)

w (mm)	Re_j	U_j^* (m/s)	ΔP_j (N/m^2)	R_j (W/m^2)
3.3	5000	26.7	528	290
	9500	51	1804	1896
	20700	110	8010	18152
13.3	20700	27.4	510	1161
	30000	39.7	1026	3387
	43800	60	2296	11450

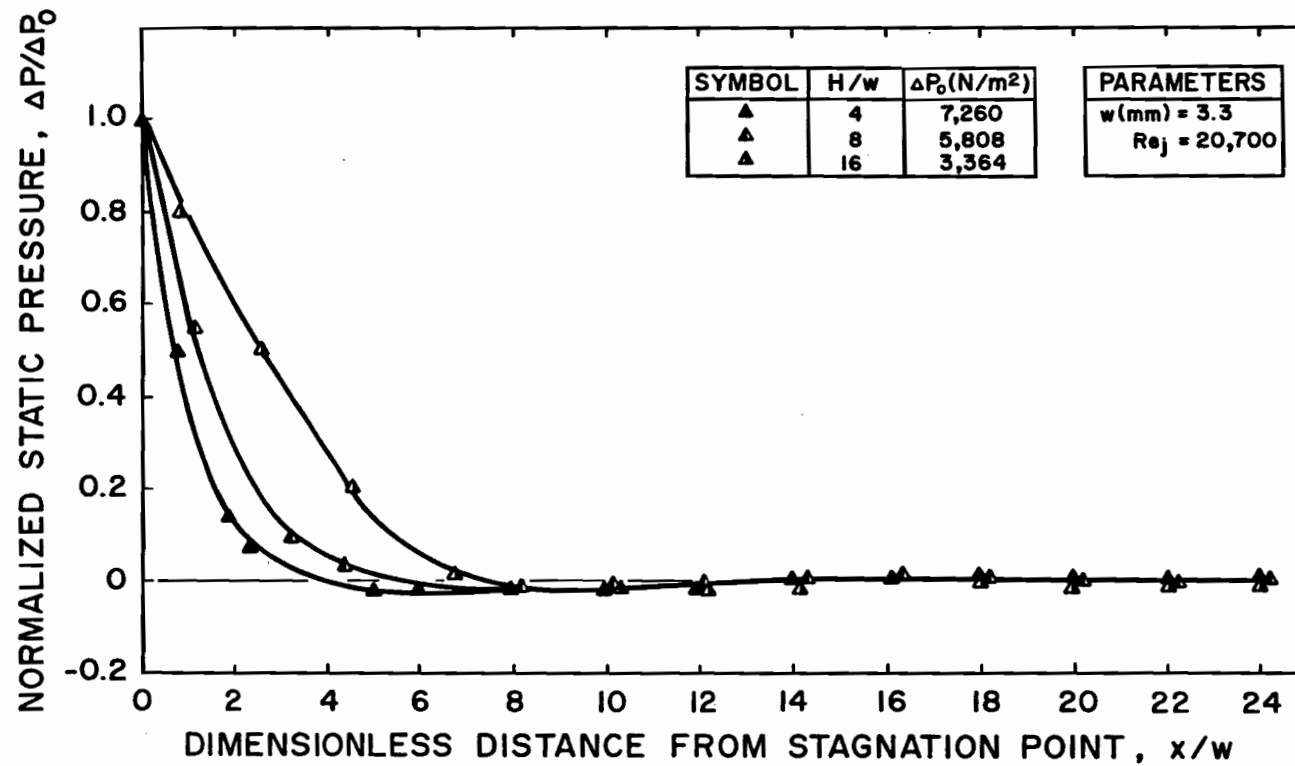


FIGURE 4.17. Lateral Profile of Static Pressure at the Impingement Surface for a Single Slot Jet

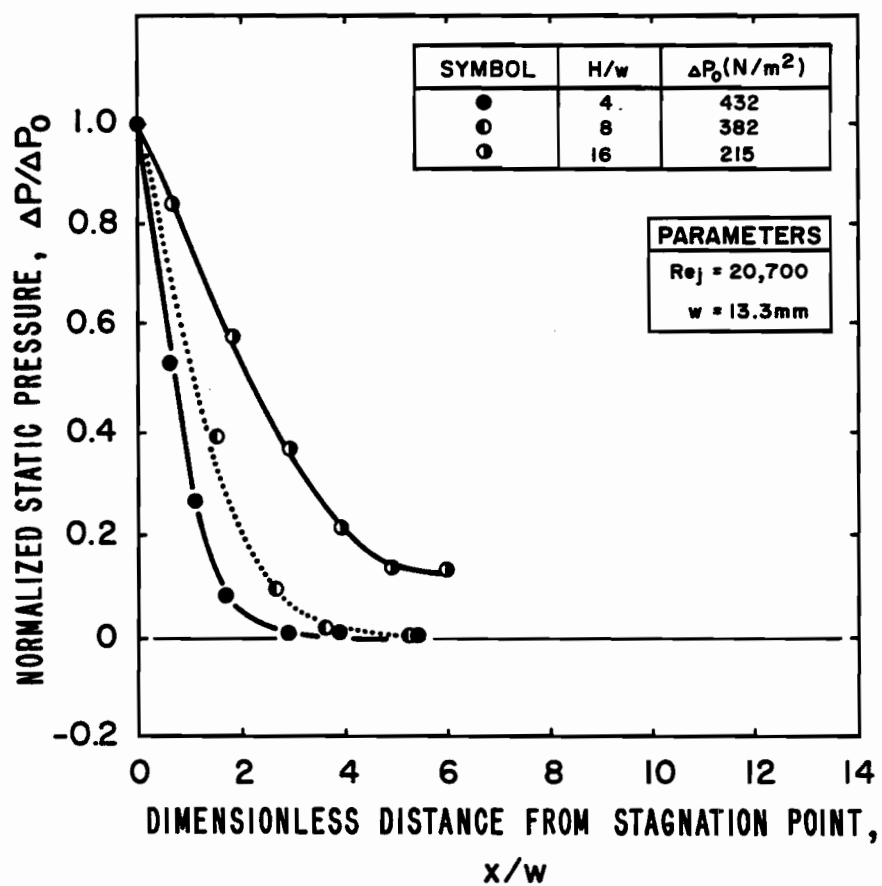


FIGURE 4.18. Lateral Profile of Static Pressure at the Impingement Surface for a Single Slot Jet

These profiles reveal that static pressure decreases sharply from its maximum value at the stagnation point to nearly ambient pressure by about $3w-8w$ from stagnation, the latter location naturally increasing in the increasing H/w . The larger the impingement surface spacing, $4 < H/w < 16$, the larger the jet spreading before impingement, hence the wider the extent of the impingement surface over which the pressure from the jet is felt, as may be seen from Figure 4.17. Within this stagnation region, $0 < x/w < 3-8$, conditions reflect lateral flow acceleration as the incoming free jet axial flow turns 90° and lateral wall jet flow starts to form. Downstream from $x/w = 3-8$ the developing wall jet is a region of flow deceleration where the static pressure increases slightly up to about $x/w = 14$, thereafter remaining steady. This flow region does not form for shorter impingement surface, i.e. $x/w = 6$ as shown in Figure 4.18.

4.5.2 Impingement Flow for the Multiple Slot Jet System

From the comprehensive tabulation of geometrical parameters of the multiple jet system given by Table 4.1, a more detailed compilation of the geometrical and flow parameters used for the impingement flow investigation is given now as Table 4.7. The values of flow cell proportions, S/H , and jet Reynolds number cover the entire range of geometrical and flow parameters. The six limiting combinations of flow cells, $S/H = 6, 3, 1.5$ for $S/w = 24$ at $H/w = 4, 8$ and 16 respectively, and $S/H = 1.5, 0.75$ and 0.375 for $S/w = 6$ at $H/w = 4, 8$ and 16 respectively, are depicted in Figures 4.19 and 4.20. For the analysis which follows reference should be made to Figures 4.19 and 4.20 because of the central role of the concept of flow cell proportions in a confined multiple impinging slot jet system. Thus with that visual representation of the range of flow cell proportions studied,

the effect of jet Reynolds number and geometrical parameters on impingement surface pressure profiles may now be examined.

For the widest flow cell, $S/H = 6$, it is evident from Figure 4.19(a) that there occurs first the usual impingement region, then a particularly long wall jet region, and finally a region around the centerline of the exit ports which has not previously been named as it does not exist in the single jet case studied by many earlier investigators, but which may logically be termed the exit port flow region. Here the wall jet type flow is succeeded by a flow from the impingement surface to the exhaust port in the confinement surface. In the exit port flow region the lateral velocities are approaching zero, the limiting value at the exit port centerline, while the normal velocity away from the impingement surface is becoming correspondingly large. The flow in the exit port flow region clearly differs from that in a wall jet where mean velocity normal to the impingement surface is smaller than that parallel to the surface. In any case, for a multiple impinging jet system with large internozzle spacings, as depicted in Figure 4.19(a), it may be expected that conditions at the impingement surface could be quite well predicted from data for a single jet for the same flow and geometrical parameters.

At the other extreme in flow cell proportions, i.e. for the narrowest flow cell, $S/H = 0.375$, Figure 4.20(c) indicates that the wall jet region effectively vanishes, there being essentially a transition from an impingement flow directly to the converse, i.e. to an exit port region flow. In this case, fluid which enters and leaves along the centerlines of the inlet nozzle and exit ports in fact travels over 6 times the spacing S in passing the distance $H = 2.67S$ from nozzle exit to stagnation point, then along the impingement surface over distance S before leaving via the exit

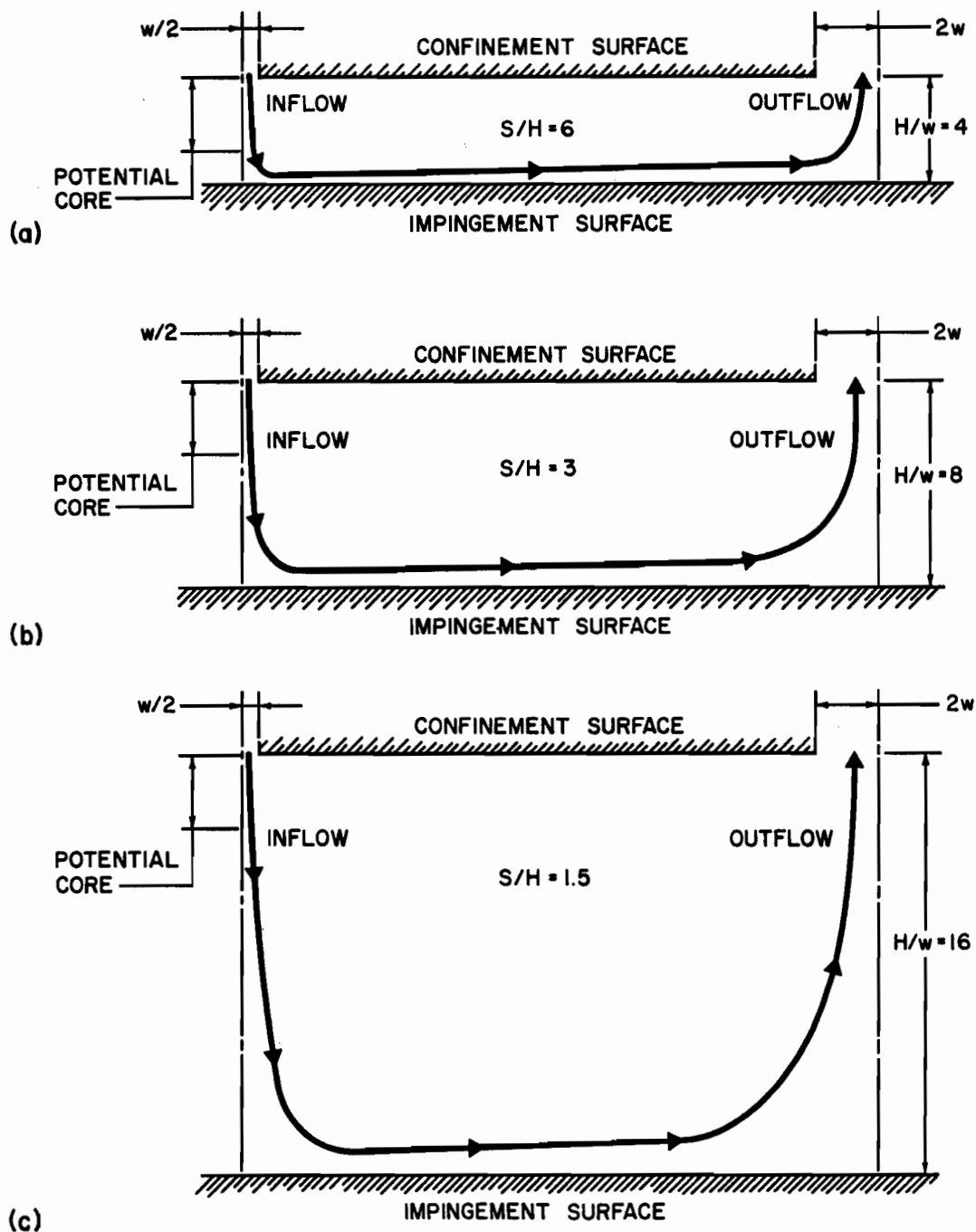


FIGURE 4.19. Schematic Diagrams of Flow Cell Proportions
 $S/H = 6, 3$ and 1.5

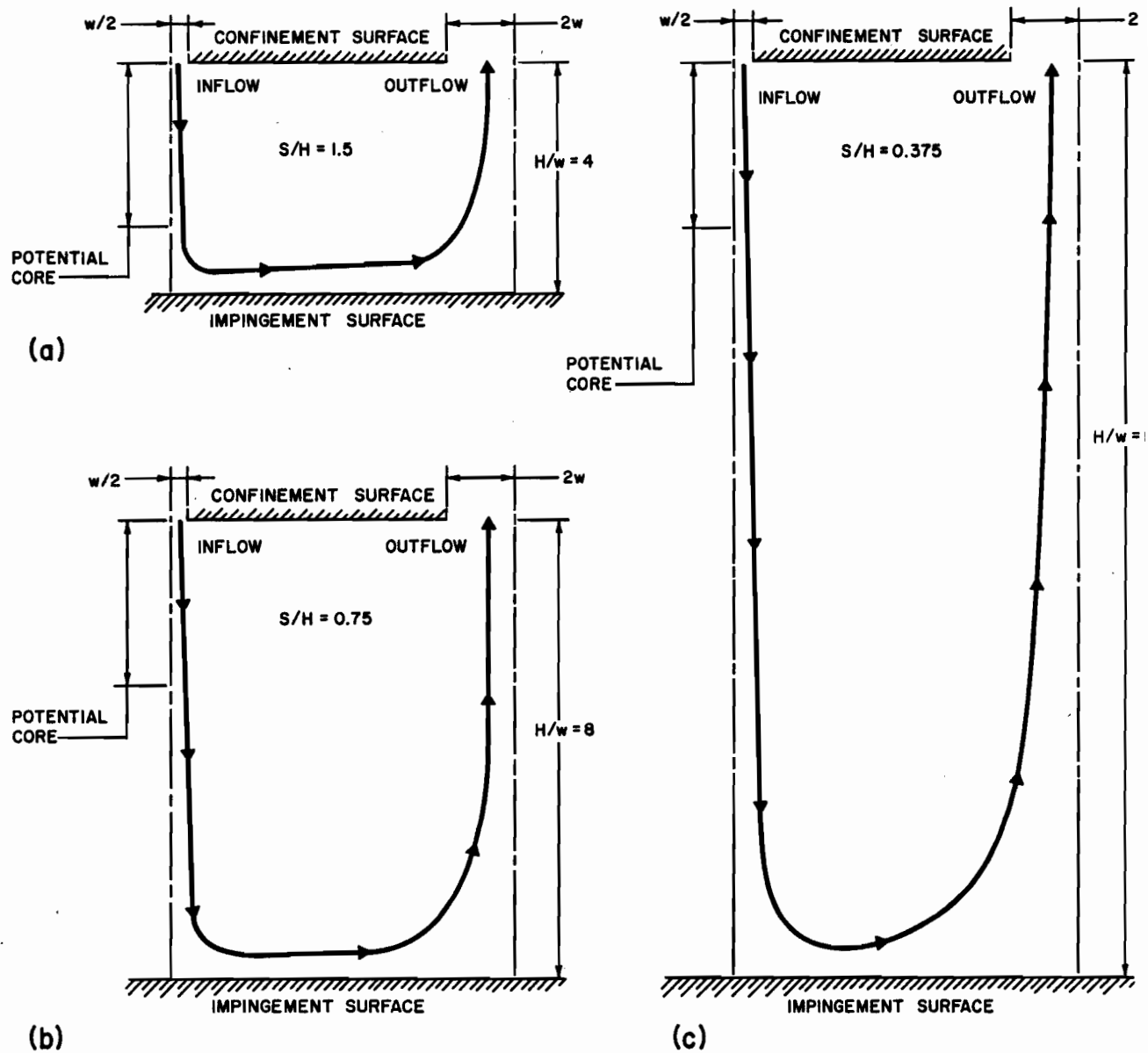


FIGURE 4.20. Schematic Diagrams of Flow Cell Proportions
 $S/H = 1.5, 0.75$ and 0.375

port centerline, another distance $H = 2.67S$. For flow cells of proportions as narrow as this it may be anticipated that extensive interaction would occur between inlet jets and the adjacent exit flows with the result that impingement surface flow and heat transfer would be greatly different relative to the corresponding single jet at the same jet Reynolds number and geometrical parameters.

Subsequently in this section criteria will be developed for distinguishing between systems of confined multiple jets of wide internozzle spacing, which behave as arrays of largely non-interacting single jets, and multiple jet systems of narrow flow cells in which adjacent inlet and exit flows interact strongly so that impingement surface conditions are significantly different from those for the corresponding single jet flow.

For one jet Reynolds number, $Re_j \approx 20700$, Figures 4.21 through 4.23 provide lateral profiles of normalized impingement surface pressure, $\Delta P/\Delta P_o$, for 3 greatly different values of flow cell proportions, $S/H = 3$, 0.75 and 0.375. On these figures the locations are shown for the six flow cells, as numbered on Figure 4.1. For the wide flow cell ($S/H = 3$) of Figure 4.21 there is for each one of the inner flow cells, i.e. from II to V, a lateral flow acceleration region with a negative pressure gradient followed by a lateral flow deceleration, positive pressure gradient region. With a narrower flow cell, $S/H = 0.75$, Figure 4.22 indicates that the region of positive pressure gradient has completely disappeared. For the narrowest flow cell, $S/H = 0.375$, Figure 4.23 indicates a yet more major change in the impingement surface pressure profiles, and hence in the flow, as will be discussed in detail subsequently.

On the other hand, the pressure profiles for the outer flow cells I and VI, as shown in Figure 4.21, are affected significantly by the presence

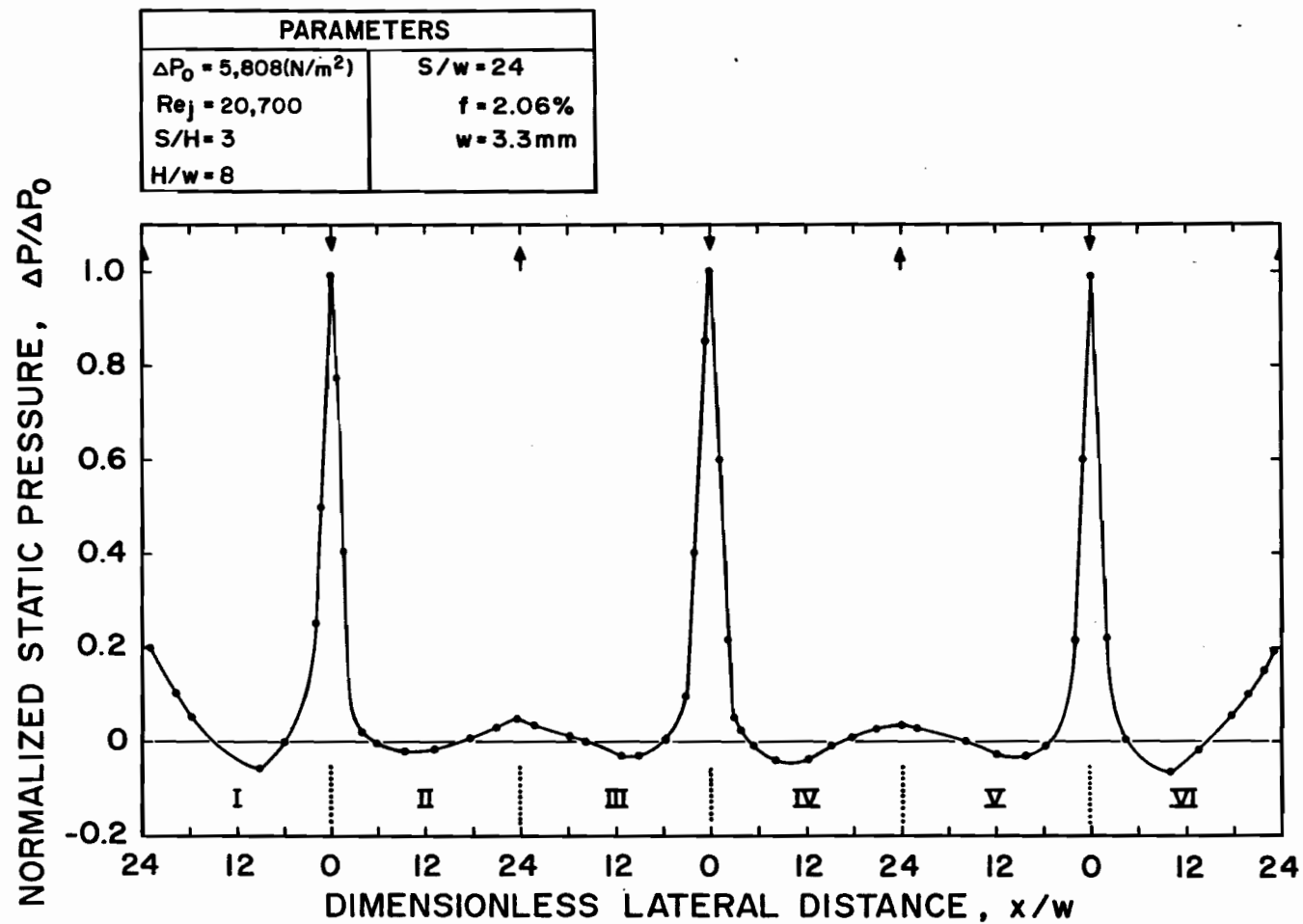


FIGURE 4.21. Lateral Profile of Static Pressure at the Impingement Surface for Multiple Slot Jets at $S/H = 3$

of the end walls. More specifically, in cells I and VI the pressure profiles over the region from stagnation out to about $x/w = 16$ correspond closely to those in flow cells III and IV, respectively. However, it is evident that beyond $x/w = 16$ the pressure profiles in cells I and VI become much steeper than in the central flow cells. Thus a multiple impinging jet system could clearly not be simulated in a test facility that comprised only a single impinging jet with two end walls and with half exhaust ports at the end walls, i.e. a two flow cell system equivalent to the combination of cell I and VI in Figure 4.21.

From inspection of the pressure profiles for cells I, II, V and VI of Figures 4.21, 4.22 and 4.23, it appears likely that a system of two inlet jets, one full exit port located centrally and two half exit ports at the ends would in fact be sufficient to give a pair of cells, centrally located, which would provide a satisfactory representation of flow cells in a multiple jet system. This observation that two inlet jets would appear to be sufficient further confirms that the use of three inlet jets in the present study provides a fully adequate representation of a multiple jet system.

While essential to illustrate the general perspective of impingement surface pressure profiles, Figures 4.21 to 4.23 are not adequate for demonstrating whether or not the central two cells of the 3-jet, 6-flow cell system used here do indeed correspond to the flow cells in the equivalent multiple jet system. For this purpose the data for all four flow cells, II, III, IV and V, of Figures 4.21, 4.22 and 4.23 are shown superimposed on the expanded lateral scale of Figures 4.24, 4.25 and 4.26, respectively. The fact that for each of the three cases a single curve adequately represents the pressure profiles from all four flow cells proves first, that the flow is symmetrical in the central region, flow cells III and IV and second, that

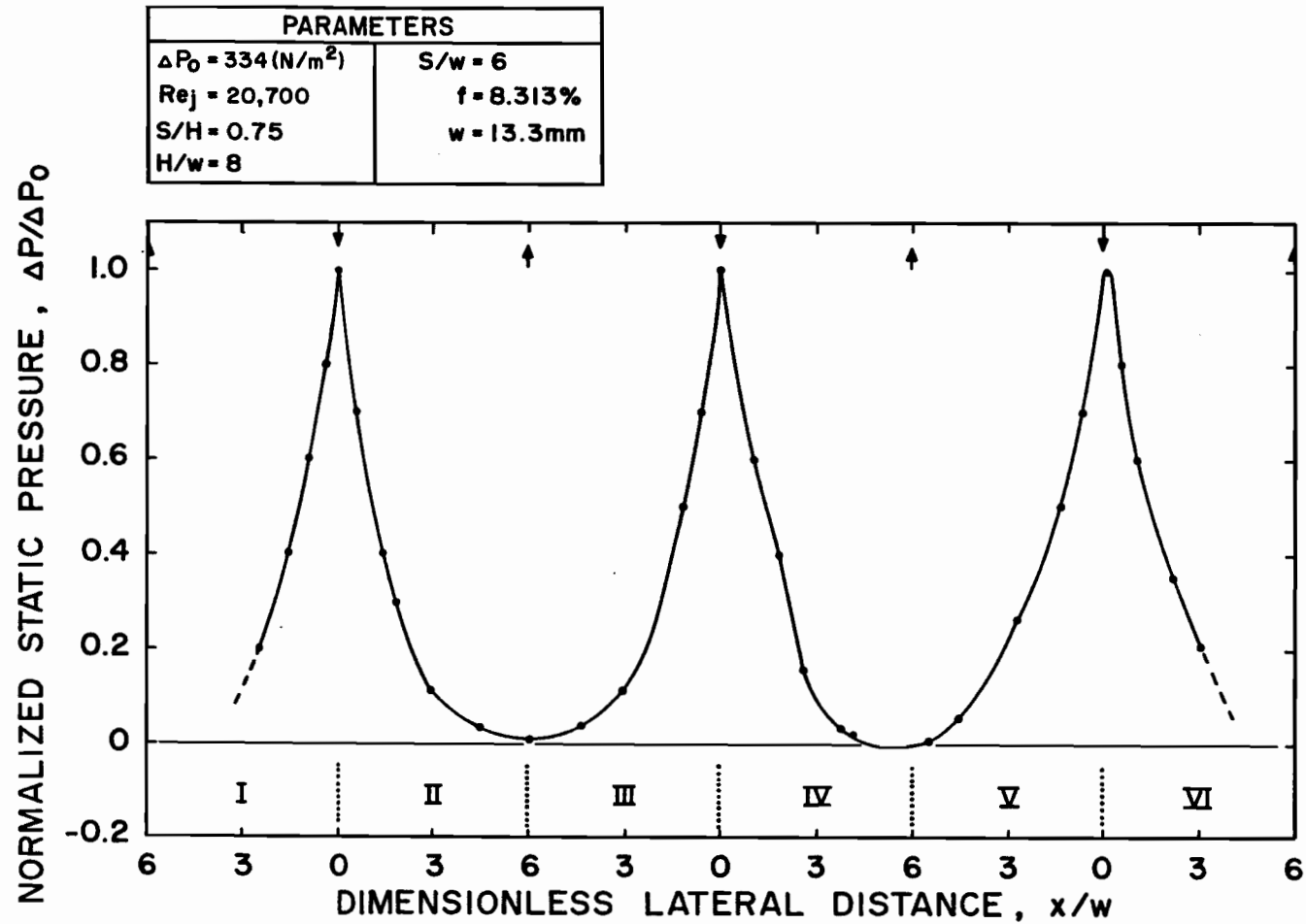


FIGURE 4.22. Lateral Profile of Static Pressure at the Impingement Surface for Multiple Slot Jets at $S/H = 0.75$

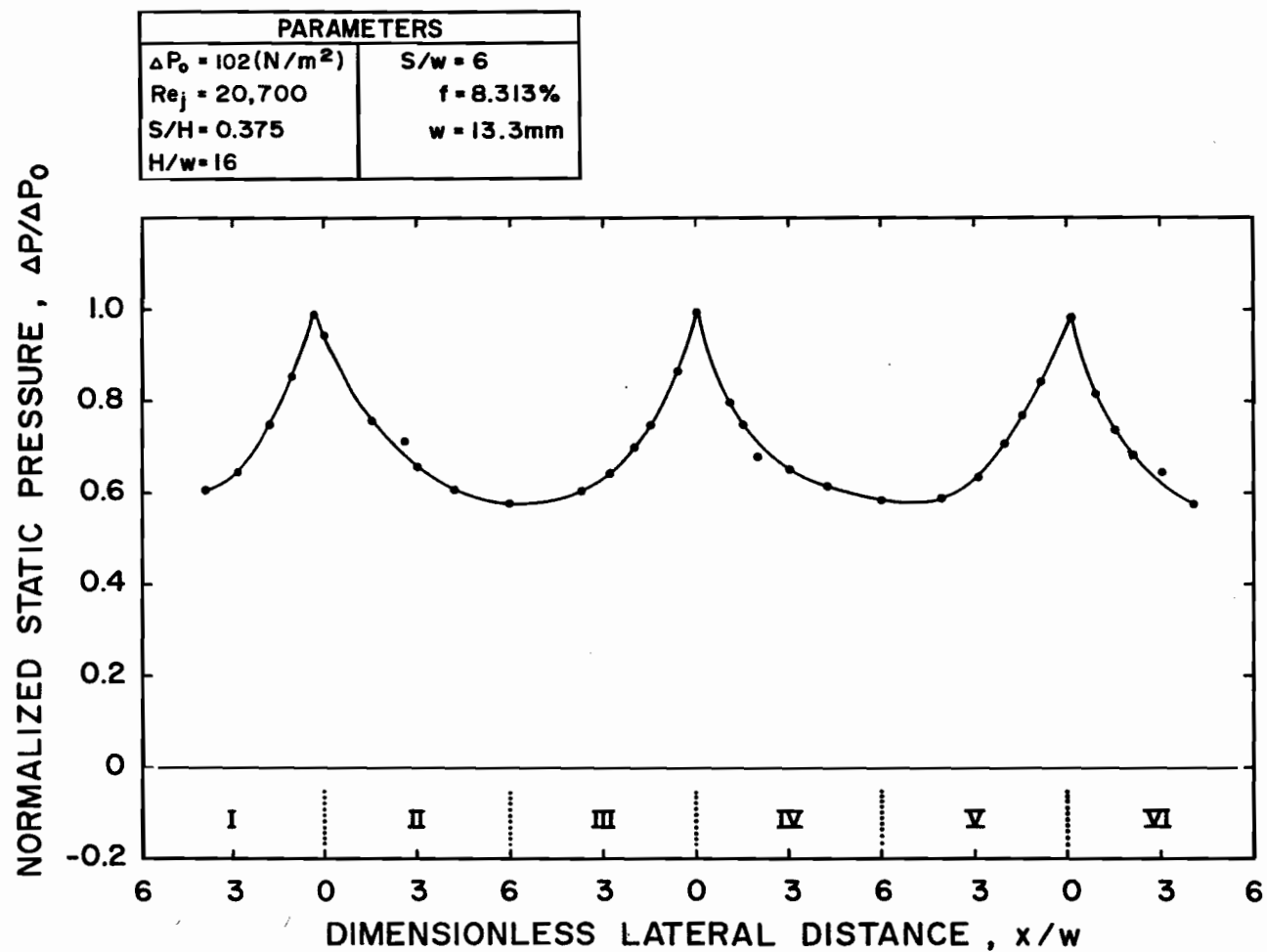


FIGURE 4.23. Lateral Profile of Static Pressure at the Impingement Surface for Multiple Slot Jets at $S/H = 0.375$

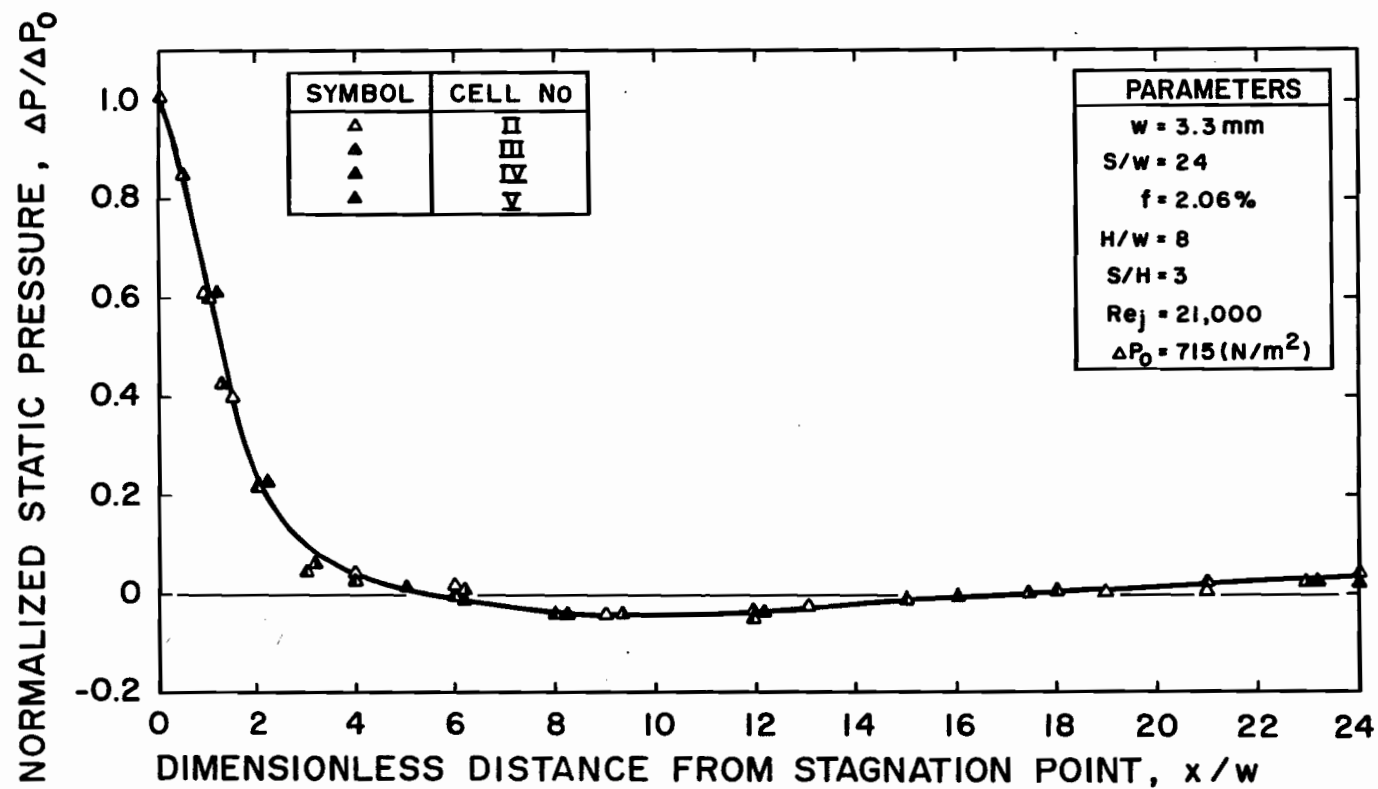


FIGURE 4.24. Superimposed Lateral Profiles of Static Pressure at the Impingement Surface for Multiple Slot Jets at $S/H = 3$

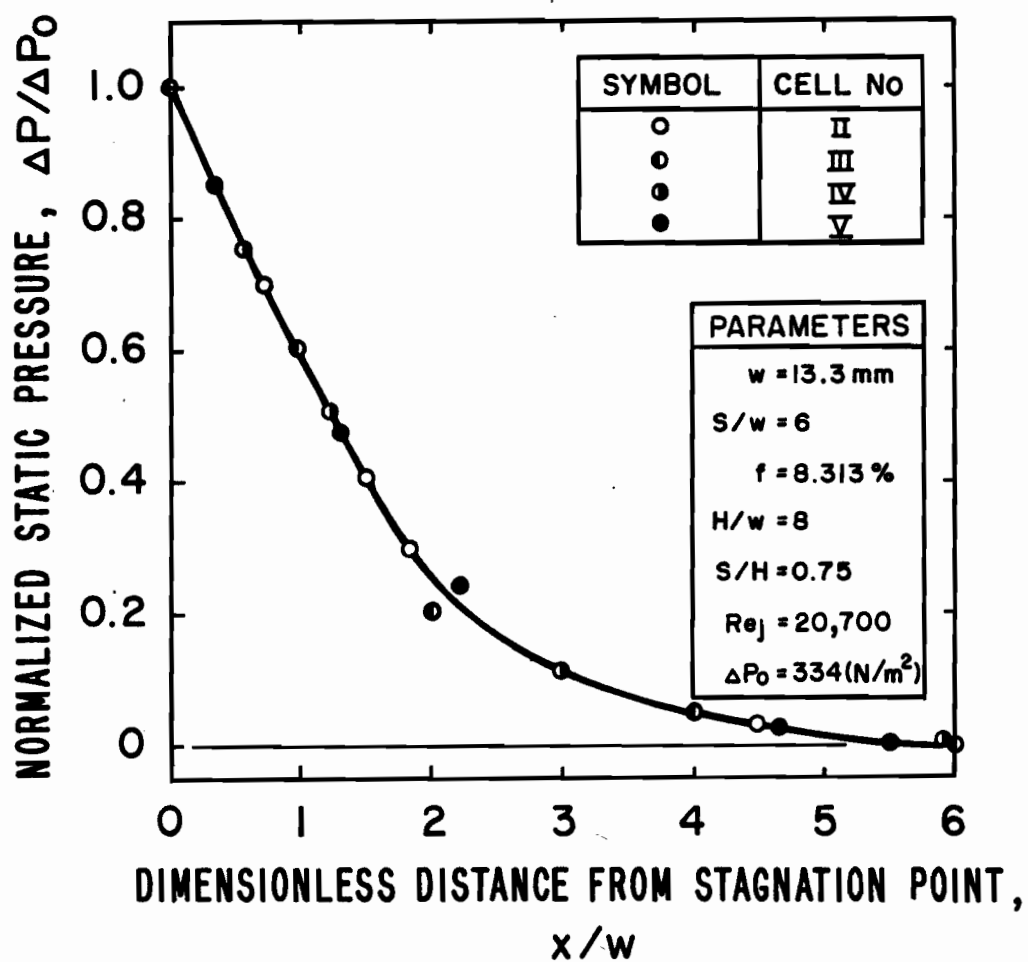


FIGURE 4.25. Superimposed Lateral Profiles of Static Pressure at the Impingement Surface for Multiple Slot Jets at $S/H = 0.75$

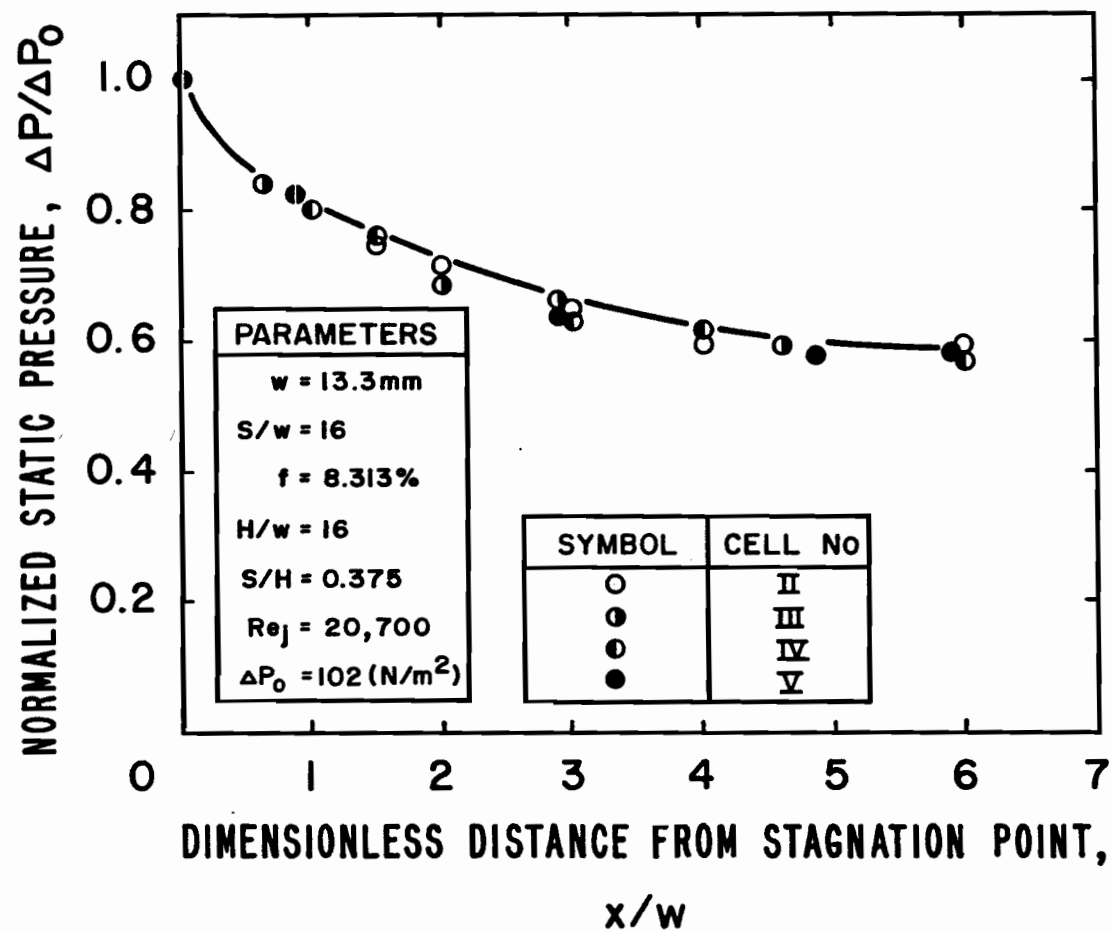


FIGURE 4.26. Superimposed Lateral Profiles of Static Pressure at the Impingement Surface for Multiple Slot Jets at $S/H = 0.375$

cells III and V are equivalent flow cells and likewise that cells II and IV are equivalent. The above proof of the postulate that this 3-jet system contains a central region which accurately represents flow in a confined multiple jet system provides assurance that the data from this experimental facility may be taken as representative of an equivalent confined multiple slot jet system with a large number of jets. Aspects of the results on Figures 4.24 to 4.26 other than this proof will be discussed subsequently.

Having established that this apparatus satisfactorily represents a multiple jet system, the effect of various geometrical parameters and jet Reynolds number may now be examined through the corresponding effects on pressure profiles at the impingement surface. Thus in contrast to Figures 4.21-4.26 pressure profiles presented subsequently are for a single flow cell which has been proven representative of a multiple jet system.

For $Re_j = 20700$, each of the next three figures, 4.27, 4.28 and 4.29, show impingement surface pressure profiles for one value of nozzle exit-to-impingement surface spacing. The absolute value of stagnation pressure, ΔP_o (N/m^2), to which lateral profiles are normalized, are tabulated in each figure. Also shown in these figures is comparative data for a single slot jet without exit ports, i.e. with outflow between the impingement and confinement surfaces as illustrated in the central part of Figure 4.1. These three figures portray effects which have already been noted in connection with Figures 4.18 to 4.26. However, the addition of reference curves for equivalent single slot jets on Figures 4.27-4.29 establishes that multiple jet pressure profiles are nearly coincident with those for a single jet except for the narrowest flow cell, $S/H = 0.375$. In the latter case, the large value of impingement surface pressure at the exhaust port centerline, i.e. about 60% of the stagnation pressure, reflects the large dissipation of

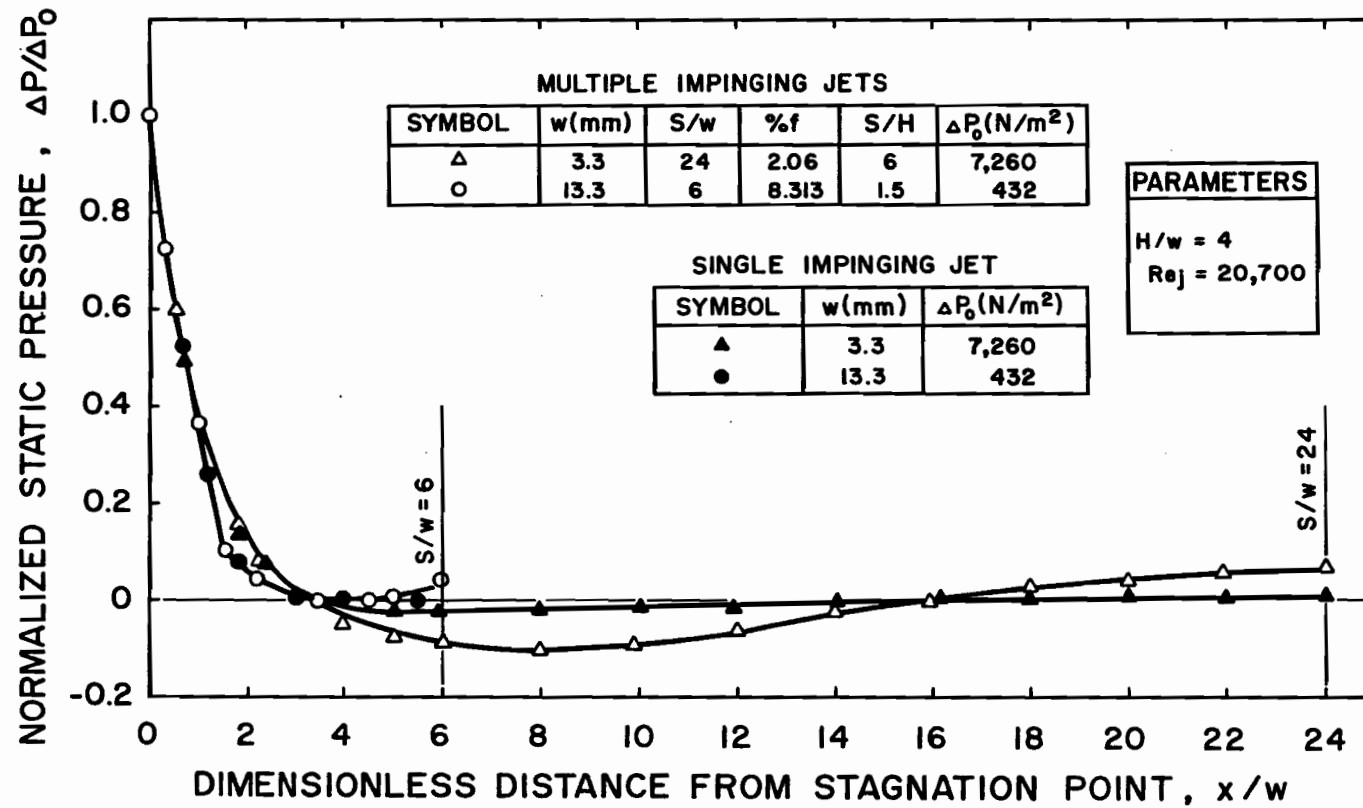


FIGURE 4.27. Lateral Profiles of Static Pressure at the Impingement Surface for Single and Multiple Slot Jets at $H/w = 4$

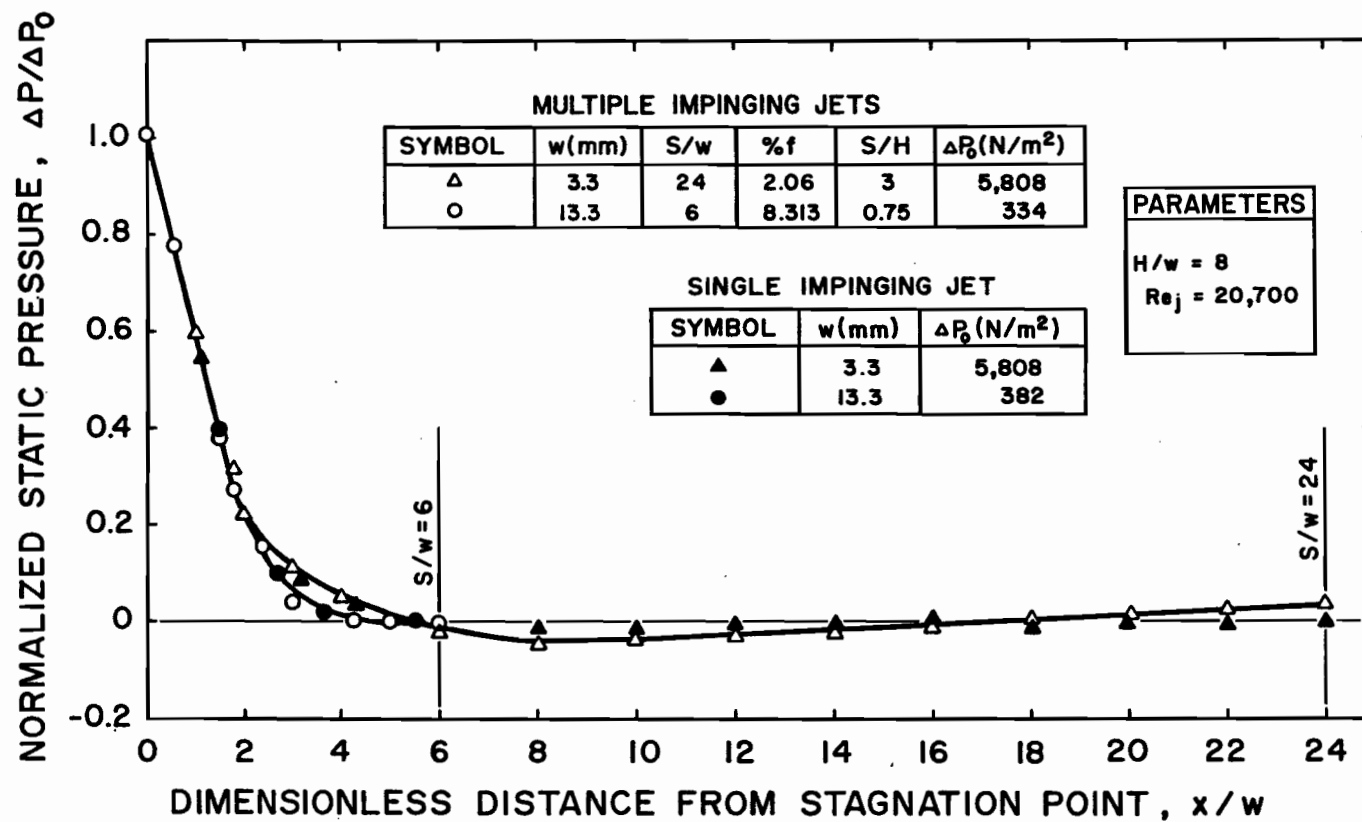


FIGURE 4.28. Lateral Profiles of Static Pressure at the Impingement Surface for Single and Multiple Slot Jets at $H/w = 8$

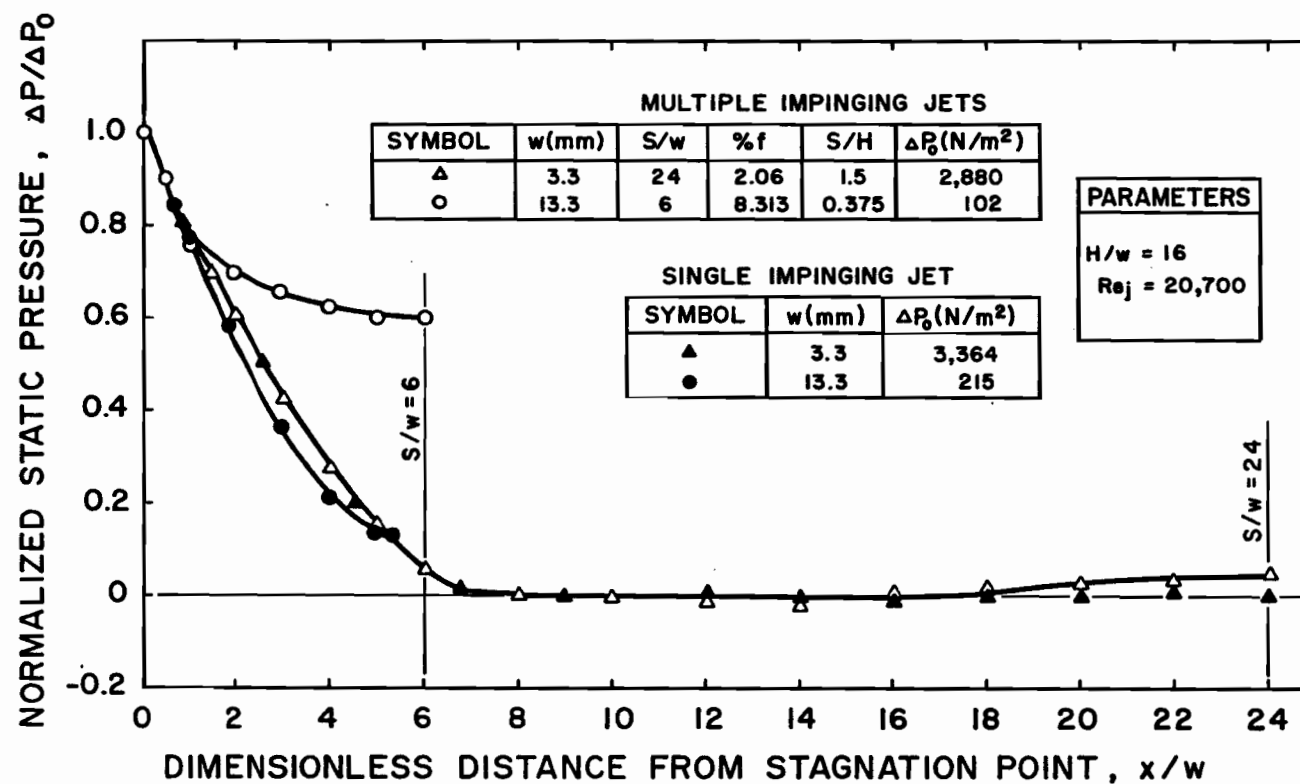


FIGURE 4.29. Lateral Profiles of Static Pressure at the Impingement Surface for Single and Multiple Slot Jets at H/w = 16

energy from the spentflow to the countercurrent inlet jet flow as the spentflow passes from the impingement surface to the exit port in flow cell as narrow as that shown on Figure 4.20(c), i.e. $S/H = 0.375$. Thus for the case of a narrow ($S/H = 0.375$) flow cell the pressure profile coincides with that for a single jet only for a very short lateral distance, i.e. to only about $1w$ from stagnation, as shown in Figure 4.29. Beyond that position the pressure profile deviates sharply from that for a single jet.

It was pointed out earlier that, as the width of the flow cell in a confined multiple slot jet system is decreased, the extent of the wall jet region decreases. For a very narrow flow cell the wall jet region effectively vanishes because of the direct transition from an impingement flow to an exit flow without a wall jet type flow ever developing. At $Re_j = 20700$ it is evident from Figures 4.28 and 4.29 that this limit is reached for a narrow flow cell of proportions S/H at some value between the limits $1.5 > S/H > 0.375$. The exact value of this limiting proportion would be the value of S/H at which the impingement surface pressure profile for the multiple jet system just starts to deviate from that for a single jet. For values of flow cells proportions, S/H , less than this limiting value, the multiple jets may be considered to be interacting in the impingement region and such a multiple jet system may not be considered to be equivalent simply to an array of single jets.

Because static pressure in Figures 4.27 through 4.29 is normalized with respect to stagnation pressure, ΔP_o , it is not evident when interaction between jets affects the stagnation pressure. Therefore stagnation pressure has been shown as a function of impingement surface spacing on Figure 4.30. For this figure ΔP_o is normalized with respect to the pressure difference across the nozzle, ΔP_j , as listed in Table 4.7(b). The data of both Figures

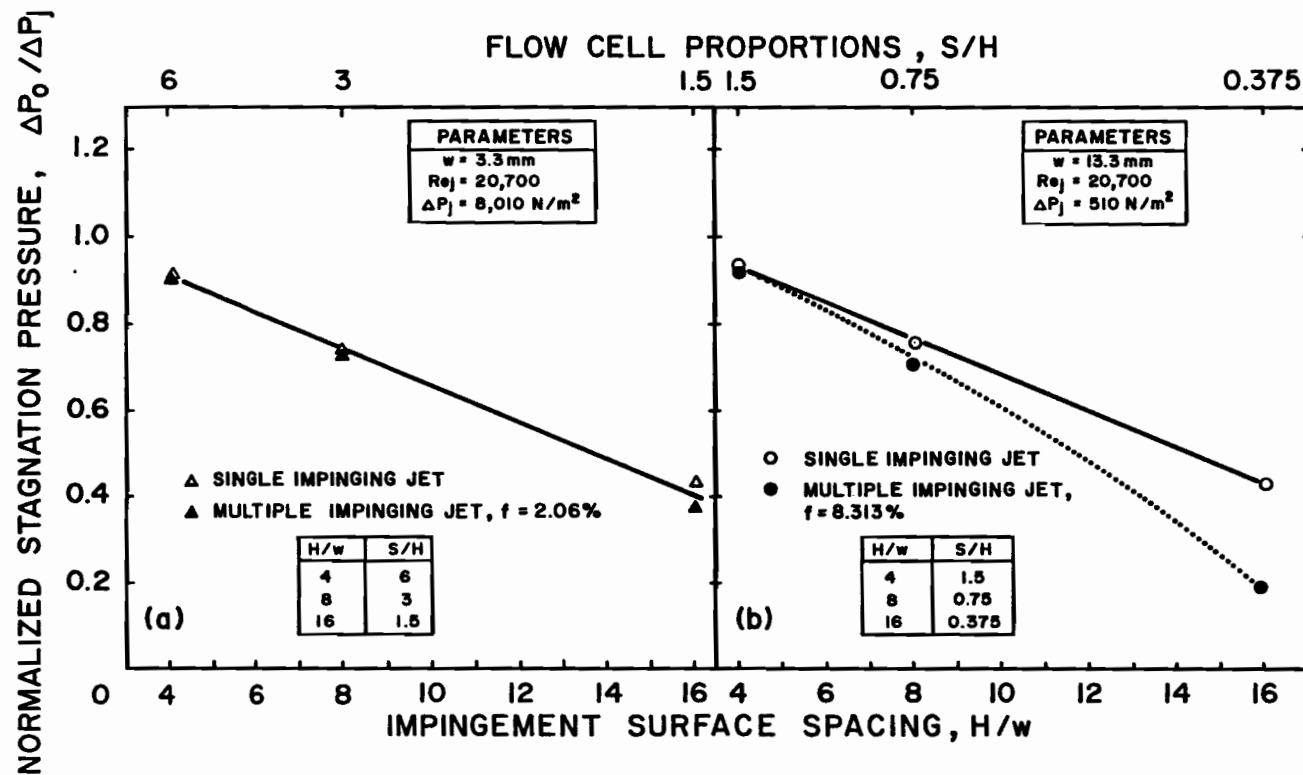


FIGURE 4.30. Effect of Impingement Surface Spacing on Stagnation Pressure for Single and Multiple Slot Jets

4.30(a) and (b) show no significant difference between multiple and single jet data for flow cells over the range $6 > S/H > 0.75$. However, Figure 4.30(b) shows that at some flow cell proportion in the vicinity of $S/H = 1$ stagnation pressure for the multiple jet system begins to drop below that for a single jet. As the correct location of the start of this deviation is unknown, the dashed line is shown only to indicate that the stagnation pressure must converge to the single jet line at some value of S/H less than 1. The display of both single and multiple jet results on Figure 4.30 parallels the similar interrelation displayed for the free jet region on Figures 4.10 through 4.12.

Figures 4.27, 4.28 and 4.29 indicate that H/w remains a parameter for pressure profiles of single and non-interacting multiple slot jets. However, as the value of H , the normalizing parameter for S , has been established, it is reasonable to investigate the utility of H as an alternate basis for non-dimensionalizing the lateral dimension of pressure profiles. This approach is investigated through the use of x/H as the lateral dimension on Figures 4.31 and 4.32. The data of these two figures, at $Re_j = 20700$, relates to two greatly different nozzle spacings, i.e. $S/w = 24$ and 6 which, with a range of confinement-to-impingement surface spacing, $H/w = 4, 8, 16$, corresponds to flow cells from very wide, $S/H = 6$, to very narrow, $S/H = 0.375$. As it is already apparent from Figures 4.23, 4.26 and 4.29 that the impingement surface pressure profiles for strongly interacting jets in flow cells as narrow as $S/H = 0.375$ are sharply different, this difference as expected carries over to the $S/H = 0.375$ profile on Figure 4.32. On the other hand, for the five profiles for non-interacting jets, $6 \geq S/H \geq 0.75$, it is significant from Figures 4.31 and 4.32 that with lateral distance normalized with respect to H , the profiles effectively collapse to a single profile

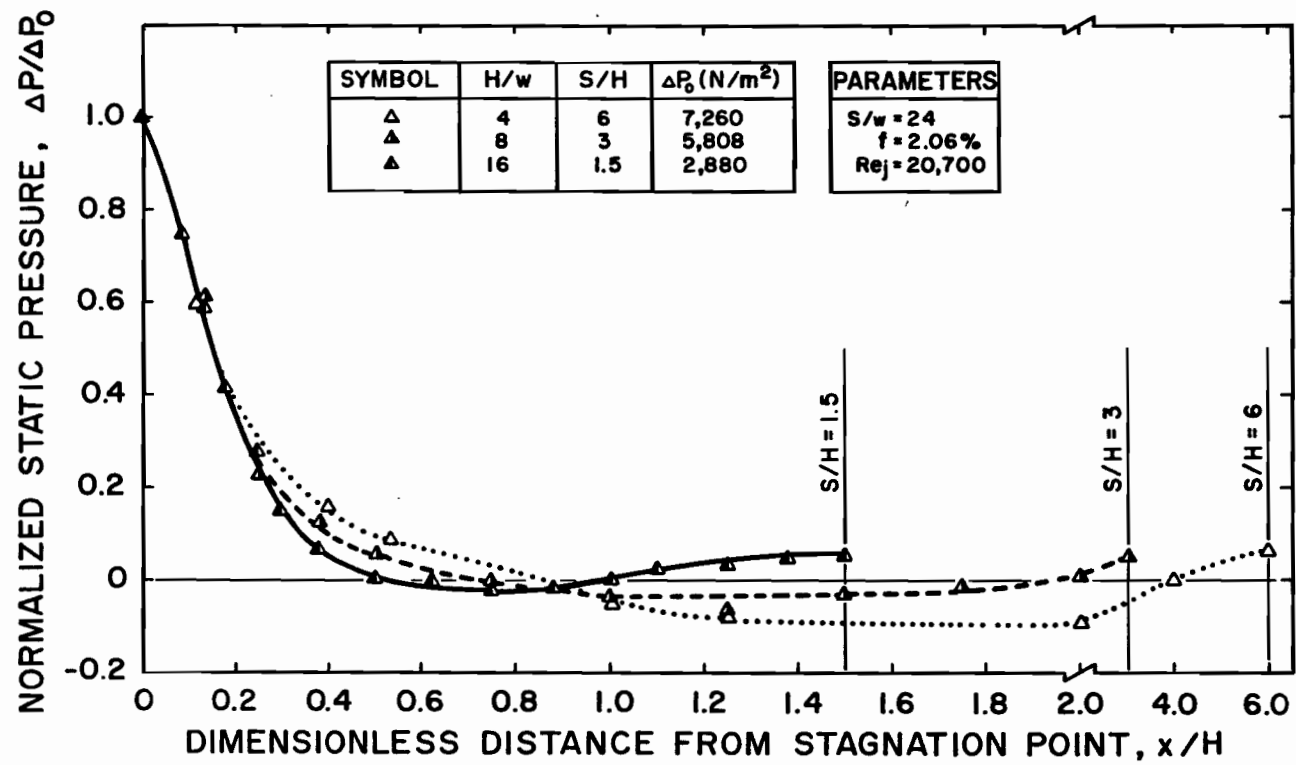


FIGURE 4.31. Lateral Profiles of Static Pressure at the Impingement Surface for Multiple Slot Jets for $f = 2.06\%$

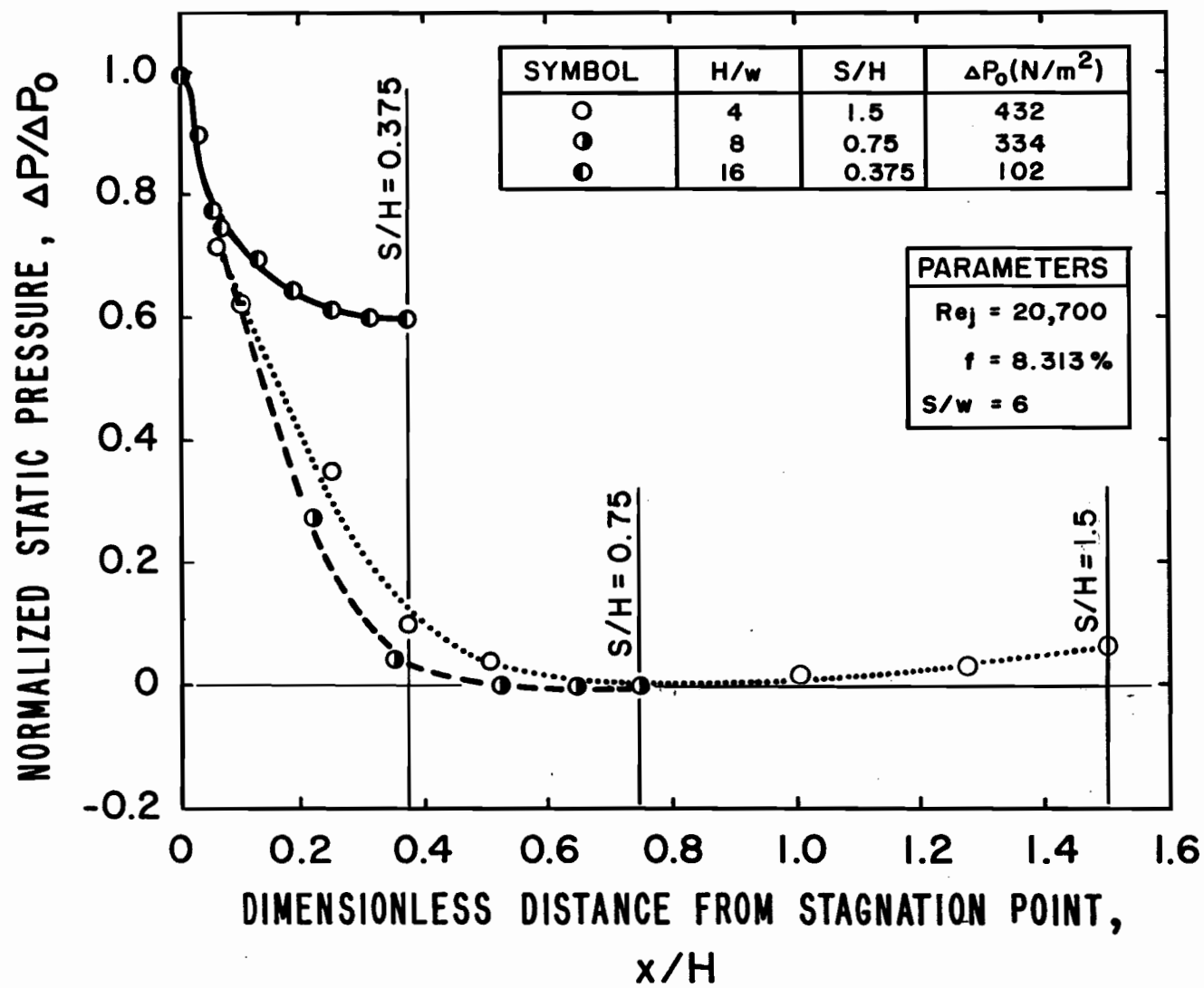


FIGURE 4.32. Lateral Profiles of Static Pressure at the Impingement Surface for Multiple Slot Jets for $f = 8.313\%$

within a reasonable variation. Specifically all half pressure widths (where $\Delta P/\Delta P_0 = 0.5$) occur at around $x/H = 0.15 \pm 0.01$, and the location for $\Delta P/\Delta P_0 = 0.05$ is also about the same for all cases, i.e. at $x/H = 0.5 \pm 0.1$.

Figures 4.27 to 4.29 have already established that there are no significant differences in impingement surface pressure profiles between single jets and multiple slot jets in flow cells of proportions $S/H \geq 0.75$ for which jets are non-interacting. This evidence may be combined with that from Figures 4.31 and 4.32 to state that, at a specific jet Reynolds number, single slot jets and multiple slot jets for flow cells of proportions $S/H \geq 0.75$ may be characterized by a single normalized impingement surface pressure profile provided lateral distance is expressed relative to H , this profile being independent of impingement surface spacing over the rather wide range tested, i.e. $4 \leq H/w \leq 16$. In this universal profile the surface pressure drops to half the stagnation pressure at about $0.15H$ from stagnation and to 5% of stagnation pressure at about $0.5H$ from stagnation. This similarity of pressure profiles at the impingement surface constitutes an interesting extension to the similarity of jet development downstream of the nozzle exit that was demonstrated particularly through Figures 4.13 through 4.16 in Section 4.4.

Although the profiles of normalized surface pressure relative to x/H effectively collapse to a single profile over the impingement region, the extent of relatively flat region of pressure profile wherein the pressure approaches that at the exhaust port varies considerably. The lateral extent of this flat region of the profiles ranges from about $5.5H$ for the case of the widest flow cell, $S/H = 6$, down to about $0.25H$ for a relatively narrow flow cell, $S/H = 0.75$, the narrowest flow cell in this series which did not give the strongly interacting multiple jet behavior represented by $S/H = 0.375$. These relatively flat regions of the pressure profiles were first presented

in the broader perspective of Figures 4.21 and 4.22.

While w is a satisfactory basis for normalizing lateral distance from stagnation point for some purposes, the above observations indicate that the maximum degree of similarity is obtained by lateral distance from stagnation point nondimensionalized with respect to impingement surface spacing H . The degree to which normalizing lateral distance with respect to impingement surface spacing, H , yields a common pressure profile at $Re_j = 20700$ provides further evidence supporting the concept that S/H is a basic characteristic variable of general utility for confined multiple slot jet systems.

For a jet Reynolds number of about 21000 an analysis has been presented through Figures 4.17 to 4.32 of conditions at the impingement surface, an analysis which has established the importance in a multiple jet system of the geometrical proportions of the flow cells, S/H , and the generalization of results possible through normalizing lateral distance with respect to impingement surface spacing, i.e. use of the nondimensional lateral position, x/H . With the aid of Figures 4.33 through 4.38 this analysis will be extended from the single Reynolds number, 21000, to the range of Reynolds number from 5000 to 44000. Figures 4.33 to 4.35 are for a wide internozzle spacing, $S/w = 24$, while Figures 4.36-4.38 are for the narrow spacing, $S/w = 6$. With this range of S/w combined with the use of impingement surface spacings in the range $4w$ to $16w$, the range of flow cell proportions, S/H , ranged from 6 to 0.375, as listed earlier in Table 4.6.

Although an appreciable spread of the data remains it is highly significant that, over this great range of geometrical and flow parameters, all the profiles are reasonably close to a common profile provided lateral distance is measured in terms of x/H . Thus whereas for the data from a single value of Reynolds number shown in Figures 4.31 and 4.32 the pressure half-width,

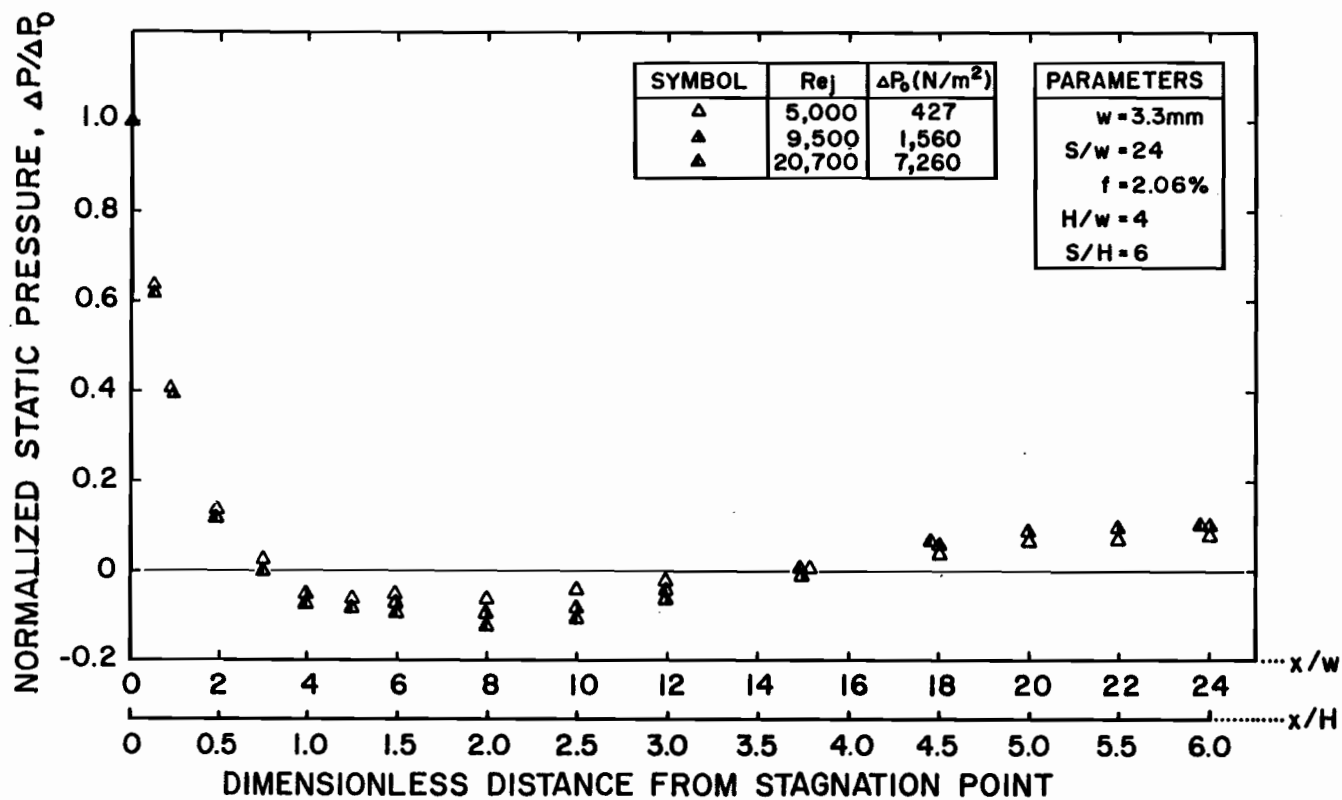


FIGURE 4.33. Effect of Reynolds Number on Lateral Profiles of Static Pressure at the Impingement Surface for Multiple Slot Jets for $S/H = 6$

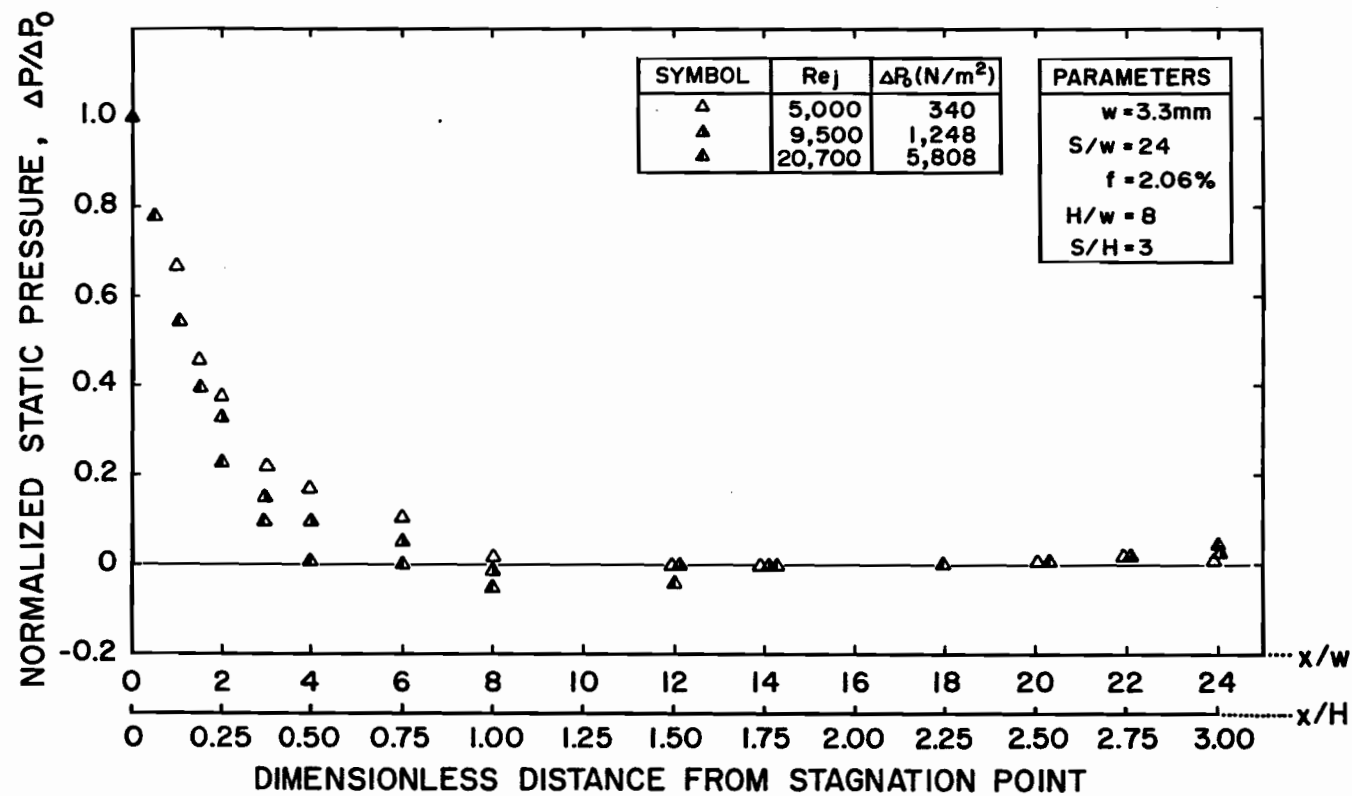


FIGURE 4.34. Effect of Reynolds Number on Lateral Profiles of Static Pressure at the Impingement Surface for Multiple Slot Jets for $S/H = 3$

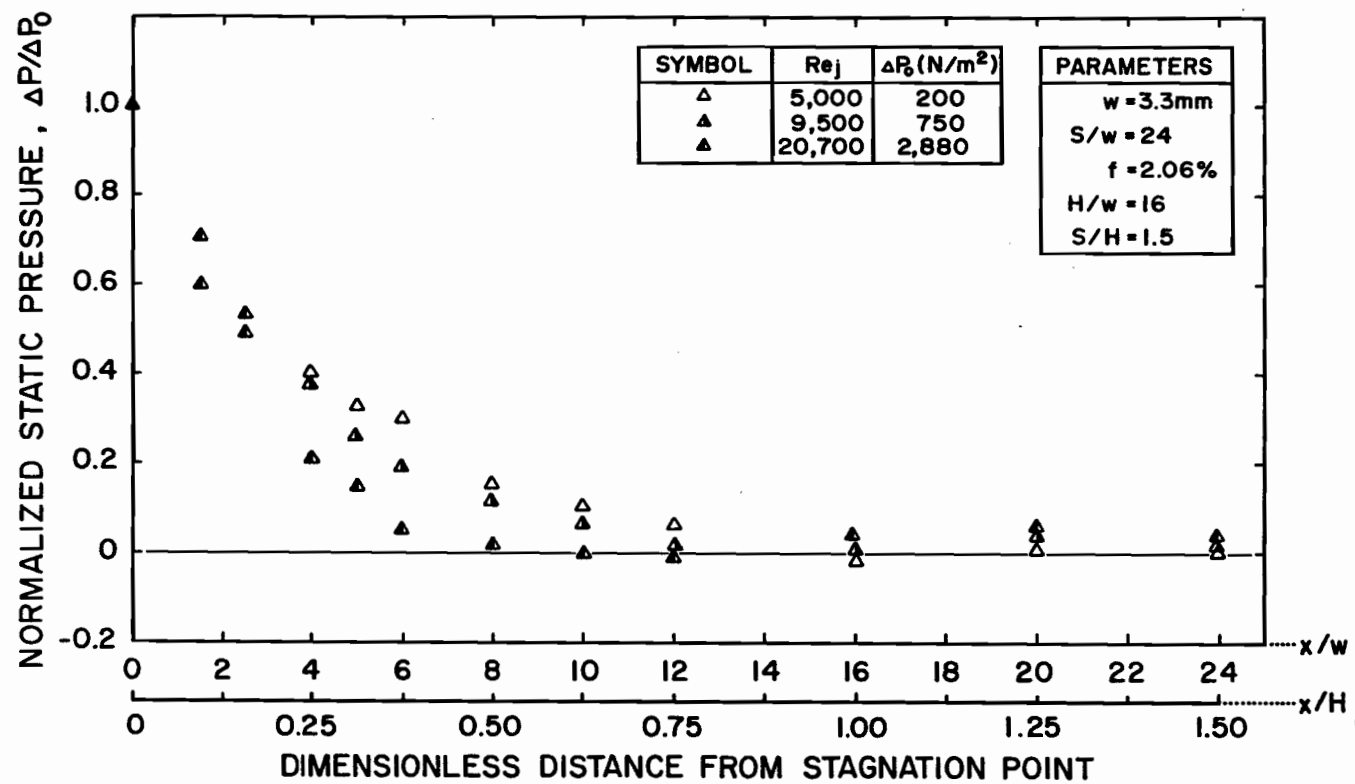


FIGURE 4.35. Effect of Reynolds Number on Lateral Profiles of Static Pressure at the Impingement Surface for Multiple Slot Jets for $S/H = 1.5$

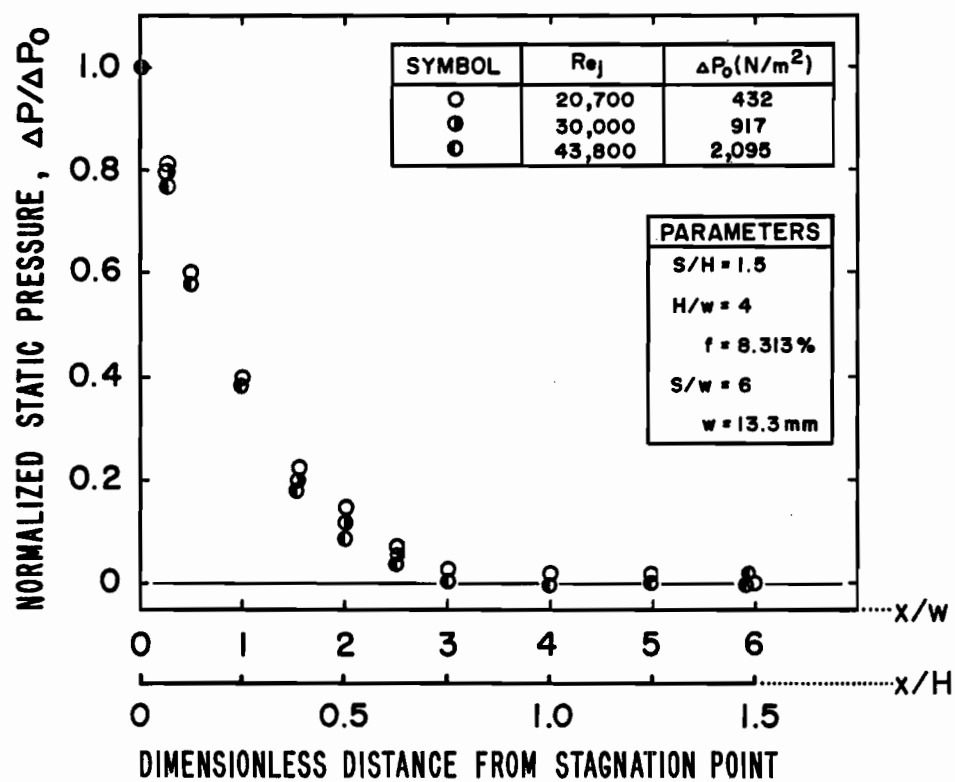


FIGURE 4.36. Effect of Reynolds Number on Lateral Profiles of Static Pressure at the Impingement Surface for Multiple Slot Jets for $S/H = 1.5$

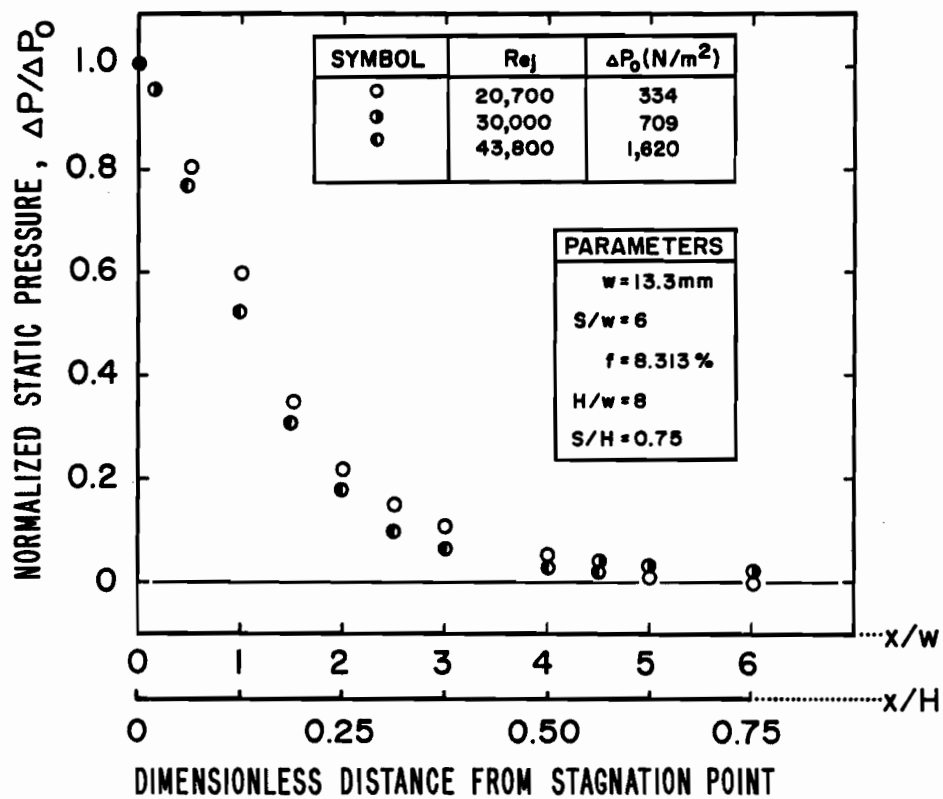


FIGURE 4.37. Effect of Reynolds Number on Lateral Profiles of Static Pressure at the Impingement Surface for Multiple Slot Jets for $S/H = 0.75$

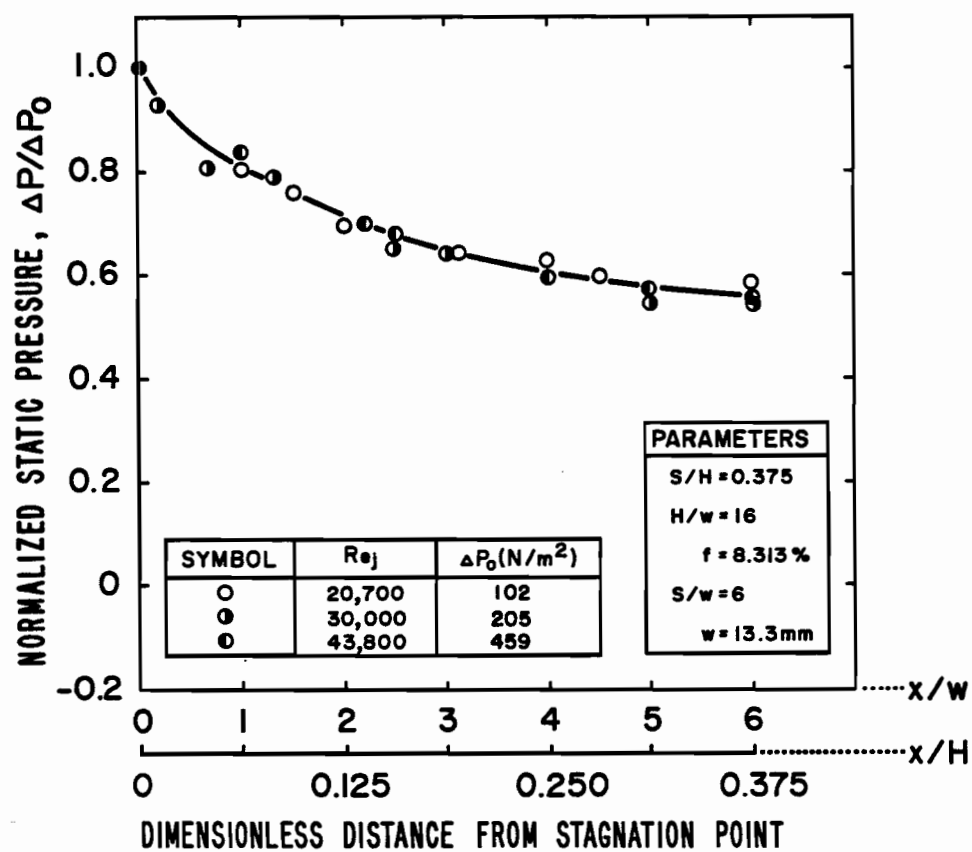


FIGURE 4.38. Effect of Reynolds Number on Lateral Profiles of Static Pressure at the Impingement Surface for Multiple Slot Jets for $S/H = 0.375$

$\Delta P/\Delta P_o = 0.5$, occurred at $x/H = 0.15$, it may be seen that the wide range of Reynolds number, 5000 to 44000, represented on Figures 4.33 to 4.38 the range in location of pressure half-width increases only to $x/H = 0.16$. This range in pressure half-width location is remarkably small considering the large range of geometric and flow variables. Although the spread of data around a common profile becomes somewhat greater for pressures less than half the stagnation pressure it may be seen for example that at $x/H = 0.5$ all the data are in the range below 20% of the stagnation pressure. In the range of less than half the stagnation pressure the profiles are slightly steeper with higher Re_j .

While Figures 4.33 to 4.37 portray systems for which the flow cells are sufficiently wide that the multiple jets are non-interacting in the impingement region, Figure 4.38 represents the strongly interacting multiple jets for $S/H = 0.375$. It is notable that this latter figure demonstrates that even for strongly interacting multiple jets, the surface pressure profiles are remarkably independent over the wide range of jet Reynolds number represented.

As the basis for analysis of the problem of interacting and non-interacting jets the present study proposes that multiple slot jet systems be viewed as an assembly of repeated "flow cells", these being defined as the volume contained by the impingement and confinement surfaces and the centerlines of adjacent inlet nozzles and exhaust ports. As the lateral and axial length of such a flow cell would be, respectively, S and H this approach suggests that a flow cell could be characterized by its dimensionless geometric proportions, S/H . However, it should also be kept in mind that there is a third dimension involved, i.e. nozzle width w . Complete similarity between flow cells would then require equality of two dimensionless ratios of the three dimensions involved, S , H and w . Thus in addition to S/H , another independent dimensionless ratio, either S/w , $f(w/2S)$ or H/w is required for

considerations of geometric similarity. In the graphical representation of results, impingement surface spacing, H/w , is usually indicated as the other dimensionless geometric parameter, although values of S/w and f are also generally indicated.

Although dimensionless analysis thus indicates that at a given Reynolds number, conditions in a flow cell are a function of S/H and H/w , only experimental results can establish the relative importance of S/H and H/w . In this respect one particularly interesting finding is that for a flow cell of intermediate proportions, $S/H = 1.5$, variation of H/w by a factor of 4, i.e. between $H/w = 4$ to $H/w = 16$, caused no significant change in the lateral profiles of normalized impingement surface pressure, $\Delta P/\Delta P_0$, from the stagnation point out to the pressure half-width, and relatively little change even out to the location where pressure was only 5% of the stagnation point pressure, ΔP_0 , as shown in Figure 4.39. Some differences in the normalized pressure profiles occurred only in the relatively long wall jet region from $0.5H$ to $1.5H$ from the stagnation point. Thus in this case S/H was sufficient to characterize flow cell conditions within the region of prime importance, the impingement region, while the second parameter, H/w , was of some importance only in the wall jet region.

4.6 Effect of Throughflow at the Impingement Surface

Prior to discussion of effect of suction on heat transfer at the impingement surface, its effects on axial flow above the impingement surface is presented and analyzed in this section.

Throughflow was achieved by maintaining a uniform reduced pressure on the suction side of the permeable impingement surface. A uniform flow on the low pressure side combined with the type of pressure profile on the impingement side that was thoroughly documented in the previous section leads to a qualitatively similar lateral profile of the pressure drop, ΔP , across

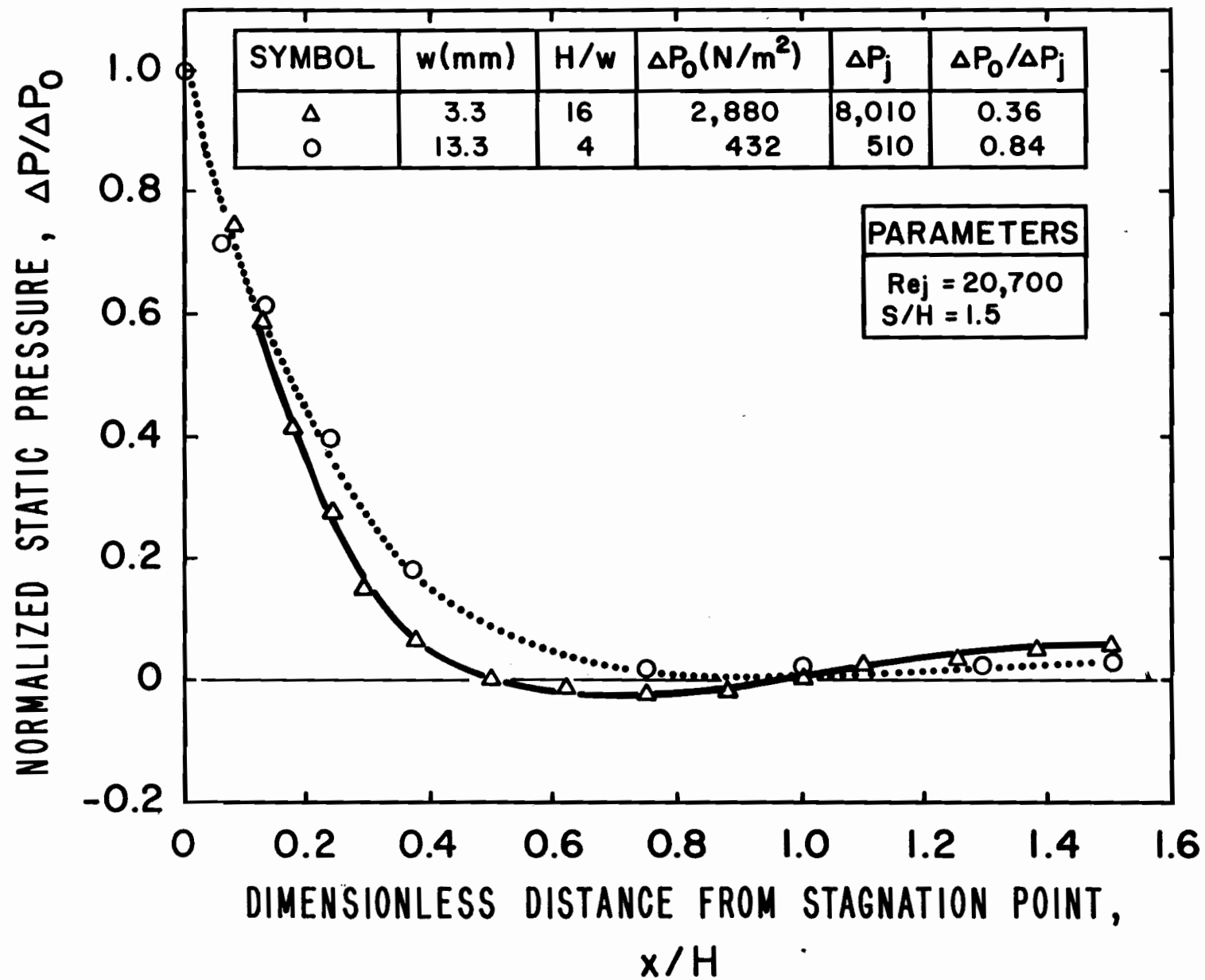


FIGURE 4.39. Effect of H/w Impingement Surface Spacing on Lateral Profiles of Static Pressure for Multiple Slot Jets for S/H = 1.5

the permeable surface, i.e. from a maximum of $\Delta P_o + \Delta P_s$ at stagnation point to about ΔP_s by $0.5H$ from the stagnation point. Such a lateral variation in ΔP_s in turn produces a lateral profile of throughflow that decreases from a maximum at the stagnation point to a nearly uniform throughflow beyond $x/H = 0.5$. This lateral variation of throughflow is reduced by minimizing the ratio, $\Delta P_o / (\Delta P_o + \Delta P_s)$. For a given jet Reynolds number this reduction can be achieved, as may be seen quantitatively from Table 4.7(a), by decreasing the axial mean velocity, i.e. by use of wide nozzle ($w = 13.3$ mm) and by using the impingement surface spacing, $H/w = 8$. Thus the pressure drop non-uniformity expressed as $\Delta P_o / (\Delta P_o + \Delta P_s)$ varies from 0.8% (for the smallest Re_j , 11400 and largest U_s , 0.3 m/s) to 12% (for the largest Re_j , 30200 and U_s , 0.2 m/s) as shown in Table 4.8. As impingement surface throughflow is a direct function of impingement surface pressure drop, the above values of percentage nonuniformity indicate the range of throughflow nonuniformity.

From Table 4.1 it may be seen that the choice of $w = 13.3$ mm and $H/w = 8$, dictated by the need to limit throughflow nonuniformity, would in turn correspond in the multiple impinging jet system to $f = 8.313\%$ and $S/H = 0.75$. Flow cells this narrow and percentage open area this high were undesirable for two reasons. First, for cells as narrow as $S/H = 0.75$ Figure 4.11 documents, by only $6w$ from the nozzle exit, that turbulence intensity is already 30% and is much higher yet away from the centerline, as established in Figure 4.9. Because of inaccuracies with hot wire anemometry measurements in such highly turbulent flows, and the objective in the present study of having reliable measurements to quantify the effects of suction on flow, it was desirable to have S/H wider than 0.75. Secondly, in the pilot plant and mill-trial Papridryer, a process proposed for drying paper which combines impingement and through-drying (Burgess et al., 1972a, b), the ranges of

TABLE 4.8. Flow Parameters of the Confined Single Jet System for Analysis of Effect of Throughflow at the Impingement Surface

Re_j	U_j^* (m/s)	U_s (m/s)	U_s/U_j^* (%)	$\frac{\rho U_s}{\rho U_j^*} \cdot \frac{1}{f}$ (%)	ΔP_{j2} (N/m ²)	ΔP_{o2} (N/m ²)	ΔP_{s2} (N/m ²)	$\frac{\Delta P_o}{\Delta P_o + \Delta P_s}$ (%)
11400	15	0.10	0.67	24.2	156	101	1300	7.2
		0.20	1.33	48.0			5200	1.9
		0.30	2.02	72.9			11700	0.8
22700	30	0.15	0.50	18.0	595	405	3000	11.9
		0.20	0.67	24.2			5200	7.2
		0.30	1.00	36.1			11700	3.3
30200	40	0.20	0.50	18.0	1042	720	5200	12
		0.25	0.63	22.7			8200	8
		0.30	0.75	27.0			11700	5.8

these parameters were, S/H from 2 to 3 and f from 1.33 to 1.66%. In order to have a wide S/H for the first reason noted, and to have S/H and f closer to the Papridryer range, the present investigation of effects of suction was carried out by converting the multiple jet system of Figure 4.1 to a single jet system by blocking the exit ports and the two outer inlet nozzles, as shown in the bottom configuration of Figure 4.1. With this configuration the values of these parameters, $f = 2.77\%$, $S/H = 2.25$, were the desired range. Finally, it should be recalled from the previous sections that a multiple jet system in the range of f and S/H may be simulated satisfactorily by single jet flow results.

For a study of effect of throughflow at the impingement surface, a key parameter is of course the range of throughflows selected. The throughflow may be expressed in three ways, i.e. as the average throughflow velocity, U_s , as the ratio of this velocity to the mean jet velocity at the nozzle exit, U_s/U_j^* , and as the ratio of the throughflow rate at the impingement surface to the jet mass flow rate at the nozzle exit, $(\rho U_s/\rho U_j^*)/f$. These ranges for the present study and for the pilot plant and mill trial Papridryer referred to earlier are as follows:

	<u>Present Investigation</u>	<u>Papridryer</u>
U_s (m/s)	0-0.3	0.045-0.26
U_s/U_j^* , %	0-2.02	0.045-0.45
$(\rho U_s/\rho U_j^*)/f$, %	0-72.9	2.7-34

The range chosen for the present study thus goes well beyond that of this industrial process.

The effect on the flow field of throughflow at the impingement surface was examined by measuring lateral profiles of axial mean velocity and axial turbulence. These profiles were determined at $z/w = 6$, i.e. $2w$ or $0.25H$

from the impingement surface. As indicated by the studies of Beltaos and Rajaratnam (1973) and Gutmark, Wolfshtein and Wygnanski (1978) discussed in Section 2.2 and by the present study, discussed in Section 4.4, the impingement region begins at about $0.20H$ to $0.3H$ from the impingement surface when the criterion is the position where the centerline mean velocity begins to deviate from the corresponding value for a free jet. Thus for the study of effect of throughflow the flow measurements were made at a location just within the limit where the effect of an impermeable impingement surface is felt on mean axial velocity. These profiles were carried out to a lateral distance $x/H = 0.15$, beyond which accuracy of the axial mean velocity starts to decrease because of sensitivity error of the hot wire system.

Although some experimental scatter is evident the lateral profiles of axial mean velocity expressed as U/U_o on Figure 4.40 clearly indicate that, over all values of U_s/U_j^* , Re_j and x/H investigated, there is a consistent trend at $0.25H$ from the impingement surface for axial mean velocity to increase with throughflow velocity at the surface. The fact that it has already been established that the presence of an impermeable impingement surface is felt by axial mean velocity as far as $0.25H$ from the surface increases the significance of the present finding that throughflow at the impingement surface causes an easily measurable effect on axial mean velocity even this far from the surface. It is interesting to note from the lines on Figure 4.40 enclosing the zero and maximum values of U_s that, for any particular value of Re_j , the increase in U caused by the maximum throughflow velocity, $U_s = 0.3$ m/s, is about constant from the centerline out to $x/H = 0.15$, at which lateral position the axial velocity is about 30% of that at the jet centerline. As the absolute amount of increase in U is about constant it follows that, for a specific U_s , the relative increase in U would be about

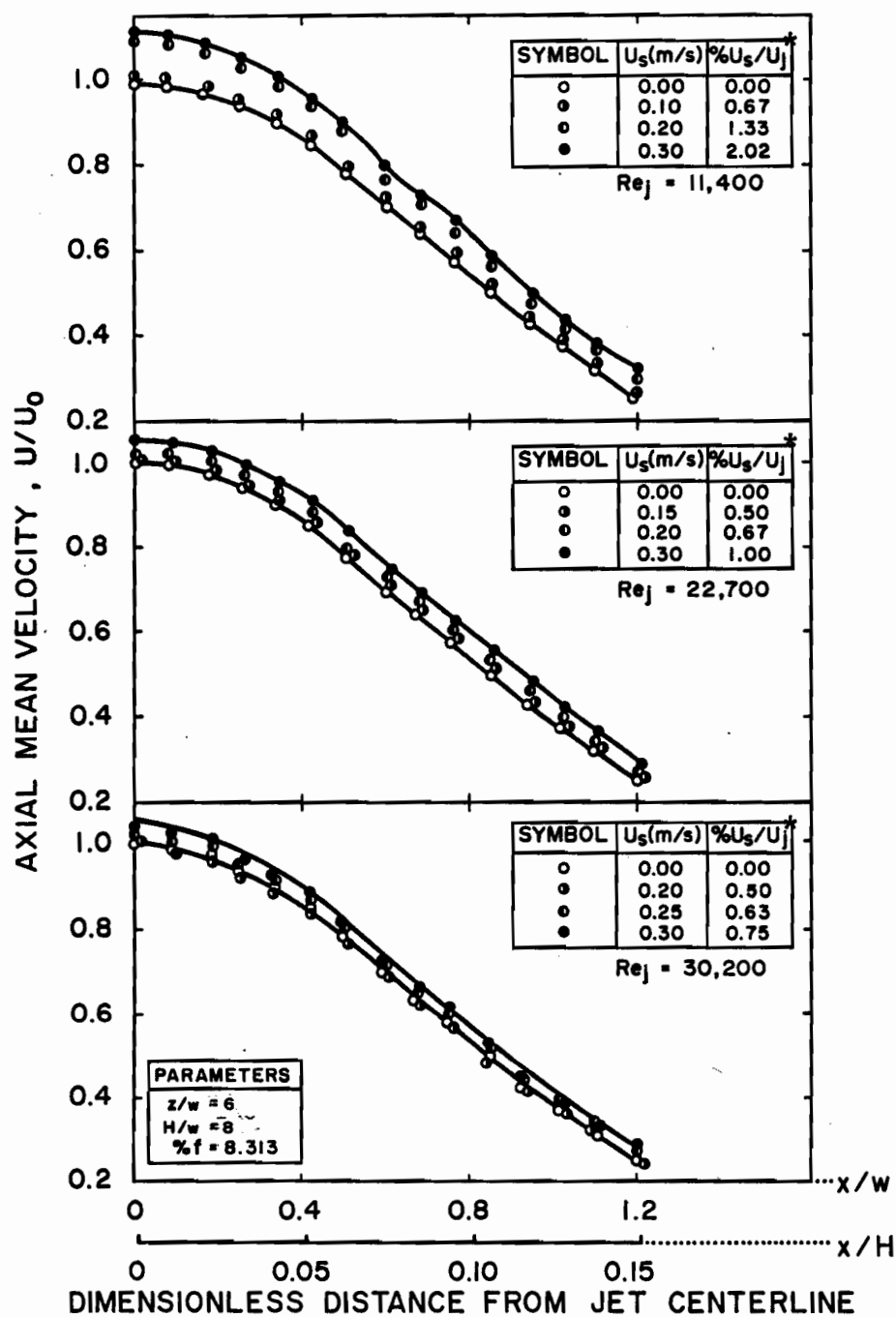


FIGURE 4.40. Effect of Throughflow on Lateral Profiles of Axial Mean Velocity

three times as high at $x/H = 0.15$ as at the centerline. The quantitative effects of maximum throughflow velocity ($U_s = 0.3$ m/s) are summarized below, although it should be kept in mind these increases are rounded off values which should not be treated as highly precise.

Re_j	Throughflow Velocity		% Increase in U/U_0 at $0.25H$ from Surface at	
	U_s (m/s)	U_s/U_j^* (%)	$x/H = 0$	$x/H = 0.15$
11400	0.3	2.02	12	28
22700	0.3	1.00	6	16
30200	0.3	0.75	3	10

The fact that the values for percent increase in U/U_0 at either the centerline or $x/H = 0.15$ are seen in the above listing to decrease in nearly inverse proportion to Re_j is a consequence of the fact that actual increase in U for a specific increase in U_s , i.e. U_s from zero to 0.3 m/s, is nearly independent of Re_j . Combining this observation with one noted earlier one may state that the absolute increase in axial mean velocity is nearly independent of both Re_j and x/H .

As axial mean velocity U increases approximately linearly with throughflow velocity U_s , independently of Re_j and lateral position and as at a specific position above the surface U_0 is some fraction of U_j^* because of similarity in decay of axial mean velocity, the linearity of U with U_s may alternatively be expressed as a linearity of U/U_0 with U_s/U_j^* , for each value of lateral position x/H independent of Re_j . A final observation with respect to the quantitative aspect is to note from the above listing of results that the percent increase in U/U_0 at $0.25H$ from the impingement surface is about 4-6

times the relative throughflow velocity, U_s/U_j^* . In general it may therefore be stated that the axial flow field in the vicinity of the impingement surface is quite sensitive to throughflow velocity at the surface.

The effects of throughflow at the impingement surface, summarized quantitatively above, may now be analyzed and compared to related studies. In the first place it should be noted that because of requirements of continuity, increases in axial mean velocity resulting from throughflow at the impingement surface require that there be a corresponding reduction in lateral flow away from the jet centerline. The only other study of effect of throughflow on the axial flow field of an impinging jet is that of Obot (1981) who for a single round turbulent jet studied the effect of surface throughflow on both axial and lateral flow. As for the present study, Obot's axial profiles were taken at $0.25H$ from an impingement surface, which in his case corresponded to a distance which was two nozzle diameters from an impingement surface located at 8 diameters from the nozzle exit. For his maximum throughflow velocity of 0.25 m/s Obot found a significant increase in axial mean velocity at $Re_j = 38000$ ($U_s/U_j^* = 0.85\%$) but not at $Re_j = 80000$ ($U_s/U_j^* = 0.42\%$). Quantitative comparison with these results is not possible not only because of the difference in nozzle geometries (round and slot) and in percentage open area, f , but also because Obot's jet was unconfined and hence produced high rates of entrainment from the surroundings.

With respect to lateral flow Obot found that the effect of throughflow on lateral mean velocity was to produce increases close to the impingement surface, including the maximum lateral velocity, and decreases away from the surface. Thus at the impingement surface the slope of the lateral mean velocity was increased. A similar increase of maximum lateral velocity accompanied by a shifting of its location closer to the surface was reported by

Baines and Keffer (1977) who over the very limited range of U_s/U_j^* up to 0.29% studied the effect of impingement surface throughflow on lateral flow for the case of a rotating drum subjected to a slot jet. At a spacing, $H/w = 10$, this increase in lateral velocity adjacent to the surface caused the local shear stress to increase by a constant amount over the entire profile and an enhancement of 12% on average shear stress at the surface when compared with that without throughflow.

As an additional aspect of the effect of throughflow on axial flow, for the same conditions of axial turbulence, was measured in the present study for the same conditions as for mean velocity, axial fluctuating velocity was found to show little significant effect of throughflow. Thus the turbulence results, presented in Figure 4.41 as lateral profiles of axial turbulence intensity, u'/U , show approximately the inverse trends to the lateral profiles of axial mean velocity, Figure 4.40. Thus relative to the case without throughflow the percent axial turbulence intensity decreases by up to about 9% at the highest throughflow rate and lower Re_j . Obot (1981) also found that the axial fluctuating velocity to be unaffected and the axial turbulence intensity to be decreased somewhat with throughflow. For lateral flow he also found the lateral fluctuating velocity to be independent of throughflow and hence that the level of lateral turbulence intensity decreases adjacent to the impingement surface and increases away from it.

In summary, the present results indicate that at $H = 0.25$ from the impingement surface, throughflow increases axial mean velocity and decreases axial turbulence intensity. Other studies indicate similar effects of throughflow on lateral flow, i.e. an increase in lateral mean velocity next to the impingement surface with a corresponding increase of slope of mean velocity at that surface, while lateral intensity of turbulence decreases

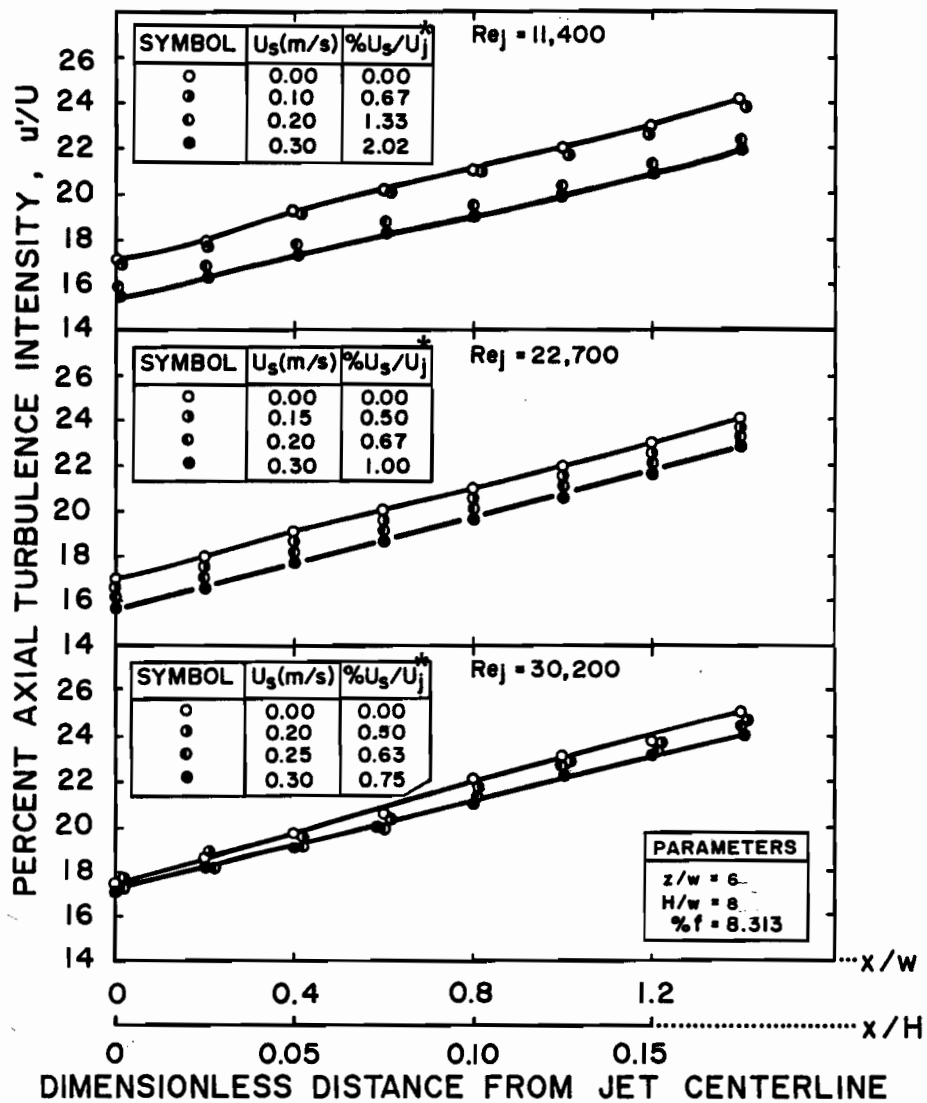


FIGURE 4.41. Effect of Throughflow on Lateral Profiles of Turbulence Intensity

adjacent to the impingement surface and increases away from it. As for both the axial and lateral flow fields the effect of throughflow on mean velocity and turbulence intensity are in the opposite direction with respect to their effect on impingement surface heat transfer, the net effect of throughflow on the latter cannot be predicted from these flow field measurements.

4.7 Summary and Conclusions

Although most studies of impinging jets are for single jets, most often for unconfined jets, some industrial applications involve the use of multiple confined impinging jets with the confinement surface parallel to the impingement surface. Two important industrial applications are the projected Papri-dryer for the drying of paper and the new technology for the cooling of vanes in turbine engines. Moreover, there is particular industrial relevance for multiple confined slot jet systems in which the spentflow (the jet flow after impingement) is discharged through exhaust ports located symmetrically between the inlet jet nozzles at the confinement surface, a system for which no analysis has been published.

To model this system an experimental facility was designed to comprise three slot jets, with two wider slot exhaust ports located between the central and the outer jets, and with a half-width slot exhaust port at each end. The confinement surface was the structural extension of the nozzle wall, hence was continuous and smooth. The impinging jet system was totally enclosed by four side walls between the impingement and confinement surfaces, thereby generating a two-dimensional flow within the multiple jet system. The two fixed dimensions were the lateral spacing between the centerlines of each inlet nozzle and the adjacent exhaust port, 80 mm, and the spanwise (transverse) dimension of the nozzle and exhaust ports, 250 mm. The impingement surface

spacing from the nozzle exit was adjustable continuously, while five nozzle widths, from 2.5 to 13.3 mm, were used.

A basic question in the use of such a test model is whether it accurately represents a similar multiple jet system with large number of jets, as would be found in an industrial application. An extensive set of impingement surface pressure profiles established that the flow within each inlet nozzle-exhaust port flow cell was completely symmetrical over the central two-thirds of the test unit, i.e. from the centerline of one of the outer jets, through the central jet, to the centerline of the other outer jet. Thus, as the evidence was that two jets might have been sufficient, the use of a three-jet system provided a reliable replication of multiple confined slot jet systems of a large number of jets.

The present study covered the following range of key geometrical parameters, nozzle width w , open (nozzle) area ratio f , and impingement surface spacing from the nozzle exit H/w , i.e. $2.5 \leq w \leq 13.3$ mm, $1.56 \leq f \leq 8.313\%$ and $4 \leq H/w \leq 24$. These ranges exceed those in the two industrial applications noted. A wide range of jet Reynolds number, $3500 \leq Re_j \leq 45000$, was studied.

In a study of multiple slot jets a central question relates to the degree of interaction between the inlet jet flows and the intervening exhaust port flows, such interaction being related to the system geometry. As noted above, variation in the dimensionless internozzle spacing, S/w , and open area ratio, f , was achieved in the present study by use of a fixed spacing, S , with nozzles of five widths, w . Extensive tests were therefore carried out to characterize the flow field of a single slot jet for these five nozzle widths over the range of Reynolds number intended for the multiple jet study. The objective of this part of the study was to establish the extent to which the mean velocity and turbulence characteristics for a given jet Reynolds

number, Re_j , were independent of nozzle width, w . In order to obtain a uniform mean velocity and turbulence intensity at the nozzle exit, short nozzles ($t/w = 1$) with an ASME standard elliptical contoured entry were used throughout. Moreover, the single jet study provided the standard of comparison against which the multiple jet system behaviour could be evaluated.

The velocity profiles at the nozzle exit for all nozzle widths was, as expected, found to be essentially flat over the central 90% of the nozzle width. The nozzle exit turbulence intensity profile over the central region was low, as expected for such short contoured nozzles, rising to the normal peak near the nozzle walls. However although the level of turbulence in the central region of the flat profile was independent of Re_j at constant w over the range of Reynolds number investigated, $10300 < Re_j < 18700$, this level of turbulence was found to be dependent on nozzle width, w , at $Re_j = 11000$. Turbulence intensity in fact increased in a small but consistent trend from 0.65% for the narrowest nozzle $w = 2.5$ mm, to 0.85% for the largest nozzle, $w = 13.3$ mm. As a fixed plenum chamber width was used throughout, the area contraction ratio, plenum chamber: nozzle width, decreased as nozzle width increased. Thus the higher nozzle exit turbulence intensity for wider nozzles is a result of correspondingly less contraction and hence less suppression of turbulence from the flow entering the nozzle.

Immediately downstream of the nozzle exit the turbulence in the free jet increases extremely rapidly from turbulence generation in the region under the nozzle walls where there is a very high lateral gradient in axial mean velocity between the jet and the surrounding fluid. Thus from about 1% turbulence at the exit, the intensity of axial turbulence by only one nozzle width downstream from the exit shows a peak of about 25% at $x/w = 0.5$. Along the jet centerline the fluctuating velocity peaks at about 10% down-

stream, while by $18w$ downstream the continuously increasing centerline turbulence intensity reaches about 20%. Lateral profiles of fluctuating velocity peak at around $x/w = 0.5$ near the nozzle exit, with the location of these peaks in u' moving out to about $x/w = 0.75$ by $16w$ downstream, due to the general outward expansion of the developing jet. By contrast lateral profiles of intensity of axial turbulence do not peak but, because of the decrease of axial mean velocity in the lateral direction, continue to increase with lateral distance out to about $x/w = 1.5$, i.e. as far out as accurate measurements could be made.

Similar to the finding by Obot (1981) for turbulent round jets, measurements in the present study established that for a slot jet the axial fluctuating velocity along the jet centerline was unaffected by the impingement surface up to $1w$ from the surface, the closest that was measured. On the other hand axial turbulence intensity along the jet centerline began to increase sharply at about $4w$ from the impingement surface when the spacing was $H/w = 19$. This increase is entirely due to a corresponding drop in axial mean velocity (that starts at around $0.2H$ from the impingement surface) with unchanged fluctuating velocity. This is similar to the finding by Gutmark, Wolfshtein and Wygnanski (1978), i.e. for turbulent impinging slot jet the deviation of centerline mean velocity and turbulence intensity does not extend further than $0.2H$ from the impingement surface.

As turbulence in a single free slot jet increases greatly in the region immediately after the nozzle exit and eventually grows to levels of about 20% by $18w$ from the nozzle, it might be expected that the small differences in turbulence intensity (0.65-0.85%) existing at the nozzle exit as a function of w would be damped out in this region of such strong generation of turbulence. In fact these differences (0.65-0.85%) continue and grow in the free

jet after discharge from the nozzle and are easily detected along the jet centerline even at $18w$ from the nozzle exit, which is as far as these measurements were extended.

The fact that the level of axial turbulence in the single free slot jet remains a small but significant function of nozzle width has consequences on the axial mean velocity characteristics as well. Thus with the higher turbulence field from larger nozzles, the lateral transport of mean momentum is correspondingly increased and the decay of axial mean velocity downstream from the nozzle exit is consequently enhanced. The length of the potential core, made dimensionless with respect to w , thus decreases slightly as nozzle width increases. The small but consistent effect of nozzle width could likewise be detected on related variables such as the locations of kinematic and geometrical origins of the single free jet and jet half-width. A small effect of nozzle width on the decay of centerline mean velocity was detected even at $18w$ from the nozzle exit, the limit of such measurements.

In summary, investigation of the mean velocity and axial turbulence characteristics of a single slot jet served to define the flow field to which that of the multiple jet system could be compared. In so doing it was found that at a constant jet Reynolds number (11000) nozzle width remained a small but consistent parameter over the entire extent of the jet flow field. The effect of increasing nozzle width from $w = 2.5$ mm to $w = 13.3$ mm at $Re_j = 11000$ is an increase in axial turbulence intensity and a more rapid decay of axial mean velocity with distance from the nozzle exit. With respect to the rates of transport phenomena at the impingement surface it will be recognized that an increase in turbulence and a decrease in axial mean velocity affect transfer rates in the opposite direction.

For a multiple slot jet system with exhaust ports alternating with in-

let nozzles it is apparent that there will be an internozzle spacing, S , sufficiently large that the impingement region conditions will be unaffected by the presence of the adjacent exhaust port flow. A multiple slot jet system with such a wide internozzle spacing becomes effectively an array of widely spaced single slot jets. Such a system may be described as one of non-interacting slot jets. Likewise it is evident that at narrow internozzle spacings, S , conditions in the important impingement region will be affected by the closely adjacent exhaust flow such that these conditions would differ significantly from those for the equivalent single slot jet. This type of system may be described as consisting of interacting slot jets. As transport phenomena in the impingement region could be predicted for a system of non-interacting jets from single jet data while special multiple jet data would be required for a system of interacting slot jets, it is important to have a criterion for distinguishing between these two types of multiple jet systems. No previous study has focussed on this problem which relates directly to the ability to design and optimize industrial scale equipment employing multiple slot jets.

As the basis for analysis of the problem of interacting and non-interacting jets the present study proposes that multiple slot jet systems be viewed as an assembly of repeated "flow cells", these being defined as the volume contained by the impingement and confinement surfaces and the centerlines of adjacent inlet nozzles and exhaust ports. As the lateral and axial length of such a flow cell would be, respectively, S and H this approach suggests that a flow cell could be characterized by its dimensionless geometric proportions, S/H . However, it should also be kept in mind that there is a third dimension involved, i.e. nozzle width w . Complete similarity between flow cells would then require equality of two dimensionless ratios of the

three dimensions involved, S , H and w . Thus in addition to S/H , another independent dimensionless ratio, either S/w , $f(w/2S)$ or H/w is required for considerations of geometric similarity. In the graphical representation of results, impingement surface spacing, H/w , is usually indicated as the other dimensionless geometric parameter, although values of S/w and f are also generally indicated.

Although dimensional analysis thus indicates that at a given Reynolds number, conditions in a flow cell are a function of S/H and H/w , only experimental results can establish the relative importance of S/H and H/w . In this respect one particularly interesting finding is that for a flow cell of intermediate proportions, $S/H = 1.5$, variation of H/w by a factor of 4, i.e. between $H/w = 4$ to $H/w = 16$, caused no significant change in the lateral profiles of normalized impingement surface pressure, $\Delta P/\Delta P_0$, from the stagnation point out to the pressure half-width, and relatively little change even out to the location where pressure was only 5% of the stagnation point pressure, ΔP_0 . Some differences in the normalized pressure profiles occurred only in the relatively long wall jet region from $0.5H$ to $1.5H$ from the stagnation point. Thus in this case S/H was sufficient to characterize flow cell conditions within the region of prime importance, the impingement region, while the second parameter, H/w , was of some importance only in the wall jet region. Thus while H/w is required for a complete description of flow cell conditions, normalized static pressure data of the present study establish that S/H is effectively sufficient over the impingement region, with H/w becoming an important factor only in the wall jet region. At a fixed value of S/H the absolute values of impingement surface pressure from the stagnation point out through the wall jet region are of course a sensitive function of H/w .

Two alternate criteria used to define the critical size of flow cell, $(S/H)_c$, which separates non-interacting (large S/H) from interacting (small S/H) multiple confined slot jet systems were the axial flow characteristics along the jet centerline of the free jet region, and pressure at the impingement surface. For a given value of S/H the degree of departure of the flow characteristics along the jet centerline and at the impingement surface relative to those for a single impinging jet indicates the extent of interaction in the multiple impinging jet system. The results of these studies are listed in Table 4.9. Although the normalized pressure profiles for the multiple jet system are not measurably different from those of a single jet until S/H is less than 0.75, the other three criteria all indicate that the value of $(S/H)_c$, the critical value separating non-interacting from interacting multiple jet systems, is between 0.75 and 1.0. As jet centerline turbulence and stagnation point pressure are the most sensitive of the four criteria used, it may therefore be concluded that $(S/H)_c$ is in the range 0.75 to 1.0. For comparison it may be noted that the experimental Papiridryers corresponded to S/H between 2 and 3, i.e. entirely in the range of non-interacting jets, while the turbine vane cooling application corresponds to S/H in the range 0.34 to 5, i.e. to both interacting and non-interacting multiple jet systems.

Another significant observation from Table 4.9 is that as S/H drops below $(S/H)_c$, interaction in a multiple jet system causes jet centerline turbulence to increase significantly while axial mean velocity drops. The resulting net effect on transport phenomena in the impingement region cannot be inferred from these results because the turbulence and mean velocity changes produce opposing trends in heat or mass transfer at the surface.

Studies of single impinging jets generally provide information concerning the wall jet region. For the multiple jet system with the widest flow

TABLE 4.9. Criteria for Transition between Non-Interacting and Interacting Multiple Confined Slot Jet Systems

S/H	Axial Flow Field along Jet Centerline for Multiple Jet System Relative to a Single Jet		Impingement Surface Pressure for Multiple Jet System Relative to a Single Jet	
	u'_o/U_o	U_o/U_{jo}	Reduction in Stagnation Pressure Relative to a Single Jet	Difference in Lateral Profiles of $\Delta P/\Delta P_o$
1	No difference	No difference	Initiated	None
0.75	Divergence begins at about $z/w = 3$; by $z/w = 6$ turbulence is twice as high for multiple jets	Velocity decay slightly faster for multiple jets after about $z/w = 3.5$	10%	None
0.50	Divergence begins earlier, at about $z/w = 1.5$	Velocity decay significantly faster for multiple jets after about $z/w = 2.5$	25% from interpolation	No data
0.375	Divergence begins almost at nozzle exit; by $z/w = 3$ turbulence is four times as high for multiple jets	Velocity decay much faster for multiple jets after about $z/w = 1.5$	50%	Completely different profiles

cell, $S/H = 6$, an extreme example of a system of non-interacting multiple jets, there is a particularly long wall jet region, about $5.5H$ in length, over all of which the surface pressure approaches that at the exhaust port. By contrast, for the narrowest flow cell, $S/H = 0.375$, there is essentially no wall jet because the impingement flow transforms directly to an exit flow away from the impingement surface. The latter case of strongly interacting jets contrasts in yet another way with the non-interacting case in that there is no region for which the impingement surface pressure drops to approach the exhaust port pressure. In fact, for $S/H = 0.375$ this pressure at the exhaust port centerline is about 60% of the stagnation pressure, an indication of the fact that the exit flow from the impingement surface to the exit port requires this much pressure drop to provide the loss due to strong interaction with the closely spaced countercurrent flow of the inlet jet.

For lateral profiles of variables in impinging jet investigations the usual practice is to de-dimensionalize lateral distance from the jet centerline with respect to the nozzle dimension, i.e. nozzle width for slot nozzles, nozzle diameter for round nozzles. While useful within a limited set of data, such nondimensional profiles do not lead to a general unification of lateral profiles. For example in the present investigation when lateral profiles of impingement surface pressure were prepared with distance from the jet centerline expressed as x/w , the lack of unification obtained may be quantified by noting that the location of the pressure half-width varies from $0.65 x/w$ to $2.7 x/w$, i.e. by a factor of 400%. However when lateral distance was de-dimensionalized with respect to impingement surface spacing, H , for data covering the range: $5000 < Re_j < 43800$, $2.5 < w < 13.3$ mm, $2.06 < f < 8.313\%$, $4 < H/w < 16$, $0.75 < S/H < 6$, $102 < \Delta P_o < 5808 \text{ N/m}^2$, it was found that the location of the pressure half-width for this extended range of vari-

ables was remarkably well defined, expressed as $x_{0.5}/H = 0.16 \pm 0.02$. Although as would be expected the variation in lateral profiles of pressure increased farther from the jet centerline where pressures for non-interacting multiple jets were lower, it may be noted for the above impressive range of parameters that by $x/H = 0.5$ the surface pressure was always less than 20% of the stagnation pressure. It is thus demonstrated that spacing, H , is a considerably more rational basis of de-dimensionalizing distance from the jet centerline for the examination of lateral profiles than is the conventionally used basis, i.e. the nozzle dimension.

As an important industrial application, the Papridryer, combines impingement flow with throughflow at the impingement surface, throughflow was studied over a range which may alternately be expressed as: U_s (0-0.3 m/s), U_s/U_j^* (0-2%), and throughflow to jet mass flow rate (0-73%). These experimental ranges are greater than those studied to date for the industrial application noted.

Throughflow at the surface was achieved by applying uniform suction to a porous bronze impingement surface. Because of the laterally nonuniform pressure profile at the jet impingement surface, throughflow will likewise be nonuniform, decreasing from a maximum at the jet centerline. The use of a wide nozzle, $w = 13.3$ mm, dictated by the need to limit throughflow nonuniformity, in turn required that only a single jet be used for the same impingement surface used with the three-jet configuration. This requirement of a single jet was a consequence of the need to maintain the percentage open area, f , and the flow cell proportions, S/H , within the desired range. Thus the single jet configuration used for the investigation of effects of throughflow corresponded to $f = 2.77\%$ and $S/H = 2.25$. As the study was carried out with a confined single jet, the results are applicable to non-interacting

multiple confined slot jet systems but not to those with internozzle spacing sufficiently close that the jets are strongly interacting, i.e. for S/H significantly less than 1.

The effect of throughflow on the axial flow field was investigated through lateral profiles of axial mean velocity and turbulence at a location $0.25H$ from the impingement surface. This position is somewhat within that for which the effect of an impermeable impingement surface is felt on centerline mean velocity. Lateral profiles of axial mean velocity at this location showed that throughflow increases axial velocity by about a constant amount over the entire lateral region from the centerline out as far as accurate measurements could be made, i.e. to about $x/H = 0.15$. It is instructive to note the effects on a percentage change basis for the case of the maximum value of throughflow used, $U_s = 0.3$ m/s. This maximum throughflow which for the range used for Re_j , i.e. 11400 to 30200, corresponds to U_s/U_j^* from 2% to 0.75%, was found to increase centerline mean velocity by from 12% to 3% and to increase mean velocity at $0.15H$ from the centerline by from 28% to 10% over this range of Re_j . Recalling that these lateral profiles were determined at $0.25H$ from the surface, i.e. within the normal impingement region, it is apparent that the axial mean velocity flow field is indeed quite sensitive to throughflow at the impingement surface.

In contrast to the significant effects found for axial mean velocity, axial fluctuating velocity was found to be unaffected by throughflow, at least at $0.25H$ ($2w$) from the surface. Consequently the axial intensity of turbulence at $0.25H$ from the surface decreases with throughflow proportional to the increase in mean velocity noted earlier.

It is interesting to observe that the effects of throughflow on the axial flow field have similarities to the effects of an impermeable impinge-

ment surface. The similarity is that in both cases the effect on axial mean velocity extends much further from the impingement surface into the oncoming flow than is the case for axial fluctuating velocity, with the result that changes in axial turbulence intensity simply reflect changes in mean velocity for an unchanged fluctuating velocity. Another general observation is that once again the effect of a variable, in this case throughflow, causes changes in mean velocity and in turbulence intensity which have the opposite effect on transport phenomena rates at the surface. Thus in all three aspects documented in this investigation, i.e. effect of nozzle width, effect of interaction between closely spaced multiple slot jets and effect of throughflow, the trend of effects on impingement surface heat transfer rates can only be determined by direct measurement of heat transfer, the subject of the succeeding chapter.

CHAPTER 5

RESULTS AND DISCUSSION: HEAT TRANSFER

5.1 Introduction

Following documentation of the flow field in Chapter 4, the present chapter is devoted to analysis of the corresponding convective heat transfer for the same system of multiple impinging slot jets with exit ports located alternately in the confinement surface. The geometrical and flow parameters of this system are detailed in Section 5.1. In Section 5.2 results from the confined system of alternate inlet jets and exit flows are compared with results from a configuration having cumulative spentflow. The effects of geometrical and flow parameters on stagnation point, local profiles and average heat transfer coefficients are discussed in Sections 5.3, 5.4 and 5.5, respectively. Finally the effect on heat transfer of throughflow at the impingement surface is analyzed in Section 5.6, followed by the summary and conclusions, Section 5.7.

5.1.1 Range of Geometrical and Flow Parameters

The confined impinging slot jet system with alternate inlet jets and exhaust ports shown schematically in Figure 5.1 is the same as that reported in Chapter 4 for characterizing the flow. This system comprised three slot jets, with two wider slot exhaust ports located between the central and the outer jets, and with half-width slot exhaust ports at each end. In this two-dimensional flow system there were two fixed dimensions, the lateral spacing between centerlines of inlet nozzles and adjacent exhaust ports, $S = 80$ mm, and the transverse dimension (not shown in this figure), always 250 mm. Im-

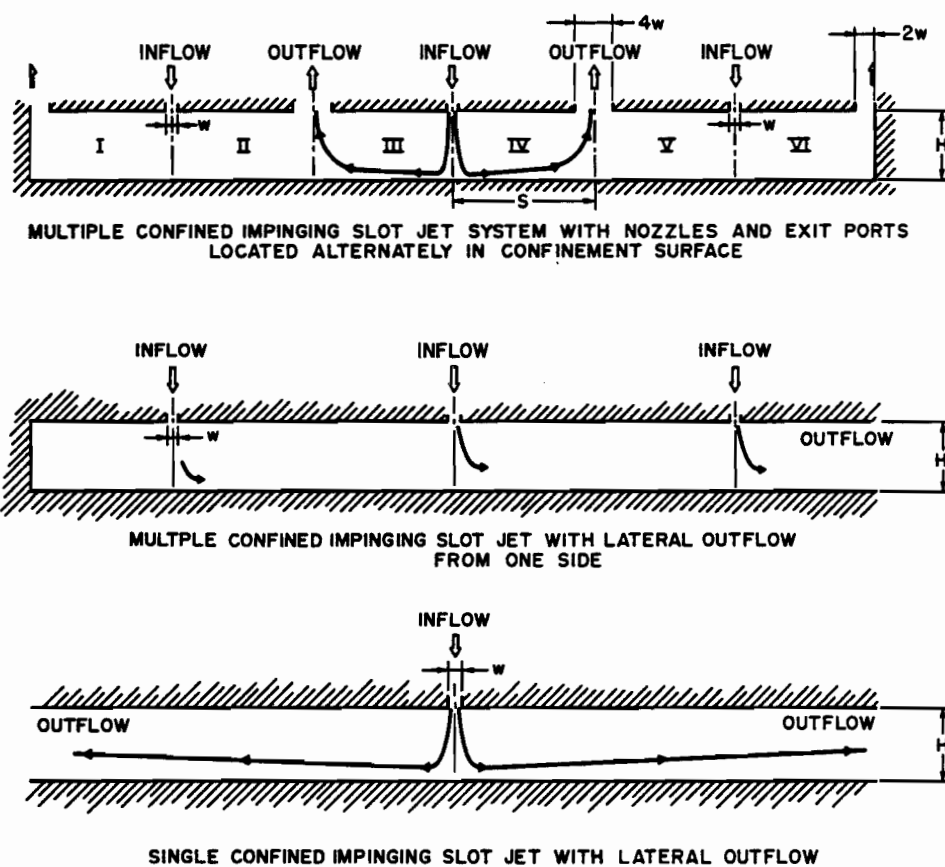


FIGURE 5.1. Impinging Jet Systems Used for Heat Transfer Measurements at the Impingement Surface

pingement surface spacing from the nozzle exit, H , was adjustable continuously, while five values of w , nozzle width, i.e. 2.5, 3.3, 5.0, 10.0 and 13.3 mm were used.

The geometrical parameters of such a system with the centerline spacing, S , fixed are conventionally represented by impingement surface spacing from the nozzle exit, H/w , and one of the three alternate parameters, nozzle width w , the percent open (nozzle) area f ($f = w/2S$), or centerline spacing, S/w . The range of these parameters is $4 \leq H/w \leq 24$, $2.5 \leq w \leq 13.3$ mm, $1.56 \leq f \leq 8.313\%$ and $6 \leq S/w \leq 32$. Analysis of the flow in Chapter 4 established the value of viewing such a multiple slot jet system as an assembly of repeated "flow cells" of lateral and axial dimension S and H , a flow cell being characterized by its dimensionless geometric proportions, S/H . In describing the multiple jet system using the flow cell parameter S/H , considerations of geometric similarity require specification of another independent dimensionless ratio, either H/w or $f(w/2S)$. The range of flow cell proportions for the heat transfer study was the same as that for the flow investigation, i.e. $6 \geq S/H \geq 0.33$.

The heat transfer study was carried out with air at ambient temperature and pressure impinging on a heated isothermal surface maintained at a ΔT of about 20°C , and which could be traversed laterally to obtain profiles of local heat transfer coefficient. The basic flow parameter is Reynolds number at the nozzle exit, $Re_j = U_j^* w / \nu_j$, for which kinematic viscosity is evaluated at nozzle exit temperature. Jet mean velocity at the nozzle exit U_j^* (m/s), pressure drop across the nozzle ΔP_j (N/m^2), and fan energy at the nozzle exit per unit heat transfer area R_j (W/m^2) are additional parameters that describe the flow. The range of these parameters is $3330 \leq Re_j \leq 29160$, $9.5 \leq U_j^* \leq 76.0$ m/s, $66.8 \leq \Delta P_j \leq 4007$ (N/m^2) and $39.7 \leq R_j \leq 8048$ (W/m^2). Details of

the equipment and of the flow system are described respectively in Chapters 3 and 4.

From the comprehensive tabulation of geometric and flow variables in Tables 4.1 and 4.2, a more detailed presentation of combinations of these parameters for the heat transfer investigation is given in Table 5.1. For each value of flow cell (S/H), the impingement heat transfer was measured for three values of Re_j as shown in Table 5.1(a), and for each of these values of Re_j the corresponding values of U_j^* , ΔP_j and R_j are presented in Table 5.1(b). For instance for $w = 2.5$ mm, $S/w = 32$, $f = 1.56\%$, local heat transfer profiles were made for 9 sets of experiments, i.e. 3 jet flow rates (Re_j) for each of the 3 values of H/w or S/H . The only exception is noted by the asterisk in Table 5.1. This table records the complete set of combinations of parameters for 52 heat transfer experiments performed on the multiple confined impinging slot jet system with nozzles and exit ports located alternately in the confinement surface.

5.1.2 Basis of Local Nusselt Number

As the analysis of heat transfer in Chapter 5 is in terms of local Nusselt number, the basis of the local heat flux measurements (discussed in Chapter 3) will now be summarized. The heat transfer profiles were obtained by traversing the isothermal impingement surface under the stationary jets. At each station the local convective heat transfer at steady state was evaluated from the power dissipated to the impingement flow from the heat flux sensor. The local heat transfer coefficient (h_x), based on the temperature difference $T_s - T_j$, was calculated as shown in Section 3.4.2. This value of h_x was then normalized in the form of Nusselt number, $Nu_x = h_x w/k$, with thermal conductivity evaluated at the nozzle exit temperature as was kinematic

TABLE 5.1. Geometrical and Flow Parameters of the Multiple Jet System for Analysis of Impingement Heat Transfer

Table 5.1(a)

w (mm)	S/w	$f, \%$	H/w	S/H	Re_j
2.5	32	1.56	8	4	3330
					5230
					10790
			16	2	3330
					5230
					10790
			24	1.33	3330
					5230
					10790
3.3	24	2.06	4	6	3410
					5400
					10270
			8	3	3410
					5400
					10270
			16	1.5	3410
					5400
					10270
			24	1	3410
					5400
					10270
5.0	16	3.125	8	2	5700
					7500
					10740
			16	1	20740*
					5700
					7500
			24	0.67	10740
					5700
					7500

Table 5.1(a) (continued)

w (mm)	S/w	$f, \%$	H/w	S/H	Re_j
10.0	8	6.25	4	2	5400
					10910
					21720
			8	1	5400
					10910
					21720
			16	0.5	5400
					10910
					21720
			24	0.33	5400
					10910
					21720
13.3	6	8.313	4	1.5	10770
					21760
					29160
			8	0.75	10770
					21760
					29160
			16	0.375	10770
					21760
					29160

Table 5.1(b)

w (mm)	Re_j	U_j (m/s)	ΔP_j (N/m ²)	R_j (W/m ²)
2.5	3330	23.4	406	148
	5230	36.8	1003	576
	10790	76.0	4007	4751
3.3	3410	18.2	245	92
	5400	28.8	614	364
	10270	54.8	2083	2352
5.0	5700	20.0	296	185
	7500	26.4	504	416
	10740	37.8	991	1171
10.0	20740	73.0	3528	8048
	5400	9.5	67	40
	10910	19.2	256	307
13.3	21720	38.2	966	2306
	10770	14.2	140	165
	21760	28.8	549	1314
	29160	38.6	970	3112

viscosity for Re_j . For the entire range of geometric and flow parameters of the present study the statistical analysis of uncertainties based on single-sample experiment and on repeated experiments is presented in Appendix 5.

5.2 Confined Multiple Slot Jet Systems with Symmetrical and One-Sided Outflow

As discussed in Chapter 2 the impingement transport characteristics are greatly affected by the interaction between the jet flow and the flow after impingement (often referred to as spentflow). This interaction decreases heat transfer at the impingement surface. However, such interaction can be prevented by constraining the flow after impingement to exit through openings in the confinement surface between successive inlet jets. The study of impingement heat transfer for such a system is the central objective of the present work. Hence as described in Chapter 3 heat transfer was studied using an experimental facility that comprised three impinging slot jets with outflow ports alternating with inlet nozzles in the confinement surface.

Two different objectives are therefore treated in this section. First, there is the need to establish that the present system does indeed accurately represent conditions in multiple jet systems with a large number of jets. Second, as the multiple jet design of the present study was chosen on the basis of supposed superiority of symmetrical outflow, this superiority should be documented quantitatively. Although these objectives are quite distinct, it is convenient to treat them consecutively because both analyses require reference to lateral profiles of local Nusselt number extending over several adjacent flow cells.

Unlike the lateral profiles of static pressure, which covered the entire impingement surface, lateral heat transfer profiles were carried out over only somewhat more than half of the impingement surface, i.e. flow cells II, III,

IV and part of flow cell I. Analysis of results established that profiles covering three central flow cells was more than sufficient.

5.2.1 Laboratory Representation of Multiple Slot Jet Systems

In Chapter 4 it was established that the impingement surface static pressure profiles in the central four flow cells of the six flow cell experimental facility (shown on top of Figure 5.1) were symmetrical and indistinguishable. Although this evidence from analysis of the flow would indicate that impingement surface convective heat transfer profiles would likewise be identical over the central two-thirds of the apparatus, this expectation was tested directly. For this purpose lateral profiles of Nu_x were obtained over about 3.5 flow cells, i.e. for part of flow cell I and all of flow cells II, III and IV. These profiles were obtained for the nine wide-ranging combinations of geometrical and flow parameters listed in Table 5.2. It may be noted that the range of geometrical parameters includes both non-interacting flow cells ($S/H > 1$) and interacting flow cells ($S/H < 1$), a concept developed in Chapter 4.

The lateral profiles of Nu_x for the nine combinations of parameters listed in Table 5.2 are presented in four sets of figures, 5.2 through 5.5. The profiles shown as dotted lines on this set of figures relate to the succeeding section and may be ignored in the present discussion. Figures 5.2 and 5.3 present, for a single Reynolds number, the profiles for $w = 2.5$ mm ($f = 1.56\%$, $S/w = 32$) and 5.0 mm ($f = 3.125\%$, $S/w = 16$), respectively. For both values of f , w or S/w (alternative parameters), profiles are presented for three values of H/w or S/H . Figure 5.4 presents Nu_x profiles at three values of Re_j for a single set of geometrical parameters. Figure 5.5 presents profiles at a single Re_j and H/w with f and S/H (or the equivalent) as variables.

For the purpose of the present section these profiles are examined only

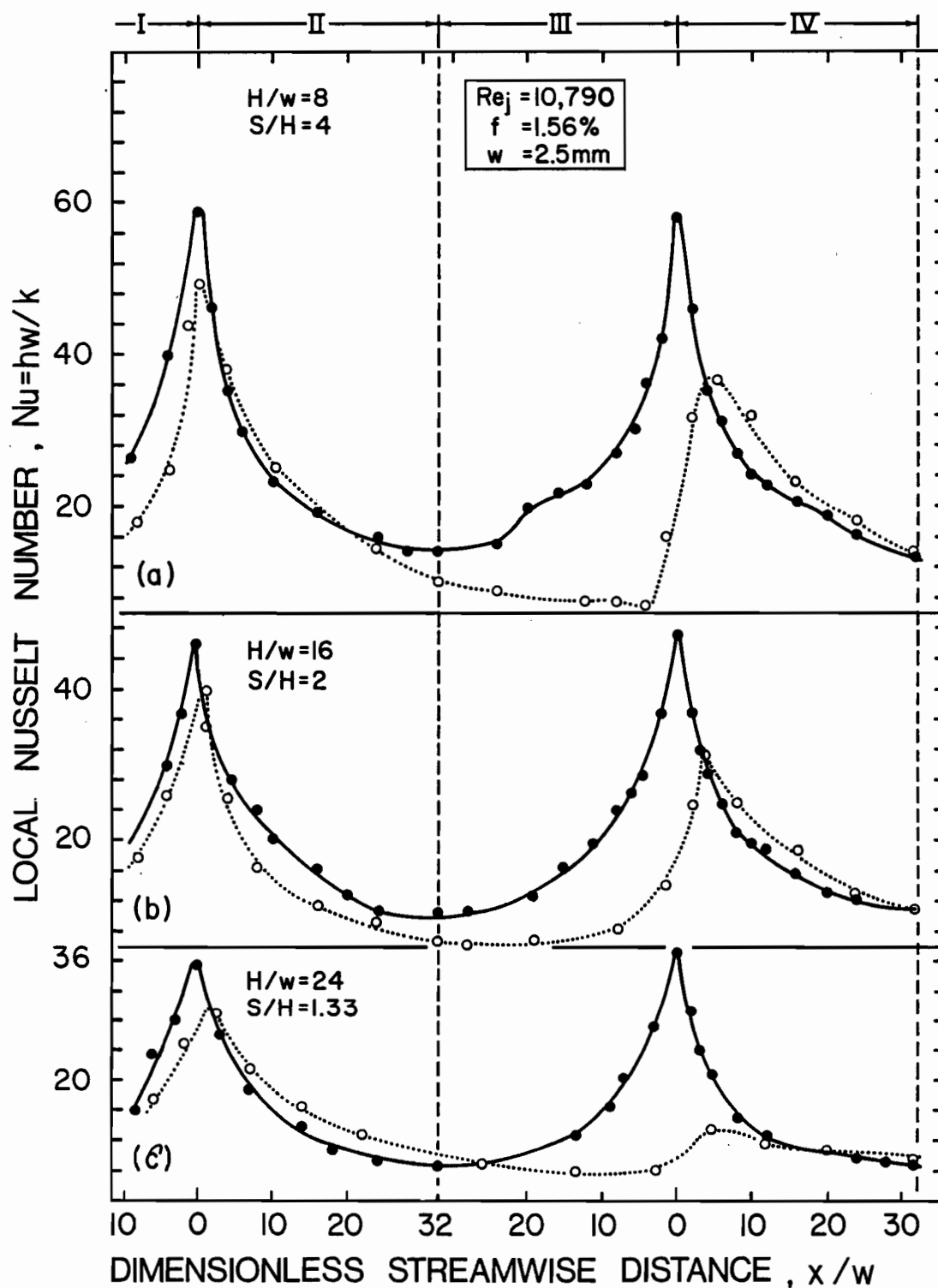


FIGURE 5.2. Effect of Impingement Surface Spacing on Lateral Profiles of Nu_x for Confined Multiple Slot Jet Systems with Symmetrical ($f = 1.56\%$) and One-Sided Outflow

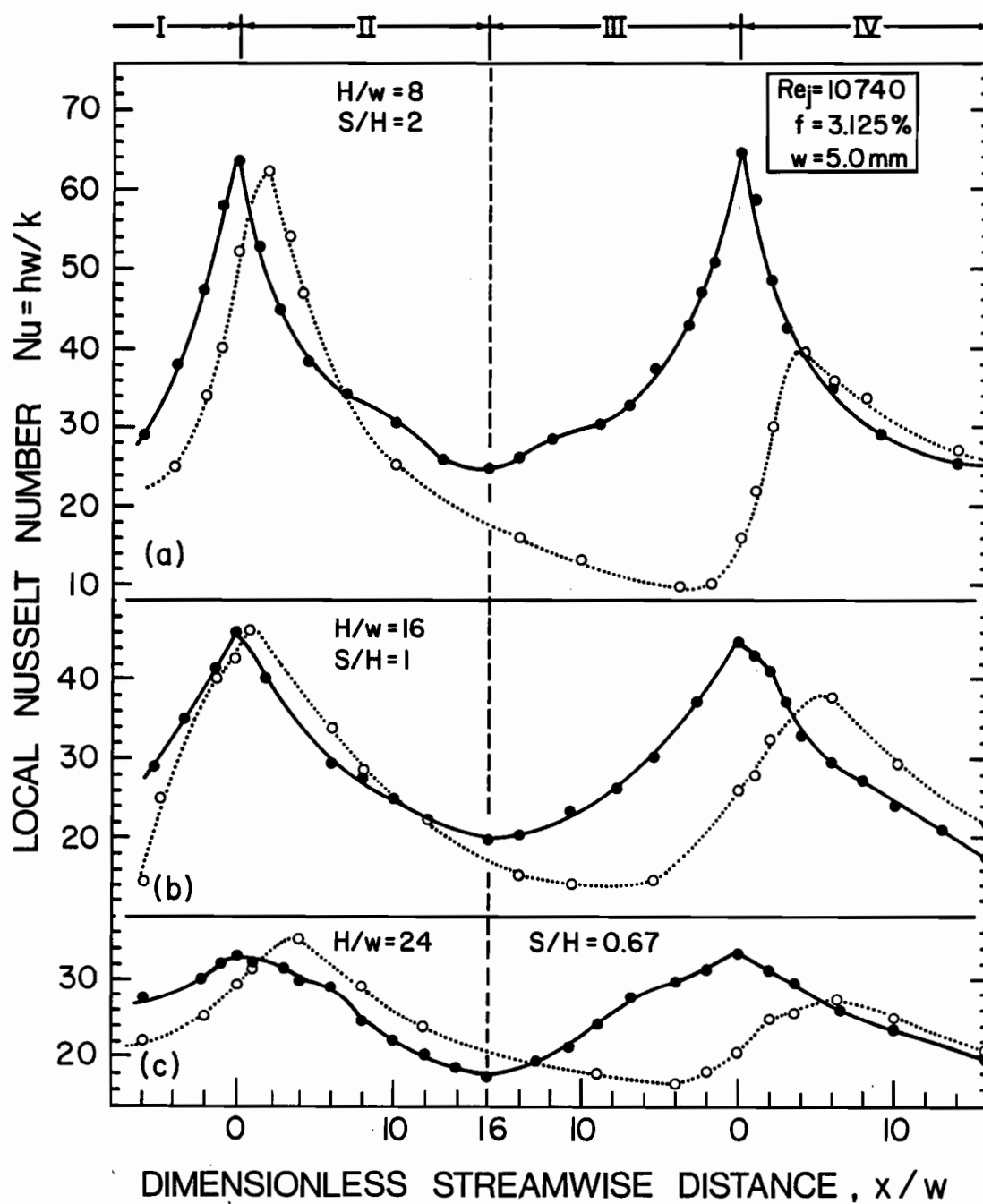


FIGURE 5.3. Effect of Impingement Surface Spacing on Lateral Profiles of Nu_x for Confined Multiple Slot Jet Systems with Symmetrical ($f = 3.125\%$) and One-Sided Outflow

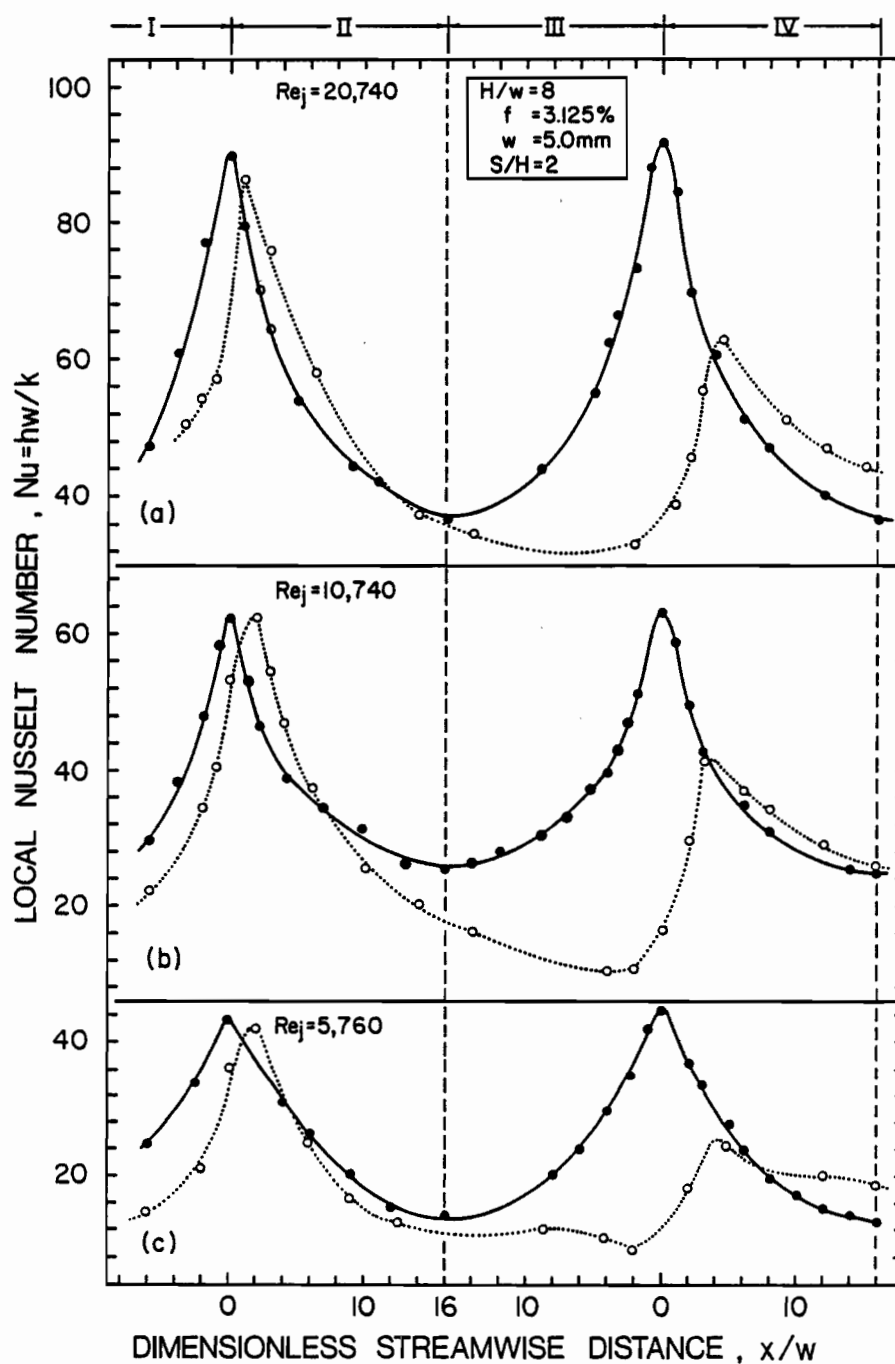


FIGURE 5.4. Effect of Jet Reynolds Number on Lateral Profiles of Nu_x for Confined Multiple Slot Jet Systems with Symmetrical ($f = 3.125\%$) and One-Sided Outflow

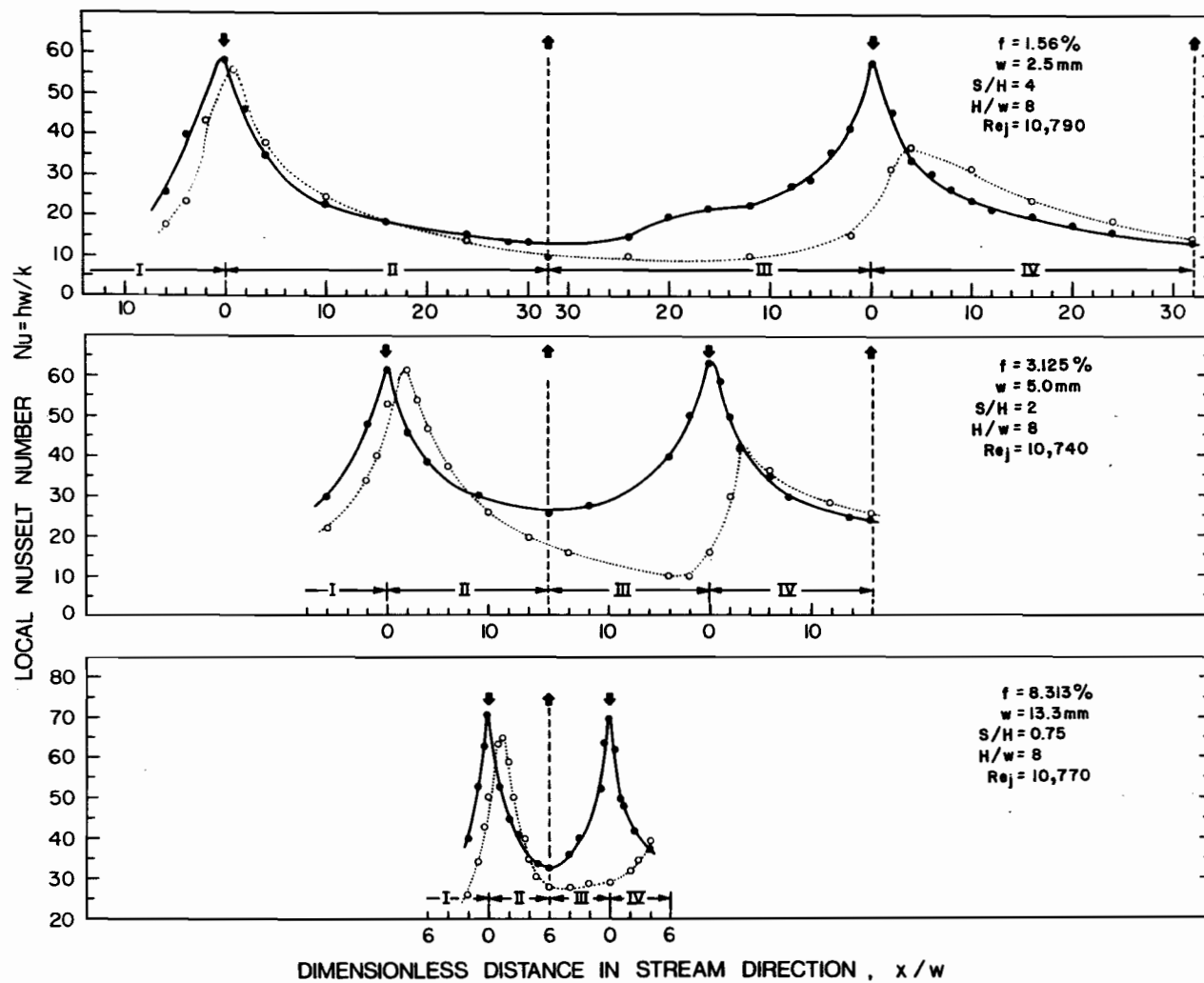


FIGURE 5.5. Effect of Percent Open Area on Lateral Profiles of Nu_x for Confined Multiple Slot Jet Systems with Symmetrical and One-Sided Outflow

TABLE 5.2. Geometrical and Flow Parameters of the Multiple Jet System for Analysis of Heat Transfer with Symmetrical and One-Sided Outflow

Table 5.2(a)

w (mm)	S/w	$f, \%$	H/w	S/H	Re_j
2.5	32	1.56	8	4	10790
			16	2	10790
			24	1.33	10790
5.0	16	3.125	8	2	5700
			8	2	10740
			8	2	20740
			16	1	10740
			24	0.67	10740
13.3	6	8.313	8	0.75	10770

Table 5.2(b)

w (mm)	Re_j	U_j^* (m/s)	ΔP_j (N/m ²)	R_j W/m ²
2.5	10790	76.0	4007	4751
5.0	5700	20.0	296	185
	10740	37.8	991	1171
	20740	73.0	3528	8048
13.3	10770	14.2	140	165

as to their degree of similarity, as analysis and interpretation of lateral profiles of Nu_x forms the subject of an entire section, 5.4. Visual inspection of the 12 distribution curves portrayed on Figures 5.2-5.5 suggests that the profiles of the three complete flow cells are indistinguishable.

Such visual comparisons as noted above are encouraging but not very precise. As a more critical test of the hypothesis that any of the central cells of the 3-jet, 6-flow cell system do indeed represent the transport characteristics of a cell in the equivalent multiple jet system, the data of cells II, III and IV of Figure 5.2 through 5.5 are shown superimposed on Figures 5.6 through 5.9. The fact that for each of the nine cases a single curve adequately represents the heat transfer profiles from all 3 cells proves first, that the flow is symmetrical in the central region, flow cells III and IV, and second, that cells II and IV are equivalent. In brief, the profiles of all flow cells of the apparatus except for the end cells, I and VI, are indistinguishable one from the other. It is therefore indicated that even in an experimental set-up comprising only two inlet jets, the central two of the four flow cells would be representative of a multijet system. This conclusion provides assurance that heat transfer data from the present experimental facility may with confidence be taken as representative of that in an equivalent confined multiple slot jet system with a large number of jets.

5.2.2 Effect on Heat Transfer of One-Sided Cumulative Spentflow

In the present section the extent of reduction of heat transfer in multiple jet systems with one-sided cumulative spent outflow is established. The standard of comparison used in this purpose is the symmetrical outflow design used for most of the work of the present study. Although the symmetrical outflow design gives superior heat transfer, as will be documented in

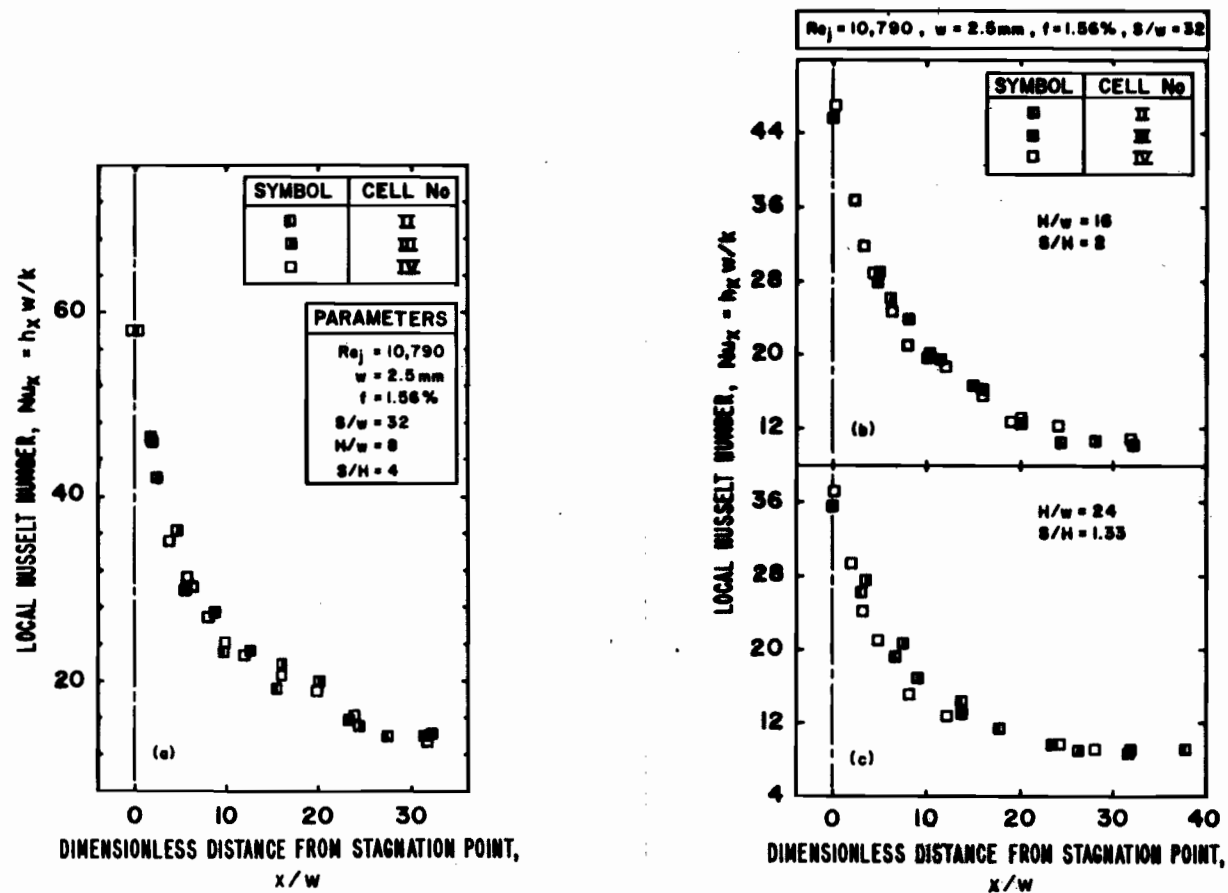


FIGURE 5.6. Superimposed Profiles of Nu_x for Confined Multiple Slot Jet Systems with Symmetrical ($f = 1.56\%$) and One-Sided Outflow

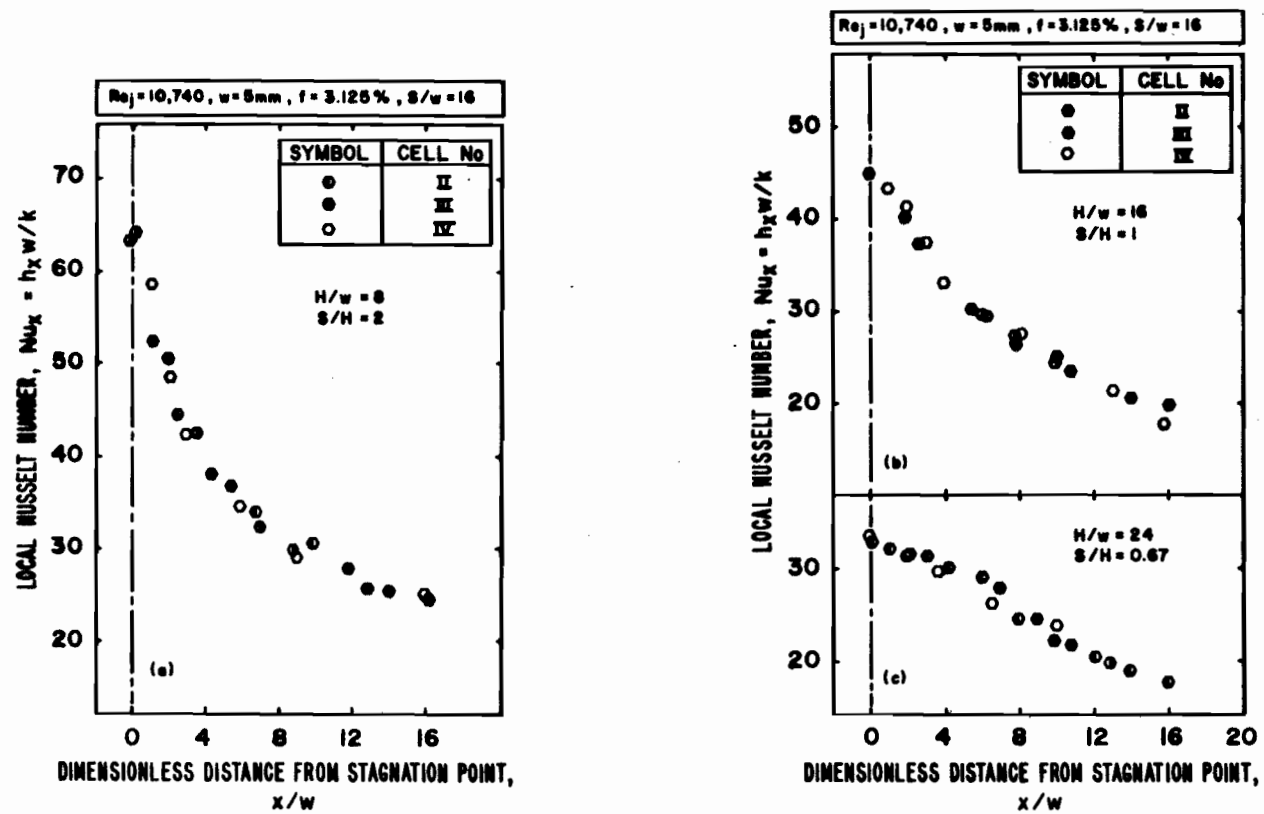


FIGURE 5.7. Superimposed Profiles of Nu_x for Confined Multiple Slot Jet Systems with Symmetrical ($f = 3.125\%$) and One-Sided Outflow

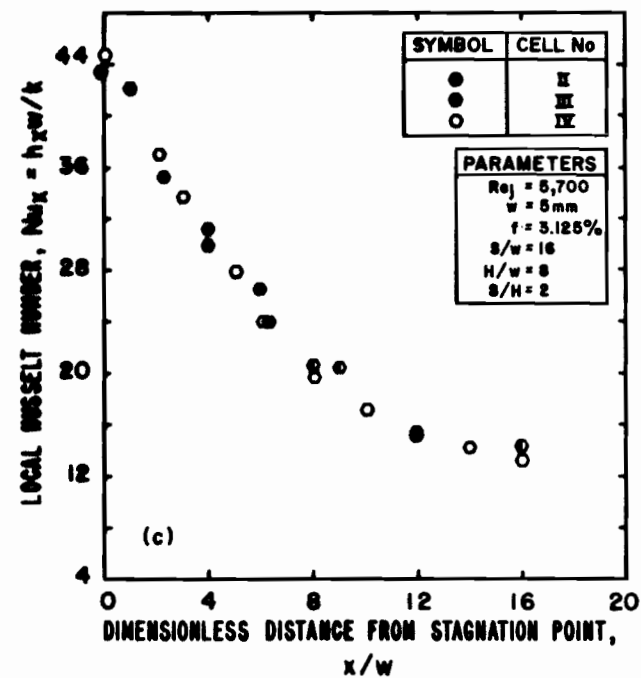
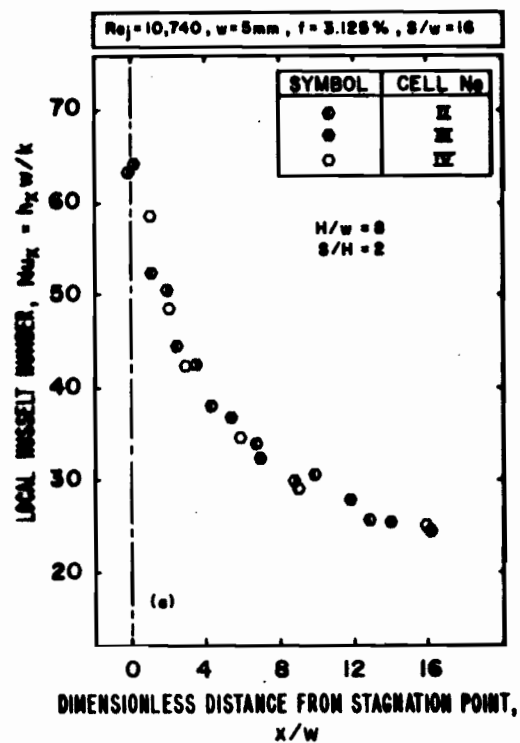
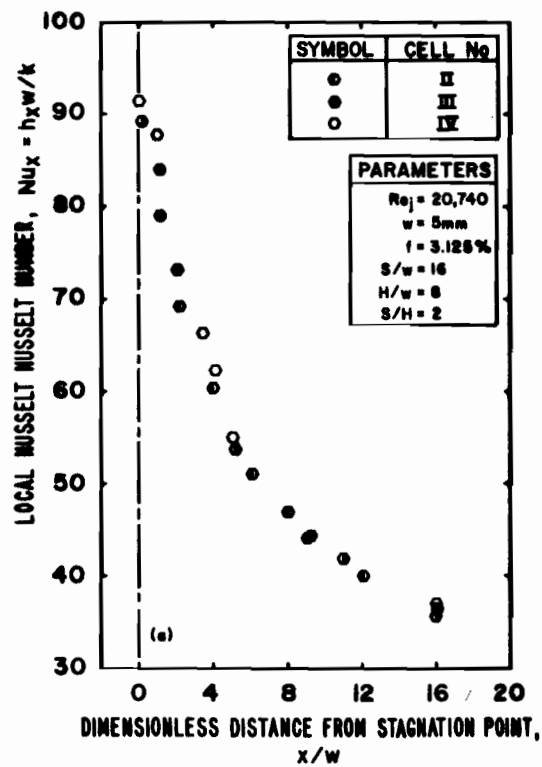


FIGURE 5.8. Superimposed Profiles of Nu_x for Confined Multiple Slot Jet Systems with Symmetrical and One-Sided Outflow and $Re_j = 20740, 10740$ and 5700

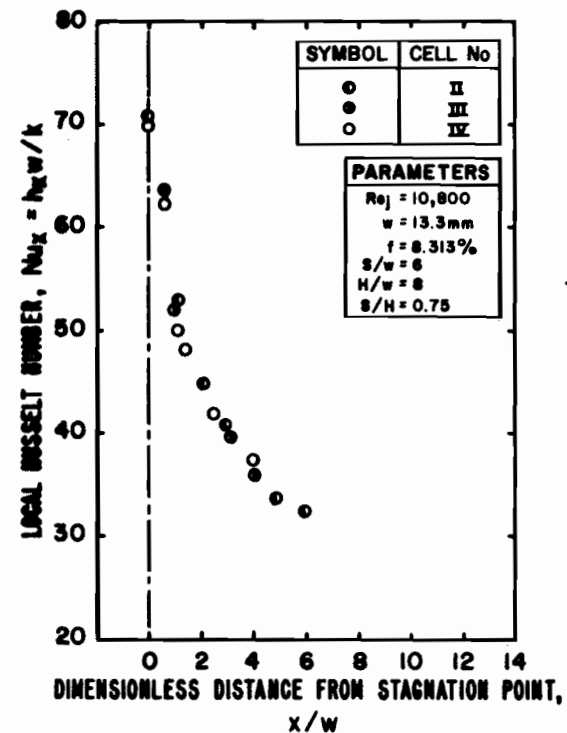
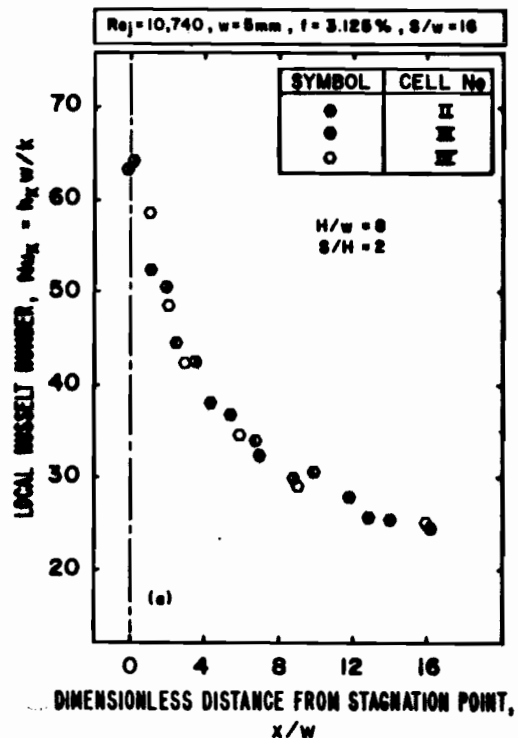
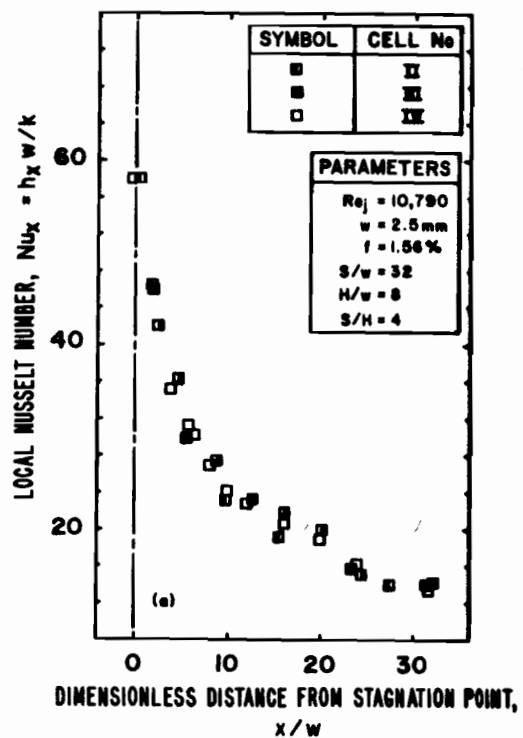


FIGURE 5.9. Superimposed Profiles of Nu_x for Confined Multiple Slot Jet Systems with Symmetrical ($f = 1.56, 3.125$ and 8.313%) and One-Sided Outflow

the present section, it should be noted that examples of industrial application exist for the use of multiple jet systems in a cumulative spentflow configuration. Thus there is specific industrial relevance to the objective of determining quantitatively the effect on heat transfer of cumulative spentflow.

A significant application utilizing a two-dimensional array of jets occurs for gas turbine airfoils, for which the jets cool the midchord region with a trailing edge discharge. The jet after impingement is constrained to flow toward the rear of the airfoil along the channel formed between the jet confinement surface and the inner surface of the airfoil envelope (the impingement surface). Thus, in this configuration spentflow from the upstream jets impose a confined crossflow on the downstream jets.

For paper drying, high velocity hoods are designed so that the exit flow openings are installed between three or more rows of jets. Thus the impingement flow from jets located at the middle of the array imposes a crossflow on the downstream jets as the flow is constrained along the channel formed between the hood and the web.

The type of one-sided lateral spentflow for which heat transfer profiles were obtained is illustrated by the middle configuration of Figure 5.1. Relative to the basic design shown at the top of Figure 5.1, this modification was obtained by blocking all the exit ports in the confinement surface and removing one end wall. The cumulative spentflow may be described by reference to the amount of spentflow exiting as a crossflow at the position of each successive centerline of the basic equipment. By contrast, with the symmetric outflow of the basic design there is of course zero crossflow at each of the five centerlines between cells. With the cumulative spentflow of the modified design there is at the cell I/II centerline a spent crossflow equal to half

of the flow of an inlet jet. At the successive centerlines between cells II/III, III/IV, IV/V, V/VI the spent crossflow cumulates successively to 1, 1.5, 2 and 2.5 times the flow of an inlet jet.

The heat transfer data at an impingement surface subjected to this type of impingement flow with cumulative spentflow are presented in the form of local Nusselt number, shown as dotted lines on the same graphs, Figure 5.2 through 5.5, as the corresponding profiles for symmetric outflow that were discussed in the previous section. At the positions corresponding to the three centerlines included in Figures 5.2 to 5.5, i.e. between cell I/II, II/III and III/IV, the respective cumulative spent crossflows equal 0.5, 1, 1.5 times the flow of an inlet jet. This crossflow causes a shift of the entire heat transfer profile in the direction of the crossflow, and causes the profiles to become reduced by an amount which increases in the direction of increasing spentflow, i.e. the reduction of Nu_x increases progressively from cells II to III to IV. Cumulative spentflow both degrades ΔT and reverses the lateral velocity in flow cells I, III and V whereas it degrades ΔT but increases lateral velocity in cells II, IV and VI. The two latter effects act in compensating directions on heat transfer. Thus reduction in heat transfer is very large in cells where lateral velocity is reversed (I, III and V) while being relatively unchanged in cells (II, IV and VI) where spentflow augments the lateral velocity.

With respect to the reduction of Nusselt number by cumulative spent crossflow there are two mechanisms involved, one relating to flow field effects, the other relating to a thermal mechanism. The flow field effect is of course that any crossflow, either of a spent outflow or of an induced crossflow, acts to destroy the unique flow field around the stagnation point which is the source of high impingement surface transport rates. The additional thermal effect is that the ΔT driving force for heat transfer is decreased by dilution

of the inlet jet flow in the spentflow which has already exchanged heat at the surface, i.e. the bulk temperature of the spentflow increases with distance downstream. This reduction in effective local ΔT for heat transfer at the impingement surface is not accounted for in the calculation of the heat transfer coefficient, which is based on the difference between T_j and T_s . Thus this thermal effect of cumulative crossflow is additive to the flow field effect.

Having made these qualitative observations as to the effect of a cumulative spent crossflow on the profiles of Figures 5.2 to 5.5, it is now appropriate to put these comparisons in quantitative form. Such a quantitative comparison is made using as a reference a complete jet profile for the symmetrical outflow case. For the cell III plus IV section under the cumulative spentflow condition, the crossflows at the three centerlines (II/III, III/IV and IV/V) correspond, respectively, to 1, 1.5 and 2 times the flow of one inlet jet. Four quantitative measures of the effect of spent crossflow are used, namely, the maximum Nusselt number, Nu_o^* ; the difference between minimum and maximum Nusselt number, $Nu_{max} - Nu_{min}$; the shift, $\Delta x/w$, in location of Nu_o ; and the average Nusselt number, obtained as follows:

$$\overline{Nu} = \frac{1}{(S/w)} \int_{x/w \text{ at II/III centerline}}^{x/w \text{ at III/IV centerline}} Nu_x d(x/w) \quad (5.1)$$

These quantitative comparisons are shown in Figures 5.10 through 5.13, which correspond to Figures 5.2 through 5.5, respectively.

For $Re_j = 10790$ and $f = 1.56\%$ and 3.125% ($w = 2.5$ and 5 mm; $S/w = 32$ and 16), the effects of spentflow on \overline{Nu} , Nu_o , $Nu_{max} - Nu_{min}$ and $\Delta x/w$ are shown as a function of impingement surface spacing in Figures 5.10 and 5.11. It should be kept in mind that in the cell III-IV region the spentflow corresponds to

* With cumulative spentflow the velocity profile slope at the wall never changes sign, hence no stagnation point exists. With cumulative crossflow the flow adjacent to the impingement surface constitutes a continuous wall jet, the thickness of which is decreased each time it comes under the influence of a jet, with the Nu correspondingly passing through a maximum.

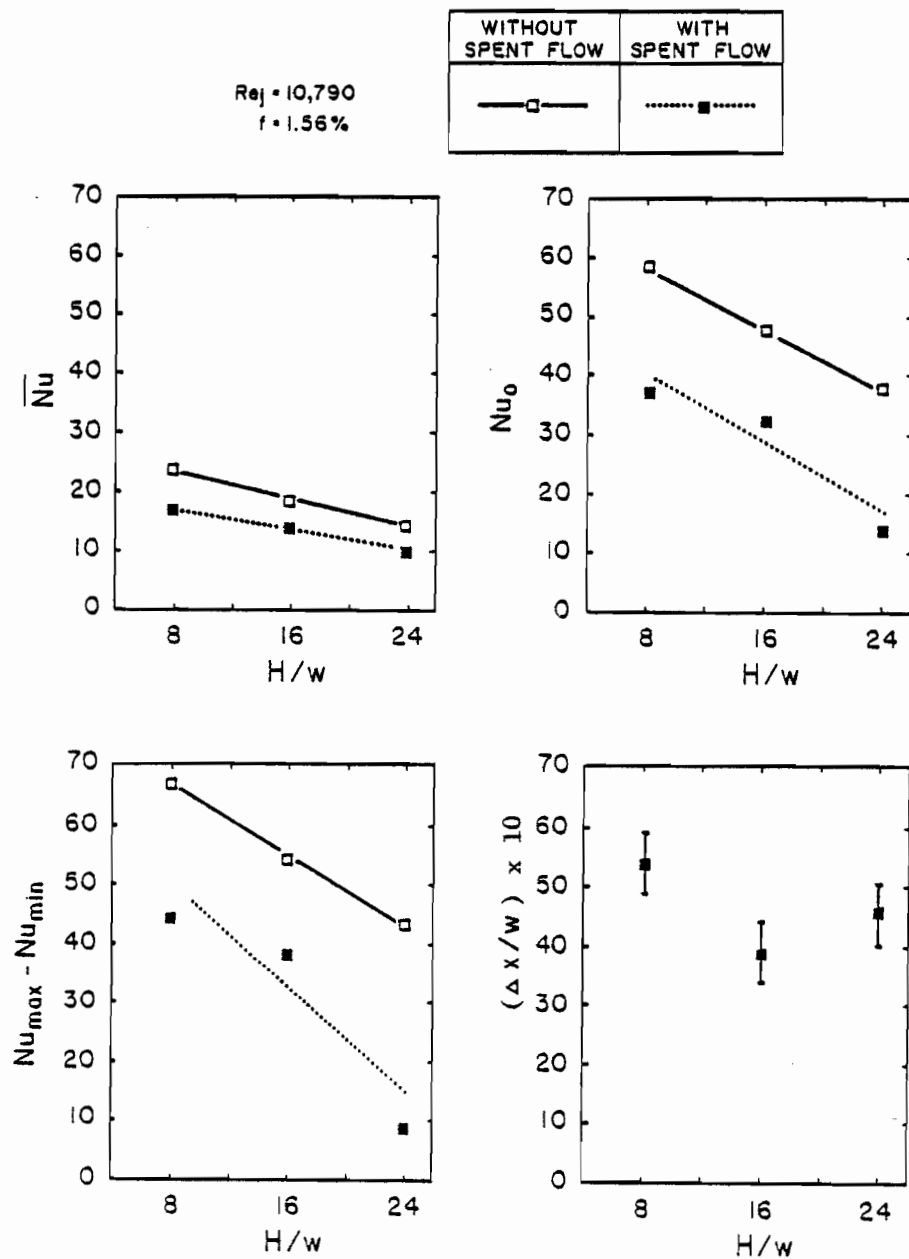


FIGURE 5.10. Effect of Impingement Surface Spacing on \overline{Nu} , Nu_o , $Nu_{max} - Nu_{min}$ and $\Delta x/w$ for Confined Multiple Slot Jet Systems with Symmetrical ($f = 1.56\%$) and One-Sided Outflow

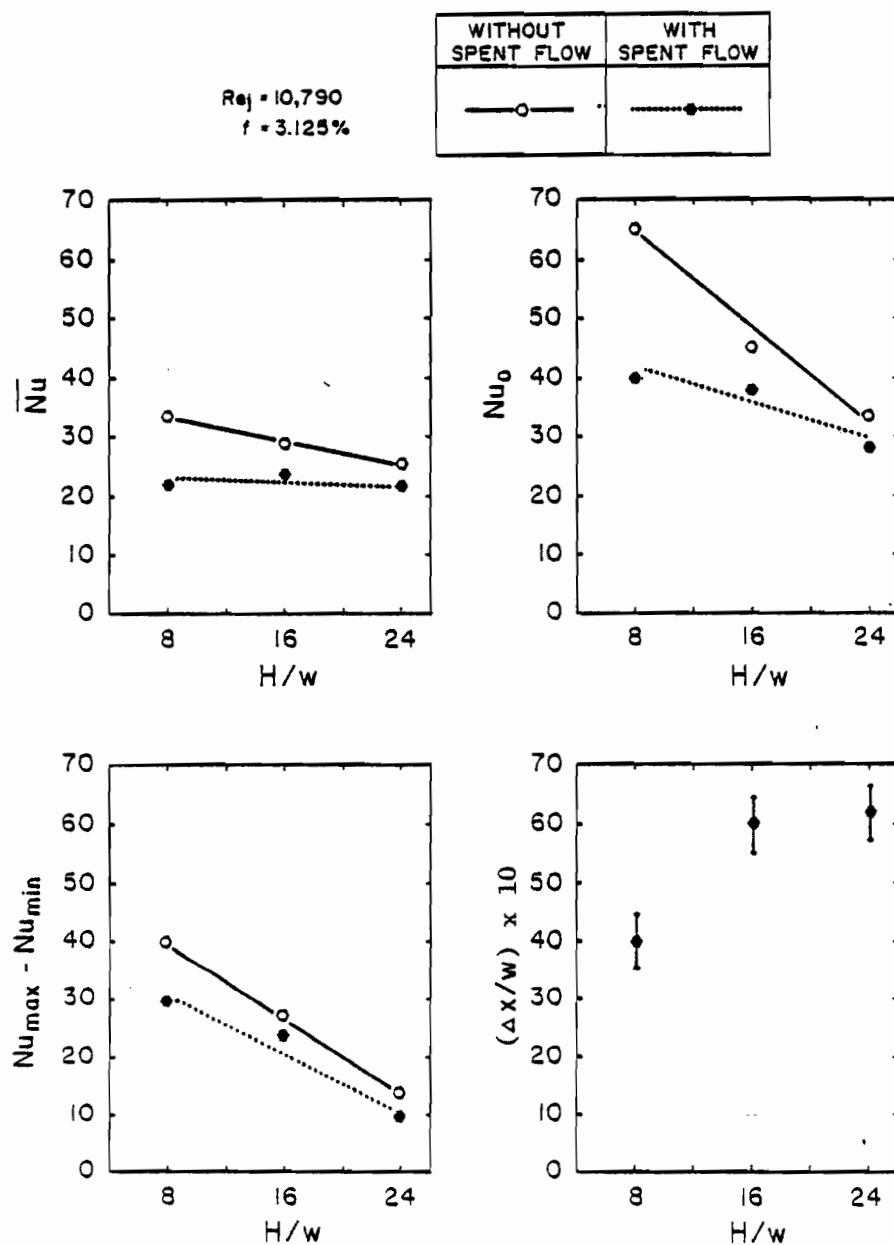


FIGURE 5.11. Effect of Impingement Surface Spacing on \overline{Nu} , Nu_o , $Nu_{max} - Nu_{min}$ and $\Delta x/w$ for Confined Multiple Slot Jet Systems with Symmetrical ($f = 3.125\%$) and One-Sided Outflow

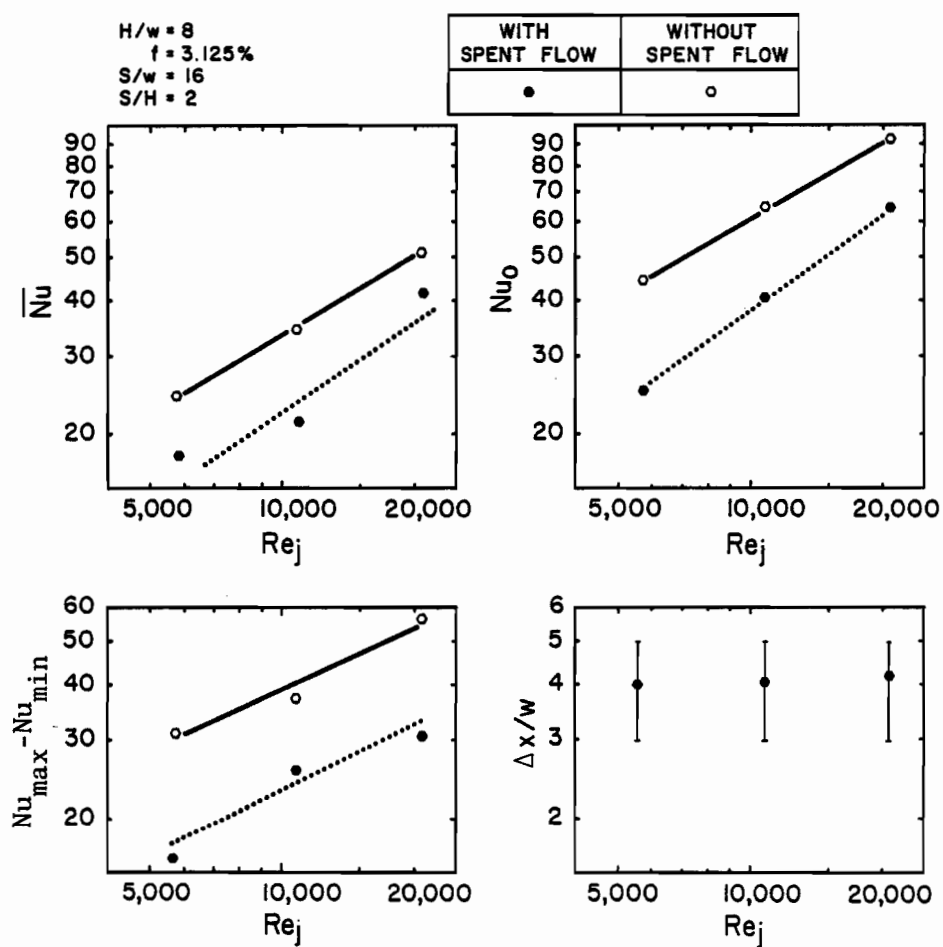


FIGURE 5.12. Effect of Jet Reynolds Number on \overline{Nu} , Nu_0 , $Nu_{max} - Nu_{min}$ and $\Delta x/w$ for Confined Multiple Slot Jet Systems with Symmetrical ($f = 3.125\%$) and One-Sided Outflow

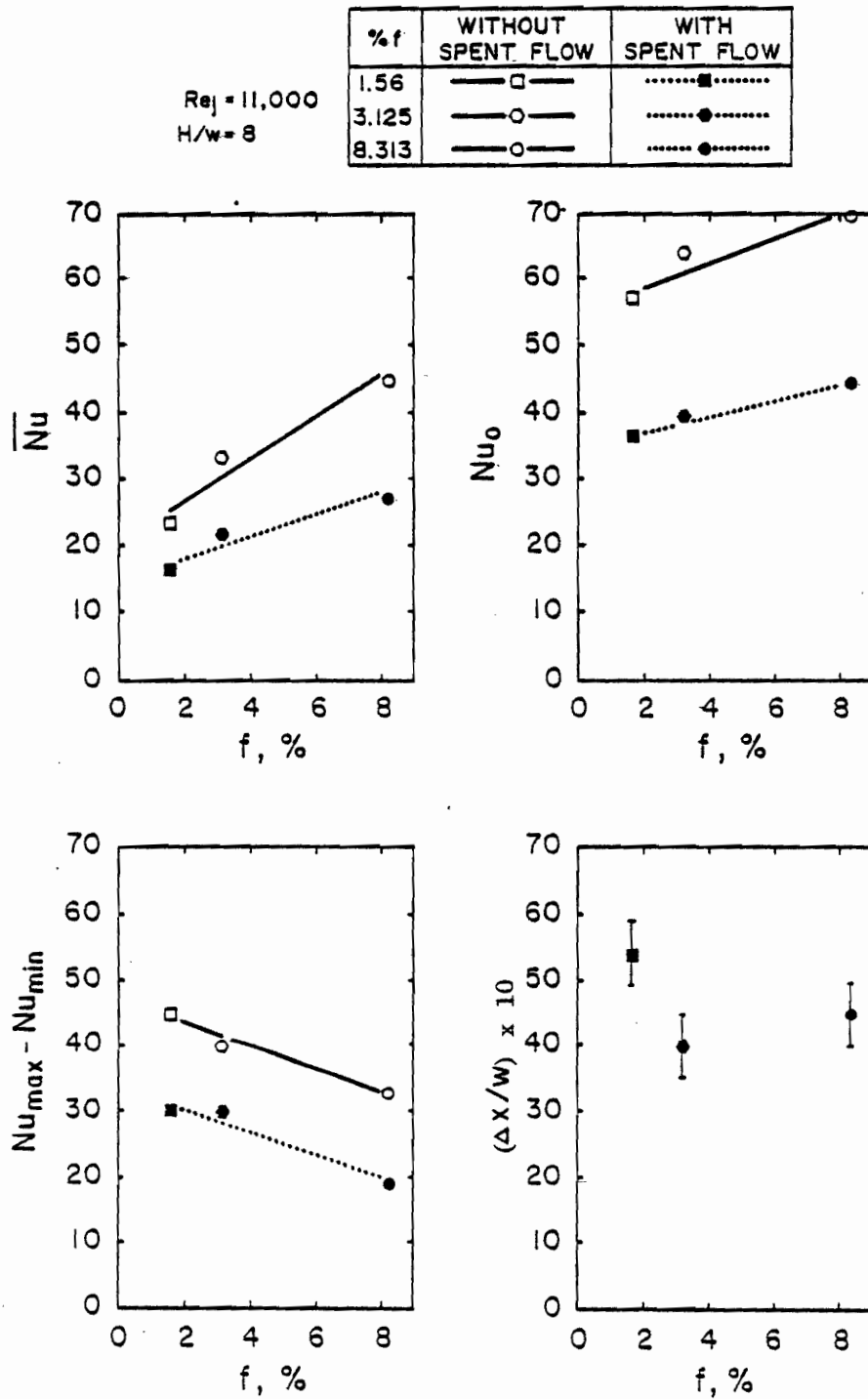


FIGURE 5.13. Effect of Percent Open Area on \overline{Nu} , Nu_o , $Nu_{max} - Nu_{min}$, and $\Delta x/w$ for Confined Multiple Slot Jet Systems with Symmetrical and One-Sided Outflow

from 1 to 2 times the flow from one inlet jet. The percentage decrease in \overline{Nu} caused by this spentflow is in the range 15% to 30%. On the other hand for this range of spacing, H/w , the spentflow decreases Nu_o by from 15% to 60%.

The finding that for the same flow and geometrical parameters a cumulative spent crossflow can cause a much higher reduction in Nu_o than in \overline{Nu} is expected. It was noted earlier that there are two mechanisms involved in the effect of cumulative spent crossflow. Degradation of the ΔT driving force for heat transfer resulting from dilution of the inlet jet fluid with the spentflow, referred to earlier as the thermal effect, applies over the entire impingement surface, hence has a similar effect on Nu_o and \overline{Nu} . The second effect noted earlier, the effect of the crossflow on the flow field, acts to destroy the stagnation point flow field which is the source of the high values of Nu_o , whereas it does not have a comparable strong effect within the wall jet flow field. Thus as one of the crossflow mechanisms operates over the impingement and wall jet regions alike while the other mechanism relates particularly to the stagnation region, the occurrence of higher reductions in Nu_o than \overline{Nu} is consistent with the controlling factors.

It can be seen from the relatively parallel curves on Figure 5.12 that the percentage reduction in Nu_o and \overline{Nu} caused by the spent crossflow, around 35-45%, does not vary significantly with Reynolds number in the range $5700 \leq Re_j < 20740$, for $f = 3.125\%$ and $H/w = 8$, ($S/H = 2$). As for the effect of nozzle open area, it is surprising to see from Figure 5.13 that the 35%-45% reduction in \overline{Nu} caused by spent crossflow does not vary significantly with f . The expectation might have been that because it is the impingement regions (which have high heat transfer coefficients) that are particularly vulnerable to a crossflow, the percentage reduction in \overline{Nu} would be higher at higher values of f because as percent open area increases, the fraction of the surface which

comprises impingement regions increases while that which comprises wall jet regions correspondingly declines.

Over the entire range of geometrical and flow parameters it is evident from Figures 5.10 through 5.13 that an amount of spentflow equal to around 1.5 times the flow from one inlet slot jet causes a shift in Nu_o in the direction of crossflow of $3.5w$ to $6w$. The limited accuracy with which it is possible to define this shift makes it impossible to relate the extent of the shift more precisely to the parameters under consideration.

Although for the present system the percentage reduction in heat transfer is found to be essentially insensitive to the variation of geometrical and flow parameters, the magnitude of the reduction is quite appreciable. It is interesting to note that for a similar crossflow of spentflow, the decrease in heat transfer in the flow cell III-IV region is much less for an array of staggered impinging round jets than for the present slot jet system. For example, under similar conditions of Re_j and S/H for an array of round jets where the spacing between neighboring holes ranged from 3 to 10-hole diameters, Saad et al. (1980) and Florschuetz et al. (1981) reported that \overline{Nu} and Nu_o in the flow cell III-IV region is only about 10% less than with symmetrical outflow, i.e. without spent crossflow. The more pronounced effect of the present multiple slot jet system is expected, since the open area of a slot jet is the upper limit of that for a row of holes as their number is increased. Furthermore for a staggered array of round holds such as described by these authors, the effect of crossflow is reduced relative to that for slot jets since the impinging jet flow for the former passes through the interhole spacing, thus not creating such a large effect of crossflow as in the case of slot jets.

In conclusion, it is established that the present multiple slot jet system with symmetric outflow does indeed accurately represent conditions in

multiple jet systems with a large number of jets. Moreover, the superiority of this system with symmetrical outflow was demonstrated quantitatively by comparing the heat transfer rate with that for the configuration with one-sided cumulative spentflow, a case of considerable industrial relevance.

5.3 Stagnation Point Heat Transfer

In the study of impingement transport characteristics the stagnation point assumes exceptional importance for its high rate of heat transfer. In order to increase the overall rate of heat transfer for a multiple impinging slot jet system the frequency of these stagnation maxima should be increased. This could be achieved by decreasing the spacing between jets, i.e. by decreasing the size of flow cell (S/H). However it is evident from results in Chapter 4 that as S/H is decreased, a critical size of flow cell, $(S/H)_c$, is reached at which interaction from the outflow extends to the jet centerline. This interaction produces significant effects on the transport characteristics at the impingement surface. In that chapter, two alternate criteria, i.e. the flow characteristics along the jet centerline and the static pressure at the impingement surface, were used to define $(S/H)_c$. As the effect on the mean velocity and turbulence characteristics of the flow field resulting from multiple jet interaction are in the direction of producing opposing trends in the transport phenomena at the surface, the resulting net effect on stagnation point heat transfer cannot be predicted.

The purpose of this section is to define the critical size of flow cell which separates non-interacting (large S/H) from interacting (small S/H) multiple impinging slot jet systems, and to determine the effects of flow and geometrical parameters on stagnation point heat transfer for both systems. Hence stagnation point heat transfer results were obtained to cover a wide

range of parameters that covers the limits of f , H/w , S/H and Re_j as shown in Table 5.1. On the other hand a larger number of values of H/w or S/H than indicated in this table were tested and are reported in subsequent figures.

Stagnation point heat transfer rates were obtained with the centerline of the heat flux sensor positioned to coincide with the centerline of the middle jet. For each experiment this coincidence of centerlines was assured by checking the symmetry of the static pressure profile at the impingement surface. The stagnation point heat transfer coefficient, h_o , was normalized in the form of Nusselt number, $Nu_o = h_o w/k$, as discussed earlier for the case of local Nu_x .

The magnitude of a small systematic error in Nu_o which is appreciable for the case of the narrower inlet nozzles may be estimated by reference to Figure 5.14. Because of symmetry of the heat transfer profile around the jet centerline only half the lateral distance need be considered. When the heat flux sensor is centered under the large nozzle ($w = 13.3$ mm), the sensor width ($s = 3.7$ mm) produces an averaging of heat transfer over an impingement lateral length equivalent to only $0.14w$ from the jet centerline. For the narrow nozzle ($w = 3.3$ mm) the lateral averaging of heat transfer is $0.56w$, i.e. 4 times larger. The relative effect of this averaging for the narrow nozzle might be assessed by comparing, for a typical heat transfer profile, the value of Nu_o for the large nozzle, i.e. averaged over $0.14w$, with that which would have been obtained for the same nozzle but averaged over $0.56w$. A test case was chosen for which the Nu_x profile around the stagnation point is quite steep, i.e. $Re_j = 10800$ and $H/w = 8$ for $w = 13.3$ mm. For this case the values of Nusselt number at position (1), (2) and (3) from the jet centerline are 70, 67.5 and 63.5, respectively. The appropriate arithmetic average for 2 sensor widths

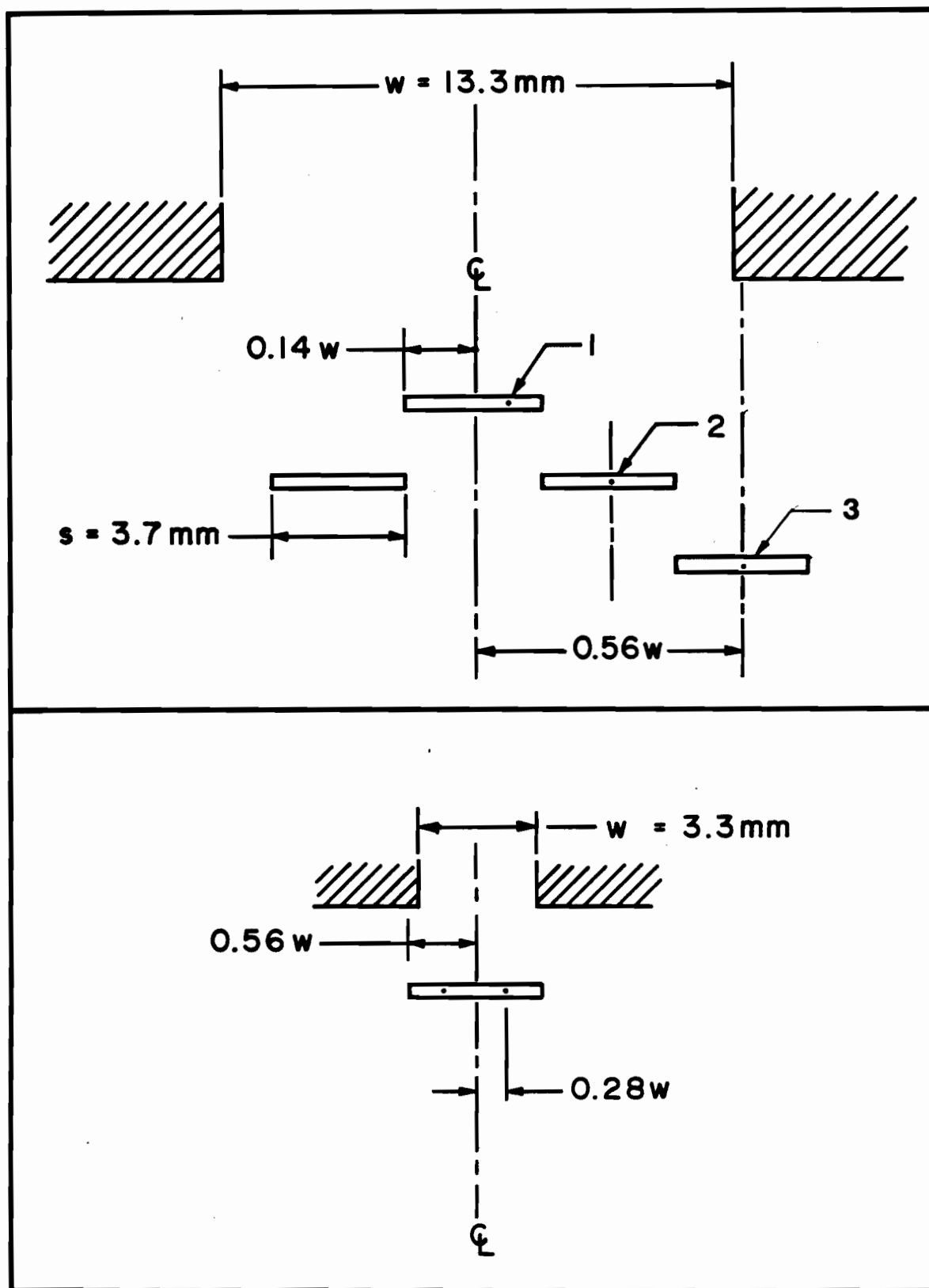


FIGURE 5.14. Schematic Presentation of the Finite Lateral Size of the Heat Flux Sensor ($s = 3.7 \text{ mm}$) with Respect to the Nozzle Width for $w = 13.3 \text{ mm}$ and 3.3 mm

that corresponds to a location of $0.56w$ from the jet centerline is $[(0.5)70 + 67.5 + (0.5)63.5]/2$. Thus for a nozzle width, $w = 13.3$ mm, a sensor four times as wide would have given a value of Nu_o of 67.13, i.e. 4.1% below the value of $Nu_o = 70$. As the systematic error which derives from the finite size of the sensor corresponds to reducing Nu_o by only about 4.1%, it was concluded that this error is acceptably small and of the same order of the uncertainty in measurement shown in Appendix 5.

Although the present study is oriented to heat transfer under multiple confined jets, the experimental program included the corresponding single confined slot jet in order to provide a base case for analysis of the multiple jet configuration. The multiple jet system was converted to the equivalent single jet arrangement shown on the bottom of Figure 5.1 by blocking the exit slots and the two side nozzles with thin sheet metal and opening both end walls to allow the spentflow to exit laterally as indicated.

The single impinging jet data presented in Figure 5.15 over the range $4 \leq H/w \leq 24$ indicate that Nu_o passes through a maximum at around $H/w = 8$. The data also indicate an effect due to nozzle width (w). Although the dependence on w over the range 3.3 to 13.3 mm is not large (Figure 5.15), it cannot be neglected, especially at the lower values of H/w .

Of these two effects on Nu_o , i.e. the maximum with respect to impingement surface spacing at $H/w = 8$ and the appearance of w as additional parameter, the former will be considered first. Impingement surface spacing affects Nu_o through the corresponding effects of H/w on the mean velocity and turbulence intensity of the impingement flow (documented in Chapter 4) approaching the stagnation point. With respect to effect of distance from the nozzle exit, Figure 4.12 provides profiles of axial mean velocity, U_o , while Figures 4.13 and 4.14 document more clearly that after the end of the poten-

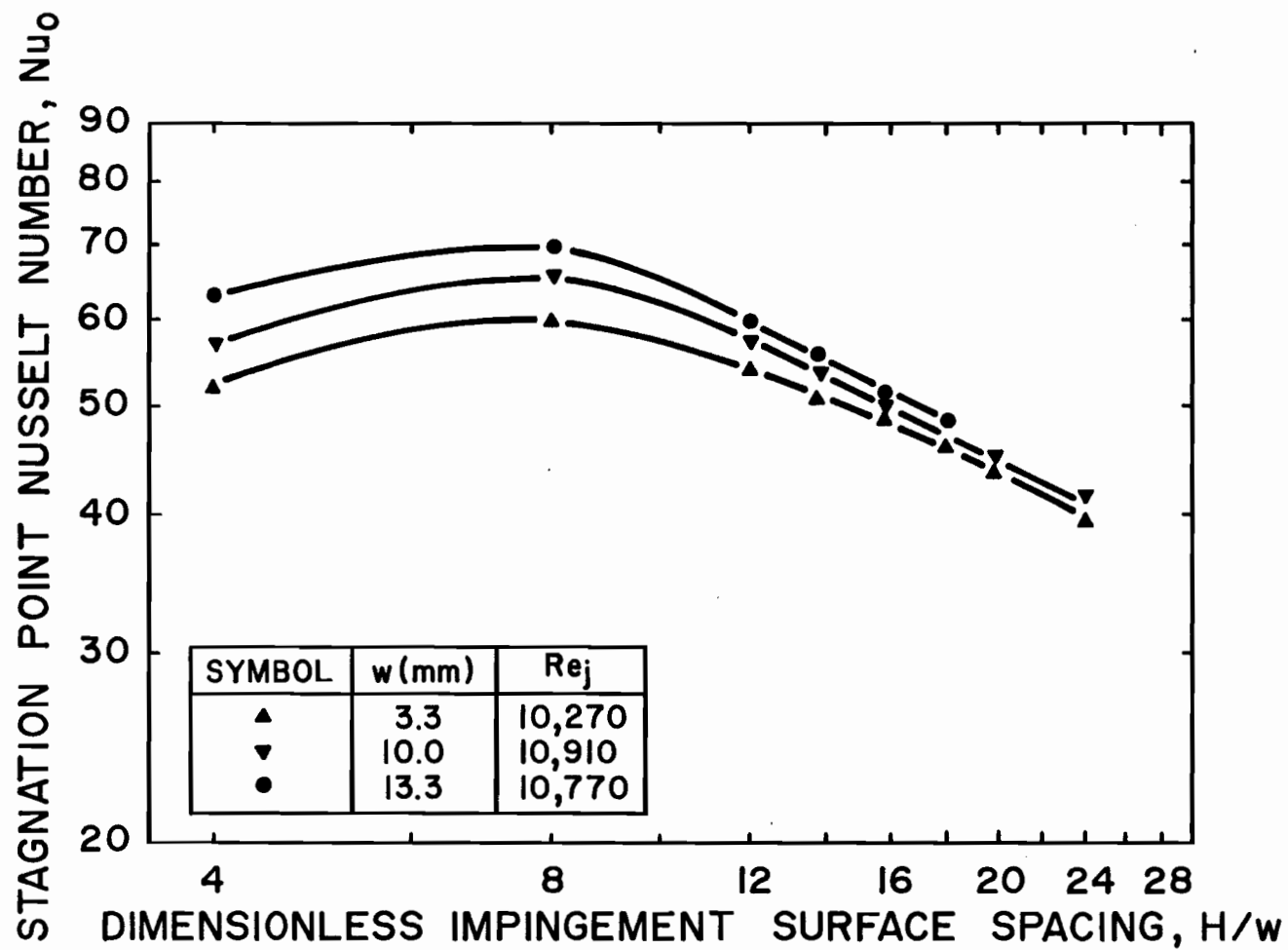


FIGURE 5.15. Effect of Impingement Surface Spacing on Nu_0 for Confined Single Impinging Slot Jet

tial core, which is about $3-4w$, U_o decays proportional to the square root of distance from the nozzle exit. It is clear that with this effect of spacing on U_o , there is a resultant effect of decrease of Nu_o with increasing spacing. However, while U_o decreases continuously with spacing, Figure 4.11 documents the increase of turbulence intensity with distance from the nozzle exit, an increase at first very sharp, but levelling out after $8w$ from the nozzle exit. Hence as impingement surface spacing increases, the effect of H/w on U_o at any particular value of w is to cause a reduction in Nu_o , while through the effect of H/w on turbulence intensity there is the opposite consequence of increasing Nu_o . Figure 5.15 clearly illustrates that for spacings up to about $H/w = 8$ the effect on Nu_o of the rapidly increasing turbulence intensity is more important than the opposing effect of decreasing U_o . Beyond $H/w = 8$ the relative importance of these two effects is reversed, i.e. the effect on Nu_o of decreasing U_o is stronger than the opposing effect of, now, more slowly increasing turbulence intensity.

This approach of analyzing $Nu_o = f(H/w)$ in terms of the concept of $Nu_o = f(Re_a, Tu_a)$ was applied quantitatively. Nu_o has previously been successfully correlated using the concept of an arrival Reynolds number derived from stagnation pressure (Gardon and Akfirat, 1966). In the present study, U_o profiles from Figure 4.12 were interpreted as equivalent to profiles of arrival Reynolds number. Thus the effect of distance from the nozzle exit on centerline turbulence intensity and centerline mean velocity of Figures 4.11 and 4.12 establish the dependence on distance from the nozzle exit for arrival Reynolds number, Re_a , and for arrival turbulence intensity, Tu_a . The dependence of stagnation Nusselt number on Reynolds number for the present study is known from results to be presented and discussed subsequently. Combination of this Nu - Re dependence with the net effect of H/w on Nu_o , indicated on Figure 5.15, makes it

possible to estimate the dependence of Nu_0 on turbulence intensity. With Nusselt number dependence expressed as turbulence intensity to some power, as for Reynolds number, this analysis indicates that for spacings in the range $4w$ to $8w$ from the nozzle exit, the turbulence exponent is about 0.41, while for spacings $8w$ to $16w$ from the nozzle the exponent is about 0.10. For a distance $4w$ to $8w$ from the nozzle the corresponding average range in turbulence intensity is 7% to 15%, while for $8w$ to $16w$ from the nozzle the intensity is in the approximate range 15% to 20%. It is reasonable that the turbulence intensity exponent, i.e. the sensitivity of Nu_0 to turbulence, would be less at levels as high as 15%-20% turbulence than at lower intensities. With respect to the occurrence of maxima around $H/w = 8$ in the Nu_0 - H/w profiles, the above analysis puts into quantitative form the qualitative observations made at the outset here and in numerous preceding studies that Nu_0 is dominated by turbulence intensity for low spacings, less than about $8w$, but by mean velocity for spacings greater than that for the maximum in Nu_0 .

The approach of analyzing the effect of H/w on Nu_0 in terms of the corresponding effects of mean velocity and turbulence intensity is applied now to a second feature of the Nu_0 results, the appearance of w as a parameter in constant Reynolds number-constant H/w results. It was documented extensively in Chapter 4 that w was a small but consistent parameter in all flow field measurements. Because the effect of w as a parameter for Nu_0 is most significant for spacings less than $8w$ (Figure 5.15), this is the region examined. It is predicted that as w increases from 3.3 to 13.3 mm the effects of w on mean velocity and turbulence intensity should contribute, respectively, a decrease of 3% and an increase of 25% in Nu_0 , i.e. a predicted net increase of about 20% in Nu_0 as compared to a measured increase of about 17%. The

fact that this analysis provides a satisfactory prediction of measured effects of w on Nu_0 is further confirmation of the validity and usefulness of the approach of interpreting effects of geometric variables w and H/w in a quantitative way through the fundamental flow field variables, Reynolds number and turbulence intensity.

In summary at fixed geometrical parameters except w there are two opposing effects on Nu_0 associated with increasing w at a fixed Re_j ; an effect on mean velocity which acts to decrease Nu_0 , and an effect on turbulence intensity which acts to increase Nu_0 . As Figure 5.15 indicates that, at $H/w = 4$, Nu_0 at constant Re_j in fact increases with increasing w , it can be concluded that for close impingement surface spacings, the effect of w in increasing turbulence intensity predominates over its effect in decreasing mean axial velocity. It should be recalled from earlier discussion that the results for Nu_0 contain a small, systematic error because of finite sensor width, an error estimated for the smallest nozzle as causing a reduction in Nu_0 of about 4.1%. From Figure 5.15 it may be concluded that at spacings in the range $16w$ to $24w$, after allowance for this systematic reduction in Nu_0 for the data at $w = 3.3$ mm there remains little significant effect of w as a parameter. By reference in Figures 4.11 and 4.12 to the effect of increasing w on turbulence intensity and mean velocity at constant Re_j at these large values of spacing, i.e. a small increase in intensity but a counterbalancing small reduction in mean velocity, the conclusion from Figure 5.15 is that combination of these opposing effects produces little net effect on Nu_0 in this range of H/w .

As understanding the effect of H/w on Nu_0 depends in part on the corresponding effects of spacing on turbulence, it is relevant to consider what is known about dependence of rate of heat transfer upon turbulence intensity. This subject was investigated by Kestin et al. (1961a, b) for the case of parallel flow on flat plates and crossflow on cylinders. They showed that free stream turbulence can affect heat transfer in three ways. First, in the absence of pressure gradients (as for parallel flow over a flat plate) increased turbulence in the free stream promotes transition from a laminar to turbulent boundary layer. Second, in the presence of a positive pressure gradient, as in diffusing flow, the transition to turbulence is also advanced. Third, in the presence of negative pressure gradient, as in stagnation flow (forward part of a cylinder in crossflow and a flat plate in an accelerating stream) the local heat transfer coefficient increases with turbulence intensity. As the impingement flow from the stagnation point is an accelerating flow, it would be expected that an increase in turbulence level in the jet would act in the direction of increasing the rate of heat transfer.

The recent measurements reported by Simonich and Bradshaw (1978) in a turbulent boundary layer in zero pressure gradient showed that grid generated free stream turbulence increased heat transfer by about 5% for each 1% root mean square increase in the longitudinal fluctuating velocity.

For single impinging slot jets the maximum Nu_0 was found to be in the vicinity of $H/w = 8$ by a number of other studies, as reported by Korger and Krizek (1966), Gardon and Akfirat (1966), Kumada and Mabuchi (1970), Schlünder et al. (1970) and Cadek and Zerkle (1970). Only Gardon and Akfirat reported measurements of axial mean velocity and turbulence intensity at the jet centerline. They reported a higher level of turbulence intensity at the nozzle exit than in the present study as they used a significantly larger nozzle length-

to-width ratio, t/w . Their case of higher turbulence at the nozzle exit produced an axial profile of turbulence along the jet centerline that, relative to the present study was higher for $0 < z/w < 8$ and lower at $z/w > 8$. In spite of this difference in profile of turbulence along the jet centerline, Gardon and Akfirat found Nu_0 to be a maximum at a spacing of about $H/w = 8$, where in fact the turbulence level of the two studies was about the same.

After analysis of the stagnation point heat transfer for single impinging slot jet, attention may now be turned to the case of multiple impinging slot jets. For the confined multiple impinging jet system with slot exhaust ports alternating symmetrically between slot nozzles shown on top of Figure 5.1, a central feature of analysis of results is the concept developed in Chapter 4 of "flow cell". It is evident from Figure 5.1 that even when the geometric and flow parameters for a single and a multiple jet system are identical, the flow field and hence the impingement surface heat transfer of the latter must be different from that for the corresponding single jet, at least over the region away from the centerline as shown subsequently in Section 5.4. However, as documented in Chapter 4, for a multiple jet system with jet nozzles and exhaust ports spaced sufficiently far apart, interaction from the outflow would not extend to the jet centerline hence to the stagnation point heat transfer. The criteria of interacting/non-interacting multiple jet system will now be investigated by examining the corresponding values of Nu_0 .

Over the entire range of jet Reynolds number the effect of impingement surface spacing or flow cell proportion on Nu_0 for the multiple impinging jet system shown on top of Figure 5.1 is presented in Figures 5.16 through 5.20 for each of the 5 values of open area over the experimental range $1.56 \leq f \leq 8.313\%$. It was noted earlier that the geometrical parameters for the multiple jet system may be defined by two independent dimensionless ratios. As percent

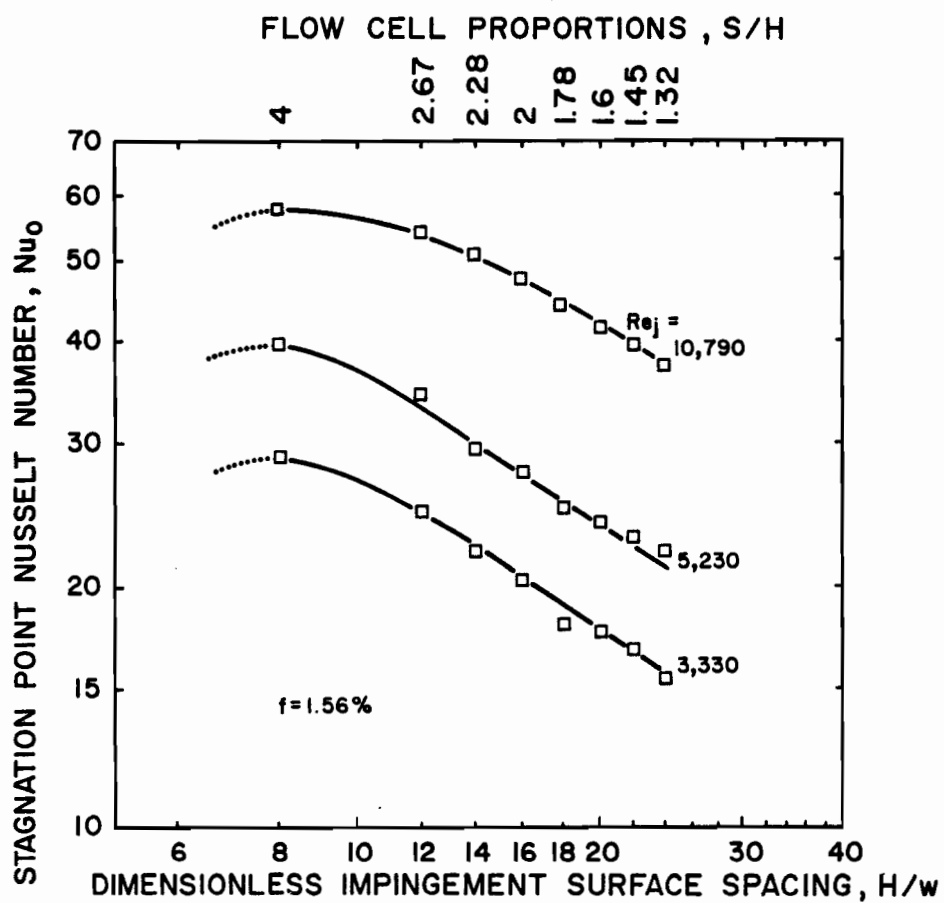


FIGURE 5.16. Effect of Impingement Surface Spacing on Nu_o for Multiple Jet System ($f = 1.56\%$)

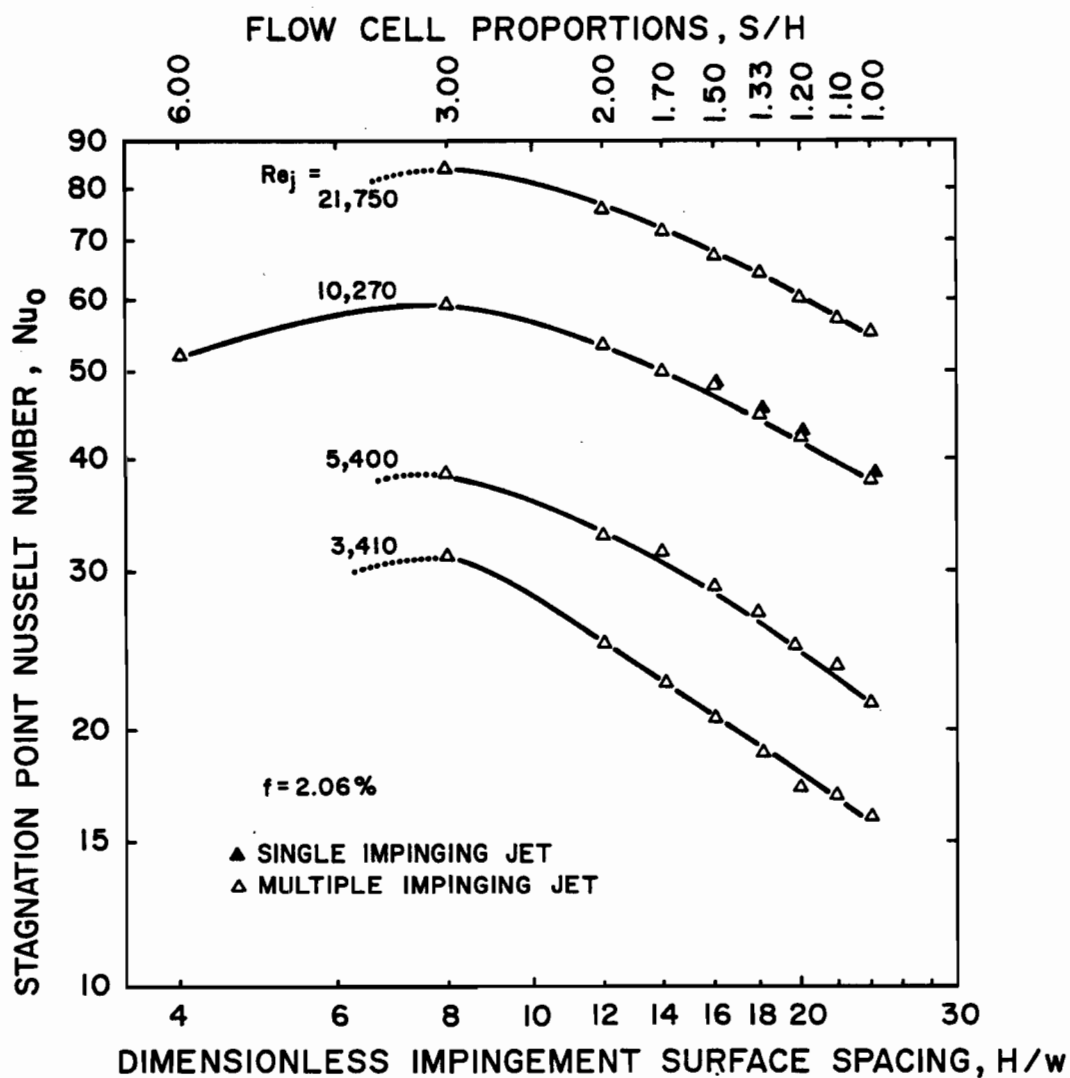


FIGURE 5.17. Effect of Impingement Surface Spacing on Nu_0 for Multiple Jet System ($f = 2.06\%$) and for Single Jet System ($w = 3.3$ mm and $Re_j = 10270$)

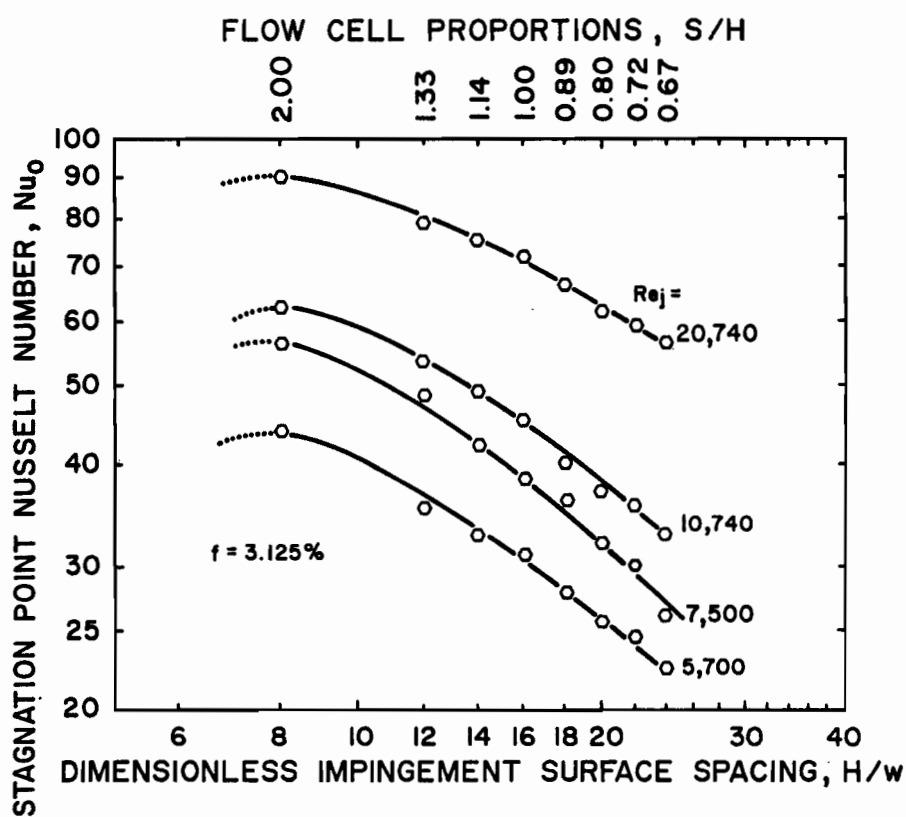


FIGURE 5.18. Effect of Impingement Surface Spacing on Nu_o for Multiple Jet System ($f = 3.125\%$)

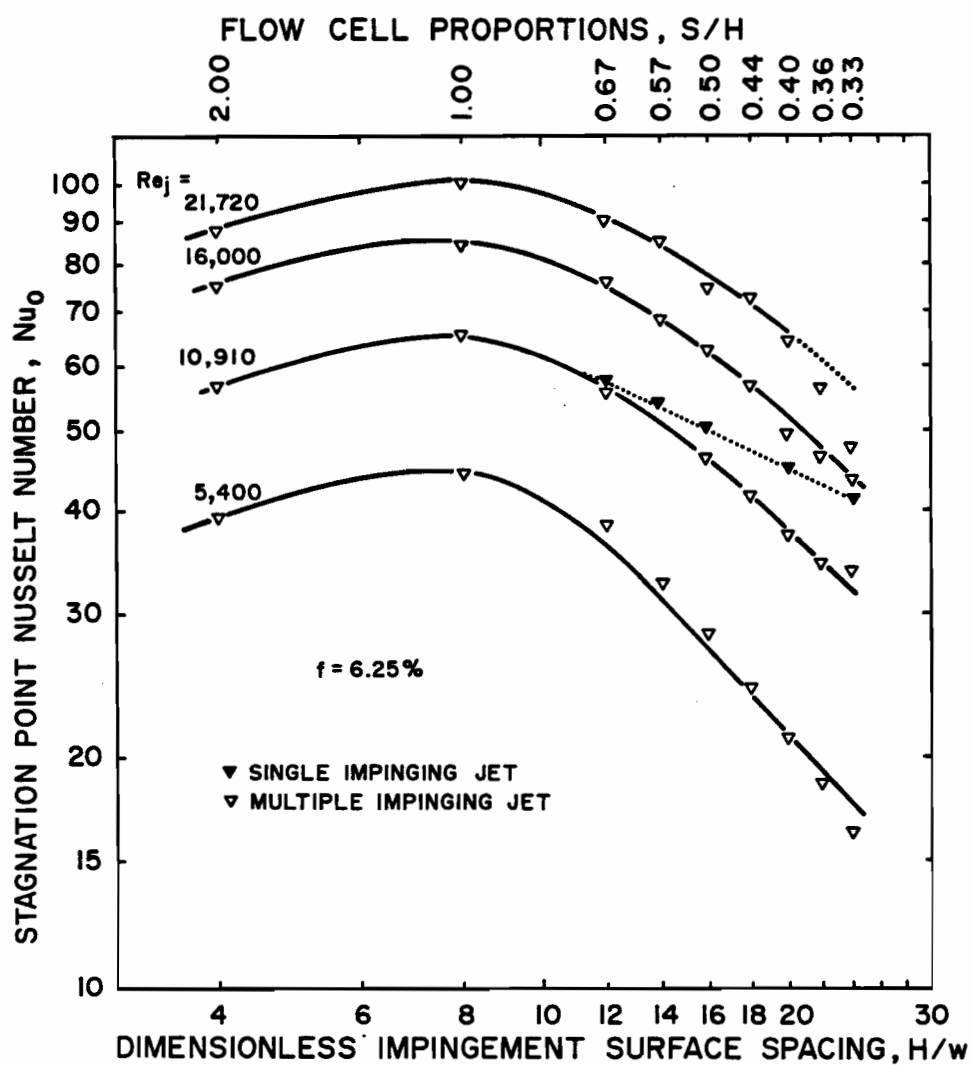


FIGURE 5.19. Effect of Impingement Surface Spacing on Nu_0 for Multiple Jet System ($f = 6.25\%$) and for Single Jet System ($w = 10.0$ mm and $Re_j = 10910$)

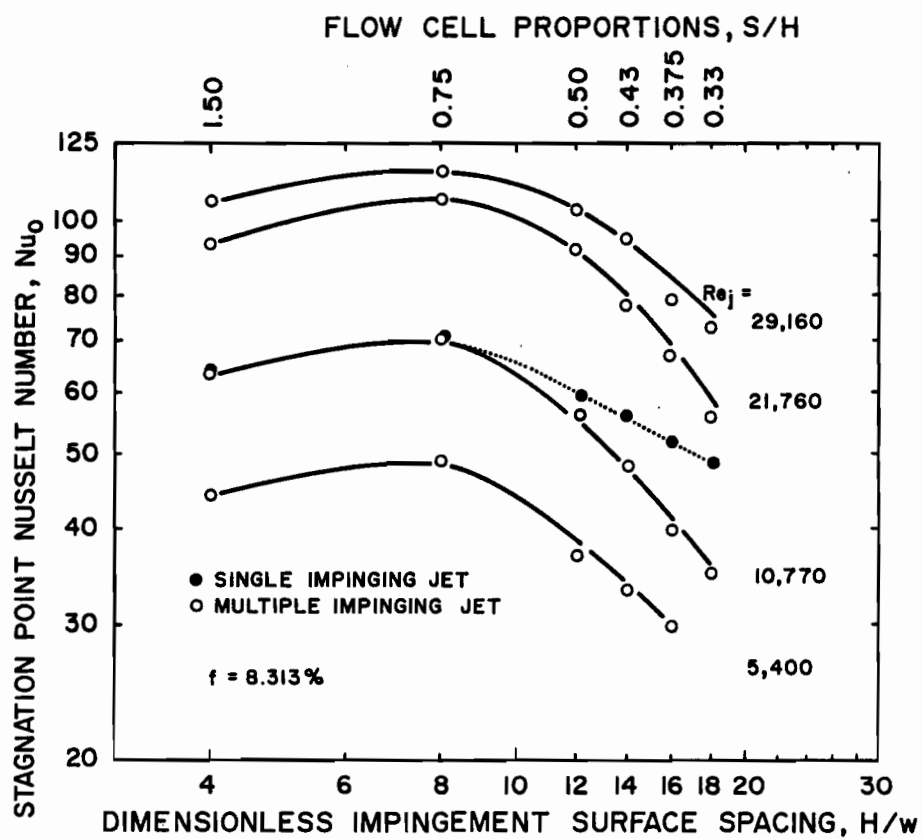


FIGURE 5.20. Effect of Impingement Surface Spacing on Nu_0 for Multiple Jet System ($f = 8.313\%$) and for Single Jet System ($w = 13.3$ mm and $Re_j = 10770$)

open area, f , has been selected as one dimensionless parameter, these figures are presented so that either S/H or H/w may be read as the other geometrical parameter.

For all values of jet Reynolds number and for all values of percent open area, on Figures 5.16 through 5.20, the profiles of Nu_o show a maximum. While the value of S/H at which the Nu_o maximum occurs varies considerably, these maxima are in all cases at about $H/w = 8$. For this purpose it is therefore evident that as the second geometrical parameter, H/w is clearly preferred over S/H . The varying relative importance of the opposing effects of H/w on axial mean velocity and turbulence intensity, as analyzed in some detail in connection with Figure 5.15 for a single jet, obviously continue to act in a similar way for the multiple jet system. The consistent occurrence of a maximum in Nu_o at about $H/w = 8$ is a consequence of these opposing effects of spacing on the flow field variables along the jet centerline.

It was noted earlier that single jet results provide the point of reference for the complex multiple jet system. The flow field analysis in Chapter 4 established that an understanding of the key factor of interaction between jets for the multiple confined slot jet case is only obtained with the choice of f and S/H rather than f and H/w as the two independent geometrical parameters. As the question of jet interaction effects is central to the analysis of Nu_o results, S/H and f is the pair of geometrical parameters required for the subsequent discussion of this section.

The comparison of single and multiple results is presented for 2.06, 6.25 and 8.313% f respectively by addition to Figures 5.17, 5.19 and 5.20 of data from Figure 5.15 for a single jet. For $f = 2.06\%$ and $Re_j = 10270$ (Figure 5.17) the data for both single and multiple impinging jets coincide down to the lower limit of S/H , i.e. to $S/H = 1$, thus indicating that for this S/H

the multiple jets are still non-interacting at the stagnation point.

For $f = 6.25\%$, Figure 5.19 shows the superposition of single jet results from Figure 5.15 for $Re_j = 10910$. As the flow cell proportions, S/H , are decreased the multiple and single jet Nu_o values remain coincident down to $S/H = 1$. By $S/H = 0.67$ the multiple jet Nu_o becomes slightly lower, while by $S/H = 0.33$ the multiple jet Nu_o is about 25% lower than for the reference single jet case. For $f = 8.313\%$ the superposition of results for $Re_j = 10770$ on Figure 5.20 shows that the multiple jet Nu_o starts to drop below that for a single jet after approximately $S/H = 0.75$ with the deviation at smaller values of S/H increasing such that by $S/H = 0.33$ the multiple jet Nu_o is about 27% lower.

The reduction of Nu_o for the multiple jet system at low values of S/H is another indication of the interaction between jets having reached the inlet jet centerline. Although single jet results were obtained at only this value of Re_j , from the similarity of slope of the curves on Figures 5.19 and 5.20 it appears that, as S/H is decreased, the effect of multiple jet interaction begins at about $S/H = 0.75$ over the range of $Re_j \geq 11000$.

With respect to the critical value, $(S/H)_{co}$, at which the effect of interaction between multiple jets just reaches the jet centerline, it is pertinent to compare the values of $(S/H)_{co}$ indicated by the criteria of Nu_o as noted above with the flow criteria summarized in Table 4.9. Thus it was recorded in this table that at $S/H = 0.75$ the interaction was already significantly felt at the jet centerline. At $S/H = 0.75$ the turbulence intensity by only 6w from the nozzle exit was already twice as high for multiple as for single jets, but the axial mean velocity was somewhat lower for multiple jets. As the data for Nu_o from Figures 5.19 and 5.20 indicate no significant difference in Nu_o between multiple and single jets at $S/H = 0.75$, it is evident that the effects on Nu_o of increased turbulence intensity but lower arrival Reynolds number, being

opposite in direction, are about equal, thus producing no net effect. Figure 5.19 indicates that the effect of interaction has lowered Nu_o perceptibly by $S/H = 0.67$. Taking the evidence of Figures 5.19 and 5.20 together it may be concluded that, using the effect of S/H on Nu_o as the criterion, the critical value of flow cell proportions at $Re_j = 11000$ is very close to $(S/H)_{co} = 0.75$.

There is no contradiction between this conclusion with respect to the value of $(S/H)_c$ and that from analysis of the flow results which indicated $1 > (S/H)_c \geq 0.75$. The finding that the value of $(S/H)_c$ is slightly lower using Nu_o as the criterion reflects the fact that the effects of interaction on the flow field (decreasing axial mean velocity but increasing turbulence) act in the opposite directions on heat transfer. Thus, over a small range of S/H just above 0.75, the effects of changes in the flow field have counterbalancing effects on heat transfer which for this very limited range of S/H leave Nu_o not significantly changed.

As the flow cell proportion drops below 0.75, i.e. below $(S/H)_c$, the same opposing effects continue, i.e. for the multiple jet case a great increase in turbulence and significant decrease in axial mean velocity relative to the single jet reference. However, the results for Nu_o at $S/H < 0.75$ indicate that the reduction of heat transfer associated with the lower mean velocity predominates increasingly over the tendency of heat transfer to increase with increasing turbulence. It is evident that beyond some high level of turbulence, further increases in intensity do not have an appreciable effect on increasing heat transfer. Recall from Figure 4.11 that the turbulence intensity for $S/H = 0.375$ had reached 20% by only $2w$ from the nozzle exit. Thus with respect to stagnation heat transfer, the dominating flow field parameter for the case of interacting multiple slot jets is axial mean velocity, not turbulence intensity.

The occurrence of multiple jet interaction at the centerline demonstrated on Figures 5.17, 5.19 and 5.20 is depicted on Figure 5.21(a) by showing the effect of S/H on Nu_o for $Re_j = 11000$. For the case of $f = 2.06\%$, even at the very large spacing of $H/w = 24$ the flow cell ($S/H = 1$) is still sufficiently wide that interaction does not reach centerline. Hence for $f = 2.06\%$, the multiple jet line shown on Figure 5.21(a) is completely coincident with the corresponding single jet line on Figure 5.15. Likewise, for the Figure 5.21(a) lines corresponding to 6.25 and 8.313% open area, the portions of the curves down to $S/H = 1$ are also identical to the corresponding single jet lines on Figure 5.15. However, for values of S/H below $(S/H)_{co}$, the drop in Nu_o is so sharp that the curves cross. Looked at from the perspective of H/w rather than S/H , the result of the strong interaction at the centerline for 6.25 and 8.313% open area systems is reflected in the reversal at high H/w from the usual effect of f (or w) on Nu_o . Similar to Nu_o at $Re_j = 11000$, the Nu_o profiles for $Re_j = 5400$ and 21700 (shown in Figures 5.21(b) and (c) respectively) appear to drop sharply at about $S/H = 0.7$, indicating that the effect of multiple jet interaction on $(S/H)_{co}$ does not vary significantly with Re_j over $5400 \leq Re_j \leq 21700$.

The effect of interaction at the jet centerline in a multiple jet system is illustrated alternately in Figures 5.22 and 5.23 where the effect of jet Reynolds number on Nu_o is shown for two particular values of dimensionless impingement surface spacing, $H/w = 8$ and 16. While for the non-interacting jets ($2 < S/H < 4$) Nu_o depends on $Re_j^{0.57}$, for the jets starting to interact $0.75 \leq S/H \leq 1$ this dependence increases to $Re_j^{0.62}$. Although this difference in exponent is not by itself significant, this trend continues as shown in Figure 5.23, where the Re_j exponent increases gradually from 0.65 to 0.72 with decreasing S/H . For a single slot jet the stagnation region boundary layer was

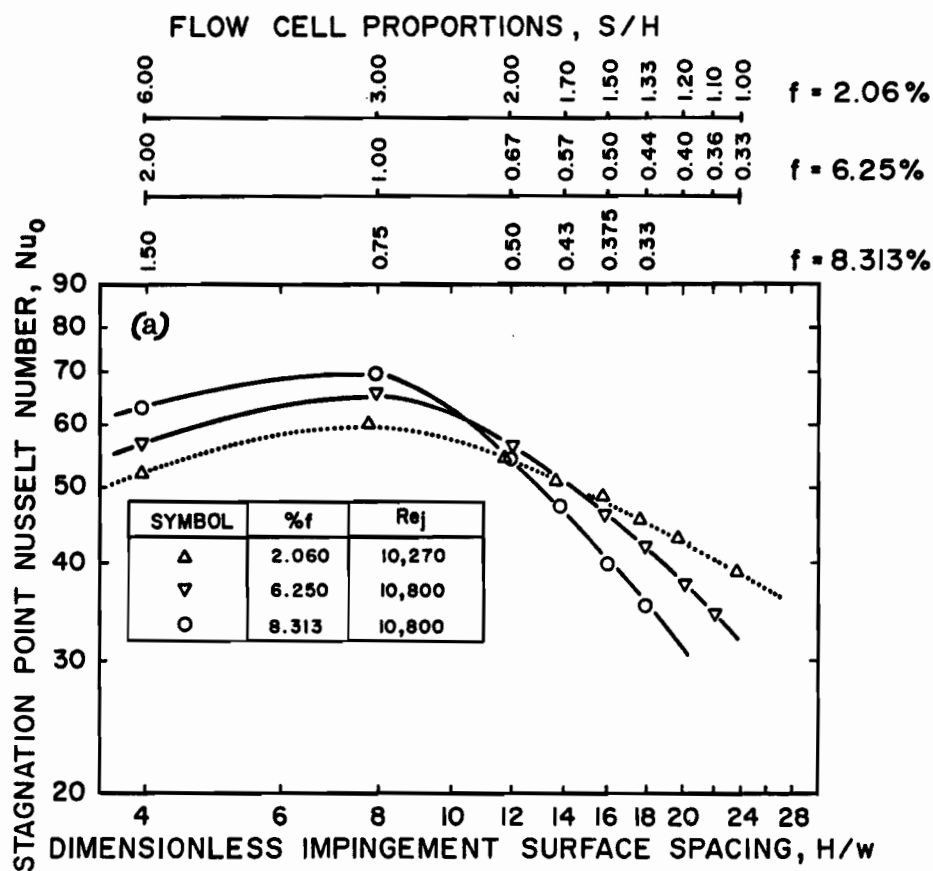


FIGURE 5.21. Effect of Impingement Surface Spacing on Nu_o for Multiple Jet System ($f = 2.06, 6.25$ and 8.313%) for $Re_j = 10800$ (nominal)

(a)

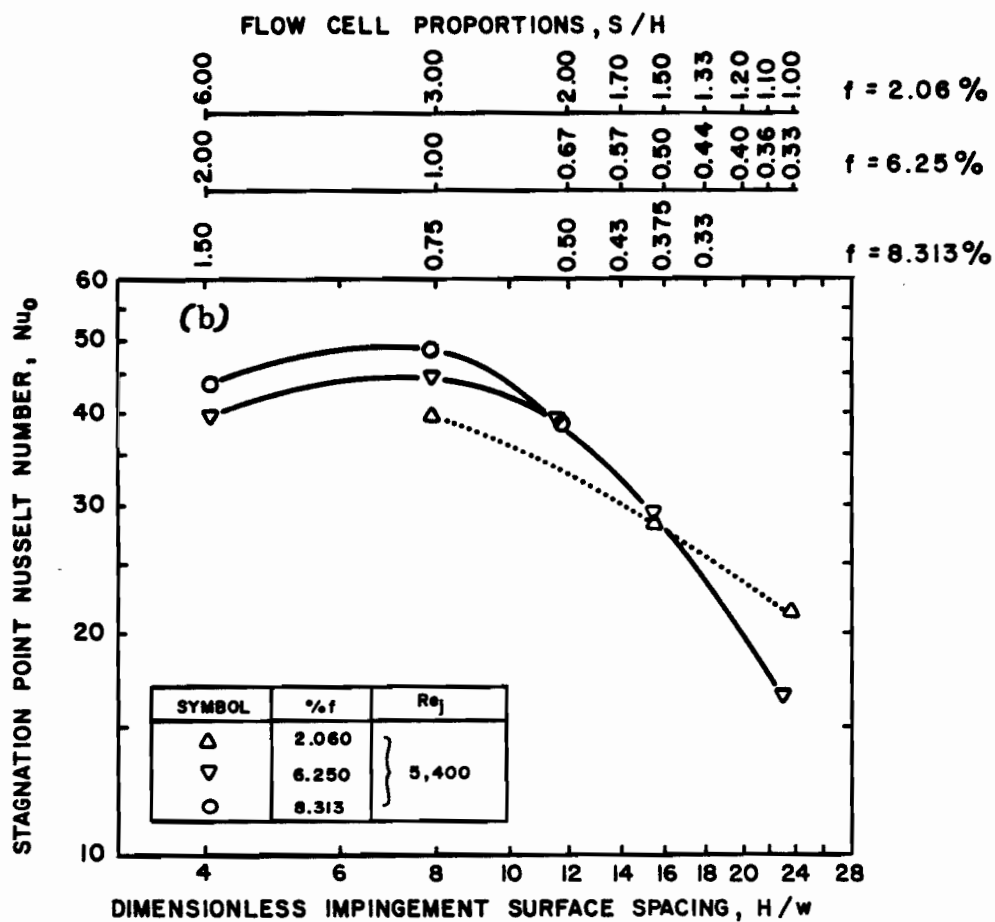


FIGURE 5.21 (b) Effect of Impingement Surface Spacing on Nu_0 for Multiple Jet System ($f = 2.06, 6.25$ and 8.313%) for $Re_j = 5400$

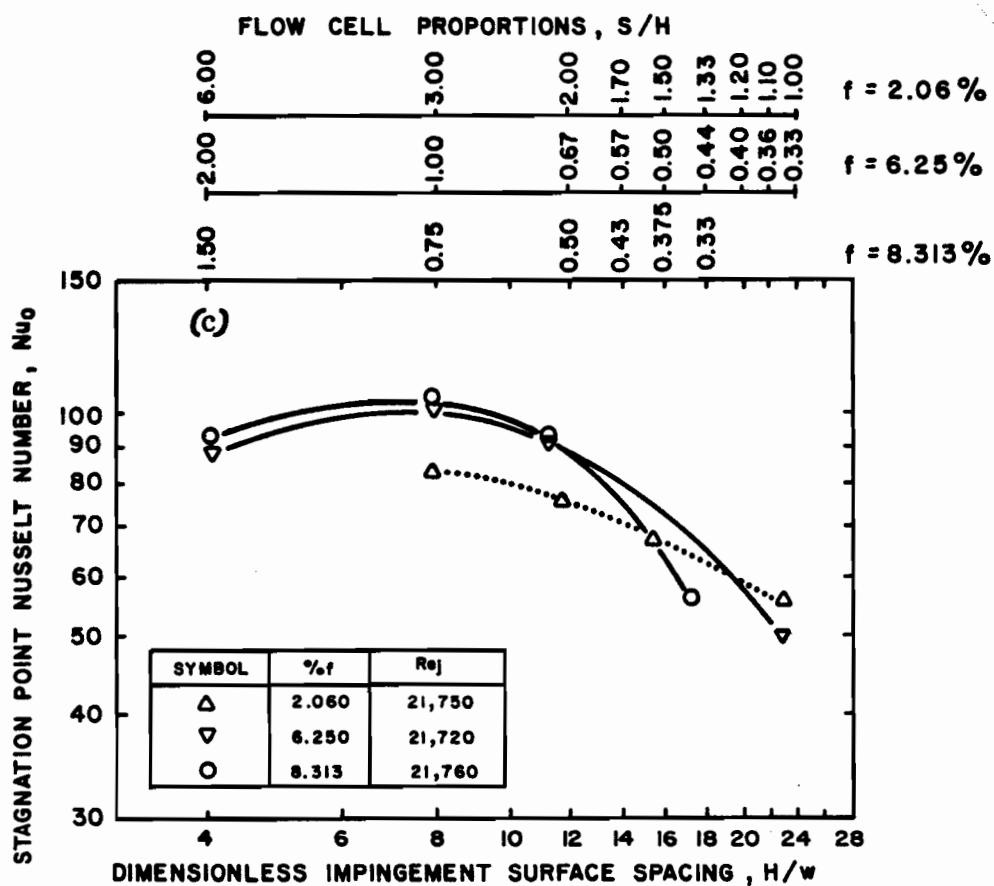


FIGURE 5.21 (c) Effect of Impingement Surface Spacing on Nu_o for Multiple Jet System ($f = 2.06, 6.25$ and 8.313%) for $Re_j = 21700$ (nominal)

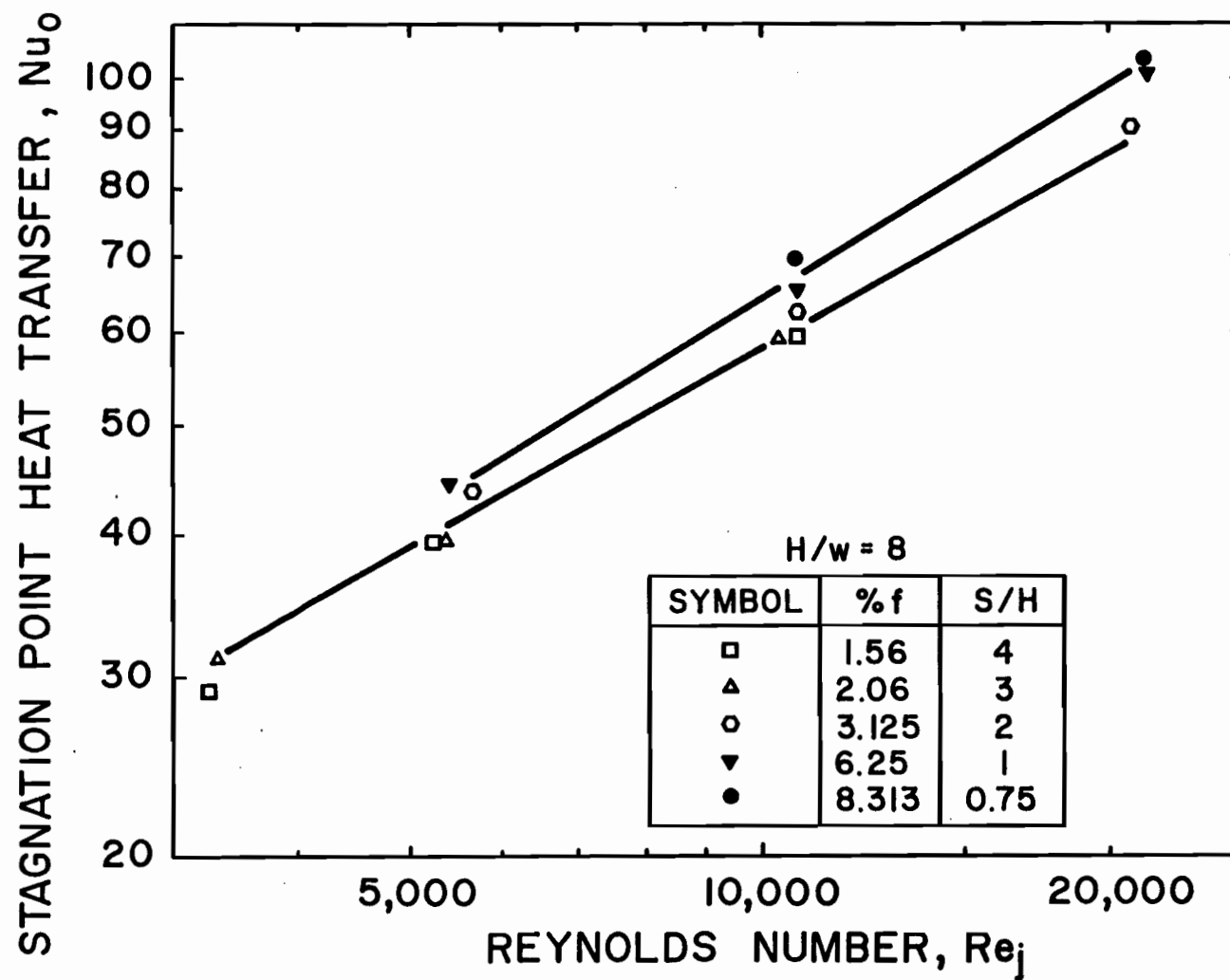


FIGURE 5.22. Effect of Jet Reynolds Number on Nu_o for Multiple Jet System ($H/w = 8$)

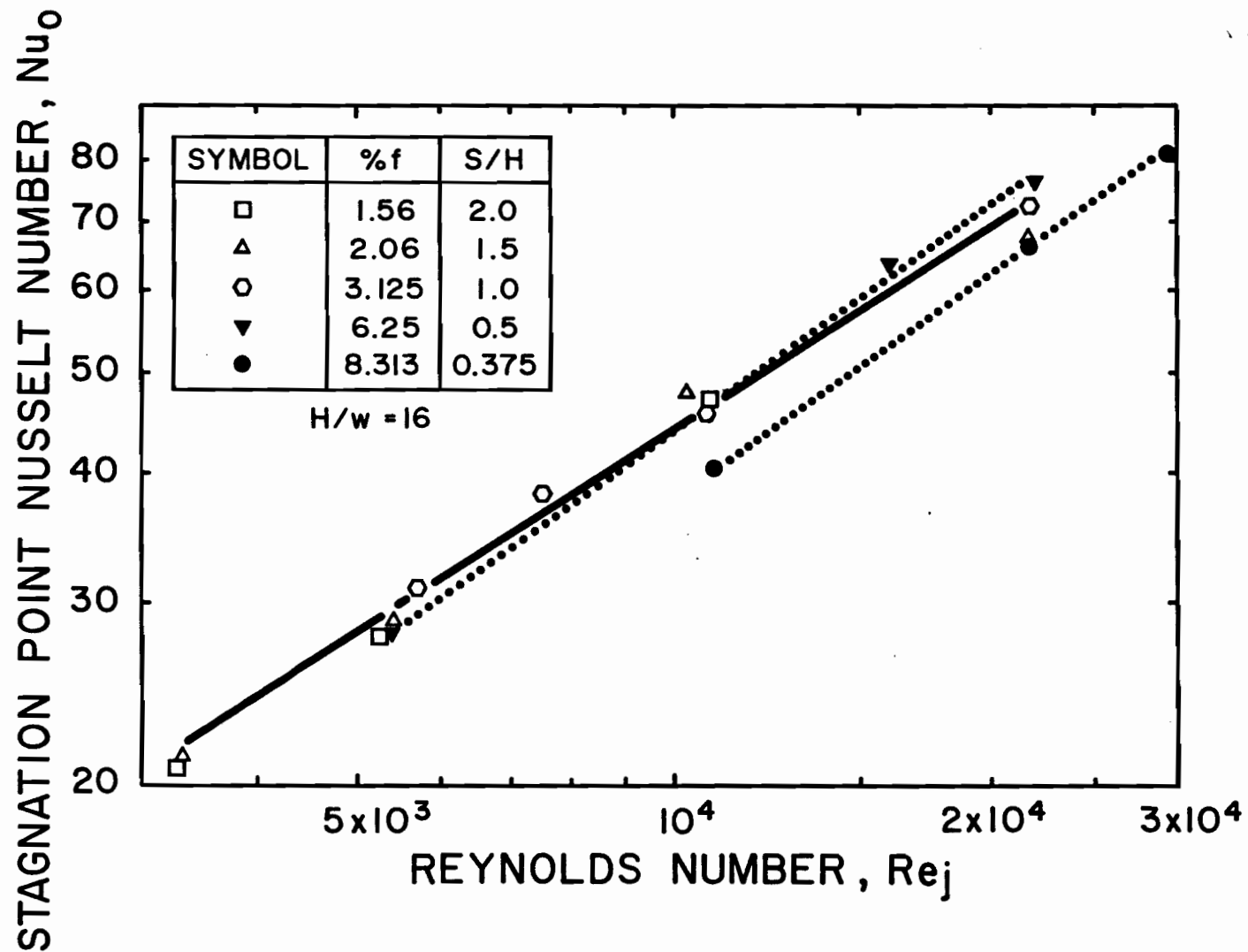


FIGURE 5.23. Effect of Jet Reynolds Number on Nu_0 for Multiple Jet System ($H/w = 16$)

assumed in various studies to be laminar, which would correspond to Nu_o proportional to $Re_j^{0.5}$. The present data show that the Re_j exponent increases from 0.57 for non-interacting multiple jets, equivalent to single jets, to 0.72 with increasing interaction at the centerline. Hence at sufficiently low values of S/H the interaction between multiple jets penetrates to the stagnation point, decreases Nu_o and changes the stagnation boundary layer in the direction of becoming turbulent. The evidence of this statement is that increasing interaction changes the Re_j exponent from 0.57 (not much above the laminar limit of 0.5) to 0.72 (not far from the limiting value of 0.8 for a turbulent boundary layer).

For very approximate purposes only, a linear regression correlation for Nu_o was obtained for all the data for $H/w \geq 8$, and is shown on Figure 5.24 with the corresponding single slot jet impinging jet correlation of Gardon and Akfirat (1966) for the case of $H/w = 8$. The higher Re_j exponent for the present study reflects the fact that some of these data are for interacting jets which, as noted earlier, are characterized by a larger Re_j exponent. Figure 5.25 shows that in spite of some major approximations associated with it, this overall representation correlates the data within $\pm 15\%$ band around the correlation line.*

5.4 Lateral Profiles of Heat Transfer

Following the discussion of stagnation point heat transfer (Section 5.3), the lateral profiles of Nu_x for the test conditions presented in Table 5.1 are analyzed in the present section.

5.4.1 Effect of Reynolds Number and Geometrical Parameters on Profiles of Nu_x

The first set of figures, 5.26 through 5.28, provides the profiles of Nu_x for the closest spacing ($H/w = 4$) over a range of Re_j . With specification of one of the dimensionless geometrical parameters by fixing H/w , the second independent geometrical variable may be specified alternately as f , S/w or

* The stagnation point mass transfer coefficients reported by Korger and Krizek (1966) for single unconfined impinging slot jet ($8 \leq H/w \leq 40$, $6040 \leq Re_j \leq 37800$) were found to be dependent on $Re_j^{0.66}$ and on $H/w^{-0.66}$. With the absence of information on the nozzle and flow characteristics it is difficult to assess the effect of these variables on the relatively higher Re_j exponent.

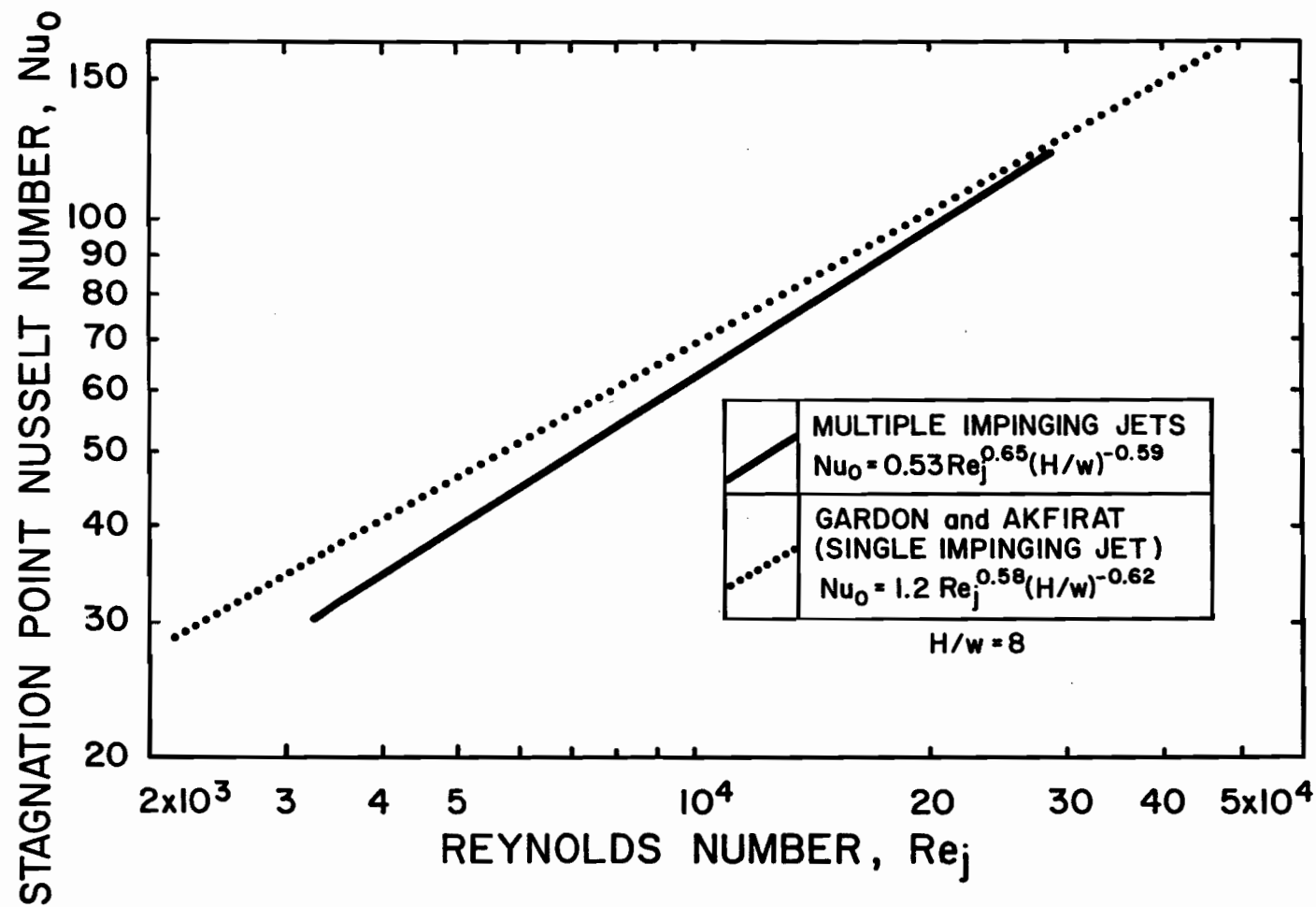


FIGURE 5.24. Stagnation Point Heat Transfer Correlation for Multiple Impinging Jet System Compared to that for Single Impinging Jet System of Gardon and Akfirat (1966)

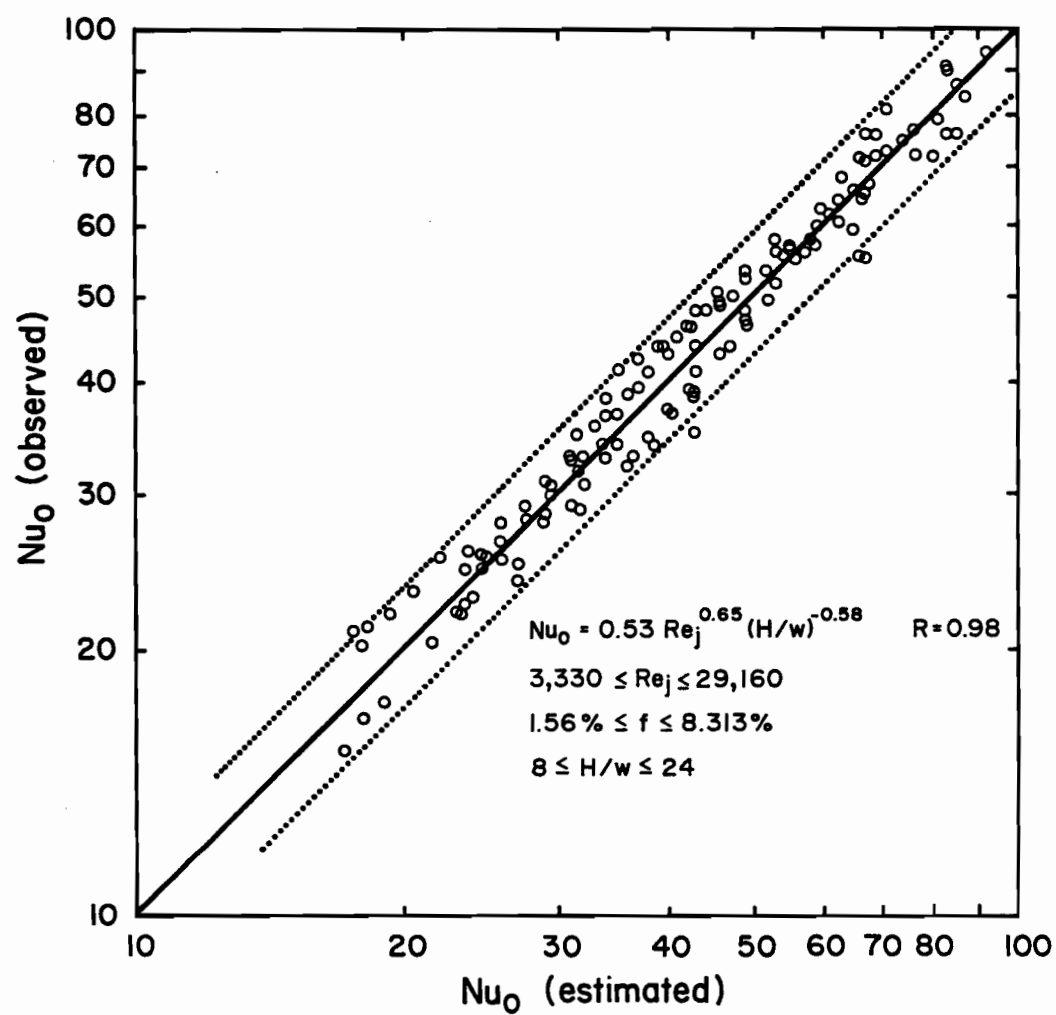


FIGURE 5.25. Bandwidth of the Scatter of Experimental Data from the Correlation Line

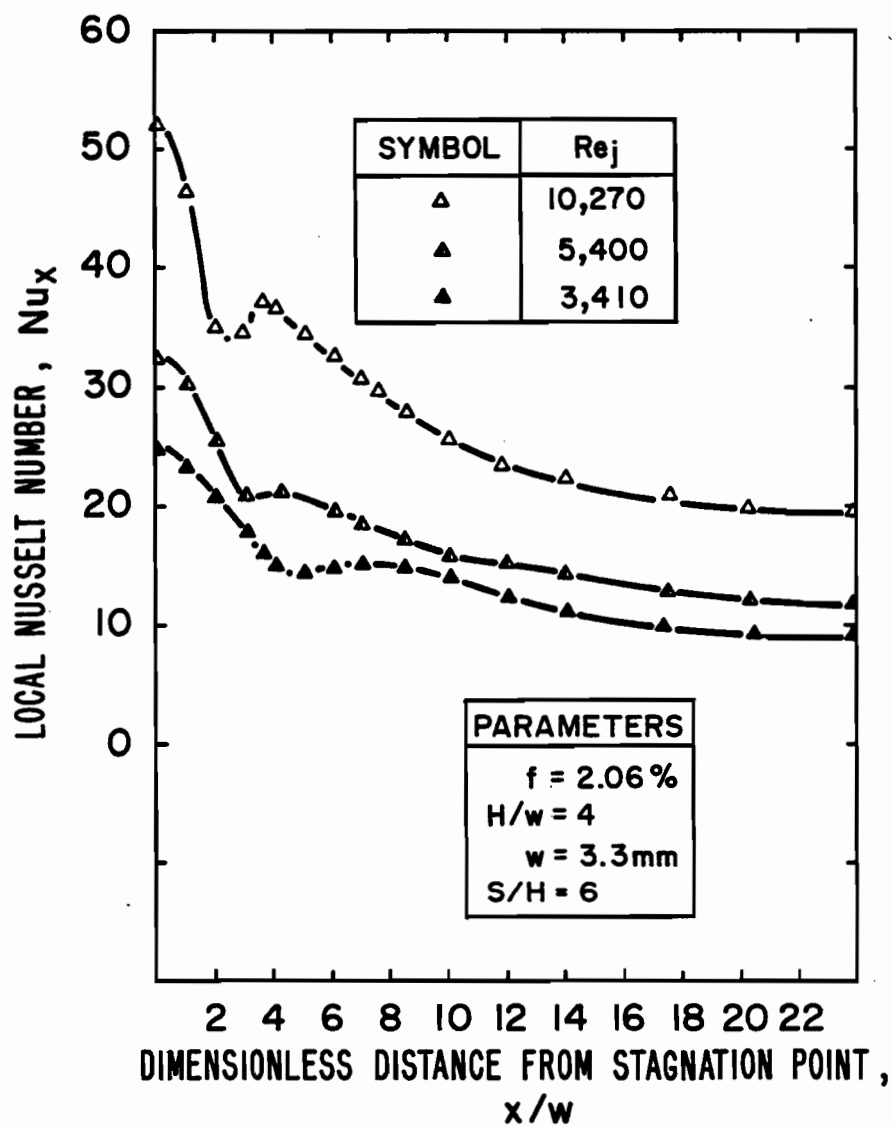


FIGURE 5.26. Effect of Jet Reynolds Number on Lateral Profiles of Nu_x for $f = 2.06\%$ and $H/w = 4$

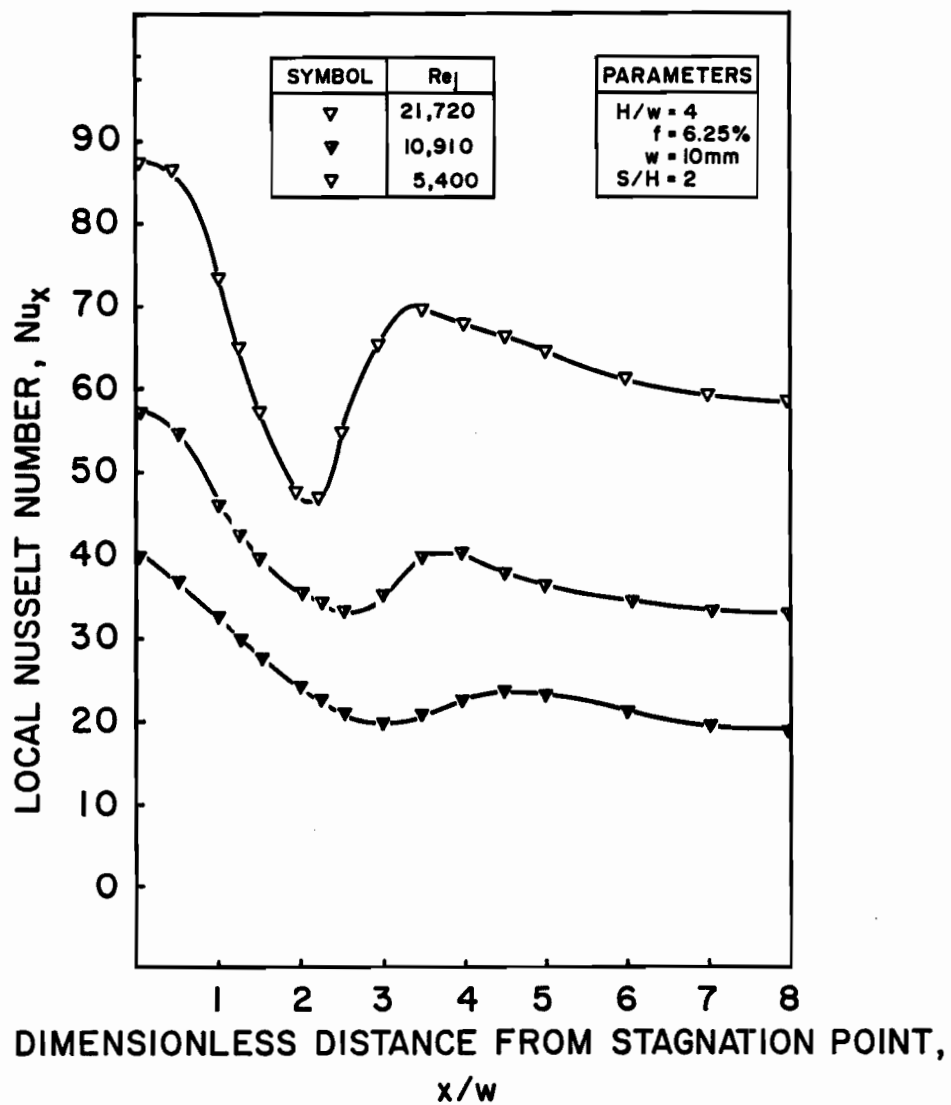


FIGURE 5.27. Effect of Jet Reynolds Number on Lateral Profiles of Nu_x for $f = 6.25\%$ and $H/w = 4$

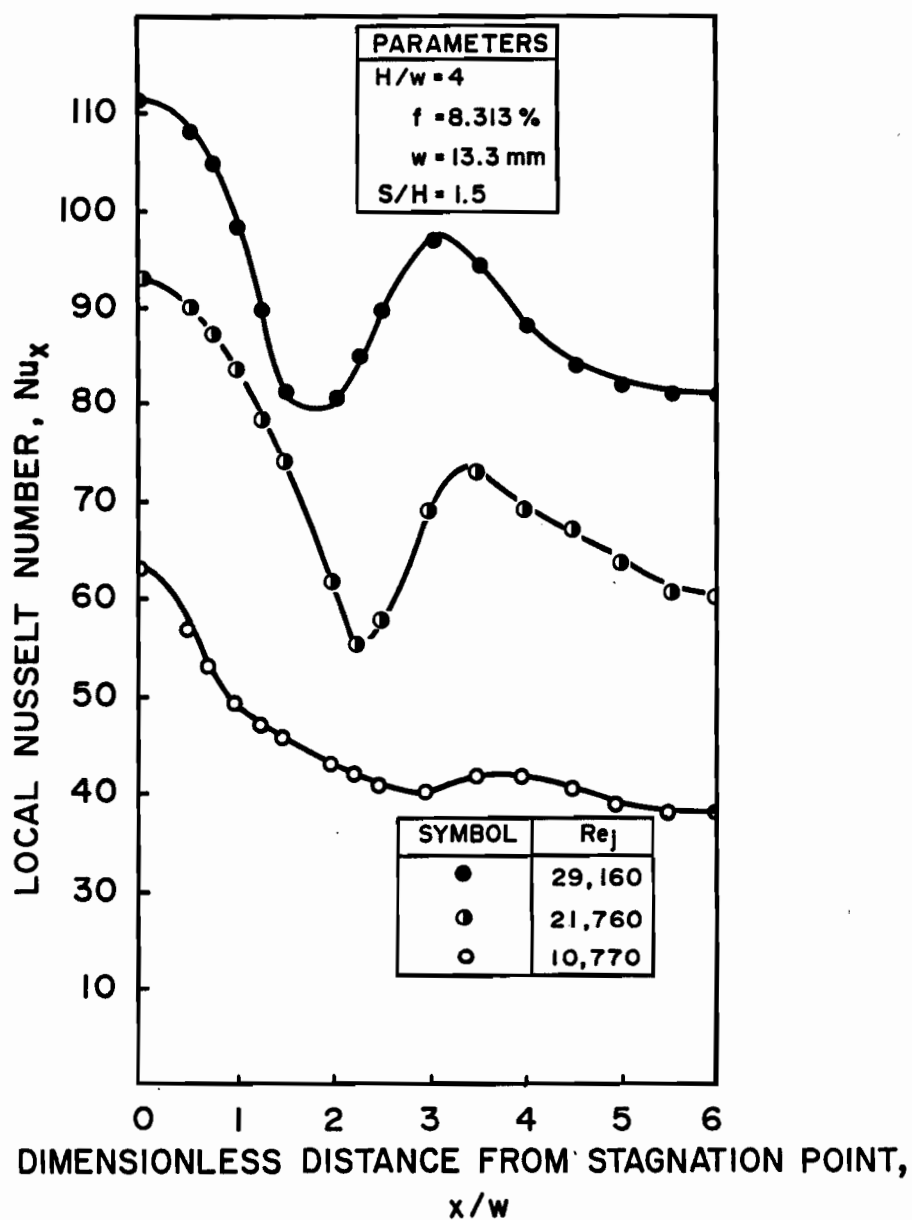


FIGURE 5.28. Effect of Jet Reynolds Number on Lateral Profiles of Nu_x for $f = 8.313\%$ and $H/w = 4$

S/H. Each of the three graphs in this set presents Nu_x profiles for one value of the second geometrical variable.

The principal features of these 9 profiles are the occurrence in each case of an off-stagnation maximum and intervening minimum. Previous investigators have identified the minimum as reflecting transition from a laminar to turbulent boundary layer, hence the designation of this position as x_T . This transition is considered complete at the location of the off-stagnation maximum, the intervening section being therefore designated the transition region.

Existence of minima in the Nu_x profiles reflects the end of the section which begins at $x/w = 0$ and over which a laminar boundary layer grows in thickness from the minimum value existing at the stagnation point. The heat transfer coefficient naturally decreases as this boundary layer grows. The increase in heat transfer coefficient over the transition region corresponds to the enhanced transport characteristics of a boundary layer which is becoming turbulent. The decline in Nu_x beyond the off-stagnation maximum simply reflects increasing thickness of the turbulent boundary layer.

For $H/w = 4$ and over the Reynolds number range 3410-29000 the minima and off-stagnation maxima occur over the ranges of distance from stagnation equal to $1.8w$ to $5w$ and $3.1w$ to $7w$, respectively. The second geometrical variable, f , S/w or S/H has no effect on the location of either of these features. Thus the variation in location of maxima and minima is due to Re_j , the direction of the effect being a shift of both the minima and maxima toward the stagnation point with increasing Re_j .

Reference at $H/w = 4$ to a laminar boundary layer over some distance out from the stagnation point for the case of slot jet as highly turbulent as was documented in Figure 4.11 warrants comment. For a single turbulent impinging jet at $2 < H/w < 8$, Gardon and Akfirat (1966), Korger and Krizek (1966), Kumada

and Mabuchi (1970), Schlünder et al. (1970) and Cadek and Zerkle (1970) all reported that stagnation region heat transfer has laminar characteristics and that at the end of this region a transition to turbulence occurs. These studies indicated that the boundary layer remained laminar in the stagnation region. Cadek and Zerkle (1970) found good agreement between theory and experiment in the stagnation region by assuming a laminary boundary layer, except for $H/w > 8$ where free jet turbulent effects were found to augment the heat transfer rates.

In the presence of a negative pressure gradient such as on the forward part of a cylinder in a crossflow, Kestin et al. (1961a, b) also reported that up to the end of this region the boundary layer is laminar, and that the presence of this negative pressure gradient stabilizes the boundary layer, thus delaying transition to turbulence. In the case of an impinging jet the presence of a similar negative pressure gradient in the stagnation region stabilizes the boundary layer in spite of the locally high turbulence levels in the free jet. A further stabilizing effect on the laminar boundary layer is the high velocity gradient near the wall at small impingement surface spacings and high Re_j , which minimize the boundary layer thickness.

Cartwright and Russel (1967), and Cadek and Zerkle (1970) over a wide range of Re_j calculated the point of transition by employing the method of Polhausen in the impingement region to predict the general flow properties, including boundary layer growth and skin friction. They then determined a stability criterion by the Tollmein-Schlichting procedure as shown in Schlichting (1968) that yielded critical values of Reynolds number as based on boundary layer displacement thickness.

For $8 < H/w < 17$ and $25000 < Re_j < 110000$, the laminar analysis of heat transfer by Cartwright and Russel (1967) fail to estimate by a considerable

margin the value measured for x_T/w . It is to be expected that such a simple analysis would fail mainly because the turbulence level in the free jet is considerably higher than that normally encountered in the aerodynamic stagnation point theory used. In fact, the boundary layer in the impingement region for the case of a turbulent jet may be considered as an unsteady layer.

As noted briefly earlier, the lateral gradient of pressure at the impingement surface is considered to play a key role in boundary layer transition from laminar to turbulent. Since a strongly negative pressure gradient stabilizes the laminar boundary layer in the stagnation region, an approximation is that transition occurs where the steep pressure gradient ends. For non-interacting multiple jet systems, i.e. corresponding to flow cells of $S/H > 0.7$ and over a range of Re_j (5000-43800) and H/w (4-16), it has been established through Figures 4.31-4.37 that the profiles of static pressure at the impingement surface display similarity when represented as a function of x/H . From these similar profiles the stagnation region, defined as the location where static pressure drops to 5% of the stagnation pressure, was found to extend laterally a distance equal to half the spacing, H . Application of these similarity findings from Chapter 4 would then imply that, for Nu_x profiles at $H/w = 4$ (Figures 5.26 through 5.28), the transition point x_T/w would be near 2. In fact it may be seen from these figures that over the Re_j range of 5400 to 29160, the values of x_T/w vary only from 1.8 to 3, thus providing further support for the concept that transition to a turbulent boundary layer occurs after the stabilizing effect of a steep lateral pressure gradient is no longer present.

As boundary layer transition from laminar to turbulent is driven by the interaction between the surface and an impingement flow which (as documented in Chapter 4) is highly turbulent, the finding that this transition occurs over a shorter distance (x_T) from stagnation as Re_j increases is expected.

Moreover, the data of Chapter 4 document the extent of the increase with Re_j of the lateral normalized static pressure gradient in the impingement region. Thus as Re_j increases it is interesting to note that there is both a larger relative drop in Nu_x (over the region $0 < x/w < x_T/w$) and correspondingly a larger relative increase in Nu_x from transition (x_T/w) to the secondary maximum. Hence the sharpness of the maxima and minima peaks increases with increasing Re_j . Rather curiously, then, higher values of Re_j act through a steeper lateral gradient in pressure, first, to maintain a laminar boundary layer for some distance from the stagnation point, but when transition does occur, the increase in Nu_x is more pronounced with larger Re_j .

Although the locations of the minima and off-stagnation maxima in Nu_x profiles are a function of Re_j , it should be pointed out that the length of the transition region, between $1w$ and $1.5w$ in all cases, is independent of Re_j . Thus the magnitude of the effects of Re_j on location of transition and of secondary maxima are evidently about the same. For the case of a turbulent round impinging jet Obot (1981) found similar effects as to the influence of Re_j on movement of the transition region. He also found that the transition from laminar to turbulent boundary layer occurs closer to the stagnation point with than without a confinement surface.

It will be recalled from the preceding section that for values of S/H sufficiently large for there to be no interaction at the jet centerline of multiple jets, a condition which applies for Figures 5.26 through 5.28 where the narrowest flow cell is $S/H = 1.5$, the Reynolds number dependence of Nu_o was with $(Re_j)^{0.57}$. That this exponent is close to the 0.5 value associated with a laminar boundary layer is of course consistent with other considerations which indicate, for the conditions of Figures 5.26 through 5.28, that the boundary layer begins as essentially laminar. Moreover the Reynolds number

dependence of Nu_x at the secondary maxima is found to be close to the 0.8 exponent associated with a turbulent boundary layer. Thus the fact that the Re_j exponent is about 0.57 for Nu_0 but about 0.8 for Nu_x at the secondary maxima provides further confirmation for this interpretation of results.

The second set of figures, 5.29 through 5.31, provides the profiles of Nu_x over a range of Re_j for the next impingement surface spacing, $H/w = 8$, with each of these five graphs prepared for a value of the second geometrical variable, i.e. f , S/w or S/H . In contrast to the profiles of Figures 5.26 through 5.28 for $H/w = 4$, the off-stagnation maxima and minima completely disappear at $H/w = 8$. Two effects both act in the direction of elimination of these features of profiles at small impingement surface spacings. First, at twice the distance from the nozzle exit the flow approaching the impingement surface is very much more turbulent, in the order of twice as turbulent, as is documented in Figure 4.11. Secondly, at twice the distance from the nozzle exit the stagnation pressure is significantly reduced, as may be seen from Figure 4.30. Thus for the case of the larger spacing ($H/w = 8$) there is a considerable reduction in the lateral gradient in impingement surface pressure, identified earlier as the source of significant stabilizing effect to maintain a laminar boundary layer until the end of the stagnation region for $H/w = 4$. Thus relative to the case for $H/w = 4$, the much more highly turbulent flow approaching the stagnation region combined with considerable reduced lateral gradients in pressure appear sufficient to eliminate the phenomena of laminar to turbulent boundary layer transition for $H/w = 8$ over the range of Re_j tested.

As the concept of transition at the edge of the stagnation region where lateral gradients in pressure become small was found to be useful in analysis of the profiles at $H/w = 4$, this concept should be applied for $H/w = 8$ as well.

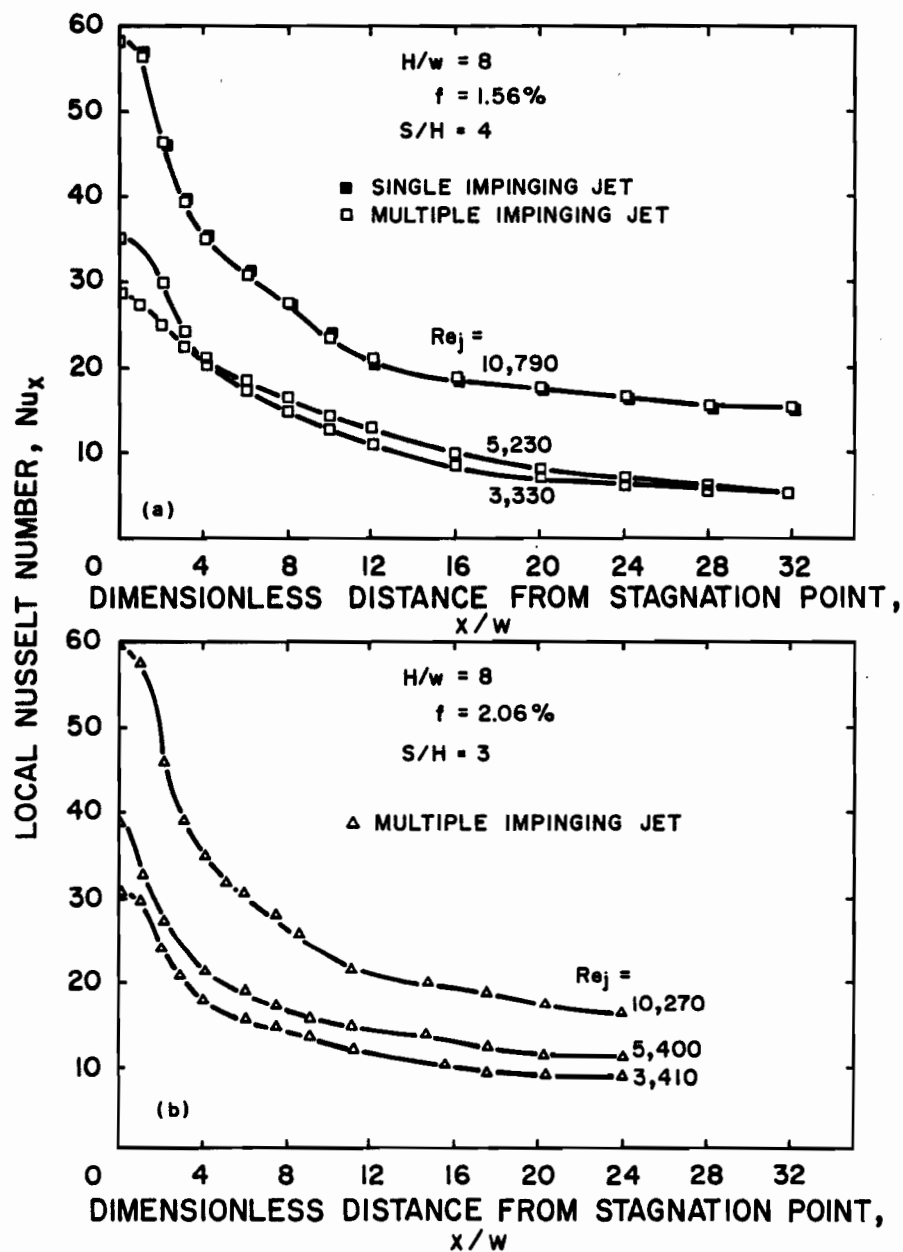


FIGURE 5.29. Effect of Jet Reynolds Number on Lateral Profiles of Nu_x for $f = 1.56$ and 2.06% and $H/w = 8$

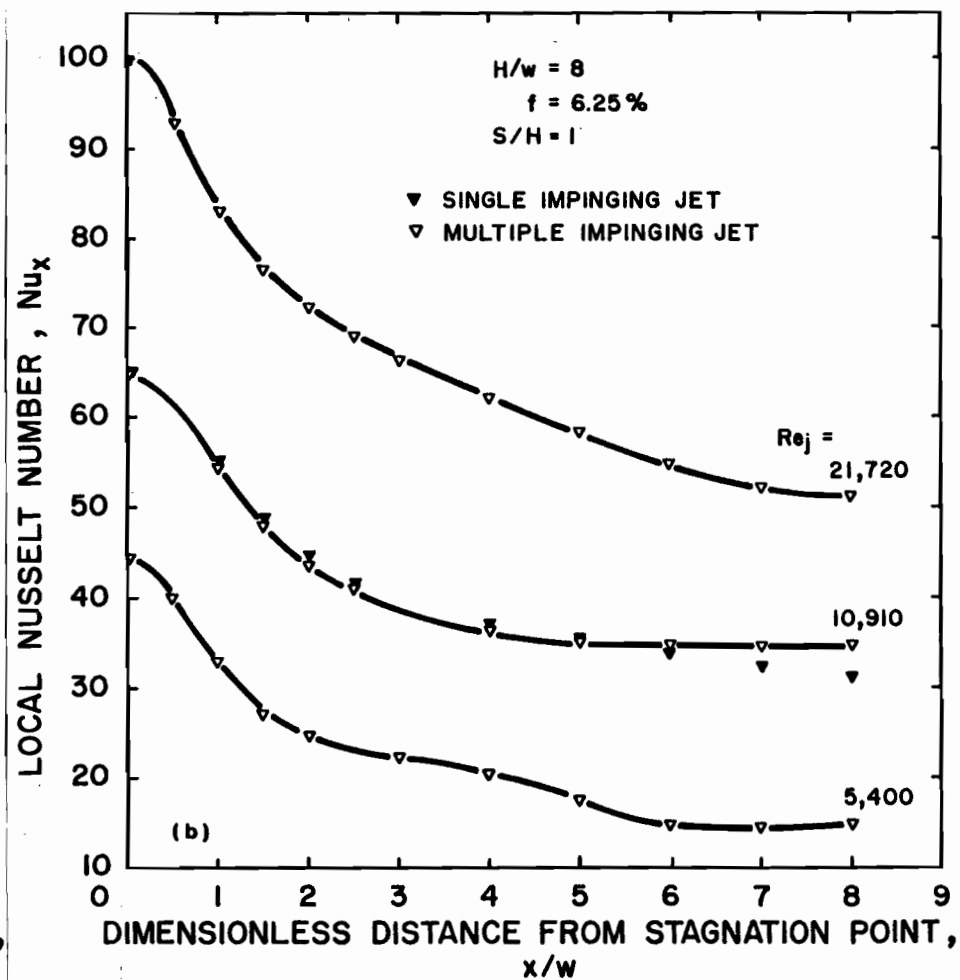
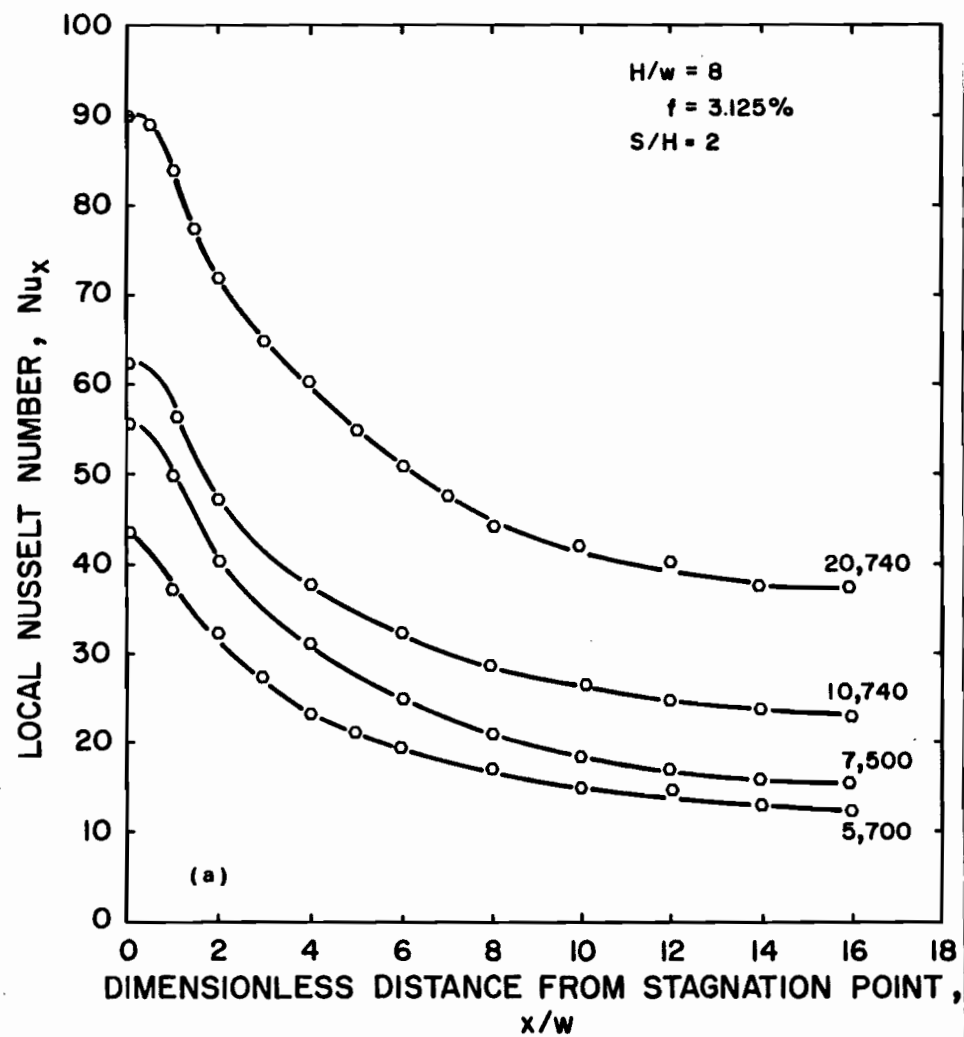


FIGURE 5.30. Effect of Jet Reynolds Number on Lateral Profiles of Nu_x for $f = 3.125$ and 6.25% and $H/w = 8$

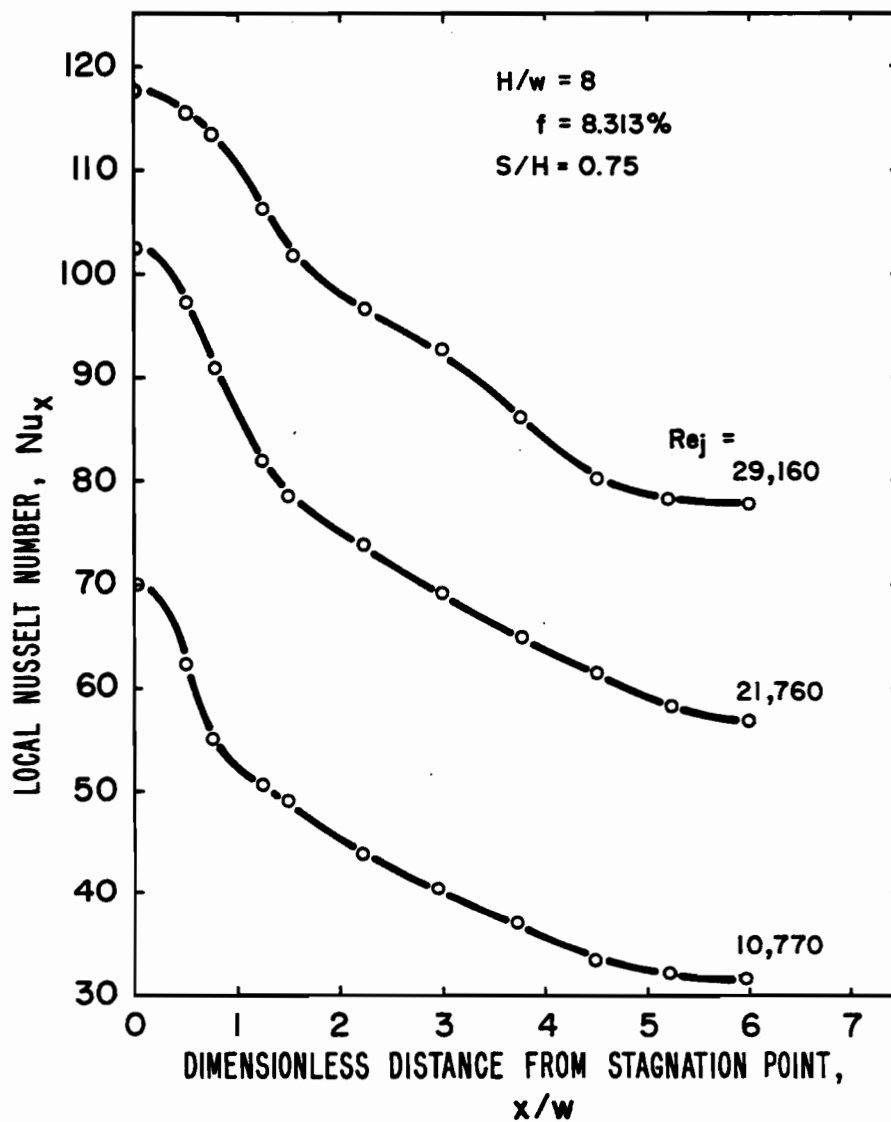


FIGURE 5.31. Effect of Jet Reynolds Number on Lateral Profiles of Nu_x for $f = 8.313\%$ and $H/w = 8$

As the similarity in pressure profiles developed in Chapter 4 indicates that the edge of the stagnation region occurs at about $x/H = 0.5$, it follows that for Figures 5.29 through 5.31, the stagnation region ends around $x/w = 4$. Examination in the vicinity of $x/w = 4$ for these 13 profiles establishes that in no case is there any indication of a sharp laminar to turbulent transition at this possible location.

It was noted at the outset that some single jet data were taken to provide a base case for evaluation of multiple jet system results. Thus on Figures 5.29(a) and 5.30(b) are superimposed two profiles on Nu_x for a single slot jet for comparison. It is evident from Figure 5.29(a) that at $Re_j = 10790$ and for $S/H = 4$ ($f = 1.56\%$), the multiple jet profile is indistinguishable from that for the equivalent single jet. From Figure 5.30(b) for the same Re_j but $S/H = 1$ ($f = 6.25\%$), the profiles likewise are indistinguishable except for the last two locations, i.e. at $x/w = 7-8$. Thus in this case the indication is for Nu_x under the exhaust port to be slightly higher than for the comparative single jet case. As the exit port width is $4w$ for $1.56 \leq f \leq 6.25\%$, it follows that the exit port is located at $2w$ from the exit port centerline, i.e. at from $x/w = 6$ to $x/w = 8$. For the case $f = 8.313\%$, the exit port is $1.5w$ from the exit centerline, i.e. at x/w from 6.5 to 8.

It may be concluded therefore that for wide flow cells, i.e. the cases for S/H of 4, 3 in Figures 5.29(a) and (b) and 2 in Figure 5.30(b), a multiple jet system may be viewed simply as an array of single jets, because the multiple jet interaction is so small as to be imperceptible on Nu_x at any location between the jet inlet to exhaust port centerlines. At $S/H = 1$ the multiple jet system is still effectively an array of single jets with the exception of evidence for a small increase in heat transfer, perhaps 10%, just for the section directly under the exit port.

The third set of figures, 5.32 through 5.34, present Nu_x profiles at the next larger spacing, $H/w = 16$. In this case for the standard range in open area, i.e. 1.56 to 8.33%, the corresponding range in flow cell proportions, S/H , is from 2 down to 0.375. As the general features remain as for $H/w = 8$, the principal interest rests with comparison with single jet results. From Figure 5.32(a) it can be seen that, as expected, the multiple jet system at $S/H = 2$ may be considered simply as an array of equivalent single jets. However, at $S/H = 0.5$ it would be expected that a significant interaction would be present, and this is apparent on Figure 5.33(b). In this case the Nu_x profile for the multiple jet case starts at stagnation at a value significantly less than that for a single jet, as was already seen on Figure 5.19 for Nu_o . The reduction in multiple jet Nu_x profile continues until the location just under the exit port, i.e. to $x/w = 6$ after which the multiple jet Nu_e is lifted to become, by $x/w = 8$, again about 10% greater than that for the comparative single jet case.

For the set of profiles at the highest impingement surface spacing, $H/w = 24$, the Nu_x profiles are shown on Figures 5.35 and 5.36, for which S/H ranges from 1.33 down to the lowest value measured in this study, $S/H = 0.33$. Again the prime interest is the single jet/multiple jet comparison. At $S/H = 1.33$, these two cases again completely superimpose, as would be expected for this size of flow cell. The profiles of Figure 5.36(b) are all quite flat, due to the marked reduction in Nu_o for S/H as low as 0.33, as was seen in Figure 5.19 for Nu_o . This large reduction in Nu_x continues away from the stagnation point until the section under the exit port is approached. Thus directly under the exit port wall, i.e. at $x/w = 6$, the multiple jet profile has been lifted back to equality with Nu_x for the single jet at the same location. By $x/w = 8$, i.e. under the exhaust port centerline, the multiple jet

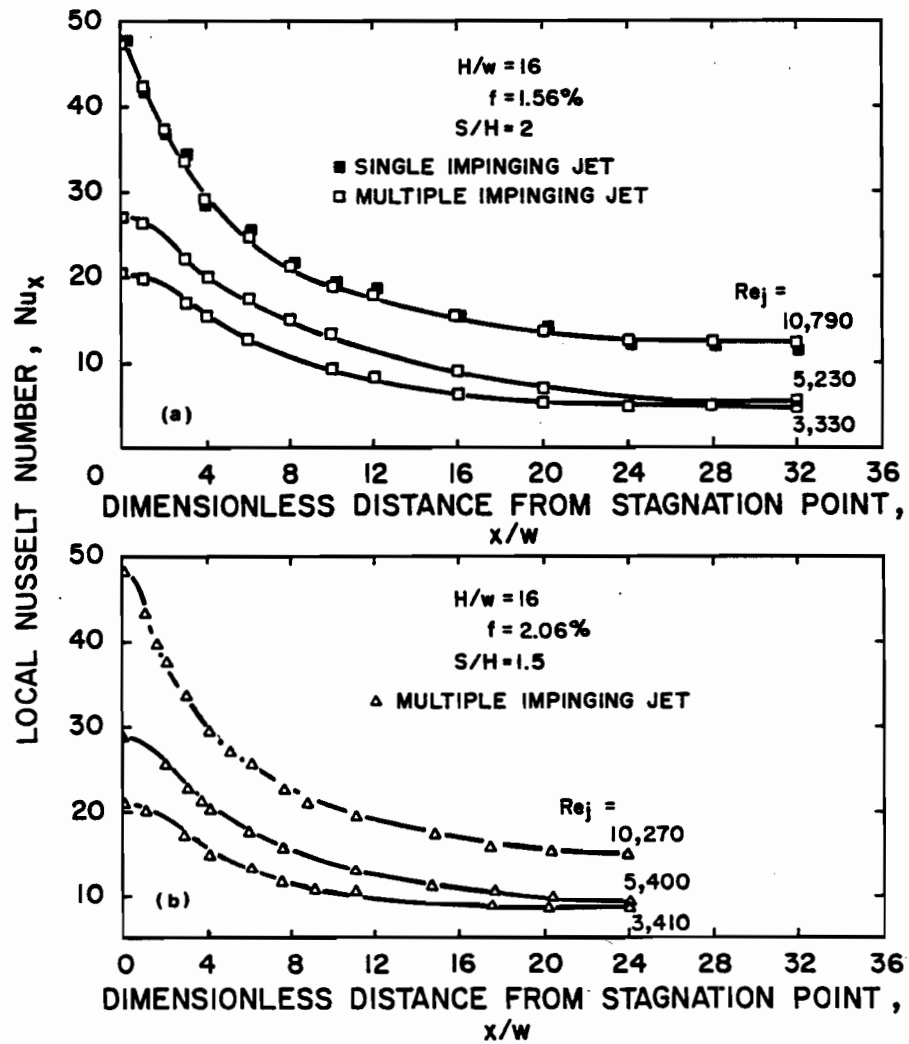


FIGURE 5.32. Effect of Jet Reynolds Number on Lateral Profiles of Nu_x for $f = 1.56$ and 2.06% and $H/w = 16$

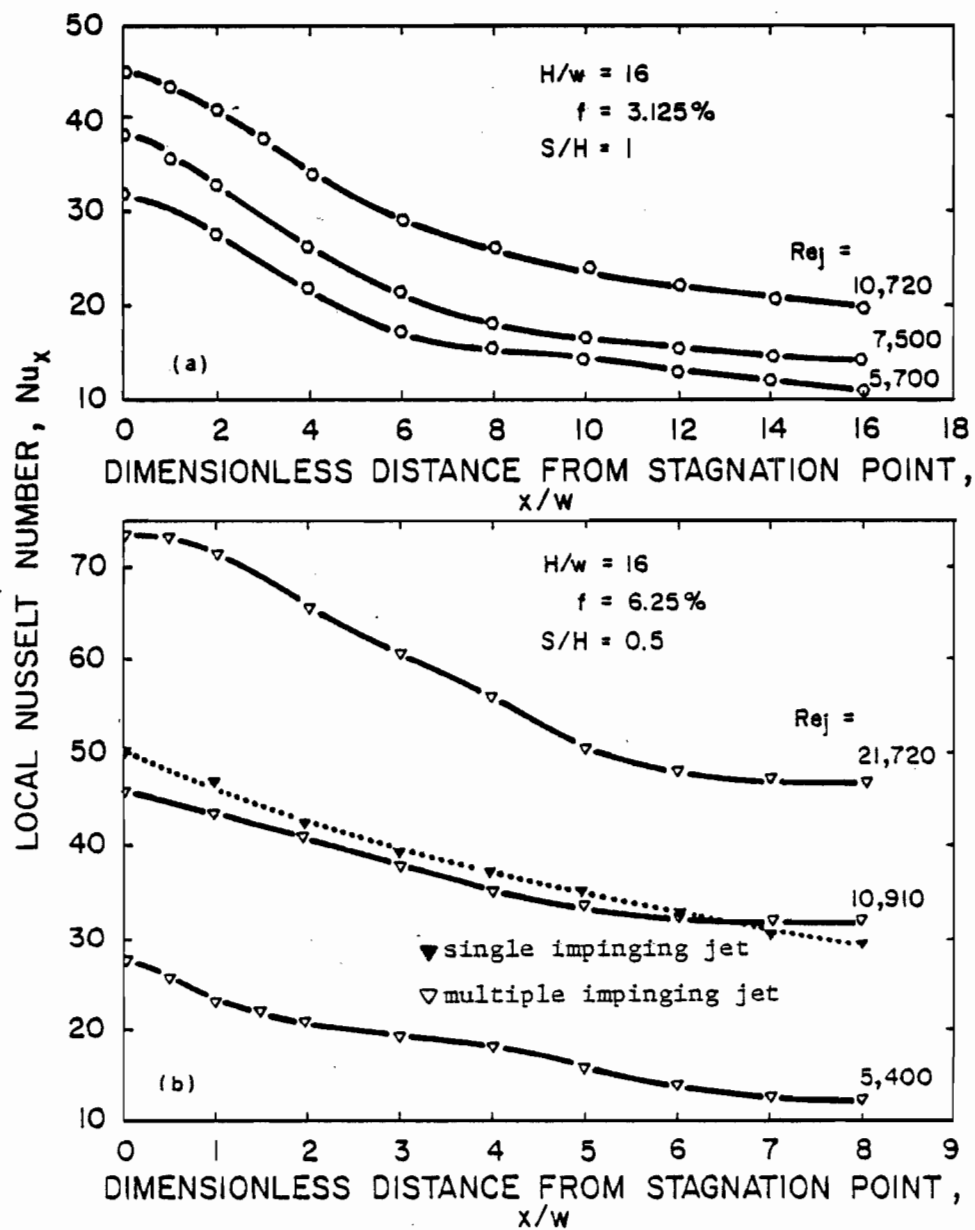


FIGURE 5.33. Effect of Jet Reynolds Number on Lateral Profiles of Nu_x for $f = 3.125$ and 6.25% and $H/w = 16$

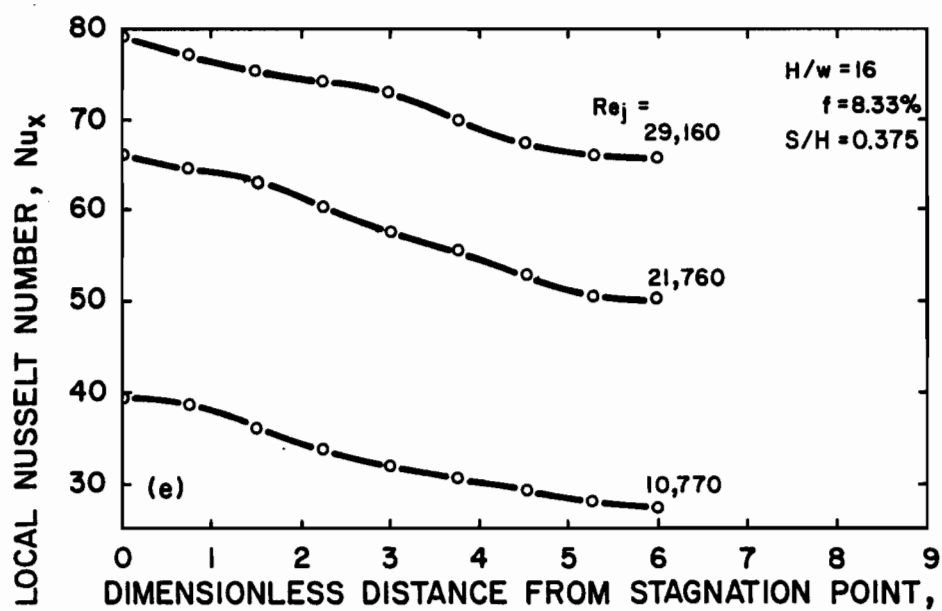


FIGURE 5.34. Effect of Jet Reynolds Number on Lateral Profiles of Nu_x for $f = 8.33\%$ and $H/w = 16$

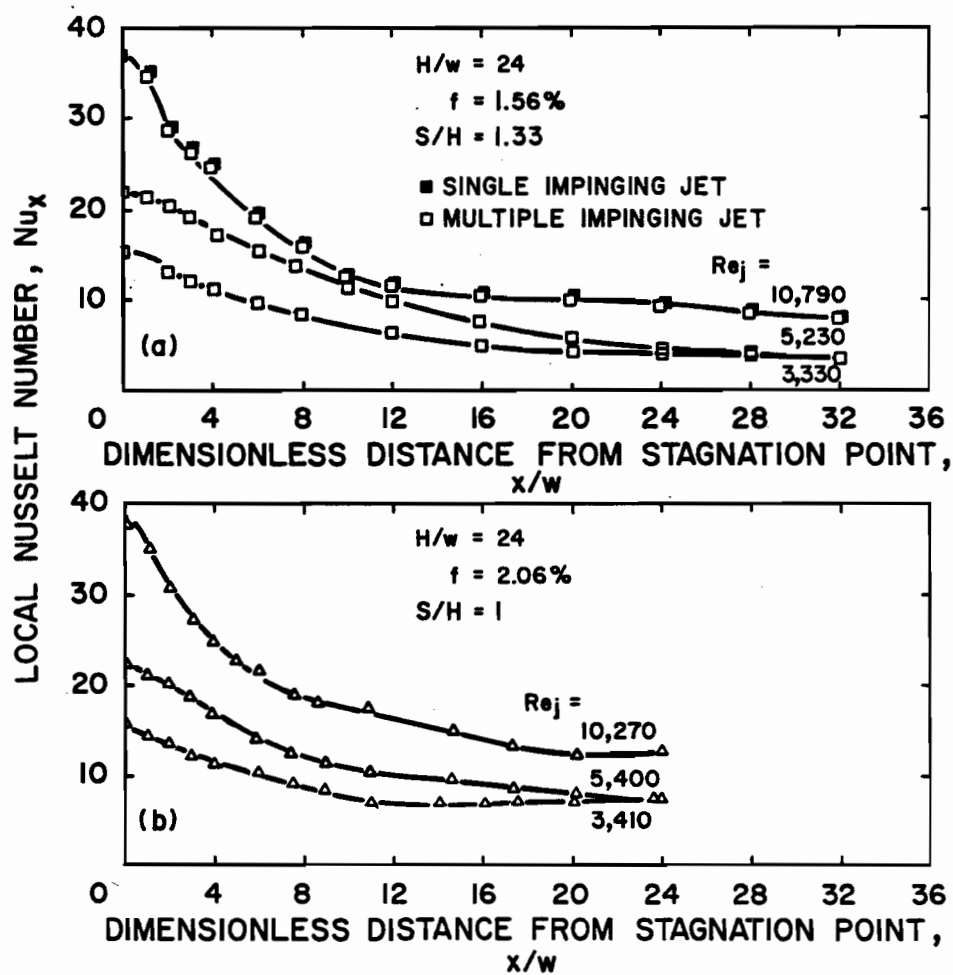


FIGURE 5.35. Effect of Jet Reynolds Number on Lateral Profiles of Nu_x for $f = 1.56$ and 2.06% and $H/w = 24$

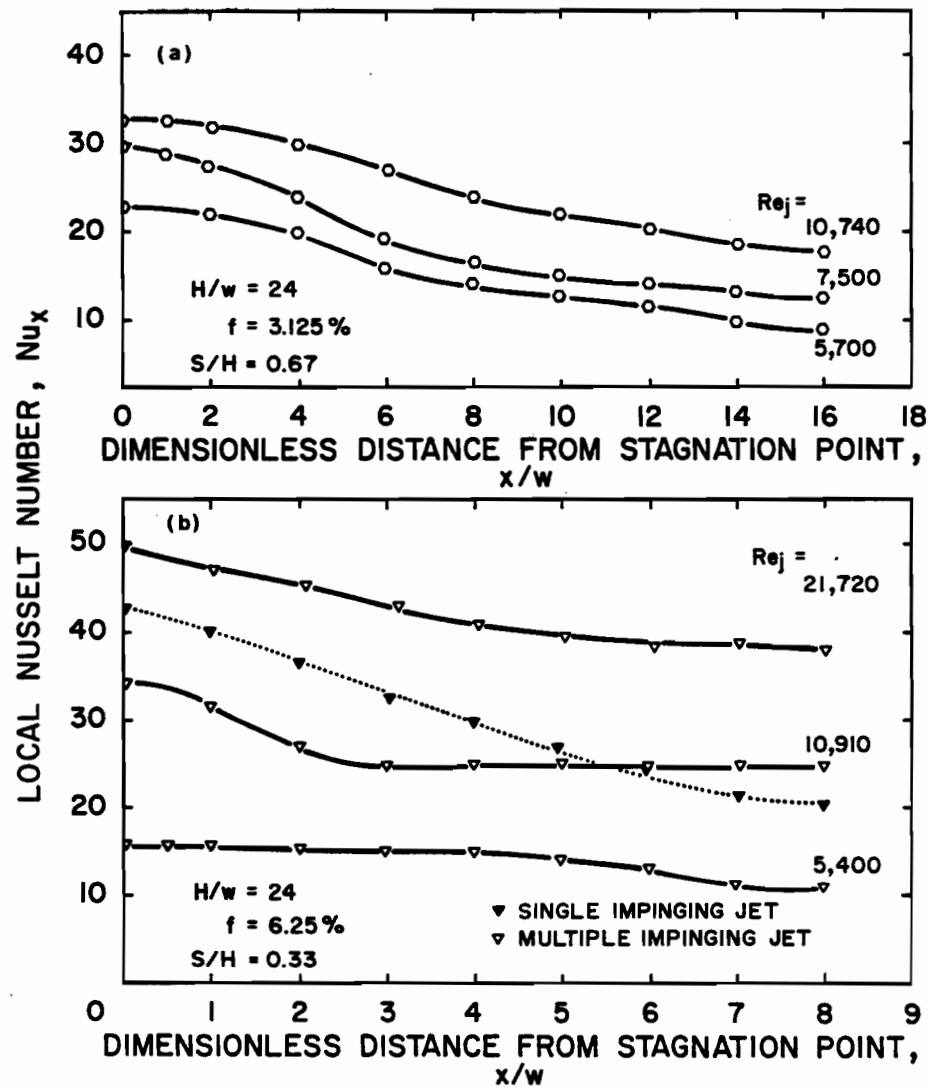


FIGURE 5.36. Effect of Jet Reynolds Number on Lateral Profiles of Nu_x for $f = 3.125$ and 6.25% and $H/w = 24$

Nu_e is about 25% higher than the comparative single jet case. The role of the local value of convective heat transfer driving force, ΔT , in this relative increase in Nu_x near the exit port region will be examined in Section 5.4.4.

Three Nusselt number profiles (Figures 5.30(b), 5.33(b) and 5.36(b)) have been noted for which Nu_e for the multiple jet case is greater than Nu_x at the same distance from the nozzle centerline for the equivalent single jet. Thus for sufficiently narrow flow cells, i.e. $S/H < 1.5$, the convergence at the exhaust port centerline of a pair of spentflows from adjacent inlet nozzles is associated with an increase in Nu_x over that for a single jet.

This flow field under the exhaust port is characterized by flow separation as the flow adjacent to the impingement surface deflects sharply near the exit centerline. Such a flow is analogous to that at the rear of a cylinder in crossflow. The exhaust port flow region and that at the back of a cylinder differ only in that separation occurs in the former case as the decelerating wall jet is constrained to flow away from a flat surface, while in the latter case, separation occurs by the deceleration of the flow along a convex surface. However, in spite of the difference in surface curvature, the dominant feature is the common phenomena of flow separation.

The enhancement of heat and mass transfer at the rear of a cylinder in crossflow has been well documented, for example in the study by Giedt (1949). In this study the variation of the rate of heat transfer around a cylinder normal to an air stream was found to be significantly affected by the separated flow field. Downstream of the stagnation region, i.e. in the back half of the cylinder Giedt (1949) reported a minimum heat transfer at a location coincident with that with zero shear stress. This condition occurs at the

position on the back of the cylinder where separation of the boundary layer from the surface is completed. Downstream from the separation point he reported a consistent increase of heat transfer rate due to increased eddy motion encountered in the separated flow region. Thus the observation of enhancement of heat transfer under the exit ports may be understood by reference to an analogous and thoroughly studied cylinder in crossflow phenomenon which is characterized by a similar region of flow separation.

5.4.2 Differentiation of Multiple from Single Jets by the Criterion of Flow Cell Proportions, S/H

A fundamental objective of the present thesis is to quantify the relationship between confined multiple and single slot jet systems. In Chapter 4 the significance was established of the dimensionless geometric parameter S/H , flow cell proportions. In Section 5.3, this parameter was found relevant for quantifying the geometric limit, $(S/H)_{co}$, over which stagnation point heat transfer, Nu_o , of multiple jets remains unchanged relative to the equivalent single slot jet. In Section 5.4.1 where there was an examination of entire Nu_x profiles, i.e. from Nu_o at the nozzle centerline to Nu_e at the exit port centerline, the same S/H ratio was found to be a relevant geometric parameter. It was noted from Figures 5.29(a), 5.32(a) and 5.35(a) that at sufficiently high values of S/H , the Nu_x profile for a multiple jet over the entire region from Nu_o to Nu_e was coincident with that for the corresponding single jet. At an intermediate value of S/H the multiple jet profile of Nu_x and the profile for the equivalent single jet were found to be coincident for some distance out from the nozzle centerline, after which Nu_x for the multiple jet becomes greater than for a single jet, as is seen on Figure 5.30(b). At still lower values of S/H , as seen on Figures 5.33(b) and 5.36(b), both types of

deviations were found, i.e. a multiple jet system with Nu_o lower but Nu_e higher than that for the corresponding single jet, so that such profiles cross at some point between the nozzle and exit port centerlines.

The behavior noted above is displayed concisely on Figure 5.37 which summarizes all experimental evidence available for viewing the heat transfer performance of confined multiple slot jet systems relative to equivalent single jets. Thus for $S/H > 1.5$, multiple slot jet systems may be simply viewed as an assembly of single jets, as the value of Nu_x from nozzle centerline (Nu_o) to exit port centerline (Nu_e) is coincident with that for the corresponding single jet. When the dimensionless width of flow cell, S/H , becomes less than 1.5, heat transfer for the multiple jet system is enhanced under the exit port and for some distance towards the nozzle centerline, while heat transfer at the nozzle centerline, Nu_o , remains the same as for a single jet. When the dimensionless spacing between nozzles is reduced below $S/H = 0.7$, interaction between the closely spaced countercurrent flows of inlet jet and exhaust streams penetrates to the nozzle centerline where it is reflected in reduction of Nu_o for a multiple jet relative to an equivalent single jet. Nu_o for multiple jets is seen to decrease very sharply as S/H is reduced below the lower critical value of 0.7. As S/H is reduced sufficiently, Nu_e also would eventually start to decrease. Although no matched sets of data for single and multiple jets in the present study were at a sufficiently low value of S/H to show this effect, this expectation is reflected in Figure 5.37 through indication of an eventual downturn in Nu_e for some flow cell width less than the lowest experimental value, $S/H = 0.33$.

These two critical values of S/H for deviation of Nu_x for a multiple jet from that for a single jet are then, $(S/H)_{ce} = 1.5$ and $(S/H)_{co} = 0.7$ for deviation of Nu_e and Nu_o , respectively. Thus for $S/H < (S/H)_{ce}$, a confined

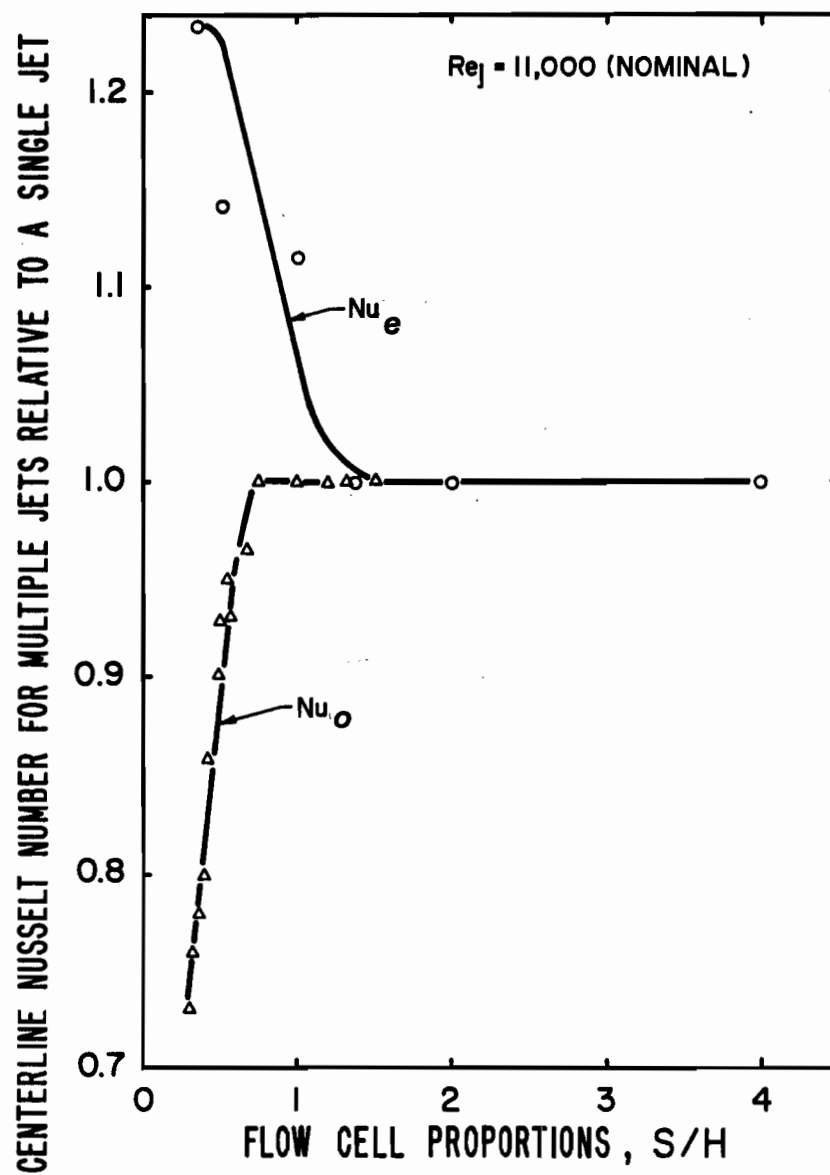


FIGURE 5.37 Effect of Flow Cell Proportion on Centerline Nusselt Number for Multiple Jets Relative to a Single Jet

multiple slot jet system ceases to be effectively an assembly of single jets, and use instead must be made of specific multiple jet data as is provided by the present study.

As the data represented on Figure 5.37 are for a nominal Re_j of 11000, the question may be posed as to whether the critical values, $(S/H)_{co}$ and $(S/H)_{ce}$, are functions of Re_j . It will be recalled that in Section 5.3, the evidence of Figures 5.21(a) and (b) indicated that $(S/H)_{co}$ was not perceptibly affected by Re_j over the range 5400 to 21700. As complete Nu_x profiles for single jets were taken in the present study only at $Re_j = 11000$, there is no direct evidence as to an effect of Re_j on $(S/H)_{ce}$. However, as $(S/H)_{co}$ is not affected by Re_j over the range $5400 \leq Re_j \leq 21700$, it seems unlikely that there would be an appreciable effect of Re_j on $(S/H)_{ce}$ over that range.

5.4.3 Effect of Flow Cell Proportion on Nu_x Profiles at Various Levels of Reynolds Number and Spacing

The point was made in Section 4.5 that, as three variables S , H and w define the geometry, two independent dimensionless ratios should in principle define geometrically similar multiple slot jet systems. Moreover in the case of lateral profiles of static pressure at the impingement surface, it was shown that a single pressure profile normalized to the stagnation point value could be obtained, Figures 4.31, 4.32 and 4.39, when lateral distance was normalized with respect to H rather than to the customarily used w . This finding of a universal pressure profile using x/H as dimensionless lateral distance suggested checking for a similar simplification for Nu_x profiles. It might be expected that because Nu_o is a function of H/w , the dependence of Nu_x profiles on H/w might be eliminated by normalizing Nu_x profiles with respect to Nu_o , leaving only dependence on a second dimensionless geometric

parameter, S/H . Figure 5.38(a) shows three Nu_x profiles as a function of x/H for a range of values of H/w but at a single value of S/H and Re_j . Figure 5.38(b) shows the corresponding profiles normalized as Nu/Nu_o . It is evident that this method of representing normalized Nu_x profiles by no means lead to a single profile. As this test was made with multiple jet data, the concept was further tested for single jet data. For a set of single jet runs at $w = 2.5$ mm and at the above value of Re_j , values of Nu_x/Nu_o were for simplicity determined at a single lateral position, i.e. at the $x/H = 0.5$ value that proved of interest in the analysis of pressure profiles in Chapter 4. It is thereby evident that for neither single nor multiple slot jets does there exist a single normalized Nu_x profile as was the case for the simpler phenomena of static pressure profiles.

As Section 5.4.2 and Figure 5.37 has established the importance of S/H as a geometric variable for multiple slot jet heat transfer, the Nu_x profiles previously presented in the series of Figures 5.26 to 5.36 are now reordered so as to show more clearly the S/H effect. Thus each of Figures 5.39 to 5.48 displays S/H as a parameter, the data being organized as a set of 4 figures (Figures 5.39 through 5.42) at $Re_j = 11000$, 4 figures (Figures 5.43 through 5.46) at $Re_j = 5500$ and 2 figures (Figures 5.47 and 5.48) at $Re_j = 21000$. Even at the same values of Re_j and H/w , profiles of Nu_x originate at different values because of two previously discussed effects, specifically, that Nu_o increases with w but decreases at sufficiently low values of S/H , as is displayed most clearly on Figures 5.15 and 5.21(a) and (b). In Figures 5.39, 5.43 and 5.47, it is seen that, for $H/w = 4$, this difference in the profiles at stagnation continues to the exhaust port. In addition to the fact that for a specific value of Re_j and H/w the profiles begin at a different value of Nu_o , the profiles may subsequently converge, diverge, sometimes crossing,

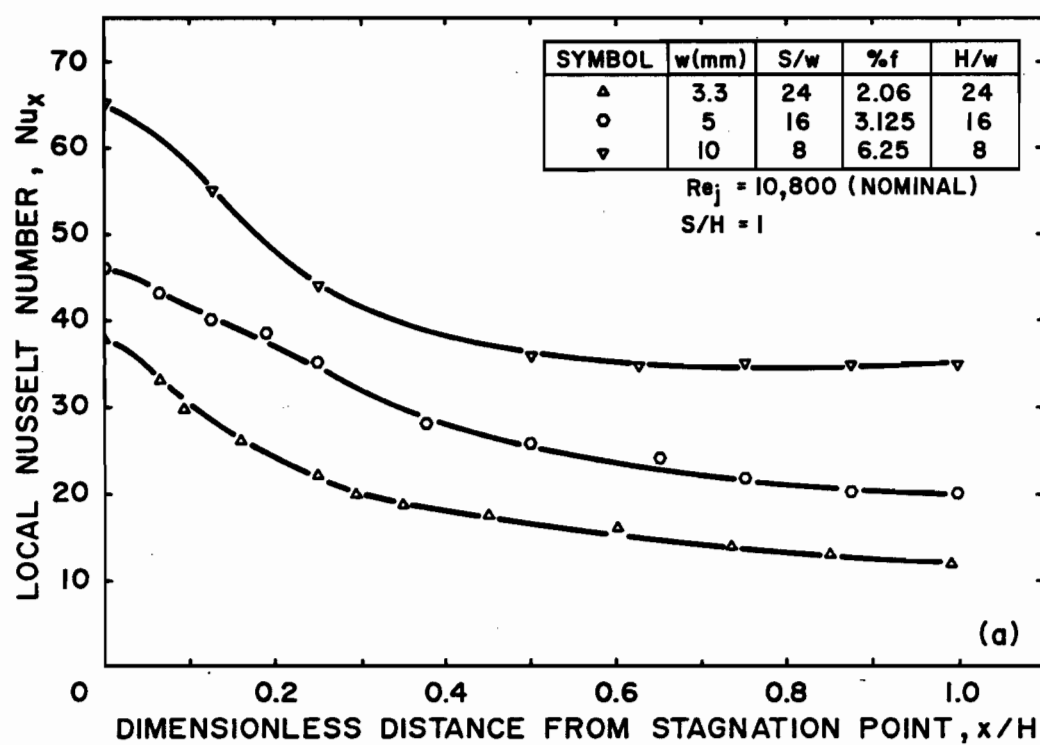


FIGURE 5.38(a) Nu_x Profiles as a Function of x/H for $Re_j = 10800$ (nominal) and $S/H = 1$

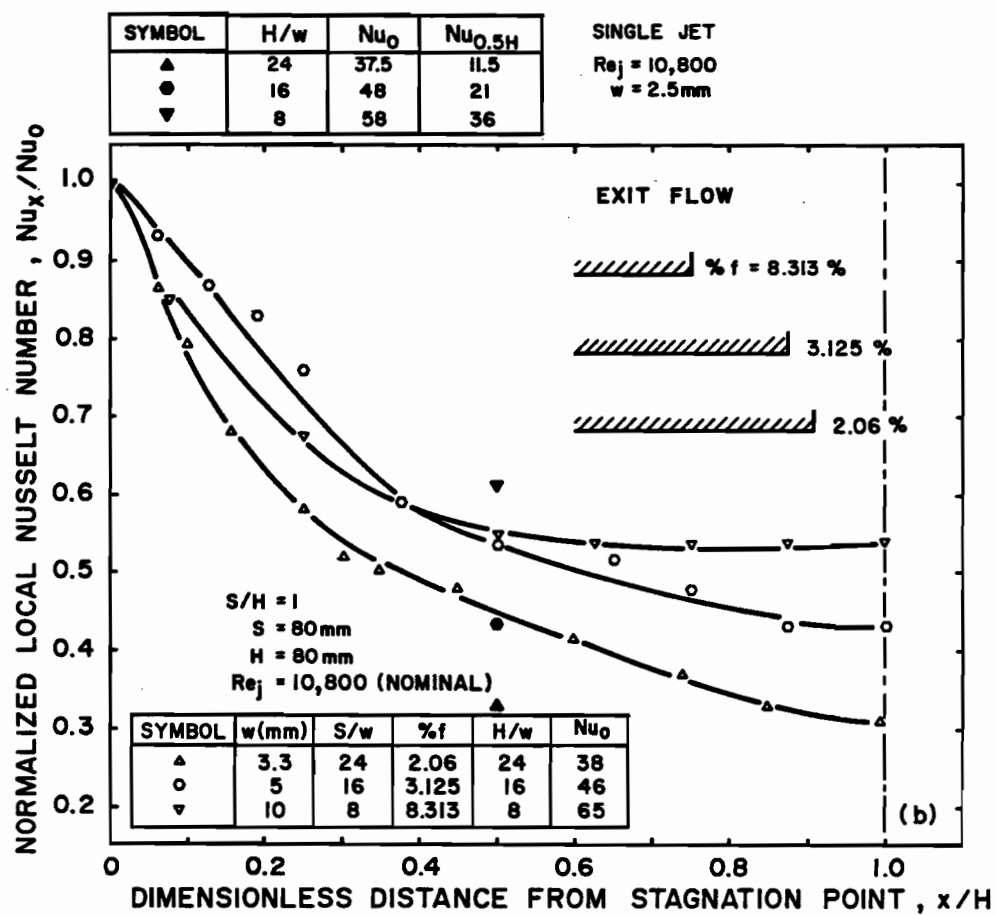


FIGURE 5.38(b) Normalized Nu_x/Nu_0 Profiles as a Function of x/H for $Re_j = 10800$ (nominal) and $S/H = 1$

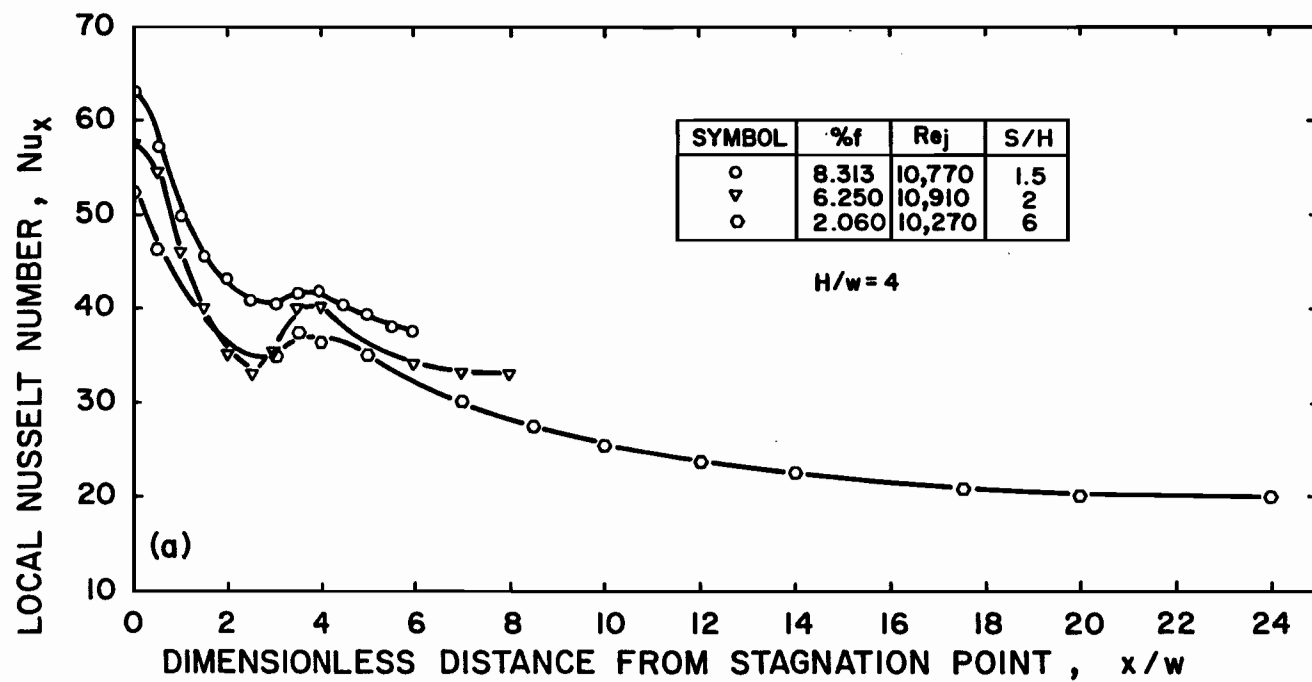


FIGURE 5.39 Effect of Flow Cell Proportion on Lateral Profiles of Nu_x for $H/w = 4$ and $Re_j = 11000$ (nominal)

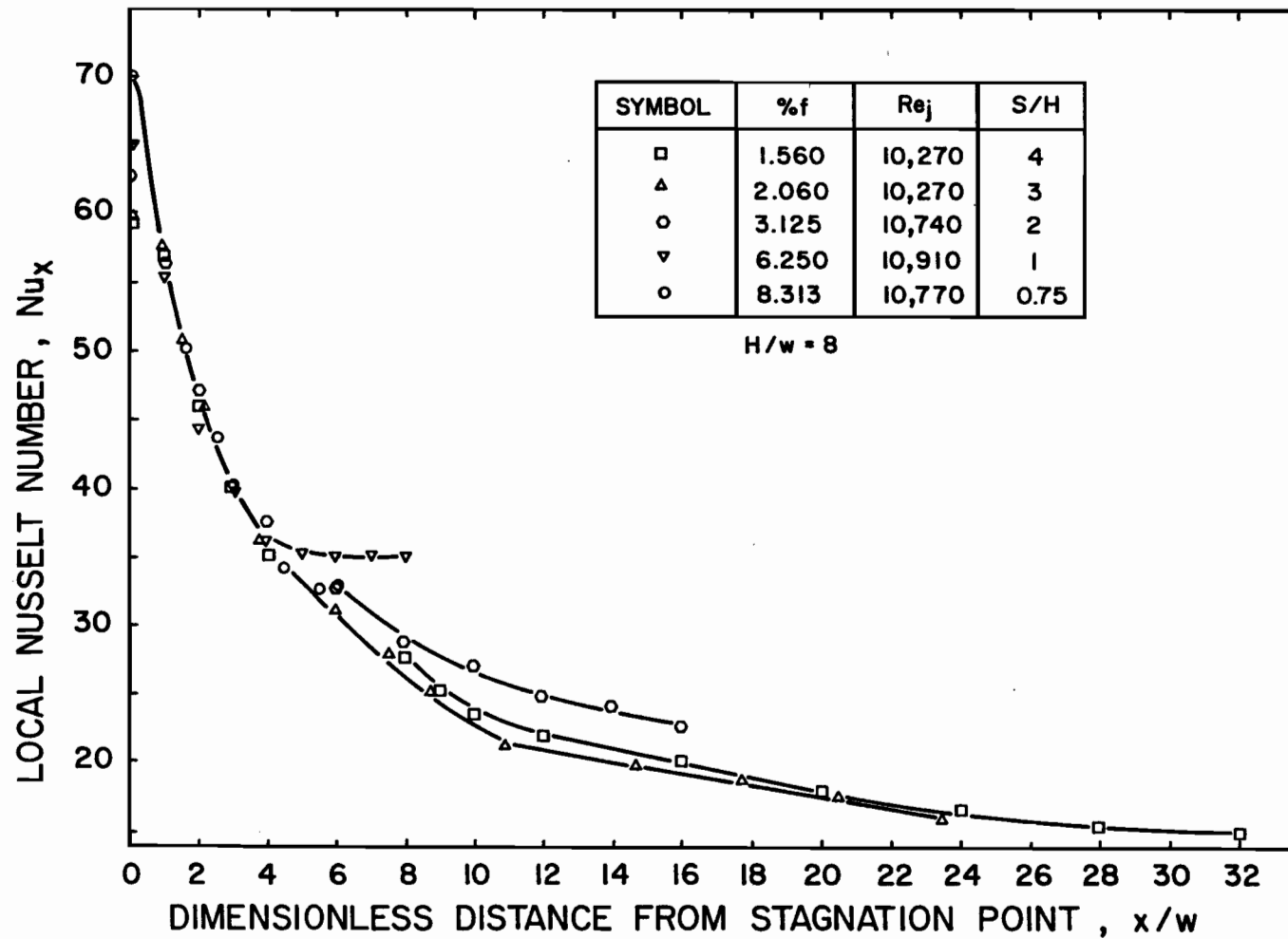


FIGURE 5.40 Effect of Flow Cell Proportion on Lateral Profiles of Nu_x for $H/w = 8$ and $Re_j = 11000$ (nominal)

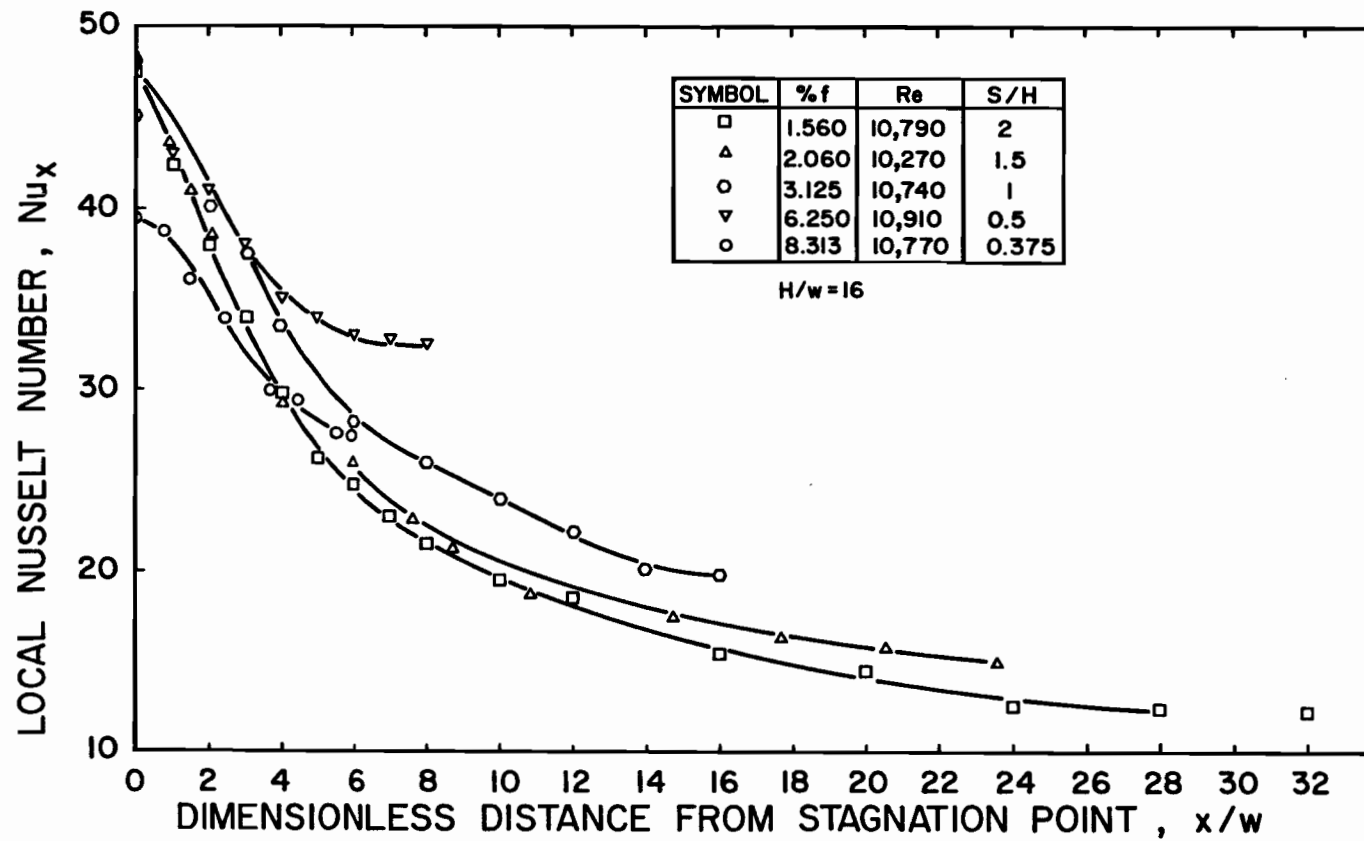


FIGURE 5.41 Effect of Flow Cell Proportion on Lateral Profiles of Nu_x for $H/w = 16$ and $Re_j = 11000$ (nominal)

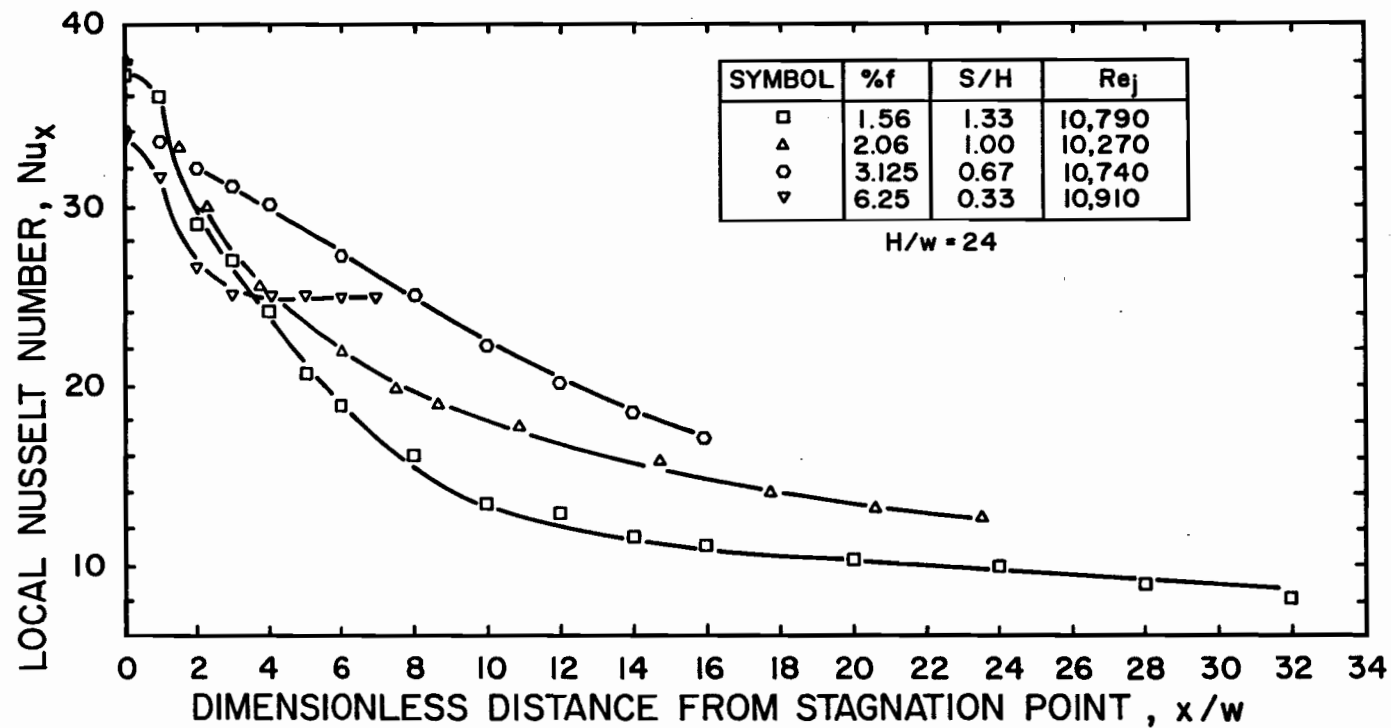


FIGURE 5.42 Effect of Flow Cell Proportion on Lateral Profiles of Nu_x for $H/w = 24$ and $Re_j = 11000$ (nominal)

sometimes not, according to the relative importance of the above-noted effects at the stagnation point and of the heat transfer enhancement under the exit ports as recorded in Section 5.4.2 and Figure 5.37.

The only previous data for a multiple slot jet system which can be compared to the present results is a run at $Re_j = 5400$, $H/w = 16$, $f = 6.25\%$, $S/w = 8$, $w = 3.175$ mm, $S/H = 0.5$ by Gardon and Akfirat (1966). Since no dimension of the plenum chamber was reported by these authors it is difficult to assess the extent of the upper confinement surface formed by the structural extension of the plenum chamber. Moreover, because these authors used a long nozzle ($t/w \geq 24$) their confinement surface was therefore always located at around $24w$ above the nozzle exit. This implies that regardless of the extent of the confinement surface, which may have produced an exit opening of around $8w$ (for a plenum chamber width, S , equal to 25 mm) the confinement surface effect would be further reduced by being located so far from the nozzle exit. With the conjecture that their confinement surface extended $4w$ from the jet centerline, their exit port would have extended from $x/w = 4$ to $x/w = 8$, i.e. a larger exit port than the comparable $x/w = 6$ to $x/w = 8$ port of the present study. The relationship between the multiple and single jet profiles of Gardon and Akfirat presented in Figure 5.45 is analogous to that found in the present study as illustrated on Figures 5.33(b) and 5.36(b) in that the profiles cross due to the opposite effects at Nu_o and Nu_e documented in the present study. Considering the difference in location and the uncertainties concerning extent of their confinement surface, the agreement between their multiple jet profile and that of the present study is reasonably satisfactory.

The only other Nu_x profile of a previous study which may be used as a reference for the present study is that of Cadek and Zerkle (1970) for a single slot jet exiting parallel to the impingement surface. In their experi-

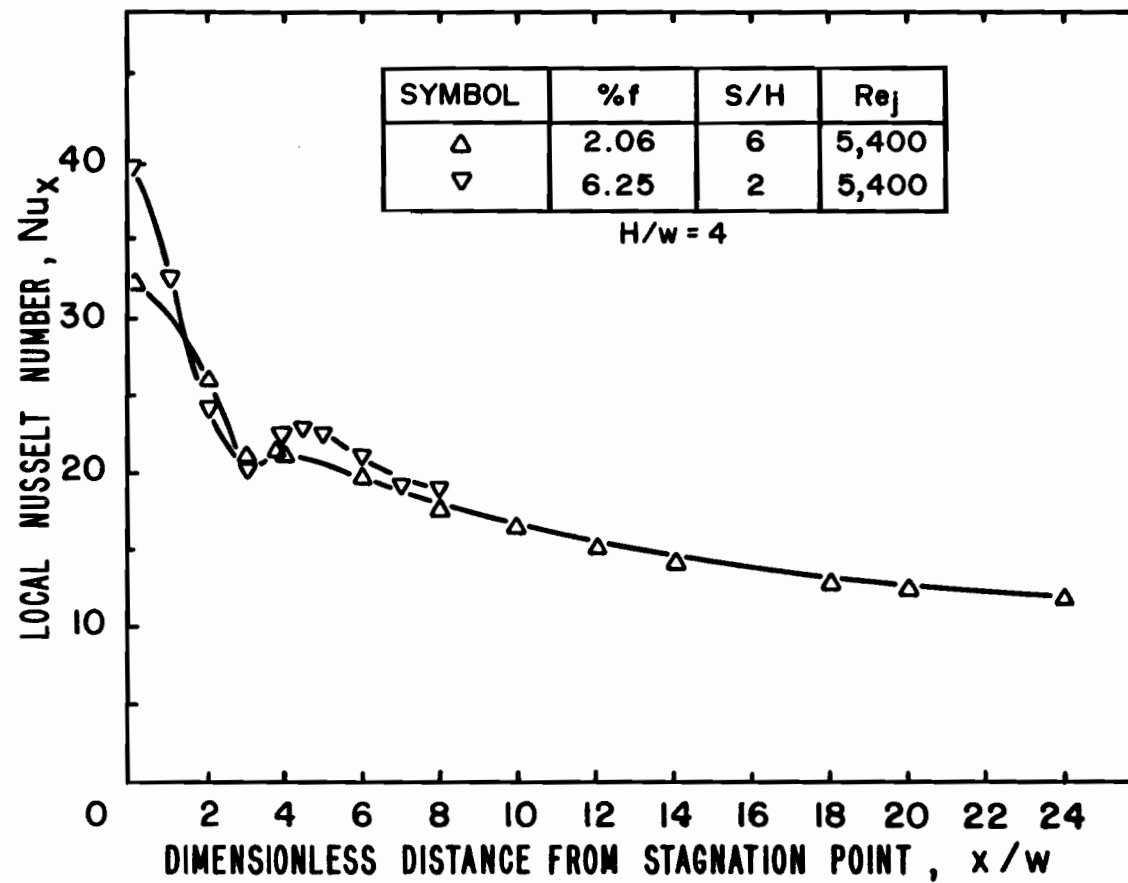


FIGURE 5.43 Effect of Flow Cell Proportion on Lateral Profiles of Nu_x for $H/w = 4$ and $Re_j = 5400$

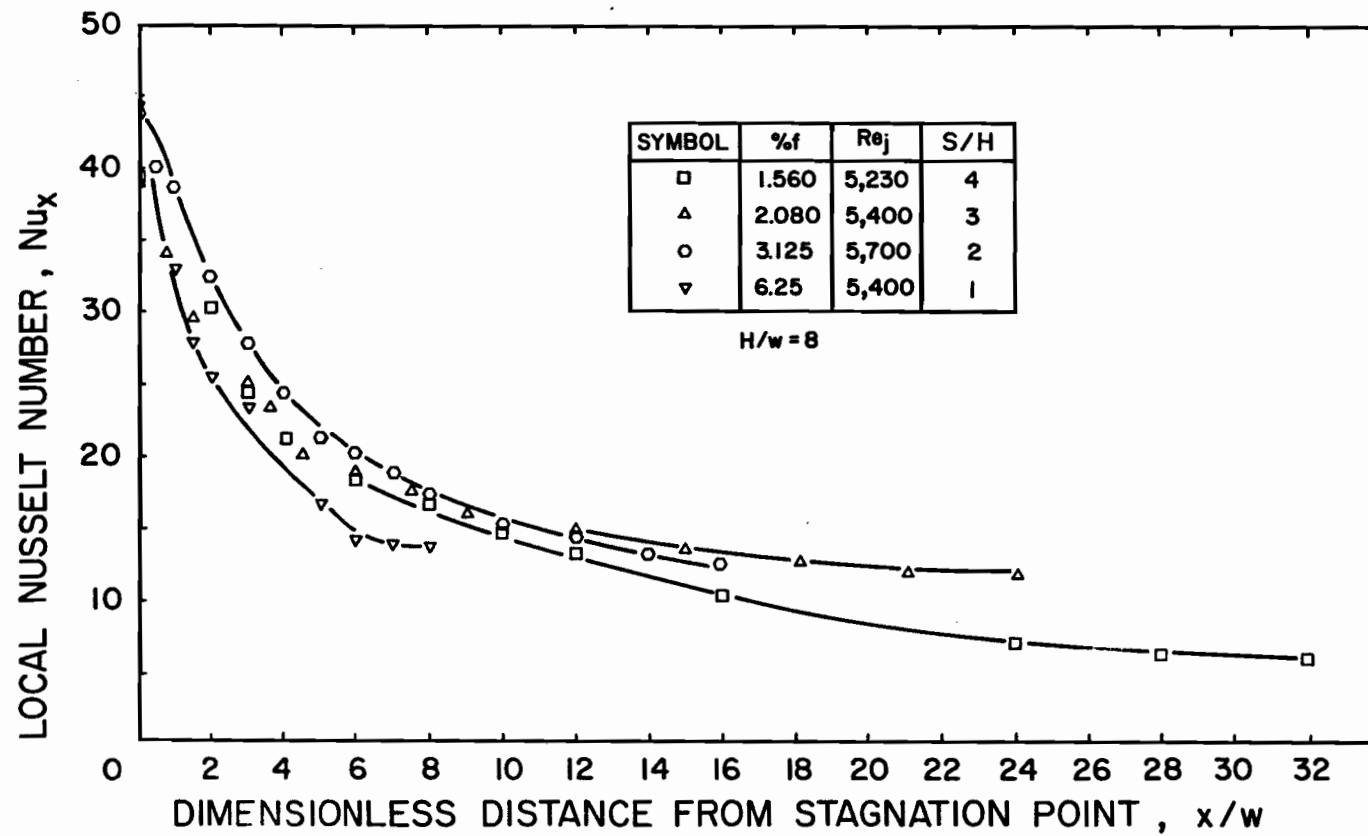


FIGURE 5.44 Effect of Flow Cell Proportion on Lateral Profiles of Nu_x for $H/w = 8$ and $Re_j = 5500$ (nominal)

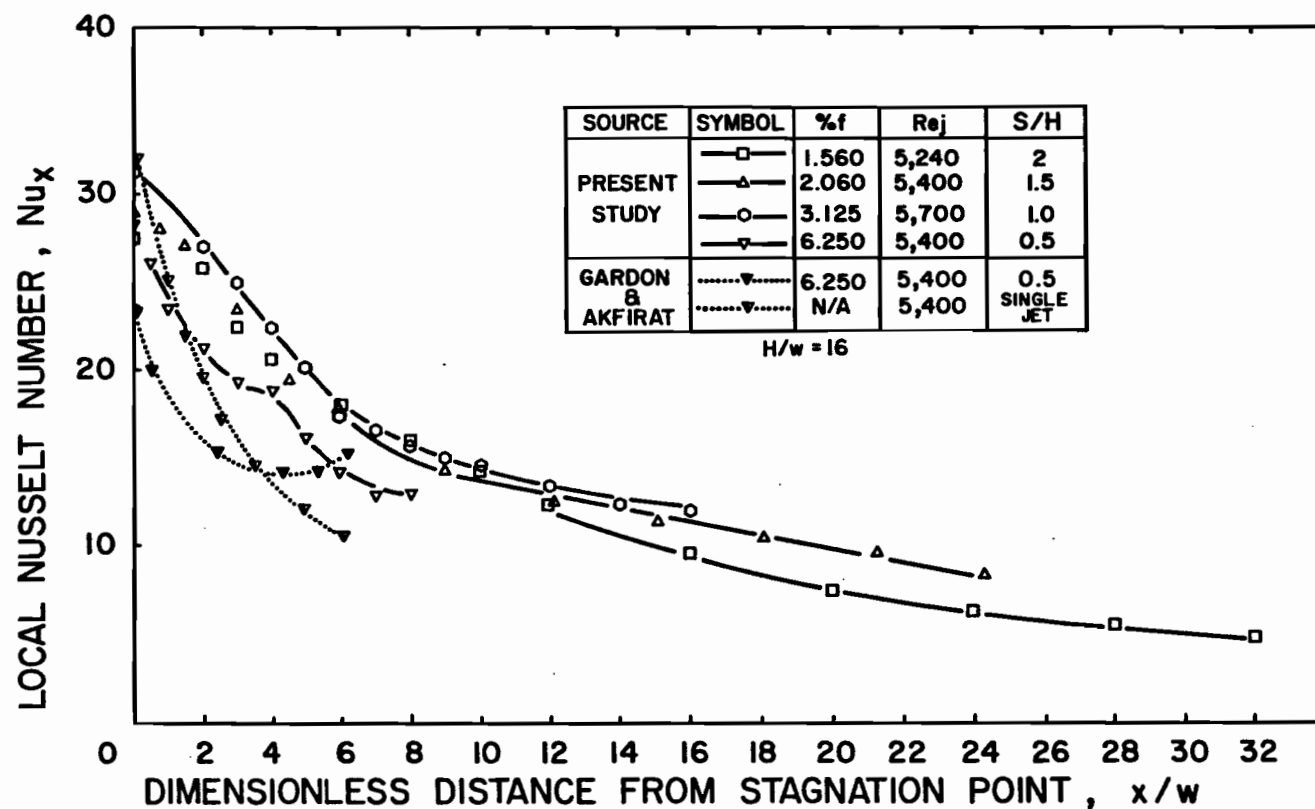


FIGURE 5.45 Effect of Flow Cell Proportion on Lateral Profiles of Nu_x for $H/w = 16$ and $Re_1 = 550000$ (nominal) and Nu_x Profiles of Gardon and Akfirat (1966)

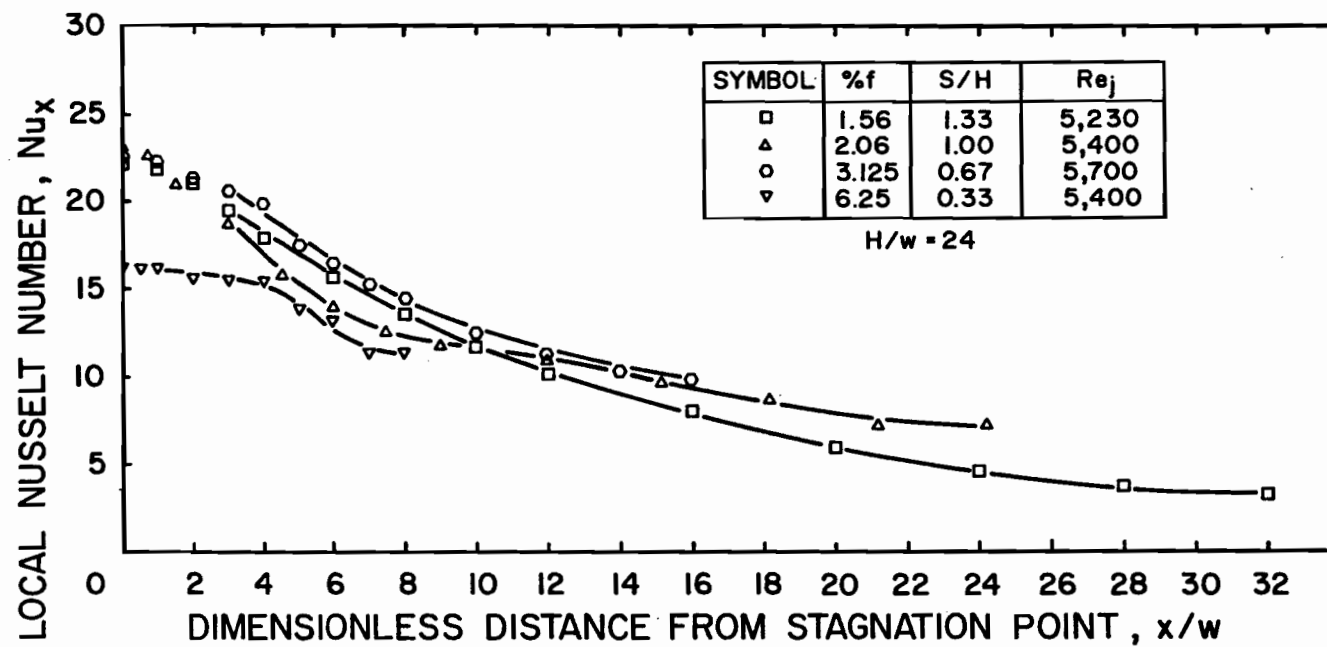


FIGURE 5.46 Effect of Flow Cell Proportion on Lateral Profiles of Nu_x for $H/w = 24$ and $Re_j = 5500$ (nominal)

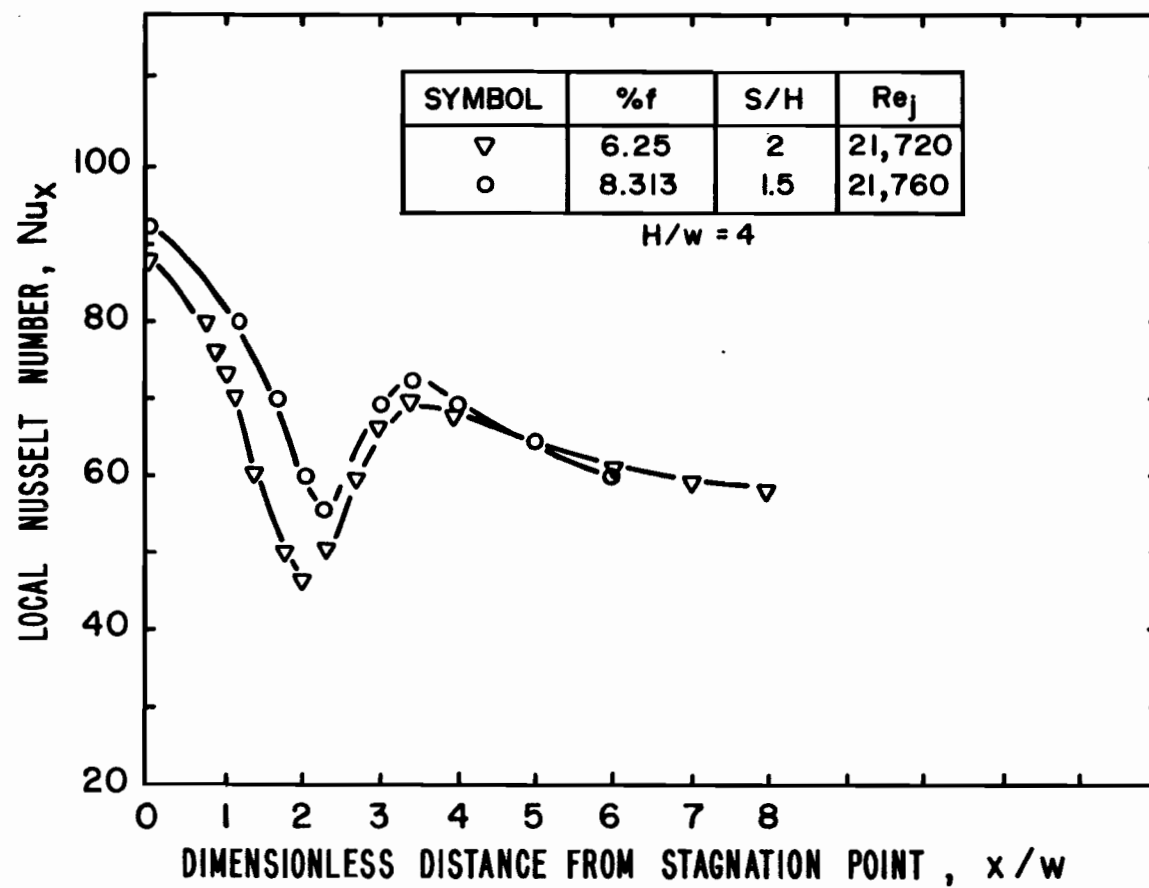


FIGURE 5.47 Effect of Flow Cell Proportion on Lateral Profiles of Nu_x for $H/w = 4$ and $Re_j = 22000$ (nominal)

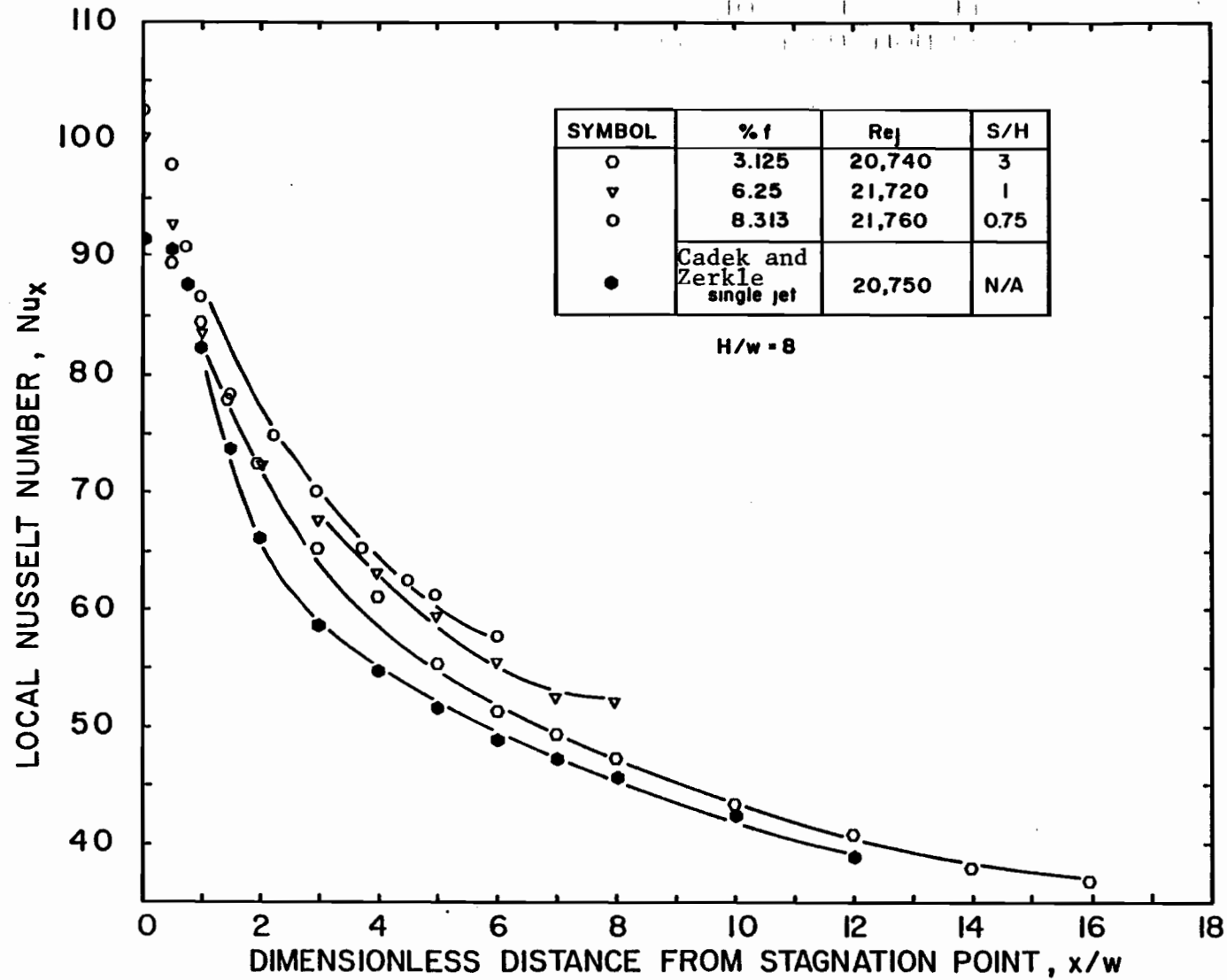


FIGURE 5.48 Effect of Flow Cell Proportion on Lateral Profiles of Nu_x for $H/w = 8$ and $Re_j = 22000$ (nominal) and Nu_x Profile of Cadek and Zerkle (1970)

mental apparatus the impingement and confinement surfaces extended respectively $12w$ and $8w$ from the nozzle centerline. Although the present study did not include any single jet measurements at the level of Reynolds number used by Cadek and Zerkle, $Re_j = 20750$, the evidence already presented establishes that single jet profiles would be indistinguishable from those for multiple slot nozzles spaced as wide as $S/H = 2$, for which a profile is shown on Figure 5.48. It may be seen that there is close agreement between the $S/H = 2$ profile and that of Cadek and Zerkle for a single jet.

5.4.4 Analysis of Confined Multiple Jets as a Closed System

The above analysis follows the pattern of all previous studies of heat transfer under impinging jets, single or multiple, unconfined or confined, in that the treatment has been that for an external flow and consequently the ΔT driving force used for conversion of heat flux to Nusselt number has been the temperature difference between the impingement surface and the jet at the nozzle exit. This pattern became established in impingement heat transfer because most studies have been of the simpler, unconfined jet case. However, as important industrial applications concern confined jet systems, the present study used an impingement apparatus closed with a confinement hood containing relatively small exhaust ports of width $4w$. For closed impingement systems the ΔT traditionally used for expression of results as Nusselt number would be exact only at the stagnation point. Beyond the stagnation point it may be considered that the appropriate ΔT driving force for use in converting local values of heat flux to local values of Nusselt number, Nu_x , should be the temperature difference between the impingement surface and the local bulk temperature of the impingement flow. This alternate analysis would treat the confined impingement system as a closed heat exchanger wherein ΔT is a vari-

able, rather than in the traditional way for impinging jet studies with nozzle exit temperature as the basis of ΔT . Profiles of Nu_x calculated using $|T_s - T_j|$ as ΔT are effectively profiles of wall heat flux, not of Nu_x . If the flow and geometrical parameters are such that the change in bulk temperature from the nozzle exit to the exhaust port produces a negligible relative change in ΔT , then there would be no significant difference between the conventional analysis as an external flow and the alternate procedure corresponding to closed heat exchanger. In this section the alternate closed heat exchanger analysis is applied to the results of the present study to determine quantitatively the importance in this case of the choice of basis for ΔT and hence of heat transfer coefficient and Nusselt number.

The change from the conventional impingement heat transfer analysis with ΔT based on T_j , to the alternate analysis with a local ΔT_x based on local bulk temperature, T_x , requires an energy balance to obtain T_x and hence ΔT_x as functions of x . As the Nu_x profiles given previously in Section 5.4.1 are effectively profiles of local heat flux, the lateral profiles of T_x derive directly from the heat flux profiles through an energy balance on the impingement flow. The lateral T_x profiles were determined for the same lw intervals in x as were the experimental values of local heat flux at the wall. Thus the integration of the impingement flow sensible heat equation was carried out as:

$$T_{x+w} = T_x + \frac{h_x (\Delta x) \Delta T_x}{(w/2) \rho U_j^* C_p} \quad (5.2)$$

The Stanton number, $h_x / \rho U_j^* C_p$, occurs as expected in this relation, and may if desired be considered as the equivalent ratio $Nu_x / Re_j Pr$. As h_x decreases with x from the nozzle to exhaust centerlines, it follows that T_x profiles

will show decreasing slope from jet inlet to flow outlet.

The local Nusselt number, Nu_{xb} , as the ratio local heat flux to local temperature difference ΔT_x may then be obtained as

$$Nu_{xb} = Nu_x \left(\frac{T_s - T_j}{T_s - T_x} \right) \quad (5.3)$$

With T_s a constant, as in the present study, ΔT_x decreases continuously from a maximum at the nozzle centerline to a minimum at the exhaust centerline.

Thus Nu_x is always an underestimate of Nu_{xb} as Nu_x is calculated for a ΔT higher than the actual local ΔT_x , except at the stagnation point where $Nu_{xb} = Nu_x = Nu_o$.

Two interesting experiments for application of this closed heat exchanger analysis are the pairs of runs shown on Figures 5.33(b) and 5.36(b) because in these cases both single and multiple jet profiles were obtained at the same conditions. Moreover these two pairs of runs are of particular interest as each pair exhibits both enhancement of heat transfer in the exit port region and depression in the stagnation region. Consequently, each of these single/multiple jet pairs of profiles cross at an intermediate point.

From the display of T_x profiles on Figure 5.49 for this single/multiple jet pair of runs, it is seen that in this case the multiple jet flow exhausts at a temperature only 1.51°C higher than at the nozzle exit. As for all runs the surface temperature T_s is effectively constant at 60°C , the T_x values of Figure 5.49 correspond to a decrease in ΔT_x from 20° at the nozzle exit to 18.5°C at the exhaust centerline. This 8% decrease in ΔT_x from inlet to outlet of the confined jet system results in the value of Nu_{xb} at the exit being likewise 8% higher than the Nu_x values which appeared on Figure 5.33(b) and

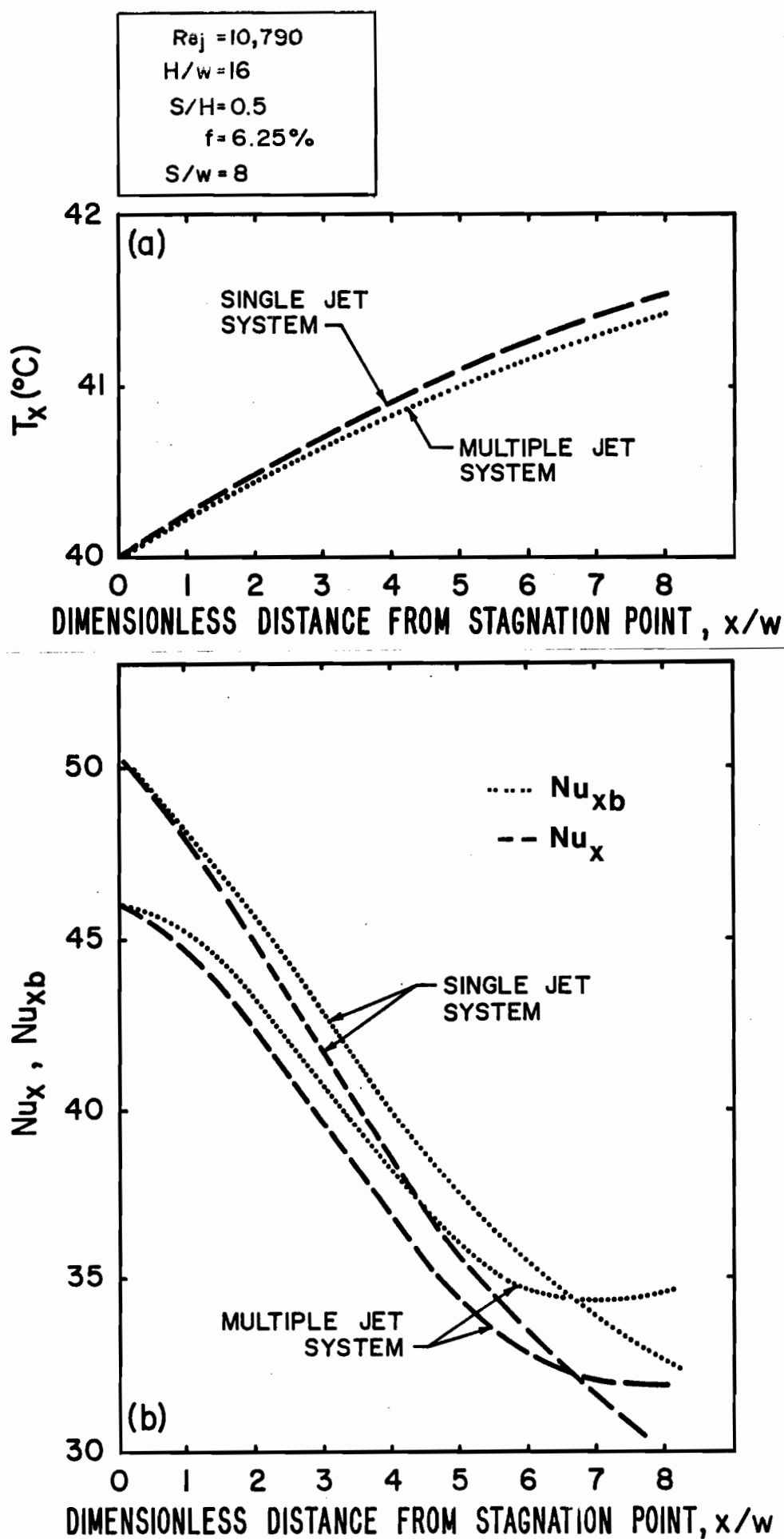


FIGURE 5.49 Lateral Profiles of T_x , Nu_x and Nu_{xb} for Single and Multiple Jet System at $Re_j = 10790$, $S/H = 0.5$ and $H/w = 16$

which are reproduced on Figure 5.49 for comparison.

For the other pair of intersecting profiles, shown originally on Figure 5.36(b), the T_x and Nu_{xb} profiles are shown on Figure 5.50. As Re_j is the same for the cases of Figures 5.49 and 5.50 but the impingement surface spacing is greater in the latter case, i.e. $H/w = 24$ in place of $H/w = 16$, the heat transfer is decreased, giving a smaller temperature rise in the impingement flow from inlet to exit. Thus there is a 1.09°C rise in this multiple jet example as compared to 1.5°C for the Figure 5.49 case. Correspondingly, the decrease in ΔT_x in this example is only from 20°C at the inlet to 18.91°C at the exit. This 6% decrease in ΔT_x is reflected in the corresponding 6% increase in Nu_{xb} at the exit, relative to the previously reported Nu_x value.

From the Nusselt number profiles for the multiple jet cases of Figures 5.49 and 5.50 it is seen that the effect of enhancement of the heat transfer coefficients associated with flow separation under exhaust ports is more evident when Nusselt number is determined using the local ΔT_x driving force. Thus for the multiple jet cases on both Figures 5.49 and 5.50 the Nu_{xb} profiles indicate an increase in Nusselt number under the exit ports whereas the Nu_x profiles indicated only a leveling out.

For a given value of Re_j the temperature rise from nozzle exit to exhaust port increases with increasing width of the impingement surface, i.e. with increasing S/w (or decreasing f). Correspondingly, for a particular value of S/w (or f), this temperature rise increases with decreasing Re_j . Thus in any experimental system the limiting cases for largest difference between the two alternate bases of expressing Nusselt number, Nu_x and Nu_{xb} , would be for low Re_j and high S/w (low f), as these conditions favor a high temperature rise and hence a large change in ΔT_x from nozzle exit to exhaust port. Several such cases for the present study are now examined.

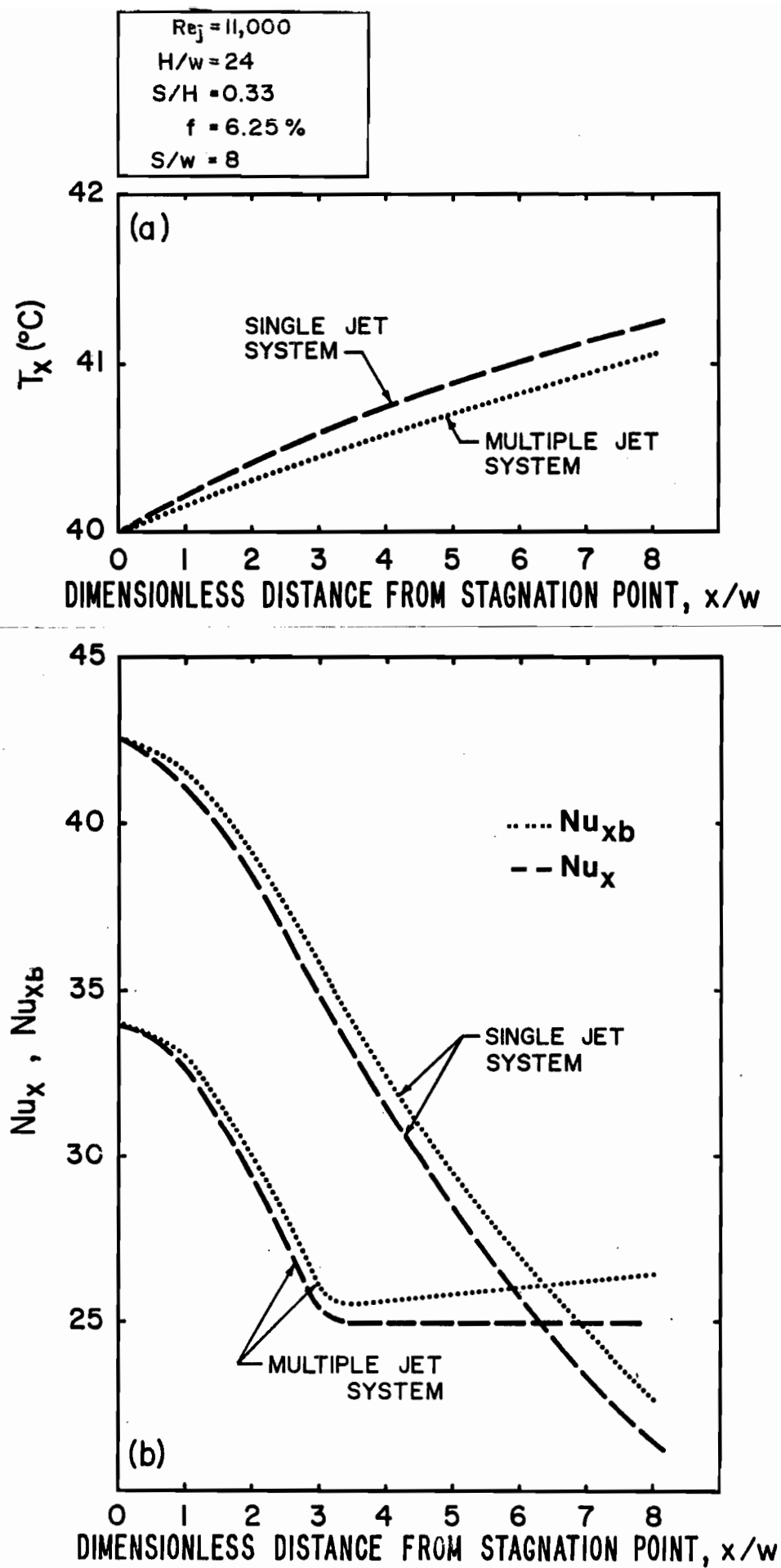


FIGURE 5.50 Lateral Profiles of T_x , Nu_x and Nu_{xb} for Single and Multiple Jet System at $Re_j = 11000$, $S/H = 0.33$ and $H/w = 24$

For the limiting case of highest internozzle spacing, $S/w = 32$ (lowest open area, $f = 1.56\%$) it is convenient to choose a case for which other experimental conditions are the same as for one of the two cases already presented. Thus Figure 5.41(a) presents T_x and Nusselt number profiles for $S/w = 32$ ($f = 1.56\%$) for the same values of Re_j and H/w as the case portrayed on Figure 5.49, for which $S/w = 8$, $f = 6.25\%$. Over the region out to $8w$ from the nozzle centerline there is not a large difference between the Nusselt number profiles of these two runs, hence the T_x profiles are likewise not dissimilar out to $x/w = 8$. However, in the case portrayed on Figure 5.51(a) the $x/w = 8$ location corresponds to only 25% of S/w . In fact the temperature rise, inlet to outlet, for the $S/w = 32$ spacing ($f = 1.56\%$) is over twice that for $S/w = 8$ ($f = 6.25\%$). The variation in ΔT_x from the stagnation point value of 20°C was correspondingly greater, i.e. about 17°C at the exit for the $S/w = 32$ case compared to about 18.5°C for the $S/w = 8$ reference case. Thus the effect on Nusselt number of the use of ΔT_x is appreciably greater for the small % open area case displayed on Figure 5.51(a) than for the larger open area run given on Figure 5.49, other conditions being the same.

As the importance on Nusselt number of the use of local ΔT_x increases at lower values of Re_j , Figure 5.51(b) provides an indication of the magnitude of the effect at the lowest Reynolds number of the present study, $Re_j = 3300$, all other conditions as for Figure 5.51(a). For this low Re_j , high S/w spacing (low open area) case the temperature rise, nozzle exit to exhaust port, is from 40°C to 44.72°C , equivalent to a decrease in ΔT_x from 20°C to 15.28°C from inlet to outlet. Corresponding to this 30% reduction in ΔT_x over the extent of the impingement surface the value of Nu_{xb} at the exhaust port, Nu_e , is around 30% higher than that reported previously as Nu_x .

The final two cases represented appear as Figures 5.52(a) and (b). The

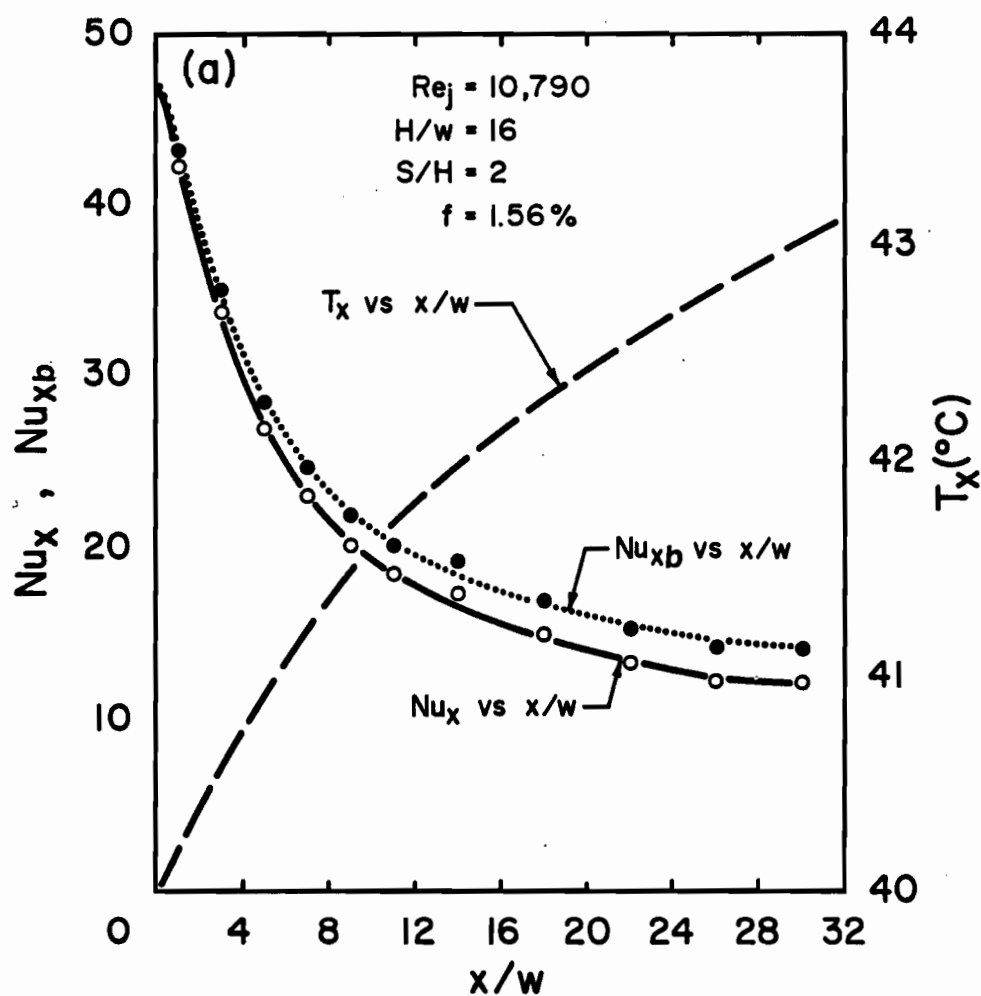


FIGURE 5.51(a) Lateral Profiles of T_x , Nu_x and Nu_{xb} for Multiple Jet System at $Re_j = 10790$, $S/H = 2$ and $H/w = 16$

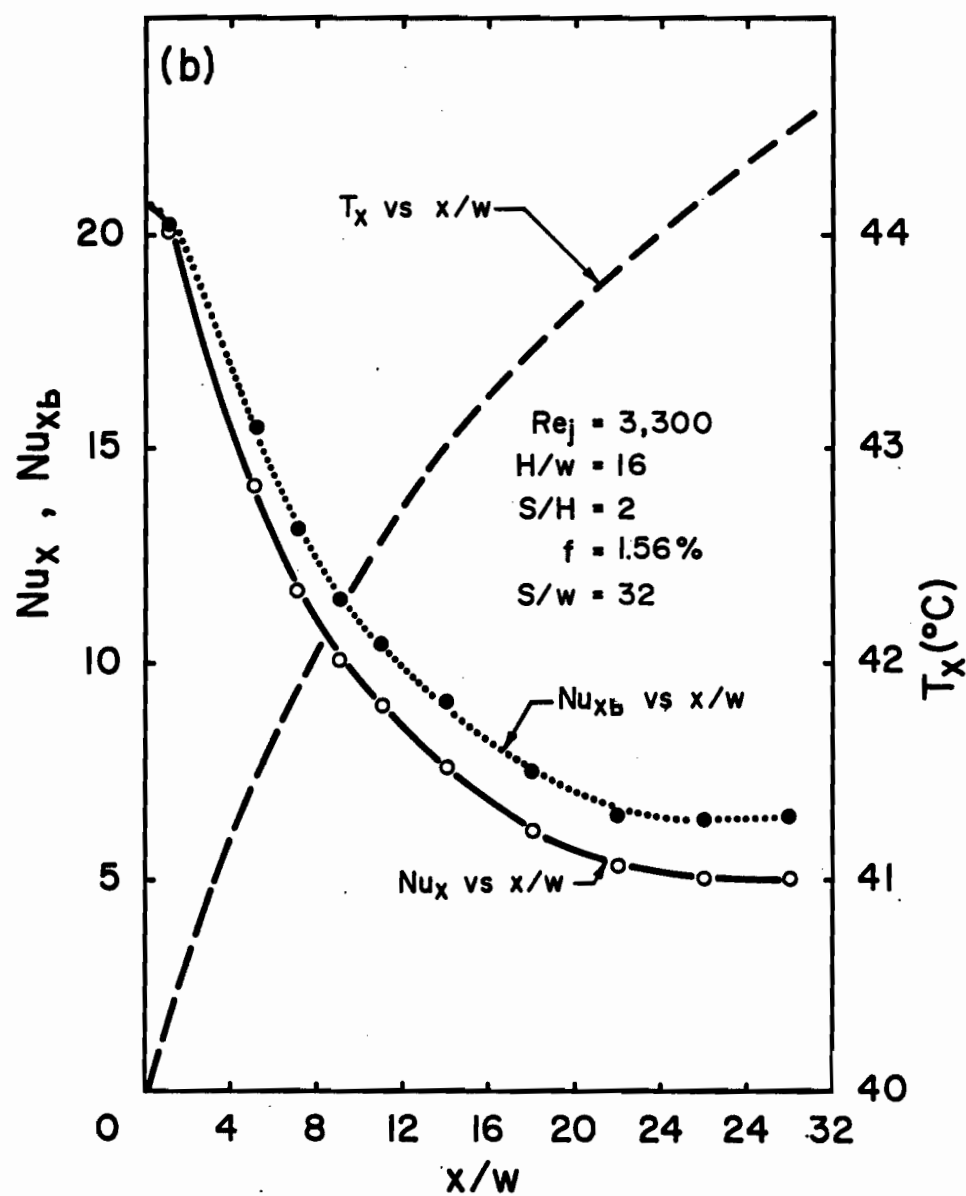


FIGURE 5.51(b) Lateral Profiles of T_x , Nu_x and Nu_{xb} for Multiple Jet System at $Re_j = 3300$, $S/H = 2$ and $H/w = 16$

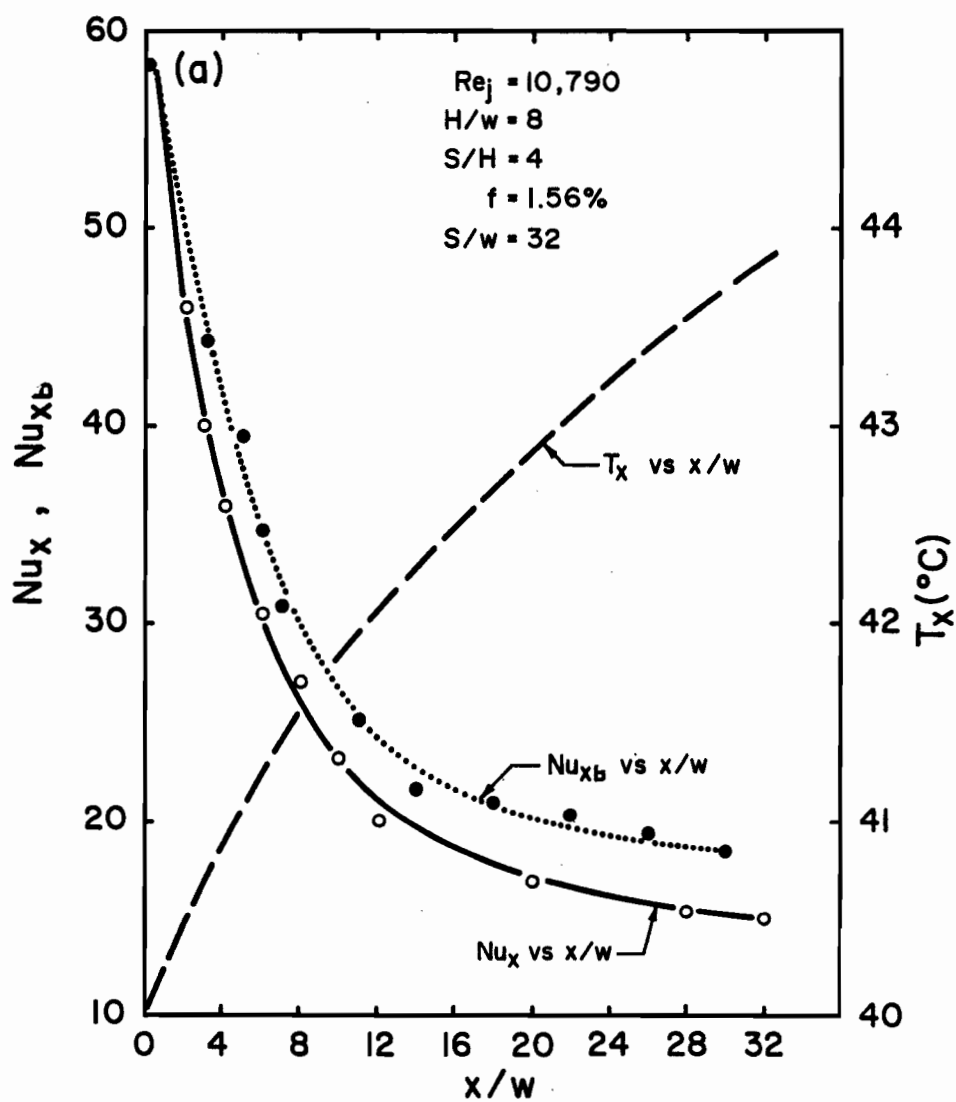


FIGURE 5.52(a) Lateral Profiles of T_x , Nu_x and Nu_{xb} for Multiple Jet System at $Re_j = 10790$, $S/H = 4$ and $H/w = 8$

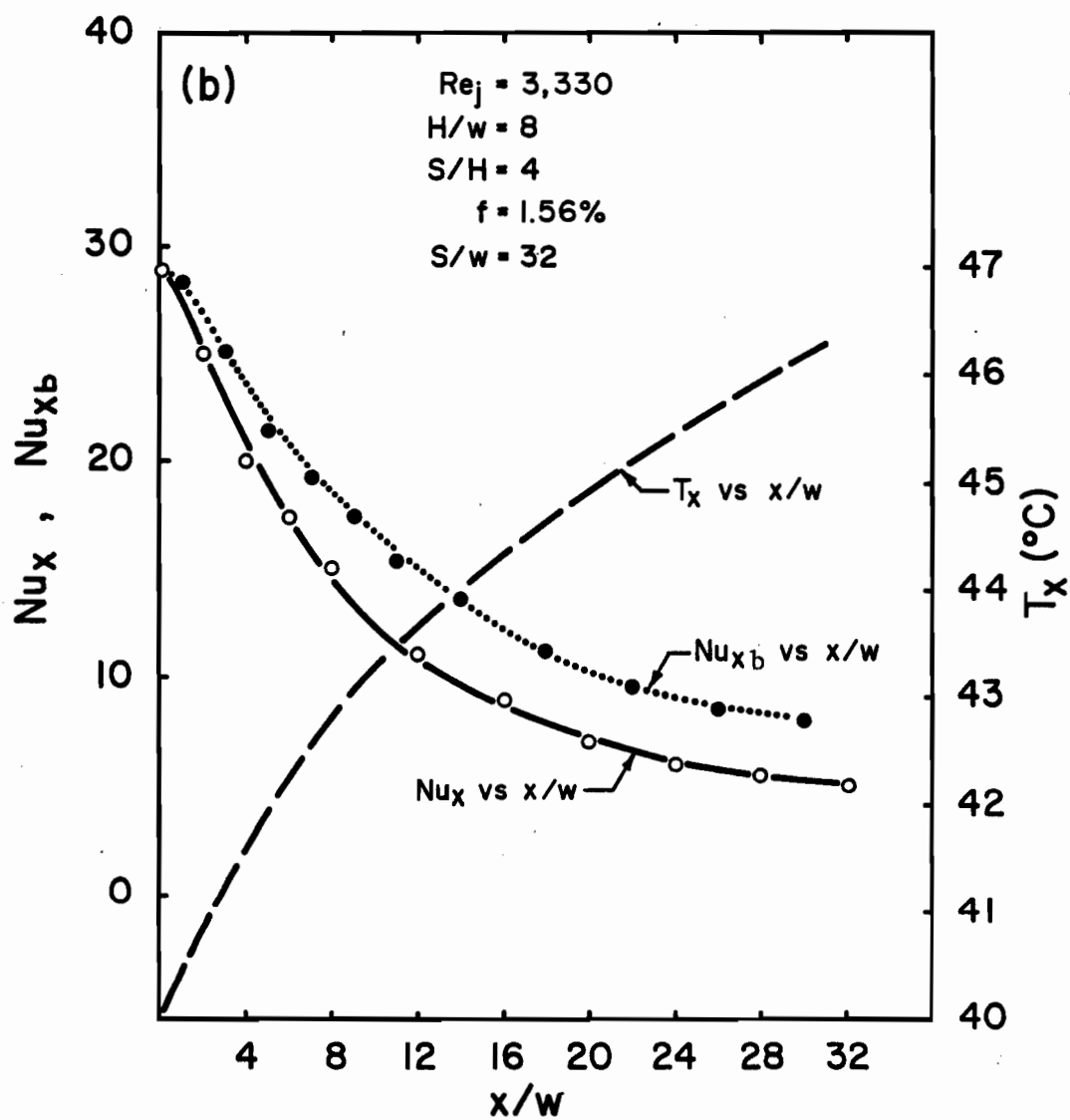


FIGURE 5.52(b) Lateral Profiles of T_x , Nu_x and Nu_{xb} for Multiple Jet System at $Re_j = 3330$, $S/H = 4$ and $H/w = 8$

run shown in Figure 5.52(a) is at the same Re_j and $S/w(f)$ as that of Figure 5.51(a), but a closer impingement surface spacing, i.e. $H/w = 8$ rather than 16w. At the closer spacing the heat transfer coefficients are naturally somewhat higher, hence the temperature rise (T_j to T_e) is larger, giving a larger reduction in ΔT from inlet to exit. Thus the increase in Nu_e associated with use of ΔT_x is greater (24%) for $H/w = 8$ spacing than for $H/w = 16$ where the correction was about 19%.

The last case, Figure 5.52(b), corresponds to the largest effect using local ΔT_x , in that at $H/w = 8$ the run portrayed has the lowest Re_j ($Re_j = 3300$) and the lowest open area ($f = 1.56\%$, $S/w = 32$) of the present study. In this case the temperature rise is from $T_j = 40^\circ\text{C}$ to $T_e = 46.2^\circ\text{C}$, hence a reduction in ΔT_x from 20°C to 14°C between nozzle and exhaust centerlines. At the nozzle exit in this extreme case Nu_{xb} is about 45% higher than Nu_x .

In conclusion, for a system of confined impinging jets, an analysis has been made of the effect of determining Nusselt number using a closed heat exchanger analysis, i.e. using a ΔT_x varying from inlet (nozzle centerline) to outlet (exhaust port centerline). This effect was quantified in relation to the conventional basis of analysis which uses a ΔT relative to T_j . With a system in which impingement surface temperature (T_s) is constant, local ΔT_x decreases continuously from its maximum value ($T_s - T_j$) at the nozzle centerline to the minimum ($T_s - T_e$) at the exit centerline. Thus use of the closed system analysis based on local ΔT_x leads to higher values of Nusselt number at all locations except at the stagnation point where the difference vanishes. The maximum difference occurs naturally at the exit centerline. For the range of flow and geometric parameters used in the present study the Nusselt number based on local ΔT_x is higher than that given in the preceding sections according to the conventional analysis by amounts ranging from insignificant

$$\overline{Nu} = \frac{1}{S/w} \int_{x/w \text{ at III/IV centerline}}^{x/w \text{ at IV/V centerline}} Nu_x d(x/w) \quad (5.4)$$

Calculation details and a complete tabulation of results is given in Appendix 2. In Section 5.4, two alternative bases of presenting heat transfer profiles were given, i.e. Nu_x and Nu_{xb} . As Nu_x is the basis used by all other investigators of impinging jet heat transfer, \overline{Nu} is computed from Nu_x to provide results on a common basis and to facilitate comparison.

Mean Nusselt number is expected to be a function of the flow parameter, Re_j and of two dimensionless parameters from the three geometric variables, H , S and w . As for the analysis of stagnation heat transfer and profiles, the two geometrical parameters chosen are the dimensionless spacing of the impingement surface from the nozzle exit (H/w) and either the flow cell proportion (S/H) or percent open area in the confinement surface (f). Mean heat transfer is then examined in three sets of figures, the first of which, Figures 5.53 through 5.56 shows for $H/w = 8, 16$ and 24 the effect of Re_j on \overline{Nu} with S/H as a parameter. The second set, Figures 5.57 through 5.59, gives \overline{Nu} as a function of S/H with Re_j as a parameter, for $H/w = 8, 16$ and 24 , respectively. The third set, Figures 5.60 through 5.64, shows explicitly the effect of H/w , with S/H shown as a parameter, for $Re_j = 5500, 11000$ and 15000 . Thus these sets of figures illustrate the dependence of \overline{Nu} on Re_j , S/H and H/w , thereby providing the basis for the general correlation, $\overline{Nu} = f(Re_j, H/w, S/H)$, presented as Figure 5.65. A comparison of results expressed as \overline{Nu} is given in Figure 5.66. Finally thermal effectiveness of the multiple jet system is shown in Figure 5.67.

Examination of the effect of flow and geometric parameters on \overline{Nu} is based closely on the findings already documented in Sections 5.3 and 5.4 for

the effect of these variables on the limiting values of Nu , i.e. Nu_o and Nu_e , and on the profiles of Nu_x between these limiting values at the inlet and exit of a flow cell of the multiple confined jet system. A key concept is the existence of two critical values of flow cell proportion, $(S/H)_{ce} = 1.5$, $(S/H)_{co} = 0.7$, as summarized clearly in Figure 5.37 of Section 5.4.2. It will be recalled that Figure 5.37 establishes the existence of three flow regimes: $S/H > 1.5$, where multiple slot jet systems are indistinguishable from an array of equivalent single jets; $0.7 < S/H < 1.5$, where heat transfer for multiple confined jets is enhanced over a region beginning at the exhaust port centerline; and $S/H < 0.7$, where stagnation point heat transfer is depressed by interaction between the inlet jet and exhaust flows in a multiple jet system of such a narrow flow cell proportion.

At specific values of H/w and S/H , Figures 5.53 through 5.55 indicate the dependence of \overline{Nu} on Re_j . Over the entire experimental region this relationship is of the type $\overline{Nu}/Re_j^n = \text{constant}$. The values of the slope n are displayed on Figure 5.56. As expected from Sections 5.3 and 5.4, \overline{Nu} dependence on Re_j becomes independent of flow cell proportion above the upper critical value, $(S/H)_{ce} = 1.5$. Although Figure 5.56 adequately confirms this expected independence for $S/H > 1.5$, the value displayed for the exponent n derives not from the limited data on Figure 5.56 but from a statistical correlation of all the experimental data for $S/H > 1.5$, as discussed subsequently. The value of the Re_j exponent in this region, 0.65, is as expected intermediate between the 0.57 exponent for Nu_o and the 0.8 exponent for fully developed turbulent flow.

As the flow cell proportion, S/H , is decreased below the upper critical value, $(S/H)_{ce} = 1.5$, Figure 5.56 shows that the Reynolds number dependence on \overline{Nu} increases significantly from 0.65 to about 0.76 at the lower

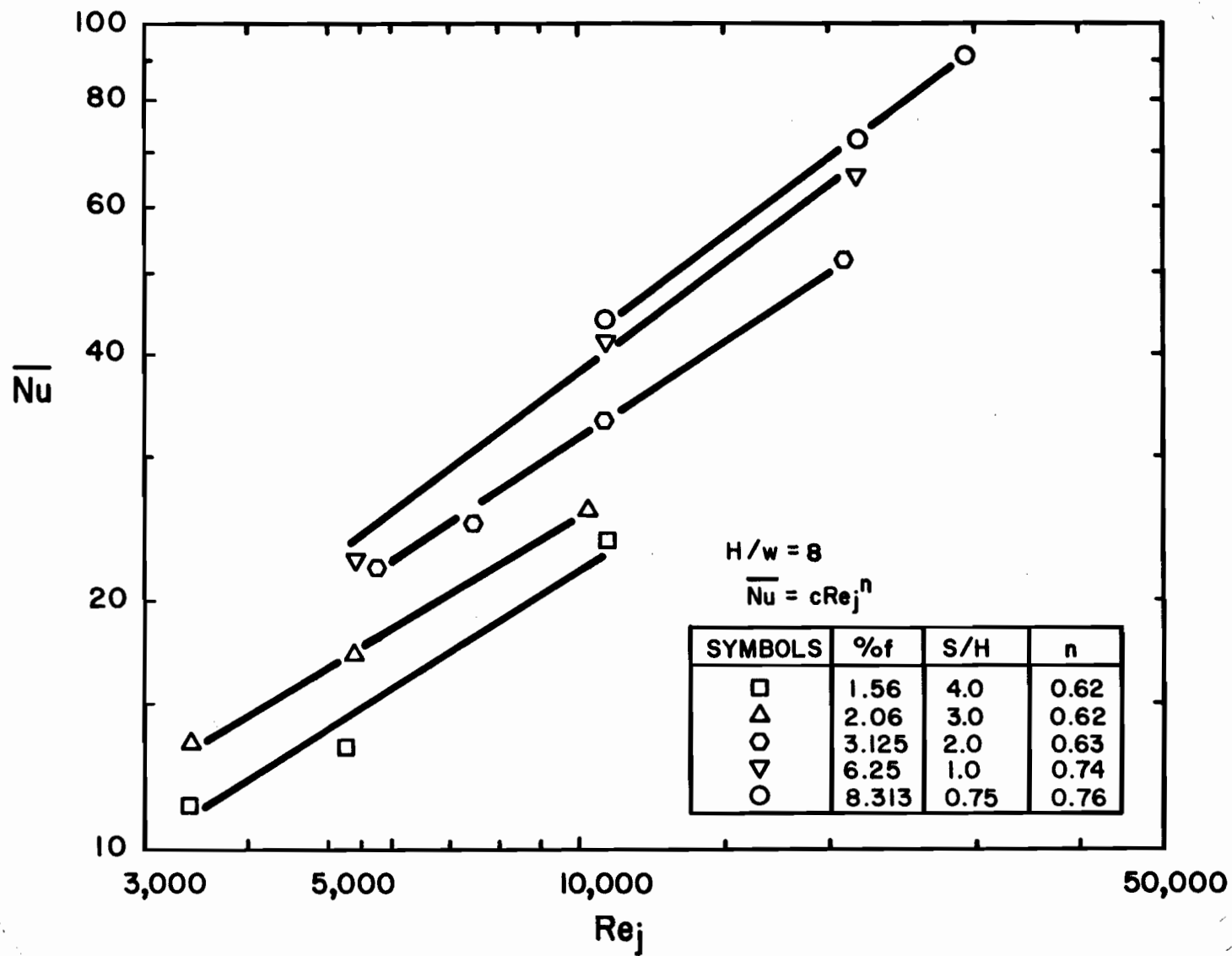


FIGURE 5.53 Effect of Re_j on \overline{Nu} for $H/w = 8$ and $0.75 \leq S/H \leq 4.0$

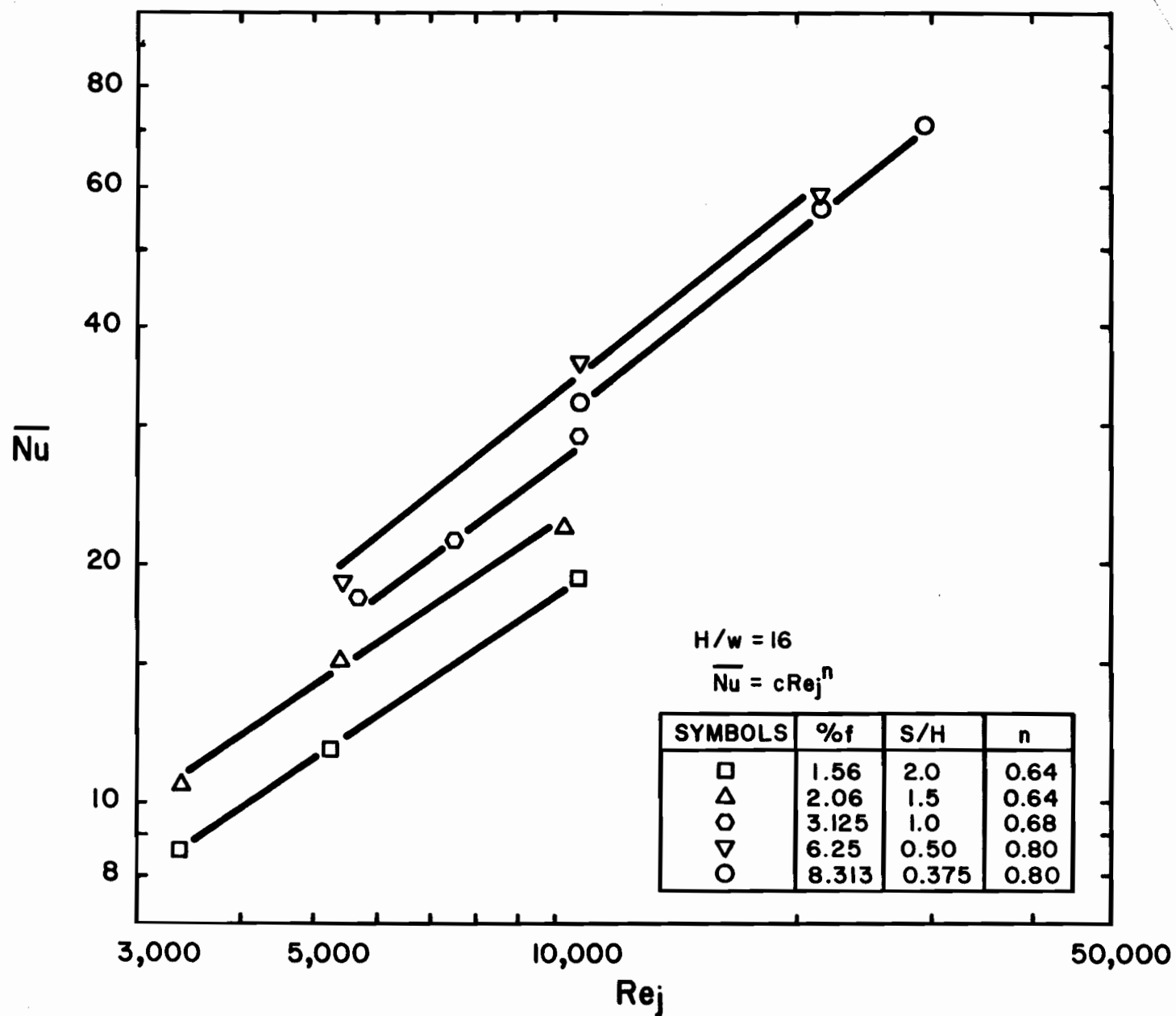


FIGURE 5.54 Effect of Re_j on \overline{Nu} for $H/w = 16$ and $0.375 \leq S/H \leq 2.0$

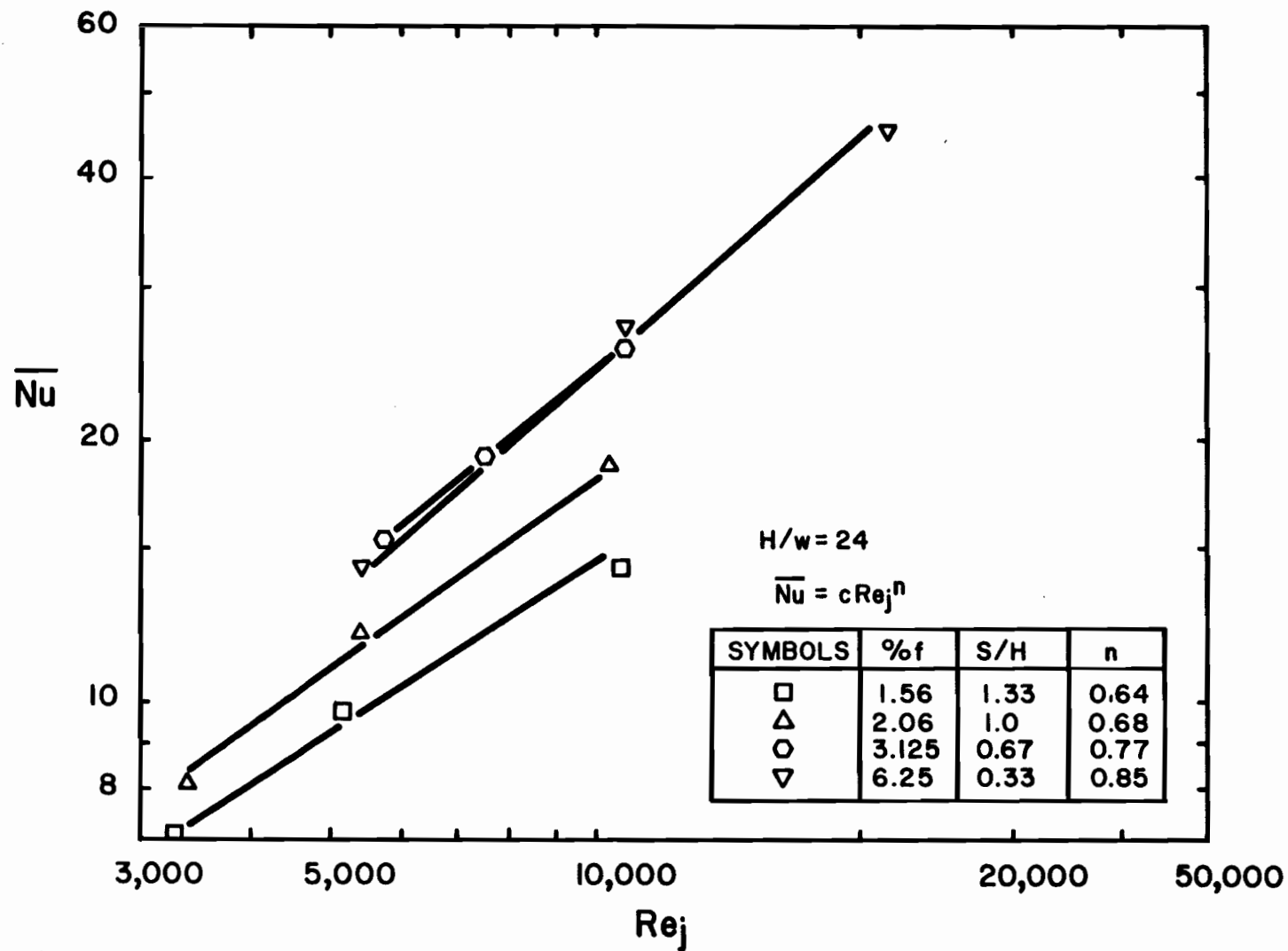


FIGURE 5.55 Effect of Re_j on \overline{Nu} for $H/w = 24$ and $0.33 \leq S/H \leq 1.33$

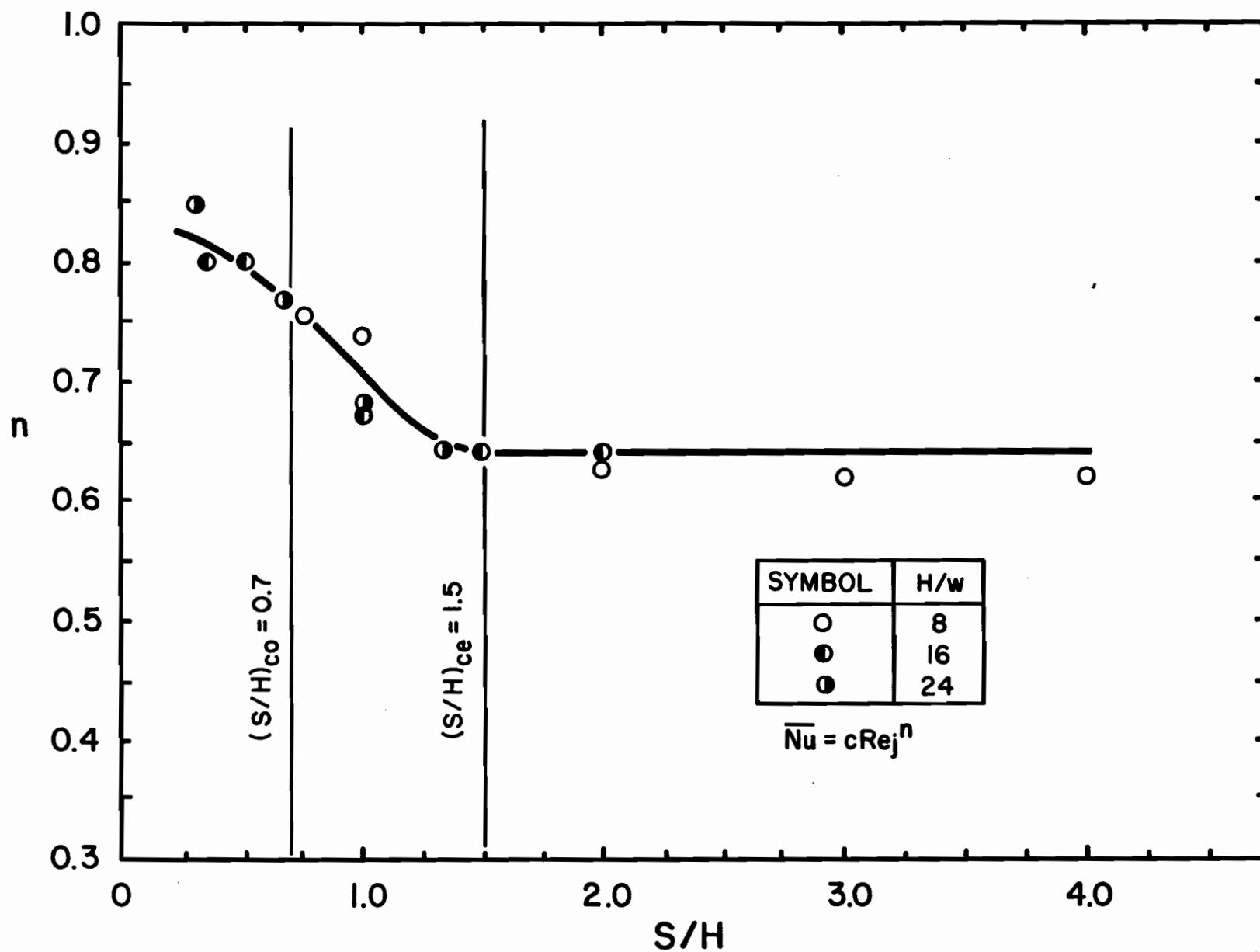


FIGURE 5.56 Effect of Flow Cell Proportion on the Slope n for $\overline{Nu} = C Re_j^n$

critical value, $(S/H)_{co} = 0.7$. The increased sensitivity of \overline{Nu} to Re_j as flow cell proportion is decreased from 1.5 to 0.7 is a reflection of increased turbulence and mixing under the exit port which causes the increase of Nu_e for S/H below 1.5, as discussed in Section 5.4. As the flow cell width is reduced below the lower critical value, $(S/H)_{co} = 0.7$, the further increase in \overline{Nu} sensitivity to Re_j is associated with the interaction of inlet jet with exhaust flow having reached the nozzle centerline, as documented in Sections 5.3 and 5.4.

For specific values of Re_j (5500, 11000 and 15000) and for $H/w = 8, 16$ and 24, Figures 5.57 through 5.59 indicate the dependence of \overline{Nu} on S/H , with Re_j and H/w as parameters. The few points in the second set of figures (5.57 through 5.59) which are derived from extrapolation of data on the first set (5.53-5.55) are identified with dashed lines. These graphs clearly indicate that mean Nusselt number passes through a maximum over this range of flow cell proportion and that, over the entire range of Re_j and H/w , the maximum value of \overline{Nu} occurs at the same value, i.e. at about $S/H = 0.5$. As the flow cell proportion is increased above $S/H = 0.5$, \overline{Nu} decreases because the dominant effect is the corresponding decrease in proportion of area which can be considered impingement region. In this connection it is pertinent to point out that in Chapter 4 it was established through Figures 4.31 and 4.32 that the limits of the impingement region was about $S/H = 0.5$ and independent of Re_j and H/w . As the flow cell proportion is decreased below $S/H = 0.5$, \overline{Nu} decreases because the advantage of more closely spaced jets is now more than counterbalanced by the reduction in impingement region heat transfer due to deleterious interaction between inlet jets and exhaust flows, as documented on Figure 5.37.

Moreover, Figures 5.57-5.59 reveal that as S/H increases above the

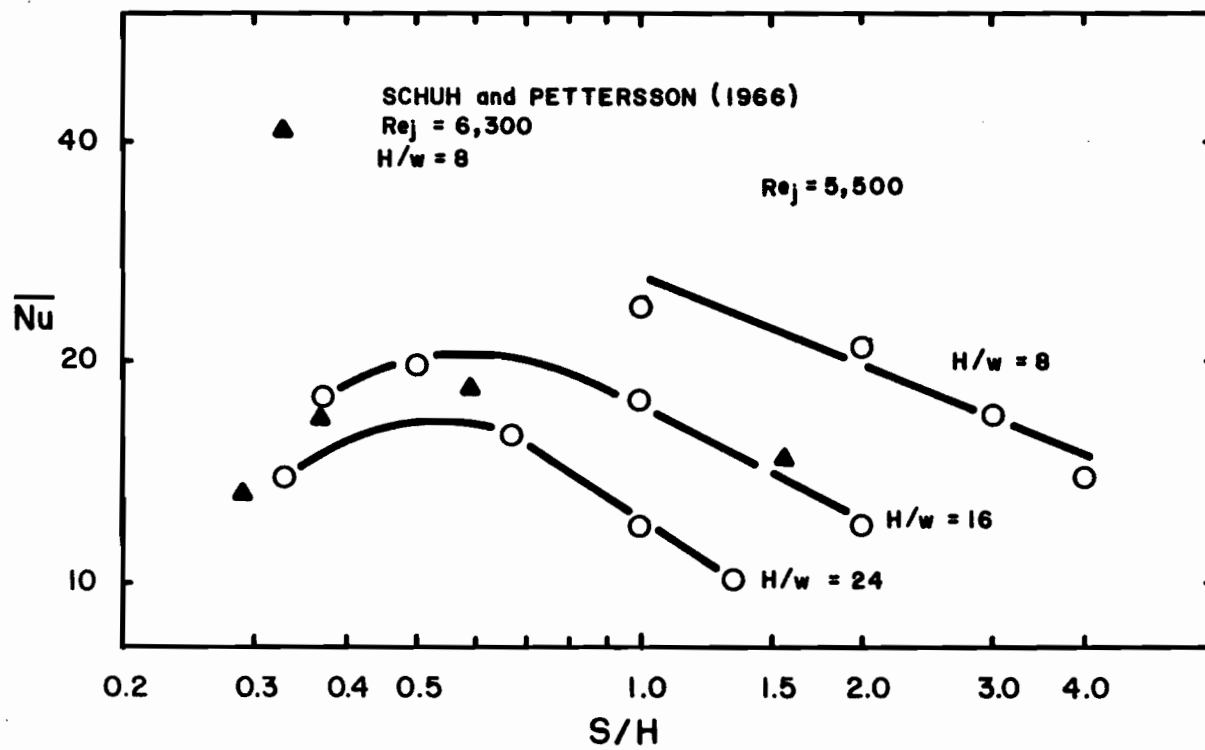


FIGURE 5.57 Effect of S/H on \overline{Nu} for $Re_j = 5500$ and $H/w = 8, 16$ and 24 and Nu of Schuh and Pettersson (1966)

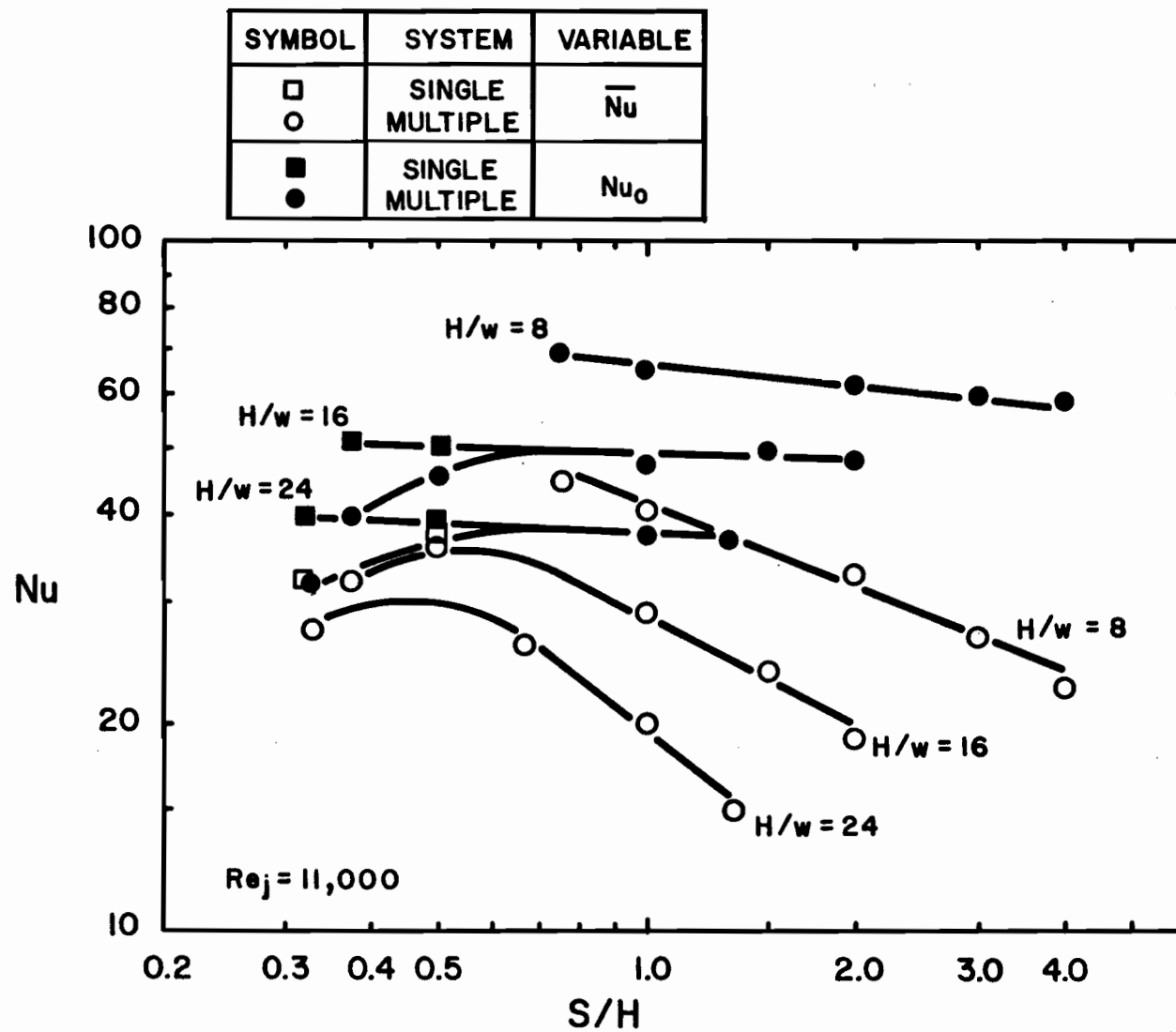


FIGURE 5.58 Effect of S/H on Nu for $Re_j = 11000$ and $H/w = 8, 16$ and 24 for Multiple and Single Jet Systems

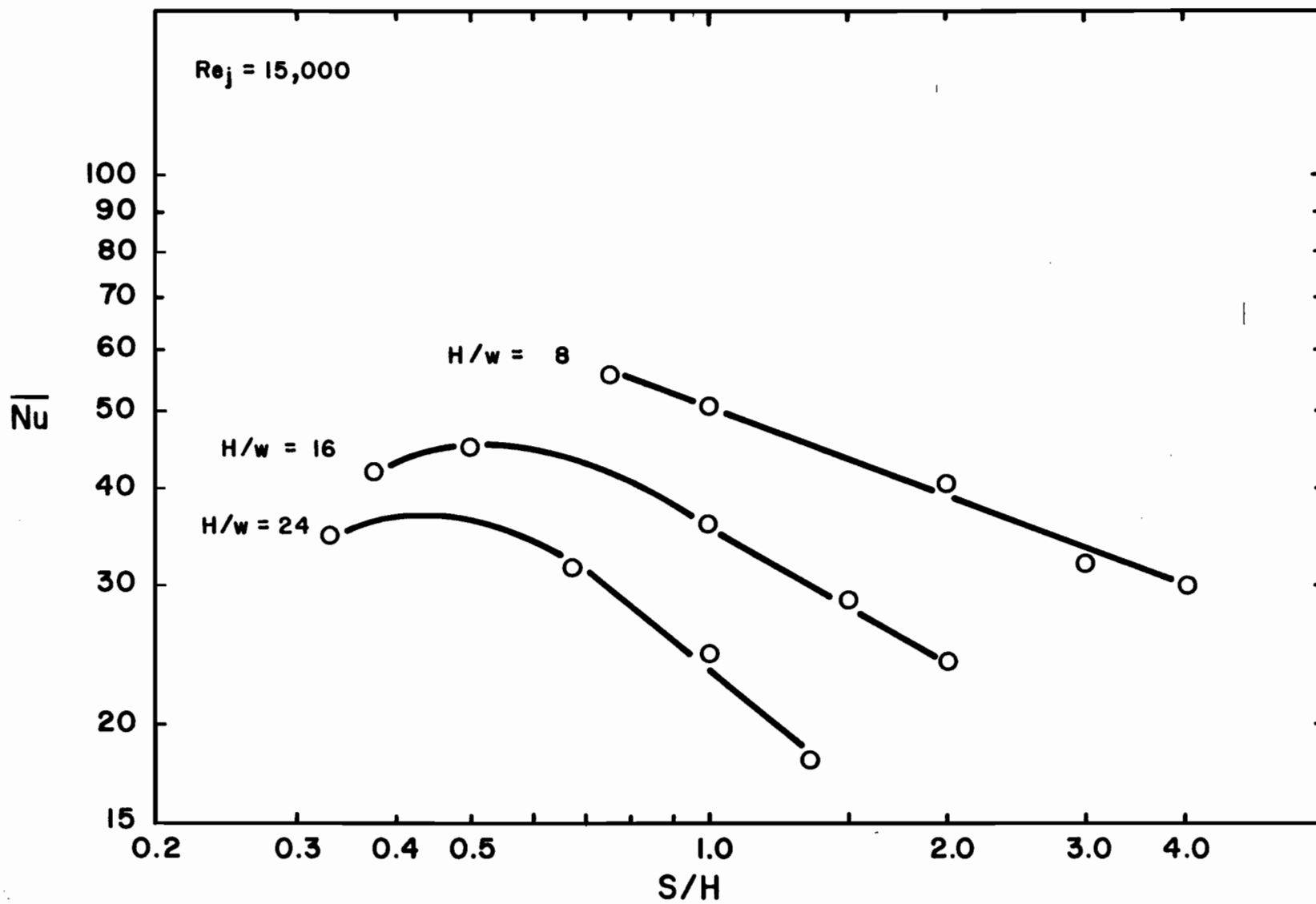


FIGURE 5.59 Effect of S/H on \overline{Nu} for $Re_j = 15000$ and $H/w = 8, 16$ and 24

value for the mean Nusselt maximum, the decrease of \overline{Nu} , expressed logarithmically, becomes linear for values of $S/H \geq 0.7$. Furthermore the onset of this region of logarithmic linear dependence occurs at the same value of S/H over the full range of Re_j and H/w investigated. It is notable that the lower limit of this region of linear dependence, $S/H = 0.7$, is also the value, $(S/H)_{co}$, below which interaction between a closely spaced inlet jet and exhaust flow depresses heat transfer at the stagnation point (Nu_o). Although there is some variation in the slope, it will subsequently be demonstrated by a multiple linear regression correlation of all the data that the dependence of \overline{Nu} on S/H may be adequately represented by $\overline{Nu}/(S/H)^a = \text{constant}$, with a single value of the exponent, $a = -0.55$, for the entire experimental range of Re_j and H/w .

On Figure 5.58 the two experimental points for \overline{Nu} for single jets have been added by comparison. For a single jet, S denotes the lateral extent of the impingement surface over which \overline{Nu} is calculated. The single jet \overline{Nu} values are for $S/H = 0.5$, $H/w = 16$, and $S/H = 0.33$, $H/w = 24$. At $S/H = 0.5$ the multiple jet \overline{Nu} is seen to be only slightly lower than for the equivalent single jet, a comparison which may be also seen from the complete profile on Figure 5.33(b). At $S/H = 0.33$ however, the multiple jet \overline{Nu} is significantly below that for the equivalent single jet due to the strong depression of Nu_o for S/H as low as 0.33, which the complete profile on Figure 5.36(b) clearly illustrated. As the single jet profiles for the flow cell proportions of 4 and 2 are indistinguishable from the equivalent multiple jet profiles of Figures 5.29(a) and 5.32(a), it is evident that the corresponding points for \overline{Nu} on Figure 5.58 would likewise be coincident with the multiple jet data shown.

Another additional feature of Figure 5.58 is the inclusion of the cor-

responding three lines of Nu_o for comparison with \overline{Nu} . The values of Nu_o for single jets are essentially independent of S/H , as indicated by the nearly zero slope of these three lines. The slight decrease of Nu_o with increasing S/H is not a result of any S/H dependence but arises because in this series of experiments an increase in S/H is associated with a decrease in slot width, w . Thus this small dependence is in fact simply the dimensional effect of nozzle width discussed in Section 5.3. The values of Nu_o for multiple jets begin to deviate from the linear, nearly horizontal relationship when S/H drops below the critical value, $(S/H)_{co} = 0.5$, as was discussed extensively in Section 5.3. However, the representation of Nusselt number with respect to S/H in Figure 5.58 is a particularly relevant method of illustrating this $(S/H)_{co}$ critical value. For each value of H/w , the pair of profiles, Nu_o and \overline{Nu} , on Figure 5.58 demonstrates how as S/H is decreased \overline{Nu} first increases, approaches the level of Nu_o , then passes through the maximum in \overline{Nu} which occurs always at $S/H = 0.5$, and finally drops for an increasingly narrow $S/H < 0.5$. It is interesting to note that for the same Re_j and H/w , the maximum in \overline{Nu} is about 70% of Nu_o .

The set of figures showing S/H dependence also serves to show a comparison with a previous multiple jet study. Thus Figure 5.57 includes data of Schuh and Pettersson (1966) for an unconfined multiple slot jet system at $Re_j = 6300$ and $H/w = 8$, expressed now in terms of S/H , not a variable recognized by them. For their four data points a maximum in \overline{Nu} appeared at some value of S/H above 0.6. Although they presented no analysis of the effect, they noted that "there are other trends, notably a maximum of the average heat transfer coefficient at about for instance $H/w = 16$ and $S/w = 14$. These details cannot be explained yet because of the complex flow pattern and lack of detailed flow investigations". A maximum in \overline{Nu} at $H/w = 16$, $S/w = 14$,

corresponds to $S/H = 0.87$, somewhat above the value of $S/H = 0.5$ which the present investigation identifies as the flow cell proportion for maximum \overline{Nu} . Moreover, the present study documents the complex flow pattern and eliminates the lack of detailed flow investigations noted by Schuh and Pettersson.

The third part of the graphical analysis of mean heat transfer, Figures 5.60, 5.61 and 5.62, illustrates the influence of H/w on \overline{Nu} , with Re_j and S/H as parameters over the same range of values. The principle overall effect is the occurrence of a quite broad maximum in \overline{Nu} at some spacing between $H/w = 4$ and $H/w = 8$. The occurrence of a more sharply defined maximum in Nu_o at $H/w = 8$ is well-known and is documented again in the present study in Figures 5.15-5.21. For ease of comparison of the cases of Nu_o and \overline{Nu} , a set of stagnation point results has been added to Figure 5.61. It may be noted that for all Re_j and S/H values of these three figures, \overline{Nu} is in fact slightly higher (up to 10%) at $H/w = 4$ than at $H/w = 8$. Thus the value of H/w for the intervening maximum in \overline{Nu} appears generally to be around $H/w = 5$.

It is apparent that for $H/w \geq 8$, logarithmic dependence of \overline{Nu} on H/w is reasonably linear, i.e. may be represented as $\overline{Nu} = c(H/w)^m$ with m independent of H/w but possibly dependent on either Re_j or S/H . For interacting multiple jets, i.e. for $S/H = 1.5$, Figure 5.63 clearly indicates the tendency in Figures 5.60 to 5.62 for \overline{Nu} to become less sensitive to H/w at lower values of S/H , but that m is independent of Re_j . As there are for $S/H \geq 1.5$ only a limited number of combinations of data to define lines at constant Re_j and S/H on Figures 5.60-5.62, there are not a sufficient number of such points to define the value of m for $S/H \geq 1.5$ on Figure 5.63. However, as it has been thoroughly documented in the present study that for flow cell proportion that wide, multiple jets become simply an array of single jets

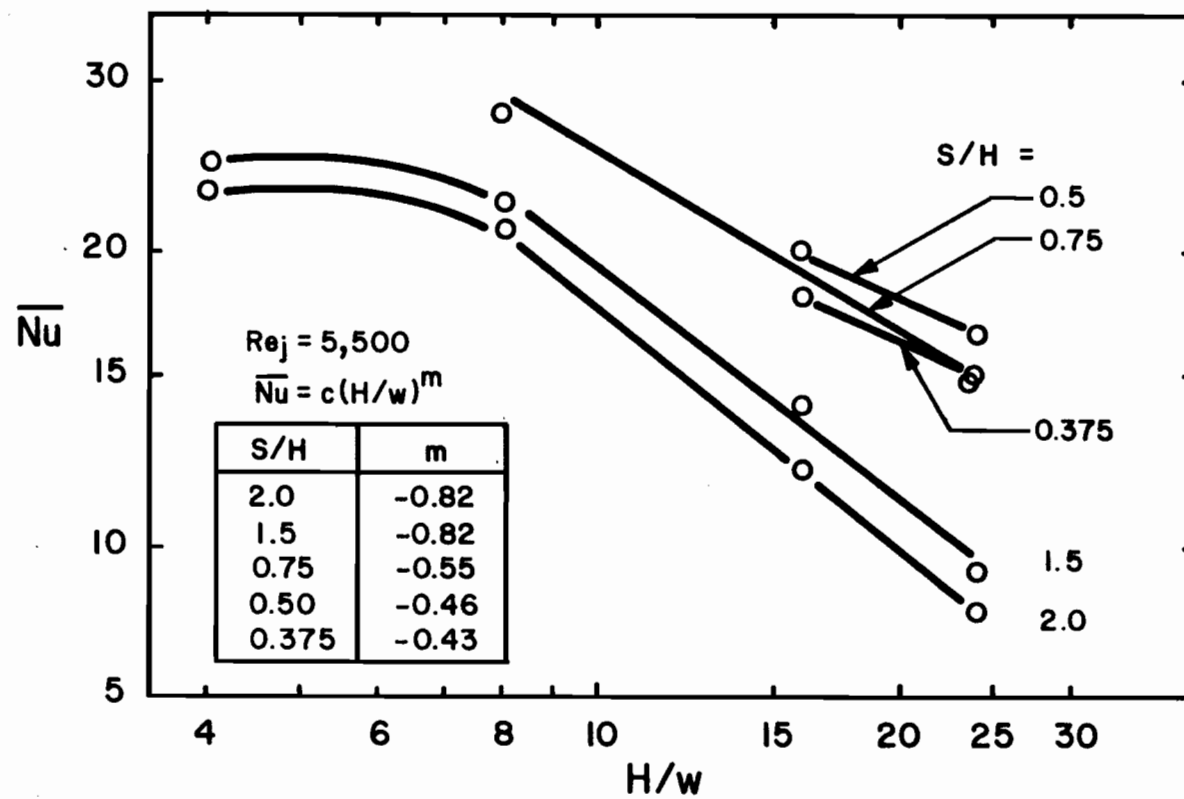


FIGURE 5.60 Effect of H/w on \overline{Nu} for $Re_j = 5500$ and $0.375 \leq S/H \leq 2$

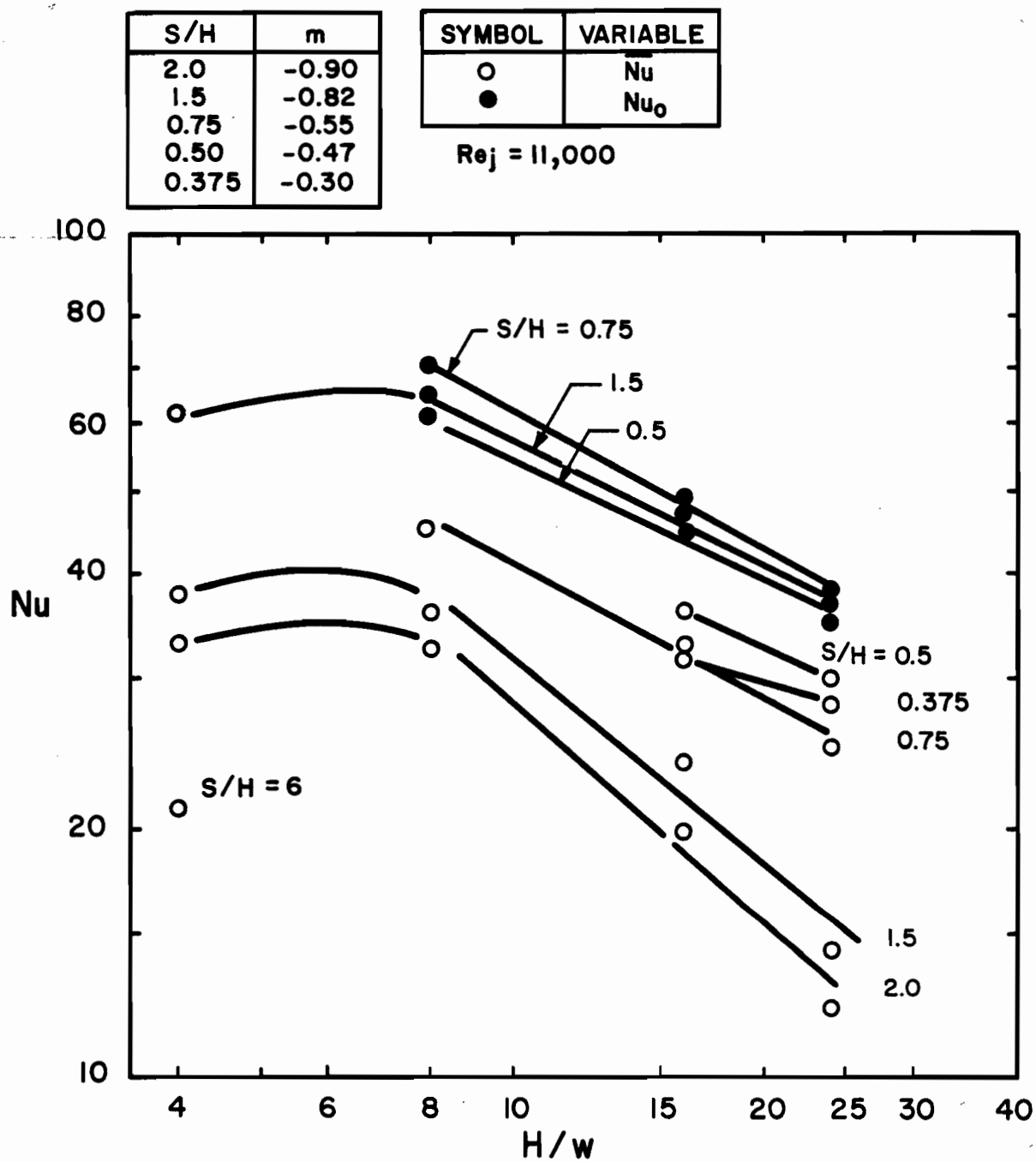


FIGURE 5.61 Effect of H/w on Nu for $Re_j = 11000$ and $0.375 \leq S/H \leq 6$

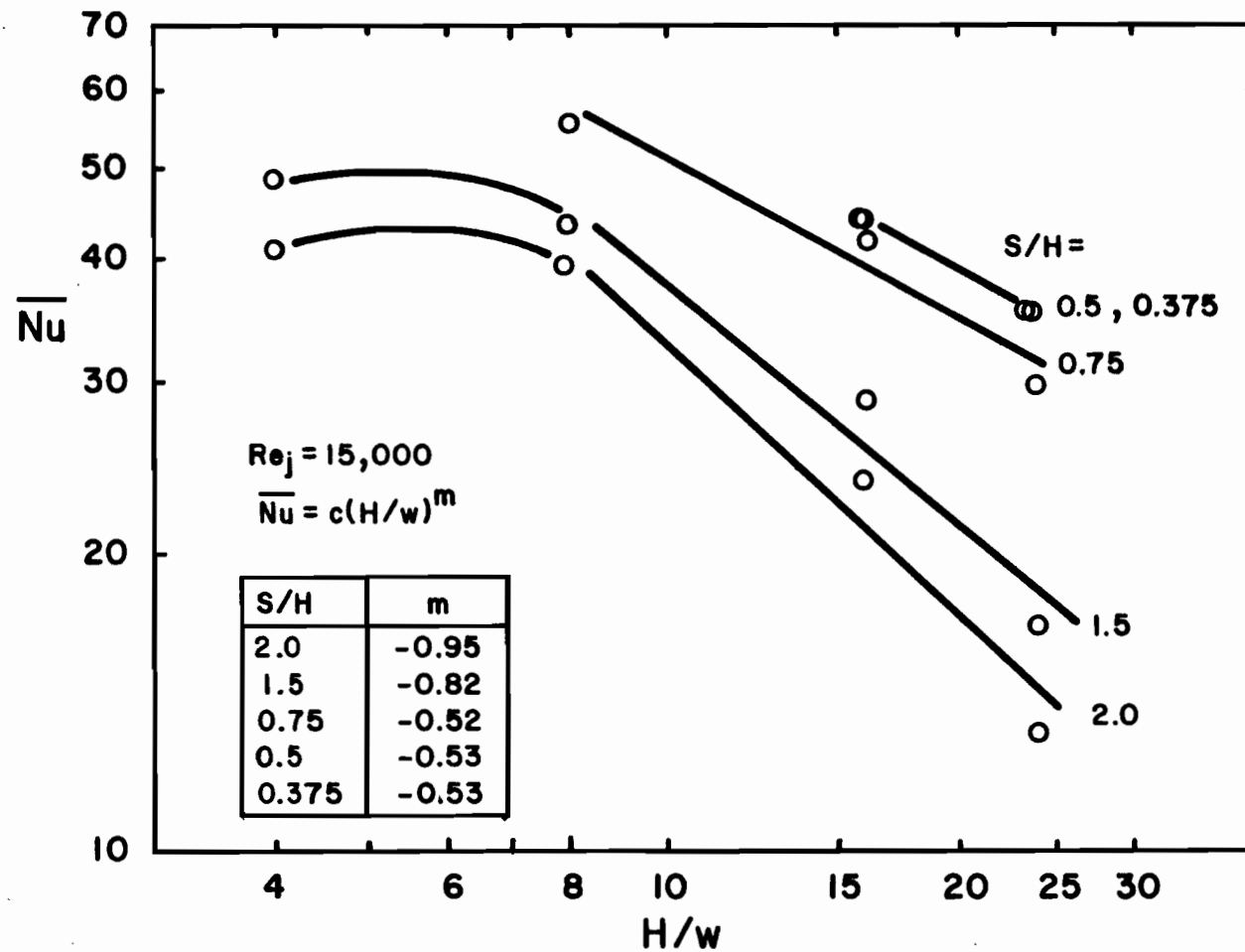


FIGURE 5.62 Effect of H/w on \overline{Nu} for $Re_j = 15000$ and $0.375 \leq S/H \leq 2$

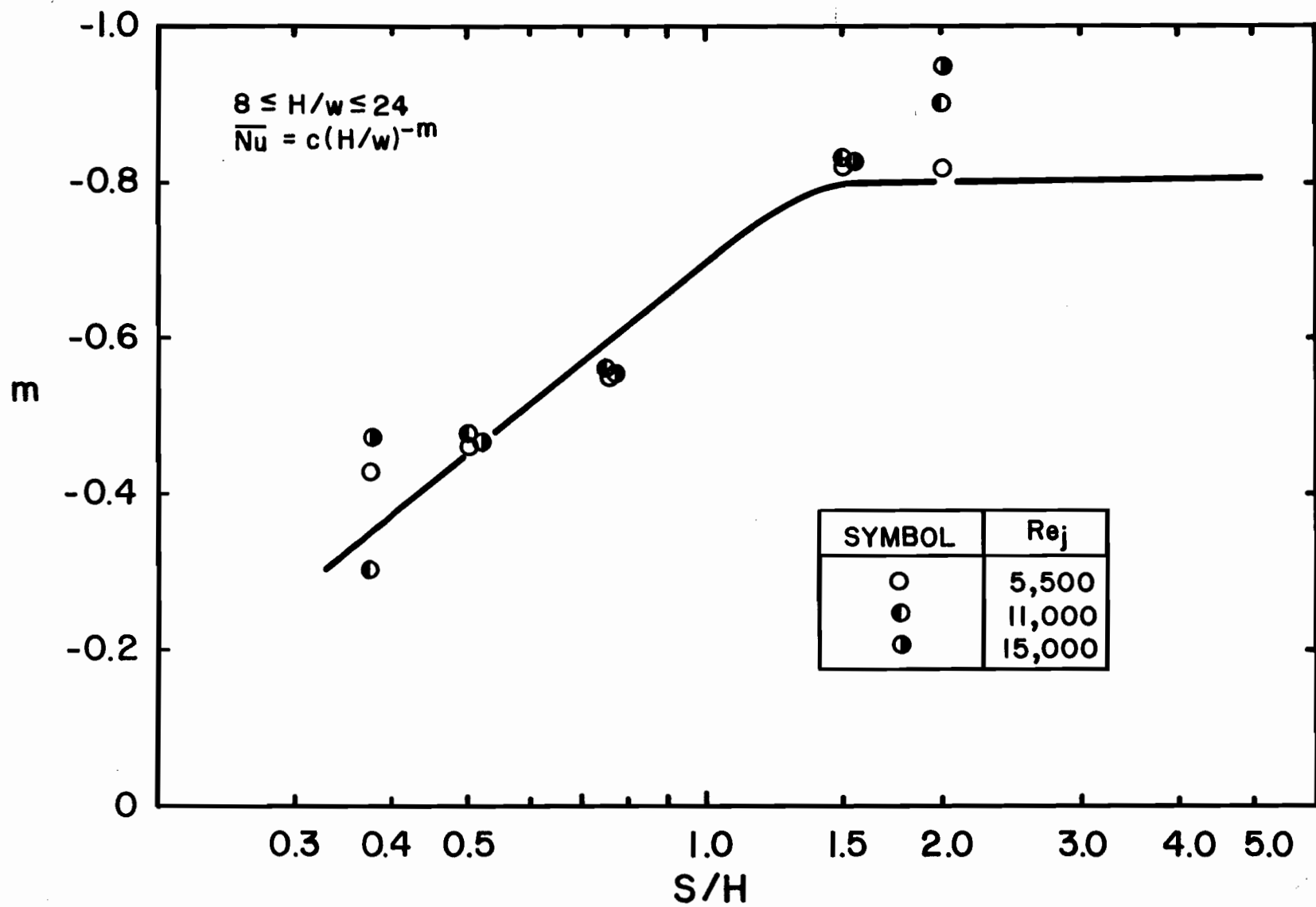


FIGURE 5.63 Effect of Flow Cell Proportion on the Slope m for $\overline{Nu} = C(H/w)^{-m}$

and all parameters such as m become independent of S/H . A multiple linear regression of all experimental data for $S/H > 1.5$ confirmed that a single value ($m = -0.8$) applied for the relationship $\overline{Nu} = c(H/w)^m$ in the non-interacting region, and is so indicated on Figure 5.63.

When H/w is chosen as one dimensionless geometric parameter it has frequently been noted in the present study that the second independent dimensionless parameter could be S/H , S/w or f . Thus while all lines on Figures 5.60 through 5.62 are at constant S/H , Figure 5.64 has been included to illustrate the equivalent representation of effect of H/w on \overline{Nu} at constant f rather than constant S/H . The same general effect prevails, although with some variation. For example, the \overline{Nu} maximum for $Re_j = 10910$ on Figure 5.64 is sharper than those of Figure 5.61 because on Figure 5.64 reduction of impingement surface spacing from 8 to 4 is also associated with an increase of S/H from 1 to 2 and the latter effect adds another contribution to the reduction in \overline{Nu} at the smallest spacing. As both flow and heat transfer aspects of the present study have established that S/H is a geometric parameter of fundamental significance, its use is in general preferable over the alternatives of f or S/w .

Examination of the form of dependence of \overline{Nu} on Re_j , S/H and H/w , as represented by Figures 5.53 through 5.64, was the first step in formulating an appropriate comprehensive correlation. This examination may be summarized as:

- (1) The effect of Re_j on \overline{Nu} is of the form $\overline{Nu} = c(Re_j)^n$, with n independent of Re_j and H/w . For non-interacting multiple jets, $S/H \geq 1.5$, n is also independent of S/H , but for interacting multiple jets n is a function of S/H as indicated on Figure 5.56.
- (2) The effect of H/w on \overline{Nu} when represented as $\overline{Nu} = c(H/w)^m$ is rea-

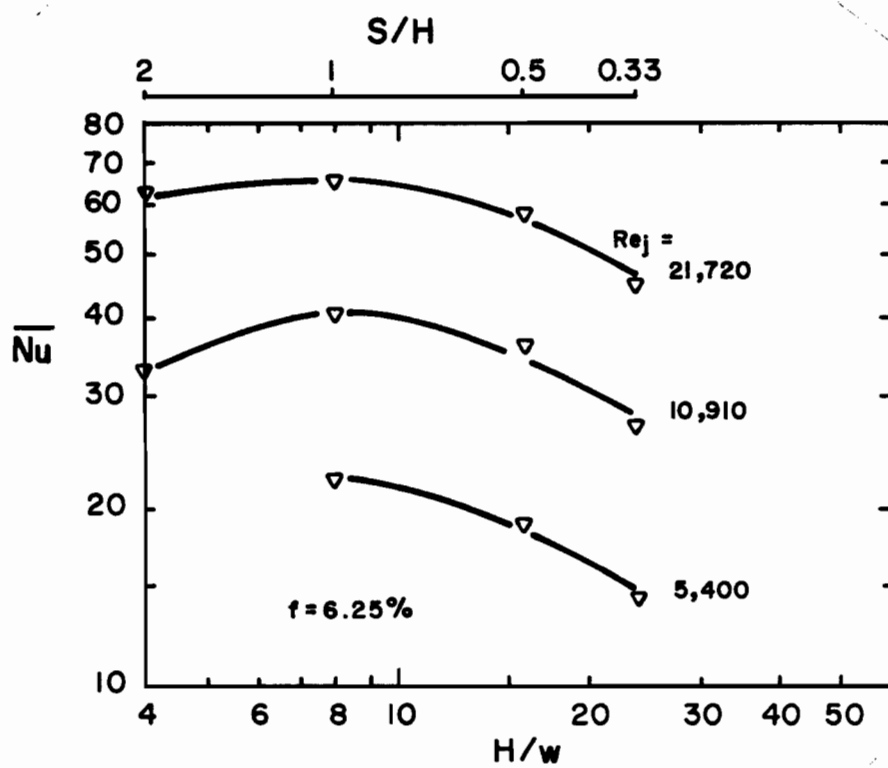


FIGURE 5.64 Effect of H/w on \overline{Nu} for $f = 6.25\%$ and $Re_j = 5400$, 10910 and 21720

sonably linear, i.e. m independent of H/w , only for $H/w \geq 8$. For spacings in this linear range of H/w the exponent m is independent of Re_j , while with respect to S/H , m is independent for non-interacting multiple jets ($S/H \geq 1.5$), but for interacting jets in narrower flow cells, m varies with S/H as indicated by Figure 5.63.

- (3) As the dependence on S/H of \overline{Nu} at constant Re_j and H/w represented on Figures 5.57 through 5.59 clearly shows a nonlinear logarithmic dependence below the lower critical flow size, $(S/H)_{co} = 0.7$, and as the exponents n and m vary with S/H for interacting multiple jets, it is clear that S/H is the most sensitive of the four dimensionless parameters to be correlated, \overline{Nu} , Re_j , S/H and H/w .

The above analysis suggests the appropriate form of correlation to be:

$$\frac{\overline{Nu}}{(Re_j)^n (H/w)^m} = c(S/H)^a \quad (5.5)$$

For non-interacting jets, $S/H \geq 1.5$, for which all three exponents are constants, a multiple linear regression gave the following form:

$$\frac{\overline{Nu}}{(Re_j)^{0.65} (H/w)^{-0.8}} = 0.63(S/H)^{-0.55} \quad (5.6)$$

The right-hand side of this equation is the line on Figure 5.65 for $S/H \geq 1.5$, while the data shown in this non-interacting region are the experimental values of \overline{Nu} , Re_j and H/w expressed as the function on the left of equation (5.6). Equation (5.6) also represents \overline{Nu} for confined single slot jets with S denoting the lateral extent of the impingement surface for which the mean Nusselt number is obtained.

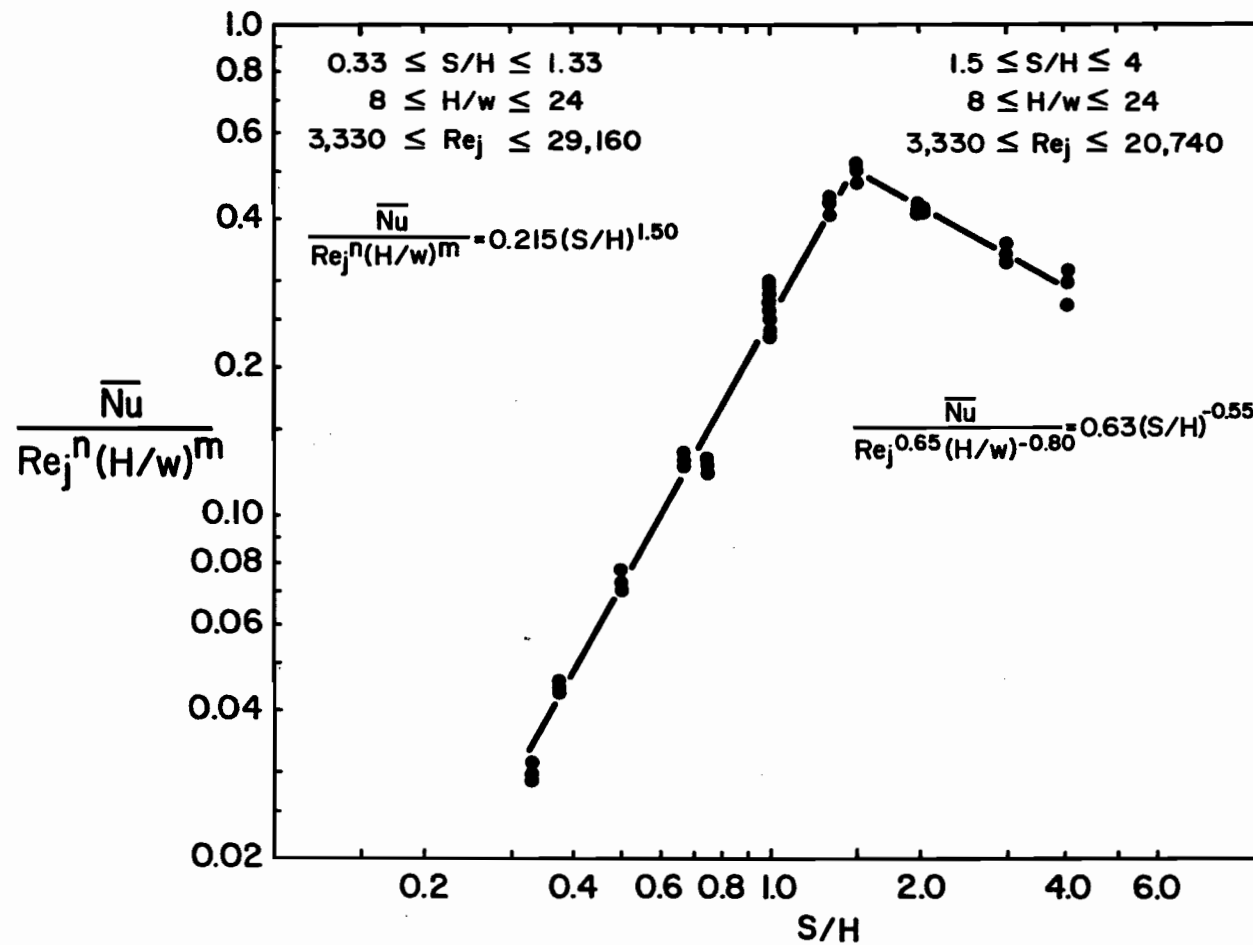


FIGURE 5.65 Average Heat Transfer Correlations for Non-Interacting and for Interacting Jets

For interacting multiple jets, the data shown on Figure 5.65 for $S/H < 1.5$ are the experimental values expressed as the function $\frac{\overline{Nu}}{(Re_j)^n (H/w)^m}$, with n and m as functions of S/H from Figures 5.56 and 5.63. The line on Figure 5.65 for $S/H < 1.5$ is the best fit of these data, which is

$$\frac{\overline{Nu}}{(Re_j)^n (H/w)^m} = 0.215 (S/H)^{1.5} \quad (5.7)$$

The only experimental range not covered by the general correlations (5.6) and (5.7), and their representation on Figure 5.65, is for spacings $4 \leq H/w < 8$ where \overline{Nu} is nonlinear in H/w , i.e. m depends on H/w . However, it was previously pointed out that there is a broad maximum in \overline{Nu} over this range of H/w and, moreover, that \overline{Nu} at $H/w = 4$ was never more than 10% higher than at $H/w = 8$. Therefore if a value of \overline{Nu} for spacing in the range $4 \leq H/w < 8$ is required, the value for $H/w = 8$ should be determined from equation (5.6) or Figure 5.65. If that value of \overline{Nu} was increased by 5%, the resulting value would be within $\pm 5\%$ of the correct value of \overline{Nu} over the range $4 \leq H/w < 8$.

Equations (5.6) and (5.7) and Figure 5.65 represent the final step in interpretation and correlation of data as \overline{Nu} in the present study. The correlation form derives from the study reported in Chapter 4 of the flow characteristics of a confined multiple impinging slot jet system, from which it was concluded that a parameter of fundamental significance was flow cell proportion, S/H . As analysis of stagnation point heat transfer and profiles in Sections 5.3 and 5.4 confirmed the importance of S/H as a key parameter, the general correlation of \overline{Nu} incorporated this variable and the limits of upper and lower critical flow cell proportion, $(S/H)_{ce}$ and $(S/H)_{co}$. Thus the final correlation, Figures 5.56, 5.63 and 5.65, illustrates a close integra-

tion into the general correlation for mean heat transfer of the characterization of the flow field as represented by the choice of S/H as a variable. The success achieved in obtaining a general correlation for \overline{Nu} through use of results of flow characterization of multiple impinging jet systems is evident in the satisfactory agreement shown on Figure 5.65 which covers the entire range from completely non-interacting to partially interacting to completely interacting multiple jet systems.

While Figure 5.65 shows the spread of data around the general correlation lines expressed as $\frac{\overline{Nu}}{(Re_j)^n (H/w)^m}$, it is also informative to observe the spread of data expressed directly as \overline{Nu} . Such a comparison is provided by Figure 5.66. Here, all the experimental data for \overline{Nu} at $Re_j = 11000$ are shown, as earlier on Figure 5.61, but on Figure 5.66 the lines shown are from the general correlations (5.6), (5.7) and associated Figures 5.56, 5.63 and 5.65. It can be seen that the general correlation adequately fits the data over the entire range from linear correlation for totally non-interacting multiple jets ($S/H > 1.5$), to the slightly nonlinear region of partially interacting jets ($1.5 > S/H > 0.7$) to the quite nonlinear region of totally interacting jets ($S/H < 0.7$). The lines of the general correlation display the broad maximum in \overline{Nu} noted earlier at around $S/H = 0.5$.

It was noted in Chapter 2 that one of the few previous studies of multiple slot jets was that of Gardon and Akfirat (1966), whose system was however one of unconfined jets. As recorded in Table 2.1 these authors obtained a logarithmic linear correlation for \overline{Nu} as a function of Re_j , f and H/w , all with constant coefficients. However it is now clear from the perspective of the flow characterization of the present study that their study likewise covered the entire range from completely non-interacting to completely interacting multiple jets, i.e. their experimental conditions correspond to a

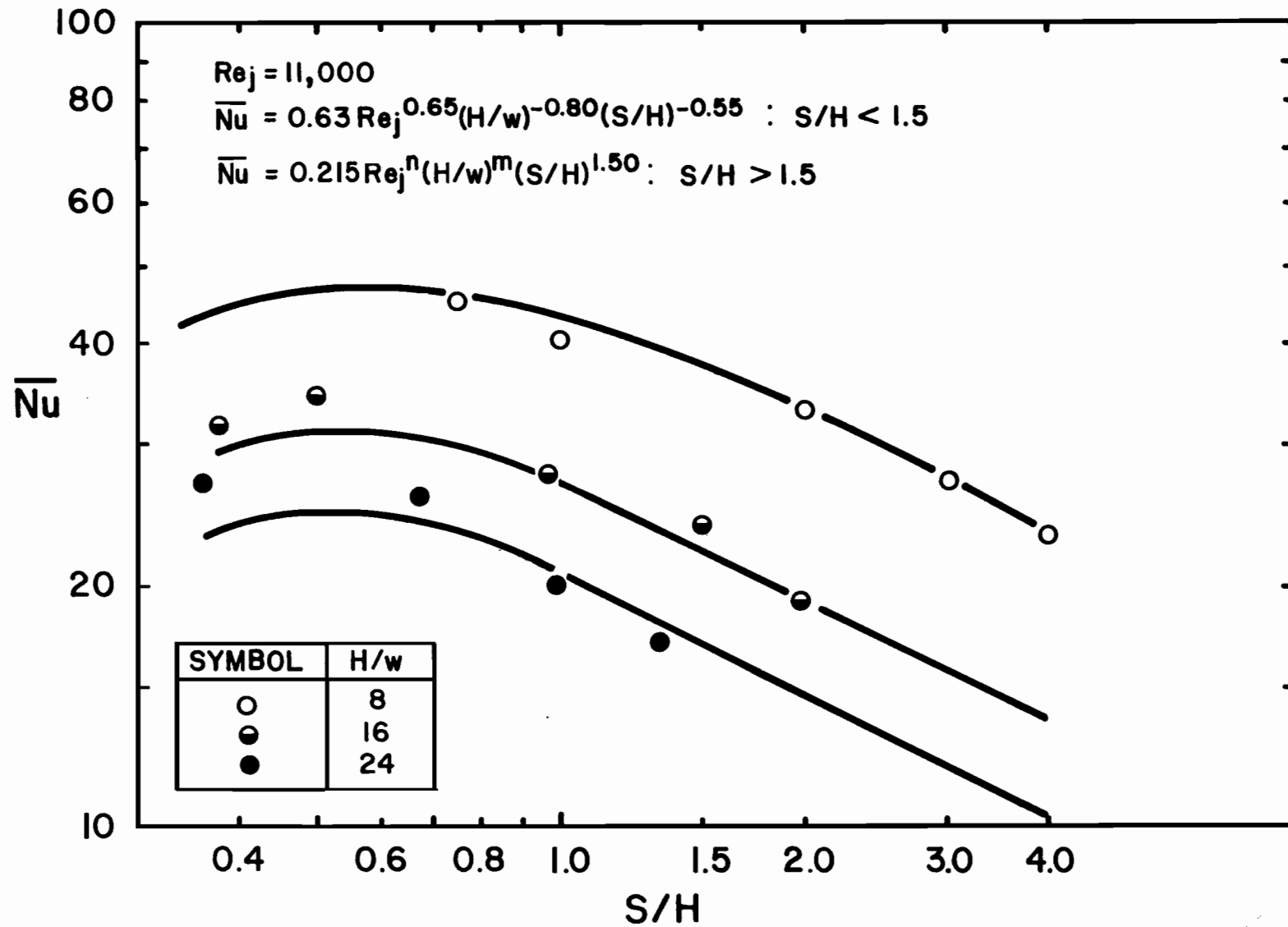


FIGURE 5.66 Average Heat Transfer for $Re_j = 11000$, $H/w = 8, 16$ and 24 and $0.33 \leq S/H \leq 4$: Correlation and Experiment

range in S/H between 0.2 and 4. Figures 5.56, 5.63, 5.65 and the associated equations (5.6) and (5.7) of the present study establish that the experimental data do not fit a single logarithmic linear relation with constant coefficients, such as that reported by Gardon and Akfirat,

$$\overline{Nu} = 0.66 Re_j^{0.62} f^{0.38} (H/w)^{-0.31}$$

On Figure 5.66 for example, it is clear that a linear correlation, i.e. with constant exponents over the entire range from interacting to non-interacting jets, would provide a significantly poorer fit to the distinctly nonlinear data. Any linear correlation such as that of Gardon and Akfirat would also be unable to represent the maximum in \overline{Nu} which occurs at about $S/H = 0.5$ for all values of Re_j and H/w , an important finding of the present study. Moreover, as multiple jet systems have markedly different flow and heat transfer characteristics in the interacting and non-interacting regions, the constants in any correlation which fails to make this differentiation become strong functions of the proportion of data taken for these distinctly different flow regimes.

As noted in Chapter 2 the other notable study of transport under multiple impinging slot jets was that of Martin and Schlünder (1973). These authors in fact report the only known previous study in which the system was closed with a confinement surface, as indicated in Figure 2.2. Unfortunately, instead of providing for spentflow to leave through exhaust ports between the nozzles in the confinement surface, they made provision for the spentflow to exit from the apparatus at the two sides perpendicular to the length of the slot nozzles. Consequently their apparatus gave transfer rates which were quite nonuniform in the direction of the slot nozzle length with maximum transfer rates at each edge. For industrial applica-

tion such nonuniformity in transfer rates in the nozzle slot direction is generally highly undesirable.

Aside from this restriction in utility of the results of Martin and Schlünder's study, they like Gardon and Akfirat obtained a single correlation for all their experimental data which, when expressed in terms of the flow cell proportion parameter of the present study, is seen to cover the range of S/H between 0.12 and 27.5, i.e. from highly interacting to totally non-interacting multiple jets. A natural consequence of this lack of differentiation as to flow is that the numerical parameters of their correlation, as for that of Gardon and Akfirat, would be a function of the proportion of experimental data taken in the interacting and non-interacting flow regimes.

However, as the form of correlation developed by Martin and Schlünder is much less simple than that of Gardon and Akfirat, they were able to deduce the conditions for maximum \overline{Nu} from their correlation. The geometric conditions for maximum \overline{Nu} as determined by Martin and Schlünder for their correlation and from the present study are listed below, together with the value of \overline{Nu} at $Re_j = 11000$ for each set of geometric parameters, the value of \overline{Nu} being calculated from the corresponding general correlation. Comparison of values for maximum \overline{Nu} for a pair of independent geometric parameters, H/w and S/H , indicates a significant difference between these two studies, i.e. H/w of 10 and 5, and S/H of 0.7 and 0.5. More interesting yet is that at the same value of Re_j , the maximum \overline{Nu} is about 30% higher for the present study. Although distinct differences in data processing and correlation procedure between these two studies have been pointed out, it appears that a some part of the large difference between the respective values of maximum \overline{Nu} must be attributed to the difference noted in spentflow patterns.

TABLE 5.3. Geometric Configuration for Maximum \overline{Nu}

Parameter	Martin (1977)	Present System
S/w	7	2.5
H/w	10	5
S/H	0.7	0.5
f, %	7	20
\overline{Nu} at $Re_j = 11000$	39.2	51.4

The few previous studies of heat transfer under multiple jets have used H/w and f as the basic geometric parameters while the analysis developed in the present study has established H/w and S/H as the preferred choice. As there are simple relationships between these parameters, it might be claimed that the choice is unimportant in that only the numerical parameters of correlations would change depending on the choice of f or S/H. This point may be examined with the aid of a tabulation of corresponding values of f and S/H over the range of H/w spacings of the present study, determined from the relation $f = \frac{1}{2(S/H)(H/w)}$. In particular, as the results of the present study indicate a maximum in \overline{Nu} at $S/H = 0.5$, an onset of jet interaction and depression of Nu_o at $S/H = 0.7 = (S/H)_{co}$, and the onset of jet interaction and enhancement of Nu_e at $S/H = 1.5 = (S/H)_{ce}$, it is of interest to calculate the values for percent open area, f, for these three values of S/H, over this range of H/w.

H/w	Open Area Ratio , f, for		
	S/H = 0.5	S/H = 0.7	S/H = 1.5
	%	%	%
4	25	17.9	8.3
8	12.5	8.9	4.2
16	6.25	4.5	2.1
24	4.17	3.0	1.4

This tabulation indicates for example that according to the spacing, H/w , multiple jets begin to interact for values of f between 8.3% and 1.4%, interaction begins to depress Nu_o at f between 17.9% and 3.0%, while the maximum \overline{Nu} occurs at f between 25% and 4.17%. Thus where each of these three key characteristics occurs at a unique value of S/H , the corresponding values of open area ratio , f , vary widely. This tabulation provides another indication of why S/H is a far more meaningful and useful dimensionless geometric parameter for multiple impinging jet systems than is open area ratio , f . It is the flow characterization component of the present study which established the importance of the previously unrecognized flow parameter, S/H and the existence of several flow regimes, and which led thereby to a much more significant analysis of Nu_o , Nu profiles and \overline{Nu} than has previously been possible.

In view of the relevance of the present data for use in design of impingement dryers such as for the Papridryer process proposed for drying paper (Burgess et al., 1972a, b), the results expressed as average heat transfer coefficient, \bar{h} (W/m^2-K) have been presented on Figures 5.67(a), (b) and (c) as a function of fan energy consumed at the nozzle exit per unit area of heat transfer, R_j (W/m^2). Reduction in \bar{h} at low values of S/H is evident on these graphs. In spite of their obvious limitations, such dimensional correlations

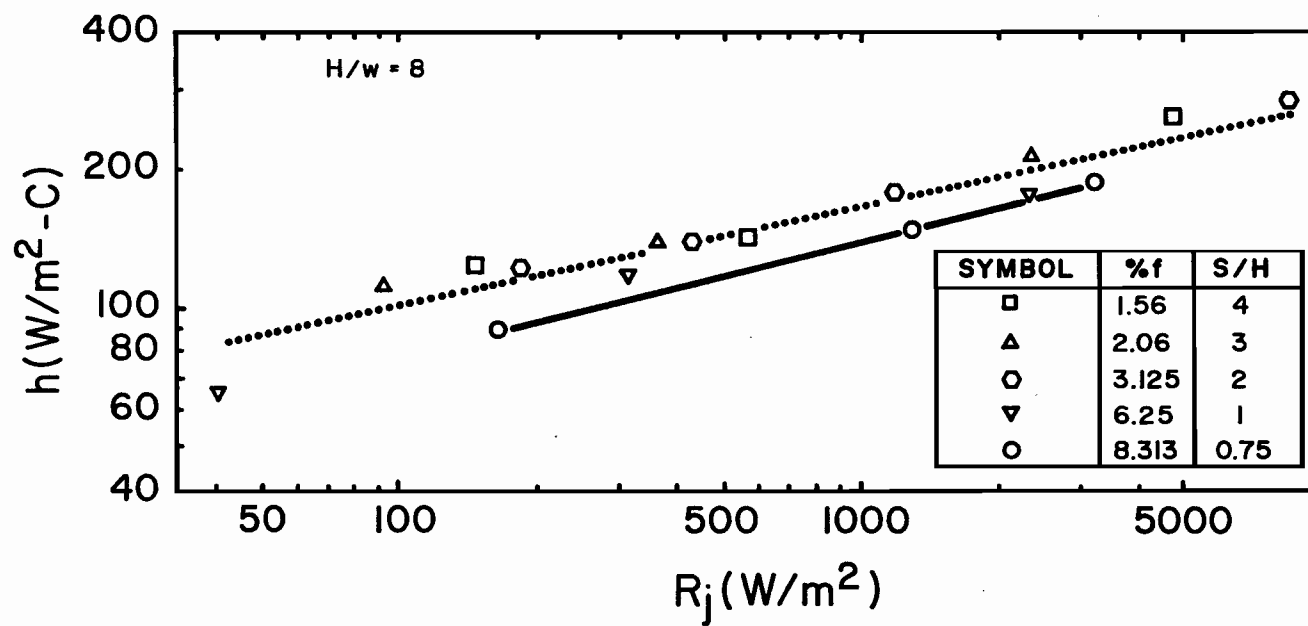


FIGURE 5.67(a) Effect of R_j on \bar{h} for $H/w = 8$ and $0.75 \leq S/H \leq 4$

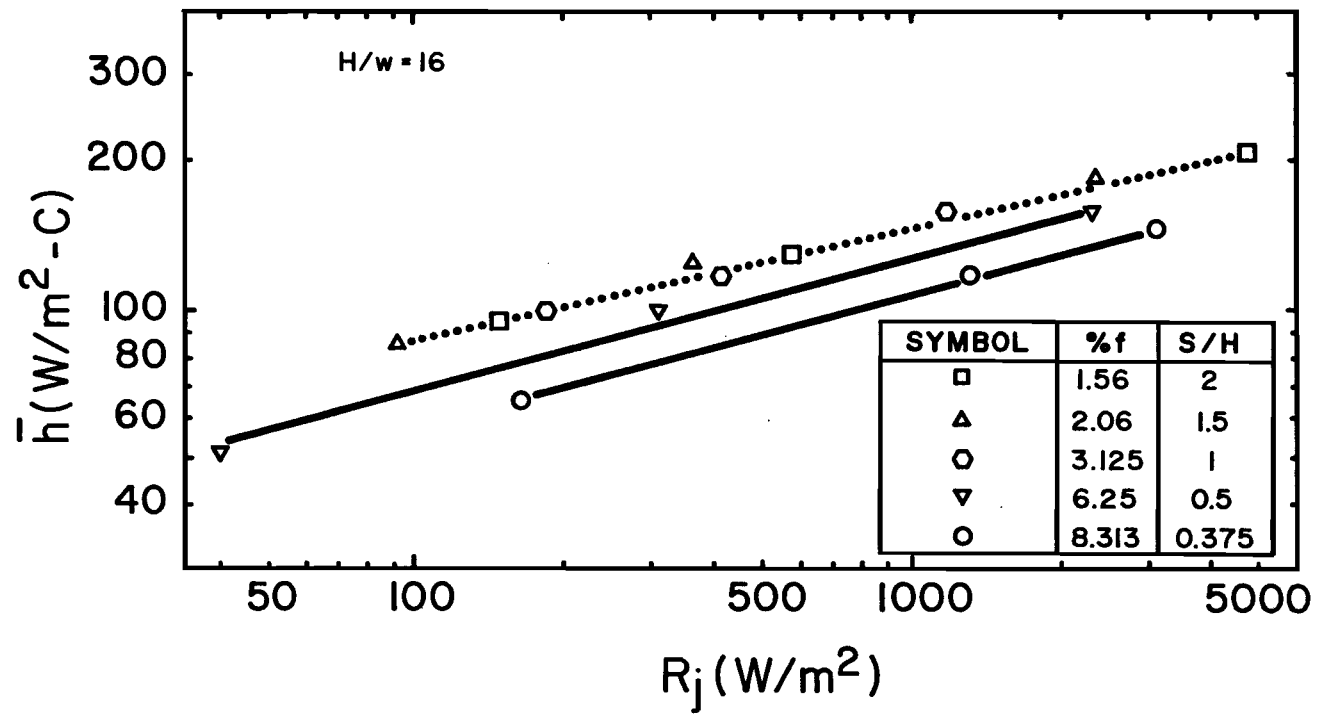


FIGURE 5.67(b) Effect of R_j on \bar{h} for $H/w = 16$ and $0.375 \leq S/H \leq 2$

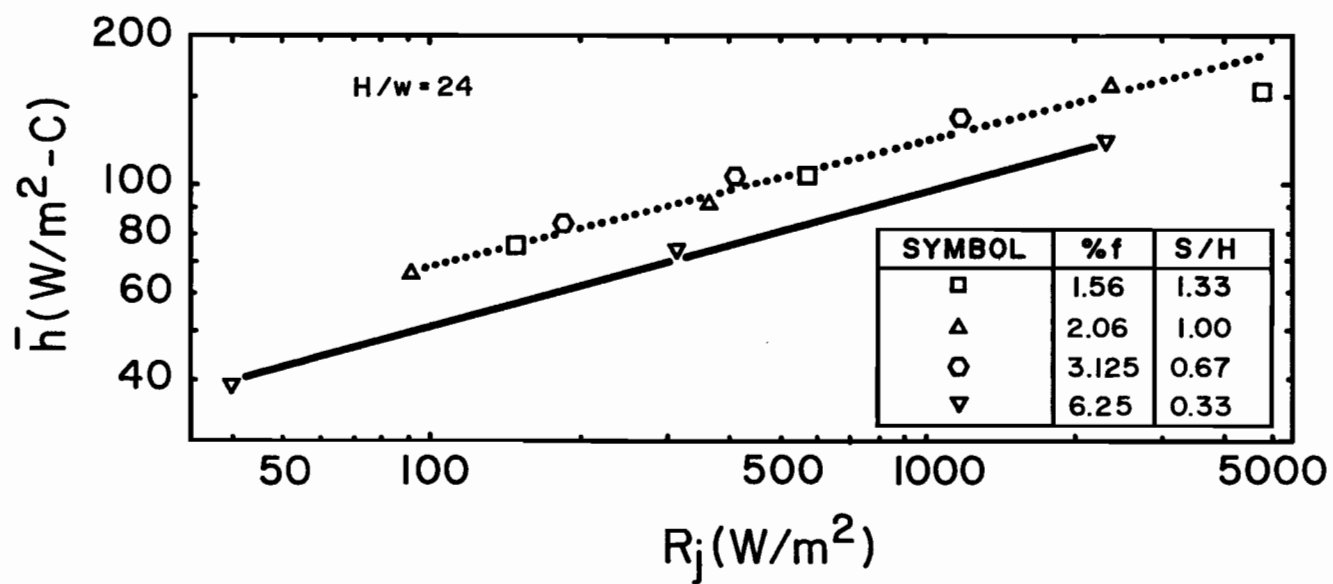


FIGURE 5.67(c) Effect of R_j on \bar{h} for $H/w = 24$ and $0.33 \leq S/H \leq 2$

are useful if applied with care. The parameter, blower rating, R_j , is widely used in industrial applications as an index of performance of impingement systems. The values of R_j listed in Table 5.1(b) for the present study, $92 < R_j < 8048$, represent an industrially important range of blower rating. The value of the nozzle discharge coefficient, shown in Appendix 3, plays a significant role in the expression of system performance as $R_j = 0.5 \rho U_j^3 f / C_d^2$, as has been discussed by Obot (1981). A simple correlation, with constant numerical parameters, of all the experimental data of the present study, expressed in terms of the dimensional variables \bar{h} and R_j , gave the following equation:

$$\bar{h} = 25.52 R_j^{0.25} (H/w)^{-0.02} (S/H)^{0.21} \quad (5.8)$$

Such dimensional equations should be used with care, with the nondimensional correlations given as equations (5.6) and (5.7) and associated Figures 5.56, 5.63 and 5.65 being more meaningful, reliable, and generally much preferred.

5.6 Effect on Heat Transfer of Throughflow at the Impingement Surface

Following presentation of the investigation of heat transfer without throughflow at the impingement surface, the results of the study of effect on heat transfer of impingement surface throughflow are now discussed. As heat transfer without throughflow was documented over a wide range of geometrical parameters, the effect of throughflow was measured for a single geometry. Thus an intermediate impingement surface spacing, $H/w = 8$, was chosen. As was noted in Section 4.6 concerning flow, the widest nozzle, $w = 13.3$ mm, was used to minimize stagnation pressure, thereby minimizing to an acceptably small level the inherent non-uniformity in local throughflow velocity.

For reasons likewise documented in Section 4.6, throughflow measurements were made with the single confined jet system shown as the bottom configuration of Figure 5.1, for which $S/w = 18$, $f = 2.77\%$ and $S/H = 2.25$. However, as the span of the lateral traversing of the impingement surface under the stationary jet is limited to about 160 mm from the stagnation point, i.e. to $12w$ with the widest nozzle, the effective geometry was $S/w = 12$, $f = 4.17\%$ and $S/H = 1.5$.

The variables for the throughflow study were three values of Re_j , 10200, 22800 and 29100 and several values of U_s , throughflow velocity, from 0.1 to 0.3 m/s. The throughflow velocities used and associated impingement surface pressures are given in Table 5.4, from which it can be seen that the maximum pressure drop non-uniformity was only 12.1%. The present heat transfer data with throughflow are in the range of parameters of the industrially important Papridryer (pilot plant and mill trial) reported by Burgess et al. (1972 a, b) as follows:

	<u>Present investigation</u>	<u>Papridryer</u>
U_s , m/s	0-0.3	0.045-0.26
U_s/U_j^* , %	0-1.11	0.045-0.45
$(\rho U_s/\rho U_j^*)/f$, %	0-40.1	2.7 -34

The ratio, $(\rho U_s/\rho U_j^*)/f$, is the amount of throughflow expressed as a percent of the nozzle exit flow rate.

The heat convected from the sensor to the jet in the absence of throughflow was calculated as:

$$Q_s = P_s - Q_{\text{rad.}} - Q_{\text{lateral cond.}} - Q_{\text{back cond.}} \quad (5.9)$$

TABLE 5.4 Flow Parameters of the Confined Single Jet System for Analysis of Effect of Throughflow at the Impingement Surface

Re_j	U_j^* (m/s)	U_s (m/s)	U_s/U_j^* (%)	$\frac{\rho U_s}{\rho U_j^*} \cdot \frac{1}{f}$ (%)	ΔP_j (N/m ²)	ΔP_o (N/m ²)	ΔP_s (N/m ²)	$\frac{\Delta P_o}{\Delta P_o \pm \Delta P_s}$ (%)
10200	13.5	0.0	0.0	0.0	135	87	0.0	-
		0.10	0.74	26.7			1300	6.3
		0.15	1.11	40.1			3000	2.8
22800	30.2	0.0	0.0	0.0	606	412	0.0	-
		0.15	0.49	17.6			3000	12.1
		0.30	0.99	35.7			11700	3.4
29100	38.5	0.0	0.0	0.0	965	666	0.0	-
		0.20	0.52	18.8			5200	11.3
		0.30	0.78	28.1			11700	5.4

where P_s is the heat into the sensor, $Q_{rad.}$ the heat loss by radiation, $Q_{lateral\ cond.}$ the heat loss by conduction to the surrounding plate and $Q_{back\ cond.}$ the conduction loss from the back of the sensor. As detailed in Appendix 5, $Q_{back\ cond.}$ was normally evaluated with a marinite insulation board, hence was a very small correction as documented in Tables A5.1 and A5.2. As it was necessary to remove the marinite board for throughflow experiments, a comparative set of runs was made without throughflow, but without this back insulation. Because the layer of warmed air below the impingement plate is relatively stagnant, this heat loss term without the insulating board was evaluated as heat conduction through a 10 mm layer of air, the temperature at this displacement being measured by five 20 AWG chromel-constantan thermocouples. The two sets of data for zero throughflow agree well on each of Figures 5.68 through 5.70 for the above-noted alternatives.

With throughflow, the heat convected from the sensor to the jet was calculated as:

$$Q_s = P_s - Q_{rad.} - Q_{lateral\ cond.} - Q_t \quad (5.10)$$

where Q_t , the heat taken from the sensor by the throughflow, is expressed as

$$Q_t = \rho U_s A_s C_p (T_{b_2} - T_s) \quad (5.11)$$

The location of the thermocouples at the impingement surface and back of the heat flux sensor, T_s and T_{b_2} , are shown in Figure 3.14. Based on experience for experiments without throughflow, $Q_{rad.}$ was neglected for the case with throughflow as the maximum value was 0.42% relative to Q_s .

SYMBOL	U_s (m/s)	U_s/U_j^* (%)	$(\rho U_s/\rho U_j^*)(1/r)$ (%)	\overline{Nu}
○	0	0	0	31.39
●	0.10	0.74	26.7	41.26
◐	0.15	1.11	40.1	40.16

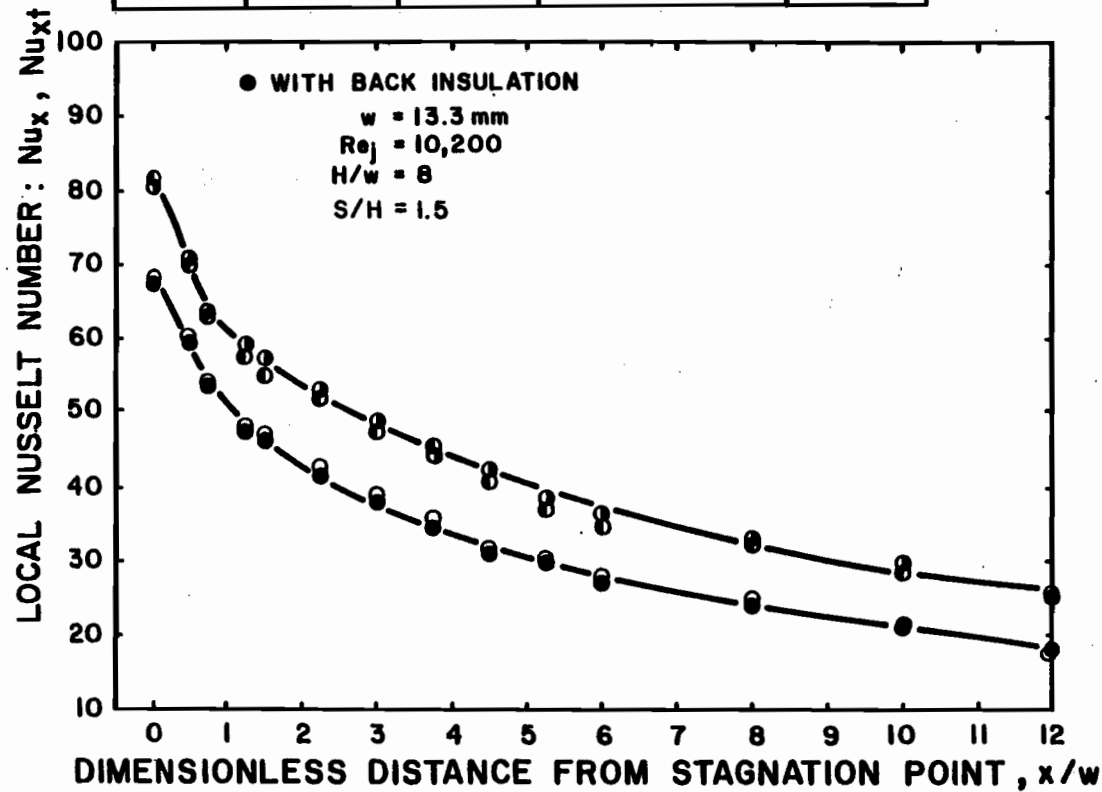


FIGURE 5.68 Effect of Throughflow at the Impingement Surface on Lateral Profiles of Nu_{xt} for $Re_j = 10200$, $H/w = 8$ and $S/H = 1.5$

SYMBOL	U_s (m/s)	U_s/U_j^* (%)	$(\rho U_s/\rho U_j^*)(1/t)$ (%)	\overline{Nu}
○	0	0	0	62.01
●	0.15	0.49	17.6	78.01
⊙	0.30	0.99	35.7	81.84

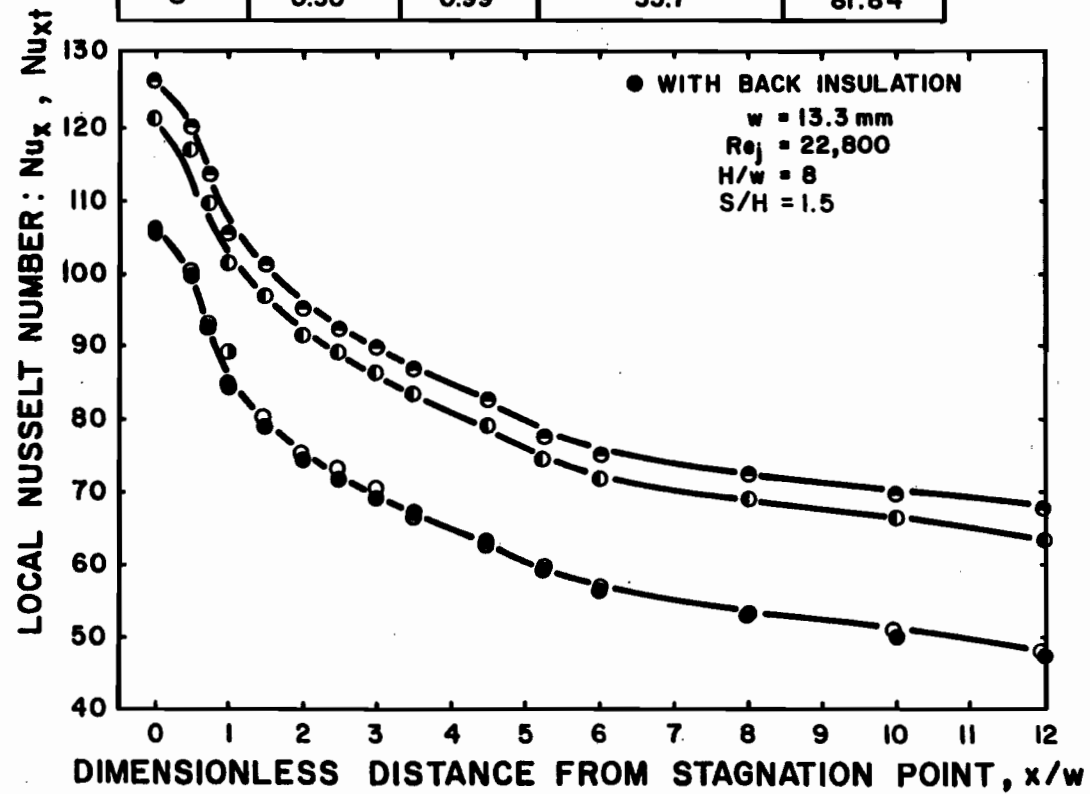


FIGURE 5.69 Effect of Throughflow at the Impingement Surface on Lateral Profiles of Nu_{xt} for $Re_j = 22800$, $H/w = 8$ and $S/H = 1.5$

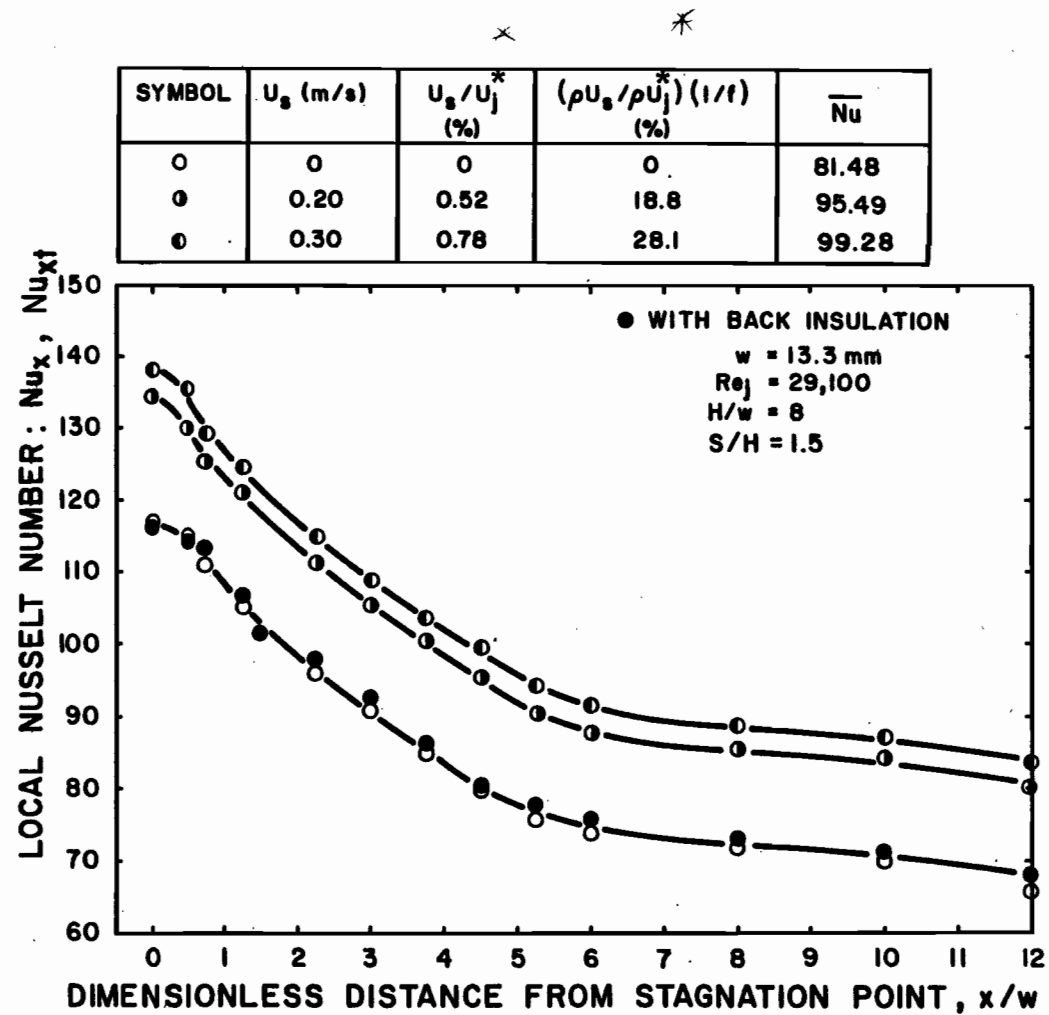


FIGURE 5.70 Effect of Throughflow at the Impingement Surface on Lateral Profiles of Nu_{xt} for $Re_j = 29100$, $H/w = 8$ and $S/H = 1.5$

The complete data are tabulated in Appendix 7, for which the values without throughflow are those measured without the insulating board at the back of the impingement plate.

The effect of throughflow on local heat transfer as a function of lateral position is expressed alternately as Nusselt number profiles in Figures 5.68 through 5.70, and as profiles of the ratio of Stanton number with and without throughflow, St_{xt}/St , on Figures 5.71 through 5.73. The choice of Stanton number as dimensionless heat transfer coefficient derives from a theoretical analysis of the effect of transpiration on convective heat transfer, discussed subsequently.

The lateral profiles of Nu_x on Figures 5.68 through 5.70 indicate that, with increasing U_s/U_j^* , heat transfer coefficient increases in most but not all cases. When an increase in U_s/U_j^* brings an increase in Nu_{xt} , it is seen on Figures 5.68 through 5.71 that the absolute magnitude of the increase is about constant from the stagnation point out to $x/w = 12$. Figures 5.71 through 5.73 in fact indicate that the percentage increase in St_x as a consequence of throughflow increases approximately linearly with lateral distance from stagnation. Occurrence of the largest relative increase in local heat transfer in the region of maximum boundary layer thickness can be attributed to the fact that throughflow reduces the thickness of both the thermal and the momentum boundary layer, thereby increasing the gradient of both velocity and temperature profiles at the impingement surface. Hence, the thicker the boundary layer, the greater the potential for increased transport rates by throughflow.

It is apparent from Figures 5.69 and 5.70 that, as U_s/U_j^* is increased from zero, Nusselt number at first increases rapidly, then less so.

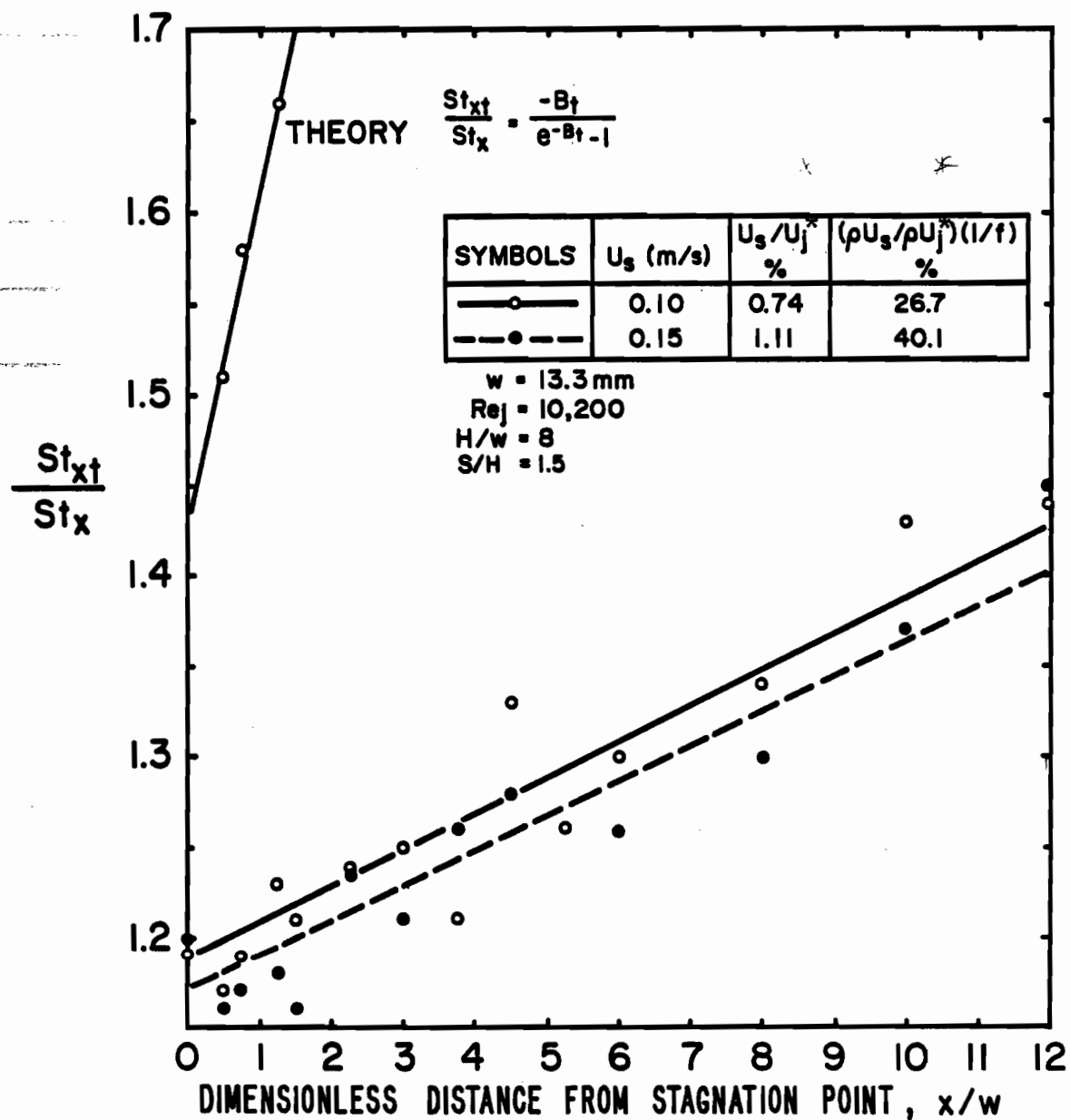


FIGURE 5.71 Effect of Throughflow at the Impingement Surface on St_{xt}/St_x for $Re_j = 10200$, $H/w = 8$ and $S/H = 1.5$: Theory and Experiment

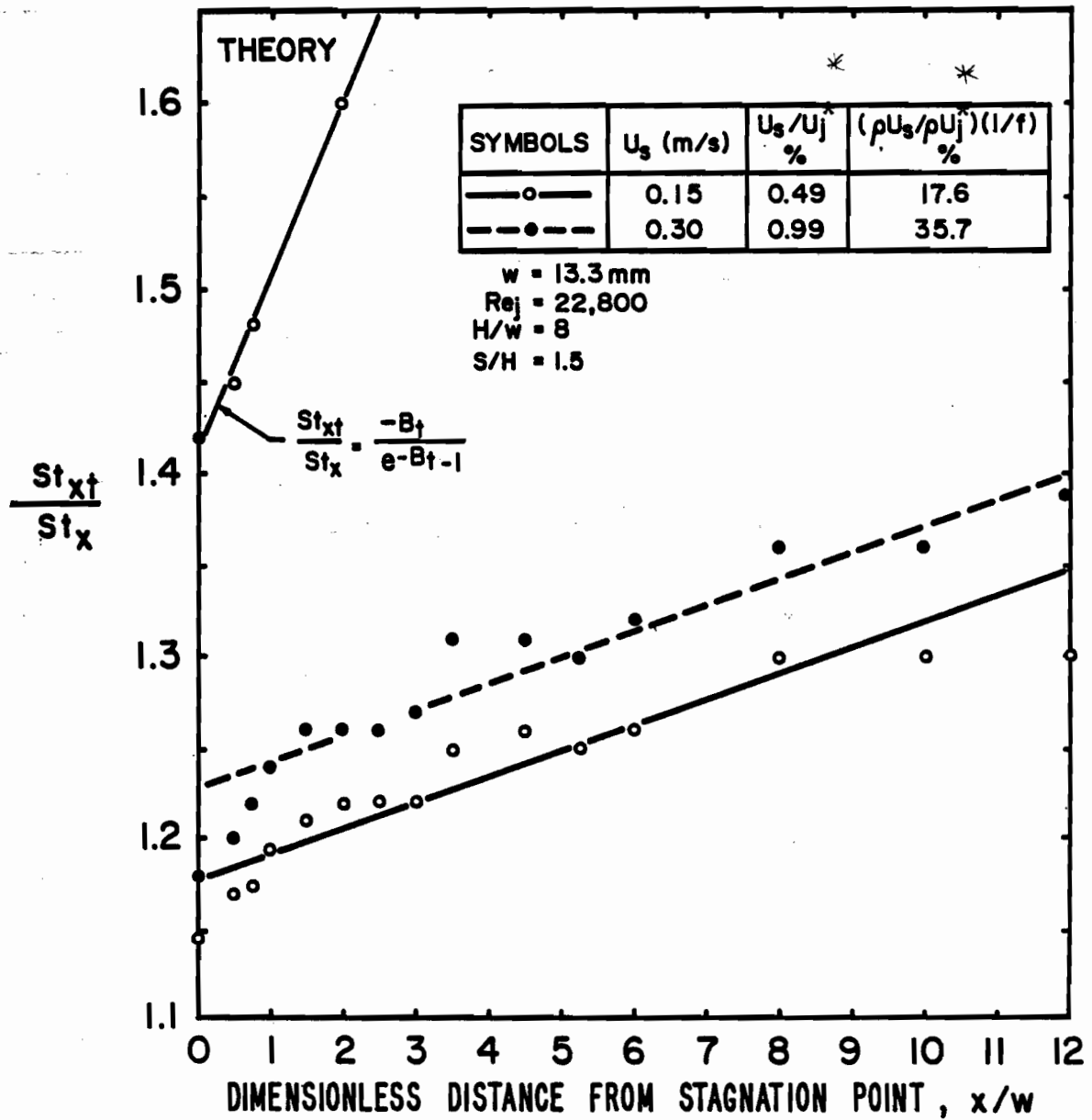


FIGURE 5.72 Effect of Throughflow at the Impingement Surface on St_{xt}/St_x for $Re_j = 22800$, $H/w = 8$ and $S/H = 1.5$: Theory and Experiment

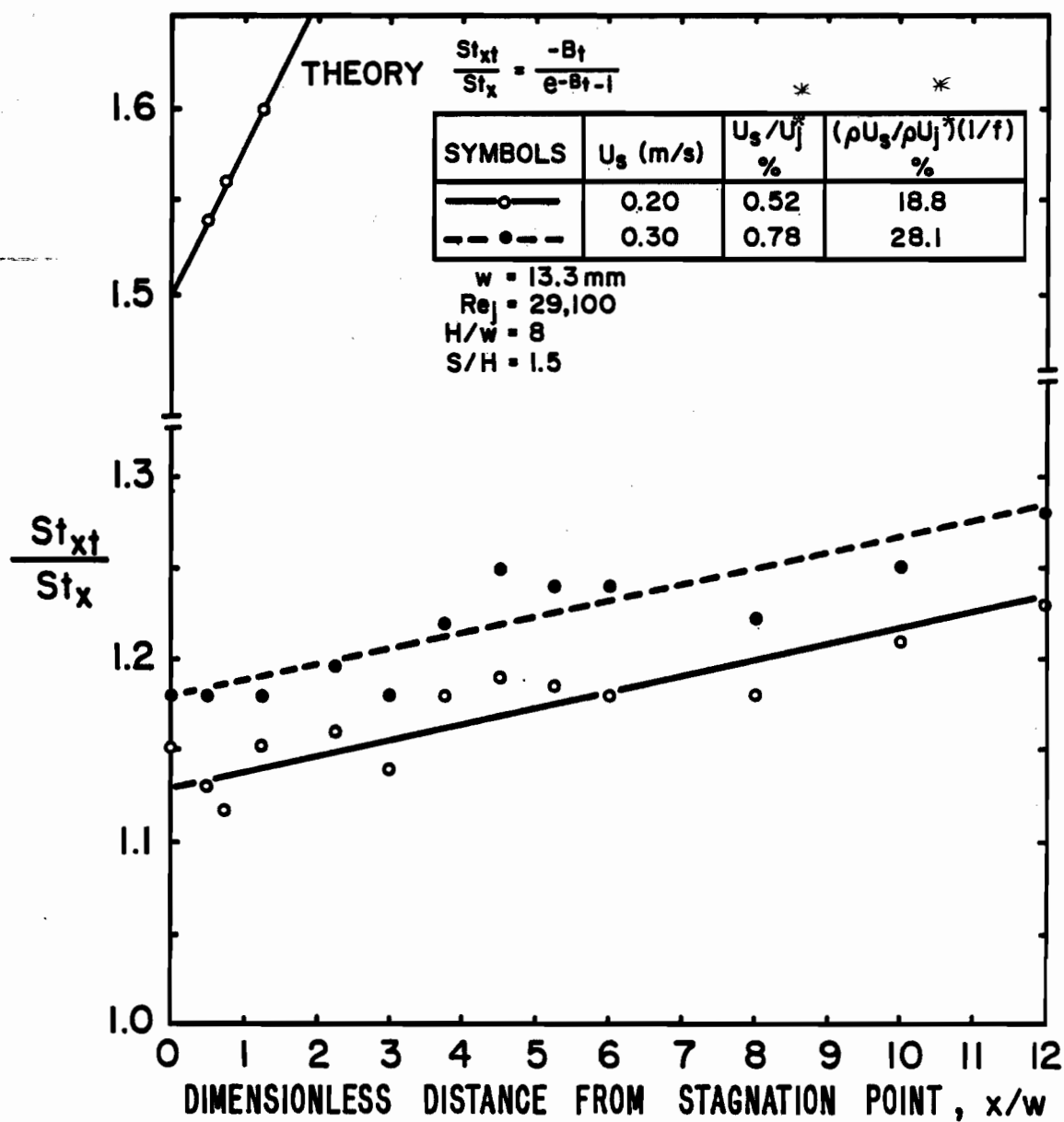


FIGURE 5.73 Effect of Throughflow at the Impingement Surface on St_{xt}/St_x for $Re_j = 29100$, $H/w = 8$ and $S/H = 1.5$: Theory and Experiment

Moreover, for the increase to the maximum measured value of relative throughflow velocity, $U_s/U_j^* = 1.11$, it is seen from Figure 5.68 that this effect actually reverses, i.e. at some high value of U_s/U_j^* less than 1.11, Nu_{xt} begins to decrease with increasing U_s/U_j^* . This same effect may be seen again on the set of profiles as St_{xt}/St_x that expresses the throughflow enhancement ratio. Thus Figures 5.72 and 5.73 show an increase in heat transfer rate at low to moderate throughflow, while a reduction in heat transfer at high throughflow is displayed by Figure 5.71. The remainder of this section is devoted to the analysis of these effects of throughflow, an analysis which relates primarily to phenomena in the boundary layer.

Also presented in Figure 5.71 through 5.73 are theoretical lines of St_{xt}/St_x calculated from the analytical approach of Mickley et al. (1954) for laminar flow and compared for the first time by van Heiningen (1981) with numerical predictions of impingement heat transfer. In their approach the actual boundary layer was replaced by a model of Couette flow. In this model it was assumed that, due to throughflow, the variations in velocity component parallel to the surface were negligible compared to those perpendicular to the wall. For zero pressure gradient and the same Reynolds number evaluated at a distance from the entrance sufficiently long to allow developed turbulent boundary layer, Kay and Crawford (1980) found that the Couette flow model satisfactorily represented their experimental measurements. For the effect of transpiration on heat transfer for a turbulent boundary layer, they expressed the Couette flow solution as

$$St_t/St = \ln(1 - b_t)/-b_t \quad (5.12)$$

The transpiration parameter, $b_t = (U_s/U_j^*)/St_t$, may alternately be represented as $b_t = \left(\frac{\rho U_s}{\rho U_j^*}\right) \frac{1}{f} / \frac{St_t}{f}$, which indicates more clearly its physical significance as the ratio of the transpired momentum flux to the surface convection heat flux with throughflow. The negative sign for the b_t term in Equation (5.12) is for the case of throughflow of the present work. Because of the implicit nature of Equation (5.12), an alternate transpiration parameter is $B_t = (U_s/U_j^*)/St$, i.e. with transpired momentum flux normalized with respect to surface convection heat flux without throughflow. Thus $B_t = \ln(1 + b_t)$. The throughflow enhancement ratio may then be expressed explicitly as

$$St_t/St = -B_t/(e^{-B_t} - 1) \quad (5.13)$$

The theoretical lines in Figures 5.71 through 5.73 are therefore calculated from Equation (5.13).

The fact that St_{xt}/St_x measured experimentally in the present study is much less than predicted by this theory can be attributed to the lower potential increase of heat transfer with throughflow in the case of the thinner boundary layer in the stagnation and early wall jet flow regions for the impinging jet case as compared to the developed turbulent boundary layer flow for the case of Mickley et al. (1954) and Kays and Crawford (1980). The difference between these theoretical predictions and experimental measurements is elaborated in connection with the succeeding figures.

In order to better assess the importance of the transpiration momentum flux ratio U_s/U_j^* , values of the throughflow enhancement ratio both at the stagnation point St_{ot}/St_o , and that averaged over the entire impingement surface ($0 \leq x/w \leq 12$) $\overline{St_t}/\overline{St}$, are displayed as a function of U_s/U_j^* and $(\rho U_s/\rho U_j^*)/f$ in Figures 5.74 and 5.75. While in Figure 5.74 the experimental values from the present study for St_{ot}/St_o show no dependence on Re_j , Figure 5.75 indicates that, for the highest value of Re_j (29100), there is a reduction in enhancement of average heat transfer due to throughflow. For average heat transfer there is at about $U_s/U_j^* = 0.008$ a clear maximum in the enhancement of heat transfer, while for stagnation point heat transfer the enhancement in heat transfer may pass through a somewhat lower maximum in St_{ot}/St_o at around $U_s/U_j^* = 0.01$. For the values of Reynolds number and geometrical parameters investigated, the maximum enhancement in convective heat transfer is about 20% at the stagnation point while the maximum increase in mean heat transfer is by about 30% at the lower Re_j range and about 22% at the highest Re_j investigated.

Also shown in these two figures are the theoretical lines from Equation (5.13) for both stagnation and average heat transfer. Although both the theoretical laminar approach by Mickley et al. (1954) and the experimental data for turbulent boundary layer of Kays and Crawford (1980) show a continuous linear dependence of St_{ot}/St_o and $\overline{St_t}/\overline{St}$ with U_s/U_j^* , the quite non-linear dependence measured in the present study indicates that the impingement jet flow field cannot satisfactorily be modelled by Couette flow.

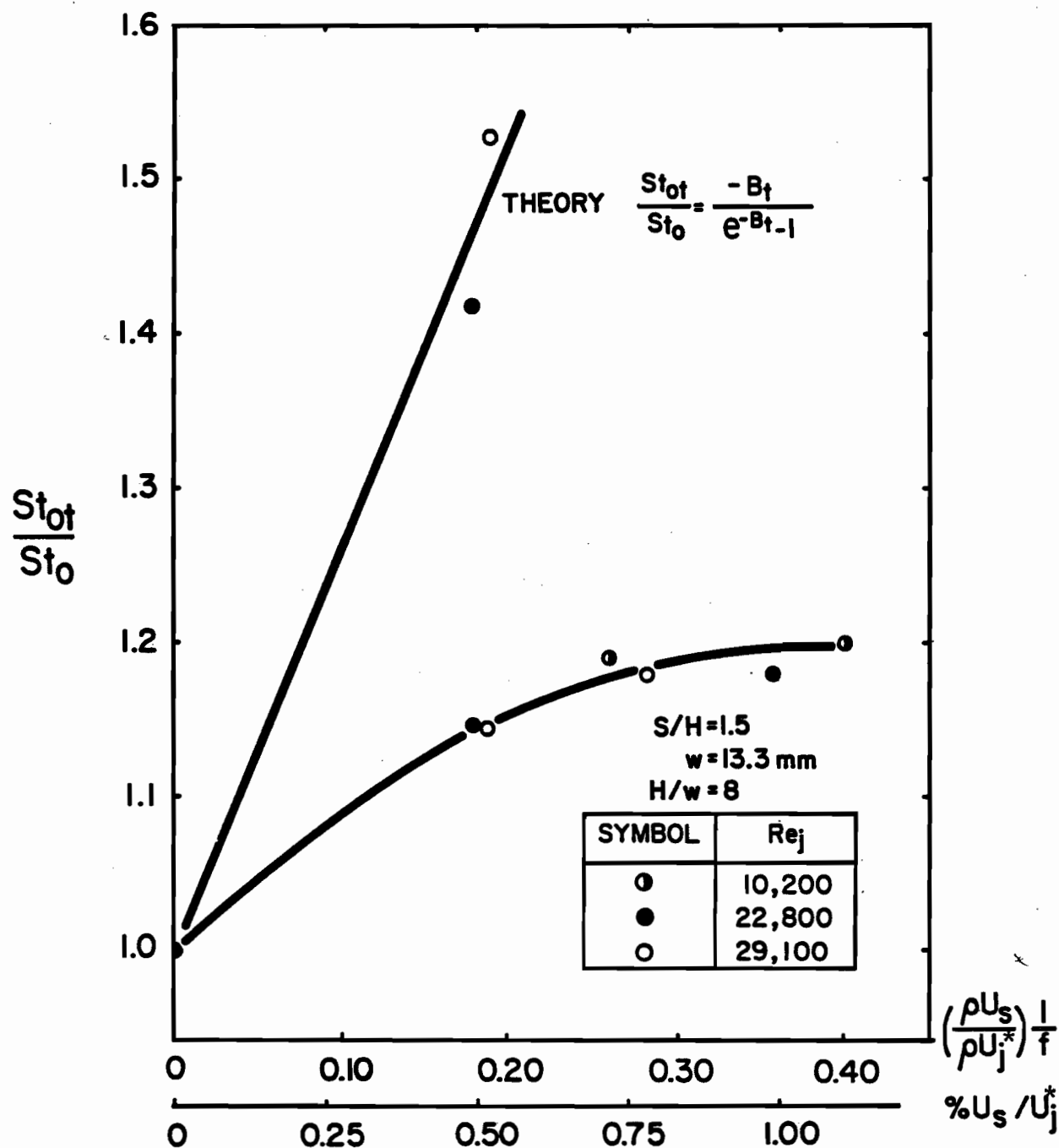


FIGURE 5.74 Effect of Throughflow at the Impingement Surface on St_{tot}/St_0 for $Re_j = 10200, 22800$ and 291000 : Theory and Experiment

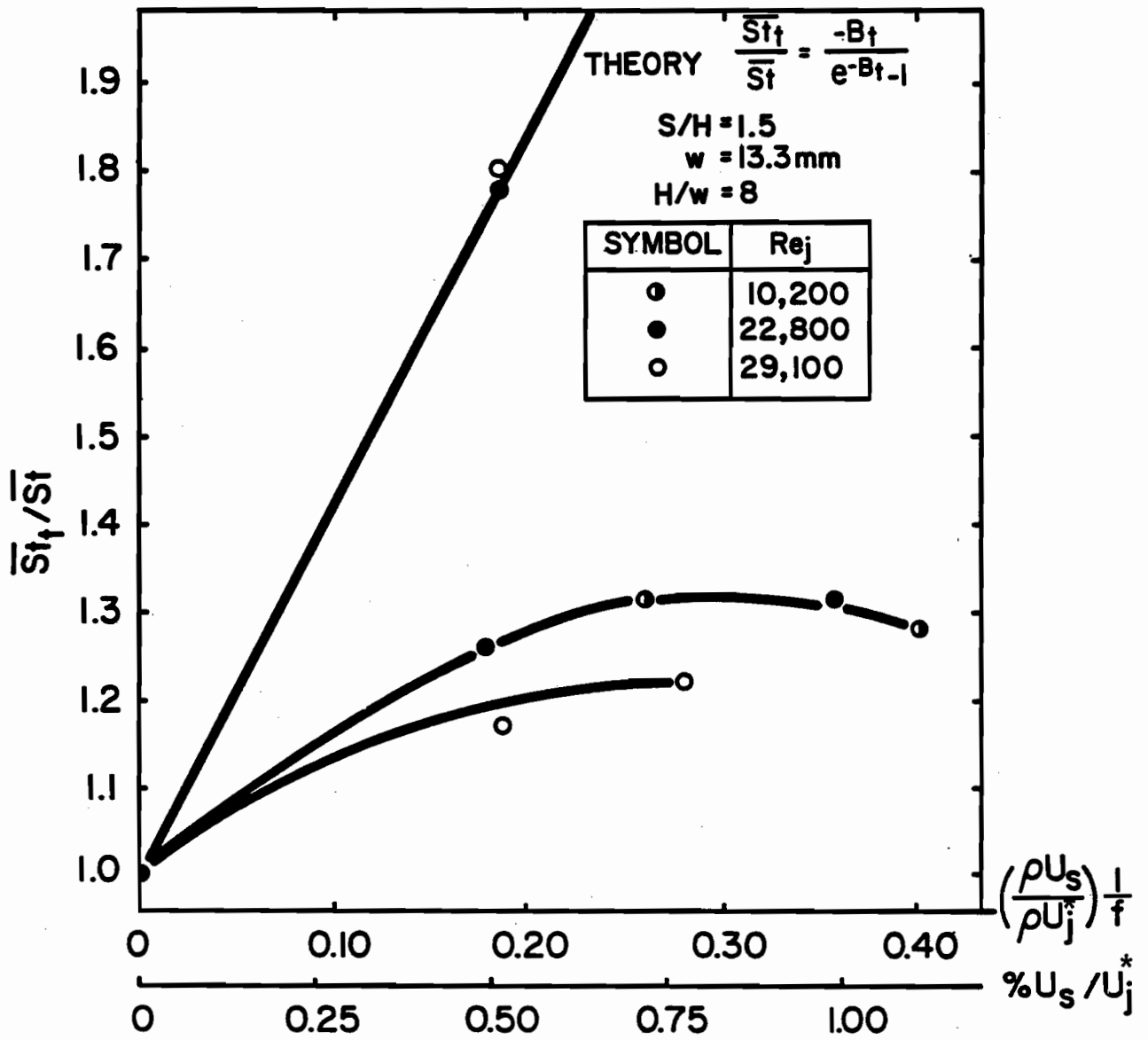


FIGURE 5.75 Effect of Throughflow at the Impingement Surface on $\overline{St}_t/\overline{St}$ for $Re_j = 10200, 22800$ and 29100 : Theory and Experiment

The mechanisms affecting rate of heat transfer with throughflow at the impingement surface may now be examined by considering the simplified enthalpy equation of the boundary layer

$$V \frac{\partial T}{\partial x} = \frac{\partial}{\partial y} \left[(\alpha + \epsilon_H) \frac{\partial T}{\partial y} \right] \quad (5.14)$$

where ϵ_H is the eddy diffusivity defined as

$$\epsilon_H = - \overline{T'v'} / (\partial T / \partial y) \quad (5.15)$$

From these equations it can be seen that the heat flux at the wall is related to lateral mean velocity, eddy diffusivity and temperature gradient at the wall. All three variables are highly affected by throughflow. With increasing throughflow it was documented by both Baines and Keffer (1977) and Obot (1980) for slot and round turbulent impinging jets respectively that the mean lateral velocity V at the impingement surface decreases with increasing U_s/U_j^* .

Regarding effect of throughflow on turbulence characteristics, it was shown in Figure 4.41 that u'/U in the flow approaching the impingement surface and at $2w$ from it decreases with increasing U_s/U_j^* . In the flow parallel to the impingement surface for a turbulent round impinging jet, Obot (1981) found that, for values of U_s/U_j^* up to about 0.4%, throughflow decreased the intensity of turbulence in the streamwise direction adjacent to the impingement surface, although the corresponding turbulence velocity was unaffected by throughflow. Obot also found that throughflow greatly increased the velocity gradient adjacent to the impingement surface.

By analogy, it may be assumed that the temperature gradient, $\partial T/\partial y$, adjacent to the surface would be correspondingly increased.

For a turbulent boundary layer subjected to throughflow, Fulachier et al. (1977) found that the turbulent shear stress and turbulent kinetic energy are significantly reduced by throughflow. Thus the various evidence noted above suggests a reduction in the value of eddy viscosity, ϵ_H , with increasing throughflow. As there appears to be a small reduction in ϵ_H in Equation (5.14) as a result of increased throughflow, the increase in heat transfer in Figure 5.74 and 5.75 is evidently due to the increase in the slope of velocity and hence of temperature adjacent to the impingement surface.

A final presentation of the effect of throughflow at the impingement surface is shown in Figure 5.76 where the experimental data, expressed as St_{ot}/St_o and $\overline{St_t}/\overline{St}$ are displayed as a function of the transpiration parameter b_t , the ratio of transpired momentum flux to surface convection heat flux with throughflow. Thus this parameter has a similarity to Prandtl number, the ratio of momentum diffusivity to thermal diffusivity. Furthermore, the equivalent presentation of this parameter as $b_t = \rho U_s C_p / h_t$ identifies b_t alternately reciprocal of Stanton number based on U_s , i.e. as the ratio of heat flow at the surface by throughflow to heat convection at the surface. For the geometry of the impingement system used, it may be seen from Figure 5.76 that the highest enhancement of average convective heat transfer by throughflow, $\overline{St_t}/\overline{St}$ (for $Re_j = 10200$ and 22800) occurs at about $b_t = 1.5$. Thus the maximum enhancement ratio occurs for conditions at which the heat flow to the surface by throughflow is approximately 1.5 times the convective heat at the surface or, expressed alternately, when

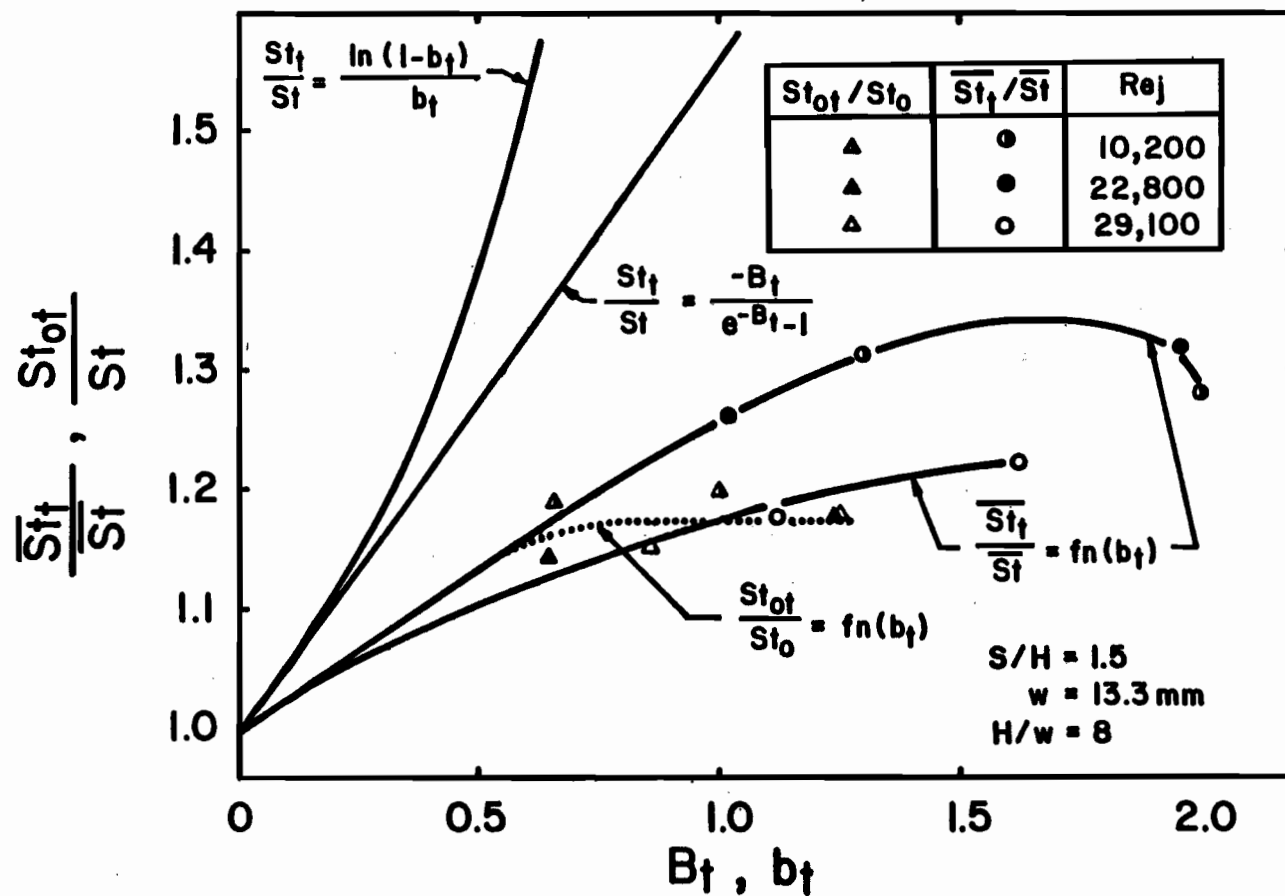


FIGURE 5.76 Effect of Throughflow Parameters B_t and b_t on $\overline{St_t}/\overline{St}$, St_{ot}/St_o for $Re_j = 10200$, 22800 and 29100

the transpired momentum flux is around 1.5 times the convection heat flux. For a throughflow greater than that corresponding to about $b_t = 1.5$, the reduction in throughflow enhancement ratio indicated on Figure 5.76 may be associated with reduction in lateral mean velocity and corresponding reduction in gradients of lateral velocity and temperature at the impingement surface.

Also presented in Figure 5.76 are the theoretical lines from the Couette flow model, presented in the alternative forms expressed in Equation (5.12) and (5.13) for the transpiration parameter as either b_t or B_t . For $B_t = 1$ the value of 1.58 for throughflow enhancement ratio ($\overline{St}_t/\overline{St}$) from the theoretical Couette flow solution is seen to be considerably greater than the value obtained for the present experiment. For the case of blowing through the boundary layer, Kays and Crawford (1980) reported experimental results which indicate St_b/St to be < 1 . They found that the boundary layer is literally blown off the surface at $b_b > 16$.

5.7 Summary and Conclusions

The central objective of the present chapter was to quantify the effect of interaction on impingement surface transport characteristics for the industrially important multiple confined slot jet system in which the spent flow (the jet flow after impingement) is discharged through exhaust ports located symmetrically between the inlet jet nozzles at the confinement surface. To achieve this objective, local rates of convective heat transfer were measured by traversing an isothermal heated impingement

surface under a system of 3 confined slot jets with symmetric exit ports. The wide selection of geometrical and flow parameters used, ($0.33 \leq S/H \leq 6$, $4 \leq H/w \leq 24$ and $3330 \leq Re_j \leq 29166$), were chosen to include the range relevant to two important industrial applications, the drying of paper and cooling of turbine vanes. From local and average rates of heat transfer the central objective of the study was satisfied by determining fundamental criteria for distinguishing between interacting and non-interacting types of multiple jet systems. This approach led to establishing general correlations for the design and optimization of systems of multiple confined slot impinging jets. The effect of throughflow on impingement heat transfer was also measured.

An extensive set of impingement surface heat transfer profiles established that heat transfer coefficients within each inlet nozzle-exhaust port flow cell were symmetrical over the central two-thirds of the 3-jet test unit, i.e. from the centerline of one of the outer jets, through the central jet, to the centerline of the other outer jet. Thus it was proven that the present 3-jet system accurately represents heat transfer conditions of a multiple jet system with a large number of jets.

For a 3-slot jet system the present study quantifies the extent of higher heat transfer with symmetric outflow relative to operation with cumulative spent flow associated with one-sided exit flow. When compared with the symmetric outflow system in the range of 5000-20000 Reynolds number and typical geometric parameters, the percentage decrease in average and stagnation point heat transfer caused by cumulative spent flow was found to be in the range 15% to 45% and 15% to 60% respectively.

The reduction was attributed to the two fundamental mechanisms; degradation of the ΔT driving force for heat transfer resulting from dilution of inlet jet fluid with spent flow, and modification of the impingement flow field by the crossflow which over half of the impingement surface reverses the lateral velocity. The thermal mechanism operates over the impingement and wall jet regions alike while the flow mechanism has its greatest effect in the stagnation region where it acts to destroy the unique flow field around the stagnation point. There is, consequently, a higher reduction in Nu_o than in \overline{Nu} . For a single slot jet at constant Reynolds number, Re_j , and constant impingement surface spacing, H/w , there remained an effect of nozzle width on impingement surface heat transfer, just as was the case in the flow study of Chapter 4. As w was increased from 3.3 to 13.3 mm at constant Re_j and H/w , there were two opposing effects on stagnation point heat transfer, Nu_o , an effect on mean velocity acting to decrease Nu_o and an effect on turbulence intensity acting to increase Nu_o . For closer impingement surface spacings, $4 \leq H/w \leq 8$, the effect of w in increasing turbulence intensity contributed to an increase of 25% in Nu_o and that in decreasing mean velocity contributed to a decrease of 3% in Nu_o , i.e. a predicted net increase of about 20% as compared to a measured increase of about 17%. For larger impingement surface spacing, $H/w > 8$, the combination of these opposing effects was found to produce increasingly smaller effects on Nu_o . Although this effect of nozzle width was greatest on Nu_o , it persisted to the exhaust port.

For multiple slot jets, a central question relates to the degree of interaction between inlet jet flows and intervening exhaust port flows, as evidenced by the corresponding effects on impingement surface heat transfer. To define the relationships between multiple jet systems and single jets, lateral profiles of local heat transfer of both were obtained for comparable flow and geometric parameters. When the single jet Nu_x profiles were used to provide the base case for evaluation of multiple jet system results, it was noted that at values of S/H above an upper critical limit, $(S/H)_{ce} = 1.5$, Nu_x profiles for a multiple jet over the entire region from Nu_o to Nu_e were coincident with those for the corresponding single jet. At an intermediate value of S/H slightly below this critical value, the multiple jet profiles of Nu_x and the profile for the equivalent single jet were found to be coincident for some distance out from the nozzle centerline, after which Nu_x for the multiple jet is greater than for a single jet. At values of S/H below a lower critical limit, $(S/H)_{co} = 0.7$, two types of deviations were found, i.e. a multiple jet system has a lower Nu_o but a higher Nu_e than for the corresponding single jet. This enhancement of heat transfer around the exit port is due to increased eddy motion encountered in the separated flow region where the flow deflects sharply from the impingement surface near the exhaust centerline. Such flow is analogous to that at the rear of a cylinder in crossflow which likewise is characterized by a region of flow separation.

When S/H is reduced below a lower critical limit $(S/H)_{co} = 0.7$, interaction between the closely spaced countercurrent flows of inlet jet and exhaust streams penetrates to the nozzle centerline where it is

reflected in reduction of Nu_o for multiple jets relative to the equivalent single jet. For Reynolds numbers of 5500, 11000 and 22000, Nu_o for multiple jets decreases very sharply as S/H is reduced below the lower critical value of 0.7 which does not vary with Re_j . There is no contradiction between this conclusion and that from analysis of flow results which indicated $1 \geq (S/H)_c \geq 0.75$. The finding that the critical value at which stagnation point conditions become affected is slightly lower using Nu_o as the criterion reflects the fact that the effects of interaction on the flow field (decreasing axial mean velocity but increasing turbulence) act in the opposite directions with respect to heat transfer. At $S/H < 0.7$, the reduction of Nu_o associated with the lower mean velocity predominates increasingly over the tendency of heat transfer to increase with the associated increasing turbulence.

As for the effect of impingement surface spacing on Nu_o for single slot jets, over the range $4 \leq H/w \leq 24$, Nu_o passes through a maximum at around $H/w = 8$, as found also by Korger and Krizek (1966), Gardon and Akfirat (1966), Kumada and Mabuchi (1970), Schlünder et al. (1970) and Cadek and Zerkle (1970). This characteristic indicates that for impingement surface spacings of up to $H/w = 8$, the effect on Nu_o of rapidly increasing turbulence intensity is more important than the opposing effect of decreasing jet centerline mean velocity. For spacings beyond $H/w = 8$, the relative importance of these two effects is reversed. For multiple impinging slot jet systems over the range of flow cell proportion S/H varying from 6 down to 0.33 and jet Reynolds number Re_j between 3330 and 29160, the Nu_o maximum also occurs at about $H/w = 8$ as a consequence of these opposing effects of spacing on the flow field

variables along the jet centerline. While for non-interacting multiple jets Nu_o depends on $Re_j^{0.57}$, this dependence increases as S/H is decreased below the lower critical value, 0.7, with this exponent eventually reaching 0.72 for $S/H = 0.375$. The increase in sensitivity to Reynolds number as multiple jets become more highly interacting reflects the effect of this interaction on the boundary layer which thereby becomes more turbulent.

Over a range of Re_j 3330 to 29160 and for the closest impingement surface spacing, $H/w = 4$, an off stagnation maximum and intervening minimum occurs in Nu_x profiles. Previous studies have associated such minima with transition from a laminar to turbulent boundary layer. From the finding of similarity in impingement surface static pressure profiles where the static pressure drops to about 5% of the stagnation pressure at a lateral distance equal to half the impingement surface spacing H , the transition point x_T/w would be near 2. The fact that all values of x_T/w were found to occur in the range 1.8 to 3 provides further support for the concept that transition to a turbulent boundary layer occurs when the stabilizing effect of a steep lateral pressure gradient is no longer present. The increase in Nu_x over the transition region corresponds to the enhanced transport characteristics of a boundary layer which is becoming turbulent. The locations of the off-stagnation maxima and minima shift toward the stagnation point with increasing Re_j . Also, the sharpness of these maxima and minima increases with increasing Re_j . Therefore, higher values of Re_j act through a steeper lateral gradient in pressure, first, to maintain a laminar boundary layer for some distance from the stagnation point, but when transition does occur, the increase of Nu_x is more pronounced at larger Re_j .

In the presence of a negative pressure gradient such as on the forward part of a cylinder in a crossflow, Kestin et al. (1961, a,b) reported that up to the end of this region the boundary layer is laminar and that the presence of this negative pressure gradient stabilizes the boundary layer, thus delaying the transition to turbulence. For the larger impingement surface spacings, i.e. $8w$, $16w$ and $24w$, the off-stagnation maxima completely disappear due to the considerable reduction in lateral gradient of impingement surface pressure from that sufficient to maintain the laminar boundary layer in the stagnation region for $H/w = 4$.

The fact that near similarity in profiles of impingement surface static pressure was found to exist when lateral distance was normalized with respect to impingement surface spacing, H , led to a check for similarity in Nu_x profiles as well. However, neither single nor multiple jet profiles showed similarity when Nu_x was expressed as a function of x/H . Thus impingement heat transfer is a more complex phenomena than static pressure.

In previous studies of single or multiple jets, confined or unconfined, heat transfer coefficients have been expressed in the form conventional for external flows, i.e. using as ΔT the temperature difference between the jet at the nozzle exit and the impingement surface, the latter usually being isothermal. For reasons of ease of comparison with results of other studies, the above convention has been continued in the present study. However, an additional analysis has been made of the effect of determining Nusselt number for this system of confined

impinging jets using a closed heat exchanger type of analysis, i.e. replacing a fixed ΔT with a ΔT_x varying from inlet (nozzle centerline) to outlet (exhaust port centerline). This procedure leads to higher values of Nusselt number at all locations except of course at the stagnation point where the difference must vanish. The maximum difference occurs at the exit centerline. For the range of flow and geometric parameters used in the present study, Nu_{xB} at the exhaust port centerline based on local ΔT_x is higher than that based on ΔT by amounts ranging from insignificant up to a maximum of about 45%. Although this perspective has been ignored in previous studies, the use of local values of ΔT_x and Nu_x is extremely important in industrial applications such as estimating the life of impinging jet cooled turbine airfoils.

Examination of the forms of dependence of \overline{Nu} on Re_j , S/H and H/w was the first step in formulating an appropriate comprehensive correlation. This examination may be summarized as:

- (1) The effect of Re_j on \overline{Nu} is of the form $\overline{Nu} = c(Re_j)^n$, with n independent of Re_j and H/w . For non-interacting multiple jets, $S/H \geq 1.5$, n is also independent of S/H , but for interacting multiple jets n is a function of S/H as indicated on Figure 5.56.
- (2) The effect of H/w on \overline{Nu} when represented as $\overline{Nu} = c(H/w)^m$ is reasonably linear, i.e. m independent of H/w , only for $H/w \geq 8$. For spacings in this linear range of H/w the exponent m is independent of Re_j , while with respect to S/H , m is independent for non-interacting multiple jets ($S/H \geq 1.5$), but for interacting jets in narrower flow cells, m varies with S/H as indicated by Figure 5.63.

- (3) As the dependence on S/H of \overline{Nu} at constant Re_j and H/w represented on Figures 5.57 through 5.59 clearly shows a nonlinear logarithmic dependence below the lower critical flow size, $(S/H)_{co} = 0.7$, and as the exponents n and m vary with S/H for interacting multiple jets, it is clear that S/H is the most sensitive of the four dimensionless parameters to be correlated, \overline{Nu} , Re_j , S/H and H/w .

The above analysis suggests the appropriate form of correlation to be:

$$\frac{\overline{Nu}}{(Re_j)^n (H/w)^m} = c(S/H)^a$$

For non-interacting jets, $S/H \geq 1.5$, for which all three exponents are constants, a multiple linear regression gave the following form:

$$\frac{\overline{Nu}}{(Re_j)^{0.65} (H/w)^{-0.8}} = 0.63(S/H)^{-0.55}$$

The right-hand side of this equation is the line on Figure 5.65 for $S/H \geq 1.5$, while the data shown in this non-interacting region are the experimental values of \overline{Nu} , Re_j and H/w expressed as the function on the left of the above equation. This equation also represents \overline{Nu} for confined single slot jets with S denoting the lateral extent of the impingement surface for which the mean Nusselt number is obtained.

For interacting multiple jets, the data shown on Figure 5.65 for $S/H < 1.5$ are the experimental values expressed as the function

$$\frac{\overline{Nu}}{(Re_j)^n (H/w)^m}, \text{ with } n \text{ and } m \text{ as functions of } S/H \text{ from Figures 5.56 and 5.63.}$$

The line on Figure 5.65 for $S/H < 1.5$ is the best fit of these data, which is

$$\frac{Nu}{(Re_j)^n (H/w)^m} = 0.215 (S/H)^{1.5}$$

A simple correlation, with constant numerical parameters, of all the experimental data of the present study, expressed in terms of the dimensional variables heat transfer coefficient \bar{h} and fan energy consumed at the nozzle exit per unit area of heat transfer, R_j , gave the following equation:

$$\bar{h} = 25.52 R_j^{0.25} (H/w)^{-0.02} (S/H)^{0.21}$$

Such a dimensional equation should be used with care, with the non-dimensional correlations given earlier being generally much preferred.

For $10200 \leq Re_j \leq 29100$ and $S/H = 1.5$, application of uniform throughflow at the impingement surface produced values of relative throughflow velocity, U_s/U_j^* , to a maximum of 1.11%. At low to moderate values of throughflow the effect was to enhance rate of heat transfer at the impingement surface. However, after an initial increase the throughflow enhancement ratio, St_{xt}/St_x passed through a maximum at about $U_s/U_j^* = 0.8\%$, becoming significantly less at the maximum value, $U_s/U_j^* = 1.11\%$.

The maximum enhancement by throughflow is about 20% at the stagnation point for all values of Re_j , while for average heat transfer the maximum enhancement is about 30% for Reynolds number 10200 to 22800 and about 22% at $Re_j = 29100$. The increase in velocity and temperature gradient at the impingement surface under conditions of throughflow provides a mechanism for the observed enhancement in convective transport. The value of the enhancement ratio, St_{xt}/St_x , based on the theoretical model of Mickley et al. (1954) is much larger than that measured experimentally. The lower experimental enhancement is attributed to the lower potential for increase in heat transfer with throughflow in the case of flow in the stagnation and early wall jet region for the impinging jet case relative to the Couette flow model of Mickley et al.

When the throughflow is expressed as a function of the transpiration parameter $b_t = \frac{U_s/U_i^*}{St_t}$ it is observed that the maximum enhancement ratio, St_t/St , occurs for conditions at which the heat flow to the surface by throughflow is approximately 1.5 times the convective heat transfer at the surface. For values of throughflow higher than those which correspond to $b_t = 1.5$, the deleterious effect on convective heat transfer associated with the severe reduction in lateral mean velocity at the impingement surface evidently predominates over the advantageous reduction in boundary layer thickness, so that in this range the net effect of increased throughflow is for a reduction in convective heat transfer.

CHAPTER 6

CONTRIBUTIONS TO KNOWLEDGE

1. Mean velocity and turbulence characteristics were documented for single and multiple slot jet systems for nozzles of ASME standard elliptical contoured entry. This flow field characterization study indicated that, in addition to the expected dimensionless variables, the effect of dimensional variables may also be present. In the present study, nozzle width over the range $2.5 \leq w \leq 13.3$ mm was found to be a significant dimensional variable with respect to both flow field and impingement surface heat transfer.
2. The significance of the dimensionless geometrical (flow cell) proportion concept has been established to quantify the relationship between the confined multiple and single slot jet systems. In this concept the present multiple slot jet system can be viewed as an assembly of repeated "flow cells", the boundaries of a flow cell being the impingement surface, the confinement surface, and the centerlines of adjacent inlet nozzles and exhaust ports. A key dimensionless geometric parameter is therefore S/H , the flow cell proportion.
3. For a multiple confined slot jet system with exhaust ports located symmetrically between jets, critical sizes of flow cell, $(S/H)_c$, have been defined as flow cells where the flow field and heat transfer characteristics at the impingement surface begin to differ from those for the corresponding single jet. The critical values

of this dimensionless geometric parameter then delimit non-interacting from interacting jet systems. The extent of this interaction in multiple jet systems is the degree of departure of flow field and heat transfer characteristics at the impingement surface from those for a single jet. The upper critical limit of $(S/H)_c$ has been established to be $(S/H)_{ce} = 1.5$, above which the multiple jet system may be viewed as an assembly of single non-interactive jets, i.e. the flow and heat transfer characteristics coincide with those for corresponding single impinging jets. The lower critical limit of $(S/H)_c$ has been found to be $(S/H)_{co} = 0.7$, below which the multiple jet system is totally interacting, i.e. the flow field and heat transfer at the impingement surface diverge at all locations from those for a corresponding single impinging jet. The intermediate region $0.7 \leq S/H \leq 1.5$ is characterised by enhancement of local Nusselt number over a region beginning at the exhaust port centerline and extending part way to the stagnation point.

4. It has been demonstrated that for non-interacting jet systems over the wide range of parameters $5000 \leq Re_j \leq 43800$, $4 \leq H/w \leq 16$ and $0.75 \leq S/H \leq 6$, the normalised profiles of static pressure at the impingement surface collapse when plotted with lateral distance is non-dimensionalized with respect to the impingement surface spacing, H . This then is a more rational basis of normalization than is the conventionally-used nozzle width. For the more complicated heat transfer phenomena, however, normalized Nusselt number profiles do not collapse for either multiple or single impinging jets.

5. The effects on local Nusselt number profiles of determining Nusselt number using a closed heat exchanger analysis has been established. This procedure leads to higher heat transfer coefficients except at the stagnation point where the two methods converge. The greatest difference in Nusselt number between these two procedures occurs at the exit flow centerline where, for the lowest Re_j tested, Nu_{xB} based on local bulk temperature difference reached a maximum of 45% higher than Nu_x based on $\Delta T = T_s - T_j$.
6. General correlations between the average Nusselt number and the flow and geometrical parameters have been developed. For non-interacting multiple jet systems with flow cells wider than the upper critical value, i.e. with $S/H > 1.5$, the correlation is

$$\frac{\overline{Nu}}{(Re_j)^{0.65} (H/w)^{-0.8}} = 0.63 \quad (S/H)^{-0.55}$$

and for interacting multiple jets, i.e. with flow cells of proportions $S/H < 1.5$, the correlation is

$$\frac{\overline{Nu}}{(Re_j)^n (H/w)^m} = 0.215 \quad (S/H)^{1.5}$$

where n and m are functions of S/H as shown in Figures 5.56 and 5.63 respectively. Average Nusselt number was found to display a maximum at $S/H = 0.5$, $H/w = 5$ for all values of jet Reynolds number.

7. The effects on axial flow field of throughflow at the impingement surface have been established for values of relative throughflow velocity, U_s/U_j^* up to 2% for $11400 \leq Re_j \leq 30200$ and $S/H = 1.5$. At $0.25H$ from the impingement surface the centerline mean velocity increases by up to 12% while the mean axial velocity at $0.5H$ from the jet centerline increases by up to 26%. In contrast, axial fluctuating velocity at $0.25H$ from the impingement surface was found to be unaffected by throughflow, hence turbulence intensity decreased corresponding to these effects on mean and fluctuating axial velocity.
8. The effect of throughflow at the impingement surface on impingement heat transfer has been determined at $10200 \leq Re_j \leq 29100$ and $S/H = 1.5$ for relative throughflow velocities, U_s/U_j^* , up to 1.11%. At the stagnation point the enhancement in heat transfer for all Re_j is about 20%. Enhancement of average heat transfer is about 30% for $Re_j = 10200$ and 22800 and about 22% at $Re_j = 29100$. The maximum enhancement ratio was found to occur when the heat flow to the surface by throughflow is around 1.5 times the convective heat transfer at the surface.

CHAPTER 7RECOMMENDATIONS FOR FUTURE WORK

1. A fundamental study of the flow field at the impingement surface with and without throughflow is highly desirable. A combination of flow visualization and hot wire (X-wire) measurements should be made to obtain valuable insights into the complex flow field and to generate turbulence data for use in numerical modelling of the multiple jet system.
2. An effort should be made to predict the flow and heat transfer characteristics using numerical techniques to solve the governing equations of momentum and energy for multiple turbulent impinging jets. Application of such a numerical prediction method to a system of multiple turbulent impinging jets with crossflow is recommended as the next step.
3. Additional experimental work should be undertaken to investigate the effect of curved impingement surfaces on heat transfer, i.e. concave surfaces and convex surfaces. Also, the effect of impingement surface motion on heat transfer should be investigated.
4. The effect of artificial roughness for augmenting heat transfer in the wall jet region and attenuation in the impingement region should be investigated for applications where more uniform lateral profiles are desirable.

5. The effect of multiple turbulent impinging jets on simultaneous heat and mass transfer (evaporation) should be investigated numerically and experimentally.
6. In various applications of impingement cooling of turbine components the channel formed between the confinement and impingement surfaces is either converging or diverging. The effect of a non-parallel channel in one-sided accelerated and/or decelerated outflow on impingement heat transfer characteristics should be investigated.
7. The effect of high temperature difference between the jet and the impingement surface on heat transfer characteristics should be investigated.
8. The combined effects of confinement and variations in impingement angle should be studied.
9. Further investigation is needed of the effect of throughflow for systems of multiple interacting impinging jets.

REFERENCES

- Abdul-Wahab, H., A.S. Mujumdar and W.J.M. Douglas (1975): Flow measurements in a bounded turbulent impinging slot jet with suction, J. Aero Soc. India.
- Abramovitch, G.N. (1963): The theory of turbulent jets; trans. by Scripta Technica, MIT Press.
- Arganbright, D.G. and H. Resch (1971): A review of basic aspects of heat transfer under impinging air jets, Wood Science and Technology, Vol. 5, pp. 73-94.
- Baines, W.D. and J.F. Keffer (1977): Shear stress measurements for an impinging jet - Effects of surface motion and suction, PPRIC Technical Report, PPR/186.
- Beltaos, S. and N. Rajaratnam (1973): Plane turbulent impinging jets, J. of Hydraulic Research, Vol. 11, #1, pp. 30-59.
- Beltaos, S. and N. Rajaratnam (1974): Impinging circular turbulent jets, Prov. of ASCE, Vol. 100, #HY10, p. 1313.
- Bradshaw, P. (1966): The effect of initial conditions on the development of a free shear layer, J. of Fluid Mechanics, Vol. 26, Part 2, pp. 225-236.
- Burgess, B.W., S.M. Chapman and W. Seto (1972a): The Papridryer Process, Part I, The basic concepts and laboratory results, Pulp and Paper Mag. Can., Vol. 73, #11, pp. 314-322.
- Burgess, B.W., Seto, W., Koller, E., and I.T. Pye (1972b): The Papridryer Process, Part II, Mill Trials, Pulp and Paper Mag. Can., Vol. 73, #11, pp. 323-331.
- Cadek, F.F. and R.D. Zerkle (1970): Local heat transfer characteristics of two-dimensional impinging air jets theory and experiment, Int. Heat Transfer Conf., FC 1.4, pp. 15-19.
- Cartwright, W.G. and P.J. Russell (1967): Characteristics of a turbulent slot jet impinging on a plane surface, Proc. Instn. Mech. Engrs., Vol. 182, Pt. 3H, pp. 309-319.
- Chance, J.L. (1974): Experimental investigations of air impingement heat transfer under an array of round jets, Tappi, Vol. 57, #6, pp. 108-112.
- Dyban, Y.P. and I.A. Mazur (1970): Heat transfer from a flat air jet flowing into a concave surface, Heat Transfer, Soviet Research, Vol. 2, #3.
- Ehrick, E.F. (1955): Some hydrodynamic aspects of valves, ASME Paper 55-A-114.
- Flora, J.J. and V.M. Goldschmidt (1969): Virtual origins of a free plane turbulent jet, AIAA Journal, Vol. 7, #12, pp. 2344-2346.

- Florschuetz, L.W., C.R. Truman and D.E. Metzger (1981): Streamwise flow and heat transfer distributions for jet array impingement with crossflow, ASME #81-GT-77.
- Folayan, C.O. (1976): Impingement cooling, Ph.D. Thesis, Imperial College, London.
- Folayan, C.O. and J.H. Whitelaw (1977): Impingement cooling and its application to combustion, Joint Gas Turbine Congress, ISME, GTSJ, ASME, Paper #07, pp. 1-7, Tokyo.
- Friedman, S.J. and A.C. Mueller (1951): Heat transfer to flat surfaces, Instn. Mech. Engr. and ASME, Proc. of General Discussion on Heat Transfer, pp. 138-142.
- Fulachier, L., E. Verollet and I. Dekeyser (1977): Resultats experimentaux concernant une couche limite turbulente avec aspiration et chauffage à la paroi, Int. J. Heat Mass Transfer, Vol. 20, pp. 731-739.
- Giedt, W.H. (1949): Investigation of Variation of Point Unit Heat Transfer Coefficient Around a Cylinder Normal to an Air Stream, Transactions of the ASME, pp. 375-381.
- Gardon, R. and J.C. Akfirat (1965): The role of turbulence in determining the heat transfer characteristics of impinging jets, Int. J. Heat Mass Transfer, Vol. 8, pp. 1261-1272.
- Gardon, R. and J.C. Akfirat (1966): Heat transfer characteristics of impinging two-dimensional air jets, J. of Heat Transfer, ASME Transaction, Vol. 8, pp. 101-108.
- Glauert, M.B. (1956): The wall jet, J. of Fluid Mechanics, Vol. 1, Part 6, pp. 625-643.
- Gosman, A.D., J.H. Whitelaw and B.E. Launder (1976): Flow, heat and mass transfer in turbulent recirculating flows - prediction and measurements, Short course notes, Chem. Eng. Dept., McGill University.
- Gosman, A.D., W.N. Pun, A.K. Runchal, D.B. Spalding and M. Wolfshtein (1969): Heat and mass transfer in recirculating flows, Academic Press, N.Y.
- Gutmark, E., M. Wolfshtein and I. Wygnanski (1978): The plane turbulent impinging jet, J. of Fluid Mechanics, Vol. 88, Part 4, pp. 737-756.
- Hill, W.G., R.C. Jenkins and B.L. Gilbert (1975): Effects of initial boundary layer conditions on jet mixing, Grumman Research Department Report RE-508, Grumman Aerospace Corporation, Bethpage, N.Y.
- Hill, W.G. (1976): Flow visualization investigation of the effects of the initial boundary layer on jet mixing, Grumman Research Department Memorandum RM-612, Grumman Aerospace Corporation, Bethpage, N.Y.
- Hill, W.G. and R.C. Jenkins (1976): Effects of the initial boundary layer state on turbulent jet mixing, AIAA Journal, Vol. 14, #11, pp. 1513-1514.
- Hinze, J.O. (1959): Turbulence, an introduction to jets measurements and theory, McGraw-Hill Inc.
- Huang, B. (1977): Prediction of flow and heat transfer under a laminar

- Huang, B., W.J.M. Douglas and A.S. Mujumdar (1978): Heat transfer under a laminar swirling impinging jet - a numerical study, 6th Int. Heat Transfer Conf., Paper Fc(b)-23, Vol. 5, pp. 311-316.
- Huang, G.C. (1963): Investigations of heat transfer coefficients for air flow through round jets impinging normal to a heat transfer surface, J. of Heat Transfer, Vol. 85, #3, p. 237.
- Kays, W.M., and M.E. Crawford (1980): Convective Heat and Mass Transfer, McGraw Hill Book Co.
- Kercher, D.M. and W. Tabakoff (1970): Heat transfer by a square array of round air jets impinging perpendicular to a flat surface including the effect of spent air, J. of Eng. for Power, Trans. ASME, Series A, Vol. 92, #1, pp. 73-80.
- Kestin, J., P.F. Maeder and H.E. Wang (1961a): Influence of turbulence on the transfer of heat from plates with and without a pressure gradient, Int. J. Heat Mass Transfer, Vol. 3, p. 133.
- Kestin, J., P.F. Maeder and H.H. Sogin (1961b): Influence of turbulence on the transfer of heat to cylinders near the stagnation point, Z. Angew. Math. Phys., Vol. 12, p. 115.
- Korger, M. and F. Krizek (1966): Mass transfer coefficient in impingement flow from slotted nozzles, Int. J. Heat Mass Transfer, Vol. 9, pp. 337-344.
- Kumada, M. and I. Mabuchi (1970): Studies on the heat transfer of impinging jets (1st Report, Mass transfer for two-dimensional jet of air impinging normally on flat plate), Bull. of JSME, Vol. 13, #55, pp. 77-85.
- Li, Y.-K. (1977): M.Eng. Thesis, Chem. Eng. Dept., McGill University.
- Li, Y.-K., A.S. Mujumdar and W.J.M. Douglas (1978): Coupled heat and mass transfer under a laminar impinging jet, presented at 85th National AIChE Meeting, Philadelphia.
- Livingood, J.N.B. and P. Hrycak (1973): Impingement heat transfer from turbulent air jets to flat plates - a literature survey, NASA TMX-2778.
- Martin, H. and E.U. Schlünder (1973): Optimierung von Schlitzdüsentrocknern auf Grund neuer Versuchsergebnisse über den Wärme-und Stoffübergang in solchen Apparaten, Chemie-Ing.-Techn. 45, Jahrg. 1973/Nr. 5.
- Martin, H. (1977): Heat and mass transfer between impinging gas jets and solid surfaces, Advances in Heat Transfer, Vol. 13, Academic Press.
- Metzger, D.E. (1962): Spot cooling and heating of surfaces with high velocity impinging air jets, Tech. Report #52, Dept. of Mech. Eng., Stanford University.
- Metzger, D.E. and R.J. Korstad (1972): Effects of crossflows on impingement heat transfer, J. of Eng. for Power, Trans. ASME.
- Michell, J.H. (1890): On the theory of free streamlines, Phil. Trans. Royal Society, Vol. 81(A), pp. 389-433.

- Mickley, H., R.C. Ross, A.L. Squyers and W.E. Stewart (1954): Heat, Mass and Momentum Transfer for Flow over a Flat Plate with Blowing and Suction, NACA TN 3208
- Minh, W.C. and S.A. Hoopes (1972): Mean and turbulent velocities for plane jet, J. of Hydraulics Division, Vol. 98, Part 2, pp. 1275-1295.
- Miyazaki, H. and E. Silberman (1972): Flow and heat transfer on a flat plate normal to a two-dimensional laminar jet issuing from a nozzle of finite height, Int. J. Heat Mass Transfer, Vol. 15, pp. 2097-2107.
- Mujumdar, A.S. and W.J.M. Douglas (1972): Impingement heat transfer - a literature review, paper presented at Tappi Conf., New Orleans.
- Murray, B.G. and T.D. Patten (1978): Heat transfer under an array of impinging jets, 6th Int. Heat Transfer Conf., Toronto.
- Obot, N.T. (1975): An apparatus for study of effect of suction on heat transfer for impinging round jets, M.Eng. Thesis, Chem. Eng. Dept., McGill University.
- Obot, N.T., A.S. Mujumdar and W.J.M. Douglas (1979): Design correlations for heat and mass transfer under various turbulent impinging jet configurations, Developments in Drying, Hemisphere Publications, pp. 388-402.
- Obot, N.T. (1981): Flow and heat transfer for round turbulent jets impinging on permeable and impermeable surfaces, Ph.D. Thesis, Chem. Eng. Dept., McGill University.
- Rajaratnam, N. (1976): Turbulent jets, Elsevier Scientific Publishing Co., Amsterdam.
- Russell, P.J. and A.P. Hatton (1972): Turbulent flow characteristics of an impinging jet, Proc. Instn. Mech. Engrs., Vol. 186, 52/72, pp. 635-644.
- Saad, N.R. (1975): Simulation of flow and heat transfer under a laminar impinging round jet, M.Eng. Thesis, Chem. Eng. Dept., McGill University.
- Saad, N.R., W.J.M. Douglas and A.S. Mujumdar (1977): Prediction of heat transfer under an axisymmetric laminar impinging jet, Ind. Eng. Chem. Fundam., Vol. 16 #1.
- Saad, N.R., A.S. Mujumdar, W. Abdel-Messeh and W.J.M. Douglas (1980): Local heat transfer characteristics for staggered arrays of circular impinging jets with crossflow of spent air, ASME presented at ASME/AIChE National Heat Transfer Conf., Orlando, Florida, #80-HT-23.
- Sato, M. and Hiroshi, Y. (1960): The stability and transition of a two-dimensional jet, J. of Fluid Mechanics, Vol. 7, pp. 53-79.
- Schauer, J.J. and R.H. Eustis (1963): The flow development and heat transfer characteristics of plane turbulent impinging jets, Tech. Report #3, Dept. of Mech. Eng., Stanford University.

- Scheuter, K.R. and G.A. Dosdogru (1971): Investigation of impinging air jet dryers with respect to possible automation, Technical Association of Graphic Arts Proceedings, pp. 224-250.
- Schlichting, H. (1968): Boundary layer theory, Sixth Edition, McGraw-Hill Book Company, N.Y.
- Schlotz, M.T. and O. Trass (1970): Mass transfer in a non-uniform impinging jet, AIChE Journal, Vol. 16, pp. 82-96.
- Schlünder, E.U., P. Krötzsch and F.W. Hernecke (1970): Chem.-Ing.-Tech., Vol. 42, p. 333.
- Schnurr, N.M., J.W. Williamson and J.W. Tatom (1972): Analytical investigation of the impingement of jets on curved deflectors, AIAA Journal, Vol. 10, #11, pp. 1430-1435.
- Schuh, H. and R. Pettersson (1966): Heat transfer by arrays of two-dimensional jets directed normal to surfaces including the effects of superimposed wall parallel flow, Proc. 3rd Int. Heat Transfer Conf., Vol. 2, p. 280 (Paper #70).
- Shen, F.C. (1962): Theoretical analysis of jet-ground plane interaction, Institute of the Aerospace Sciences, Paper #62.
- Simonich, J.C. and P. Bradshaw (1978): Effect of free-stream turbulence on heat transfer through a turbulent boundary layer, J. of Heat Transfer, Vol. 100, pp. 671-677.
- Sparrow, E.M., R.J. Goldstein and M.A. Rouf (1975): Effect of nozzle-surface separation distance on impingement heat transfer for a jet in a cross-flow, Trans. ASME, J. of Heat Transfer, Vol. 97, pp. 528-533.
- Sparrow, E.M. and L. Lee (1975): Analysis of flow field and impingement heat and mass transfer due to a non-uniform slot jet, Trans. ASME, Series C, J. of Heat Transfer.
- Sparrow, E.M. and T.C. Wong (1975): Impingement transfer coefficients due to initially laminar slot jets, Int. J. Heat Mass Transfer, Vol. 18, pp. 597-605.
- Subba Raju, K. and E.U. Schlünder (1977): Heat transfer between an impinging jet and a continuously moving flat surface, Wärme-und Stoffübertragung, Thermo- and Fluid Dynamics, Vol. 10, pp. 131-136.
- Townsend, A.A. (1976): The structure of turbulent shear flow, Cambridge University Press.
- van Heiningen, A.R.P., A.S. Mujumdar and W.J.M. Douglas (1976_a): On the use of hot and cold-film sensors for the skin friction and heat transfer measurements in impingement flow, letters in Heat and Mass Transfer, Vol. 3, p. 523.
- van Heiningen, A.R.P. (1981): Ph.D. Thesis, McGill University, Montreal.

- van Heiningen, A.R.P., A.S. Mujumdar and W.J.M. Douglas (1976b): Numerical prediction of the flow field and impingement heat transfer caused by a laminar slot jet, Trans. ASME, J. of Heat Transfer, Vol. 98, #4, pp. 654-658.
- van Heiningen, A.R.P., A.S. Mujumdar and W.J.M. Douglas (1977): Flow and heat transfer characteristics of turbulent slot jet impinging on a moving wall, Turbulence Shear Flow Symposium, Penn. State University.
- Wolfshtein, M. (1967): Convective process in turbulent impinging jets, Ph.D. Thesis, Imperial College, London.
- Yokobori, S., N. Kasagi, M. Hirata and N. Nishiwaki (1978): Role of large-scale eddy structure on enhancement of heat transfer in stagnation region of two-dimensional, submerged, impinging jet, 6th Int. Heat Transfer Conf., Toronto, Paper Fc(b)-22, pp. 305-310.

APPENDIX 1VALUES OF FLUCTUATING VELOCITY FOR $Re_j = 11000$ TABLE A1.1. Fluctuating Velocity at the Jet Centerline for
 $w = 2.5 \text{ mm}$

z/w	$z \text{ (mm)}$	$u' \text{ (m/s)}$
0.0	0.0	0.50
1.2	3.0	0.85
4.6	11.5	5.42
5.7	14.3	6.35
7.2	18.0	8.37
10.1	25.3	8.60
12.9	32.2	8.60
15.4	38.5	8.52

TABLE A1.2. Fluctuating Velocity at the Jet Centerline for
 $w = 3.3 \text{ mm}$

z/w	$z \text{ (mm)}$	$u' \text{ (m/s)}$
0.0	0.0	0.38
1.6	5.3	1.12
4.0	13.2	3.28
6.6	21.8	5.87
8.8	29.0	6.57
12.5	41.2	6.40
15.2	50.2	6.04
18.0	59.4	5.87

TABLE A1.3. Fluctuating Velocity at the Jet Centerline for
 $w = 5.0$ mm

z/w	z (mm)	u' (m/s)
0.0	0.0	0.27
1.5	7.5	0.62
4.5	22.5	2.86
6.6	33.0	4.25
9.0	45.0	4.64
10.1	50.0	4.64
12.6	63.0	4.60
18.0	90.0	3.98

TABLE A1.4. Fluctuating Velocity at the Jet Centerline for
 $w = 10.0$ mm

z/w	z (mm)	u' (m/s)
0.0	0.0	0.14
0.7	7.0	0.27
1.6	16.0	0.48
2.6	25.0	0.78
3.3	33.0	1.20
4.0	40.0	1.41
4.6	46.0	1.67
8.0	80.0	2.42
10.5	105.0	2.42
12.0	120.0	2.34
13.8	138.0	2.31
14.9	149.0	2.29
16.0	160.0	2.19
18.0	180.0	2.11

TABLE A1.5. Fluctuating Velocity at the Jet Centerline for
 $w = 13.3 \text{ mm}$

z/w	$z \text{ (mm)}$	$u' \text{ (m/s)}$
0.0	0.0	0.12
1.3	16.6	0.44
3.0	39.9	0.99
4.6	61.8	1.60
6.4	79.2	1.74
8.2	109.1	2.00
9.2	131.5	1.98
10.9	145.0	2.00
12.7	169.0	1.96
14.9	198.0	1.88
16.2	215.5	1.80
17.0	226.1	1.77
18.0	329.4	1.74

APPENDIX 2

VALUES OF AVERAGE HEAT TRANSFER COEFFICIENTS OVER THE
ENTIRE RANGE OF GEOMETRICAL AND FLOW PARAMETERS

TABLE A2.1. Average Heat Transfer Coefficient for $f = 1.56\%$

w (mm) (S/w)	H/w	S/H	Re_j	R_j (W/m ²)	\overline{Nu}	\overline{St}/f	\bar{h} (W/m ² -K)
2.5 (32)	8	4	3330	148	11.38	0.306	123.73
			5230	576	13.03	0.223	141.58
			10790	4751	24.00	0.201	260.00
	16	2	3330	148	8.69	0.233	94.40
			5230	576	11.86	0.203	128.92
			10790	4751	19.20	0.161	208.00
	24	1.33	3330	148	7.04	0.189	76.47
			5230	576	9.65	0.165	104.92
			10790	4751	14.20	0.119	154.00

TABLE A2.2. Average Heat Transfer Coefficient for $f = 2.06\%$

w (mm) (S/w)	H/w	S/H	Re_j	R_j (W/m ²)	\overline{Nu}	\overline{St}/f	\bar{h} (W/m ² -K)
3.3 (24)	8	3	3410	92	13.56	0.269	111.63
			5400	364	16.75	0.210	137.94
			10270	2353	26.05	0.172	214.45
	16	1.5	3410	92	10.50	0.211	86.23
			5400	364	15.10	0.191	124.00
			10270	2353	22.22	0.146	182.93
	24	1	3410	92	8.00	0.160	65.70
			5400	364	12.04	0.151	99.14
			10270	2353	19.15	0.126	157.71
	4	6	3410	92	13.2	0.264	108.68
			5400	364	17.5	0.221	144.08
			10270	2353	27.1	0.180	223.12

TABLE A2.3. Average Heat Transfer Coefficient for $f = 3.125\%$

w (mm) (S/w)	H/w	S/H	Re_j	R_j (W/m ²)	\overline{Nu}	\overline{St}/f	\bar{h} (W/m ² -K)
5.0 (16)	8	2	5700	185	22.40	0.187	121.40
			7500	416	25.50	0.134	138.20
			10740	1171	33.00	0.138	178.90
			20740	8048	51.90	0.110	282.10
	16	1	5700	185	18.10	0.151	98.10
			7500	416	21.40	0.121	116.00
			10740	1171	29.00	0.122	157.20
			20740	8048	51.90	0.110	282.10
	24	0.67	5700	185	15.43	0.129	83.30
			7500	416	19.00	0.121	103.25
			10740	1171	25.20	0.106	136.60
			20740	8048	51.90	0.110	282.10

TABLE A2.4. Average Heat Transfer Coefficient for $f = 6.25\%$

w (mm) (S/w)	H/w	S/H	Re_j	R_j (W/m ²)	\overline{Nu}	\overline{St}/f	\bar{h} (W/m ² -K)
10.0 (8)	4	2	5400	39.7	23.74	0.098	64.50
			10910	307	32.80	0.068	88.90
			21720	2306	63.19	0.066	171.24
	8	1	5400	39.7	22.28	0.092	60.53
			10910	307	40.86	0.084	110.70
			21720	2306	65.17	0.068	176.61
	16	0.5	5400	39.7	18.73	0.077	50.88
			10910	307	36.07	0.075	97.75
			21720	2306	58.50	0.058	158.53
	24	0.33	5400	39.7	14.34	0.059	38.97
			10910	307	27.03	0.056	73.25
			21720	2306	44.95	0.047	121.81

TABLE A2.5. Average Heat Transfer Coefficient for $f = 8.313\%$

w (mm) (S/w)	H/w	S/H	Re_j	R_j (W/m ²)	\overline{Nu}	\overline{St}/f	\bar{h} (W/m ² -K)
13.3 (6)	4	1.5	10770	165	43.08	0.068	87.78
			21760	1314	66.79	0.052	136.09
			29160	3112	85.49	0.049	174.20
	8	0.75	10770	165	44.08	0.069	89.82
			21760	1314	72.15	0.056	147.02
			29160	3112	92.35	0.054	188.18
	16	0.375	10770	165	32.07	0.050	65.35
			21760	1314	57.55	0.045	117.27
			29160	3112	71.37	0.041	145.43

APPENDIX 3

CALCULATION OF REYNOLDS NUMBER

For an incompressible flow through an elliptical ASME nozzle installed at the outlet of a plenum chamber, the discharge may be expressed in the form

$$m = C_d w \ell Y \left[\frac{2 \Delta P_j \rho}{1 - \beta^4} \right]^{0.5} \quad (\text{A3.1})$$

where C_d = nozzle discharge coefficient
 w = nozzle width
 ℓ = nozzle transverse length
 ΔP_j = pressure drop across the nozzle
 ρ = density at plenum chamber pressure and temperature
 β = ratio of nozzle width to plenum chamber width
 Y = expansion factor

The results presented in Figure A3.1 were determined from equation (A3.1). The expansion factor was determined from fluid meter applications (1971). For $U_j^* \leq 40$ m/s, the pressure drop across the nozzle was measured using a micromanometer while for $U_j^* > 40$ m/s, a U-tube manometer was used.

For each one of the five ASME nozzles, $w = 2.5, 3.3, 5.0, 10.0$ and 13.3 mm, the discharge coefficient C_d is plotted versus Re_j . C_c refers to the nozzle/plenum chamber width ratio. The agreement between the present results and those of Metzger (1962) is satisfactory.

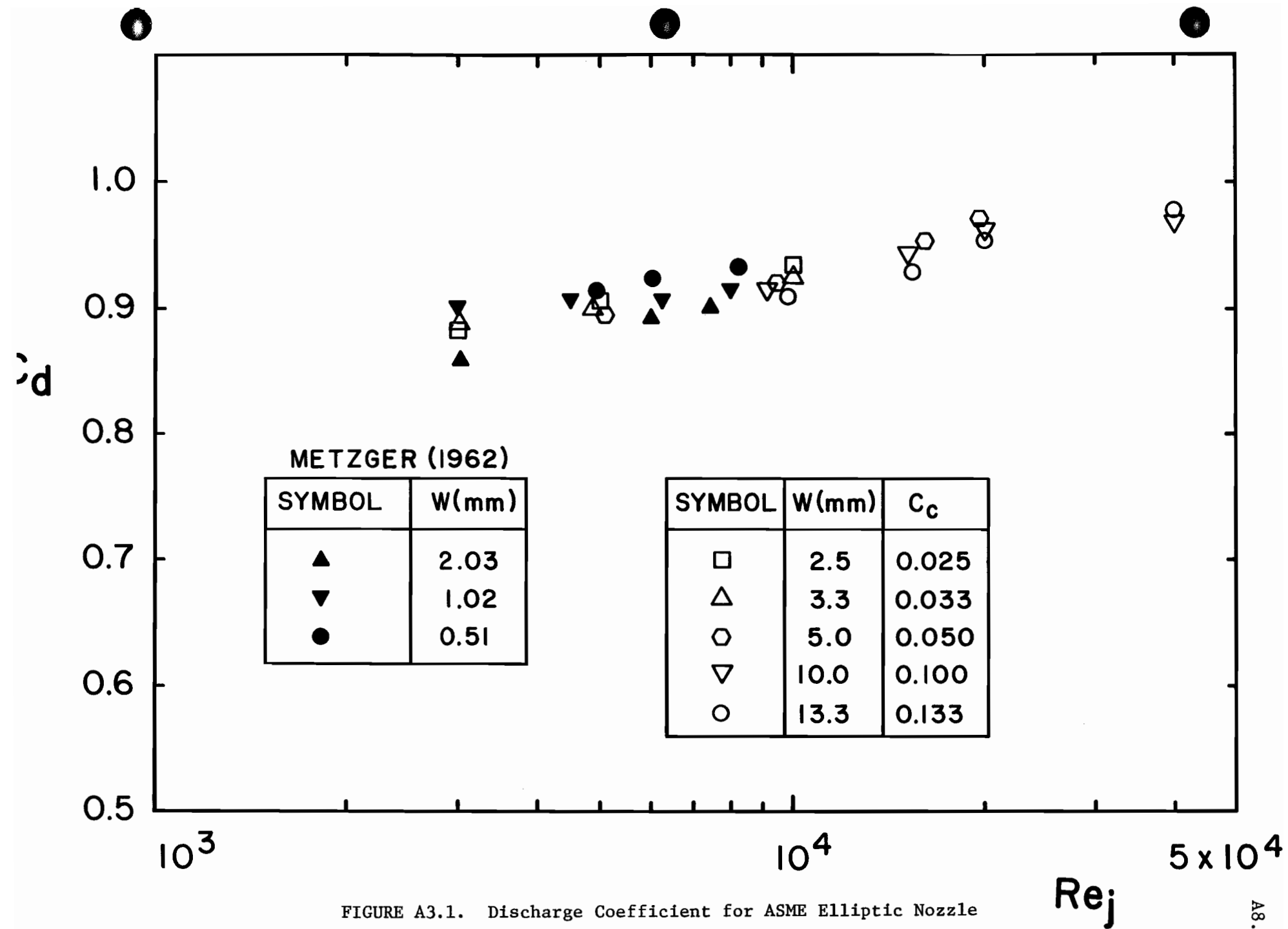


FIGURE A3.1. Discharge Coefficient for ASME Elliptic Nozzle

For flow and heat transfer runs, the pressure drop across the nozzle, ΔP_j , was measured through two pressure taps installed flush; the first (5 mm inside diameter) on the inside wall of the plenum chamber and the second (1 mm inside diameter) on the midspan 1 mm above the nozzle exit. For the higher pressure range, $1200 \leq \Delta P_j \leq 8000 \text{ N/m}^2$, the uncertainties in ΔP_j (measured with a U-tube manometer) were $\pm 40 \text{ N/m}^2$. For the mid-pressure range $200 \leq \Delta P_j \leq 1200 \text{ N/m}^2$ and the lower pressure range $100 \leq \Delta P_j \leq 200 \text{ N/m}^2$ (measured with a micromanometer) the uncertainties were $\pm 10 \text{ N/m}^2$ and $\pm 2 \text{ N/m}^2$, respectively. The jet Reynolds number was calculated from the pressure drop across the nozzle, ΔP_j , and the nozzle discharge coefficient as follows:

$$\text{Re}_j = \frac{wC_d}{\nu} \sqrt{\frac{\Delta P_j}{0.5\rho}} \quad (\text{A3.2})$$

The uncertainties expressed in terms of jet Reynolds number are shown for the flow runs and heat transfer runs in Tables A3.1 and A3.2, respectively.

TABLE A3.1. Uncertainties in Re_j for the Study of Flow at the Impingement Surface

w (mm)	U_j^* (m/s)	ΔP_j (N/m ²)	$\pm \Delta P_j$ (N/m ²)	Re_j	$\pm \Delta Re_j$
3.3	26.7	528	10	5000	47
	51	1804	10	9500	26
	110	8010	40	20700	52
13.3	27.4	510	10	20700	202
	39.7	1026	10	30000	146
	60	2296	40	43800	380

TABLE A3.2. Uncertainties in Re_j for the Study of Heat Transfer at the Impingement Surface

w (mm)	U_j^* (m/s)	ΔP_j (N/m ²)	$\pm \Delta P_j$ (N/m ²)	Re_j	$\pm \Delta Re_j$
2.5	23.4	406	10	3330	40
	36.8	1003	10	5230	26
	76.0	4007	40	10790	53
3.3	18.2	245	10	3410	69
	28.8	614	10	5400	44
	54.8	2083	40	10270	98
5.0	20.0	296	10	5700	95
	26.4	504	10	7500	74
	37.8	991	10	10740	54
10.0	73.0	3528	40	20740	117
	9.5	66.8	2	5400	80
	19.2	256	10	10910	211
13.3	38.2	966	10	21720	112
	14.2	140	2	10770	77
	28.8	549	10	21760	197
	38.6	970	10	29160	150

REFERENCES

1. ASME Research Report on Fluid Meters, ASME, New York, N.Y. (1971).
2. Metzger, D.E. (1962): Spot cooling and heating of surfaces with high velocity impinging air jets, Tech. Report #52, Dept. of Mech. Eng., Stanford University.

APPENDIX 4DESIGN CRITERIA FOR THE HEAT FLUX SENSOR

The heat flux sensor used in this study was designed to measure the local convective heat flux from an isothermal surface. The fundamental design criteria were the following:

- (i) the preservation of a (nearly) isothermal surface
- (ii) the provision of high resolution in local heat transfer measurements
- (iii) the assurance of minimum and measurable heat loss over a wide range of convective heat transfer
- (iv) the allowance of measuring convective heat transfer with throughflow.

To allow the measurement of convective with throughflow the sensor was made of porous bronze like the rest of the heat transfer surface as described in Section 3.4. The thermo-physical properties of this material are: $\rho = 520.4 \text{ kg}_m/\text{m}^3$, $C_p = 377 \text{ J/kg-K}$, $k = 6.923 \text{ W/m-K}$. To heat the sensor a 26 AWG insulated Inconel heating wire was embedded in a groove on its lower surface as shown in Figures 5.13 and 5.14. The sensor was thermally insulated from the surrounding plate and instrumented with thermocouples as shown in Figure 3.15 so that the sensor heat loss could be obtained experimentally as discussed in Appendix 5.

The transverse length of the sensor was made long enough to allow sufficient throughflow from its open area. In addition this length was to be shorter than 250 mm (the overall transverse length of the impingement surface) to avoid wall effects (due to presence of side walls). Hence the transverse

length of the heat flux sensor was set at 78.5 mm, a region over which the static pressure measurements showed a uniform profile even for the largest impingement spacing $H/w = 24$.

The lateral length of the sensor had to satisfy two conflicting criteria; first it has to be quite narrow to provide essentially local measurements of heat transfer and second it has to be large enough to permit the through-flow to pass through the open area not blocked by the heating wire. On the other hand the finite lateral length of the sensor when subjected to a large gradient of heat transfer as in the stagnation region should show a small temperature variation at the surface.

The sensor (and hence the impingement plate thickness) was selected to be large enough to permit development of a (nearly) uniform temperature profile at the surface.

To select the sensor dimensions on a quantitative basis the classical problem of two-dimensional steady heat conduction was solved numerically for sensors of various thickness and lateral dimensions. Figure A4.1 shows the physical model and the appropriate boundary conditions for simulation of the heat conduction process. The governing elliptic partial differential equation was solved using DSS (Distributed System Stimulator) which is a package program developed by Zellner (1970) to solve sets of partial differential equations.

For the purpose of simulation it was assumed that the back and side surfaces of the sensor were well-insulated and that the power from the heating wire was dissipated totally through convection from the top surface where a linear distribution of convective heat transfer was imposed as a boundary condition. Because of symmetry at the heating wire centerline, only a half of the sensor was simulated.

For a surface heat flux condition (equivalent to a convective heat transfer coefficient $\bar{h} = 300 \text{ W/m}^2\text{-K}$) and for a sensor thickness of 10 mm, the maximum temperature variation at the surface of the sensor over a lateral length of 3.7 mm was found to be less than 0.1°C . At the insulation side the temperature distribution across the thickness of the sensor is shown in Figure A4.2. Thus the dimension chosen for the heat flux sensor shown in Figure 3.13 were found to meet all the requirements of the optimal sensor.

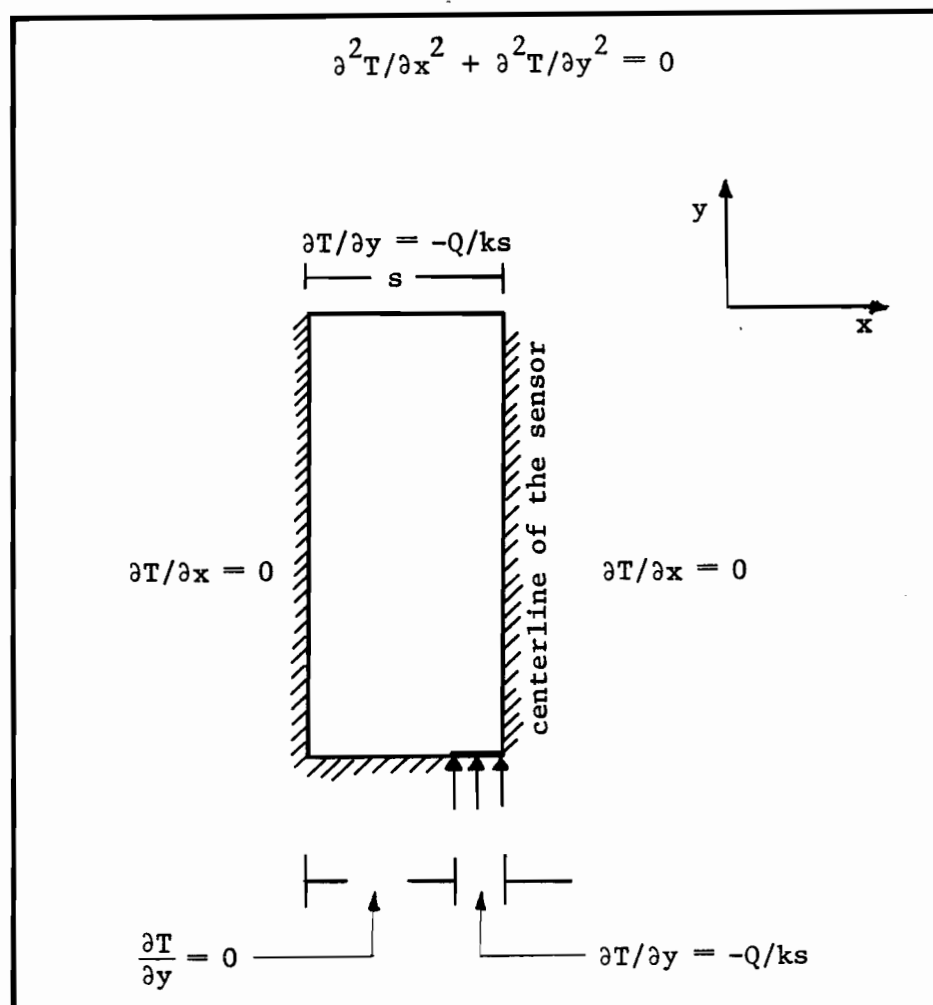


FIGURE A4.1. Boundary Conditions for the Heat Flux Sensor Numerical Simulation

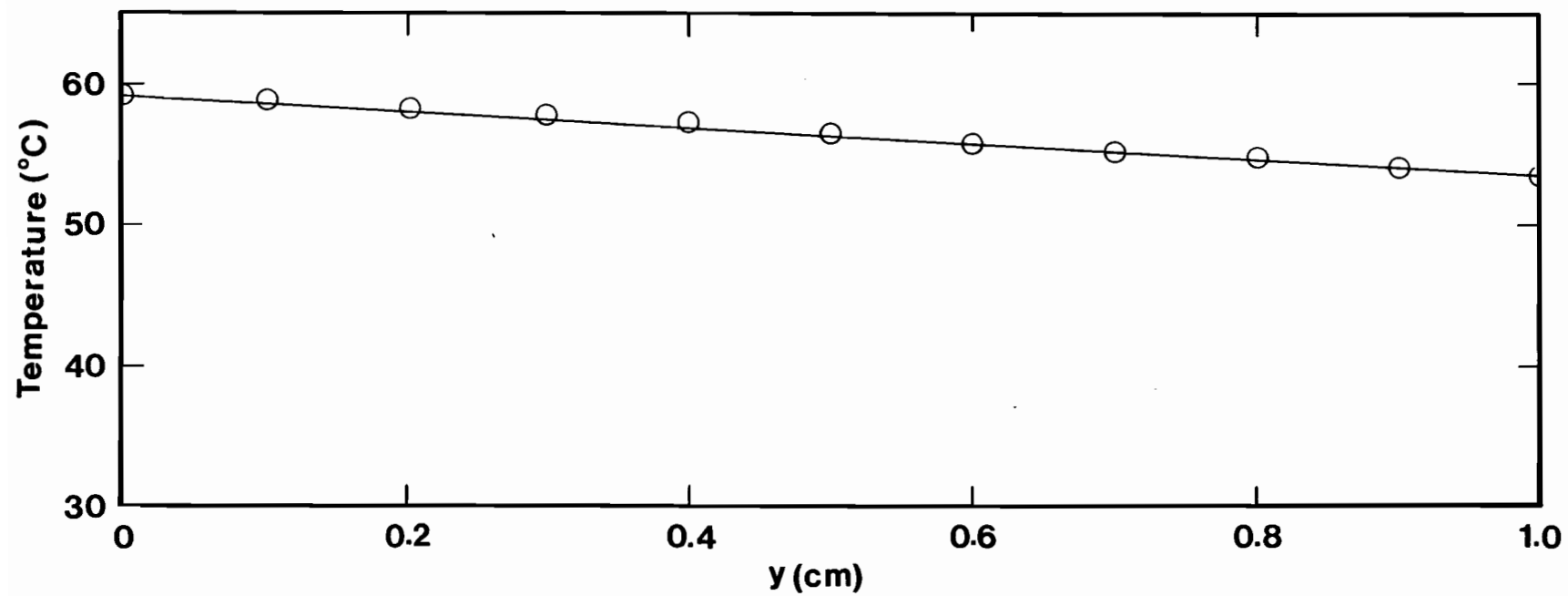


FIGURE A4.2. Temperature Profile Throughout the Thickness of the Heat Flux Sensor

REFERENCE

1. Zellner, M.G. (1970): DSS-distributed system simulator, Ph.D. Dissertation, Lehigh University, Bethlehem, Pa.

APPENDIX 5

HEAT TRANSFER ERROR ANALYSIS

A5.1 Analysis of Uncertainties Based on Single-Sample Experiments

At steady state condition, the heat transfer coefficient (h_x) is obtained from the following heat balance equation for the heat flux sensor:

$$P_s = Q_s + Q_{\text{cond.}} \quad (\text{A5.1})$$

Rate of heat into the sensor Rate of heat dissipated out the free surface Rate of heat loss by conduction through insulation

Each term is expressed as follows:

$$P_s = V_h (V_p / R_p) - (V_p / R_p)^2 R_{lw}$$

$$Q_s = Q_{\text{conv.}} + Q_{\text{rad.}} = h_x A_s (T_s - T_j) + q_{\text{rad.}} A_s$$

$$Q_{\text{cond.}} = B(\bar{T}_s - \bar{T}_w) + C(T_{b2} - T_{b1})$$

where P_s = heat into the sensor, W

V_h = voltage across the heating wire, volts

V_p = voltage across the precision shunt

R_p = resistance of the precision shunt, ohms

R_{lw} = resistance of the lead wire, ohms

$Q_{\text{conv.}}$ = heat transfer by convection, W

$Q_{\text{rad.}}$ = heat transfer by radiation, W

$Q_{\text{cond.}}$ = heat transfer by conduction, W

T_j = jet temperature at the nozzle exit, °C

T_s = temperature of the sensor free surface at steady state, °C

T_w = temperature of the impingement surface at 1 mm from the sensor and at steady state, °C

T_{b1} = temperature at the back of the insulation, °C

T_{b2} = temperature at the back of the sensor, °C

T_{b3} = temperature at the back of the impingement plate 1 mm from the sensor, °C

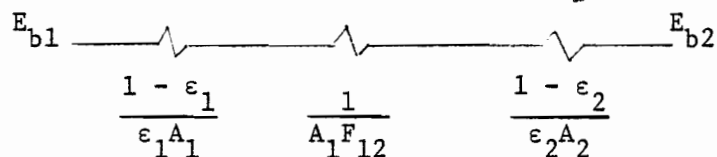
A_s = free surface area of the sensor, mm²

B, C = conductance of marinite, W/K

$\bar{T}_s = 0.5(T_s + T_{b2})$

$\bar{T}_w = 0.5(T_w + T_{b3})$

The radiation network for two surfaces that see each other and nothing else is (Holman, 1976):



$$q_{\text{rad.}} = (E_{b1} - E_{b2}) / \left(\frac{1 - \epsilon_1}{\epsilon_1 A_1} + \frac{1}{A_1 F_{12}} + \frac{1 - \epsilon_2}{\epsilon_2 A_2} \right) \quad (\text{A5.2})$$

$$q_{\text{rad.}} = \sigma (T_s^4 - T_j^4) / \left(\frac{1 - \epsilon_1}{\epsilon_1 A_1} + \frac{1}{A_1 F_{12}} + \frac{1 - \epsilon_2}{\epsilon_2 A_2} \right) \quad (\text{A5.3})$$

where

E_{b1} = energy of a black body at the temperature of the porous bronze plate

E_{b2} = energy of a black body at the temperature of the aluminum plate

σ = Stefan-Boltzmann constant = $5.669 \times 10^{-8} \text{ W/m}^2 \cdot \text{K}^4$

ϵ_1 = emissivity of the porous bronze assumed to be equal to that of copper = 0.025 (Perry (1972))

ϵ_2 = emissivity of aluminum = 0.04 (Perry (1972))

F_{12} = shape factor = 1 (assuming that surfaces 1 and 2 only see each other)

$A_1 = A_2 = A$ = surface of the impingement and confinement surface

$$\Sigma R = \frac{1 - 0.025}{0.025(A)} + \frac{1}{(A)(1)} + \frac{1 - 0.040}{0.040(A)} = \frac{64}{A} \text{ m}^{-2}$$

Let $T_j = 40^\circ\text{C}$, $T_p = 60^\circ\text{C}$

$$\text{Hence } q_{\text{rad.}} = \frac{\left(5.669 \times 10^{-8}\right) \frac{\text{W}}{\text{m}^2 \text{K}^4} \left((60 + 273)^4 - (40 + 273)^4\right) \text{K}^4}{(64/A)_m^{-2}} \times \frac{1}{A \text{ m}^2}$$

$$q_{\text{rad.}} = 2.39 \frac{\text{W}}{\text{m}^2}$$

This value is 0.0195% and 0.39% respectively of the maximum (12500 W/m^2) and the minimum power (600 W/m^2) supplied to the sensor. The radiation loss, $Q_{\text{rad.}}$, is considered to be negligible and equation (A5.1) becomes

$$h_x = \frac{1}{A_s (T_s - T_j)} \left[V_h (V_p / R_p) - (V_p / R_p)^2 R_{\ell w} - B(T_s - T_w) - C(T_{b2} - T_{b1}) \right] \quad (\text{A5.4})$$

While the thermal conductance, B , accounts for the lateral conduction between the sensor and the impingement plate, the other value of thermal conductance, C , accounts for the conduction through the back insulation; their values are $kA_L/\Delta x$ and $kA_s/\Delta y$ respectively where the thermal conductivity of marinite is $k = 0.108 \text{ W/m-K}$.

The thermal conductance for lateral conduction between the heat flux sensor and the impingement plate is:

$$B = kA_L/\Delta x \quad (\text{A5.5})$$

$$\text{i.e. } B = [0.108] \{ [(3.7)(10.0)(2) + (78.5)(10.0)(2)] 10^{-6} \} [10^3/0.37]$$

$$B = 0.48 \text{ W/K}$$

The thermal conductance for conduction between the heat flux sensor and the back insulation is:

$$C = kA_s / \Delta y \quad (A5.6)$$

$$\text{i.e.} \quad C = [0.108][(3.7)(78.5)10^{-6}][10^3/10]$$

$$C = 0.00314 \text{ W/K}$$

Hence equation (A5.4) becomes

$$h_x = \frac{1}{A_s(T_s - T_j)} \left[V_h(V_p/R_p) - (V_p/R_p)^2 R_{\ell w} - 0.48(\bar{T}_s - \bar{T}_w) - 0.00314(T_{b2} - T_{b1}) \right] \quad (A5.7)$$

This equation represents the functional relation between the heat transfer coefficient and the measured variables. The uncertainties in the variables V , A_s , R and T are all independent and the above equation is continuous and has derivatives. Therefore the uncertainty in heat transfer coefficient associated with each measured x_i is $(\partial h_x / \partial x_i) \delta x_i$.

To illustrate the uncertainty two examples are given; the first is the upper limit of the present measurements representing stagnation point heat transfer for $f = 1.56\%$ ($w = 2.5 \text{ mm}$), $H/w = 8$ and $Re_j = 10790$, and the second is the lower limit of the present measurements representing heat transfer at $x/w = 8$ for $f = 6.25\%$ ($w = 10.0 \text{ mm}$), $H/w = 24$ and $Re_j = 5400$. The values of x_i , uncertainties and percentage uncertainty are presented in Tables A5.1 and A5.2 for the upper and lower bounds on h_x , respectively. Also the uncertainties in heat transfer coefficient associated with each measurement x_i in a derivative form from equation (A5.7) are listed below:

$$\partial h_x / \partial V_h = \frac{1}{A_s(T_s - T_j)} (V_p/R_p)$$

$$\partial h_x / \partial V_p = \frac{1}{A_s (T_s - T_j)} \left[V_h / R_p - \frac{2V_p}{R_p^2} R_{\ell w} \right]$$

$$\partial h_x / \partial R_p = \frac{1}{A_s (T_s - T_j)} \left[- \frac{V_h V_p}{R_p^2} + \frac{2V_p^2}{R_p^3} R_{\ell w} \right]$$

$$\partial h_x / \partial R_{\ell w} = \frac{1}{A_s (T_s - T_j)} \left[- (V_p / R_p)^2 \right]$$

$$\begin{aligned} \frac{\partial h_x}{\partial A_s} = & - \frac{1}{A_s^2 (T_s - T_j)} \left[V_h (V_p / R_p) - (V_p / R_p)^2 R_{\ell w} - 0.48 (\bar{T}_s - \bar{T}_w) \right. \\ & \left. - 0.00314 (T_{b2} - T_{b1}) \right] \end{aligned}$$

$$\begin{aligned} \frac{\partial h_x}{\partial T_s} = & - \frac{1}{A_s (T_s - T_j)^2} \left[V_h (V_p / R_p) - (V_p / R_p)^2 R_{\ell w} - 0.48 (\bar{T}_s - \bar{T}_w) \right. \\ & \left. - 0.00314 (T_{b2} - T_{b1}) \right] \end{aligned}$$

$$\begin{aligned} \frac{\partial h_x}{\partial T_j} = & \frac{1}{A_s (T_s - T_j)^2} \left[V_h (V_p / R_p) - (V_p / R_p)^2 R_{\ell w} - 0.48 (\bar{T}_s - \bar{T}_w) \right. \\ & \left. - 0.00314 (T_{b2} - T_{b1}) \right] \end{aligned}$$

$$\frac{\partial h_x}{\partial \bar{T}_w} = \frac{0.48}{A_s (T_s - T_j)} \quad , \quad \frac{\partial h_x}{\partial \bar{T}_s} = \frac{-0.48}{A_s (T_s - T_j)}$$

$$\frac{\partial h_x}{\partial (T_{b2} - T_{b1})} = \frac{0.00314}{A_s (T_s - T_j)}$$

$$h_x = \frac{1}{A_s(T_s - T_j)} \left[v_h (V_p/R_p) - (V_p/R_p)^2 R_{lw} - 0.48(T_s - T_w) - 0.00314(T_{b2} - T_{b1}) \right] \quad (A5.8)$$

The total rms error is then

$$\delta h_x = \sqrt{\sum_{L=1}^n \left[\left(\frac{\partial h_x}{\partial x_i} \right) \delta x_i \right]^2} \quad (A5.9)$$

The maximum and minimum values of convective heat transfer coefficients calculated from equations (A5.7), (A5.8) and (A5.9) are $h_x = 622 (\pm 14) \text{ W/m}^2\text{-K}$ and $h_x = 31.6 (\pm 9.4) \text{ W/m}^2\text{-K}$, respectively. An examination of Tables A5.1 and A5.2 reveals that the primary source of error in heat transfer measurements is \bar{T}_s . Since the error reported in these tables are based on the maximum error that the instrumentations can produce, the expected total error might in general be lower than this maximum. In order to assess the uncertainties due to real experimental measurements a statistical analysis of uncertainties based on repeated tests is shown in the subsequent section.

A5.2 Statistical Analysis of Uncertainties Based on Repeated Experiments

Five sets of replicate experiments were performed to generate the data for statistical analysis. These experiments, consisting of measurement of the local heat transfer distributions, were performed over a period of 3 months. Two sets of flow and geometrical conditions were tested that cover the upper and lower bounds of the entire range of parameters. The upper limit is presented by $w = 2.5 \text{ mm}$ ($f = 1.56\%$), $H/w = 8$ ($S/H = 4$) and $Re_j = 10790$ and the limit by $w = 10.0 \text{ mm}$ ($f = 6.25\%$), $H/w = 24$ ($S/H = 0.33$) and $Re_j = 5400$.

TABLE A5.1. Error Analysis for High Heat Transfer Testing Conditions

x_i	Value of x_i	δx_i	$\frac{\partial h_x}{\partial x_i} \delta x_i$ (W/m ² -K)	$\frac{1}{h} \frac{\partial h_x}{\partial x_i} \delta x_i$ (%)
V_h (volt)	1.512	0.004	1.738	0.278
V_p (volt)	0.249	0.002	4.937	0.792
R_p (ohm)	0.102	0.001	-6.026	-0.966
R_{lw} (ohm)	0.020	0.004	-4.243	-0.680
A_s (mm ²)	290.45	1.50	-3.225	-0.517
T_s (°C)	61.70	0.08	-2.571	-0.413
T_j (°C)	42.33	0.08	2.575	-0.413
\bar{T}_w (°C)	70.24	0.08	-6.826	-1.096
$T_{b2} - T_{b1}$ (°C)	9.8	0.16	0.089	0.014
\bar{T}_s (°C)	70.32	0.08	6.826	1.096

$$h_x = 622.59 (\pm 14.08) \text{ W/m}^2\text{-K}$$

TABLE A5.2. Error Analysis for Low Heat Transfer Testing Conditions

x_i	Value of x_i	δx_i	$\frac{\partial h}{\partial x_i} \delta x_i$ (W/m ² -K)	$\frac{1}{h} \frac{\partial h}{\partial x_i} \delta x_i$ (%)
V_h (volt)	0.363	0.004	0.419	1.327
V_p (volt)	0.062	0.001	0.572	1.812
R_p (ohm)	0.102	0.001	-0.348	-1.10
R_{lw} (ohm)	0.020	0.004	-0.254	-0.807
A_s (mm ²)	290.45	1.50	-0.163	-0.516
T_s (°C)	60.08	0.08	-0.127	-0.40
T_j (°C)	40.12	0.08	0.127	0.401
\bar{T}_w (°C)	60.56	0.08	-6.621	-20.96
$T_{b2} - T_{b1}$ (°C)	0.4	0.16	0.087	0.274
\bar{T}_s (°C)	60.62	0.08	6.621	20.96

$$h_x = 31.6 (\pm 9.4) \text{ W/m}^2\text{-K}$$

The objectives of the statistical analysis were to test the homogeneity of variance and to find the 95% confidence interval for h_x .

The following tests were used to perform the analysis:

- (a) Bartlett's test as described in Himmelblau (1970), which is a commonly used test to detect differences among two or more variances; their homogeneity is determined by comparing the logarithm of the average variance with the sum of the logarithms of the separate variances. The formulas necessary for the use of this test are based on the hypothesis, $H_0: \sigma_1^2 = \sigma_2^2 = \dots = \sigma_n^2 = \sigma^2$ and the presumption that the variances measured are normally distributed. If the test hypothesis is correct a pooled s^2

$$s^2 = \frac{\sum_{i=1}^K v_i s_i^2}{\sum_{i=1}^K v_i} = \frac{1}{n} \left(\sum_{i=1}^n (P_i - 1) s_i^2 \right) \quad (A5.10)$$

where n = number of samples

P_i = number of replicates in a sample

v = degrees of freedom

has an χ^2 distribution with a mean of σ^2 and v degree of freedom.

Bartlett showed that

$$\Lambda = -\frac{1}{c} \sum_{i=1}^n P_i \ln \left(\frac{s_i^2}{s^2} \right) \quad (A5.11)$$

where

$$c = 1 + \frac{1}{3(n-1)} \left(\sum_{i=1}^n \frac{1}{P_i} - \frac{1}{\sum_{i=1}^n P_i} \right)$$

has an approximate χ^2 distribution with $(n-1)$ degrees of freedom.

(b) The 95% confidence interval is obtained as:

$$h_x - t_{1-\frac{\alpha}{2}} s_x \leq \bar{h}_n \leq h_x + t_{1-\frac{\alpha}{2}} s_x \quad (\text{A5.12})$$

From Table A5.3

$$c = 1 + \frac{1}{3(n-1)} \left(\sum_{i=1}^n \frac{1}{P_i} - \frac{1}{\sum_{i=1}^n P_i} \right) = 1 + \frac{1}{3 \times 13} \left[\frac{14}{5} - \frac{1}{14 \times 5} \right] = 1.071$$

$$s^2 = \frac{1}{\sum_{i=1}^n P_i - n} \sum_{i=1}^n (P_i - 1) s_i^2 = \frac{1}{14 \times 5 - 14} \sum_{i=1}^n 4 \times s_i^2 = 10.70$$

$$\Lambda = -\frac{1}{c} \sum_{i=1}^n P_i \ln \left(\frac{s_i^2}{s^2} \right) = -5 \sum_{i=1}^{14} \ln \left[\frac{s_i^2}{10.70} \right] = 6.34$$

For $\alpha = 0.05$ with $(n-1) = 13$

$$\chi^2 = 22.36$$

Since $\Lambda < 23.68$, the hypothesis of equal variance for different x/w is acceptable. Hence, the variation from the mean is the same.

The maximum standard error is used to calculate the confidence interval. From Table A5.3 this is observed at $x/w = 2$ and $s_x = 1.991$ using 95% confidence interval.

$$t_{1-\frac{\alpha}{2}} = 2.132$$

Hence, h_x is subject to a variation of

$$\begin{aligned} &= \pm 2.132 \times 1.991 \\ &= \pm 4.245 \text{ W/m}^2\text{-K} \end{aligned}$$

$$c = 1 + \frac{1}{3(n-1)} \left(\sum_{i=1}^n \frac{1}{P_i} - \frac{1}{\sum_{i=1}^n P_i} \right) = 1 + \frac{1}{3 \times 9} \left[\frac{10}{5} - \frac{1}{10 \times 5} \right] = 1.073$$

$$s^2 = \frac{1}{n \sum_{i=1}^n P_i - n} \sum_{i=1}^n (P_i - 1) s_i^2 = \frac{1}{10 \times 5 - 10} \times 4 \times 23.988 = 2.3988$$

$$\Lambda = -\frac{1}{c} \sum_{i=1}^n P_i \ln \left(\frac{s_i^2}{s^2} \right) = -\frac{5}{1.073} \sum_{i=1}^{10} \ln \left[\frac{s_i^2}{2.3988} \right] = 11.261$$

For $\alpha = 0.05$ with $(n-1) = 9$

$$\chi^2 = 16.92$$

Since $\Lambda < 16.92$, the hypothesis of equal variance for different x/w is accepted.

The confidence interval is calculated for the value of x/w corresponding to the maximum standard error. This is observed at $x/w = 1$ with a value $s_{\bar{x}} = 1.249$ using 95% confidence interval from Table A5.4.

$$t_{1-\frac{\alpha}{2}} = 2.132$$

Thus variation in h_x of $\pm 2.132 \times 1.249 = \pm 2.66 \text{ W/m}^2\text{-K}$ is found.

In conclusion, the above statistical analysis indicates that for each of the 2 sets of data the variance is homogeneous. The variation in h_x from 95% confidence interval (based on maximum standard error in h_x) was found to be ± 4.25 and $\pm 2.66 \text{ W/m}^2\text{-K}$ for the first ($625 \leq h_x \leq 160 \text{ W/m}^2\text{-K}$) and second ($44 \leq h_x \leq 29 \text{ W/m}^2\text{-K}$) set of data, respectively.

TABLE A5.3. Repeated Experiments for $f = 1.56\%$, $H/w = 8$
and $Re_j = 10790$

i	x/w	Expt. #1 $Y_1 (h_x)$	Expt. #2 $Y_2 (h_x)$	Expt. #3 $Y_3 (h_x)$	Expt. #4 $Y_4 (h_x)$	Expt. #5 $Y_5 (h_x)$
1	0	622.6	624.8	628.1	620.3	624.1
2	1	614.0	605.3	609.3	609.4	616.3
3	2	505.4	504.2	500.2	503.5	512.3
4	3	429.3	432.1	433.3	435.2	437.1
5	4	380.4	381.0	378.2	383.4	383.9
6	6	336.9	329.9	335.8	336.1	339.8
7	8	298.9	297.1	296.2	295.1	301.9
8	10	255.4	256.3	252.4	252.1	260.2
9	12	239.1	232.4	235.2	231.2	239.2
10	16	206.5	201.5	202.1	204.1	209.1
11	20	195.6	192.3	190.1	191.3	197.3
12	24	179.3	173.4	170.1	171.3	176.2
13	28	168.5	166.3	163.5	164.3	169.5
14	32	163.0	162.0	159.3	160.0	164.2

i	\bar{Y}	$\Sigma(Y_i - \bar{Y})^2$	$s_i^2 = \frac{\Sigma(Y_i - \bar{Y})^2}{P_i - 1}$	Standard Error, $s_{\bar{x}}$ $(s_i^2/P_i)^{0.5}$
1	623.98	33.11	8.277	1.286
2	510.90	74.94	18.73	1.936
3	505.12	79.308	19.83	1.991
4	433.40	35.44	8.86	1.331
5	381.38	21.65	5.41	1.040
6	335.70	55.06	13.02	1.613
7	297.84	28.35	7.09	1.190
8	255.28	43.67	10.92	1.478
9	235.42	54.81	13.70	1.655
10	204.66	39.95	9.99	1.413
11	193.32	36.53	9.13	1.351
12	174.06	55.77	13.94	1.670
13	166.42	26.85	6.71	1.159
14	161.70	16.68	4.17	0.913

TABLE A5.4. Repeated Experiments for $f = 6.25\%$, $H/w = 24$
and $Re_j = 5400$

i	x/w	Expt. #1 $Y_1 (h_x)$	Expt. #2 $Y_2 (h_x)$	Expt. #3 $Y_3 (h_x)$	Expt. #4 $Y_4 (h_x)$	Expt. #5 $Y_5 (h_x)$
1	0	44.3	42.4	40.7	40.4	41.2
2	0.5	44.0	41.3	41.5	40.7	40.9
3	1	44.0	44.1	38.3	39.2	40.5
4	2	42.5	42.2	38.2	38.9	40.5
5	3	42.2	42.5	37.9	38.7	39.2
6	4	42.3	40.2	37.0	38.2	38.5
7	5	37.5	38.0	36.0	35.8	36.2
8	6	36.2	34.9	35.0	34.2	34.9
9	7	31.4	31.5	30.9	29.3	33.9
10	8	31.6	31.0	30.2	28.9	33.4

i	\bar{Y}	$\Sigma(Y_i - \bar{Y})^2$	$s_i^2 = \frac{\Sigma(Y_i - \bar{Y})^2}{P_i - 1}$	Standard Error, s_x $(s_i^2/P_i)^{0.5}$
1	41.6	9.3	2.325	0.682
2	41.68	7.13	1.782	0.597
3	41.22	31.22	7.805	1.249
4	40.46	14.73	3.683	0.858
5	40.10	17.78	4.445	0.943
6	39.24	16.93	4.233	0.920
7	36.70	3.88	0.970	0.440
8	35.04	2.09	0.523	0.323
9	31.4	10.92	2.73	0.739
10	31.02	11.17	2.79	0.747

REFERENCES

1. Kline, S.J. and F.A. McClintock (1953): Describing uncertainties in single sample experiments, Mech. Eng., p 3.
2. Himmelblau, D.M. (1970): Process analysis by statistical methods, John Wiley and Sons, Inc.
3. Holman, J.P. (1976): Heat Transfer, fourth edition, McGraw-Hill, Inc., N.Y.
4. Perry, J.H. (1972): Chemical Engineer's Handbook, fourth edition, McGraw-Hill, Inc., N.Y.

APPENDIX 6

UNCERTAINTIES IN STATIC PRESSURE AT THE IMPINGEMENT SURFACE

w (mm)	S/w	$f, \%$	H/w	S/H	Re_j	ΔP_o (N/m ²)	$\Delta P_o / \Delta P_j$	$\pm \Delta P_o$ (N/m ²)
3.3	24	2.06	4	6	5000	427	0.8	5
					9500	1560	0.86	34
					20700	7260	0.9	34
			8	3	5000	340	0.64	5
					9500	1248	0.69	34
					20700	5808	0.72	34
			16	1.5	5000	200	0.38	5
					9500	750	0.41	5
					20700	2880	0.36	34
13.3	6	8.313	4	1.5	20700	432	0.84	5
					30000	917	0.89	5
					43800	2095	0.91	34
			8	0.75	20700	334	0.65	5
					30000	709	0.69	5
					43800	1620	0.70	34
			16	0.375	20700	102	0.2	5
					30000	205	0.2	5
					43800	459	0.19	5

APPENDIX 7

VALUES OF SURFACE HEAT FLUX WITH AND WITHOUT THROUGHFLOW

TABLE A7.1. Local Heat Flux at the Impingement Surface for
 $H/w = 8$, $Re_j = 10200$ and $U_s = 0, 0.1$ and 0.15 m/s

x/w	$U_s = 0.0$ m/s		$U_s = 0.10$ m/s		$U_s = 0.15$ m/s	
	$q_{\text{convection}}$ (W/m ²)	$q_{\text{loss by conduction}}$ (W/m ²)	$q_{\text{convection}}$ (W/m ²)	$q_{\text{loss by throughflow}}$ (W/m ²)	$q_{\text{convection}}$ (W/m ²)	$q_{\text{loss by throughflow}}$ (W/m ²)
0	2769	33.4	3333	510	3333	765
0.50	2456	33.2	2883	441	2850	654
0.75	2184	31.1	2602	398	2566	589
1.25	1957	30.2	2415	370	2334	536
1.50	1920	30.0	2334	357	2233	512
2.25	1725	29.3	2152	329	2111	484
3.0	1592	28.8	1997	306	1928	442
3.75	1482	28.3	1790	274	1875	430
4.50	1299	27.6	1725	264	1640	376
5.25	1259	27.4	1583	242	1462	335
6.0	1137	26.9	1482	227	1429	328
8.0	1015	26.5	1360	208	1319	303
10.0	853	25.8	1218	186	1165	267
12.0	710	25.2	1031	157.8	1031	237

TABLE A7.2. Local Heat Flux at the Impingement Surface for
 $H/w = 8$, $Re_j = 22800$ and $U_s = 0, 0.15$ and 0.3 m/s

x/w	$U_s = 0.0$ m/s		$U_s = 0.15$ m/s		$U_s = 0.30$ m/s	
	$q_{\text{convection}}$ (W/m ²)	$q_{\text{loss by conduction}}$ (W/m ²)	$q_{\text{convection}}$ (W/m ²)	$q_{\text{loss by throughflow}}$ (W/m ²)	$q_{\text{convection}}$ (W/m ²)	$q_{\text{loss by throughflow}}$ (W/m ²)
0	4330	36.9	4949	1135	5120	2350
0.5	4068	35.8	4758	1092	4884	2242
0.75	3788	34.7	4442	1019	4113	1886
1.0	3448	33.4	4121	946	4275	1962
1.5	3262	32.6	3938	904	4100	1882
2.0	3049	31.8	3719	853	3857	1770
2.5	2966	31.5	3621	831	3755	1723
3.0	2866	31.0	3504	804	3646	1673
3.5	2700	30.4	3390	778	3536	1623
4.5	2548	29.8	3211	737	3350	1537
5.25	2412	29.2	3025	694	3146	1444
6.0	2314	28.8	2927	672	3057	1403
8.0	2152	28.2	2805	644	2939	1349
10.0	2071	27.9	2692	618	2822	1295
12.0	1970	27.5	2574	590	2741	1258

TABLE A7.3. Local Heat Flux at the Impingement Surface for
 $H/w = 8$, $Re_j = 29100$ and $U_s = 0, 0.2$ and 0.3 m/s

x/w	$U_s = 0.0$ m/s		$U_s = 0.2$ m/s		$U_s = 0.3$ m/s	
	$q_{\text{convection}}$ (W/m ²)	$q_{\text{loss by conduction}}$ (W/m ²)	$q_{\text{convection}}$ (W/m ²)	$q_{\text{loss by throughflow}}$ (W/m ²)	$q_{\text{convection}}$ (W/m ²)	$q_{\text{loss by throughflow}}$ (W/m ²)
0	4750	35.8	5473	1675	5603	2572
0.5	4669	35.5	5278	1615	5501	2525
0.75	4547	35.0	5075	1553	5258	2413
1.25	4263	33.8	4913	1503	5055	2320
1.5	4141	33.4	-	-	-	-
2.25	3898	32.4	4227	1385	4669	2143
3.0	3735	31.7	4263	1304	4425	2031
3.75	3451	30.6	4060	1242	4222	1938
4.5	3248	29.8	3857	1181	4060	1863
5.25	3086	29.1	3654	1118	3836	1761
6.0	3004	28.8	3552	1087	3735	1714
8.0	2923	28.5	3451	1056	3573	1640
10.0	2842	28.2	3443	1054	3552	1630
12.0	2680	27.5	3268	1000	3431	1575

